UNIVERSITY OF SOUTHAMPTON

School of Ocean and Earth Science

Seasonal and Interannual Sea Surface Height Variability in the Nordic Seas

Anna Izabela Kaczmarska

Thesis for the degree of Doctor of Philosophy

September 2011

UNIVERSITY OF SOUTHAMPTON

ABSTRACT

FACULTY OF ENGINEERING, SCIENCE & MATHEMATICS
SCHOOL OF OCEAN & EARTH SCIENCES

Doctor of Philosophy

Seasonal and Interannual Sea Surface Height Variability in the Nordic Seas

Anna Izabela Kaczmarska

The Nordic Seas are the regions of exchanges between the Arctic and the Atlantic oceans. Furthermore, they are the regions of deep-water formation. By providing a substantial part of the source waters for North Atlantic Deep Water the Nordic Seas influence the global thermohaline circulation. Therefore, an understanding of the Nordic Seas circulation and its variability is needed to determine how changes in the high latitude climate affect the global thermohaline circulation and the regional and global climate system. Although, the summer circulation in the region is known from in-situ and other measurements, knowledge about the winter circulation is limited because of the unavailability of data from the ice-covered seas. However, Peacock and Laxon (2004, J Geophys Res, 109, C07001) showed that it is possible to derive sea surface height anomaly (SSHA) from satellite altimeter data in the ice-covered seas. This thesis makes use of the novel satellite-altimeter data derived from ice-covered seas combined with the altimeter records from the open ocean. Envisat altimeter monthly SSHA in 2002-2009 have been used and corrected by applying a set of relevant geophysical corrections. For the first time the variability of the sea level and the surface currents was described in the ice-covered ocean of the Nordic Seas and over such a long record. The driving mechanisms causing this variability were also investigated using statistical analysis and the results provided the clues about the mechanisms causing the observed variability. It was found that sea level varied greatly seasonally and interannually in the ice-covered regions of the Nordic Seas, especially in the autumn and winter. Therefore, most of the existing measurements are biased towards the least variable season and could therefore underestimate the interannual variability of the circulation. Empirical Orthogonal Functions were used to identify the most important modes of variability. Possible explanations behind the variability were hypothesized and addressed by the statistical analysis of the SSHA and freshwater, heat and momentum fluxes (EOF, MCA, CCA, Pearson point-to-point correlations). Finally, the anomalous surface geostrophic currents were calculated from SSHA and the mean seasonal cycle and the inter-annual variability of the surface circulation was described. The final aim of this thesis was the description of the EGC variability along its path using the previously obtained anomalous surface currents. The numerical ocean model (NEMO) was used to analyze the vertical structure of the EGC and develop a method of the transport calculation. Mean seasonal cycle and annually averaged anomalous transports of EGC were described in 2002-2009.

Contents

List of figures

List of tables

DECLARATION OF AUTHORSHIP

I, Anna Izabela Kaczmarska

declare that the thesis entitled

Seasonal and Interannual Sea Surface Height Variability in the Nordic Seas.

and the work presented in the thesis are both my own, and have been generated by me as the result of my own original research. I confirm that:

- this work was done wholly or mainly while in candidature for a research degree at this University;
- where any part of this thesis has previously been submitted for a degree or any other qualification at this University or any other institution, this has been clearly stated;
- where I have consulted the published work of others, this is always clearly attributed;
- where I have quoted from the work of others, the source is always given. With the exception of such quotations, this thesis is entirely my own work;
- I have acknowledged all main sources of help;
- where the thesis is based on work done by myself jointly with others, I have made clear exactly what was done by others and what I have contributed myself;
- none of this work has been published before submission.

Signed: ……..

Date:…….

ACKNOWLEDGEMENTS

I am very grateful to my supervisors: Sheldon Bacon, Alberto Naveira Garabato and Seymour Laxon for their care and support during my PhD. I would like to thank them for sharing their knowledge and providing valuable discussions during the last 4 years. I am also grateful for their encouragement and motivation. I am very thankful to Sheldon and Alberto for the time I spent on the RRS James Cook and a wonderful adventure I was part of during the ANDREX cruise.

My sincere thanks go to Andy Ridout for his help with the altimetry data processing and corrections. Thanks to Seymour Laxon for providing the altimetry data, which was the major motivation for this PhD. I am also thankful for his support and hospitality during my many visits in UCL, London.

I would like to thank Dr Robert March for checking on my progress and being my PhD Panel Chair. I am also grateful to my PhD examiners: Dr Kevin Oliver and Prof. Philip Woodworth for reviewing this thesis and an interesting discussion during my viva.

Thanks to my PhD and postdoctoral friends at NOCS for their friendship, support and the great time we had together. I am glad I could meet you and by knowing you, get to know about many different countries. I am especially grateful to my best friend: Maria Paola Clarizia for believing and motivating me and for the organization of my viva celebrations. I also would like to thank my friends who played volleyball with me at NOCS, especially my thanks go to Dr Graham Quartly for organizing everything. Finally, I would like to thank my office mates: Ibrahim, Khairul, Aurelie, Katriona and Jade for their friendship and a nice atmosphere they created in our office.

To finish, I would like to thank NERC for funding my PhD and ECMWF for the atmospheric products I used for one of my results chapters.

CHAPTER 1: INTRODUCTION

Radiative processes continuously warm low latitudes and cool high latitudes. The role of the ocean and atmosphere is therefore to transport heat (energy) meridionally from low latitudes to the polar regions. There are still large uncertainties how much heat is transported by the ocean and the atmosphere. The meridional heat transport is divided nearly equally into three parts: ocean transport, atmospheric transport and the latent heat transport (Bryden and Imawaki, 2001). However, the ocean plays a very important role in the meridional heat transport and also affects the atmosphere by the heat exchange processes through air-sea interactions. The meridional overturning circulation (MOC) is a major part of the global climate system consisting of warm and salty surface currents transporting heat to the high latitudes and cool, deep currents that return to the low latitudes (Figure 1.1). In the North Atlantic, warm and salty Atlantic waters travel into the Nordic Seas. The Atlantic waters lose a lot of heat to the atmosphere along the current path. When they enter the Nordic Seas they are still saltier and warmer than the surrounding waters. Then the current splits into several branches and some of them transport the Atlantic waters further north to the Arctic. In the Arctic Mediterranean (the Arctic Ocean together with the Nordic Seas), the Atlantic waters are further cooled and therefore become denser, which results ultimately in a deep southward flow of dense and cold water. The Atlantic waters that were transformed in the Arctic Ocean return as the deep waters to the Atlantic via the Nordic Seas and contribute to the North Atlantic Deep Water (NADW). Convection and deep-water production also occurs within the Nordic Seas in the Greenland and Iceland Seas and the transformed waters also contribute to the NADW. Therefore, the newly formed deep waters renew the deep waters of the world ocean and promote a returning northward flow at the surface and the global thermohaline circulation (Figure 1.1). It was estimated that about 75% of the Atlantic waters entering the Arctic Mediterranean is transformed into denser overflow waters (Hansen and Osterhus, 2000). The Nordic Seas are therefore unique and very important for the global ocean circulation. They also are a major exchange region between the Arctic and Atlantic Oceans and therefore act as a ‘buffer’ zone between them. The upper layers of the eastern part of the Nordic Seas are dominated by warm and salty Atlantic waters, whereas the western part is dominated by the cold and

fresh Polar water flowing south to the Atlantic as the East Greenland Current (EGC). The hydrographic properties of the Nordic Seas waters may be sensitive to the changes in the import and export of Atlantic and Polar waters. The circulation in the area may be also sensitive to changes in air-sea interaction and ice processes. The increased export of the Polar waters and sea-ice through the EGC might suppress deep-water formation. Additionally, changes in the wind may also shift the polar waters more to the east, which would cause similar consequences (Bjork et al. 2001, Blindheim et al. 2000). The above reasons are only a small fraction of the motivation behind the monitoring of the circulation of the Nordic Seas. Any changes occurring in the Atlantic MOC or in the Arctic Ocean would influence the Nordic Seas, which makes them also a great location for detection of changes occurring in the Arctic and the North Atlantic.

The measurements in the Nordic Seas started in 19th century (e.g. Knudsen, 1899) and the Nordic Seas are one of few regions where such long records exist. However, due to hard atmospheric conditions occurring there, most of these measurements were gathered in the summer and mainly in the proximity of the land in the south and south-eastern part of the Nordic Seas. In the western part our knowledge about the mean circulation and its variability is limited to only a few locations (Fahrbach et al., 2001, Woodgate et al., 1999, De Steur et al., 2009). Another problem is that the measurements in the western part were gathered mainly in the summer season and there are only very few long-term observations in the area, which are nevertheless sensitive to large uncertainties, especially during the winter season (Fahrbach et al., 2001, De Steur et al. 2009). Studies of ocean variability in the Arctic Mediterranean have been limited by the latitudinal limit of satellite coverage and by the presence of seasonal and permanent sea ice cover. Altimetry coverage was extended to 81.5°N when the European ERS and Envisat satellites were deployed. Peacock and Laxon (2004) showed for the first time that altimetry measurements of the ocean sea surface height could be used to study ocean variability in the ice-covered part of the ocean. Their method was a great improvement for the monitoring of ice-covered oceans but has not been much used since their publication. This study applies this novel technique to study the circulation in the Nordic Seas with a special focus on the East Greenland Current

(EGC) variability and transports. The altimetric data provides a framework and a major motivation for this thesis. We are especially interested in the EGC because our knowledge about its variability is very limited, especially during the winter season but also even in the summer. The current directly connects the Arctic with the Atlantic and provides a major sink of freshwater for the Arctic (Schlichtholz and Houssais, 1999). The reason why very few long-term measurements of EGC exist is because it is covered by sea-ice during the whole year from north-eastern Greenland to the Fram Strait (Fig 1.7). During the winter, sea-ice extends further south to Cape Farewell and covers the whole current (Fig. 1.7). Sea-ice conditions are described in the later sections of this chapter and show that sea-ice is also present during the summer along the East Greenland Current (EGC), on the east Greenland shelf and in the Greenland Sea. In the remainder of this chapter, the importance of the EGC and Nordic Seas for global and regional climate will be further described. The altimetry from the ice-covered ocean provides a unique tool to monitor the circulation in the ice-covered part of the Nordic Seas. This is therefore the first study to describe the circulation variability in the whole Nordic Seas in the 7-year period starting in November 2002 when ENVISAT satellite was launched. Furthermore, this study makes a first estimate of the EGC transport variability along its path in the Nordic Seas, from 80.5°N to 69°N.

The structure of this thesis is as follows: The remainder of this chapter provides a general overview of the Nordic Seas, it sets this study in the context of current knowledge, and it describes the aims and objectives of the thesis. Chapter 2 gives a detailed description of the data and methods used for this study. The results are divided into three independent chapters; each one focuses on a particular problem. Chapter 3 describes the variability of the sea level in 2002-2009. Chapter 4 explains which mechanisms could drive the observed sea level variability. Finally, Chapter 5 describes the mean seasonal cycle and the variability of an annually averaged surface geostrophic circulation in the Nordic Seas. Furthermore, its major part focuses on the transport variability of the EGC obtained using surface currents. The thesis is summarized and concluded in Chapter 6, in which suggestions for the future research are proposed.

1.1 Overview- Nordic Seas Circulation

The Nordic Seas are a region of exchanges between the Arctic and the Atlantic oceans. Furthermore, they are regions of deep-water formation. Therefore, an understanding of the Nordic Seas circulation and variability is needed to determine how changes in the high latitude climate could affect the global thermohaline circulation and global and regional climate.

The upper branch of the global MOC conveys warm and salty Atlantic water to the Nordic Seas (Figure 1.1). The Atlantic water crosses the Greenland-Scotland ridge and continues flowing northward on the eastern side of the Nordic Seas as the Norwegian Atlantic Current (NwAC). In the Nordic Seas the current divides into three main branches that flow further north towards the Arctic (Figure 1.3): (i) Fram strait recirculation, (ii) Barents Sea branch, which continues into the Arctic and (iii) Fram Strait branch, which also continues into the Arctic. The Fram Strait branch is called the West Spitsbergen Current (WSC) and flows northward along the continental slope to the Fram Strait where part of it recirculates and returns directly to the Nordic Seas (Schauer et al., 2004, Schlichtholz and Houssais, 1999), with the remainder continuing into the Arctic. This recirculating branch contributes to the MOC by the direct flow through Denmark Strait (Mauritzen, 1996) or through preconditioning of dense water formation in the Greenland gyre (Gascard et al., 2002). The second branch of the NwAC, the North Cape Current (NCC) crosses the Barents Sea shelf and also continues into the Arctic where it is modified by the ice-formation process on the Arctic shelf. In effect it becomes denser returning to the Nordic Seas as a deep-water mass as part of EGC and contributing to the NADW. There is strong evidence that past changes occurring in the MOC and in deep water formation could change the global climate (Ganopolski et al. 1998). Simulations of future climate by numerical models of the ocean and atmosphere show that due to warming resulting from increased anthropogenic gas emissions, the North Atlantic MOC could weaken (Schmittner et al. 2005). Bryden et al. (2005) suggested that such a weakening could already be occurring but their estimate was prone to many uncertainties and was not confirmed yet with the mooring array installed at 26.5°N (Cunningham et al. 2007). However, the observations showed that the inter-annual

variability of the north Atlantic MOC is large and therefore the monitoring of the MOC needs to be done over a long time before detecting any changes in its strength.

The climate of north-western Europe is warmer than other locations located at similar latitudes. The combination of westerly winds and the large heat capacity of the ocean is one of the causes of the exceptionally warm European climate (Rhines at al., 2008). However, the surface component of the MOC also transports northwards large quantities of heat keeping the North Atlantic and eastern part of the Nordic Seas ice free (Seager et al. 2002). The heat stored in the ocean can be released to the atmosphere in the winter, which keeps the European climate relatively mild. Therefore, any changes in the North Atlantic branch of the MOC would cause changes in the regional European climate and influence the living conditions of people living there. However, not only European climate could be affected because the amount and characteristics of Atlantic water entering the Nordic Seas also influence sea-ice processes in the Arctic (Spielhagen et al., 2011) which in effect could cause changes in the freshwater export from the Nordic Seas and deep water production, which in turn would affect the global MOC and the climate system.

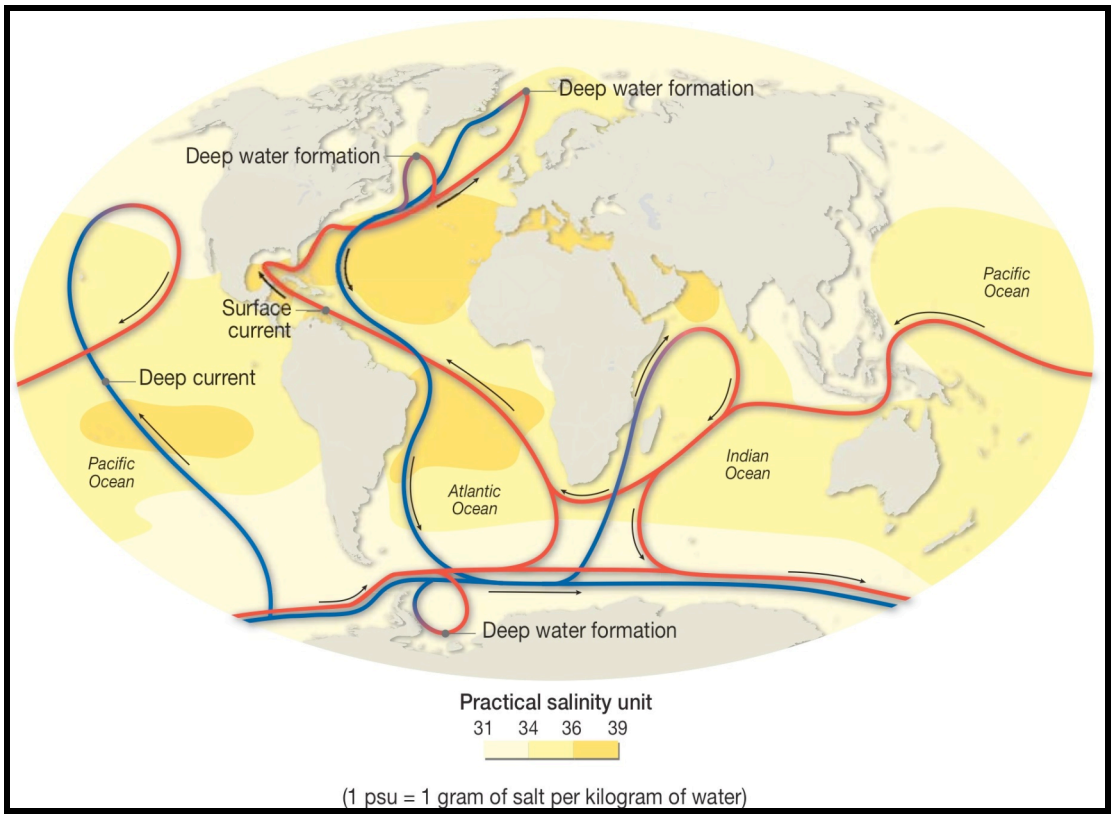

Figure 1.1 Schematic showing global Meridional Overturning Circulation. The surface currents are showed in red and deep currents are showed in blue. The locations of the deep-water formation are also showed. Note that Arctic Ocean is not presented (Source: UNEP/GRID Arendal Maps and Graphics Library).

1.2. Ocean Circulation in the Nordic Seas

1.2.1 Bathymetry

The Nordic Seas are restricted to the west by Greenland and to the east by Norway (Figure 1.2). Fram Strait (sill depth 2600m) provides the deepest connection of the Arctic Ocean with the other world oceans. The other connection between the Arctic and Nordic Seas is through the Barents Sea but is limited to depths of about 250m (with maximum depth of about 450m). The Nordic Seas together with Labrador Sea are the only deep areas in the world ocean that have the conditions favourable for the transformation of the warm and saline surface water into deep dense water that returns equatorwards. However, the Nordic Seas are separated from the North Atlantic by the Greenland-Scotland Ridge, which the intermediate and surface waters have to pass the keep the MOC running. Therefore, bathymetry of the Nordic Seas influences the exchanges between the Arctic Mediterranean and the North Atlantic.

The interior of the Nordic Seas is weakly stratified and therefore bathymetry strongly influences the ocean circulation. Many previous studies showed that the circulation follows the topographic contours and is mainly barotropic (Jakobsen et al. 2003, Voet et al. 2010, Koszalaka et al. 2010). On the other hand, geostrophic currents flow along the topographic contours and topographic obstacles are able to direct the flow and restrict exchanges between the basins. For example, Denmark Strait (640m deep) only allows the surface and intermediate waters to pass through and directs the deepest waters to the east where they can exit through the North Atlantic by the deep openings in the Greenland–Scotland Ridge: Faroe Bank Channel (maximum depth ~850m) and Iceland-Faroe Ridge. The oceanic ridges separate the interior of the Nordic Seas into four deep basins. The Norwegian and Lofoten basins make together the eastern part and are separated by the shallow Voring Plateau. The western part consists of the Greenland Basin to the north and Iceland Sea to the south and are separated by the Jan Mayen fracture zone. The Greenland Basin is also restricted to the east by the Mohn's Ridge and to the north by the Greenland Fracture Zone.

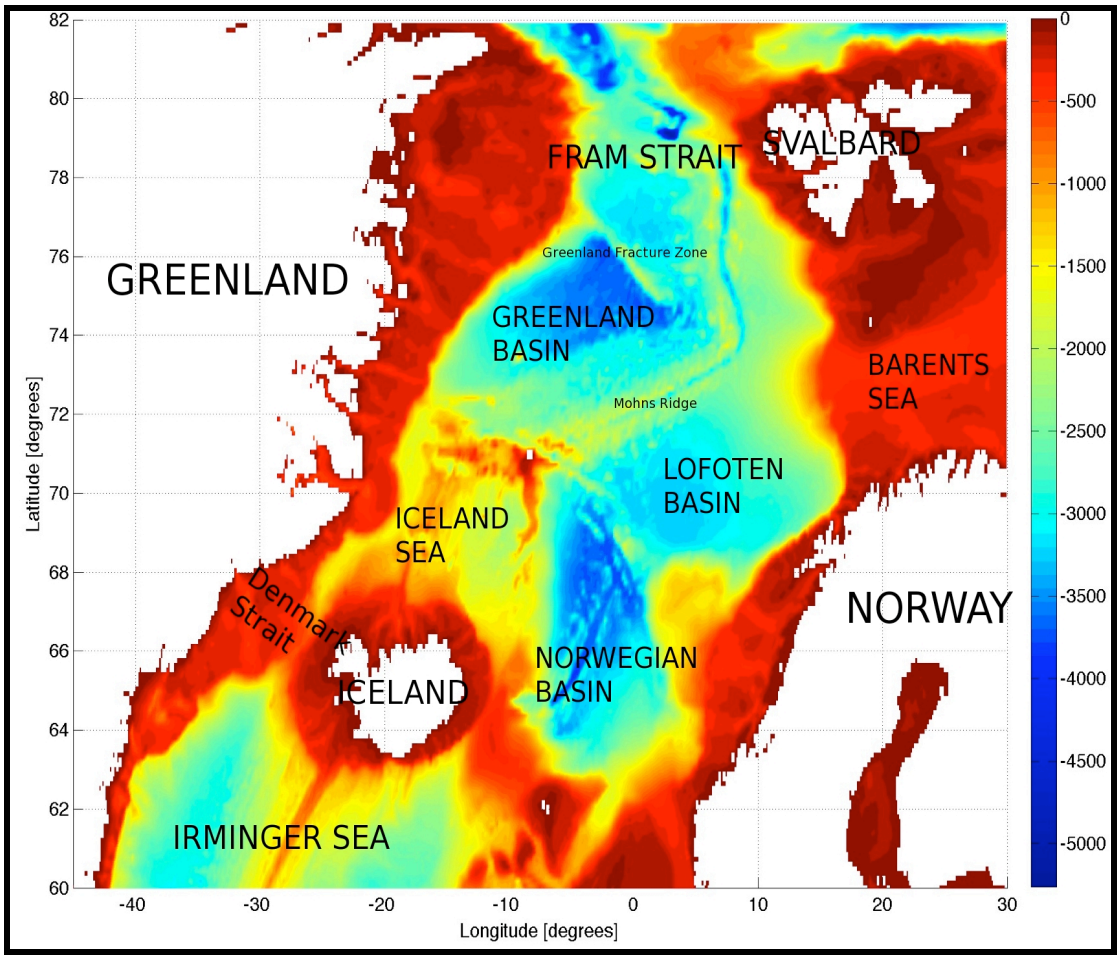

Figure 1.2. Bathymetry of the Nordic Seas constructed using ETOPO1 1-minute global relief (Amante and Eakins, 2009).

1.2.2. Mean surface circulation and its variability

The Nordic Seas control major exchanges between the Arctic and Atlantic oceans. The most important features of the surface circulation are the East Greenland Current (EGC) transporting cold and fresh water from the Arctic to the North Atlantic, and the continuation of the North Atlantic Current, called the Norwegian Atlantic Current (NwAC), carrying warm and saline water masses north along Norwegian coast and to the west of Spitsbergen (WSC) through the Fram Strait towards the Arctic (Figure 1.3). The general pattern of the circulation in the Nordic Seas was known for a long time because the ship observations and geostrophic estimates of the currents started very early in the area (e.g. Pettersson, 1900, Helland-Hansen and Nansen, 1909). The knowledge about the circulation changed in the last decades. Four cyclonic gyres limited by the topography were discovered (Poulain et al., 1996). Major current systems were described and a lot of measurements of currents and their characteristics were performed. New techniques were developed in the recent years to study ocean circulation: moored arrays, Argo floats, surface drifters, satellite observations of sea level, winds, waves etc. The application of those techniques contributed to the understanding of the mean circulation and its variability in this important region (e.g. Woodgate et al. 1999, Fahrbach et al. 2001, Schauer et al. 2004, Skagseth et al. 2004, Jakobsen et al. 2003, Voet et al. 2010, De Steur et al., 2009, Koszalka et al. 2011). This section briefly introduces the general circulation and its variability. The most interesting regions relevant to this study are further described in the later sections.

In general the upper layers of the Nordic Seas consist of warm and salty Atlantic water in the east and fresh and cold polar waters in the west. Furthermore, there are two major cyclonic gyres in the Greenland and Norwegian Seas located between the two boundary currents. The surface circulation in the Nordic Seas is illustrated in Fig. 1.3. The stratification and dynamics in the large parts of the Nordic Seas are affected equally by salinity and temperature, e.g. Bjork et al. (2001), who found that the topographic steering in the area is strong which is a result of the strong barotropic circulation. It was suggested that the barotropic circulation together with topographic obstacles, like Greenland-Scotland Ridge, affect the freshwater and heat budgets in the Nordic Seas (Bjork et al., 2001). On the eastern part of the Nordic Seas the fresh

and narrow Norwegian Coastal Current flows northwards from the Baltic Sea along the coast of Norway (not shown in Fig.1.3, Orvik et al. 2001). There are also two branches of the NwAC transporting saline and warm Atlantic waters, one follows the Norwegian continental slope and the other flows towards the Greenland Sea (Jakobsen et al., 2003). The two branches connect with each other and spread towards Fram Strait as the WSC and towards the Barents Sea as the NCC. To the west, the EGC exports Polar waters from the Arctic along the eastern continental slope of Greenland. It recirculates in the Greenland and Iceland Seas mixing there with the Atlantic waters. Before crossing Denmark Strait it divides into two branches. The eastward branch is called the East Icelandic Current (EIC) and continues to the east of Iceland, whereas the western branch crosses Denmark Strait and continues to Cape Farewell. The four cyclonic gyres are located between the major current systems and separated from each other by oceanic ridges (Section 1.2.1).

Many studies have shown that the circulation in most of the Nordic Seas strengthens during winter (Orvik et al. 1999 for the NwAC at 63°N, Woodgate et al. 1999 for the EGC at 75°N, Fahrbach et al. for the EGC and WSC at 78.5°N, Nost and Isachsen 2003 and Skagseth et al. 2004). The strengthening is especially strong for the eastern boundary currents and jets associated with topographic gradients. In some areas the strengthening may be 15 cms^{-1} stronger than the mean current (Jakobsen et al., 2003) but in most areas corresponds to about 20% of the mean flow (Jakobsen et al., 2003). The evidence suggests that the flow is stronger during the winter due to anomalously strong winds occurring in that season (See section 1.3.1 and Chapter 4) and the barotropic response of the ocean to this forcing (Jakobsen et al. 2003). On the other hand, in the summer the winds are weak and the baroclinic forcing mainly drives the circulation (Jakobsen et al., 2003). Nost and Isachsen (2003) observed that the strengthening occurs along f/H contours, which suggest that the variability is controlled by the topography and the anomalous Ekman transport. Recent findings of Voet et al. (2010) show that the seasonal variability is the greatest in the Greenland and Norwegian Basins and comparable there to the mean flow. They also found that the higher frequency (monthly to annual) variability plays an important role in the Lofoten Basin and its magnitude is similar to the magnitude of the seasonal signal.

Wind forcing is also an important driving mechanism for the inter-annual variability,

especially for the eastern boundary currents and it was argued that it was responsible for the weaker Atlantic flow observed during the second half of the 1990s (Jakobsen et al., 2003). Orvik et al (2001) showed that the North Atlantic wind stress curl is the major forcing for the inter-annual variability of Norwegian Atlantic Slope Current, the major branch of the NwAC. Orvik and Skagseth (2003) found a high level of lag correlation between the zonally integrated wind stress curl at 55°N and the volume transport in the Norwegian Sea at 62°N.

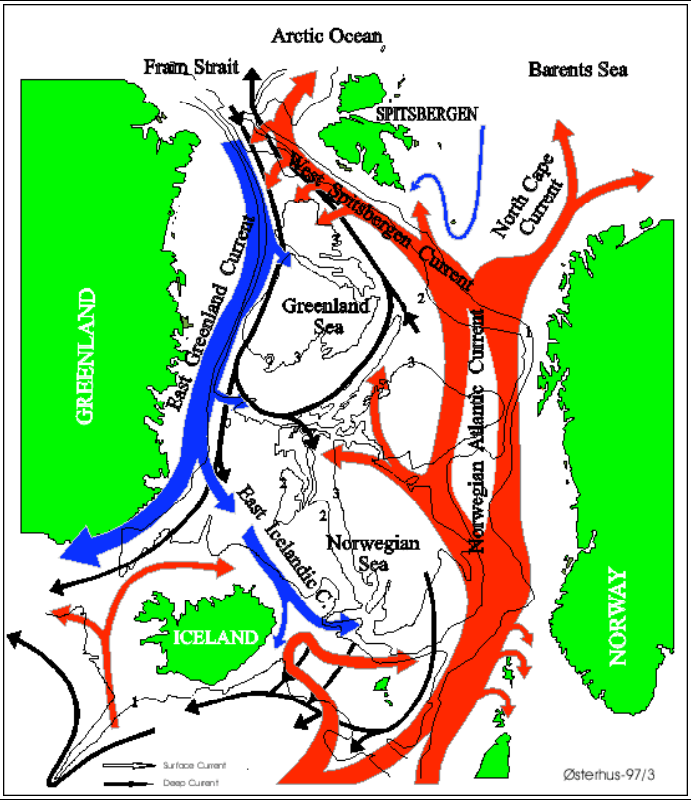

Figure 1.3. Surface circulation in the Nordic Seas (in blue and red). Warm and saline Atlantic water is marked in red. Cold and fresh water transported from the Arctic by the East Greenland Current is marked in blue. (Source: Eliasen et al., 2000)

1.1.3 Exchanges through Fram Strait

Fram Strait is a broad and deep trench that separates Greenland and Spitsbergen, enabling exchanges between the Nordic Seas and the Arctic (Fig.1.3). Waters of Atlantic and Polar origin, characterized by contrasted hydrographic properties, meet here. This exchange system is limited in the vertical direction by the sill depth of about 2600 m (Schlichtholz & Houssais, 1999). At the surface, the East Greenland Polar Front separates cold, low salinity polar water west of the front from the warmer and more saline Atlantic water on the eastern side (Foldvik et al. 1988). At greater depths, the interactions are controlled by the timing and strength of the convection sites (Rudels, 1995). It was reported that the inflow of the warm and salty Atlantic water mass, carried by the West Spitsbergen Current, is important for the final characteristics of deep and intermediate water masses formed in the Arctic (Rudels et al. 1994). On the other hand, the formation of deep and intermediate waters in the Iceland and Greenland Seas should be controlled by the amount of sea ice and fresh Polar Water advected from the north by the East Greenland Current (Schlichtholz & Houssais, 1999). Therefore, an understanding of Fram Strait dynamics is important in the context of deep-water formation and its variability.

In general, the circulation in Fram Strait comprises an inflow, a recirculation and an outflow. However, the flow is complex with large spatial and temporal variability. Considerable uncertainty still exists about the transports through Fram Strait, in spite of several years of moored current measurements and ice transport observations at 78.5°N within the EU VEINS (Variability of Exchanges In the Northern Seas) and ASOF-N (Arctic and Subarctic Ocean Fluxes) programs. This is largely due to the strong recirculation occurring in the strait and to the presence of both baroclinic and barotropic eddies, which increase the gross northward and southward flows across the section (Hopkins, 1991, Gascard et al., 1995). The northward and southward transports estimated from the current measurements are above 10 Sv, with a net southward transport of 2-4±2 Sv (1 Sv = 10^6 m^3 s^{-1}) (Fahrbach et al., 2001, Schauer and Fahrbach, 2004). However, large monthly variability was also reported (e.g. Fahrbach et al., 2001and Schauer et al., 2004).

The inverse model solution of Schlichtholz and Houssais (1998) of the summer circulation suggested that a branch of WSC turns westward to the north of 81°N and recirculates south merging with another branch of WSC that recirculates at 79°N. This caused much larger southward flow at 79°N (6.5Sv) when comparing to the northward flow of WSC (1.5Sv). They also argued that the flow pattern in the Fram Strait must have a substantial barotropic component and is forced by the bottom pressure torque, which includes a baroclinic contribution determined by the density distribution relative to the topography. Later *in situ* mooring observations confirmed that the two major currents have a substantial barotropic component which was estimated as 5 cms^{-1} for the EGC and 20 cms^{-1} for the WSC, and the baroclinic components are very similar (5 cms^{-1}).

1.1.4 Convection and Deep-water Formation

The Greenland and Iceland Seas contribute significantly to the production and export of North Atlantic Deep Water and therefore help to drive the global thermohaline circulation. Previous studies found that the deep water of the Greenland Sea has become gradually warmer and more saline from 1970 (Bonisch et al., 1997, Karstensen et al., 2005). It was argued that the horizontal exchange between the Greenland Sea and the Arctic Ocean through Fram Strait increased, that generated the above changes in the Greenland Sea deep water. Observations have shown increasing salinities over last decade in the region with very large values reported in 2003 (Hansen & Osterhus, 2000). Hatun et al. (2005) have shown that the salinity anomalies are highly dependent on the dynamics of the North Atlantic subpolar gyre. On the other hand, climate models predict an increase in freshwater supply from the Arctic into the Nordic Seas due to sea-ice melting and some observations indicate that the freshening is already occurring (Curry et al., 2003, Curry & Mauritzen, 2005). As a consequence of the freshening various models predict that the North Atlantic thermohaline circulation could weaken. The impact either of the freshening or of the higher salinities on the thermohaline global circulation is not known and therefore more research must be performed to understand the process and its implications.

Several authors have suggested the EGC to be the main source for the waters ventilating the North Atlantic Ocean through the Denmark Strait (e.g., Strass et al., 1993; Mauritzen, 1996; Rudels et al., 2002, 2005). Jeansson et al. (2008) showed that East Greenland Current (EGC), at least in spring 2002, was the main source for the North Atlantic Deep Western Boundary Current and for the Atlantic Meridional Circulation by transporting waters from the Arctic Ocean, including the Atlantic layer as well as deeper layers, from the West Spitsbergen Current and from the Greenland Sea.

1.1.5 East Greenland Current

The East Greenland Current is of particular interest in this research because it is the main and the largest current flowing from the Arctic to the North Atlantic (Fig. 1.4). It carries cold and fresh water and sea ice southward along the eastern coast of Greenland, from Fram Strait to Cape Farewell, via the Greenland Sea and the Denmark Strait. The current carries water of relatively low density and therefore follows the Greenland Continental shelf within about 100 km: part of the EGC recirculates in the Greenland Sea Gyre (Hopkins, 1991). The properties of the intermediate and deep waters in the EGC change significantly from Fram Strait to the Greenland Sea due to mixing with recirculating waters (Rudels et al. 2004). The salinity of the polar surface water increases downstream together with the thickness of the fresh surface layer, maintaining a constant freshwater content. Furthermore, more than 90% of ice transported from the Arctic is carried south by the EGC (Woodgate et al. 1999). Estimates of the transport of ice range from 1530 km^3 $year^{-1}$ (Martin and Wadhams, 1999) to 5000 km^3 $year^{-1}$ (Foldvik, 1988).

Three major water masses of the EGC were described by Aagaard and Coachman (1968) (See Fig. 1.4). Numerous current velocity measurements have been made: Aagaard and Coachman, 1968; Foldvik et al., 1988; Muench et al., 1992; Bersch, 1995. The velocities reported ranged from 8 cm s^{-1} in the Fram Strait (winter 1989; Muench et al. 1992) to 30 cm s^{-1} close to Cape Farewell (September 1991; Bersch, 1995). The current is surface and bottom intensified (at 75°N), with annual means of 24 cm s^{-1} at the surface and 6-10 cm s^{-1} at 60 m above the bottom (Woodgate et al., 1999). The summary of recent studies of EGC transports is shown in Table 1.1. Current meters moored across the EGC at 75°N in 1994-1995 showed a large seasonal variation of the current, ranging from 11 Sv in summer to 37 Sv in winter (Woodgate et al., 1999). The annual mean transport was found to be 21±3 Sv and consisted of a wind driven part (ca. 19±3 Sv for the 9-month long period) with a strong seasonal variability and a thermohaline-driven part (8±1 Sv for the 9-month long period) with little seasonal variation (Woodgate et al., 1999). Woodgate et al. (1999) concluded that the spatial coherence of the current is strong from year to year, indicating small interannual variability in comparison to seasonal cycle. The moorings located in the Fram Strait (78˚ 50 N) from 1997 to 1999 also showed great monthly variability of the southward

transport through the Fram Strait (10-25 Sv) with a maximum occurring in the autumn (December) or spring (April to June) and a mean transport of 13.7±1.7 Sv (Fahrbach et al., 2001). However, in the later years of the mooring observations no clear seasonal cycle was observed (Schauer et al., 2004, De Steur et al. 2009).

The vertical structure of the current also changes downstream. In the Fram Strait the baroclinic and barotropic components have similar magnitudes of about 5 cm s^{-1} (Fahrbach et al. 2001), whereas in the Greenland Sea (75°N) the barotropic component dominates (70%; Woodgate et al., 1999). Schlichtholz et al. (2005) found that the barotropic contribution coincides with the maximum in the bottom density gradient and occurs in the Greenland Gyre at about 75°N. Foldvik et al. (1998) and Schauer et al. (2004) showed that the southward current in the Fram Strait (78.5°N) extends to the bottom. Woodgate et al. reported that the flow has a uniform direction in the whole water column further south, at 75°N.

Study	Time	Location	Transport estimation [Sv]	Velocity range [cm s-1]	Other findings
Fahrbach et al. (2001) (moored current meters)	1997-1999	Fram Strait 79°N	11.1±1.7	9.2±2	Small annual (±2Sv) and large semi-annual (±8 Sv) variability
Schlichtholz and Houssais (1999), (an inverse modelling study)	Summer 1984	78.9°N	6.2		Increasing speed of the current from Fram Strait downstream
Woodgate (1999), (moored current meters)	1994-1995	75°N	21±3	24 (at the surface) 11 (at 60m above the bottom)	Large seasonal variability: 11±5Sv (summer) 37±5Sv (winter)
Woodgate (1999), (moored current meters)	1987-1994	75°N	20±2		Low interannual variability, Seasonal variability range: 16-26±3Sv

Table 1.1 Results obtained by the previous studies of EGC.

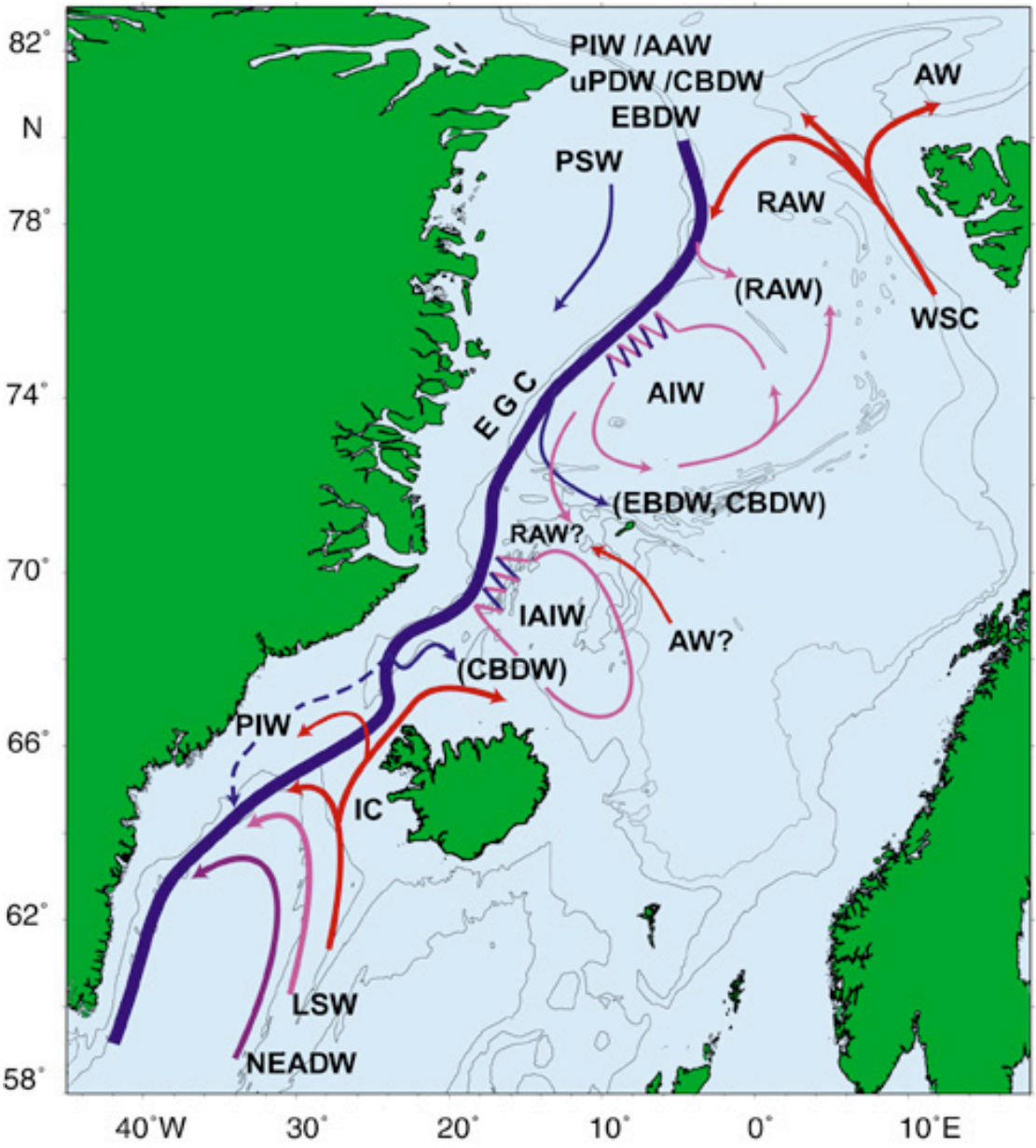

Figure 1.4.Schematic illustration of water masses contributing to the East Greenland Current from the Fram Strait to the south of Denmark Strait, adopted from Rudels et al. (2002) by Jeansson et al. (2008). Abbreviations: **AAW** – Arctic Atlantic Water; **AW** – Atlantic Water; **AIW** – Arctic Intermediate Water; **IAIW** – Iceland Sea Arctic Intermediate Water**; CBDW** – Canadian Basin Deep Water; **EBDW** – Eurasian Basin Deep Water; **EGC** – East Greenland Current**; IC** – Irminger Current**; LSW** – Labrador Sea Water; **NEADW** – Northeast Atlantic Deep Water; **PIW** – Polar Intermediate Water; **PSW** – Polar Surface Water; **RAW** – Re-circulating Atlantic Water; **WSC** – West Spitsbergen Current; **uPDW** – upper Polar Deep Water. Different colors indicate different temperatures of the currents from the warmest (red) to the coldest (blue).

1.3 Atmospheric forcing

The Nordic Seas are influenced mainly by the Icelandic low-pressure system and by the high pressures over the Arctic Ocean (Hopkins, 1991). Furthermore, anomalously low temperatures over the Greenland ice sheet cause strong pressure gradients around Greenland (Proshutinsky and Johnson, 1997). The oceanic circulation is partly driven by the atmospheric forcing including fluxes of momentum, heat and freshwater. It also affects the sea-ice formation and melting and export of sea-ice from the Arctic (e.g. Vinje et al. 1998, Widell et al. 2003). The most important modes of the atmospheric variability in the Nordic Seas are the North Atlantic Oscillation, which describes the variability of the coupled Icelandic low and Azores high and the Arctic Oscillation, which describes the variability of the Arctic high and mid-latitudes low. Both modes of variability can affect the circulation in the Nordic Seas and therefore will be further discussed in the remaining of this section. Existing knowledge about the atmospheric circulation in the North Atlantic and Nordic Seas was recently reviewed by Furevik and Nilsen (2005). Furthermore, more information about the atmospheric forcing of the Nordic Seas circulation is provided in Chapter 4.

1.3.1. Atmospheric modes of variability in the Nordic Seas

North Atlantic Oscillation

The North Atlantic Oscillation (NAO) is the dominant mode of variability of sea level pressure in the North Atlantic, characterized by out-of-phase atmospheric pressure anomalies between temperate and high latitudes over the Atlantic region. There are many definitions of the NAO; it has been defined in the past as the leading Empirical Orthogonal Function (EOF) of the mean sea level pressure over the Euro-Atlantic sector or the 2nd EOF of the streamfunction at 850hPa (Ambaum et al., 2001). It generally explains more than 40% of the variance in these atmospheric fields during the winter season (Barston and Livesey, 1987, Hurrell and van Loon, 1997, Ambaum et al. 2001). The NAO can also be defined as a difference in the atmospheric sea level pressure (SLP) at two stations at the centers of action (index). The mode expresses variations in meridional atmospheric pressure gradient, therefore variations in strength of westerly winds. A low-pressure system over Iceland (the Icelandic Low) and a high-pressure system over the Azores (the Azores High) control the direction and strength of westerly winds into Europe. The relative strengths and positions of these systems vary on

monthly to annual timescales and this variation is known as the NAO. The centers of action can also change their strength and position independently to each other. A large difference in the pressure at the two stations (a high index year) leads to increased Westerlies and, consequently, cool summers and mild and wet winters in central Europe and the North Atlantic Ocean (Figure 1.5). In contrast, during the low index Westerlies become weaker and cold winters and storm tracks move south toward the Mediterranean Sea.

The NAO has its strongest signature in the winter months (December to March) when its positive (negative) phase exhibits an enhanced (diminished) Iceland Low and Azores High (Hurrell et al., 2003). Positive NAO index winters are associated with a northeastward shift in the Atlantic storm activity, with enhanced activity from Newfoundland into northern Europe and a modest decrease to the south (Hurrell and van Loon, 1997; Alexandersson et al., 1998). Positive NAO index winters can be also characterized by more intense and frequent storms in the vicinity of Iceland and Greenland and Norwegian Sea (Serreze et al., 1997; Deser et al., 2000). In the Nordic Seas, the NAO can affect wind speed, latent and sensible heat flux, evaporation and precipitation, wave climate, sea surface height, sea ice extent and freshwater transport through Fram Strait by the EGC (Dickson et al., 1988, 2002, Aagaard and Carmack 1989) and characteristics and distribution of water masses (Dickson et al. 2000). Furthermore, changes in the poleward moisture flux caused by the NAO can affect sea-ice production and thus deep-water formation in the region (Dickson et al. 2000). All of the above effects could cause significant changes in the global thermohaline circulation.

The North Atlantic Oscillation plays a very important role for the variability of sea level and circulation in the Nordic Seas. Dickson et al. (2000) noticed that the positive phase of the NAO may lead to an increasingly intense and widespread influence of Atlantic waters in the Nordic Seas, although the exact mechanisms are not known (Furevik and Nilsen, 2005). The positive NAO increases heat flux and in effect drives the Icelandic Low more to the east (Bengtsson et al., 2004), which causes further warming in the Norwegian and Barents Seas. The shift of the Icelandic Low to the east can intensify the advection of polar water and sea ice transport through Fram Strait, cooling the waters off the east coast of Greenland (Hilmer and Jung, 2000). On the other hand, the intense freshwater flux through Fram Strait causes weakening of the Icelandic Low that results

in cooling in the Norwegian and Barents Seas (Dukhovskoy et al., 2004). The NAO can influence the circulation by the wind forcing, by the divergence/convergence in the Ekman transport, which changes the elevation of the sea level and causes a horizontal pressure gradient and acceleration of the flow (See Chapter 4). This ocean response occurs on relatively short time scales (~days) but the wind can also cause slower changes in the internal density structure of the currents. The density structure can be also modified by the atmospheric freshwater and heat fluxes (Chapter 4).

Previous observations showed that the inflow of the Atlantic water into the Nordic Seas is affected by NAO indicating a stronger inflow during its positive phase (Orvik et al., 2001, Furevik and Nilsen, 2004 and Skagseth et al. 2004). However, it was argued that the relationship occurs for the branches of the NwAC but not for the total inflow (Hansen et al. 2003) and that more cyclonic wind causes more recirculation and mixing with Faroe-Shetland branch (Hansen et al. 2003) what results in strengthening of the eastern branch of the NwAC and weakening of the western branch during the positive NAO. On the other hand, Dickson et al. (2000) suggested that the total inflow of Atlantic water increases during positive NAO and some previous observations of the warming of the Atlantic waters also support this argument (Furevik 2000, Ingvaldsen et al. 2003, Schauer et al. 2004, Furevik et al. 2006).

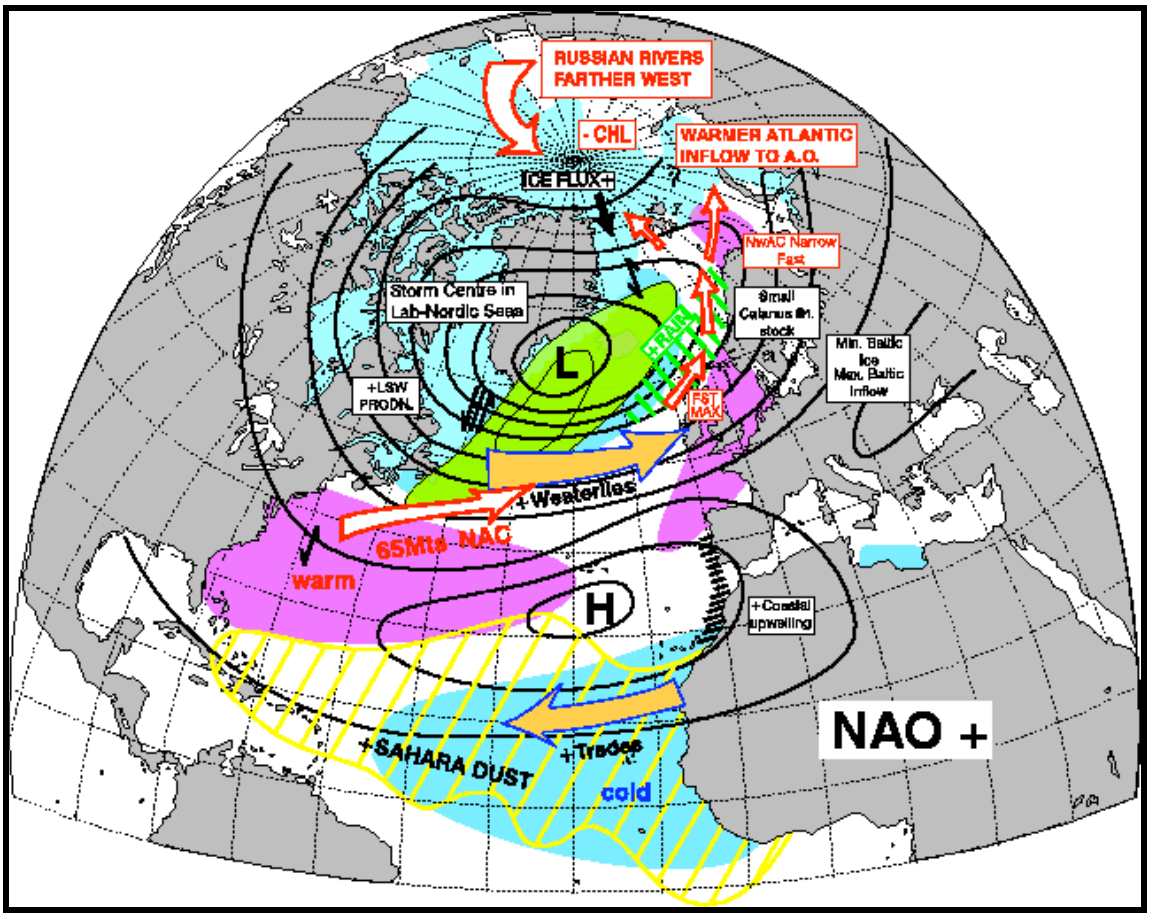

Figure 1.5. Schematic illustrating positive phase of the North Atlantic Oscillation. (Source: http://www1.secam.ex.ac.uk/cat/NAO)

Arctic Oscillation (AO)

The Arctic Oscillation is defined as a first Empirical Orthogonal Function (EOF) of the mean sea level pressure field over the whole Northern Hemisphere (Kutzbach 1970, Thompson and Wallace 1998). Its importance was recognized by many previous studies (e.g. Thomson and Wallace, 1998, 2000 and Thomson et al. 2000). The mode explains about 25% of variance in the mean sea level pressure field and shows two same-signed centers of action over the Pacific and Atlantic Oceans (Ambaum et al., 2001, Figure 1.6). In the AO pattern (Figure 1.6) the Pacific center of action has same sign as the Azores center of action, but the Pacific center corresponds to the Aleutian low, whereas the Azores center corresponds to the Azores high. An increase of the AO index (a difference of the mean atmospheric pressure at two sites: Azores and Aleutian) relate to the strengthening of the Azores high and weakening of the Aleutian low.

The NAO and AO timeseries are highly correlated but the differences in patterns suggest different underlying basic physical mechanisms (Ambaum et al. 2001). The NAO describes a mechanism that is local to the Atlantic region, whereas Thomson and Wallace (2000) suggested that the AO maybe a representation of the zonal symmetric mode modified by the zonal asymmetric forcing (e.g. topography). The distinction between the NAO and AO has been recognized by Wallace (2000) who argued that the two modes could describe different mechanisms of the Northern Hemisphere atmospheric variability. Unlike the NAO, the AO does not reflect the correlations between the surface pressure variability of its centers of action (Ambaum et al, 2001). Therefore, Ambaum et al. (2001) argued that AO is mainly a reflection of similar activity in the Atlantic and Pacific oceans and describes a tendency in these basins for anticorrelation between the geostrophic winds near 35°N and 55°N. The positive phase of the AO corresponds to the strengthening of the polar and subtropical jets over the Euro-Atlantic region and to weakening of the Pacific jet. The low-index state corresponds to one subtropical jet and high-index state to a double jet in the Atlantic basin (Ambaum et al., 2001). This suggests that the AO may also reflect the changes in the atmosphere states from one jet to two jets (Ambaum et al. 2001).

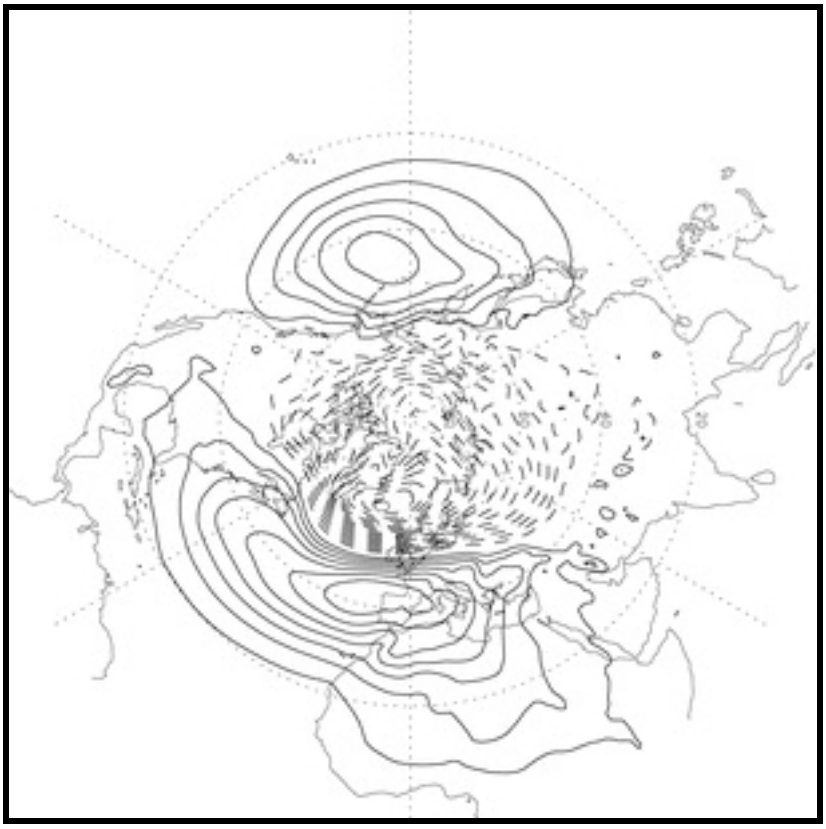

Figure 1.6. First EOF of winter mean sea level pressure showing Arctic Oscillation Pattern. The contour interval is 0.5hPa. (Source: Ambaum et al., 2001)

1.4 Sea Ice in the Nordic Seas

Arctic climate has shown some dramatic changes in recent decades in sea ice extension, temperature, precipitation, river run off and the atmospheric circulation (Serreze et al., 2000, Comiso et al. 2008, Overland et al. 2008, Simmonds et al. 2008, Peterson et al. 2008). Over the last decade, Arctic sea-ice extent has reached record minimum values. In September 2005 a new record low was set, which was broken again soon after in 2007. In 2008 the sea-ice extent was only slightly greater when compared to the 2007 record. Greater transport of sea-ice through Fram Strait was also observed (Kay et al. 2008, Kwok 2008). Much research was done to investigate the causes of this decline and many explanations were proposed (Zhang et al., 2008, Comiso et al. 2008, Kay et al. 2008). Simmonds and Keay (2009) showed that the decline was related to the strength of cyclones in the Arctic and suggested that ice-extent and thickness is vulnerable to the anomalous atmospheric forcing. Giles and Laxon (2008) investigated the sea-ice thickness in that period and found that the average thickness decreased in the Western Arctic. They suggested a number of factors, which might contribute to the decrease: duration of melt season, greater exposure of the Arctic Ocean over summer to the solar radiation. However, more research needs to be done to explain the causes of the sea-ice decline. The dramatic decline of sea-ice, which continues from 1953 until present, together with the very low extent observed in recent years, provided arguments about the future ice-free Arctic Ocean and the changes in the Arctic and global circulation. The decline of sea-ice extent and thickness has many serious consequences for the global and regional climate. Firstly, the reduced albedo would cause changes in the global energy balance and more warming in the Arctic. This would affect greatly marine ecosystems and biodiversity. More freshwater in the surface layers increases stratification which reduces deep-water formation. As a result the global overturning circulation and therefore the global and regional climate could be affected and the whole climate could even transform into a different equilibrium state.

The northwestern part of the Nordic Seas is covered by sea-ice over the year making it difficult to make any in situ measurements in the area (Figure 1.7). Furthermore, during the winter, sea-ice covers the whole eastern Greenland shelf (Figure 1.7). This makes the regions like Fram Strait, EGC and Greenland Sea hardly accessible and makes it almost impossible to gather any *in situ* measurements from those important regions. As

a result our knowledge about the circulation in the ice-covered regions is still very limited. More research in the ice-covered ocean is needed to understand the local circulation, especially in the time of the recent sea-ice decline and high latitude climate warming. This study is the first to show how the circulation in the ice-covered regions of the Nordic Seas varied during the recent 7 years.

Sea ice minimum, summer:
September 2007

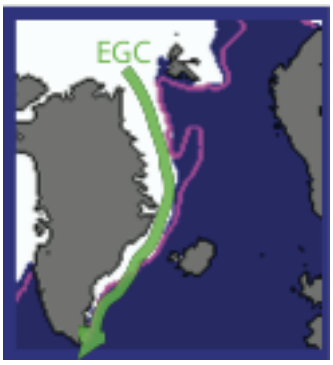

Sea ice maximum-winter
February 2009

Figure 1.7. An example of sea ice minimum extent during the summer (September 2007) and the maximum during winter (February 2009) shown in white. The magenta line shows the 1979 to 2000 average extent for September and February. East Greenland Current (EGC) is illustrated in green. Figures taken from US National Snow and Ice Data Centre.

1.5 Recent climate change observed in the Arctic Mediterranean

Over recent years the climate over the North Atlantic and the Arctic has undergone some significant changes. Since 1960 the westerly winds in the region strengthened and caused dry and cold winters in the southern Europe and mild and wet winters in northern Europe (Hurrell, 1995). Changes were also observed in the Nordic Seas, which became more saline and warmer from 1990s (Holliday et al. 2008) and the Arctic sea-ice cover that decreased in extent and thickness (Giles and Laxon, 2008). The temperature of the Atlantic waters entering the Arctic increased since 1990s (Polyakov et al., 2011), which could have implications for the declining Arctic ice cover.

Many climate models suggest that warming in high latitude regions could be much greater when compared to the rest of the world and may reach about 3-4°C by the end of this century (Randal et al, 2007, IPCC report, Chapter 8). Many models also show that the Arctic Ocean may be nearly ice-free during the summer at the end of the first half of this century (Wang and Overland, 2009, Zhang and Walsh, 2006). There is also evidence that the increased freshwater flux from the Arctic changed the salinity distribution in the Greenland Sea in the top 800m layer (Bonisch et al. 1997). The freshening was also observed in the upper layers of the western Norwegian Sea (Blindheim et al., 2000). Numerical simulations also show the freshening of the upper Arctic Ocean and the weakening of the North Atlantic MOC (Griffies and Bryan, 1997). There is growing evidence that the changes could be caused by anthropogenic greenhouse gas emissions (Houghton et al. 2001). Model experiments showed that the increased atmospheric concentrations of CO_2 changed the tropical sea surface temperature, especially in the Indian Ocean, which could be one of the factors responsible for the observed climate change (Furevik and Nilsen, 2005). If the model results are right the future anthropogenic forcing may result in further warming, and the recent trends in the observed changes may be sustained, which would cause great changes in the Arctic Mediterranean and further affect the global climate.

1.6 Altimetry – how it works?

Altimetry data provides the framework for this thesis. Therefore it is important that the reader is familiar with the principles of altimetry and its limitations. This section describes how the altimeter collects the data and what exactly it measures. Furthermore, it will be explained how to derive the surface geostrophic currents from the measured sea level signal. More detail about the limitations and processing steps of the measured sea level signal can be found in Chapter 2.

The radar altimeter transmits short pulses of energy towards the ocean surface and receives the reflected signal (waveform). The return echo provides information about the global distribution and variability of sea surface height (SSH), amplitude of oceanic waves and wind speed. The time difference between the transmitted and received signal gives the distance between the satellite and the sea surface (range). The SSH is measured relative to the reference surface (ellipsoid), and consists of two components: the marine geoid and the elevation of sea level due to movements in the interior ocean (Figure 1.8). The geoid is the gravitational equipotential of the Earth, defined as the ocean surface in the absence of external forcing and internal motion (Wunsch and Stammer, 1998).

Changes in the height measured by the altimeter are generated not only by the geostrophic flows, but also by other geophysical processes including tides, seasonal heating (steric effect) and changes in the atmospheric pressure (inverse barometer effect). In order to estimate the geostrophic flow, these other contributors to the sea surface height must be removed. After the removal the geostrophic velocities can be obtained from:

$$Vg = \frac{g}{f}\frac{\partial \zeta}{\partial x}$$

$$Ug = -\frac{g}{f}\frac{\partial \zeta}{\partial y} \qquad \text{EQ 1.1}$$

Where f is the Coriolis parameter [s^{-1}], Ug and Vg are the horizontal components of geostrophic velocity in the x and y direction [ms^{-1}], g is gravitational acceleration [ms^{-2}] and ζ is the sea surface elevation [m].

The above equations mean that the measurement of sea surface slope yields estimates of the surface geostrophic velocity. If the information about the ocean interior is available

(the vertical structure of currents), the interior geostrophic velocity profile can be obtained. However, the absolute currents can be only measured if the geoid is known, which is true for length scales greater than about 500 km (Wunsch and Stammer, 1998). At shorter spatial scales the geoid is not known and the measurements can only provide information about the variability of the circulation relative to the altimeter-derived mean sea level (sea surface height anomaly-SSHA). Therefore changes in the sea surface height measured by the altimeter are associated with steric changes, caused for example by seasonal changes in solar radiation, redistribution of mass in the ocean caused by the dynamic variations in the currents (Wunsch, 1994, Wunsch and Stammer, 1998) and a mass input from precipitation/evaporation and river runoff/ melting (Vinogradov et al., 2008).

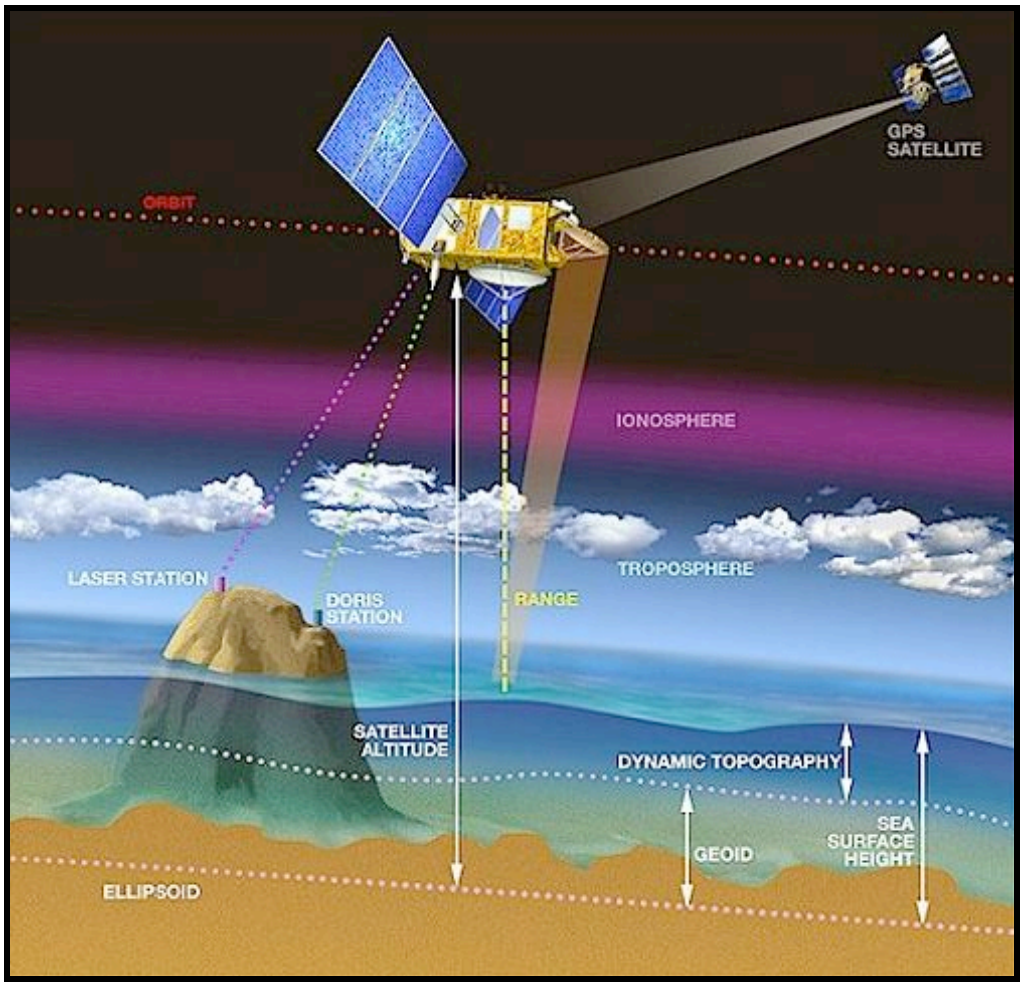

Figure 1.8. Principle of the altimetry measurement. (Source: http://www.aviso.oceanobs.com/en/altimetry/principle/basic-principle/index.html)

1.7 Aims and objectives

The earlier sections of this chapter demonstrated the importance of the Nordic Seas circulation in the global and regional climate system. It was also showed that the high latitude climate has undergone some dramatic changes during recent years and the circulation in the Nordic Seas was also affected. On the other hand it was argued that knowledge of the circulation is still limited, especially in its western part, where sea-ice is present. Therefore, the main aim of this study was to contribute to the understanding of the Nordic Seas circulation with a special focus on the ice-covered seas.

The major objective was to describe the variability of the sea level in the whole Nordic Seas in 2002-2009 using sea surface height anomaly (SSHA) measured by the Envisat altimeter. This objective required production of the SSHA on a regular grid, of adequate resolution and accuracy, and therefore pre-processing of the data and development of a method to connect SSHA from the open ocean with data from ice-covered regions (Chapter 2). The analysis of the SSHA variability required the application of harmonic analysis and EOF analysis to the data. The next objective was to explain the observed sea level variability and find its driving mechanisms. This required examination of the possible driving mechanisms and an application of various statistical methods, which could identify those mechanisms.

The second major objective was to describe the surface circulation in the Nordic Seas using the SSHA. Due to the limited length of the analysed data, the investigation focused on the mean seasonal cycle and the annually averaged surface currents. The next stage of the study focused on the EGC. The main aim was to show how the EGC transport varied in 2002-2009. However, this aim required knowledge about the vertical structure of the current and its relation to the current surface velocity. Therefore, the couple ice-ocean numerical model (NEMO) was used to gather this information and the method of transport estimation was developed.

CHAPTER 2: DATA AND METHODS

2.1 Introduction

The main part of this chapter describes data and the pre-processing steps performed to create a final product of the sea surface height anomaly used in the analysis of the following chapters. The sea surface height (SSH) data were delivered by the Centre of Polar Observation and Modelling at University College London, and provided the major motivation for this project. Due to the number of technical issues and limitations of these data, Section 2.2 describes the corrections applied to the measured SSH. Furthermore, processing steps and errors associated with the altimetry data are described here. The remainder of this chapter describes different data sets that also contributed to the analysis. Section 2.3 describes the ECMWF products of air-sea exchanges of momentum, heat and freshwater used later in the subsequent analysis of Chapter 4. Finally, Section 2.4 describes the numerical model output used in the analysis described in Chapter 5.

2.2 Sea Surface Height

2.2.1 Data description

Sea surface height (SSH) was measured by the radar altimeter (RA-2) on board the Envisat satellite from November 2002 to October 2009. The data analyzed here consist of two data sets that were processed using different retracking techniques: SSH from the open ocean, and from sea-ice covered ocean. The SSH data and the geophysical corrections (Section 2.1.2) were provided by the Centre of Polar Observation and Modelling at the University College London as 18 Hz along-track SSHA organized into cycles (35 days) and calendar months. In total eighty-four months were used for this PhD, starting from November 2002. On average only 5% of data was missing in any month when considering the final girded data used in the analysis of the remainder of this thesis (Figure 2.1). There were two episodes when the RA-2 altimeter stopped collecting the data and needed to be rebooted (ESA, ENVISAT Instrument Availability Interruptions, 2011). This resulted in about 25% of data missing in March 2003 and 20% and 32% of data missing in May and June 2006. The number of missing data also showed seasonal variations. Generally, from December until May there was about 10% or less missing data and from June to November there was on average only 2.5% of missing data. The spatial distribution of the missing data is shown in Figure 2.2. as a percentage of the total time when a given grid point had no data. The most data (more than 50%) were missing in the Belgica Bank (Greenland northern shelf) and along the coasts, which could be caused by the Nioghalvfjerdsfjorden Glacier floating into the shallow Belgica Bank (Bacon et al., 2008) that changes the altimetric waveform shape. Furthermore, about 10-20% of data was missing along a few zonal bands across the Nordic Seas to the south of 68°N. This could be caused by the organization of the satellite tracks in the southern Nordic Seas (See for example Figure 2.5). About 10-20% of data was also missing along the Greenland continental shelf, a narrow region from the Denmark to the Fram Strait. In the region where the ice-edge occurs, e.g. in the Greenland Sea and to the south of Svalbard, about 10% or data was missing. The rest of the Nordic Seas had good altimeter spatio-temporal data coverage and less than 5% of data was missing there.

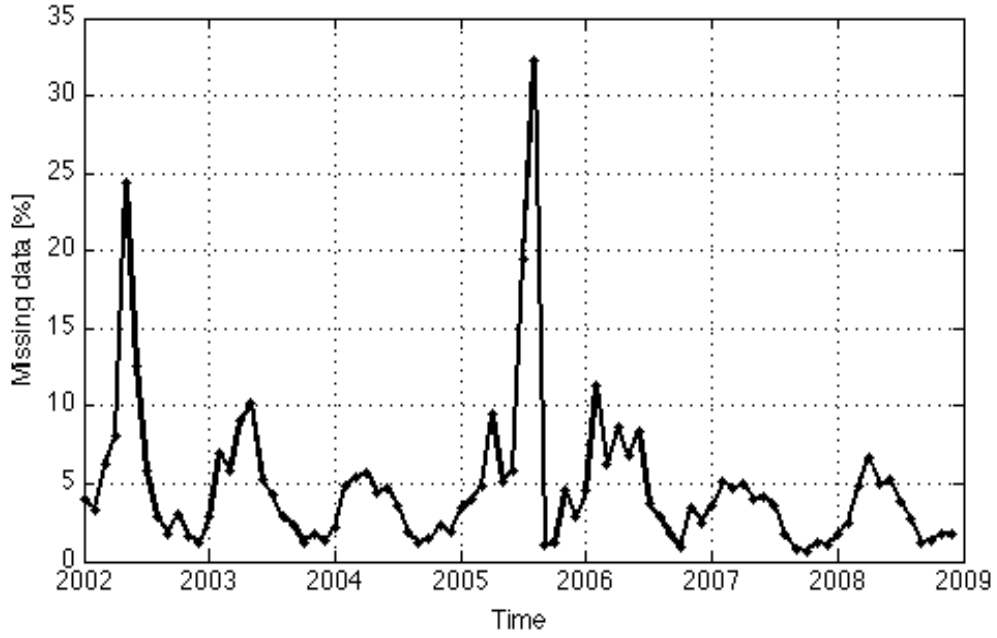

Figure 2.1. Time series of the percentage of the missing SSH data. The labels of the X-axis show November in a given year

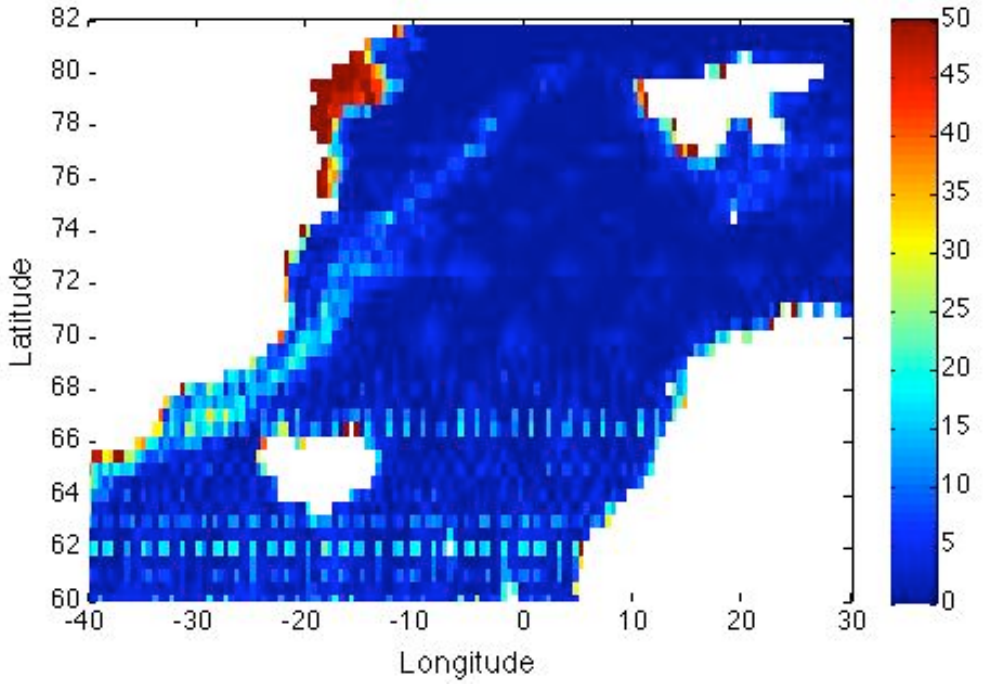

Figure 2.2. Spatial distribution of the missing SSHA data presented as a percentage of time missing.

Return echo from the open ocean

The RA-2 altimeter on board the Envisat satellite is a pulse limited altimeter and therefore the shape of the averaged return signal is dictated by the length of the pulse. A flat surface, which is rough on the scale of the radar wavelength (of order centimeters), is called a diffuse scatterer and therefore the reflected energy from that surface is proportional to the illuminated area. As a result the averaged return exhibits a linear initial rise, followed by a flat region that is eventually attenuated. The resulting form of the mean radar echo as a function of time is shown in Figure 2.3. The shape of the return echo from the ocean can be estimated by the Brown model (Brown, 1977) and six parameters can be obtained by comparing the theoretical model with the real averaged waveform. The epoch at mid-height is defined to be the half of the power received by the altimeter and it provides the time delay of the predictable return of the radar pulse (estimated by the tracker algorithm) and thus the time the radar pulse took to travel the satellite-surface distance (or 'range'). The SSH is the difference between the satellite height in reference to the World Geodetic System 1984 ellipsoid (European Organization for the Safety of Air Navigation, 1998) and the altimetric range computed from the waveform received by the altimeter (See Chapter 1).

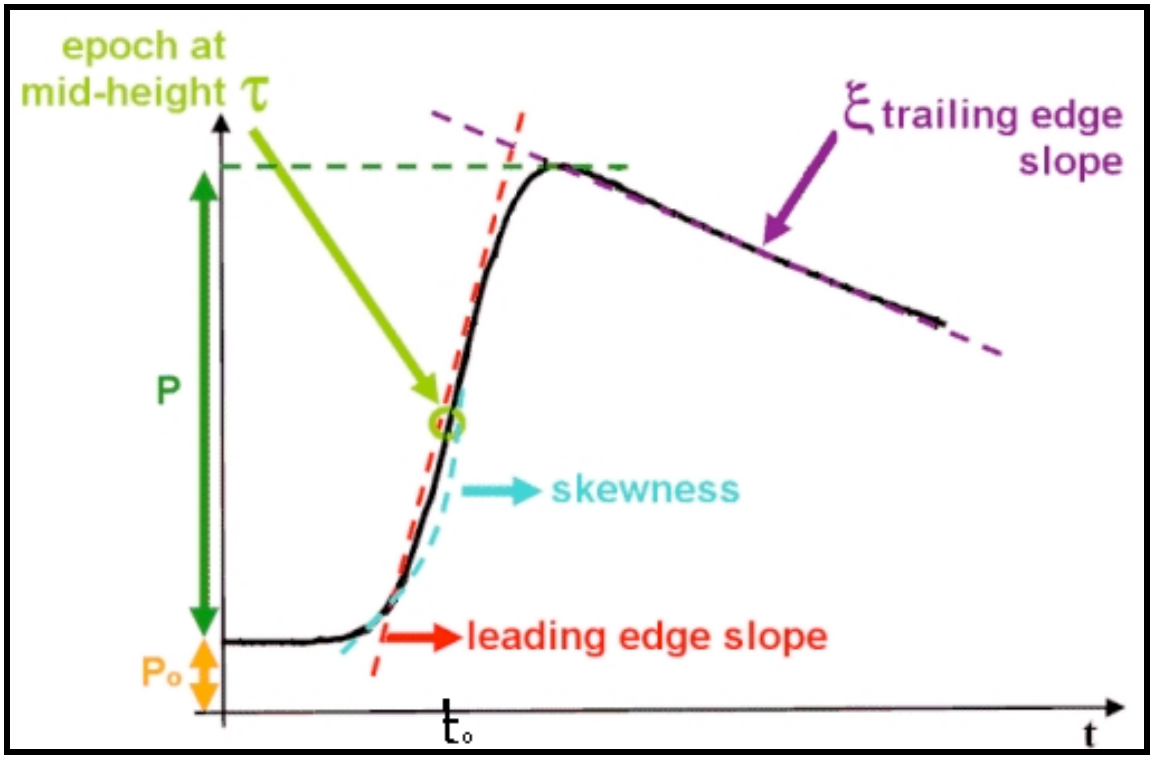

Figure 2.3. Average waveform of the altimeter return signal reflected by the ocean surface shows the power returned (P) in time (t). The slope of the leading edge ξ relates to the wave height and its skewness relates to the ocean wave skewness. P_0 is the thermal noise level. The time delay to the mid-point of the leading edge τ relates to the satellite altitude and sea level height *(Source: ESA http://earth.eo.esa.int/)*.

Return echo from the ice–covered ocean

The radar echo received by an altimeter from any surface is dependent on the surface roughness on scales similar to the radar wavelength (2.2 cm for ERS-2 and for Envisat). Drinkwater (1991) showed that even when a small fraction of the surface has a roughness of 3 mm (for ERS-2), it dominates the return signal received by altimeter. This returned signal has the shape of a sharp peak and is called "specular". The comparison of Ku-band (13.575 GHz) airborne radar altimetry with aerial photography proved that the specular returns originate from the water between the ice floes (leads) (Drinkwater, 1991; Laxon, 1994). In the areas of mixed small ice floes and leads, specular echoes can dominate the return signal even at high ice concentrations (Peacock and Laxon, 2004). The comparison of signals originating from leads and the open ocean is shown in Figure 2.4. The separation between the two waveforms was performed by

CPOM using the technique described by Peacock and Laxon (2004). The return waveform from the ice-covered ocean was modelled by the Gaussian function, from which the SSH was calculated and additional processing steps were performed by CPOM in the same way as described by Peacock and Laxon (2004). Figure 2.5 provides an example, which indicate where the two different retrackers were used.

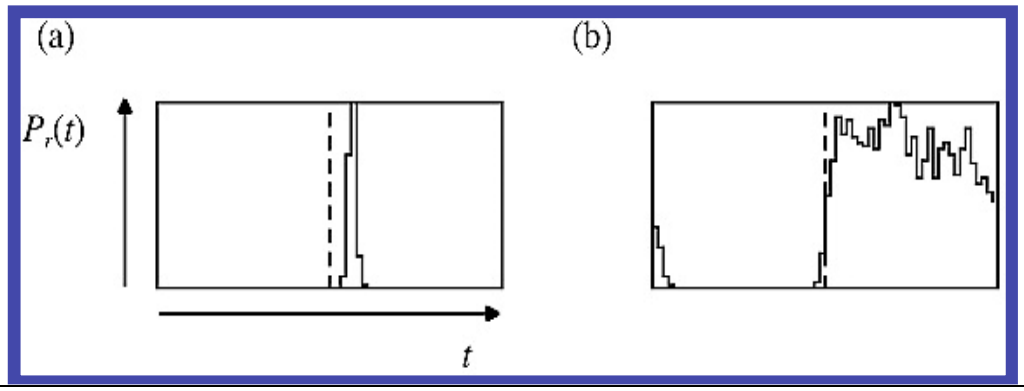

Figure 2.4.Typical ERS altimeter waveforms acquired from an ice-covered sea: (a) specular waveform, and (b) diffuse waveform (open ocean). The waveforms show received power $P_r(t)$ *(counts)* at the altimeter versus time *t (bins)*. Note that the power peak of specular waveform is typically three times greater than for the diffuse waveform. Source: Peacock & Laxon (2004).

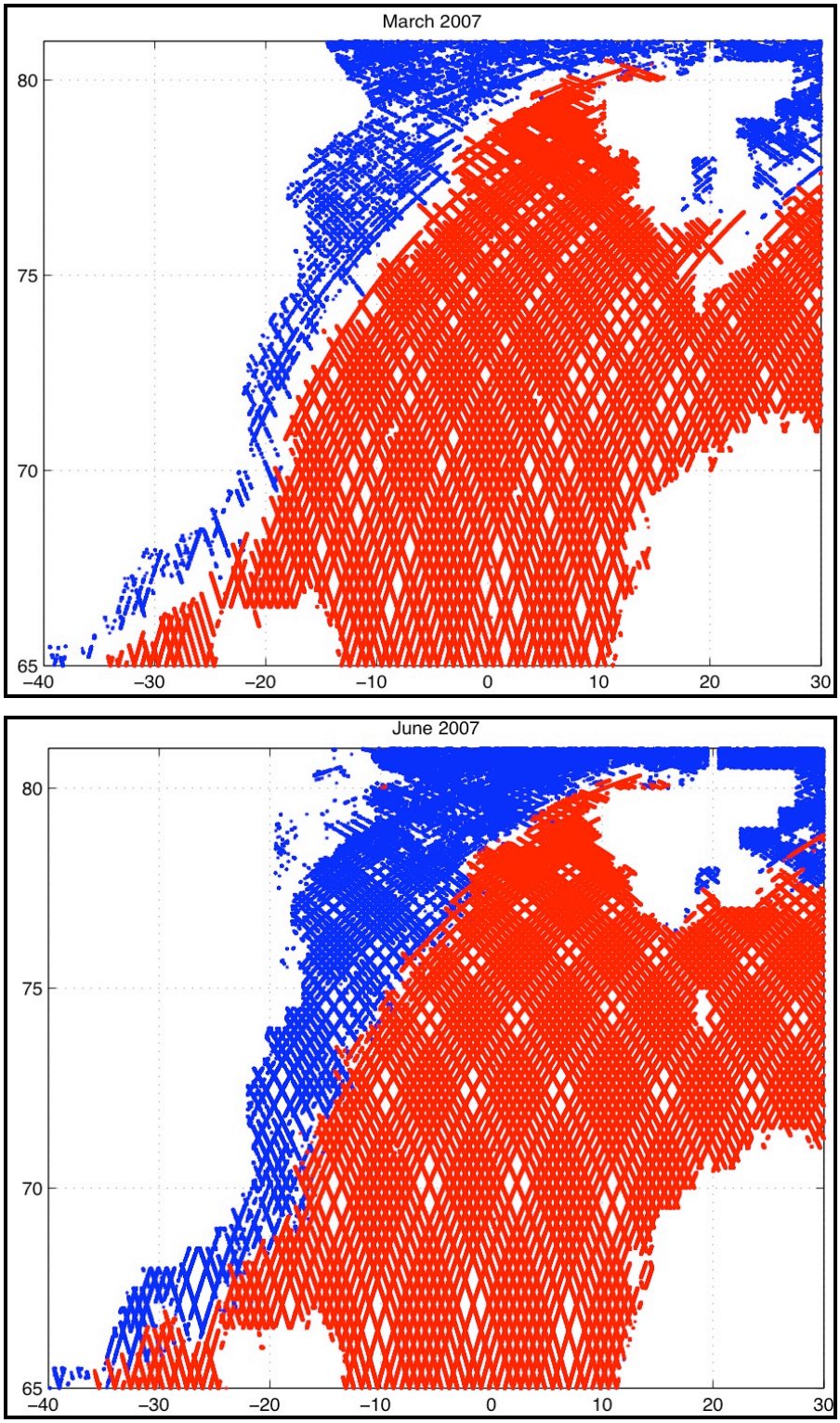

Figure 2.5. Example where Peacock & Laxon retracker was used (blue) and where the standard ocean retracker (red) for March (top) and June (bottom) 2007.

Summary of the Post-processing steps

The SSH retrieval from the ocean and ice-covered seas were done by CPOM, who also delivered the SSH data with all the geophysical corrections applied as 18 Hz along-track data (Section 2.1.2). The mean SSH (Figure 2.9) was subtracted from the 18 Hz SSH to create the sea surface anomaly (SSHA). Due to the different retracking methods used to obtain the SSHA in the ice-covered and open ocean an offset in height between the two datasets emerged. CPOM did not understand a physical reason for the offset and therefore it was decided to take the statistical approach to understand its behavior and develop a method to correct for it. Therefore, the data was divided into two monthly data sets: open ocean and ice-covered ocean. The 18Hz along-track data was very noisy and needed data quality check and filtering. Firstly, the missing values and outliers were removed by taking away the absolute values of SSHA greater than one meter from each dataset. Furthermore, the values greater/smaller than three standard deviations from the mean were removed. The nature of the offset and the method of its removal are described in Section 2.1.3.

2.1.2 Corrections and errors

In order to use the data and correctly interpret it, one must have an understanding about sources of errors and various corrections applied to the data. The altitude of the ocean with respect to the reference ellipsoid can be calculated by subtracting from the satellite-to-Earth's-surface range measured by the altimeter, the independently known satellite orbit height. In order to get the sea level height the return signal needs to be adequately processed. Firstly the signal needs to be corrected for instrument and platform errors. Secondly, the orbit of the satellite needs to be accurately determined and sea surface and refraction effects need to be removed from the signal. There are four sources of errors in sea surface height retrieval: altimeter noise, atmospheric errors (including ionospheric), sea state bias and orbit errors. The atmospheric errors and sea state bias can be further reduced by applying the relevant corrections. The corrections were applied by CPOM to the SSH and are presented in Table 2.1. The characteristics of the errors and corrections are described below.

Correction type	
Ionospheric	Value in WAP (Waveform Product, Cudlip & Milnes, 1994, using International Reference Ionosphere, 1994), (Bent Model)
Dry Tropospheric Wet Tropospheric	Computed by CPOM from ECMWF surface pressure, humidity and temperature (6-hourly)
Inverse barometer	Mog2D model for periods shorter than 20 days and standard IB static correction for periods longer than 20 days
Ocean Tide	FES95.2.1 (Le Provost et al., 1998)
Long period tide	Cartwright and Taylor (1971), Cartwright and Edden (1973)
Loading Tide	CSRV3.0
Earth Tide	Value in WAP data based on Cartwright-Taylor-Edden tables (Culdip et al. 1994)
Pole tide	Wahr (1985)
Mean Sea Surface	The newest Mean Sea Surface generated from Envisat RA-2 SSH data (2002-2008) calculated by CPOM (Figure 2.8)
Sea State Bias (Applied to the open ocean)	BM3 model (This correction is set to zero in the ice-covered ocean)

Table 2.1.Corrections applied to the along-track 18Hz SSH data.

The greatest error in the SSH is usually caused by the uncertainties in the orbit determination. This error is a long wavelength (greater than 1000 km) error that should be treated as a sum of random and systematic errors associated with a single range estimate or monthly (or longer) averages over hundreds of kilometers. However, thank to the DORIS (Doppler Orbitography and Radio-positioning Integrated by Satellite) and SLR (Satellite Laser Ranging) tracking the Envisat radial root mean square error is about 2.5-3cm (Doornbos and Scharoo, 2004), which is a great improvement when comparing with older ERS satellites. The second error source, an altimeter noise, can be treated as a random noise in the measurements and dominates short temporal and small

spatial scales. This component of the error increases with the Significant Wave Height (SWH) and stabilizes at SWH=3 m reaching about 25 mm (Fu et al., 1994, for TOPEX).

Atmospheric errors can be further divided into dry and wet tropospheric errors. All tropospheric gases, except water vapor and liquid water, make the dry troposphere. Therefore, a dry atmospheric range delay depends on the amount of mass between the sensor and sea surface (sea level pressure) and reaches 2.7 mm per 1-mbar change in the atmospheric pressure (Martin, 2002). The wet tropospheric error is caused by the range delay due to the presence of water vapor and liquid water in the atmosphere. The Ionospheric correction accounts for charged particles in the ionosphere and can be modelled or determined directly by dual-frequency altimeters.

The last source of error in the SSH retrieval is a sea state bias generated by the ocean waves. This error can be also divided into two parts: electromagnetic bias (EM), and skewness bias. EM bias occurs because the troughs of waves are better reflectors than the crests, therefore the mean surface appears to be depressed below mean sea level. From observations, the EM bias is negative and linearly proportional to 2-3% of SWH and depends on the geographic region and wind speed (Chelton et al., 2001). For example for TOPEX and JASON-1, for SWH= 2 m, depending on geographical area, the EM bias is 40-60 mm (Fu et al., 1994). The EM error is difficult to remove and is the second largest error in the altimetry measurements. The skewness bias is due to the assumption that the waves have a Gaussian shape. This error also depends on the SWH and reaches the maximum of ±40 mm when SWH= 10 m (Chelton et al., 2001). The skewness bias could be reduced by postprocessing because it is due to an instrument error. However, in practice it is difficult to separate EM from skewness bias and the two errors are grouped into a single sea state bias.

The above errors can be reduced by applying various corrections to the altimetry measurements. For example, use of a combination of DORIS laser tracking and GPS positioning with numerical orbit models significantly reduces the orbital errors (Chelton et al., 2001). Furthermore, in order to be able to calculate the geostrophic surface currents, both tides and the inverse barometer effect must be removed from the data. The inverse barometer correction is a correction for variations in SSH due to atmospheric pressure variations and can reach a maximum ±15 cm in the Southern

Ocean (Wunsch and Stammer, 1998). The inverse barometer correction (a static response) has got a standard deviation of about 5-7 cm in the Nordic Seas when considering the monthly data and about 2cm when considering annually averaged data (Ponte, 2006). Recent study of Ponte (2006) suggests that the application of the inverse barometer correction can reduce the monthly SSHA variance by about 20-50% and up to 40|% of the annually averaged SSHA variance in the regions to the north of 60°N. The correction can be obtained from the dry tropospheric correction and meteorological models. The model results of Ponte et al. (1991) confirm that over most open ocean regions the ocean response to atmospheric pressure forcing is mostly static. The deviations from the inverted barometer response are in the range of 1 to 3 cm root mean square (RMS), with most of the variance occurring at high frequencies (ESA, RA-2/MWR Level 2 User Guide, 2011).

Ocean Tidal model

The global standard deviation (SD) of the SSH due to the oceanic tides is between 10-60 cm with larger amplitudes in the coastal regions and marginal seas (Fu and Cazenave, 2001). Therefore, tidal SSH variation can be twice larger than the magnitude of the dynamical SSH (SD=5-30 cm) and because of that can be regarded as a noise and must be removed in order to recover the dynamical part of the SSH. The tidal model that is used to remove the oceanic tidal effects from the SSH must be therefore as accurate as possible, otherwise the errors for the tidal frequencies would propagate into the alias frequencies (tidal aliasing). The Envisat and ERS-2 satellites rotate the Earth in 35 days (one cycle) and therefore the diurnal tidal constituents K1 (23.93 h) and P1 (24.07 h) could be aliased into an annual cycle (Mork and Skagseth, 2005). However, in the Nordic Seas the semidiurnal tides dominate (Gjevik and Straumer, 1989); Furthermore, Mork and Skagseth (2005) confirmed that there was no aliasing into the annual cycle in the Nordic Seas for the ERS-2 altimeter, that have got the same orbit characteristics as Envisat. The semidiurnal tides could be aliased into 95 days period (3-4 months).

Many models use the variety of altimeters to obtain the tidal constituents. However, in the Arctic and Nordic Seas only ERS-1, ERS-2 and Envisat altimeters were collecting the data to the north of 66°N. Therefore, the tidal models are less accurate in these regions when compared to the regions that are located south of 66°N. The most

energetic tidal constituents in the Nordic Seas are M_2, S_2, K_1, and O_1 (Padman and Erofeeva, 2004). The M_2 has the greatest amplitude that reaches 1.8m in the southern Barents Sea and about 1m south of Denmark Strait (Figure 2.6). There are two amphidromic points in the Nordic Seas in the semi-diurnal tidal maps located in the close proximity to the Denmark Strait and east of Iceland (Figure 2.6). The diurnal tides K_1 and S_1 have much smaller magnitudes in the Nordic Seas that vary from zero in the central Nordic Seas to about 15 cm close to the coast of Greenland (Figure 2.6). Therefore the greatest errors associated with the oceanic tidal corrections should be caused mainly by the errors of the M_2 tidal harmonic. This statement can be supported by mean tidal current speed map (Figure 2.7), which shows that the greatest currents occur in the proximity of the semi-diurnal amphidromic points: in the Denmark Strait, east of Iceland and southern Svalbard. The currents there reach about 20 cms^{-1} but are less than 4 cms^{-1} in the majority of the Nordic Seas. Therefore, we expect the largest errors to occur in the regions that have the greatest tidal currents. Because the errors associated with the ocean tidal correction can be a significant part of the total SSH error budget, sensitivity tests were performed by CPOM and the 'best' model was chosen to remove the SSH contribution due to the oceanic tides. Firstly the Envisat SSH was generated in the whole Arctic for cycles 21 to 26 (time periods: 2003/10/10 - 2004/05/06) and some along-track smoothing was applied to remove the instrument noise. Three tidal models were used to obtain SSH contribution due to the oceanic tides that was subtracted from the original SSH. The models tested were: Arctic Ocean Tidal Inversion Model (Padman and Erofeeva, 2004), GOT00.2 standard Envisat model (Schrama and Ray, 1994) and FES95.2 (Le Provost et al., 1998). Finally, the SSHA differences were generated by CPOM at the crossovers points of the satellite tracks and the root mean square of the differences were calculated for each tidal model. The results are presented in Figure 2.8 and show that FES95.2 provides the 'best' correction for the oceanic tides in the Arctic. Therefore, the FES95.2 was used to remove the effect of oceanic tides on SSH (Table 2.1).

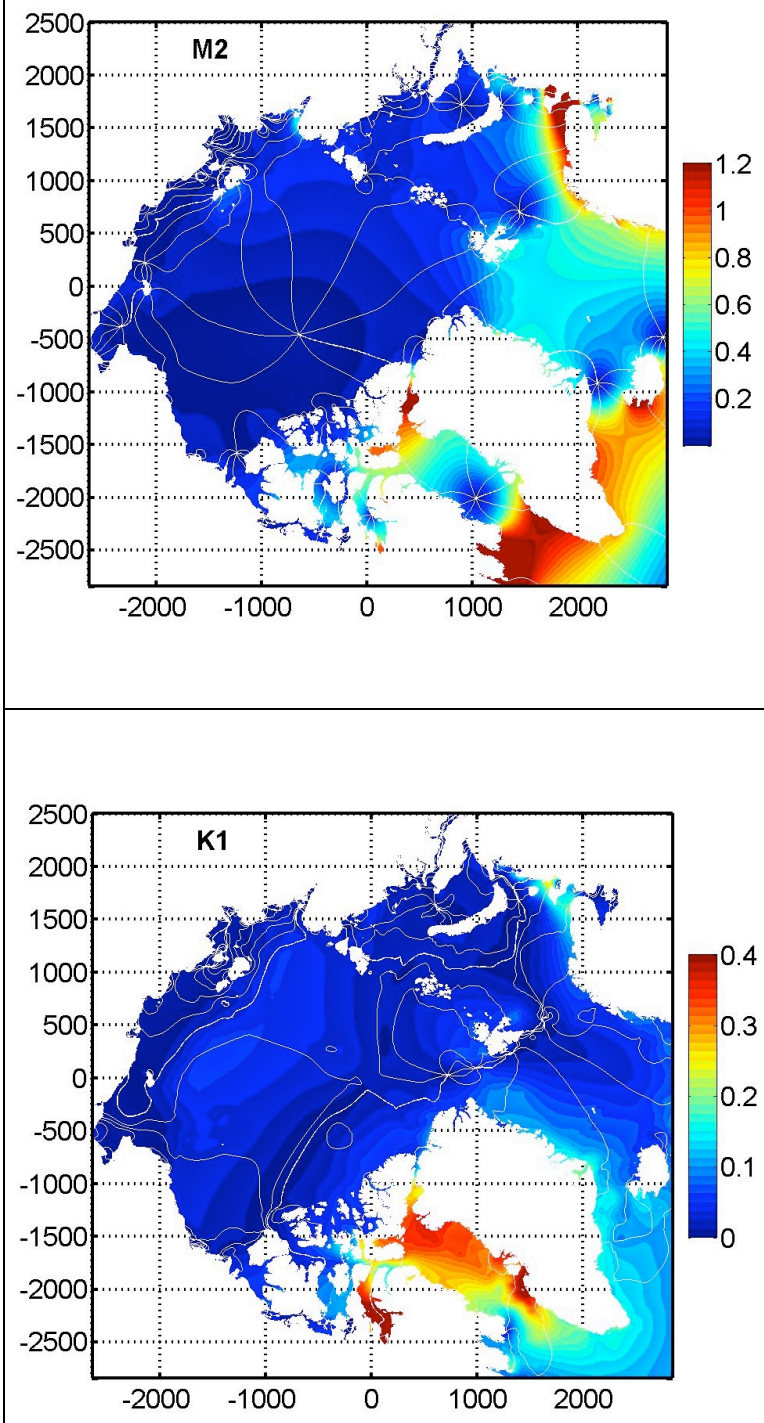

Figure 2.6. Amplitude [m] and phase (white contours) for tidal harmonics M_2 K_1 for the Arctic Ocean Tidal Inversion Model (AOTIM-5). Peak M_2 amplitudes are close to 1.8 m in the southern Barents Sea near the entrance to the White Sea. Source: Padman and Erofeeva (2004).

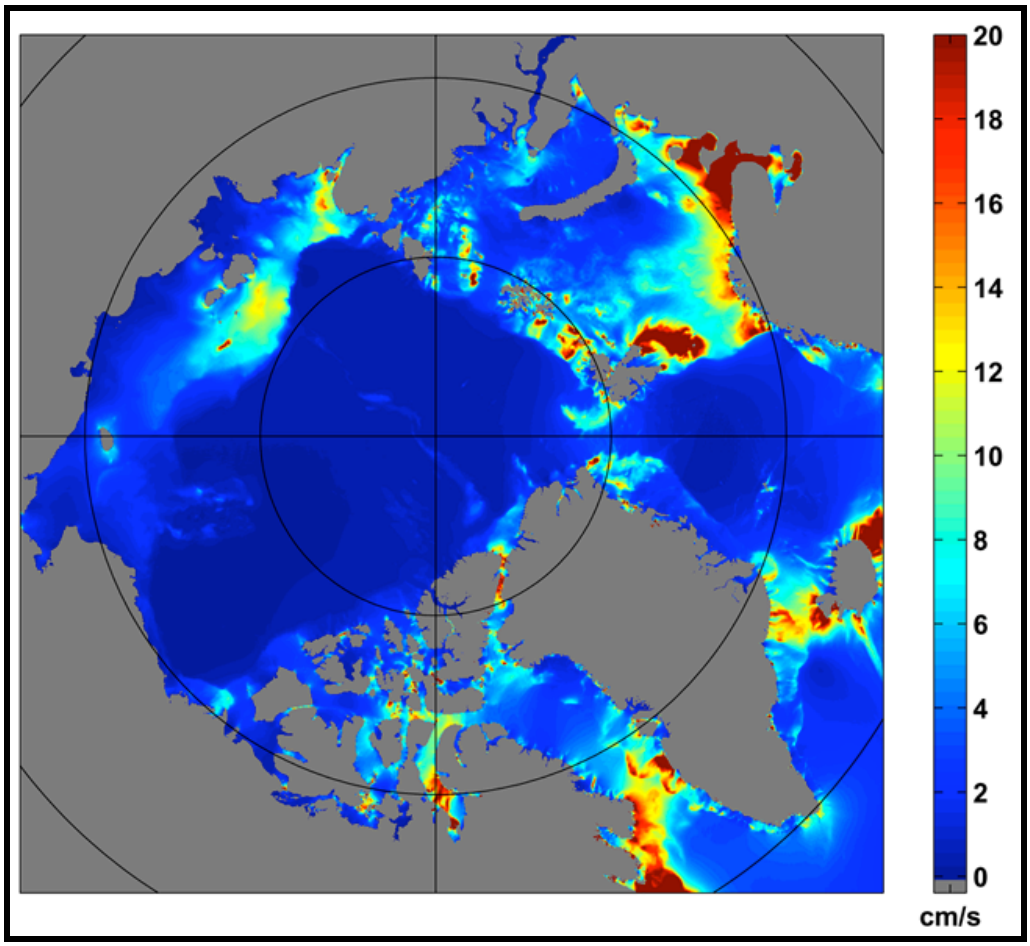

Figure 2.7. Mean tidal current speed (cm s^{-1}) based on simulating 14 days of hourly total tidal speed from the 8-constituent inverse solution AOTIM-5. Source: Padman and Erofeeva (2004).

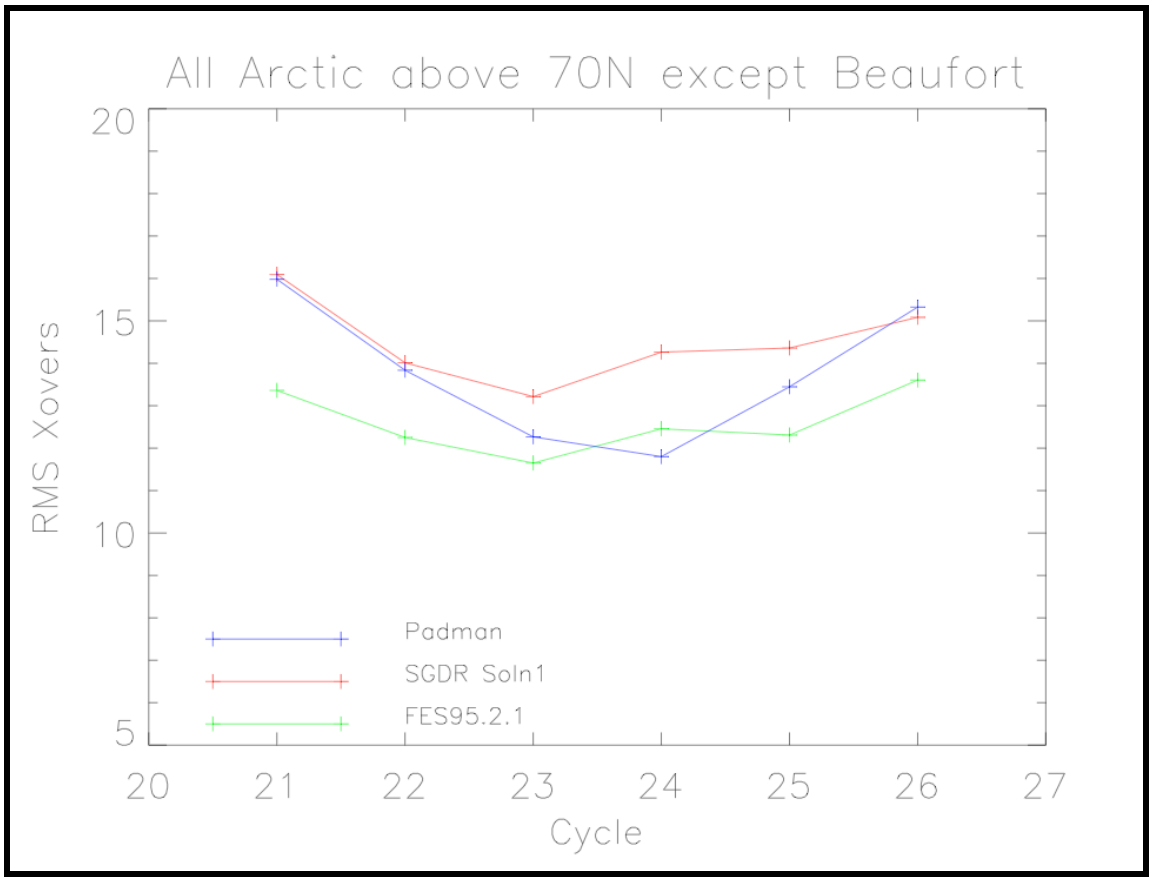

Figure 2.8. Root mean squared (RMS) crossover SSHA differences for different tidal models: AOTIM-5 (Padman and Erofeeva, 2004), GOT00.2 standard Envisat model (Schrama and Ray, 1994) and FES95.2.1 (Le Provost et al., 1998). Source Ridout and Laxon (2011, personal communication).

Standard Tidal Corrections

Several of the tidal corrections listed in Table 2.1 were subtracted from the range measurements by applying 'standard' models that have been successfully used for previous satellite altimeter missions such as ERS-1, ERS-2 and TOPEX/Poseidon. These corrections are the solid earth tide, long-period tides and pole tide.

1.Solid Earth Tide- The solid earth tide is the periodic movement of the Earth's crust caused by gravitational interactions between the Sun, Moon and Earth. The magnitude of this tide is about 30cm (Cartwright and Taylor (1971), Cartwright and Edden (1973)), and its effect was subtracted from the range estimate before calculating SSH.

2. Ocean tide diurnal and semidiurnal.

2. Geocentric Long Period Tide in the ocean- expressing the disturbance of the geoid by the sun and moon, have no longitudinal dependence and is characterized by periods exceeding two weeks (Wunsch, 1967). These long-period tides have amplitudes of less than 1 cm and approximate the to static equilibrium in the ocean. The accuracy of the solid earth tide height and the equilibrium long period ocean tide is better than 1 mm (ESA, RA-2 Level-2 user guide, 2011).

3. Loading tide, including long period loading- it is caused by the elastic response of the Earth's lithosphere to the load of the ocean and its self-attraction. The vertical displacement caused by ocean-loading is of the order of several tens of millimeters in polar regions although it is primarily restricted to the vicinity of the coastline.

4. Pole tide is an ocean response to the variation of the solid Earth to the centrifugal potential generated by the small perturbations of the Earth's rotation axis. The correction has got a high accuracy of the order of 1mm and mainly occur at periods of 12 months and 14 months (ESA, RA-2 Level-2 user guide, 2011). The pole tide correction was computed as described by Wahr (1985) and subtracted from the satellite range estimates.

Mean Sea Surface

Mean Sea Surface height (MSS) was generated by CPOM from the Envisat tracks as an along-track time average. CPOM used the 'best' 8 passes from the start of the mission in 2002 to the end of 2008 for each of the 501 satellite tracks in the repeat cycle (Ridout and Laxon, Personal communication, 2011). Laxon and Ridout (Personal communication, 2011) investigated the waveforms of many satellite tracks and noticed that in the summer one or two passes had very little noise on the specular returns over the sea ice and the elevation profiles were extremely similar. Therefore for each of the 501 arcs the best 8 examples of the very low noise passes were put in the average. The produced MSS that was subtracted from the SSH, is shown in Figure 2.9. Because the MSS was an average over a shorter period (i.e. 6 years) than the analyzed signal (i.e. 7 years) and it was an approximation to the real MSS (only 8 tracks were used for its construction) the resulted SSHA still had a time residual mean that I removed in order to create the SSHA time series with the zero time mean. This was done after the offset was added to the data from the ice-covered ocean (See Section 2.1.3) and the SSHA was mapped into the regular grid (described below).

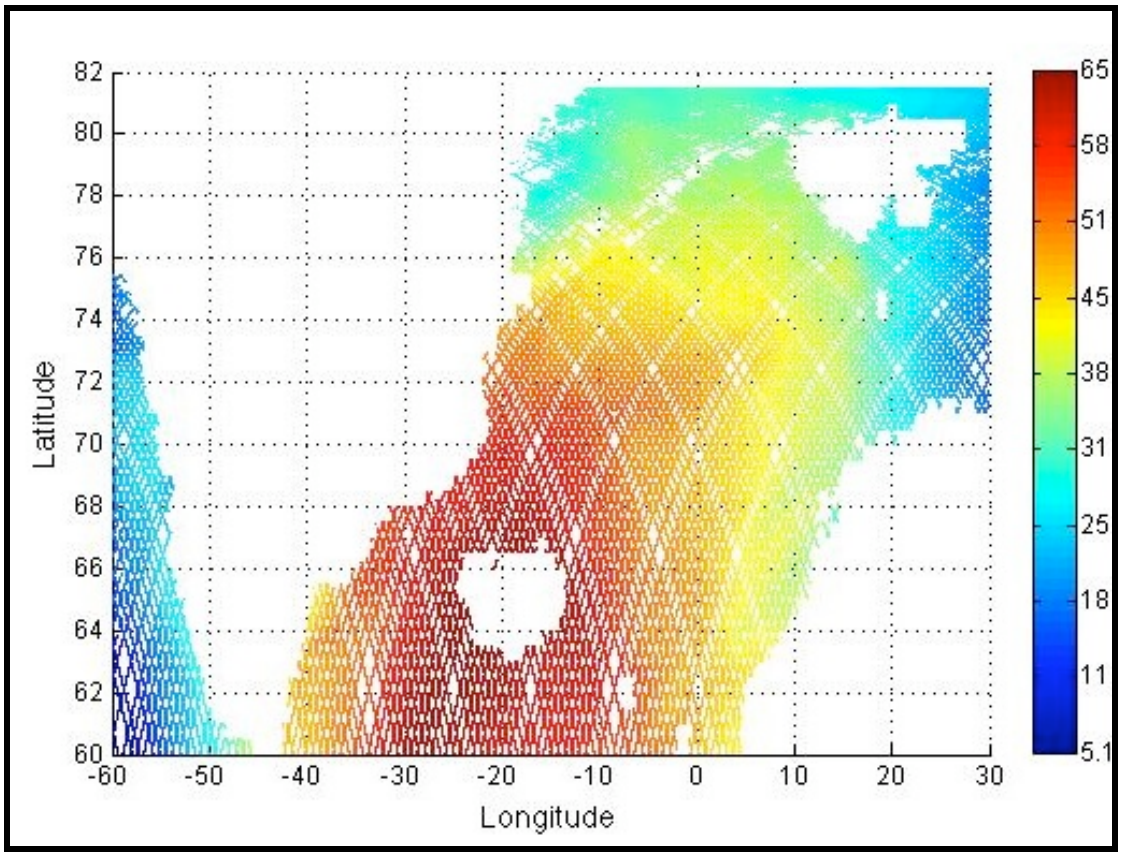

Figure 2.9. Mean Sea Surface (2002-2008) height generated from the Envisat SSH [m] .

Errors in the ice-covered ocean

The errors associated with measurements of SSH in ice-covered seas are greater than for those in ice-free regions (Peacock and Laxon, 2004) and therefore require more explanation. The additional errors in the ice-covered ocean could be caused by the high-powered specular radar echoes and additional uncertainties in orbit determination and atmospheric and ocean tidal correction (Peacock and Laxon, 2004). The total error for the 18 Hz along-track SSHA in ice-covered seas should be very similar to or less than 9.4 cm obtained for the whole Arctic using ERS-2 data (Peacock and Laxon, 2004). The total error for the ERS-2 SSH measurements in the ice-free regions was found to be 6.4 cm for the ERS-2 global ocean (Scharroo and Visser, 1998). The RA-2 altimeter on board Envisat is a newer, more advanced altimeter and other previous studies have confirmed it is more accurate than the ERS-2 altimeter (Janssen et al. 2007, Faugere et al. 2006). Therefore, we can assume that the upper limit of the RA-2 error is equal to the ERS-2 error and is about 10 cm in the ice-covered ocean and 8 cm in the open ocean when accounting for the sea state bias. However, we must also note that the total error is dependent on the location and spatial and temporal scales considered.

Mapping data into a regular grid

Spatial averaging can significantly reduce the total mapping error. The median filter is very efficient way of reducing the instrument error, which is characterized by the white noise process (Cherniawsky et al. 2004). Also the block averaging acts in a similar way and reduces the instrument noise and other errors that have their spatial scales smaller than the grid size. However, the mapping process into the regular grid decreases the resolution of the data. One therefore must compromise to obtain not too coarse resolution of the accurate data. Because of the above arguments various grid sizes and averaging methods were tested to obtain the appropriate resolution monthly maps of SSHA of required accuracy. The mapping was performed by block averaging 18Hz monthly data, where the same weighting of data is applied to each data point in the grid box, and by Gaussian weighting, where the weighting decreases with distance from the centre of the grid box in the same way in both directions. Grid sizes of 0.5°x0.5°, 1°x 0.5°, 2°x1° were tested. It was decided to use the smallest grid size (0.5°x0.5°) for the analysis of Chapter 3 and 4 because it was found that the grid size does not affect the results greatly but it provides the greatest resolution. For the analysis performed in Chapter 5 the more accurate Gaussian gridding with lower resolution of 1°x 0.5° was used, because the better accuracy of the SSHA was needed. The interpolation was done using a Gaussian function with isotropic distance weighting from the center of the grid box towards boundaries with the search radius of 60km and the full width half maximum equal to 100km. The later analysis described in Chapters 3-5 was performed on the monthly corrected and mapped SSHA.

2.1.3 Method of offset removal

Due to the different retracking methods used to obtain the SSHA in the ice-covered and open ocean an offset in height between the two datasets emerged. CPOM did not understand a physical reason for the offset and therefore it was decided for the purposes of this PhD to take the statistical approach to understand its behavior and develop a method to correct for it. The problem of the offset was not reported previously in the literature and therefore in this section the nature of the offset is investigated and a method of its removal is designed. There are no possible physical reasons that could explain the offset between the SSHA from the open ocean and its ice-covered part. The only candidates that could cause it may be different retracking models used for the SSHA retrieval from the two different environments. Therefore, one can state that the height offset between SSHA from the open and the ice-covered ocean is attributed to the different processing techniques used to obtain SSHA measurements in the ice-covered seas and in the open ocean (Peacock and Laxon, 2004). Because the exact reasons are not know the statistical approach was taken to investigate its nature and behavior. Firstly, the nature of the offset was investigated, by addressing these questions: Does the offset vary in time and space? Is it a constant value? If so, can it be easily removed? A method of the offset removal was established and is described below in the remainder of this section.

The Envisat RA-2 radar altimeter measures the SSH at a frequency of 18 Hz, corresponding to data points spaced by 0.37 km along the ground track of the satellite. However, not all the points along the track are statistically independent from each other. In order to estimate the number of independent data points in the data set, one needs to find the decorrelation length scale, which can be obtained by computing a mean autocorrelation function along the ground track for many orbits (altimeter tracks). In order to estimate the offset, the monthly SSHA is then spatially averaged into square boxes of the size corresponding to the decorrelation scales. Therefore, each point in the new, processed data is statistically independent from the others.

The decorrelation scales were calculated using two different approaches: by calculating (i) a mean power spectral density, and (ii) the mean autocorrelation function of the along track SSHA. In both cases only long orbits, with more than 70% data coverage across the basin were used for the estimation (about 30 orbits x 40 months= 120 orbits).

Furthermore, an individual orbit was not taken into account when the gaps in the data were greater than 1 degree of latitude/longitude. That reduced the number of orbits used for averaging to about 100, but it was enough to produce a smooth autocorrelation function and spectrum. Due to the length of the orbits in two data sets, only the open ocean SSHA was taken into account for this calculation.

Mean Along-track Autocorrelation Function of Sea Surface Height

The aim of the analysis is to estimate the monthly offset assuming it does not change in one month. Therefore the autocorrelation function is assumed to be the one-dimensional autocorrelation function of the SSHA versus the altimeter distance. The autocorrelation of discrete time series is simply the correlation of the signal against a time-shifted version of itself. The autocorrelation ***R*** at lag ***k*** for a discrete process $X \in [X_1, X_2, X_3 ... X_n]$ with known mean μ and variance σ^2 in time ***t*** is:

$$R(k) = \frac{1}{(n-k)\sigma^2} \sum_{t=1}^{n-1} [X_t - \mu][X_{t+k} - \mu] \qquad \text{EQ. (2.1}$$

Where ***R*** is a correlation coefficient with a range *[-1 – 1],* with *1* indicating a perfect correlation and *-1* indicating a perfect anti-correlation. This applies for any positive integer where the time lag is smaller than the total length of the signal *(k<n)*.

The decorrelation scale of the SSH informs about typical spatial (the altimeter is moving in space) and temporal (the altimeter is moving in time) scales of variability. Furthermore, it provides information about physical characteristics of the ocean dynamics. For example, sea surface height anomaly (SSHA) measured on the edge of a mesoscale eddy should not be correlated with the SSHA of another eddy. Therefore, decorrelation scale also informs about the scales of the circulation in the region. However, the long periods (wavelengths greater than the eddies) also influence the decorrelation, their effects can be evident as oscillations of the autocorrelation function. Furthermore, long periods also cause the correlation to decay more slowly. Spatial and temporal averaging improves an estimation of the scales and was performed in this study. Autocorrelation functions were calculated for each orbit (ground track) and then averaged to produce the final estimate of the decorrelation scale. It was assumed that the

decorrelation scale for the SSHA is isotropic in both horizontal directions. The result is shown in Figure 2.10 as a two-sided autocorrelation function plotted against lag (distance). Note that the maximum value is located for a lag equal zero. It can be seen in Figure 2.10 that the autocorrelation coefficient *(R)* decays rapidly from 1 at zero lag to about 0.35 at lag=10, which corresponds to 65% decrease in the correlation during the first 3.7 km. A similar decay of autocorrelation function was obtained for simulated random white noise, which suggests that the altimeter measurements taken along very small distances (less than 3.7 km) are dominated by the altimeter instrument noise, which is random (white) and occurs for the short spatial scales. For the along-track measurements separated by distances greater than 3.7 km and up to *ca.* 30 km the correlation coefficient decays slowly, indicating a moderate correlation between these points. The autocorrelation function becomes flat when the distance reaches about 25-30 km, therefore the points separated by greater distances than about 50-60 km are uncorrelated with each other. This point was picked up for the further analysis as an indicator of the average decorrelation scales in the Nordic Seas.

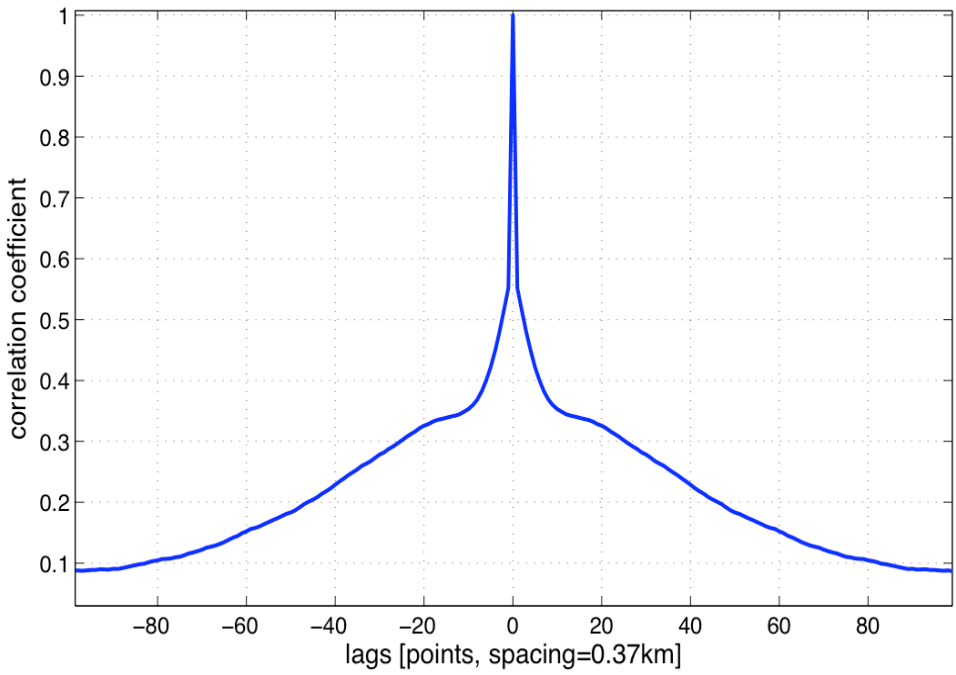

Figure 2.10. Mean Autocorrelation function calculated for the Nordic Seas. Lags correspond to the distance along the track of Envisat satellite. The spacing between the lags is 0.37 km.

Along-track Spectrum of the Sea Surface Height

Power spectral density (PSD) describes how the power (or variance) of a time series is distributed with frequency. A spectrum of the along-track SSHA informs about the scales of the circulation (e.g. diameters of eddies, sub-basin and basin scales of circulation etc.) and therefore computing the spectrum is a different method of estimating the decorrelation scale.

The spectrum of an along-track SSHA was computed for each orbit using Welch's method (Welch, 1967) and a Hamming window (Emery and Thomson, 2001). The same orbits were used as for the autocorrelation method. All obtained spectra were averaged together. The averaged spectrum is shown in Figure 2.11 and describes a gradual flow of energy from the low to high frequencies (large to small spatial scales respectively). The slope of the spectrum changes at about 0.2 Hz (50 km), which indicates a change in the scales of circulation from the large scales, which are dominated by a geostrophic flow (the low frequencies), to the smaller scales dominated by eddies. The break point in the spectrum corresponds to the diameter of the largest eddies which is approximately 50 km. It can be concluded from Figures 2.10 and 2.11, that the upper limit of the decorrelation scale is about 50 km.

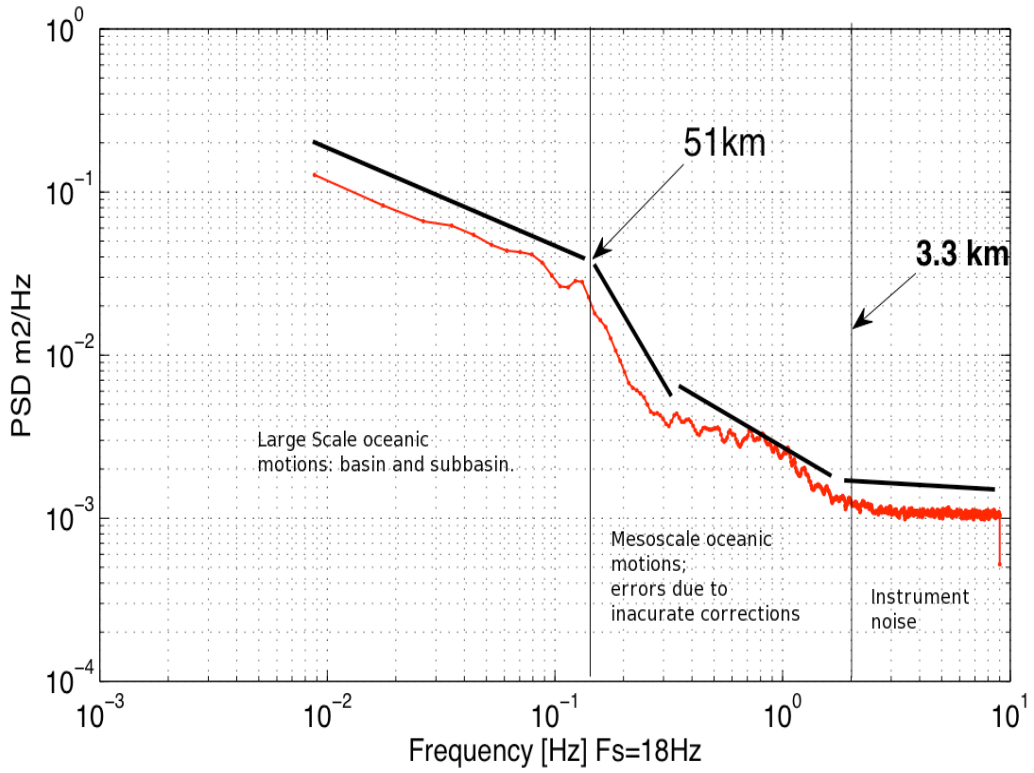

Figure 2.11. Mean along track spectrum. Y-axis – Power Spectral density [PSD: $m^2\ Hz^{-1}$], X axis – Frequency [Hz]. The sampling frequency (Fs) is equal to 18 Hz, thus the spectrum is calculated from ½ Fs=9Hz to 0.01 Hz. Note that 1 Hz corresponds to 7 km.

Offset estimation

The spectral analysis and the mean autocorrelation function showed that the average decorrelation scales in the investigated region are certainly less than 50 km. Underestimation of the decorrelation scale could produce errors in the further analysis. Therefore 50 km was used as the upper limit of decorrelation scale. In reality the mean decorrelation scales could be less than 50 km, because the scale computed here is an average over the whole Nordic Seas and it could vary with a position. Therefore, it was decided that the offset should be estimated using 50 km x 50 km boxes. The method of offset estimation is described below.

In order to grid the data into 50 km boxes, the coordinates of each measurement were converted from degrees to km. The distances in meridional (North-South) and zonal (East-West) were calculated from a reference point located at 58°N, 61°W. Each data set (open ocean and ice-covered ocean) was averaged into squares of side 50 km (blockmean) and the resulting means for each data set were located on the same grid locations. The offset was obtained by subtracting the monthly mean ice value from the monthly mean ocean value for grid boxes where both were found in the same time period. The resulting histogram of the offset distribution is shown in Figure 2.12. The mean of the population is 17.69 cm with standard deviation equal to 10.17 cm and a standard error of 16 mm. The results show that the SSHA in the ice-covered seas is on average 17.7 cm lower than the SSHA in the open ocean. The Kolmogorov-Smirnov (K-S) test was performed on the offset data to check whether the offset has a normal distribution. However, the data did not pass the test, which could be caused by the outliers within its distribution caused by the errors in the SSHA. Fitting a Gaussian function to the offset frequency distribution (Figure 2.12) confirmed that the offset corresponds to a Gaussian distribution in the proximity of its mean but its tails do not fit it well. The monthly mean offset was found to have a normal distribution, which was confirmed by passing the K-S test with 95% significance levels.

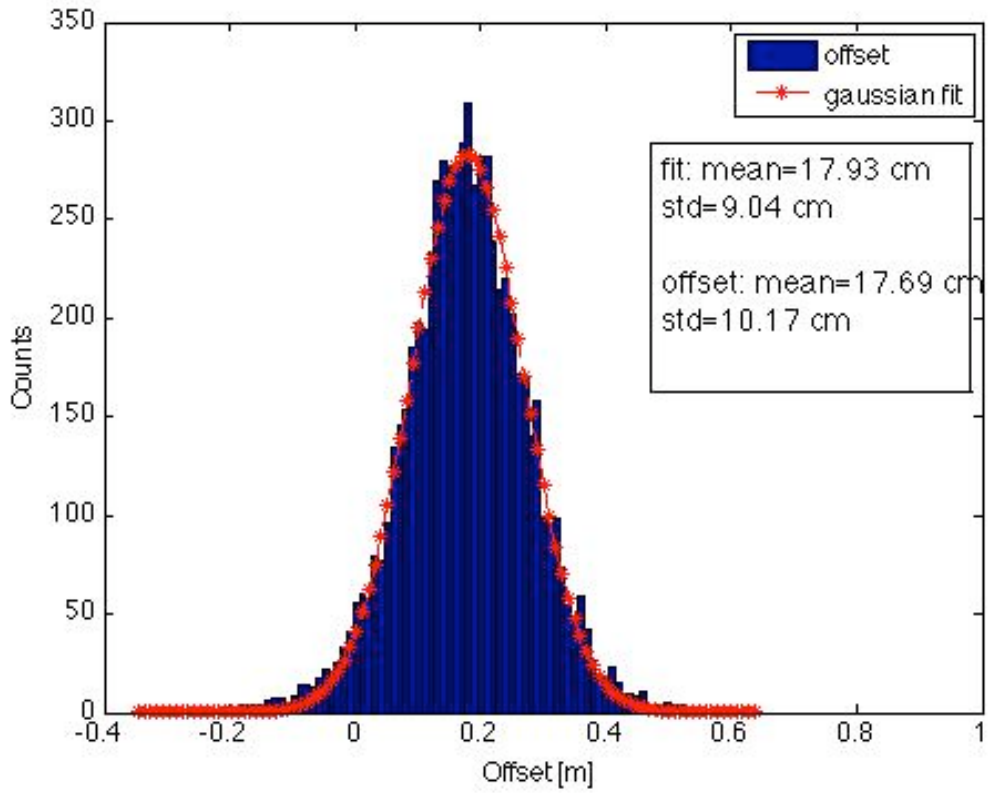

Figure 2.12.Histogram of the offset (blue) and the Gaussian fit (red).

The time series of monthly means of the offset are shown in Figure 2.13. The linear regression was applied to the data visible in Figure 2.8 to see if there is a linear trend is present. The slope was found to be 0.00021m/month and 0.00335m/month for the data weighted by the monthly standard deviation about the monthly mean and the standard error for these estimations was 0.00015m/month and 0.00219m/month. The slope was found statistically not different from zero according to the results of Student t-test with p-values equal to 0.18 for the non-normalized and 0.13 for the normalized data. Therefore, the statistical tests confirmed that the monthly offset estimations do not have any linear trend in the analyzed time period. Variations visible in the monthly means could be caused by natural variability of the ocean circulation within a month, variations in the number of points used for averaging, inaccurate sea state bias correction and noise in the measurements. The greatest number of the independent offset estimations and therefore the greatest accuracy was during the summer from June to August with maximum of 194 estimates in July 2003 and minimum in March 2003 (only 3 estimates). On average 78 estimates of the offset were done in a month.

The offset was calculated in the overlapping regions between the two datasets, which are the regions where the ice edge occurs. The important problem in the offset estimation is that the measurements in these regions can have the greatest errors due to the large number of missing data and therefore the variation of the offset is quite large, its range is equal to about 15 cm. The mean monthly offset was found to be 17.63 cm with a standard deviation of 3.57 cm. In summary, the offset in the data was found to be random with no temporal or spatial trends. The precision of the mean offset estimation is very high (standard error = 16 mm) due to the large number of independent measurements in the overlapping regions over the 7 years. The above results confirm that adding the offset mean to the SSH from the ice-covered ocean is an appropriate method of removing the height difference between the two data sets. Therefore, in order to correct for the offset, 17.63 cm were added to the ice-covered SSH dataset (18Hz).

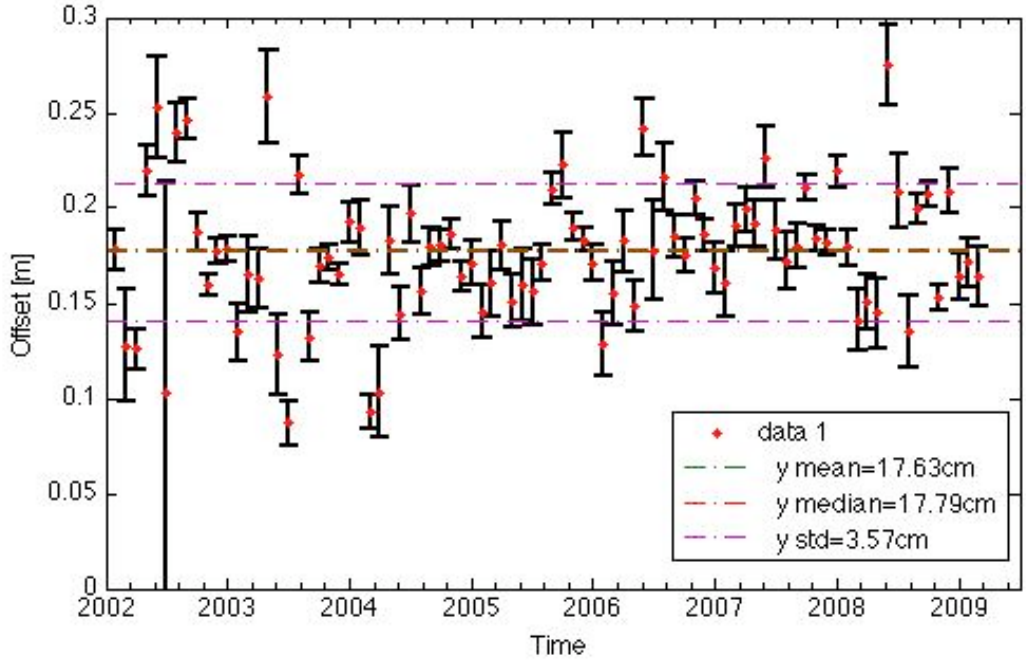

Figure 2.13. Monthly offset: mean and the error bar showing 95% confidence intervals about the mean. The labels of the X-axis show September in a given year.

2.3 Atmospheric products

2.3.1 ECMWF products

The monthly means of air-sea fluxes and wind stress (analyzed in Chapter 4) were obtained from the ERA-Interim model reanalysis produced by European Centre for Medium-Range Weather Forecasts (ECMWF) (Dee et al. 2011). In this section the description of the dataset is presented. The fluxes include only local fluxes between an atmosphere and ocean and not into account local and remote terrestrial (river run-off, glacier melting) and sea-ice freshwater sources.

The ECMWF model assimilates in-situ observations including meteorological reports, measurements from ship and land stations, measurements made by radiosondes and aircraft and remotely sensed satellite measurements that include data from altimeters, scatterometers and microwave sensors. The number of assimilated data per day has increased from 10^6 in 1989 to 10^7 in 2010 due to the increased satellite measurements (Dee et al., 2011). Despite the large number of data assimilated, the output fields are sensitive to the model physics and have their own limitations and errors (Trenberth et al., 2009). Furthermore, the resolution of the fields is quite low and is equal to 1.5˚ in both directions (~125 km). The main characteristics of the relevant ECMWF products are presented below. More detailed description of the model physics, assimilated fields and the performance of the system were described by Dee et al. (2011).

Net Heat Flux [W m^{-2}]

The surface heat budget can expressed as the net total heat flux at the air-sea interface:

$$\mathbf{QT = QS - QU = QS - QE - QH - QB} \qquad \textit{Eq. 2.2}$$

Where QS is the solar (shortwave) radiation flux, QU is net upward heat flux emitted by the ocean, QE is latent heat flux (evaporation), QH is sensible heat flux and QB the net outgoing long-wave radiation flux.

The turbulent terms (QE and QH) are estimated from the ECMWF model surface meteorology fields, and the short-wave and long-wave terms are obtained from the

radiative transfer component of the atmospheric model. The sensible heat flux is an order of magnitude smaller than the latent heat flux but it is important in the regions where very cold air is advected over the ocean from the neighboring land. This component of the net heat flux can be therefore important in the Nordic Seas. Both turbulent heat fluxes (latent and sensible) can be estimated from the near sea surface wind speed, air-sea temperature difference and air-sea humidity. However, the relationship is poorly known at the high wind speeds (Josey, 2010). The shortwave radiation is the function of solar elevation, cloudiness and albedo, whereas the long-wave radiation is the difference between the upwelling and downwelling radiation and depends on the sea surface and air temperatures, humidity and cloudiness. The ECMWF net heat flux is underestimated in the Nordic Seas, because it does not include the ice-ocean heat flux in the ice-covered ocean (Simonsen and Haugan, 1996).

Evaporation [m]

Evaporation is the same as the latent heat flux (QE) in Eq. 2.2

Precipitation [m]

The estimation of precipitation by the reanalysis model is based on the temperature and humidity that are derived by the model from the assimilated observations (Dee et a. 2011). In the regions where the in-situ observations are sparse, greater uncertainty in the precipitation can be caused by lack of measurements from rain sensors (Weller et al., 2008). This in effect would affect the net freshwater flux that often has a greater error in comparison to the net heat flux error (Josey, 2010).

Wind Stress [N m^{-2}]

Assimilation of QuickSCAT data by the ECMWF model from 2002 resulted in a major improvement of the wind products. The reanalysis wind stress is in good agreement with remotely sensed observations and in-situ wind measurements (Simmonds et al. 2007, Jakobson et al. 2009).

2.4 Numerical Ocean Model Output

Ocean general circulation model (OGCM) output was used in the analysis of Chapter 5. The OGCM is the Nucleus for European Modelling of the Ocean (NEMO) model output from the National Oceanography Centre, Southampton, UK (Barnier et al., 2006). The model global mean spatial resolution is 0.25° but increases poleward. In the Nordic Seas the horizontal resolution of the model is about 16 km at the 60^0N and about 12 km at 80^0N. The model has 75 vertical levels and is interfaced with the ice model (Louvain la-neuve Ice Model) and with several atmospheric general circulation models (Madec, 2008). The model uses the ORCA tri-polar, curvilinear Arakawa C grid (Madec et al., 1999) and the ETOPO2 (Smith and Sandwell, 1997) bathymetry that is interpolated onto the model grid (median over each grid cell). The model was forced by the DFS3 set of surface fluxes, developed through DRAKKAR consortium to develop ORCA025-NEMO system (Marsh et al., 2010). Series of control experiments were run recently by Grist et al. (2010) and it was found the model has got a realistic representation of the Atlantic MOC. The model grid in the Nordic Seas is presented in Figure 2.14. In this study the monthly means of the model sea surface height and both components of the ocean and wind velocity from January 1968 to December 2007 (40 years) were used for the analysis described in Chapter 5.

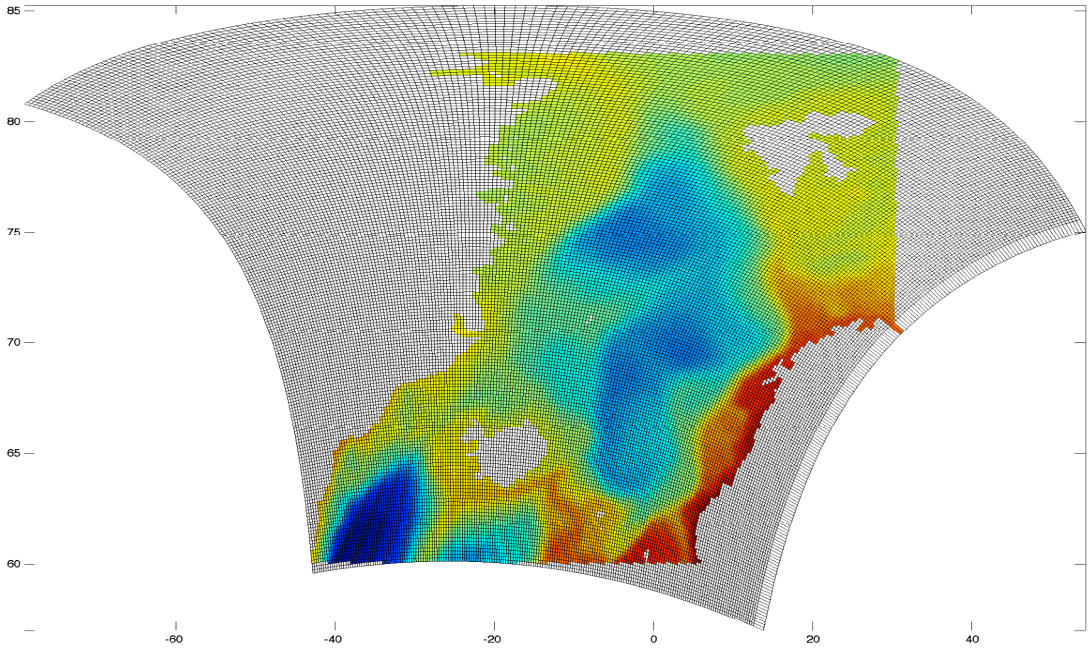

Figure 2. 14. Example of the NEMO grid in the Nordic Seas, the color shows mean SSH in 2000-2007.

CHAPTER 3: SEA LEVEL VARIABILITY IN THE NORDIC SEAS.

3.1. Introduction.

As shown in Chapter 1, our knowledge about variability of the circulation in the Nordic Seas is limited mostly due to the difficulty of gathering in-situ and remotely sensed data from the region. Very little data is available during the winter when sea ice covers a substantial part of the Nordic Seas. Very important regions in terms of the local and global climate are covered by sea ice not only during winter. Fram Strait, the East Greenland Current and the Greenland Sea are hardly accessible during winter but also during other seasons (see Chapter 1). The East Greenland Current is the main current carrying liquid freshwater and sea-ice from the Arctic to the Atlantic via Fram Strait, the main connection between the Arctic and the Atlantic oceans. Only by obtaining data from the ice-covered regions we can fully understand the changes in the Nordic Seas and their effects on the global thermohaline circulation. The new data processed by applying the novel technique of Peacock and Laxon (2004) to the Envisat altimetry is used here to describe for the first time the variability of the sea surface height (SSH) in the whole Nordic Seas on seasonal to interannual timescales during the recent 7 years: from November 2002 to October 2009. The SSHA data analyzed here were corrected and processed as described in Chapter 2 (Section 2.2) and consist of the monthly and mapped (blockmean) data (0.5°x0.5° grid). The analysis of the sea level variability is followed by the investigation of the forcing mechanisms causing the variability. This examination is started with analysis of the links between the SSHA variability and the North Atlantic Oscillation (NAO) and Arctic Oscillation (AO) that are obvious atmospheric forcing candidates for the regional SSHA (See Chapter 1). A more detailed analysis of the atmospheric forcing is performed in Chapter 4. In section 3.2 the mean seasonal cycle of the SSH in the Nordic Seas is described and this is followed by the analysis of the inter-annual SSH changes in Section 3.3. Harmonic functions are used to describe the amplitude and phase of SSH in Section 3.4. In order to explain the spatial and temporal SSH variability, Principal Component Analysis (PCA) is used in Section 3.5. The relationship between SSH and the NAO and AO is investigated in Section 3.6. Finally this chapter is summarized and discussed in Sections 3.7 and 3.8.

3.2. Mean seasonal cycle of sea surface height anomaly in the Nordic Seas.

The mean seasonal cycle of the sea level height anomaly (SSHA) in the Nordic Seas is shown in Figure 3.1, where the data have been averaged into calendar months for January to December. It can be seen that in January sea level is high (about 10 cm) off the east coast of Greenland and depresses to the centre of the basin, reaching an anomaly of -15 cm and increasing again towards Norwegian coast. From May the sea level becomes higher in the centre of the Nordic Seas and lower close to the Greenland and Norwegian coasts. The height of the sea surface increases further in time in the Greenland and Norwegian Sea gyres and decreases in the areas corresponding to the EGC and the Norwegian Atlantic Current. September is characterized by a strong gradient perpendicular to the East Greenland coast. The sea level is lower to the west and higher to the east, reaching a maximum of 20 cm above the mean in the Norwegian Gyre and along the Norwegian coast. A maximum of about 20 cm is reached in the whole basin in October and then starts falling again from November, reaching a minimum of – 20 cm in April.

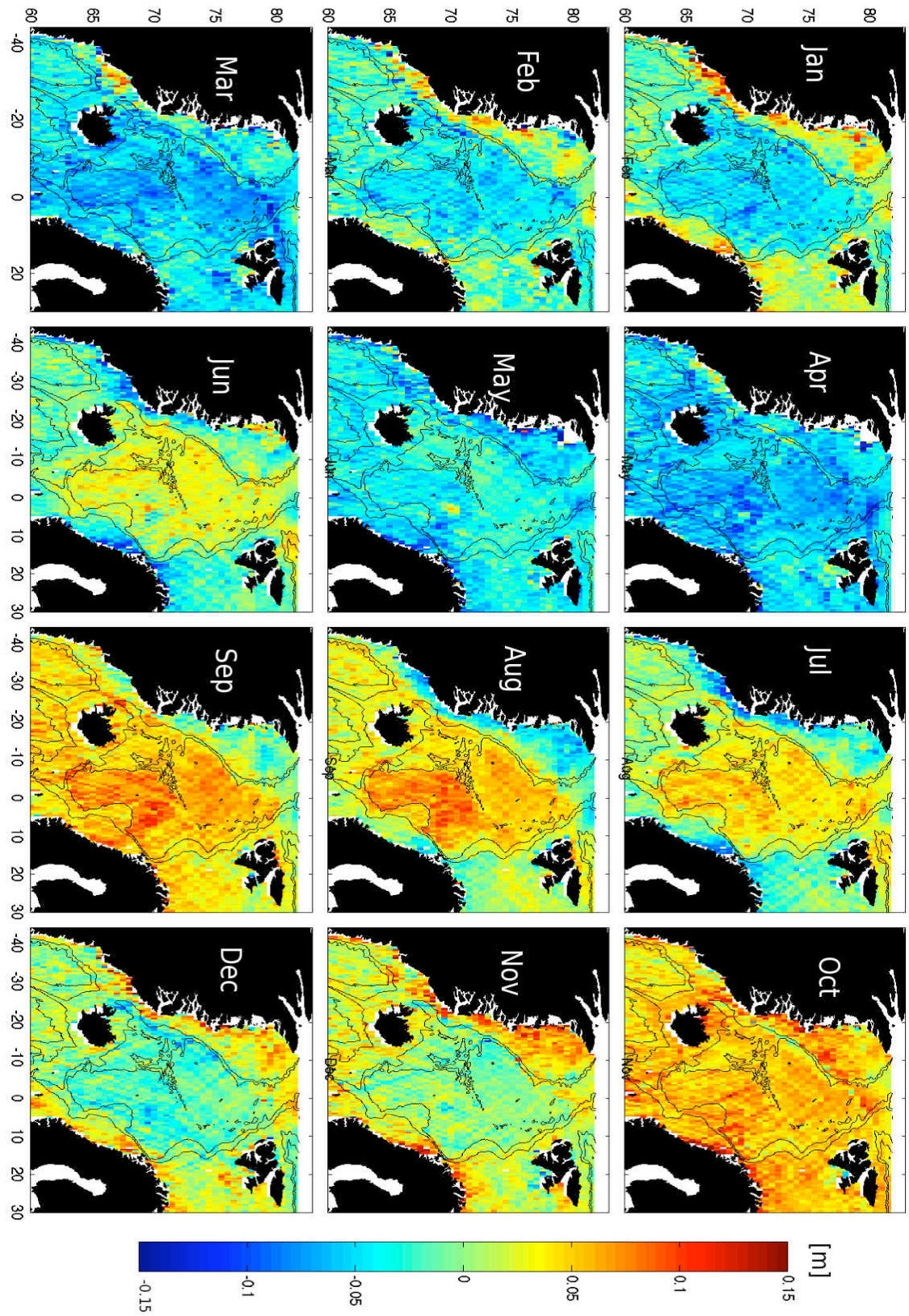

Figure 3.1. Mean seasonal cycle of sea level height anomaly [m] with 1000 m and 2000 m depth contours (black). Maps are averaged into calendar months for the period: November 2002 – October 2009.

3.3. Interannual variability of the sea level in the Nordic Seas.

Figure 3.2 shows the variability presented as a standard deviation (no detrending) of SSHA in the Nordic Seas in the investigated time period (November 2002 – October 2009). The greatest variability in the Nordic Seas was observed along the Norwegian and East Greenland coasts, with the amplitude reaching 15 cm (Figure 3.2), during the period from November 2002 to October 2009. Also high variability with amplitudes reaching 10 cm was observed in the Norwegian and Greenland Seas and along the ice-edge extending from Svalbard to Greenland. Furthermore, the sea level in the coastal zones to the north of Iceland and south of Svalbard varied with amplitudes exceeding 10 cm in the analyzed 7 years. High variability in SSHA was also observed in the Lofoten Basin (Figure 3.2) that could be caused by the high anticyclonic eddy activity observed in this region in the past (Rossby et al., 2009, Kohl et al. 2007). Furthermore, the high variance in SSHA along the Norwegian coast could be associated with the Norwegian Coastal Current (Johannessen et al., 1989). A significant increasing linear trend in SSHA was also found on the eastern continental shelf of Greenland, in the Denmark Strait and Barents Sea (Figure 3.2 bottom). However, the inspection of the SSHA in these regions indicated that the sea level increased until 2007 and decreased again after that. The major contribution of this section was the finding that the sea level varies greatly in the ice-covered part of the Nordic Seas. This finding provided many questions that will be addressed in the remaining of this Chapter: What causes this variability? In which months this variability occurs? Which periods are contributing to this variability?

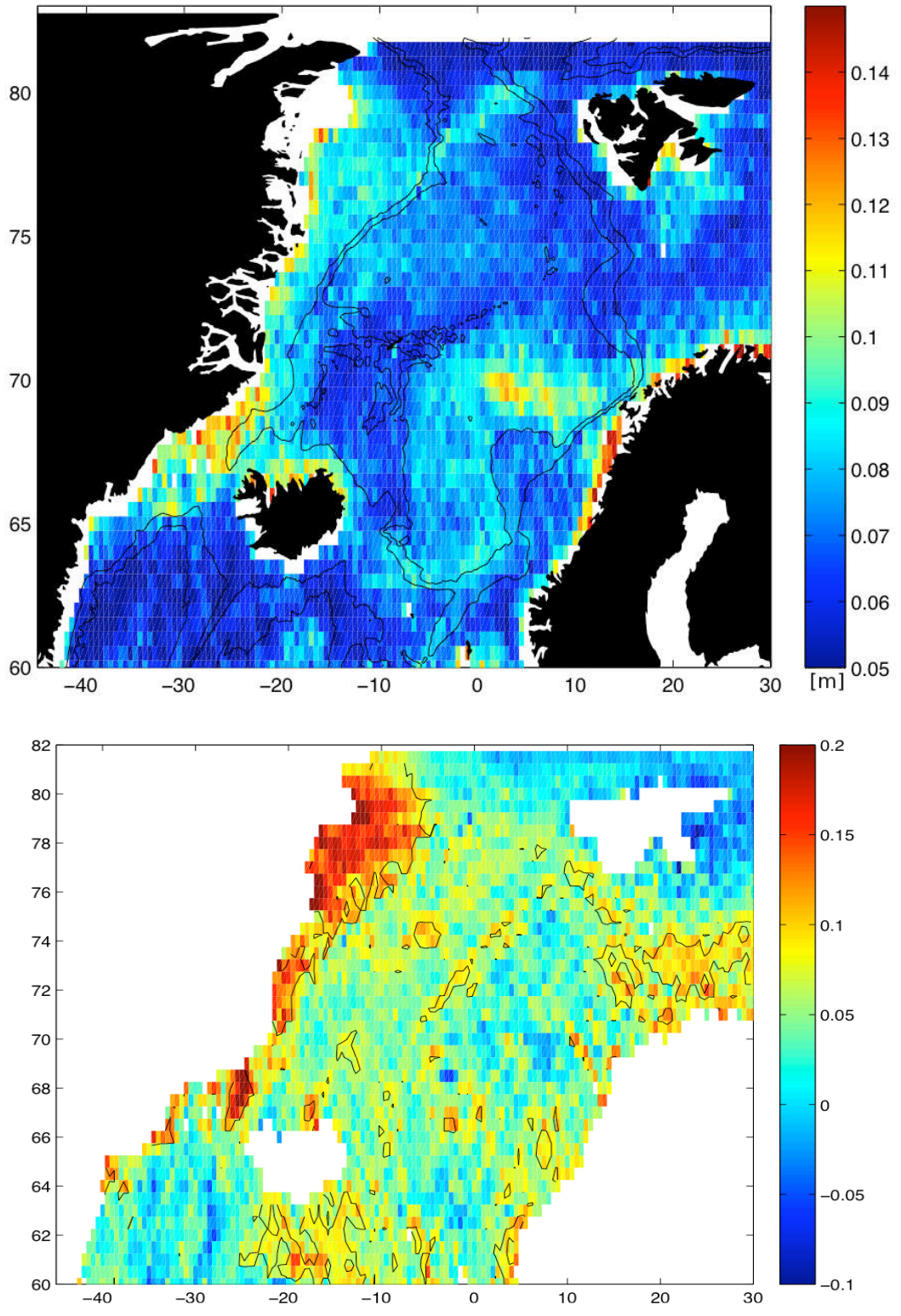

Figure 3.2. Top: Standard deviation [m] for 7 years (Nov 2002-Oct 2009) of SSHA in the Nordic Seas with 1000 m and 2000 m depth contours (black). Bottom: Trend [cm/month] with 95% significance level contoured in black.

The inter-annual variability of SSH was estimated by calculating the standard deviation of sea surface height anomaly in each calendar month for the seven years of observations (no detrending). The variability in SSH is shown in Figure 3.3. A few areas show very high variability with amplitudes reaching 10-15 cm. Among them is the east Greenland continental shelf that appears very patchy from January to April (winter) and shows exceptionally high amplitudes in October. The ice concentration contour, over plotted in Figure 3.3, indicates that increased October variability along the continental shelf of Greenland can be associated with ice processes: transport of the sea ice through the Fram Strait or changes in the formation and melting rates. De Steur et al. (2009) also found increased variability of the liquid freshwater export in the EGC at 78.5°N during September.

During spring and early summer the inter-annual variability is small (less than 10cm) and becomes greater in the autumn and winter. Some of the variability shown in Figure 3.3 can be associated with noise in the data, especially in the regions of strong tides where the tidal correction could be inaccurate (e.g. in Denmark Strait, see Chapter 2). Also the satellite tracks are visible because the signal to noise ratio is smaller for Figure 3.3 when comparing to Figure 3.1. Figure 3.3 shows the monthly variability in relation to the monthly mean (Figure 3.1) and therefore was obtained with less averaging. Also the individual monthly SSHA maps have got a higher noise level and therefore satellite tracks can be distinguished. This also could be associated with the nature of the errors and grid size used to map the along-track SSHA data. In the later Section the variability will be further analyzed by application of the Principal Component Analysis. The method can also be useful to indicate statistically what is the noise level in the mapped SSHA (Section 3.5).

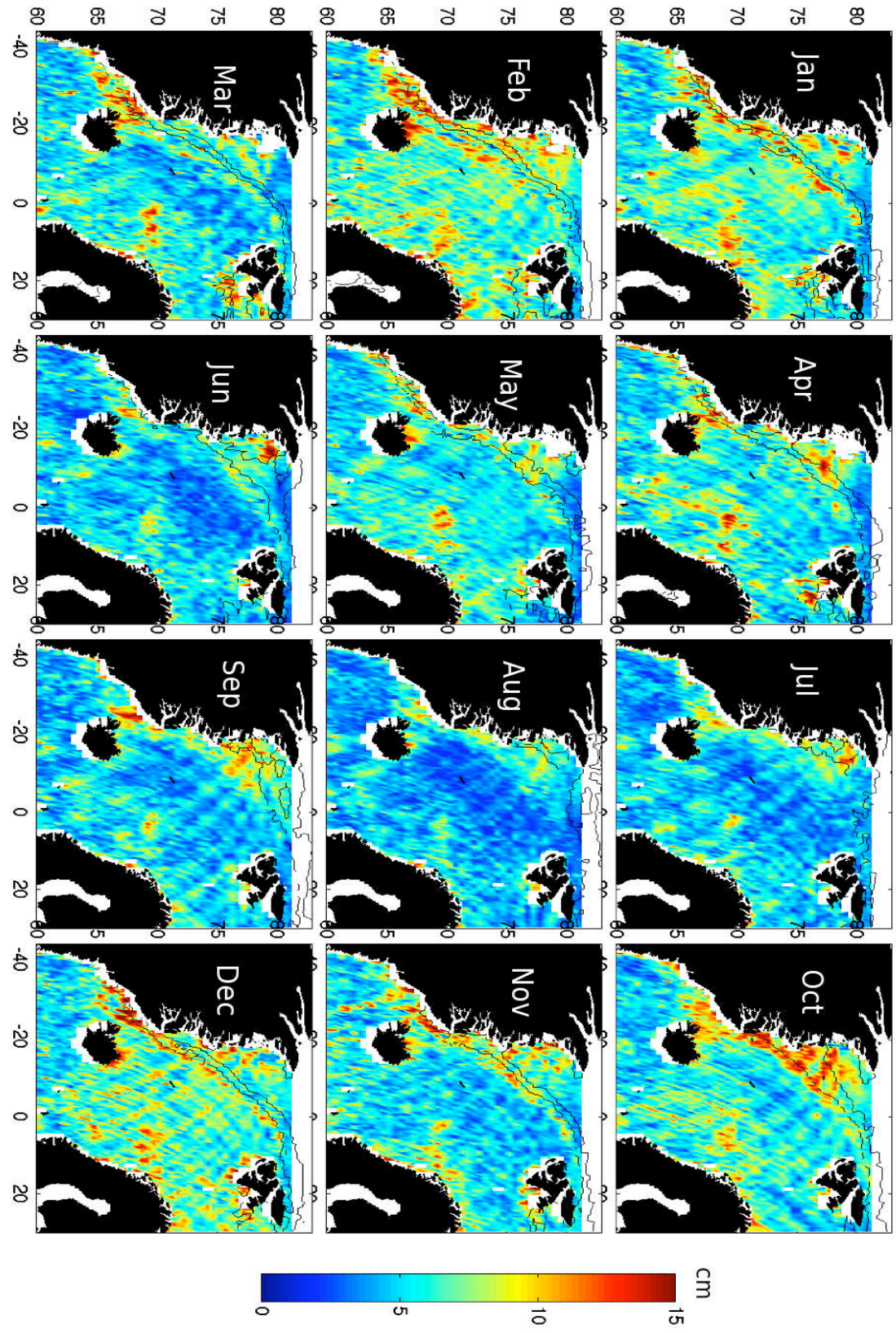

Figure 3.3 Inter-annual variability of sea level presented as standard deviation of SSHA in a given month [cm] with over plotted contours of 75% and 85% mean sea-ice concentration for a given month (black) in 2002-2009.

3.4. Harmonic Analysis.

Harmonic functions of various frequencies were fitted to the SSH data at each grid point (location) to find the most important frequencies in the SSH signal:

$$SSH(time,longitude,latitude) = A\ sin(\omega t + \varphi) \qquad \text{EQ.3.1}$$

where A is fitted amplitude, ω is frequency and φ is phase of the sine wave. Prior to the harmonic analysis the altimeter data were detrended (the average and linear trend were removed from each grid point) and missing data were linearly interpolated in time. Furthermore, the regions with fewer than 20 months of data available were removed. On average only 5% of data were missing during the 7 year long period (See Chapter 2). There were a few periods when problems with the satellite occurred (March 2003, May and June 2006) that caused an increase in the number of missing data (but only up to about 30%).

It was found that the annual cycle is the dominant signal in the SSH time series and explains on average about 36% of the total SSHA variance. The amplitudes of different harmonics averaged over the whole Nordic Seas are shown in Figure 3.4. The mean amplitude of the annual frequency in the Nordic Seas is 4.5 cm whereas the higher frequencies have much smaller amplitudes, about 1.5 cm. The spatial pattern of the amplitude and phase of, and variance described by, the annual harmonic is shown in Figure 3.5. The annual amplitudes vary between 2-12 cm, with the largest amplitudes observed in the deep basins: the Greenland, Norwegian and Lofoten Basins and along the Norwegian coast. The smallest annual amplitudes are associated with EGC, Irminger Sea and Barents Sea. The results are consisted with the observations of Mork and Skagseth (2005) indicating a similar spatial pattern of the annual harmonic in the Nordic Seas. However, the amplitudes they observed in the ice free regions of the Nordic Seas were lower (4-8 cm), which could be due to: greater spatial averaging, different time of their observations (May 1995 - February 2002) and different altimeter used (ERS and TOPEX merged). The results show that most of the variability in SSH can be explained by the annual harmonic in the deep basins of the Nordic Seas, where the amplitudes are high (Figure 3.5). Part of this contribution could be also noise, which could also have significant amplitude at the annual frequency. Many applied atmospheric corrections and orbit errors could therefore contribute to the annual signal.

Furthermore, the number of missing data also varies annually causing the greater total error in the winter (Section 2.2.1). However, the pattern of missing data (Figure 2.2) is not similar to Figure 3.5. The errors caused by atmospheric corrections are much smaller than the observed amplitudes of the annual signal (Chapter 2, Chapter 3: Section 3.5). The maximum of sea level occurs earlier in the deep basins of the Nordic Seas (August and September) and later at the continental shelf of Norway and Greenland and in the shallow seas. The phase (month of the maximum SSHA) contours overlay isobaths and the maximum amplitude in the annual cycle propagates from the interior of the Nordic seas outside, towards boundaries and shallow regions. At the eastern border of the Nordic Seas the maximum occurs in October and November whereas at the western border the phase changes gradually from the deep areas towards the coast of Greenland and the maximum occurs there much later than for the rest of the Nordic Seas (October to December/January). The spatial annual phase pattern is consistent with the previous studies of Mork and Skagseth (2005) and Furevik and Nilsen (2005) in the ice-free regions. However, our results suggest the outward propagation of the annual signal from the interior towards the shallower areas whereas the previous findings [Mork and Skagseth (2005), Furevik and Nilsen (2005)] show the eastward propagation. That disagreement is caused by the lack of SSH data in the ice-covered regions in the previous studies, especially during the winter, when the maximum in the annual cycle occurs in the ice-covered regions.

The semi-annual harmonics are important in the western Fram Strait and Norwegian Sea where the amplitudes can reach up to about 5 cm (Figure 3.6). This finding is consistent with the mooring observations in the Fram Strait where no clear annual signal was found but higher frequencies dominated the signal (Fahrbach et al., 2001). Furthermore, the higher amplitudes of semi-annual harmonics were found in the Lofoten Basin, where mesoscale activities are important (Rossby at al., 2009). Recent observations (Poulain et al. 1996) and results of numerical models (Kohl et al., 2007) found a semi-permanent anticyclonic eddy in the same area.

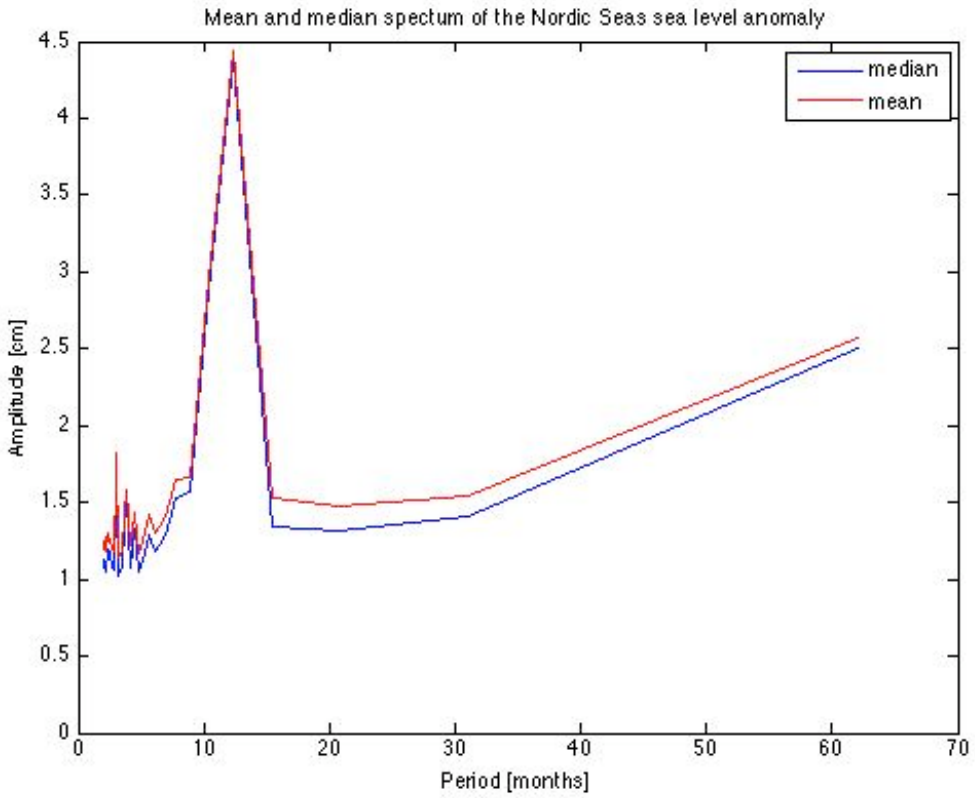

Figure 3.4. The mean amplitudes of different harmonic (sine) functions averaged over the whole Nordic Seas. X-axis shows period of the oscillation and Y-axis shows the amplitude in cm.

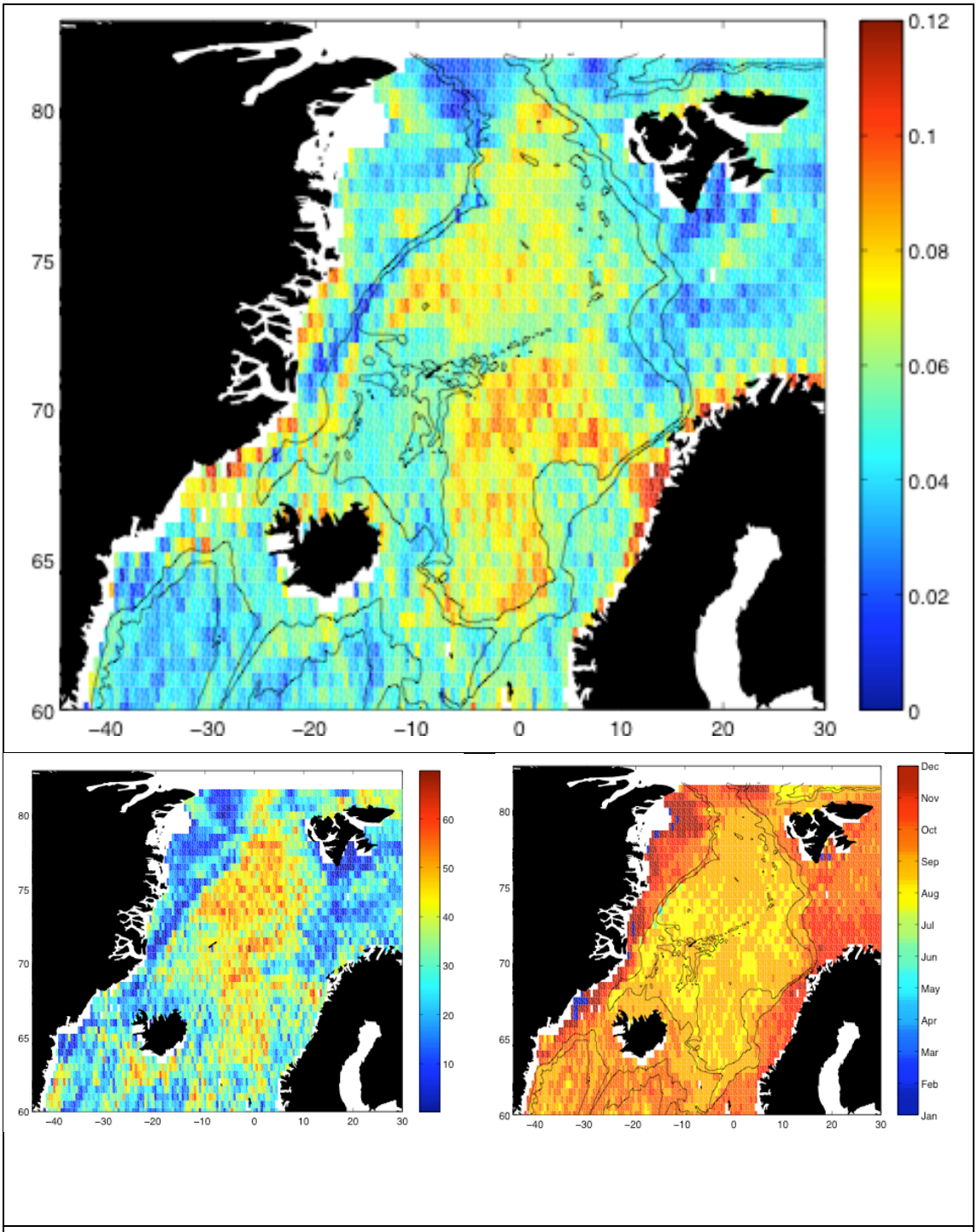

Figure 3.5. Map of the annual amplitude [m] (top), variance explained [%] (bottom left) and phase presented as month when maximum SSHA occurs (bottom right). 1000 m and 2000 m depth contours are also plotted in black (top and right bottom).

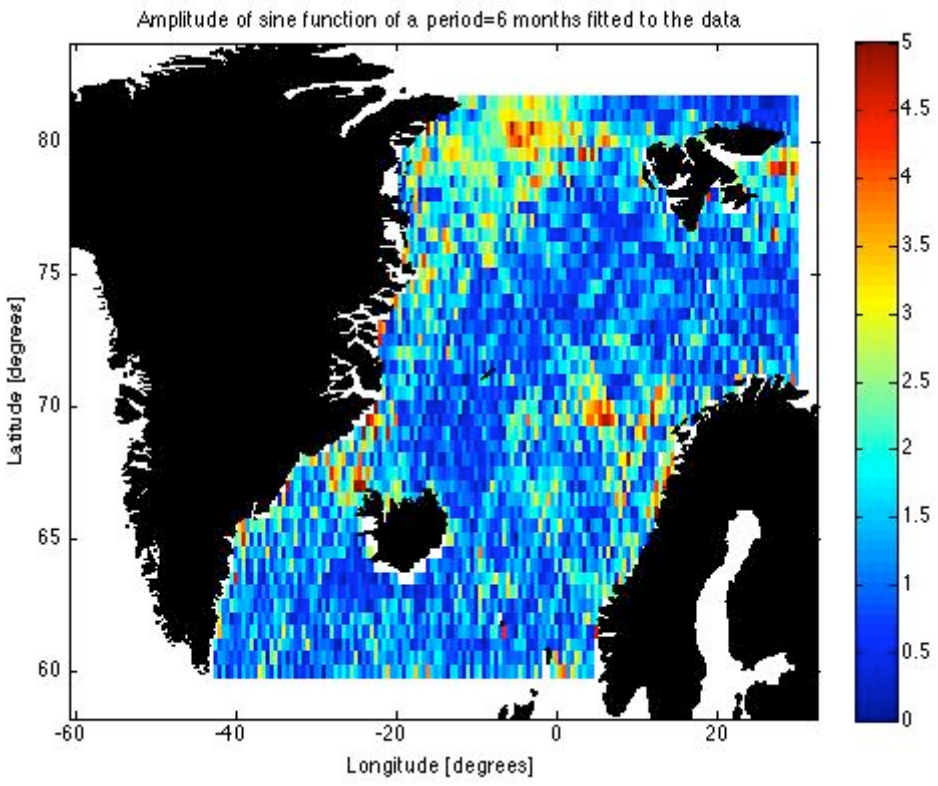

Figure 3.6.Map of the semi-annual amplitude of SSHA. Color Scale in cm.

3.5 Principal Component Analysis (PCA) of sea surface height.

In order to examine the spatial and temporal patterns of variability an Empirical Orthogonal Function analysis was performed. The Empirical Orthogonal Functions (EOFs) were calculated using Singular Value Decomposition (SVD; Linz and Wang, 2003) on the non-normalized SSHA data (covariance matrix):

$$SSHA(time,space\ (longitude\ x\ latitude)=U\sum V^T \qquad EQ.\ 3.2$$

Where U and V are orthogonal and $\sum$ is diagonal, the columns of U are the eigenvectors of $SSHA*SSHA^T$, columns of V are the eigenvectors of $SSHA^T*SSHA$ and singular values are the square roots of the non-zero eigenvalues of both $SSHA*SSHA^T$ and $SSHA^T*SSHA$ matrixes. A column of the SVD input represents time series of SSHA at one location point. The columns of V^T are the EOFs (spatial patterns of the modes of variability) and $U\sum$ are the coefficients of the EOFs (their Principal Components). Each EOF and its Principal Component (PC) defines a mode of variability, and their product recovers the signal, which this mode of variability describes. Therefore, the EOF analysis takes all the variability in the time evolving field and breaks it into standing oscillations patterns (EOFs) and its time series (PC). The EOFs are orthogonal to each other and their PCs are uncorrelated in time. The robustness of the mode was also investigated by repeating the analysis with: normalized data, weighted area data and decreasing the size of the region. These three approaches produced the same modes of variability as the one presented in Figures 3.8 and 3.10.

The aim of this section is to use EOF analysis to extract various modes of the spatial and temporal variability from the altimeter data and also to determine whether the EOF analysis can identifies the noise (assuming the noise is incoherent). Prior to the plotting, the spatial eigenvectors (EOFs) were multiplied by the square root of the corresponding eigenvalue, so they are scaled to represent the amplitude in real units per one standard deviation of the corresponding principal component (PC). On the other hand, the principal components were normalized by their standard deviation (no units). The amplitude of each PC, when multiplied by the associated scaled spatial pattern, recovers that part of time-series of the SSHA, which is related to that EOF. The EOF were obtained for the unfiltered SSHA and the seasonally filtered SSHA (Section 3.5.2).

The statistical significance of the EOF modes was tested using the method of Overland & Preisendorfers (1982). Firstly the autocorrelation time scale was calculated by

$$T_{SCALE} = \int_0^{t^*} a(t)dt \qquad \text{EQ.3.3}$$

where *a(t)* is a mean autocorrelation function and *t** is time needed for the function to reach zero. The time scale was *1.68* months for the unfiltered SSHA and *2.26* months for the seasonally filtered SSHA. The effective number of degrees of freedom was calculated by

$$dof = \frac{N}{Tscale} \qquad \text{EQ. 3.4}$$

Where *N* is the length of the record (84 months). It was found that the unfiltered SSHA has *50* effective degrees of freedom and the seasonally filtered SSHA have *37* effective degrees of freedom.

In order to determine which EOFs are significant and also to find what is the noise level in the SSHA data, one hundred sets of random, normally distributed data (with a mean of zero and standard deviation of one) of the same spatial size as the original SSHA data were generated and the EOF of those data were calculated. The temporal size of the random data had a dimension of the effective degrees of freedom. The obtained eigenvalues were compared to the real eigenvalues of normalized SSHA. The EOF mode is significant at 95% confidence level when its eigenvalue exceeds the eigenvalue of the randomly generated fields for 95% of time. The results showed that the first 3 EOF modes were significant above the noise level of 2.4% of the total variance. The significant modes account for 48.6% of variance in the data set.

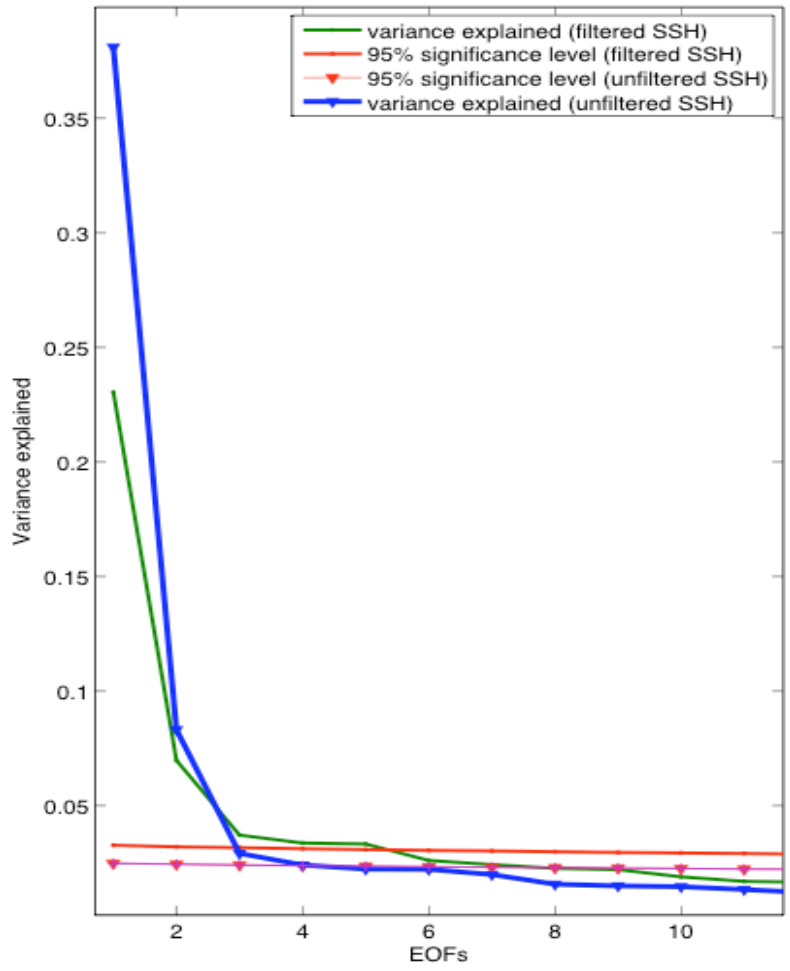

Figure 3.7. Results of Monte Carlo simulations (red) of singular values for EOFs on unfiltered (blue) and seasonally filtered SSH (green). Y-axis shows variance explained in % divided by 100 and the X-axis shows numbers of EOFs starting from the most important.

In addition to the Monte Carlo simulations, the modes were tested for uniqueness using the method of North et al. (1982). The method states that if the sampling error of a particular eigenvalue is comparable to or larger than the difference between the neighboring eigenvalues, than that mode is not unique and is comparable to the sampling error. Table 1 shows the properties of the significant modes that are distinct following the rule of North et al. (1982). It was found that mode 4 and all subsequent modes are not distinct and also not significant according to both methods. Furthermore, the first three EOFs obtained from unfiltered data are significant and distinct according to both methods. However, in the case for the EOF obtained for the seasonally filtered data, the Monte Carlo method suggests the first 3 modes are significant but North's method suggests the 3rd mode is not distinct. This suggests that the noise level of this mode is comparable to the size of a dynamical signal. Therefore, the filtered 3rd EOF needs to be analyzed and interpreted with caution.

Mode number	Variance %	Eigenvalue λ_j	Eigenvalue difference $\lambda_j - \lambda_{j+1}$	Sampling error $\rho\lambda_j$
1	35.80 [20.91]	7.74 [2.91]	5.60 [1.82]	1.19 [0.45]
2	9.88 [7.85]	2.14 [1.09]	1.49 [0.56]	0.33 [0.17]
3	3.02 [3.84]	0.65 [0.54]	0.15 [0.06]	0.10 [0.08]

Table 3.1.The percentage of the variance explained and the eigenvalues of the significant modes. Also the differences between the eigenvalue and the neighboring eigenvalue for each mode are listed with the associated sampling error. The values in the square brackets show the same properties for the EOF of seasonally filtered SSH. ρ is $\sqrt{2}/n$ where n is a number of independent samples.

3.5.1 PCA of the non-filtered data.

The three leading EOF structures of SSHA and their PCs are shown in Figure 3.8 All three leading PCs show oscillations of sea level at the annual and semi-annual frequencies. The first three components explain 49% of variance in the data.

First Principal Component

The first EOF explains 35.8% of the variance in SSH in the Nordic Seas and shows an oscillation mainly with annual frequency. The PC shows that the sea level is generally much lower during winter (January to April) and higher during summer. The 1st PC shows also a minimum in October 2006 corresponding to the exceptionally high sea level in that period. Its spatial structure is characterised by oscillations mainly in the deep basins and closely matches the topography (Figure 3.8). The amplitude of the 1st EOF changes at the continental shelves and the mid-oceanic ridges. This mode can be called a basin-wide coherent mode because it could correspond to the annual spin-up and spin-down of the circulation in the deep basins (This hypothesis will be tested later in Chapter 4). It explains most of the variability in the deep basins and up to 80% of variability in the Greenland Gyre (Figure 3.9).

The spatial structure of the 1st EOF is very similar to the annual harmonic shown in Figure 3.4. However, the annual cycle expressed by the 1st EOF is not simply the annual harmonic. The temporal differences between the 1st EOF and the annual harmonic confirm that the annual cycle in the Nordic Seas cannot be characterized only as a sine wave. The correlation coefficient (R equal to 0.77) between the first PC and the annual harmonic function indicates that the 1st EOF is highly correlated to the annual harmonic but the annual harmonic can explain only 60% of variance in the first PC. Also the differences between the two signals can be as large as the amplitude of the annual harmonic.

Second Principal Component

The spatial pattern of the second EOF shows depression of the sea level towards Greenland and Norwegian coasts and explains 10% of the total variance in the data (Figure 3.8). Because the sea level gradient relates via geostrophy to the surface currents, the second PC could be interpreted as the annual spin-up and spin-down of the Nordic Seas boundary current system (This hypothesis will be further tested in Chapter 4). The eastern (the Norwegian Continental Shelf) and western (the East Greenland Continental Shelf) margins are in phase with each other but in antiphase with the internal Nordic Seas. The structure of the PC also follows continental shelves and the bathymetric contours. The 2nd principal component shows that the pattern oscillates mainly with annual frequency with the maximum in late spring (May to July) and the minimum in late autumn (Nov-Jan). There are also longer period changes of this pattern, evident as a gradual decrease of the sea level until December 2006 and a gradual recovery to the original values after that time. This mode of variability explains most of the variance at the Continental Shelf of Greenland [up to 60%] and Norway [50-60%] and in the Southern Barents Sea [30%] (Figure 3.9).

The 2nd EOF could be caused by the wind stress curl over the Nordic Seas that increases in the winter causing the sea level to rise at the borders and to drop in the central Nordic Seas. The opposite happens in the summer, when the wind stress curl decreases, so the sea level decreases at the borders (East Greenland and Norwegian coasts) and increases in the inner Nordic Seas. Further investigation needs to be done to explain and confirm the physical meaning of the 2nd mode of variability. The 2nd mode will be compared with long-term moored current data and wind stress curl over the Nordic Seas (Chapter 4).

Third Principal Component

The structure of the third EOF corresponds to the high (positive anomaly) sea level anomaly at the western border and low (negative anomaly) at the eastern, at the Norwegian continental shelf (Figure 3.8, bottom left). Since the gradient of sea level relates to geostrophic currents, one can interpret the 3rd EOF as oscillations of the two boundary currents: EGC and NwAC. The oscillations are in antiphase between the two currents and the internal Nordic Seas are nearly flat. The 3rd mode of variability indicates that 3% of variance is caused mainly by the annual and semi-annual oscillations of the East-West sea level gradient. Also this mode represents a long-term increasing trend in the sea level gradient between the two margins from November 2002 to June 2008.

Most of the variability is explained by mode three at the Northern Greenland Continental Shelf [25%], Denmark Strait [20%], Norwegian Continental Shelf [20%] and East and South Svalbard coastal areas [35%] (Figure 3.8). The mean seasonal cycle (Figure 3.1) also shows similar variations between the two regions. At the western side, sea level is lower in September and higher in February, whereas at the western side the opposite happens. The 3rd EOF structure could be a result of seasonal asymmetry in the buoyancy loss by the two boundary currents (hypothesis). In the winter the EGC is covered by sea ice and there is no heat exchange between the atmosphere and the ocean whereas in the same period the NwAC is ice-free and therefore loses heat to the atmosphere (buoyancy loss). The forcing mechanisms of this mode will be further investigated in the next chapter.

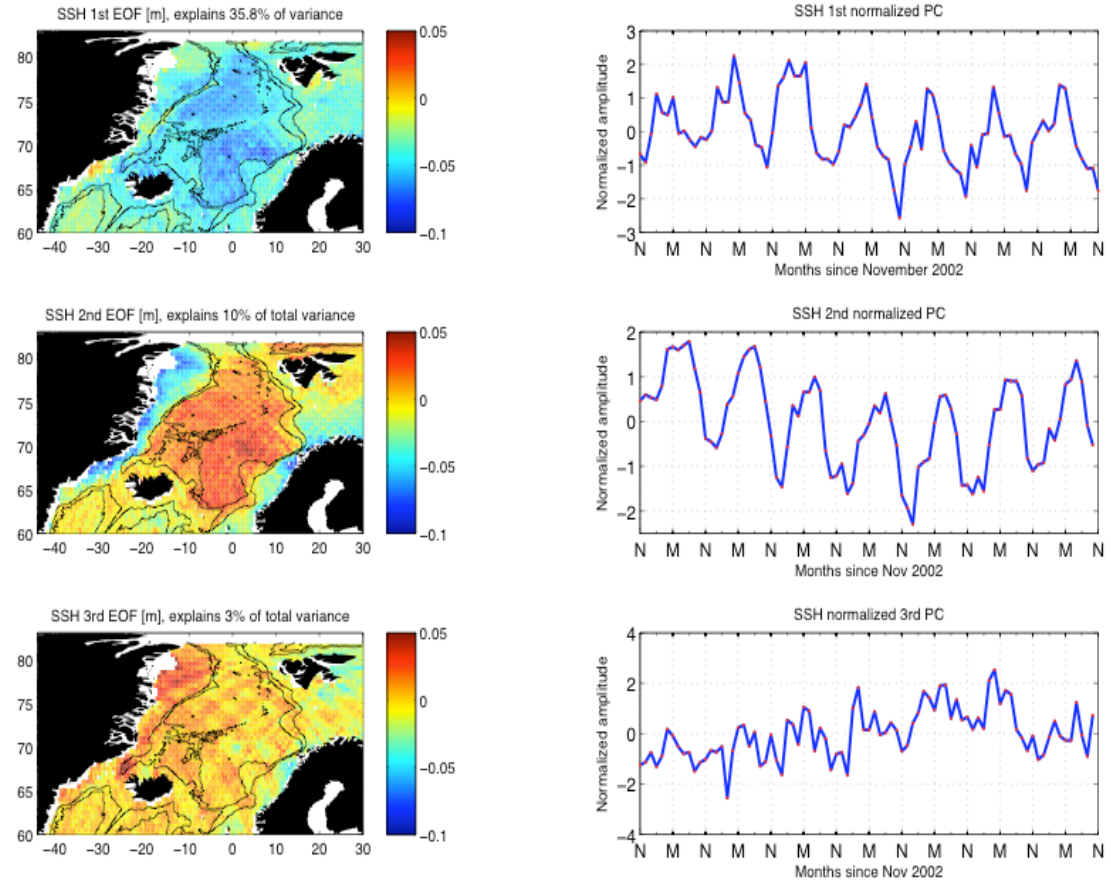

Figure 3.8. First three EOFs (left) and PCs (right) of 7 years of Envisat sea surface height anomaly. The x-axis for PC shows months since November 2002. The spatial patterns (left) have units in meter relevant to one standard deviation of their corresponding principal component; PCs are normalized by their standard deviation (no units), but when EOF pattern and its PC are multiplied they recover part of the signal described by the mode.

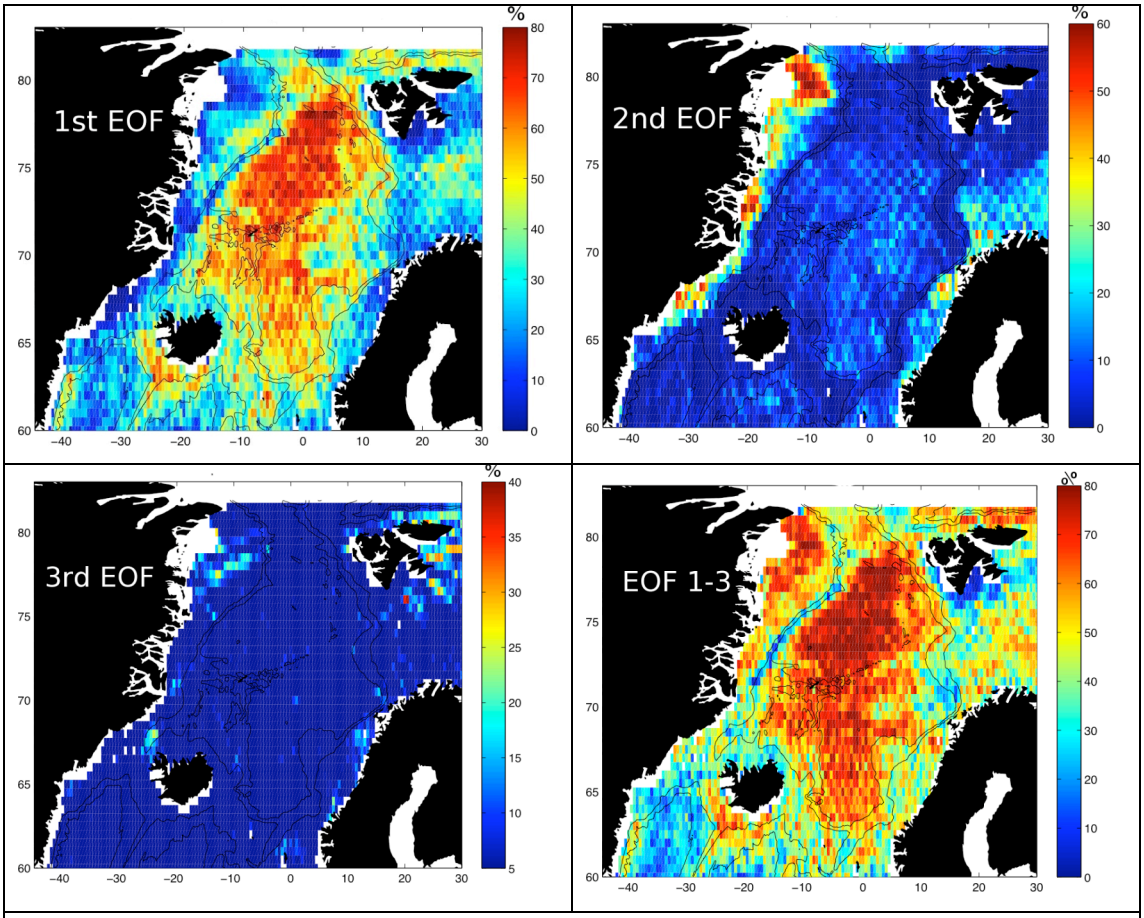

Figure 3.9.Variance explained [%] by the first three EOFs. Starting from the top left: 1st ,2nd, 3rd and the first three EOFs summed.

The higher order Principal Components

The first three EOFs of SSHA explain up to 90% of total variance in the Greenland and Norwegian basins (Figure 3.9). Also a high proportion of the variance [60-70%] is explained by these modes in the Lofoten Basin and Iceland Sea, Northern Continental Shelf of East Greenland, Southern Continental Shelf of Iceland, and off northern Svalbard. The three first EOFs also perform moderately well in explaining the variability in the Barents Sea and Norwegian continental shelf [40-50%]. However, only a very small part of variability [10%] can be explained by the first three EOFs in the Irminger Sea, along the ice edge over the EGC and in the region of southern Svalbard. In order to better explain the variability in these regions more EOFs need to be added. This means that these regions have more complicated, higher frequency variability that cannot be adequately reconstructed with a few EOFs. In order to explain about 50% of variability along the eastern continental shelf of Greenland, where also the ice-edge often occurs, a minimum of 25 EOFs need to be considered. If we want to describe 90% of variance in the region then 50 EOFs are required. This could mean the region along the Greenland continental slope could have: i) high noise due to observation error (However, the observed variability is much greater than the error caused by the offset- See Figures 2.12 &3.2) ii) a high noise content which could be caused by the natural high variability, iii) low natural variability not captured by the 3EOFs or iv) the 3 EOFs do not capture well the regional variability at this location because they focus on the large-scale patterns.

3.5.2 PCA of the data with seasonal cycle removed.

In the previous section it was shown that the seasonal cycle represents a large fraction of the variability in the greater part of the Nordic Seas. Therefore, the EOF analysis is sensitive to this high amplitude, energetic annual signal. In order to study sea level variability at less energetic frequencies the seasonal cycle needs to be filtered out from the data at every location. Therefore, the next part of this section investigates the interannual variability by repeating the EOF analysis on the de-seasonalized SSHA data (no detrending was done). The mean seasonal cycle (Figure 3.1) was subtracted from the data and the EOFs were calculated in the same way as for the unfiltered data.

First Principal Component

The removal of the seasonal cycle from the SSHA data does not greatly change the structure of the 1st EOF (Figure 3.10). The total variance explained by this mode is now over 10% lower and equals 21%. The 1st mode of variability still explains most of the variance in the deep basins [up to 70%] but also about 80% of variance at the East Greenland Continental Shelf (Figure 3.11). A much lower fraction of the variance is described at the southern continental shelf of Iceland [20-40%]. Also the amplitudes of the EOF pattern have decreased by about 4 cm (50%) in the deep basins. That indicates that a seasonal signal is a main contributor to the sea level variability in these areas. On the other hand the amplitude at the East Greenland continental shelf increased from 2-4 cm to 4-6 cm. The 1st PC now shows oscillations with semi-annual and inter-annual frequencies but the long-term variability is similar to the non-filtered 1st PC.

Second Principal Component

The 2nd EOF has a spatial and temporal structure similar to the 2nd EOF of the non-filtered data. After removal of seasonal cycle the amplitude of the 2nd EOF decreased proportionally to the variance explained by the mode from about 10% to 8%. The mode still explains the highest variances (25-45%) at the Greenland Continental Shelf, Norwegian Sea and Barents Sea (Figure 3.11). The corresponding PC reaches the maximum amplitude at the beginning of the record (November 2002) gradually decreasing until January 2006, than increases again (Figure 3.10).

What is the consequence of the removal of the seasonal signal on the EOFs?

The removal of the seasonal cycle does not change the spatial structure of the first two EOFs. Also the time series remain similar except the seasonal oscillations were removed. However, the spatial structure of the 3rd EOF changes after the seasonal cycle was removed prior to the EOF analysis. The pattern has more visible altimeter tracks and the gradient between the east and west border is not as strong as before. This may suggest that the annual signal is in fact an important contributor to the 3rd EOF and removing the annual frequencies leaves a smaller signal in the 3rd EOF, which becomes comparable to the noise level (Section 3.5). The removal of the seasonal cycle prior to the analysis also causes removal of the long-term trend in the 3rd PC, what suggests that this trend was caused by a shift in the mean annual signal.

The higher order principal components

The three first EOFs of the seasonally filtered SSHA explain about 33% of the total variance in the seasonally filtered SSHA. The majority of the variance can be explained by the 3 modes along the eastern Greenland continental shelf (up to 80%) and in the central Nordic Seas, especially in the Greenland, Norwegian, Lofoten and Icelandic Basins (50-80%) (Figure3.11). However, the three first EOFs explain very little variance in the Irminger Sea, region along the eastern continental slope of Greenland, Svalbard shelf and continental shelf of Norway (Figure 3.11). Therefore, the three most important modes of variability describe mainly the sea level variability at the central part and the western boundary of the Nordic Seas.

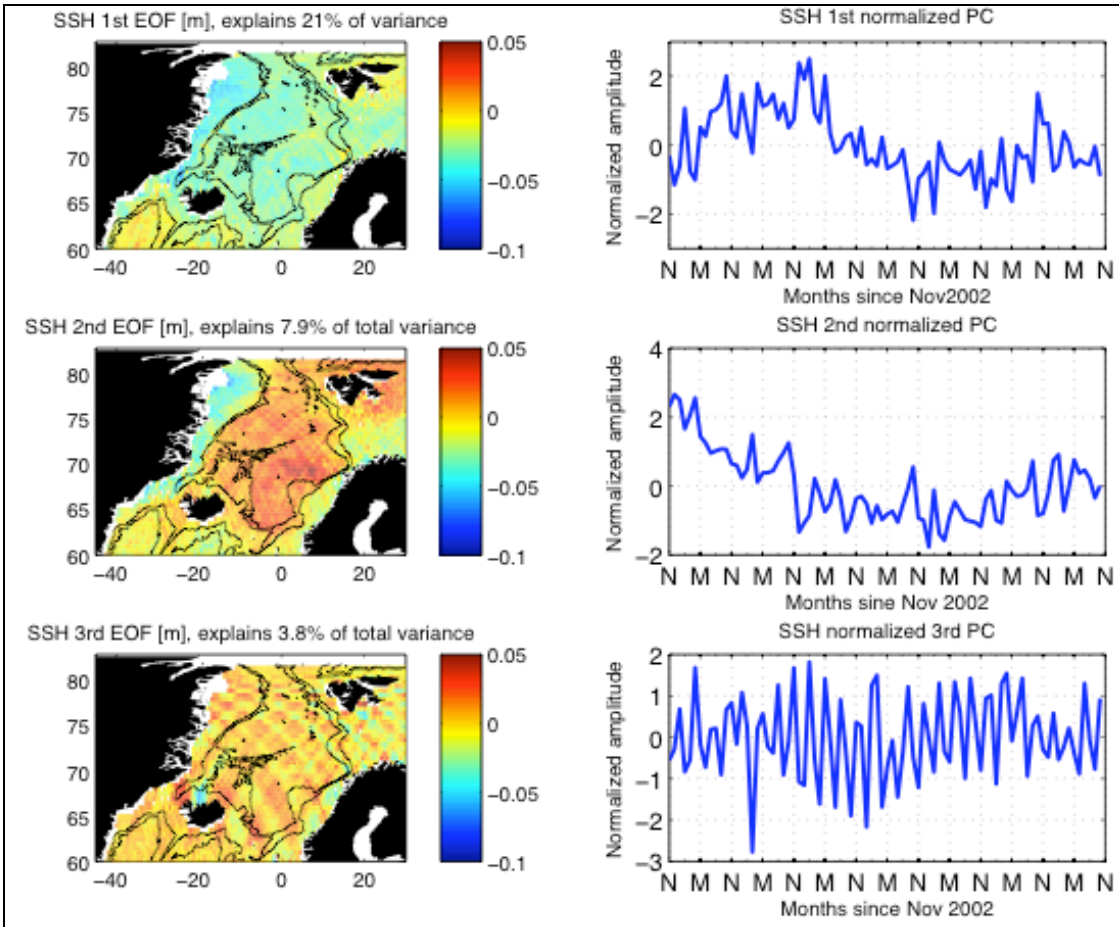

Figure 3.10. First three EOFs (left) and PCs (right) of 7 years of Envisat SSHA with the mean seasonal cycle filtered out. X-axis for PC shows months since November 2002. The spatial patterns (left) have units in meter relevant to one standard deviation of their corresponding principal component; PCs have no units because they were normalized by their standard deviation.

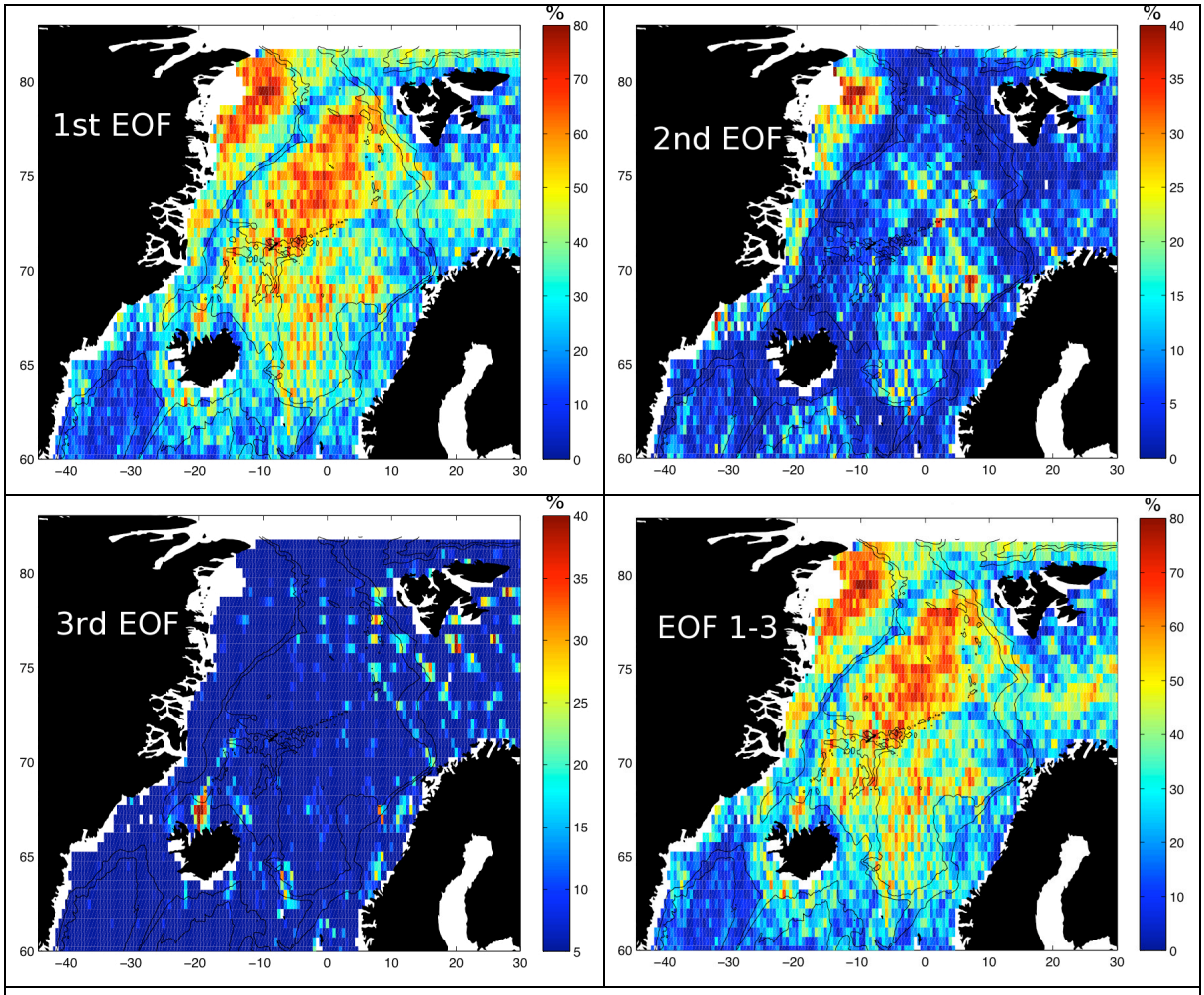

Figure 3,11. Variance explained [%] by the first three EOFs after a removal of seasonal cycle. Starting from the top left: 1st ,2nd, 3rd and all three first EOFs.

3.6. Relation of sea surface height to North Atlantic Oscillation (NAO)

Further analysis focuses on the possible forcing mechanisms that may cause sea level to vary on the annual to interannual timescales. In the remaining part of this chapter the beginning of this investigation is reported; more detailed analysis is performed in Chapter 4. Due to the importance of the NAO for the variability of sea level in the Nordic Seas, this section investigates the sensitivity of sea level to the NAO. The monthly SSHA is firstly related to the monthly NAO index (Jones et al. 1997, http://www.cru.uea.ac.uk/cru/data/nao.htm). The NAO index is defined as the difference between the normalized SLP over the Gibraltar and southwest Iceland (Reykjavik). The NAO index defines 'high' (positive) and 'low' (negative) states of the NAO depending on the meridional pressure gradient between the Azores high and the Icelandic low. Due to the dominance of the winter NAO, which has got a positive sign in the period of interest, a relationship between the winter NAO index and winter SSHA is further investigated by computing correlations and comparing EOFs of the wintertime SSHA and the winter NAO index.

NAO Index

In the last 7 years the annual NAO index was mainly weakly negative, with an exception in the period from September 2005 to January 2006 (Figure 3.12 green line). In the second half of the record the NAO index showed greater variability with strong positive and negative amplitudes from May 2006 and more pronounced seasonal cycle. It can be seen that the NAO index was generally positive during the winter and negative for the summer, becoming more negative if longer averages are taken into account. If only the winter average is considered (See Figure 3.17), the NAO index time series can be divided into two periods, both with positive NAO index (NAO+). The first period (2003-2005) was characterised by a relatively low interannual variability with values of the index not changing significantly from year to year. In the winter of 2006 the NAO+ increased, reaching a maximum in 2007. It decreased in 2008, reaching a low positive value in 2009.

It can be seen in Figure 3.12 that the NAO index can be characterised by a small negative annual mean in the first half of the record and a larger negative index in the second half. Furthermore, the first half of the record shows less variability and smaller magnitudes than the second. The results of Mann-Whitney non-parametric statistical test confirmed that the first and the second halves are statistically different at 95% confidence level if 3-monthly (or longer) averaged NAO index is considered. The statistical results confirm a change in the wind forcing in 2006 that could affect significantly SSH and ocean circulation. It was checked using the same statistical test that the first three PCs also follow the same change (significant at 99% confidence level). For the PC1 dividing into two periods between March 2005 and August 2006 gives significant results. For the PC2 and PC3 there is a wide range of the division times due to the long-term trends in the time series.

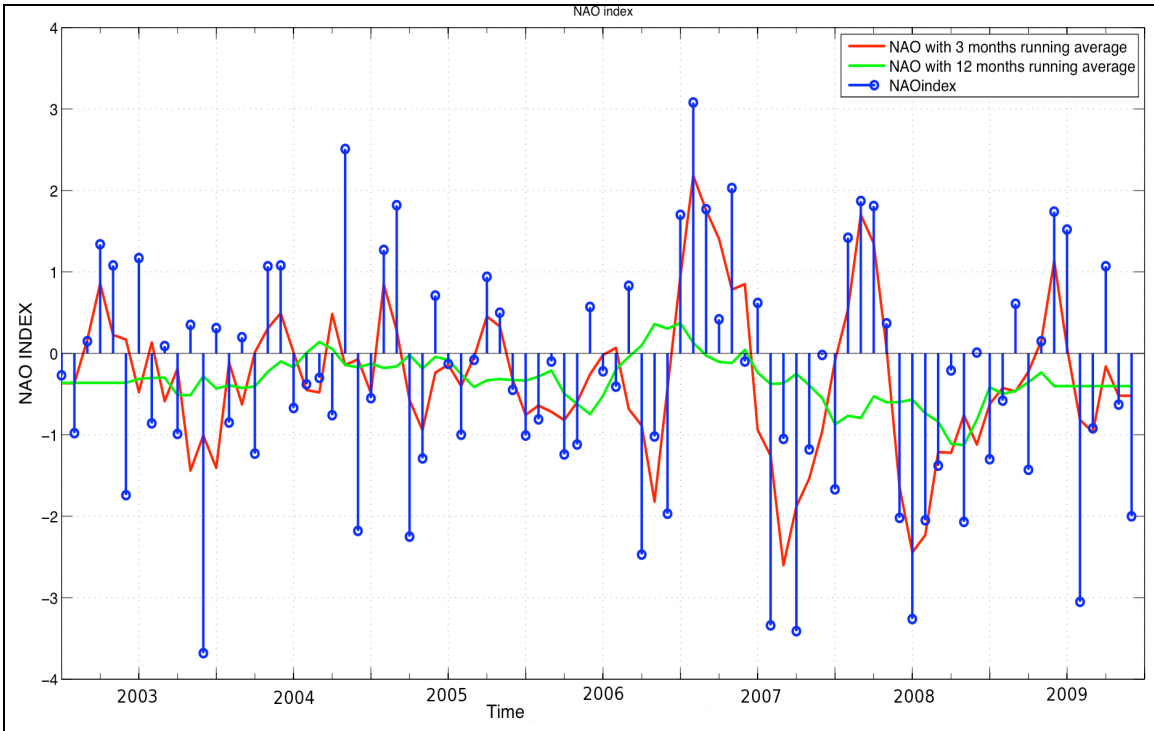

Figure 3.12. NAO index from November 2002 to October 2009, monthly (blue), 3-month averaged (red), annually averaged (green). The labels on X-axis indicate May in a given year.

Negative correlations (significant at 95% confidence level) are observed between the monthly NAO indices and SSHA in the interior of the Nordic Seas, particularly in the deep basins (Figure 3.13). The spatial structure of the correlation map (Figure 3.13) is very similar to the spatial structure of the 2nd EOF of the monthly SSHA (Figure 3.7). Furthermore, a similar fraction of the total variance is explained by the NAO index in the SSHA data, about 10% of variance can be explained by the NAO in these regions. The correlations of the monthly NAO index with the EOFs of the unfiltered monthly SSHA are significant at the 95% confidence level for all the first three EOFs with the strongest and the most significant for the 3rd EOF (R1=0.27 p=0.012, R2=-0.27 p=0.013, R3=-0.29 p=0.008). Correlating the three-month averages (moving average) of the same EOFs with the NAO index increases the correlation of the 2nd EOF and NAO index (R=-0.32 p=0.003) but does not change the correlations of the other modes. On the other hand, the same correlations for the seasonally filtered EOFs and the NAO index are significant only for the 3rd EOF (R=-0.26 p=0.016, and R=-0.40 p=0.00017

for the 3-monthly averaged signals). The correlations for the seasonally filtered NAO and SSHA are similar to the results of Furevik and Nilsen (2005) but only significant at the Norwegian continental shelf (Figure 3.13). The results suggest the NAO index is highly correlated to the 3 first SSHA modes of variability on the seasonal timescales. If we consider other frequencies then only 3rd EOF was found to be correlated to the NAO index.

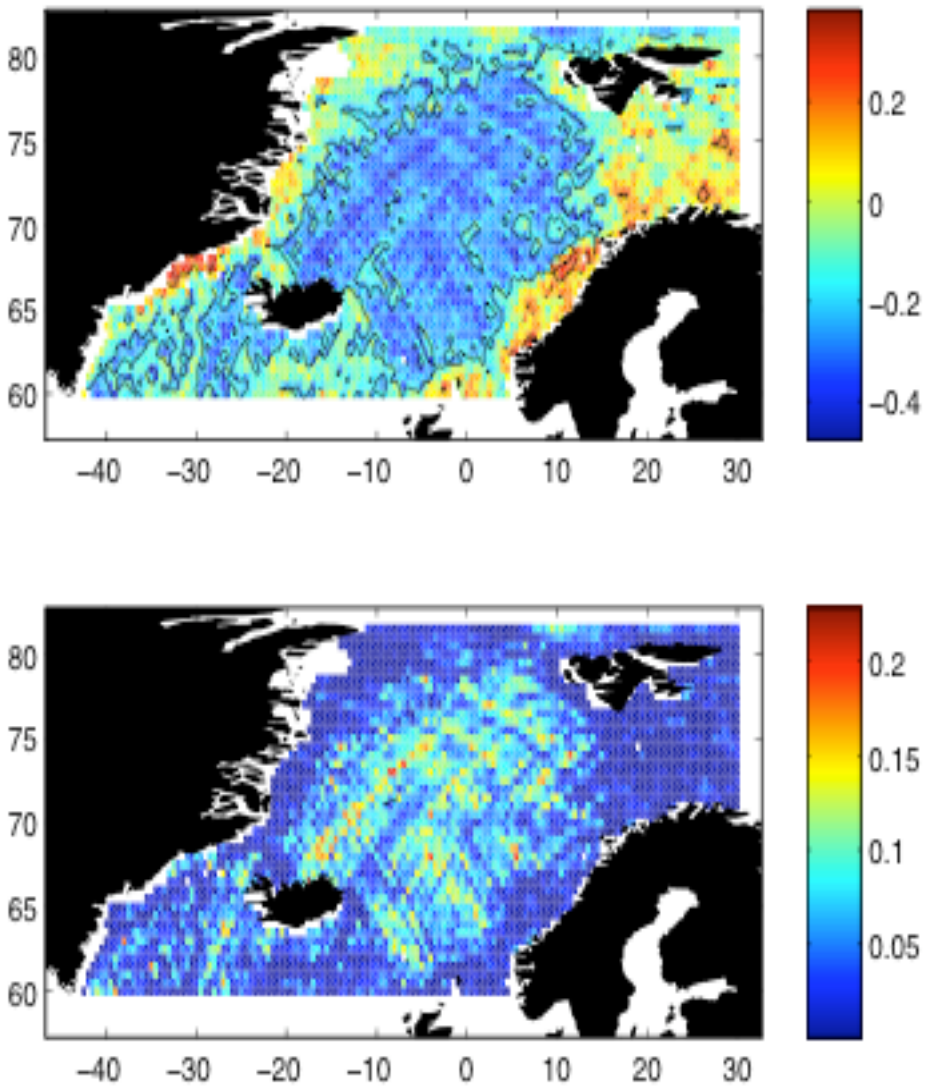

Figure 3.13. Correlation coefficient [R] between the monthly NAO index and monthly sea level (top) with 95% significance level contour in black; and variance explained by the monthly NAO index in the monthly SSHA [%] (bottom).

Arctic Oscillation index

Also the Arctic Oscillation (AO) could affect sea level and water masses in the Nordic Seas. Here, we use the AO index from the National Weather Service Climate Prediction Center (NOAA, US) obtained by projection onto the leading principal component of NCEP Sea Level Pressure (SLP) at 1000hPa for the area north of 20 N. In fact the NAO and AO indices are very similar to each other, especially for the winter season; the correlation coefficient between the two indices is 0.89 for the winter period only and 0.66 for the monthly indices, both highly significant at 99% confidence level (Figure 3.14). This is due to the dominance of the Atlantic sector on the AO and because the Pacific contribution to the AO is very small (Hurrell 1996; Deser 2000). Correlation coefficient for the monthly SSH and AO shows positive and significant values (up to 0.5) along the continental slopes of east Greenland and Norway and in the Barents Sea (Figure 3.15). In fact the map of variance explained by the AO matches the map of variance explained by the 2nd EOF of SSH (Figure 3.9). Moreover, there exists a significant correlation between the AO index and the 2nd PC of SSH (0.27 for the non-filtered PC and 0.31 for the seasonally filtered PC, both significant at 99% confidence level). That suggests the AO may be one of the drivers of the 2nd EOF both on the annual and interannual timescales.

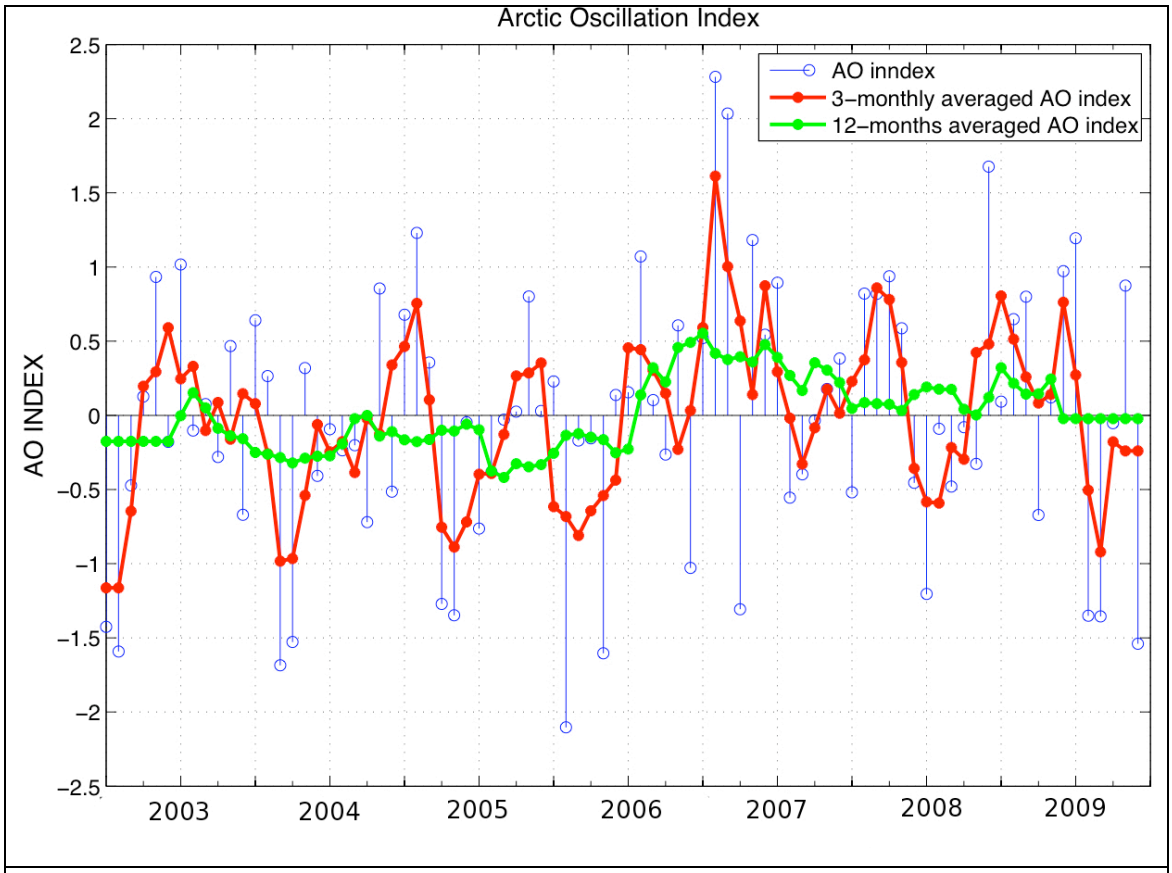

Figure 3.14. AO index from November 2002 to October 2009, monthly (blue), 3-month averaged (red), annually averaged (green). The labels on X-axis indicate May in a given year.

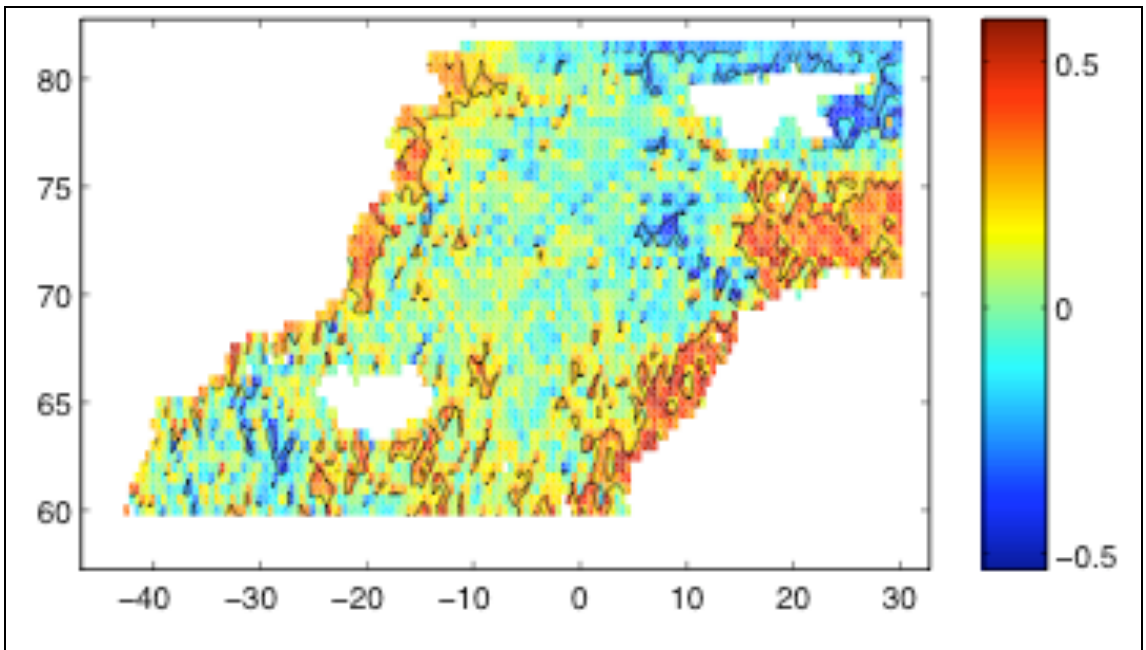

Figure 3.15.Correlation coefficient (R) for the AO index and SSHA with 95% confidence contour (black).

3.6.1 PCA of winter only data and its relation to NAO.

Winter in the North Atlantic is a time of year generally associated strongly with the North Atlantic Oscillation; following Jones et al. (1997), the sea level variability is investigated by treating each extended winter (December-January-February-March) as a whole. Therefore, height anomalies are averaged over four months for each winter. Correlation coefficient, explained variance and corresponding p-values are calculated at each grid point between the averaged wintertime sea level and the NAO index (Figure 3.16). The results show that the sea level variability is positively correlated with NAO during winter in the shallow ocean (less than 1000m deep). Very strong positive correlations (and significant with 95% confidence level) are found at the Eastern Greenland continental shelf, Norwegian and Iceland continental shelf and in the Barents Sea (Figure 3.16). Also strong and negative correlations were observed in the shallow waters off southern Svalbard (also significant at 95% confidence levels).

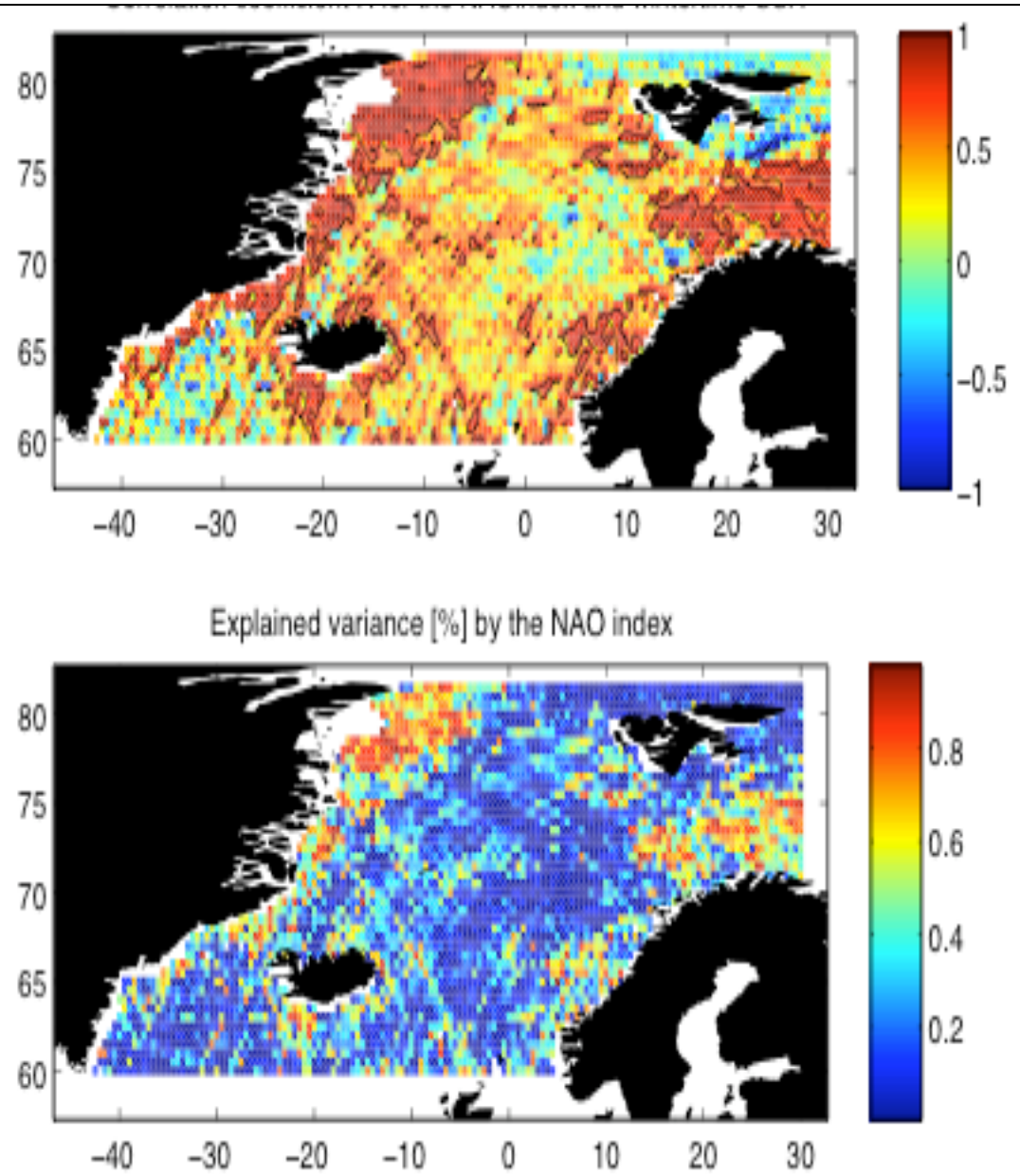

Figure 3.16. Correlation coefficient [R] between the winter NAO index and wintertime sea level (top) with 95% confidence level (black); and variance explained by NAO index in the wintertime SSHA [in % divided by 100] (bottom) .

In order to analyze wintertime temporal and spatial variability, EOFs of the non-normalized wintertime height anomalies were calculated. Only the first two EOFs are significant, explaining 65% of the total variance in the averaged winter sea surface height. There is a strong leading EOF that explains 42% of variance. It has similar structure to the 1st EOF of the non-filtered monthly sea surface height (Figure 3.17). The largest part of a total winter variance is explained in the deep basins and East Greenland continental shelf similarly to the 1st EOF of monthly SSHA. However, the amplitude explained by this mode is now larger, reaching 12 cm in the deep basins and Denmark Strait (50% increase). This increased amplitude suggests that the winter sea level variability is the strongest among all the seasons in these regions.

The 2nd EOF explains 23.5% of the total winter sea surface height variability and its structure and principal component are very similar to the 2nd EOF of the monthly SSHA (Figure 3.17). Also the amplitude explained by this mode has similar values and long-term trend corresponding to the stronger gradient in the sea level between the margins and the interior of the basin during winter 2003 and 2004 and the reversal of that gradient from 2005 to 2008.

The leading EOF of the wintertime sea level is anti-correlated to the NAO index (Figure 3.17). The correlation coefficient R is equal to -0.73 and it is weakly significant at the 90% confidence level. The 2nd principal component also shows anti-correlation with the NAO of moderate value [R=-0.55] but is only significant at the 80% confidence level. The low confidence level is probably caused by the limited number of years in the analysis. However, adding the two principal components strengthens the correlation to R=-0.92 and increase the level of significance of R to 95%. In interpreting the correlation one needs to be careful with the correlation's sign that is chosen randomly during EOF analysis for the 1st EOF. Consequently, all the next EOFs have the sign that is related to the previous one. Therefore, the negative correlations between the NAO index and the wintertime EOFs can be in fact positive. This explanation can be supported by positive correlations observed between the wintertime SSHA and the NAO index.

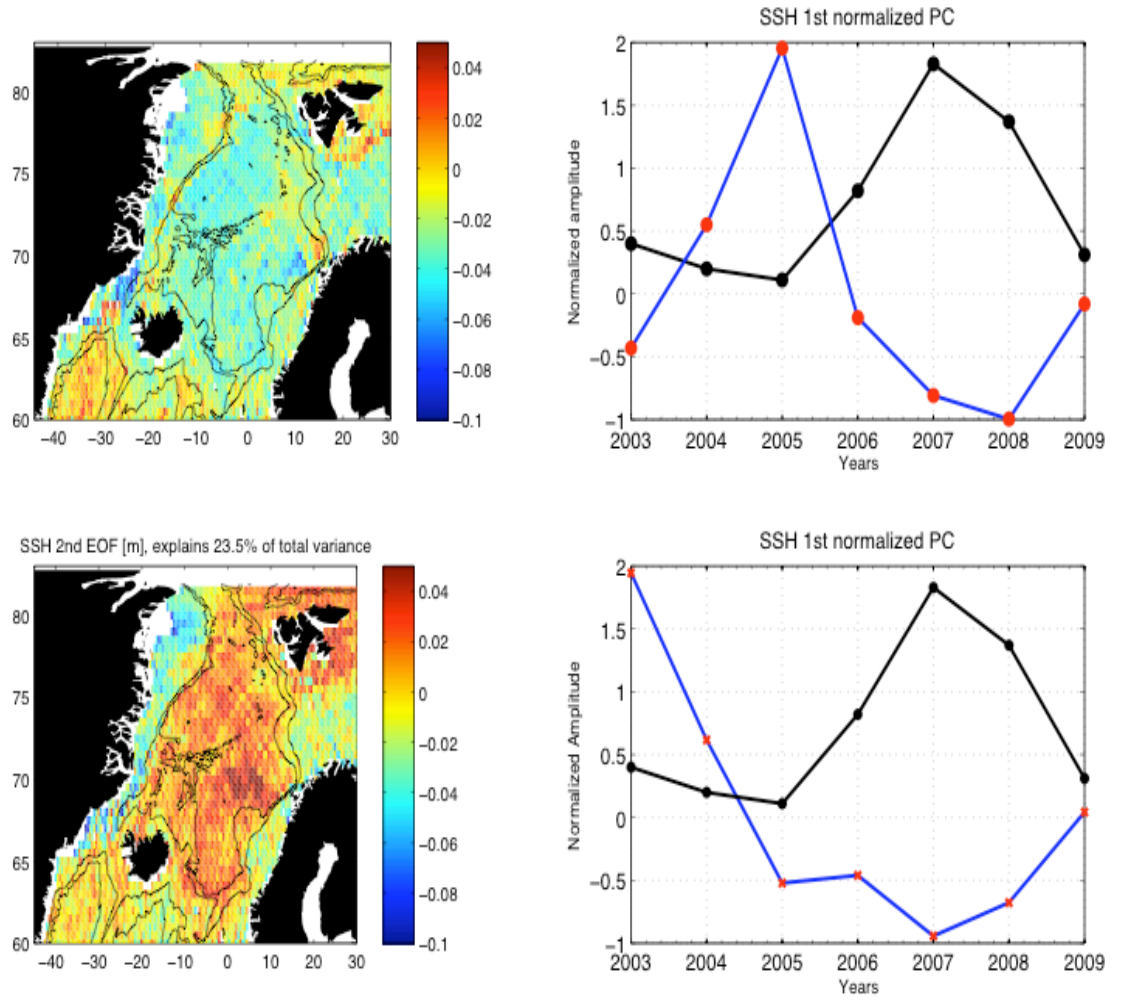

Figure 3.17. 1st (top left) and 2nd (bottom left) EOF of mean wintertime (DJFM) SSHA. In each case the principal component (blue) is shown together with the mean winter North Atlantic Oscillation Index (black) (top and bottom right).

Why are the correlations between the NAO index and SSHA different for the monthly and wintertime data?

To summarize, correlations between the NAO index and SSHA are negative and significant in the central Nordic Seas (deep basins) for the monthly data but positive and significant at the margins of the Nordic Seas (shallow water) for the wintertime data. To explain these differences, the correlations for each season were investigated. It was found that the NAO is generally positive during extended winter period but negative for the rest of the year. Averaging months from January to October into the yearly means and correlating the two variables results in the negative correlations (significant at 95% of confidence level) in the Central Nordic Seas (not shown here). Furthermore, the phase difference in the annual cycle of SSHA between the margins and the interior of the Nordic Seas combined with different sign of the NAO index for the winter clarifies the negative correlations for the wintertime NAO and SSHA at the Continental Shelf.

3.6. Summary

Sea level in the Nordic Seas varies greatly on the annual and inter-annual time scales. During the last 7 years the greatest variability occurred at the continental shelf of Norway and Greenland and in the Norwegian Sea (SD=15 cm). Considering the interannual variability (Figure 3.3) the greatest contributors to the variability were winter months (December, January, February) for the whole area and October/November for the interannual variability at the Greenland Continental Shelf. It was found that the mean seasonal cycle was a large contributor to the variance of the total signal. The mean change in the variance over the whole Nordic Seas after removal of the mean seasonal cycle was 36%. The contributions of the mean seasonal cycle to the total variance differed regionally from 10% at the Greenland Continental Shelf and Barents Sea to 60-70% in the Greenland Sea. The harmonic sinusoidal function fitted to the data has maximum amplitude of 12 cm at the Norwegian continental shelf and Norwegian Sea. The semi-annual harmonic function fitted to the SSHA data indicate important contributions of the semi-annual signal at the Greenland continental shelf (up to 5 cm). The EOFs of the monthly unfiltered SSHA determined three important independent modes of variability that oscillate with large annual and inter-annual frequencies. The three modes explain 49% of the total variance, and regionally up to 80% of the variance can be explained by the first 3 modes in the deep basins and the Greenland continental shelf. However, only a small part of the variability (10%) can be explained by the first 3 EOFs at the ice-edge, Irminger Sea and off southern Svalbard, indicating complicated, high frequency variability in these regions. The removal of the seasonal signal does not change greatly the structure of the first two modes; the corresponding time series no longer have annual oscillations but the long-term trend is the same as for the unfiltered PCs. This could be caused by the winter variability, which dominates the variability in the region and therefore can affect the EOFs.

It was found that the North Atlantic Oscillation has a strong effect on Nordic Seas' sea level. Strong negative correlations were found between the monthly NAO indices and SSHA in the deep basins of the Nordic Seas. On the other hand, significant positive correlations were found for the wintertime period only in the shallow waters of the Nordic Seas: the continental shelves of Iceland, Greenland and Norway, and the Barents Sea. Correlations between the monthly NAO indices and EOFs of monthly SSHA

confirmed a strong relationship between the NAO and all the first 3 EOFs. However, this relationship does not exist for the seasonally filtered EOFs suggesting that the seasonality in NAO is strongly related to the seasonality of SSHA. On the other hand there exists a significant relationship between winter SSHA and the NAO that was confirmed by the correlations of the wintertime EOFs of SSHA and the NAO index. Furthermore, correlations of SSHA and AO indices showed strong annual and inter-annual relationship between the 2nd EOF and AO index. The results indicate that the Arctic Oscillation may be one of the driving mechanisms for the 2nd EOF of SSHA.

3.7. Discussion.

A gap in our knowledge was filled by this study by describing the sea level variability in the ice-covered part of the Nordic Seas. This study contributed a significant knowledge about the variability of sea level and circulation in the ice-covered regions of the Nordic Seas. It was found that the sea level is very variable in the ice-covered regions especially at the eastern Greenland continental shelf and at the sea-ice edge. It was also found that these regions show high inter-annual variability from September to April. The harmonic analysis showed that the annual frequencies are the greatest contributors (36%) for the total signal and can reach up to 12 cm in the Norwegian Sea and Norwegian coast. On the other hand, the annual amplitudes are small in the ice-covered part of the Nordic Seas except Greenland Sea (7 cm) and southern east Greenland continental shelf in the proximity of Denmark Strait (8 cm). The maximum in the annual cycle is reached the earliest (August/September) in the interior of the Nordic Seas. In fact this region is limited by the 1000 m depth contour. The maximum in annual amplitude propagates toward shallower regions outside of the centre of the basin. In the ice-covered regions, at the east continental shelf of Greenland, the maximum occurs the latest (December/January).

Seasonal amplitudes, described here as a mean over the 7 year period and the annual harmonic function fitted to the data at each location, show similar patterns in the ice free regions to the amplitudes found in the open ocean by Mork and Skageth (2005). However, this study found amplitudes that are greater by few centimeters from the previous research, with the biggest differences occurring along the coast of Norway. A higher spatial averaging in the Mork and Skagseth's study could cause this disagreement or it could be due to the different period studied. The results of Furevik and Nilsen (2005) support our findings of the propagation of the maximum amplitudes in the seasonal cycle from the deep basins to the shallow seas and coastal ocean. However, the phase difference that Furevik and Nilsen reported suggests a westward propagation of the annual sea level amplitude. That discrepancy between our results and the previous findings is probably caused by the lack of data at the East Greenland Continental Shelf in Furevik and Nilsen's study.

Merging the altimeter measurements from the open ocean and from the ice-covered part of the ocean allowed the detailed description of modes of variability as EOFs in the whole Nordic Seas. It was found that the first three modes are significant and can be explained with help of physical forcing mechanisms. The most important EOF is very similar in structure to the annual harmonic and shows basin-wide coherent oscillations with annual and lower frequencies. The second mode of variability follows the 1000 m depth contour and shows antiphase oscillations between the interior of the Nordic Seas and the borders. The mode oscillates at annual and inter-annual frequencies with an apparent decrease (increase) until 2006 and a recovery after that. The third mode of variability shows a long term increasing trend in sea level at the continental shelf of Greenland and opposite trend at the continental shelf of Norway.

The analysis of the forcing mechanisms suggest a strong relationship between the NAO index and SSHA in the deep basins that is coherent at the annual frequencies. That suggests the NAO can be one of the drivers of the seasonal variability in the sea level in the deep basins of the Nordic Seas. On the other hand, there exists a strong relationship between the wintertime NAO and SSHA in the shallow regions of the Nordic Seas. This suggests that NAO also affects the sea level in the region on the longer time scales (inter-annual), especially in the shallow waters of the Nordic Seas during the winter. The previous study of Isachsen et al. (2003) found a similar first mode of variability with a strong seasonal cycle for a period 1995 - 2001. They used a barotropic model forced by local winds, was and were able to reconstruct much of the variability in the Norwegian Gyre on seasonal to inter-annual time scales. The two modes of variability described here have a strong topographic dependency, which was observed also by others who argued it is mainly wind-driven (Isachsen et al. 2003, Poulain et al. 1996, Orvik and Niiler 2002 and Jakobsen et al. 2003). Correlations with the Arctic Oscillation index also have revealed a strong relationship between the AO and the 2nd EOF coherent on annual and inter-annual frequencies. This supports the hypothesis that AO could be one of the drivers of the 2nd EOF.

The two first EOFs, described here, indicate also seasonal weakening and strengthening of the currents along the topographic contours that was observed before by Orvik et al. (2003) for the NwAC. Significant correlations of SSHA and the NAO index suggest a strong dependency of sea level to the local wind forcing related to NAO. The correlations found here could mean that the wind stress curl that is more cyclonic over

the winter depresses the sea level in the interior of the Nordic Seas and increases the sea level along the surrounding coasts. The correlations of SSHA and NAO index suggest that process occurs on the annual time scales whereas the correlations of SSHA and AO suggests there may be also inter-annual changes in this process (2^{nd} EOF). The forcing mechanisms will be further investigated in the next chapter.

CHAPTER 4: ANALYSIS OF THE LOCAL ATMOSPHERIC FORCING OF SEA LEVEL VARIABILITY IN THE NORDIC SEAS.

4.1 Introduction

The aim of this chapter is to investigate correlations between the sea surface height and the local atmospheric forcing. Due to the time limitation and unavailability of data the non-local and terrestrial forcing are beyond the scope of this study (e.g. river-run off, glacier melting, sea-ice melting, advection by the currents etc.). The meteorological variables that might be important in driving sea surface height variability are identified and their influence on the sea level is described in section 4.1.1. Furthermore, different sources of the atmospheric variables are discussed in section 4.1.1 and the most appropriate dataset is chosen. We begin the investigation of possible relationships between the sea surface height anomaly (SSHA) and the other atmospheric variables by looking at the annual cycle of the atmospheric fields and the spatial correlation patterns between the atmospheric fields and SSHA (Section 4.2). In section 4.3 the results of the EOF analysis for all atmospheric fields are compared and regressed with the time series of the EOFs of SSHA. Finally, the coupling between the sea level and the atmospheric fields is investigated using Maximum Covariance Analysis (MCA) in Section 4.4. Each section is summarized separately and the most important results are discussed in Section 4.5. Finally, the main conclusions of this chapter are expressed in Section 4.6.

Air-sea fluxes

Air-sea fluxes can affect sea level height directly and/or indirectly and therefore are considered as major drivers of the local SSH variability. Fu and Cazenave (2001, Chapter 2) argue that the sea-level variability can be divided into two categories dependent on the spatial scales. For the scales larger than about 500km the variability is caused mainly by the ocean response to the air-sea fluxes and winds and for the scales smaller then 500km the variability is caused by the mesoscale eddies and ocean currents. Wunsch and Stammer (1997) estimated the global average root mean squared

variability of sea level to be about 12cm excluding tides, where the larger scales (greater than 500km) contribute about 9cm (including the inverted-barometer response) and the smaller 8cm, which are caused mainly by the ocean currents and eddies. In the Nordic Seas the mean along-track autocorrelation function of SSHA (see Chapter 2) shows that the characteristic horizontal scales of mesoscale oceanic motions are smaller or equal to about 100 km. Kuragano and Kamachi (2000) investigated the spatial and temporal scales of sea level variability in many different locations and showed that in the high latitudes the larger scale sea level variability is also more isotropic when compared with other regions (zonal and meridional spatial scales have similar magnitudes), what could suggest more locally forced response of the ocean in these regions. However, it is difficult to distinguish between the changes of sea level in a given location caused by the changes in the water masses driven by the local and non-local forcing because the two processes can occur at the same time (Fu and Cazenave, 2001). These changes can be caused by the local atmospheric forcing but also by advection/diffusion.

Changes of Sea Level Due to the Buoyancy Forcing

Thermohaline circulation is influenced by the density/buoyancy of seawater and therefore changes in the surface density flux affect the local and global circulation. The surface density flux consists of the haline and thermal contributions. The thermal contribution depends on the net air-sea heat flux and the haline contribution depends on the net freshwater flux that can be defined as a sum of the difference between the evaporation and precipitation at the sea surface and the terrestrial freshwater and ice freshwater inputs. The thermal component dominates the surface density flux in the warm seas like Mediterranean (Josey, 2003) and model results show that it could also dominate in the Greenland Sea (Grist et al. 2007). The net air-sea heat flux expresses whether the ocean gathers or radiates the heat from/to the atmosphere. The positive heat flux during the summer indicates a heating of the sea-surface that directly results in the increase of SSH. It also decreases the surface density of seawater and increases stratification. The opposite situation happens in the winter in the Nordic Seas when the net heat flux is negative due to the strong winds in the area (Furevik et al. 2009, Grist et al. 2007). This makes seawater in the surface layer colder and denser which decreases SSH (negative SSHA) and it is an important preconditioning process for the deep convection and dense water formation in the Nordic Seas (Marshall and Schott, 1999). The dense water formation process in the Nordic Seas is very important for the

formation of the North Atlantic Deep Water (Dickson and Brown, 1994) and the Atlantic deep circulation and it plays key role for the global climate (Broecker et al., 1985).

On the other hand, evaporation/precipitation control the loss/gain of freshwater by the surface layer of the ocean. Positive (freshwater loss) evaporation increases seawater density and decreases SSH, whereas positive precipitation (freshwater gain) decreases the surface density of the ocean and causes SSH to increase. The net flux of freshwater in and out the ocean can be therefore described as evaporation minus precipitation (E-P). Notice that also river runoff and ice melting contribute to the total net freshwater flux but these sources are beyond the scope of this study. The main characteristic of the net freshwater flux is that it controls the sea surface salinity and, as a consequence, the stability of the water column. A positive freshwater flux (E>P) results in the decrease of SSH and increase of the surface density. Due to the nonlinearity of the equation of state of seawater, salinity variations dominate surface density flux at low temperatures and can be the most important in the subpolar ocean where deep water forms (Josey, 2010).

To sum up, evaporation, precipitation and net heat flux can change the surface density of the ocean and affect the thermohaline circulation. A negative net heat flux, and a positive net freshwater flux increase the surface density of the ocean and decrease SSH. On the other hand, positive heat flux and negative freshwater flux (P>E) decrease the surface density of seawater, which increases stability of the water column and SSH in the area. Furthermore, because heat and freshwater fluxes cause changes in the local surface density field, they can also cause changes in the horizontal gradients of density and sea level and therefore affect the geostrophic circulation. Imagine a situation when the increased precipitation occurs only in the interior of the Nordic Seas. This would affect the horizontal gradient of SSH across the Nordic Seas and cause the main boundary currents to weaken. On the other hand, the increased freshwater input at the borders of the Nordic Seas would result in the higher SSH along the borders and lower offshore, what would cause a strengthening of the EGC and NwAC. The above example demonstrates that the patterns of the air-sea fluxes could provide clues for changes in the sea surface height patterns and oceanic circulation. We should also expect the deep-water formation to be affected by the changes caused in the buoyancy loss. A few studies suggest that the changes in the location of the dominant area for deep-water

formation, which occurred in the past, were caused by the changes in the buoyancy loss due to variability strongly correlated with NAO (Dickson et al. 1996, ASOF, 2008).

Wind Driven Circulation and Its Effect on Sea Level

The wind can also be treated as one of the air-sea fluxes because it fluxes momentum into/out of the ocean. It also affects the turbulent heat fluxes and therefore also affects evaporation and net heat flux variability. The stronger the wind the more heat is exported from the ocean to the atmosphere. The dynamical response of the upper-ocean to the wind forcing is described by Ekman theory (Gill, 1982). However, the altimeter cannot "see" the Ekman layer because it does not form a pressure boundary layer and causes motion only at the surface layer of the ocean (Wunsch and Stammer, 1997). Altimeters can see gradients in SSH and therefore only the flow, which extends to the greater depth in the ocean (Wunsch and Stammer, 1997). One of direct consequences of the Ekman transport that can be seen by the altimeter is upwelling/downwelling along a coast. If the wind has a component along the coast, the water in the Ekman layer is transported offshore or inshore. The direction of the net transport is approximately 90 degrees to the right of the wind stress direction (Northern hemisphere) and due to the mass continuity this flow needs to be compensated by the flow from the opposite direction at a depth causing upwelling or downwelling. As a result sea level decreases (upwelling) or increases (downwelling), which causes horizontal pressure gradients in the water column and produces a geostrophic flow along the coast in the same direction as the wind (Tomczak and Godfrey, 1994). In the Nordic Seas, the northerly wind blowing along the eastern Greenland coast could produce inshore surface Ekman transport and downwelling, which would result in the increased sea level at the Greenland coast and sea level slope away from the coast. That would also produce a southerly geostrophic flow along the coast, which could strengthen EGC transport. The same situation could occur for the southerly wind blowing along the Norwegian coast causing the northerly geostrophic transport along the Norwegian coast and increased NwAC transport.

Another consequence of the Ekman transport is a vertical movement of water caused by convergence/divergence in the wind-driven surface layer. This motion is called Ekman pumping/suction (Podolsky, 1987) and it is proportional to the curl of the wind stress and the Coriolis parameter. When the curl is positive (cyclonic) it causes divergence in

the Ekman layer and a sea level decrease due to upwelling. It is therefore associated with the surface transport of water outside the region of the cyclone and a rise of the thermocline in the area of upwelling. On the other hand, anticyclonic winds (negative curl) cause convergence in the surface Ekman layer that produces downwelling and depression of the thermocline. This also results in the increase of the sea level. The vertical motion of water caused by this process is relatively weak (about 10m/year) but can drive ocean gyres, along-shelf flows and currents like Antarctic Circumpolar Current (Fu and Cazenave, 2001, Chapter 2). But how does this process work? The positive curl of the wind increases momentum of the water column, which has to respond by changing its shape. It can respond by stretching (widening cross-sectional area), which would results in the increased vorticity and acceleration of the currents, or by increasing its length which would not generate vorticity and not accelerate the currents. However, on the Earth the water column can change its volume even without changing cross-sectional area by moving meridionally and this would generate meridional currents. The velocity generated by the suction with vertical velocity of 30m/year, Coriolis parameter $f=10^{-4}$ s^{-1} in the area with depth of 1000 meters would generate the flow of about 0.5 cm s^{-1}.

The ocean can respond to the mechanical wind forcing as a movement of the entire water column, which is called a barotropic mode. However, it can also respond in a baroclinic way by the vertical movement of the constant density surfaces. This mode can be modified by the mechanical forcing of wind but also by the buoyancy forcing caused by the surface density flux described above. The ocean response has also different time scales for the both modes. The barotropic response is much faster than the baroclinic that occurs at the longer time scales: from seasonal to decadal. However, the two adjustment processes to the local forcing occur simultaneously with the barotropic dominance at the shorter periods and the increasing baroclinic importance with time (Olbers and Lettmann, 2007).

In the Nordic Seas the positive wind stress curl in the central Nordic Seas causes divergence, local upwelling and onshore transport away from the centre towards the surrounding coasts. The wind stress is not spatially uniform in the Nordic Seas. Land acts as a lateral boundary, which causes Ekman divergence close to the land and results in the change of the surface elevation (depression), thinning of the mixed layer and a distortion in the pressure gradient field together with baroclinic/barotropic flow

anomalies. If the wind stress has a parallel component to the coast the ocean responds by increasing or decreasing the SSH along the coast and generating an alongshore current that is proportional to that wind stress component. This will also generate pressure gradients and modify internal density field of the fluid through fast-propagating barotropic waves and slower baroclinic waves. After some time the flow becomes stationary and can be described by the Sverdrup theory (Sverdrup, 1947), which relates the meridional volume transport away from the boundaries to the wind stress anomaly. However, it does not include the effects of topography and stratification, which is important for the Nordic Seas. Furevik and Nilsen (2005) argue that when topography is included the Ekman pumping in the central Nordic Seas would produce a flow across f/H contours via vortex stretching. On the other hand the stratification would make the effects of topography less important but the time it requires to remove the effect of topography is very long (Anderson and Killworth, 1977). The effects of topography make it difficult to relate the Sverdrup response of the ocean to the wind forcing (Willebrand et al., 1980) especially in the weakly stratified regions like Nordic Seas (Furevik and Nilsen, 2005) where the flow has a similar speed to the first baroclinic Rossby wave speed (about 1cm s^{-1} Killworth et al., 1997). More recent model studies (Hughes and de Cuevas, 2001) showed that the wind stress curl, in the regions where the flow interacts with the bottom topography, is also balanced by the bottom pressure torque with the bottom pressure playing an important role when the alongshore wind is present at the coast. This means that the bottom pressure torque would dominate over viscous and nonlinear terms for the barotropic flow and would cause the flow along the f/H contours (Hughes and de Cuevas, 2001).

Atmospheric Pressure Forcing

The atmospheric pressure forcing is a less effective mechanism for generating ocean response than the wind or buoyancy forcing (Fu and Cazenave, 2001, Chapter 2). The main response of the ocean can be described as a static response where an increase of the atmospheric pressure by 1mbar would cause a decrease of sea level by about 1cm. This response is called the “inverted barometer” (See Chapter 2) and it is not associated with any movement of water. The atmospheric pressure field has a large spatial and temporal variability and therefore the resulting sea level variations could be as large as 15 cm (Southern Ocean) and if not corrected, would cause SSH data to be difficult to analyze for studying the ocean circulation (See Chapter 2 for corrections used).

On the other hand, wind can be described as a direct response of the atmosphere to the atmospheric pressure spatial differences. Because changes in the atmospheric pressure cause changes in the wind field, the atmospheric pressure has a direct impact on the wind stress and wind-driven circulation. This could affect Ekman transport, wind-driven upwelling/downwelling and Sverdrup transport. The mean atmospheric pressure at the sea level can be also used as a good indicator of the large-scale atmospheric modes of variability such as NAO, AO or the Scandinavian High.

Air-sea fluxes data sources

The above arguments showed that the local forcing might drive sea level in the Nordic Seas. The most important meteorological variables are those associated with the wind and buoyancy forcing. Therefore, the fields for the subsequent analysis should include mean sea level pressure, wind stress, precipitation, evaporation and the net heat flux.

These air-sea fluxes can be obtained from the surface meteorology reports, satellite observations and atmospheric model reanalysis, which assimilate most of the available data. In order to investigate the local driving mechanisms of sea level variability we need a product that has the same temporal resolution as SSHA and the highest possible spatial resolution in the Nordic Seas, provides data in the ice-covered ocean and all identified air-sea fluxes with the highest possible accuracy. Due to the above reasons we cannot use the NOC climatology (Berry and Kent, 2009) or surface meteorology records that are heavily under-sampled in many areas and biased towards regions of frequent ship tracks. Remotely sensed products suffer from uncertainties in the turbulent heat fluxes because there is no method of measuring near-surface atmospheric temperature and humidity from space. Model reanalysis air–sea fluxes assimilate all available remotely sensed and *in situ* data and provide the global coverage also in the ice-covered regions. That makes these products the best suited for the purposes of the analysis of this chapter. However, one needs to remember that these products have their own limitations (See Chapter 2) and are dependent on the model physics (Trenberth et al. 2009). Currently, there are two major model reanalysis products: National Center for Environmental Prediction/National Center for Atmospheric Research (NCEP/NCAR) and European Centre for Medium-Range Weather Forecasts (ECMWF). There is supported evidence that the NCEP/NCAR reanalysis may overestimate air-sea fluxes in high latitudes. Renfrew et al. (2002) showed that this discrepancy could be as large as

about 50% for the sensible heat flux in the Labrador Sea and may be caused by the coarse treatment of the ice-edge. Yu et al. (2004) also showed that the surface heat flux algorithms of NCEP/NCAR models are not correct for the areas with large differences between the temperatures of air and sea, which occurs in the Nordic Seas. The newest generation of reanalysis and the latest improvement of ECMWF reanalysis is ERA-Interim (Simmons et al. 2006). It has a greater horizontal and vertical resolution than NCEP/NCAR and ERA-40 and compares well in the Greenland Sea with the NOC climatology, remotely sensed fluxes and the regional climate model (REMO) of Max Planck Institute for Meteorology (Latarius and Quadfasel, 2010). Because of the many advantages described above the ECMWF ERA-Interim air-sea fluxes are used in the analysis of this chapter.

4.2 Relationship between SSHA and other atmospheric fields

In the previous chapter it was found that there exists a phase difference in the annual harmonic of the SSH between the interior of the Nordic Seas and the shallower parts, the borders of the Nordic Seas. Investigation of the annual cycle of various atmospheric fields could point us to the drivers of that phase difference. Therefore, the next subsection focuses on the annual cycles of various atmospheric fields. The annual harmonics are calculated in the same way as for the SSHA and the same time of the record is used (See Chapter 3).

4.2.1 Annual cycle of atmospheric fields

Mean Sea Level Pressure

The annual amplitudes of mean sea level pressure are the highest (up to 800Pa) in the central Nordic Seas, over deep basins and in the Irminger Sea (Figure 4.1). The sharp gradient in the annual mean sea level pressure is evident above the east Greenland continental slope and the Norwegian continental slope and Norwegian coast. The seasonal signal is a large contributor to the total signal of mean sea level pressure and locally explains up to 50% of variance in the central Nordic Seas. It was found that the spatial mean of the annual signal contributes 37.6% to the total variance of mean sea level pressure. The maximum in seasonal cycle occurs the earliest (April) over land and propagates south from northern Greenland to the Nordic Seas from May to June. In the areas of the maximum annual amplitudes the maximum mean sea level pressure occurs in June. The pressure decreases through the year from May/June reaching minimum in January.

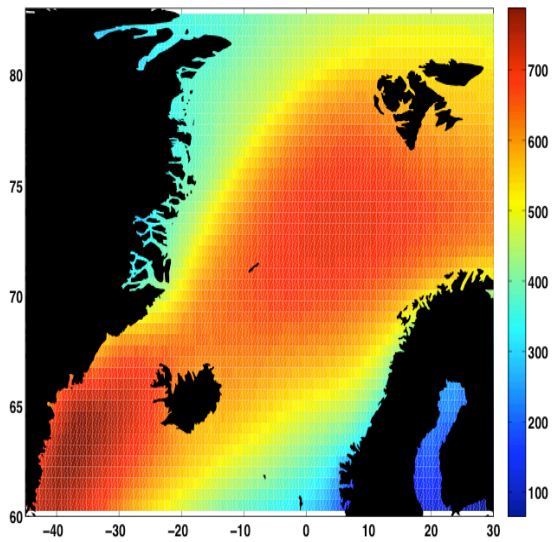

A) Amplitude [Pa]

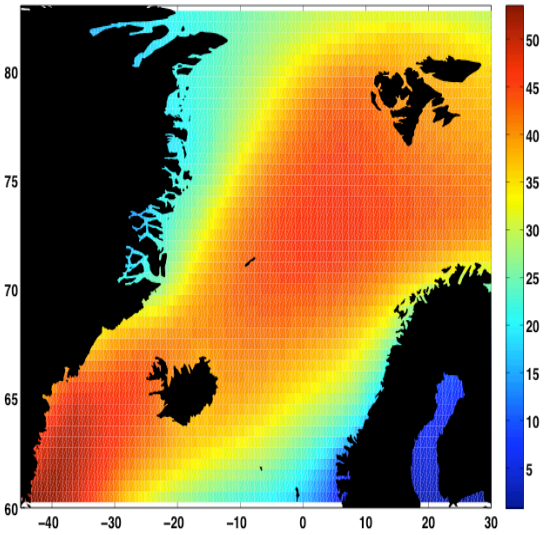

B) Variance explained [%]

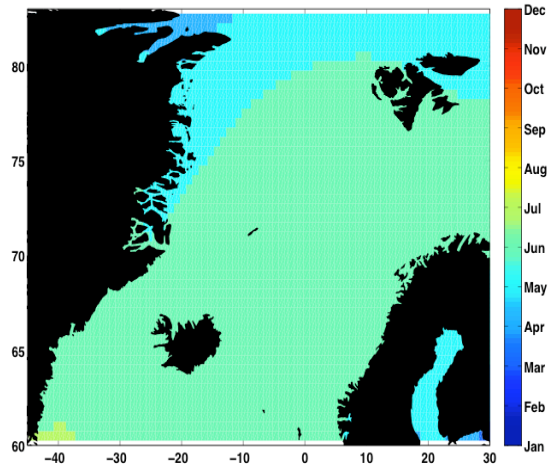

C) Phase

Figure 4.1. Annual cycle of mean sea level pressure: A) Amplitude (Pa), B) Variance explained (%), Phase (month when maximum in the atmospheric pressure occurs).

Zonal Wind Stress

The mean pattern of the zonal wind stress is positive (Easterlies) in the region along the eastern coast of Greenland located between 40^0W, 70^0N to 20^0W, 80^0N and along the Norwegian coast and south-eastern part of the Nordic Seas (not shown). The Westerlies (negative zonal wind stress) dominate south of 70^0N in the Irminger Sea and also around Svalbard. Generally, the winds are stronger during the winter reaching maximum strength in January. Therefore during the winter, the zonal wind stress become more negative in the Irminger Sea and more positive in the south-eastern part of the basin. The annual frequency contributes about 13% to the total signal and locally its major contributions come from a region along the eastern Greenland coast where it explains up to 70% of the local variance. The maximum wind stress occurs the earliest along the Greenland and Norwegian coasts (December) and one month later in the central Nordic Seas and Barents Seas (Figure 4.2).

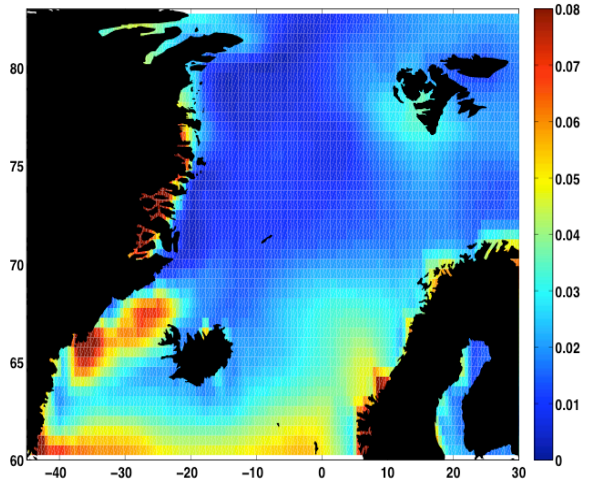

A) Amplitude [N m^{-2}]

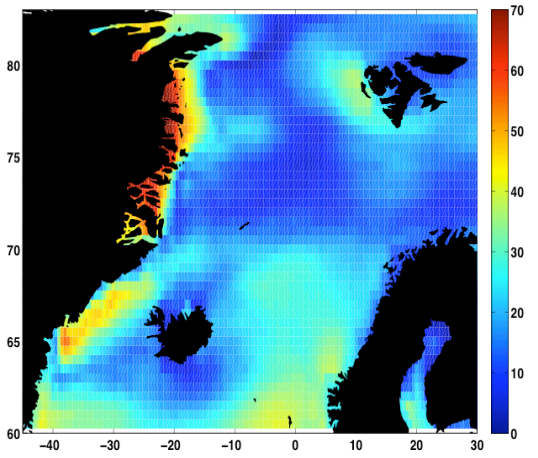

B) Variance explained [%]

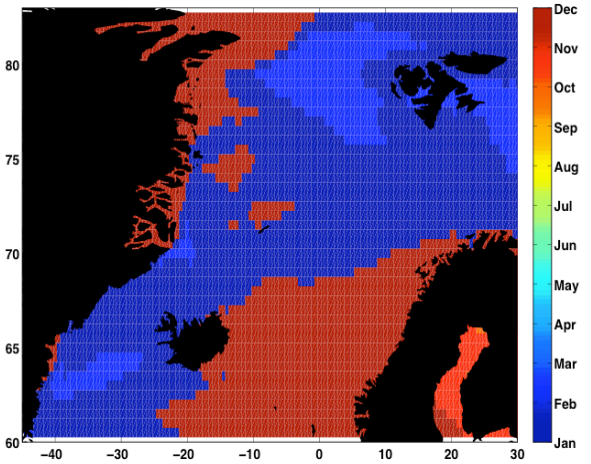

C) Phase

Figure 4.2. Annual cycle of zonal wind stress: A) Amplitude [N m^{-2}], B) Variance explained [%], C) Phase, month when the strongest wind stress occurs the (month of the maximum absolute wind stress).

Meridional Wind Stress

The annual mean of the meridional wind stress is negative (Northerly winds) along the eastern Greenland coast and positive (Southerly winds) along the Norwegian coast (not shown). These regions can be also characterized by the greatest amplitudes of seasonal variability (Figure 4.3). The seasonal cycle of meridional wind stress accounts for the 16.3% of variance in the total signal. Locally it can explain up to 70% of variance along the southern coast of Greenland. Also it has a large contribution to the total variance at the eastern Greenland continental shelf and along the Norwegian coast where it can reach up to 0.1 Nm^{-2} and explains 50% of the local variance (Figure 4.3). The maximum meridional winds (absolute values) occur in the winter. The winds reach maximum strength in December along the coasts of Greenland and Norway and in the Irminger and Iceland Seas and one month later in the rest of the Nordic Seas (Figure 4.3).

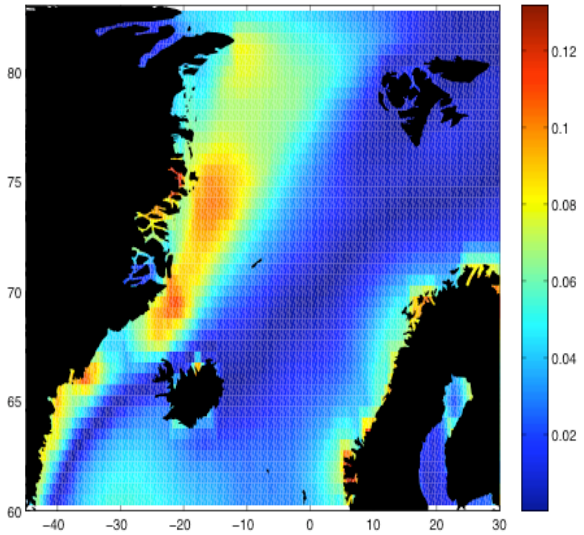

A) Amplitude [Nm^{-2}]

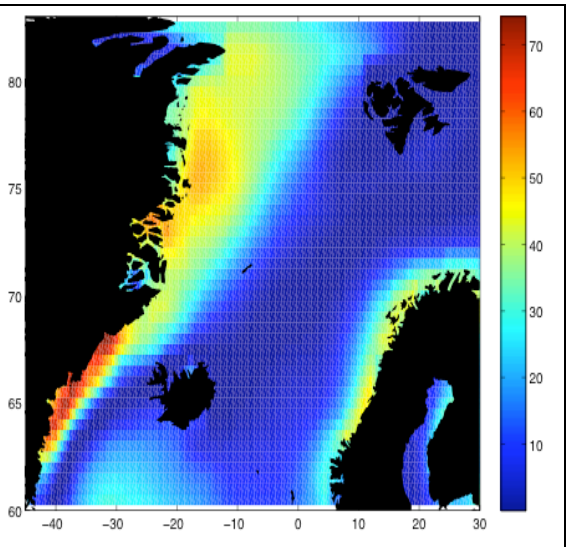

B) Variance explained [%]

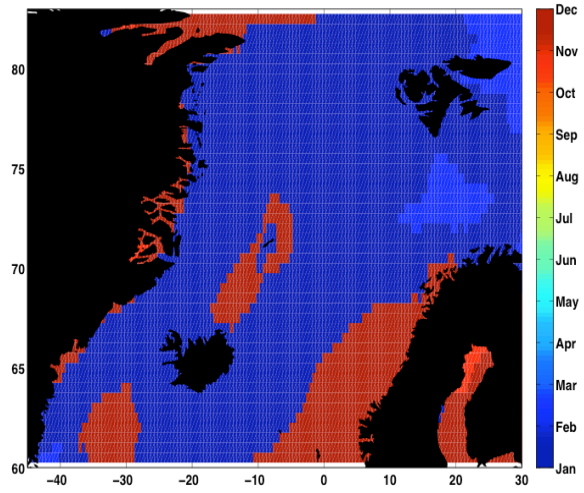

C) Phase

Figure 4.3. Annual cycle of meridional wind stress: A) Amplitude [Nm^{-2}], B) Variance explained, C) Phase, month when the strongest winds occur (month of the maximum of the absolute wind stress).

Wind Stress Curl

The mean annual pattern of the atmospheric circulation in the Nordic seas can be characterised by the cyclonic winds (positive wind stress curl) in the whole region except a few regions, where the winds are anticyclonic: Irminger and Barents Seas and a narrow region to the north of 75^0N along the Greenland coast (not shown).

Wind stress curl is related to the wind stress and therefore the mean sea level pressure. It has a strong annual component, which accounts for 15.3% of its total variance and locally can explain up to 70% of variance (region south of Denmark Strait, Figure 4.4). The annual contribution is the greatest in the Denmark Strait, Norwegian continental shelf and in the region from the eastern Fram Strait to the southwest, towards Denmark Strait. Furthermore, along the coast of Greenland the annual amplitudes in the wind stress curl are large (Figure 4.4). The maximum winds occur in the winter from December to January (Figure 4.4). The wind stress curl is cyclonic (positive) almost everywhere in the Nordic Seas except Irminger Sea and a very narrow region next to northern Greenland coast from October to April. The wind stress curl is stronger (more cyclonic or anticyclonic) in the winter (October- April) and it is much weaker in the summer in the whole basin with few regions that have large wind stress curl during the whole year: Denmark Strait, western Svalbard and along the Greenland and Norwegian coasts. Considering only the anomalies of the wind stress curl, the positive anomalies occur in the winter (October – June) and negative in the summer in the regions where the cyclonic winds dominate and the opposite anomalies occur for the regions where the anticyclonic winds dominate.

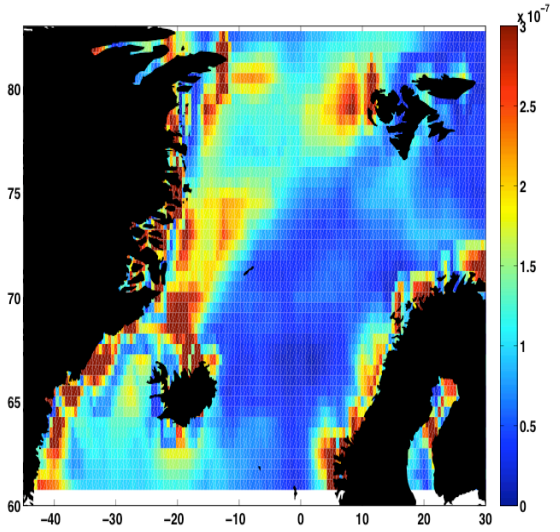

A) Amplitude [Nm^{-3}]

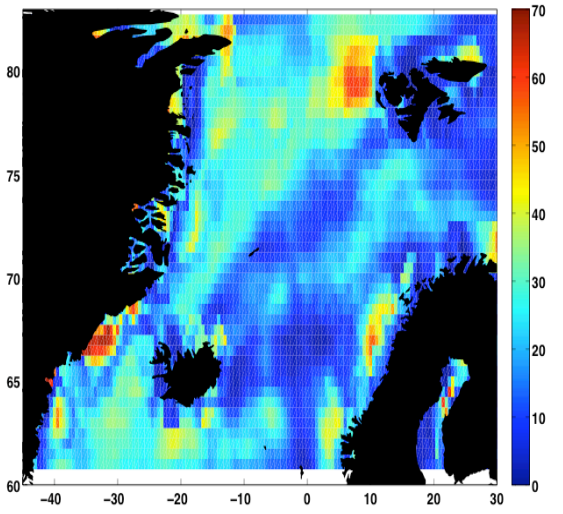

B) Variance explained [%]

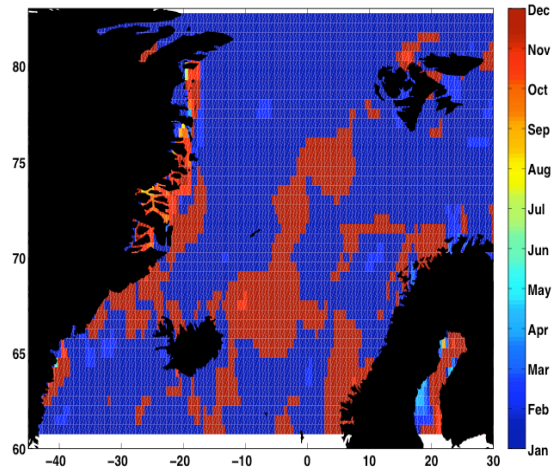

C) Phase

Figure 4.4. Annual cycle of wind stress curl: A) Amplitude [Nm^{-3}], B) Variance explained [%], Phase (month when the maximum absolute wind stress curl occurs-the strongest winds).

Total Net Heat Flux

The net heat flux is defined as positive downwards and therefore its annual mean is negative almost in the whole Nordic Seas except the ice-covered region of Greenland continental shelf where its mean is almost zero. The ocean loses heat to the atmosphere most of the time with the exception in the ice-covered regions at the northern Greenland shelf that almost do not exchange heat with the atmosphere. The greatest heat loss occurs during the winter (September to April) with the maximum heat loss occurring in the regions where strong winds dominate: along the sea-ice edge and in the Greenland Basin (-70 Wm^{-2}). On the other hand, in the summer (July and August) the ocean gains heat from the atmosphere at the Greenland continental shelf (positive heat flux of about 1 Wm^{-2}). Heat flux in the Nordic Seas has large annual variations with the largest amplitudes reaching 70 Wm^{-2} along the ice-edge where the wind stress curl is also the strongest. Its annual harmonic contributes 50.7% to the total variance (Figure 4.5). The amplitude of the annual harmonic is close to zero over the ice and along the eastern coast of Greenland. It reaches maximum at the ice-edge and in the region spreading from the eastern Fram Strait towards southwest. The maximum amplitudes occur at the same regions as for the maximum wind stress curl with the maximum heat loss occurring also in the winter (November to January). Considering only the anomalies relative to the annual mean, the negative anomalies were found during the winter (October-April) and positive anomalies during the summer (May – September) in the whole Nordic Seas.

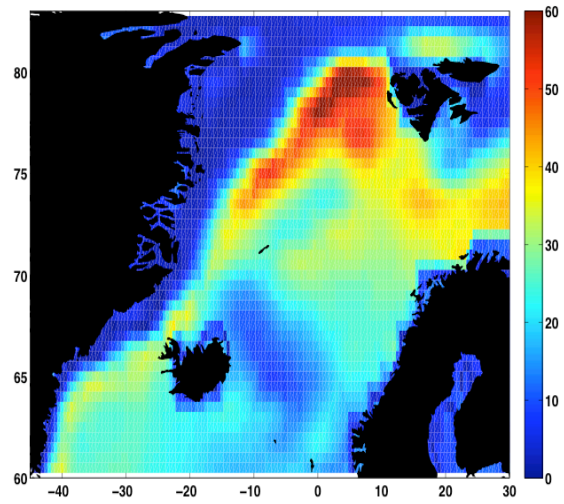

A) Amplitude [Wm^{-2}]

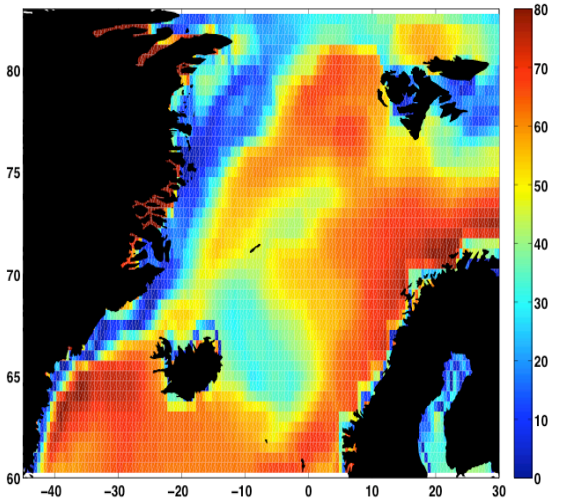

B) Variance explained [%]

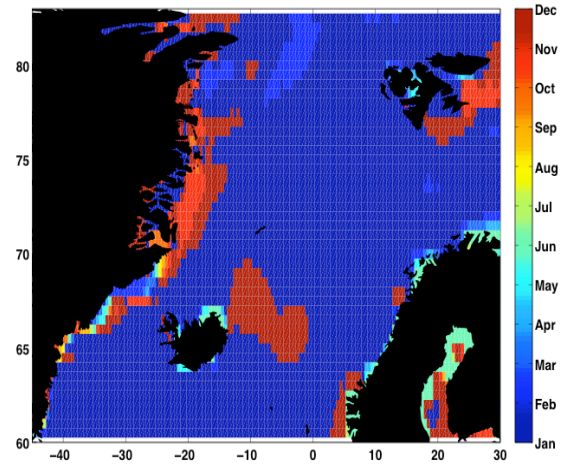

C) Phase

Figure 4.5. Annual cycle of total heat flux: A) Amplitude [Wm^{-2}], B) Variance explained [%], Phase (month when maximum heat loss occurs)

Evaporation

The annual mean of evaporation is negative in the whole Nordic Seas, which means the ocean loses heat to the atmosphere due to evaporation. The maximum heat loss occurs in the south-eastern part of the Nordic Seas and in the Irminger Sea. The annual cycle of evaporation is a major contributor to the total variance of the signal; it accounts for 54.6% of the total variance and locally explains up to 80% of variance (Figure 4.6). The annual harmonic is important in the whole region, except the eastern continental shelf of Greenland, which is the area of the sea-ice presence. The less negative (less heat loss) evaporation occurs in the summer from April until September and the ocean loses more heat (more negative evaporation) during the winter from October until March. The anomalies (relative to the annual mean) of evaporation are negative (ocean losing heat) in the whole area during the winter (October – March) except the ice-covered regions where the anomalies are almost zero. During the rest of the year the anomalies increase reaching the maximum values in July and decrease again and become negative in October.

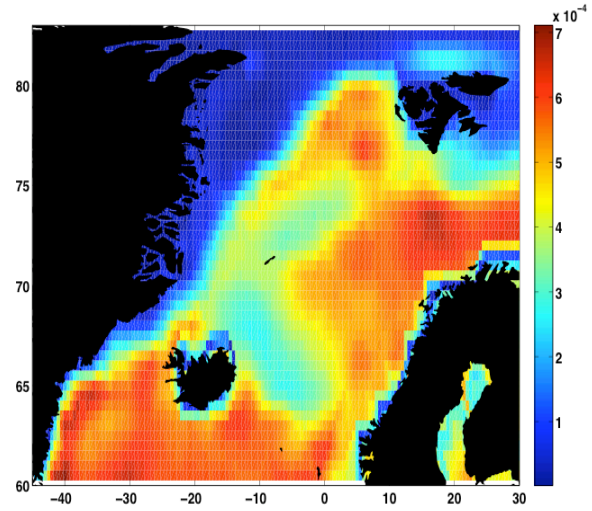

A) Amplitude [m]

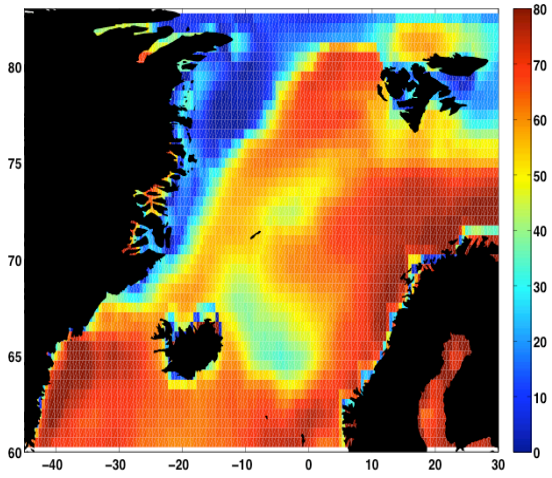

B) Variance explained [%]

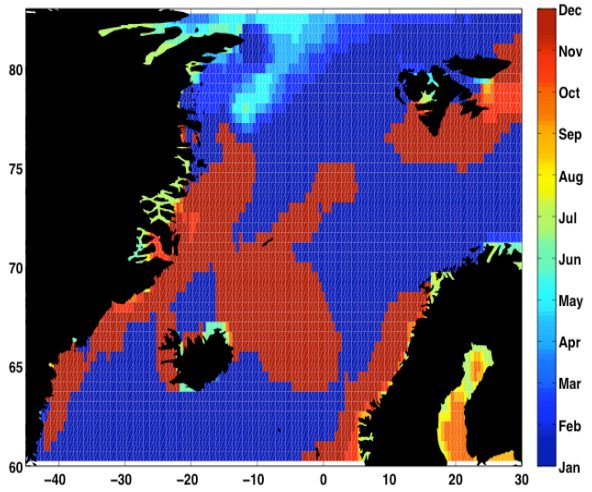

C) Phase

Figure 4. 6. Annual cycle of evaporation: A) amplitude [m], B) Variance explained [%], Phase (month when maximum evaporation occurs)

Precipitation

The annual cycle of precipitation accounts for 41.5% of the total variance. It has a small contribution in the deep basins and the northern part of Nordic Seas but higher amplitudes to the south of 70^0 N. Therefore, precipitation could be important in driving the seasonal cycle of sea level in the Irminger Sea and along the southern coast of Norway. The increased precipitation in the winter along the southern borders cause sea level increase in the region and a sea surface slope that decreases offshore which causes a southward geostrophic current at the western side and a northward current at the eastern. Therefore, the increased precipitation in the winter strengthens the mean circulation in the Nordic Sea, especially in the southern regions of the two major boundary currents. However, even in the areas where the amplitudes of the annual cycle are small, the local variance explained is high and reaches 70% almost everywhere. Again, only at the continental shelf of Greenland the seasonal cycle explains little variance. The phase of the annual harmonic is almost the same in the whole region and the maximum occurs during the winter (November to February) (Figure 4.7).

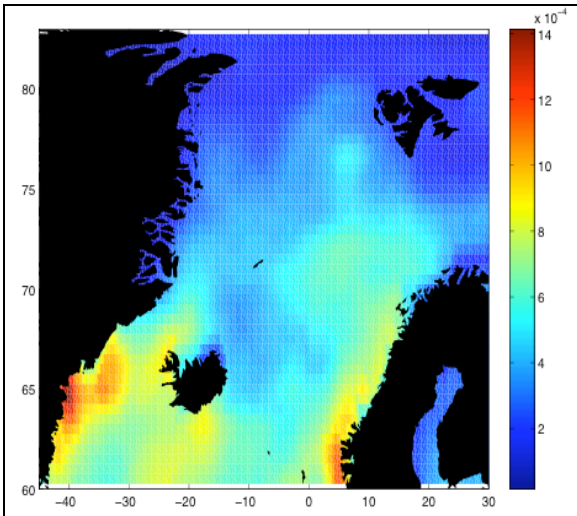

A) Amplitude [m]

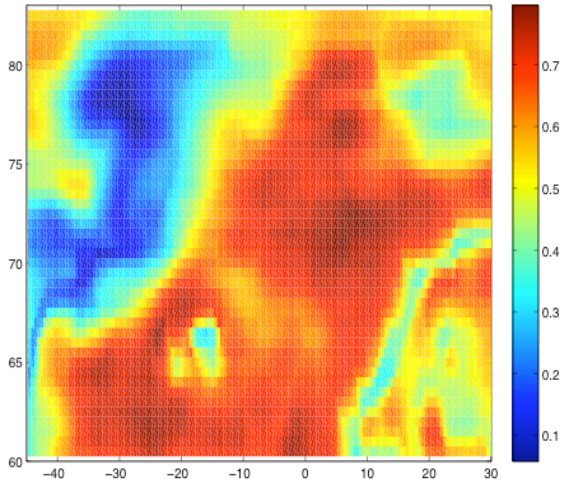

B) Variance explained [%]

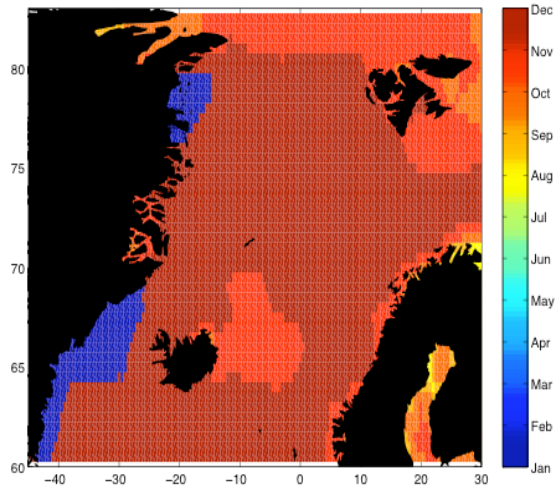

C) Phase

Figure 4. 7. Annual cycle of precipitation: A) Amplitude [m], B) Variance explained [%], Phase (month when maximum precipitation occurs).

Freshwater Flux

The freshwater flux was calculated as a difference between evaporation and precipitation (E-P). Its annual mean is negative in the whole Nordic Seas, meaning that precipitation exceeds evaporation and the ocean is gaining freshwater. In the ice-covered regions along the eastern Greenland coast the ocean gains much less freshwater (about -0.5 x 10^{-3} m) than in the other regions. The greatest net input of freshwater occurs at the southern coasts of Greenland and Norway, which are also characterised by large annual precipitation. The annual harmonic of the freshwater flux accounts for a major part of the total variance. It explains 56% of the signal's variance but locally 80% can be accounted by the seasonal signal almost in the whole region (Figure 4.8.B). The greatest amplitudes, reaching up to 1.6 x10^{-3}m, occur in the Irminger Sea and the region associated with the NwAC. Only along the Greenland coast and in the area where sea-ice is present the annual signal is small. The phase is also almost the same for the whole Nordic Seas and the maximum freshwater input occurs in the winter in the whole region (Figure 4.8). The phase pattern is more similar to the precipitation phase pattern and one can argue that the precipitation controls freshwater flux in the Nordic Seas at the annual timescale. Freshwater flux anomalies, relative to the annual mean, are negative in the winter in the whole region except the ice-covered ocean. In March the anomalies are close to zero also in the Norwegian Sea and increase towards positive values until May in the whole region. They continue to be positive until August but decrease and reach negative values again in September.

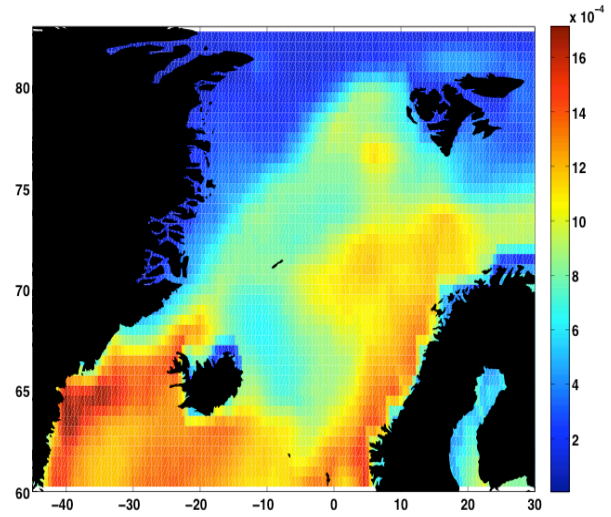

A) Amplitude [m]

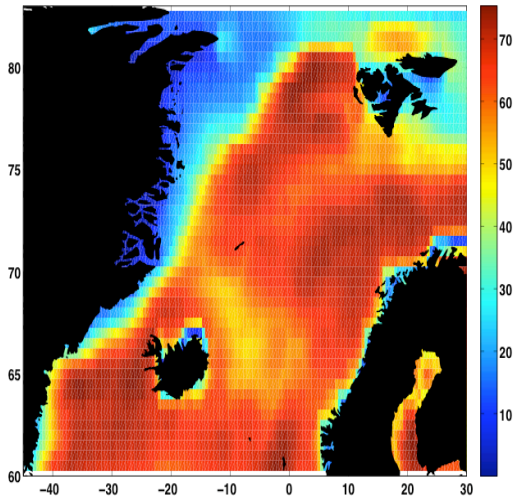

B) Variance explained

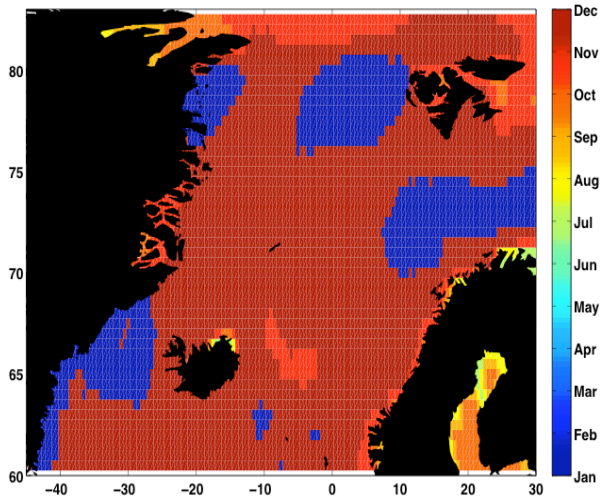

C) Phase

Figure 4.8. Annual cycle of freshwater flux: A) Amplitude [m], B) Variance explained [%], Phase (month when maximum freshwater input occurs).

Summary

All of the atmospheric fields have pronounced annual cycles and therefore their annual harmonics account for the substantial part of variance in the total signal. The largest proportion of variance accounted by the annual frequency was found in the freshwater flux (56%), evaporation (55%), heat flux (51%) and precipitation (41%). In the case of mean sea level pressure and all wind fields, the annual cycle accounts for much smaller proportion of variance: mean sea level pressure (38%), wind stress curl (15%), meridional wind stress (16%), zonal wind stress (13%). The reason for these smaller variances could be that the annual amplitudes of the wind stress fields are more localized and occur at the smaller regions when comparing to the mean sea level pressure or heat flux for which the annual cycle accounts for the majority of variance almost in the whole of the Nordic Seas.

All of the air-sea fluxes show strengthening during the winter which coincides with the behaviour of the atmospheric low-pressure centre in the central Nordic Seas. Therefore winter in the area is characterised by increased wind stress and wind stress curl, increased net heat loss and evaporation, precipitation and freshwater input into the ocean. The analysis of the phase of the annual cycle shows that there are some spatial delays in the timing of the maximum strength but these phase differences are usually of the order of 1-2 months. For example, all the wind fields reach their maximum the earliest along the coasts of Greenland and Norway and one month later in the other regions of the Nordic Seas. There are also small (1-2 months) annual phase differences between the atmospheric variables. For example the net freshwater flux has maximum input into the ocean in December, whereas the maximum heat loss and wind strength occur in January in the same area.

How can seasonal cycles of air-sea fluxes affect the seasonal cycle of sea level?

All of the air-sea fluxes can locally affect the sea level height. Precipitation causes freshwater input to the ocean and therefore increases SSHA. On the other hand, evaporation removes the freshwater from the ocean system and causes sea level to decrease. These effects are combined here into freshwater flux that is a difference between evaporation and precipitation. In the Nordic Seas the freshwater input dominates during the year but during the summer there is a small freshwater output from the ocean into the atmosphere. The increased freshwater input during the winter

along the southern coasts of Greenland and Norway would cause the local sea level rise in these regions and a sea surface slope that decreases offshore. As a result the mean geostrophic currents should strengthen in the southern Nordic Seas. On the other hand there is an increased freshwater input in the central Nordic Seas during the winter that causes a sea level slope which decreases inshore and causes a geostrophic current in the opposite direction to the mean circulation, therefore decreasing the southward transports to the north of Denmark Strait. However, in the same area, along the sea-ice edge, the increased net heat loss decreases SSH and causes a SSH slope that decreases offshore and therefore strengthens the EGC during the winter and increases its transport. Furthermore, much stronger winds along the coasts of Norway and Greenland can produce downwelling, which increases sea level and causes a geostrophic current in the direction of the wind. In a consequence, the EGC and NwAC accelerate and the circulation strengthens. The more cyclonic wind stress curl in the central Nordic Seas decreases the sea level in the central Nordic Seas which produces an ocean transport away from the central basins and also causes an increased geostrophic flow in the central Nordic Seas and in the major boundary currents. Therefore, during the winter most of the air-sea fluxes cause changes in the SSH that result in the strengthening of the circulation and increased transports in the region. The analysis of the annual harmonic shows that some of the fluxes (i.e. freshwater flux) can increase the circulation in one area and decrease elsewhere in the same month.

The analysis of the atmospheric annual cycles suggests that the SSHA annual cycle could be a delayed sea level response to the atmospheric annual forcing. The maximum SSHA occurs in the central Nordic Seas in August/September (Chapter 3), which is 1-2 months later after the occurrence of the minimum in the oceanic heat loss in the same region and one month after the weakest winds. On the other hand the sea level reaches a minimum in the same area in February and March, which is 1-2 months later than the maximum heat loss and the strongest winds in the area. The more cyclonic wind stress curl and the increased heat loss would be the most important for the time of the minimum SSH in the central Nordic Seas because they both cause sea level depression during the winter. For the borders of the Nordic Seas – the continental shelves of Greenland and Norway – the maximum in the sea level height occurs from October to December. The timing of this maximum coincides with the maximum wind stress along the coasts of Greenland and Norway that produces downwelling along the coast and

causes sea level rise. At the western side of the Nordic Seas (northern Greenland shelf) the winds are also anticyclonic which also cause the local sea level rise.

Sea-ice is a natural barrier to the local winds and can cause a change of their direction. It also limits the heat exchange with the atmosphere and therefore affects evaporation, freshwater and heat fluxes. Therefore, not surprisingly, the analysis of the annual cycle showed that all the fields had large horizontal gradients in the annual amplitudes across the ice edge during the investigated time period. A similar variability was found in the SSHA field (see Chapter 3) and the above analysis suggests this variability could be caused by the local forcing at the ice-edge and is not caused by errors in the altimetry data. Also the atmospheric fields have much smaller amplitudes in the ice-covered ocean, which means that we should expect a different response to local forcing in the ice-covered part of the Nordic Seas.

4.2.2. Correlations between SSHA and Other Atmospheric Fields.

Before moving to more complicated ways of exploring the relationship between SSHA and various atmospheric fields, simple correlations between the fields are investigated. The spatial correlations can test if the atmospheric variables are correlated with the sea level and how strong these relationships are. The strength and a sign of the correlation can inform how the local forcing affects SSHA and which areas are the most sensitive to this forcing. For the unfiltered and seasonally filtered pairs (a pair of monthly corrected and mapped SSHA and an atmospheric field) and for every grid point, Pearson's correlation coefficient is calculated, together with its 95% significance level and the percentage of the local variance explained in the SSHA signal.

Significant positive correlations between SSHA and the mean sea level pressure were found in the central Nordic Seas (Figure 4.9). The removal of the seasonal cycle from the data has not affected the spatial pattern of the relationship between the two fields; therefore one can conclude that there exists a significant in-phase relationship between sea level and the mean sea level pressure in the central Nordic Seas on monthly to interannual timescales. Furthermore, significant negative correlations were found at the continental shelf of Norway indicating the importance of the local seasonal pressure forcing (Figure 4.9). The sign of the correlation provides information about the relationship between the two variables and thus how sea level may respond to the local forcing. Therefore, the correlations between the atmospheric pressure and sea level show that when atmospheric pressure increases, sea level also increases in the central Nordic Seas but decreases at the borders and in the shallower areas. The pressure forcing cannot directly drive these changes but the wind and other air-sea fluxes that are affected (driven) by the changes in the pressure field can. Therefore, one can expect to find similar correlation patterns for the sea level and other atmospheric variables.

Indeed, similar spatial patterns in correlations were found between SSHA and freshwater flux (Figure 4.16), SSHA and evaporation (Figure 4.13) and SSHA and precipitation (Figure 4.15). The same correlation patterns between SSHA and the three atmospheric fields also indicate that these atmospheric fields are strongly correlated and could be indirectly driven by the atmospheric pressure variability. Therefore, the correlations show that the increase of the mean sea level pressure decrease the strength of the winds, evaporation, heat loss and their combined effect causes (or are correlated

with) sea level increase in the central Nordic Seas. The opposite effect on SSHA, which is also correlated with the increased atmospheric pressure, has a decreased precipitation and freshwater output in the area which would cause the sea level to drop if no other atmospheric forcing is present. However, the freshwater output is too small to compensate for the heat gain during the summer and a net effect is therefore sea level rise (positive SSHA anomaly) during the summer and sea level reduction in the winter.

Spatial correlation patterns of evaporation and SSHA (Figure 4.13) and net heat flux and SSHA (Figure 4.14) show very similar relationships, which is not surprising because evaporation is one of the terms in the net heat flux equation (See Chapter 2). They both show that when evaporation and heat loss decrease in the summer, the sea level increases in the central Nordic Seas and at the northern Greenland shelf – the area, which is ice-covered during the year. On the other hand, similar changes in the evaporation and heat flux are negatively correlated with the sea level at the Norwegian continental shelf, which show that these changes cannot be driven by the heat flux or evaporation because increased evaporation or heat loss cannot cause a local sea level rise. The negative correlations could also mean that while the ocean is losing heat to the atmosphere the sea level increases, which means there must be another opposing and stronger process causing sea level increase in the area. The variance explained by the heat flux and evaporation reaches 20-25% in the central Nordic Seas and about 15% at the Greenland shelf. For the seasonally filtered fields the significant and positive correlations are obtained only along the northern continental shelf of Greenland and north of Svalbard, the areas that are ice-covered during most of the year (Figure 4.13). The sign of the correlation suggests that if heat loss weakens (becomes more positive) the sea level increases, that is the same response of sea level as reported earlier for the annual period. The heat flux and evaporation can explain about 20% of the variance in the filtered SSHA.

The spatial correlation patterns for the sea level and freshwater flux are very similar to the one found for evaporation and SSHA and opposite to the pattern for SSHA and precipitation if one considers the seasonal signal alone (Figures 4.13, 4.15, 4.16). Positive correlations were found for precipitation and SSHA at the Norwegian continental shelf (Figure 4.15), which means that the increased precipitation would cause a local sea level rise. This is consistent with the theory (See section 4.1.1) and

suggests that precipitation could be one of the drivers of local seasonal sea level changes in that region. The variance explained by precipitation in the area reaches 30-40% of the SSHA variance but it explains only the seasonal variability (Figure 4.15). The correlation pattern for freshwater flux and SSHA is similar to the one found for evaporation and SSHA except in the ice-covered regions where it does not show any significant correlations (Figure 4.16). On the other hand, if the seasonal cycle is not present in the data, the pattern is similar to the one obtained for precipitation and SSHA, showing that increased freshwater input causes sea level rise in the central Nordic Seas. However, the sign of freshwater flux is opposite to the precipitation and therefore the pattern suggests that more freshwater input (more negative) is associated with sea level rise along the Norwegian continental shelf and less freshwater input (more positive) in the central Nordic Seas is associated with sea level rise. The second argument is not consistent with the theory and one can therefore conclude that freshwater flux cannot be responsible for sea level rise in the central Nordic Seas during the summer (seasonal changes) and at the other frequencies (monthly to interannual) but it is possible that it may drive the sea level variability along the Norwegian continental shelf at the seasonal frequencies.

At the borders of the Nordic Seas wind stress plays an important role in sea level variability. It was shown in the previous section that seasonal variations in the wind stress are greatest at the eastern Greenland continental slope and along the Norwegian shelf. Significant correlations were found in these regions for the filtered and unfiltered SSHA and the meridional wind stress and wind stress curl (Figures 4.11 and 4.12). The patterns are very similar for the unfiltered and seasonally filtered fields and show that more southerly winds along the Greenland continental slope and sea-ice edge are associated with the more positive sea level. The southerly winds would cause an upwelling along the ice-edge and therefore sea level decrease; also weaker northerly winds would cause sea level to drop. Therefore, the meridional wind cannot explain the sea level behaviour along the ice-edge. However, the anticyclonic wind (negative wind stress curl) is also significantly correlated to the SSHA in the same area, which means that an increase in the anticyclonic wind is associated with the sea level increase along the ice-edge. This is consistent with the Ekman theory because the anticyclonic wind causes local downwelling and sea level rise. Therefore one can conclude that wind stress curl can be one of the drivers of SSHA along the ice-edge and at the northern

Greenland continental shelf, where negative correlations are found (Figure 4.12). In total, about 20-25% the unfiltered SSHA variance and 15-20% of the filtered SSHA variance can be explained by the wind stress curl.

Significant positive correlations between SSHA and zonal and meridional wind stresses were found also along the continental shelf of Norway, which suggests that the stronger the south-westerly wind in (more positive anomaly) the higher the sea level along the Norwegian continental shelf. This is in agreement with Ekman theory (See Section 4.1.1), which states that the wind blowing in the direction parallel to the coast produces the net surface flow that is directed 90 degrees to the right of the wind at the Northern hemisphere. Therefore, along the Norwegian continental shelf this process produces local downwelling, which manifests as a higher sea level (Figures 4.10, 4.11). A similar situation occurs along the Greenland coast where the more northerly wind causes downwelling and local sea level rise (Figure 4.11). Furthermore, positive correlations for SSHA and zonal wind stress also show that more easterly wind in the Barents Sea and off southern and northern Svalbard is also associated with more positive sea level, which might be caused by downwelling in the area (Figure 4.10). On the other hand, SSHA in the Norwegian and Iceland Seas correlates negatively with the zonal component of the wind (Figure 4.10).

The significant correlations found in the central Nordic Seas between the zonal wind stress and SSHA cannot be supported by the theory, but may be caused by the low atmospheric pressure system and cyclonic winds which produce Ekman suction and upwelling that manifests in the sea level reduction. Wind stress can explain locally in these regions from 15-25% of the SSHA variance.

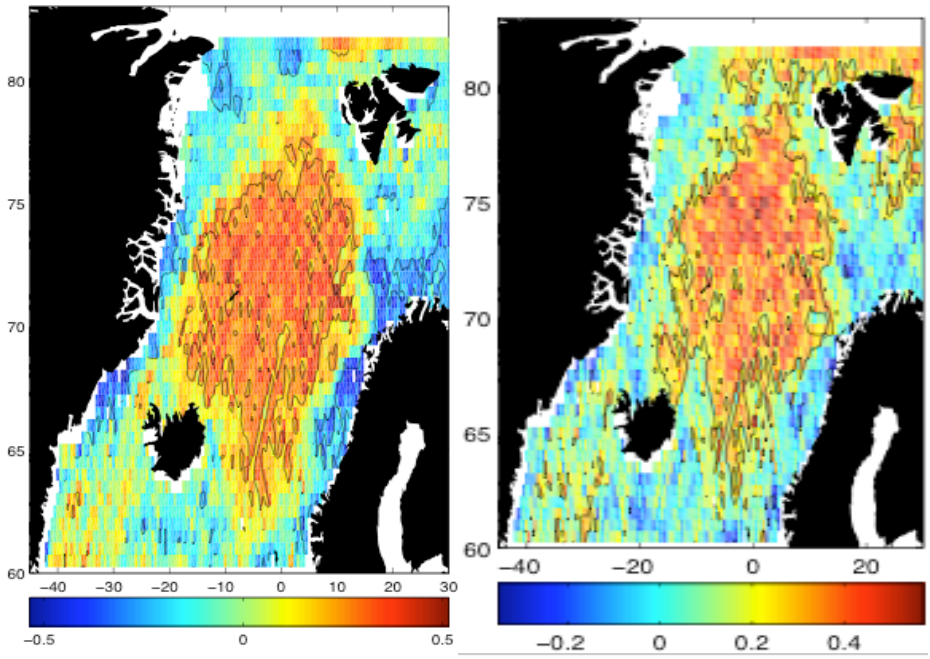

Figure 4. 9. Correlation coefficient (R) between SSHA and mean sea level pressure for the unfiltered (left) and seasonally filtered (right) fields. Significant correlations were contoured in black.

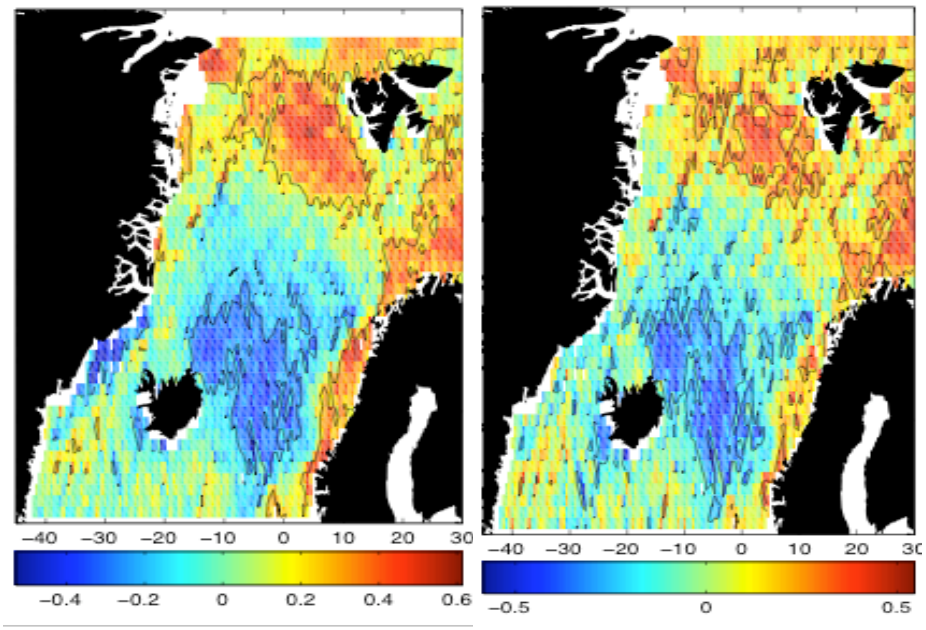

Figure 4. 10.Correlation coefficient (R) between SSHA and zonal wind stress for the unfiltered (left) and seasonally filtered (right) fields. Significant correlations were contoured in black.

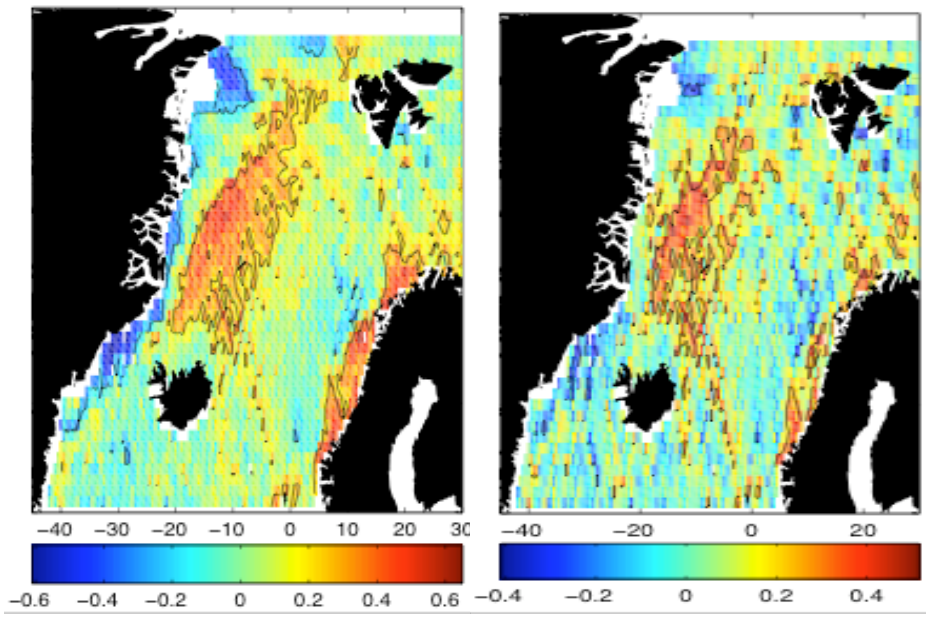

Figure 4. 11. Correlation coefficient (R) between SSHA and meridional wind stress for the unfiltered (left) and seasonally filtered (right) fields. Significant correlations were contoured in black.

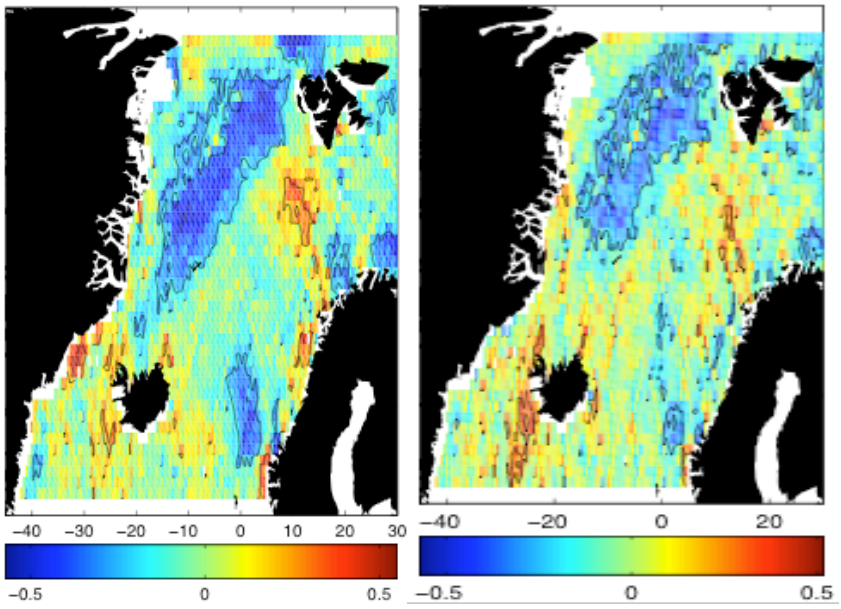

Figure 4.12. Correlation coefficient (R) between SSHA and wind stress curl for the unfiltered (left) and seasonally filtered (right) fields. Significant correlations were contoured in black.

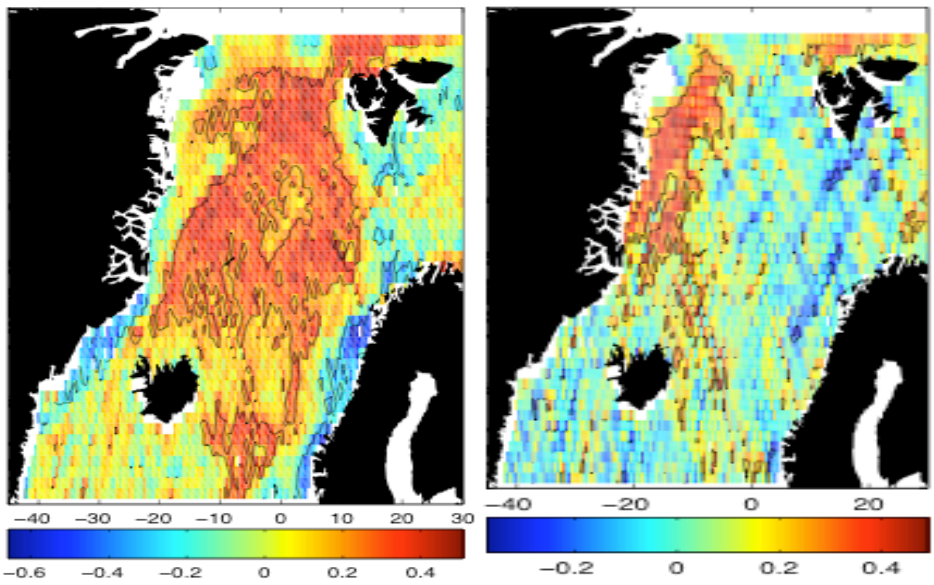

Figure 4.13. Correlation coefficient (R) between SSHA and evaporation and for the unfiltered (left) and seasonally filtered (right) fields. Significant correlations were contoured in black.

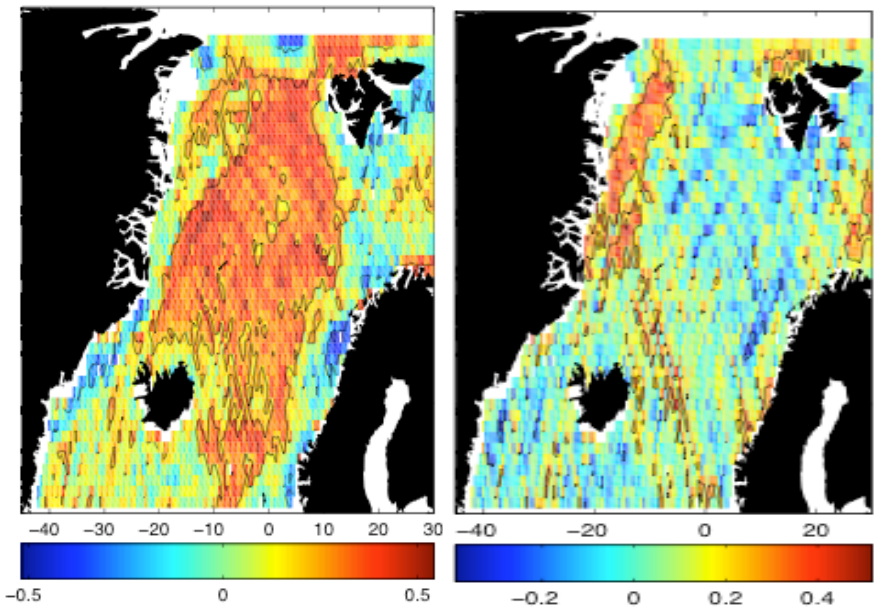

Figure 4. 14. Correlation coefficient (R) between SSHA and heat flux for the unfiltered (left) and seasonally filtered (right) fields. Significant correlations were contoured in black.

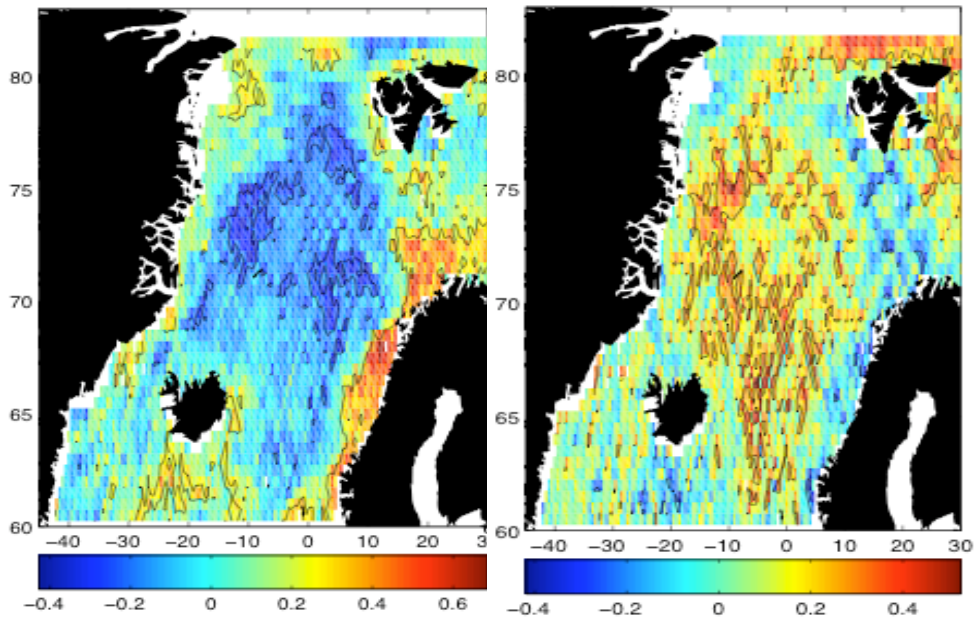

Figure 4. 15. Correlation coefficient (R) between SSHA and precipitation for the unfiltered (left) and seasonally filtered (right) fields. Significant correlations were contoured in black.

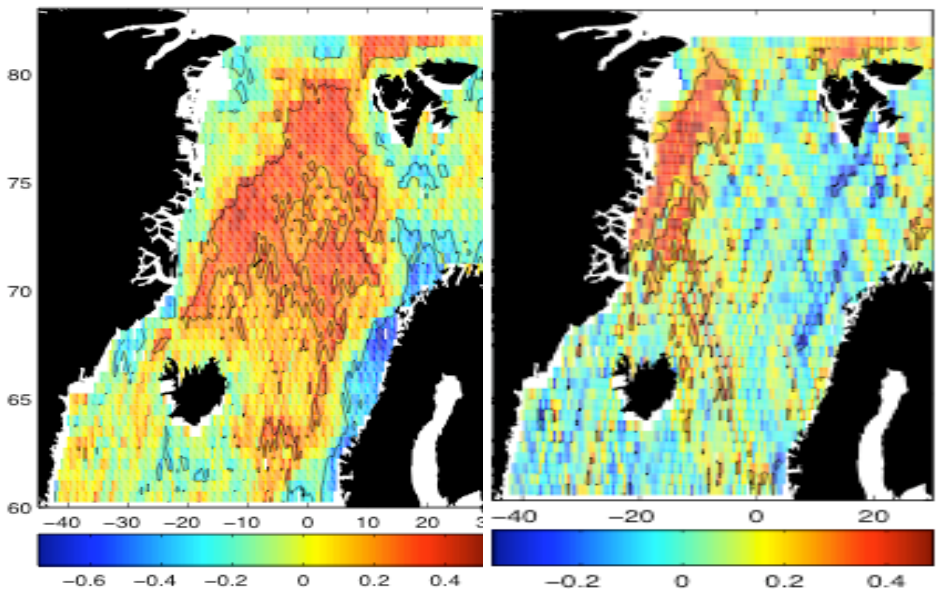

Figure 4. 16..Correlation coefficient (R) between SSHA and freshwater flux for the unfiltered (left) and seasonally filtered (right) fields. Significant correlations were contoured in black.

CHAPTER 4: RESULTS PART II

Summary

The analysis of the spatial correlations indicated the importance of all the atmospheric variables for the sea level variability. Significant correlations were found between SSHA and all the atmospheric fields at annual and other frequencies. On seasonal timescales, positive correlations were found in the central Nordic Seas between SSHA and mean sea level pressure, freshwater and heat fluxes and evaporation and in the same area negative correlations were found between SSHA and precipitation. On the other hand, all the wind fields correlate significantly on the seasonal timescale with SSHA at the borders of the Nordic Seas, along the ice-edge and in the Greenland Sea. Also seasonal variations in the Norwegian Sea are in-antiphase relationship with the zonal wind stress component.

Considering seasonally filtered data, the same correlation patterns were found for SSHA and mean sea level pressure, wind stress curl together with both wind components and freshwater flux, suggesting these atmospheric fields can be important candidates for forcing SSHA not only at the seasonal timescales but also at other periods. Evaporation and heat flux were correlated with SSH along the northern Greenland continental shelf. The sign of the correlation changed from positive to negative for SSH and precipitation after the removal of seasonal cycle.

The correlation analysis showed that air-sea fluxes can cause sea level variability that can be supported by the theory. The three main conclusions are:

1. Heat flux can drive sea level variability along the northern Greenland shelf, the area covered by the sea-ice during most of the year (seasonal and other periods) and in the central Nordic Seas during the summer when the other sea-air fluxes are weak or not present.
2. Precipitation and freshwater input can drive sea level variability along Norwegian Continental shelf but only at the seasonal time scales.
3. Wind stress curl can drive sea level variability along the ice-edge and wind stress can drive sea level along the borders of the Nordic Seas and in the shallower parts of the ocean by causing local downwelling and sea level rise in these areas.

4.3 Principal Component Analysis (PCA) of the atmospheric fields and the relationship between their PCs and the PCs of SSH.

So far the seasonal cycle of the atmospheric variables has been described and point-to-point correlations between SSHA and other fields were analyzed. The correlations indicated that all the atmospheric fields are significantly correlated with the SSHA but the correlations indicated that none of the atmospheric variables cannot explain a dominant amount of SSHA variance. In this section EOFs of the atmospheric fields are presented and the relationships between the principal components of SSHA and principal components of other atmospheric fields are analyzed. The spatial patterns of atmospheric EOFs can provide clues for similarities between the atmospheric fields and SSHA and therefore indicate which field could force particular modes of SSHA variability. The obtained EOFs are also used as a basis for a subsequent comparison in section 4.4. The EOFs and PCs of all atmospheric fields are obtained using the same method as for SSHA (See Chapter 3). When computing the covariance matrices, calculations were performed with and without weighting the fields by the square root of latitude as suggested by North et al. (1982). However, it was found that both methods give very similar results. The relationship between different atmospheric fields and sea level is investigated in Section 4.3.2 by analyzing the correlations between the corresponding principal components. The significance for all atmospheric EOFs was checked using Monte Carlo simulations in the same way as in Chapter 3.

The previous section showed that the seasonal cycle is a major contributor to the total variance of many fields. Therefore, one can expect the 1st EOF of the unfiltered data to show large annual oscillations and to describe the seasonal cycle. However, it does not mean that this EOF oscillates only with the annual frequency but can also oscillate with higher or lower frequencies. If the mode can explain most of the variance at other frequencies than the annual, the removal of the seasonal signal prior to the EOF would not change its structure and order. On the other hand, it may happen that different patterns emerge, or the order of the EOFs changes if the variability at the other frequencies has different structure. Therefore, the final effect of the filtering out of the seasonal signal depends on the variance explained by this mode after the seasonal cycle is removed. Furthermore, some EOFs can be important only at a certain frequency (i.e.

annual) and therefore repeating the analysis without the seasonal signal might provide the clues for the most important variability at other, less energetic frequencies.

4.3.1 Empirical Orthogonal Functions of the atmospheric fields.

Mean Sea Level Pressure [Pa]

The spatially averaged temporal autocorrelation function indicated that the mean sea level pressure field has 56 degrees of freedom, and 77 when the seasonal cycle is removed. The results of Monte Carlo simulations indicated that only 3 (4) EOFs are significant for the unfiltered (filtered) data. There is almost no difference in the EOF patterns when comparing EOFs of unfiltered to seasonally filtered data (Figure 4.17). Furthermore, their principal components look almost the same at both longer and shorter periods than seasonal. The first EOF accounts for 79% and 66% of the total variance in the unfiltered and filtered field respectively, implying that the mode is the most important for all frequencies. Only the first EOF has a clear annual cycle (Figure 4.17). Its spatial pattern has the largest amplitude in the central Nordic Seas, and it can be recognized as the Icelandic Low. The area of low pressure extends from Irminger Sea to the Barents Sea with two centres: one in the Irminger Sea and another one in the central Nordic Seas, north of Norway.

The only difference between the two first EOFs of mean sea level pressure is that the seasonally filtered one has only one centre. Therefore it can be argued that the second centre occurs mainly at the annual frequency. A similar mode of variability is often referred to in the literature as describing mean sea level pressure due to the North Atlantic Oscillation (e.g. Furevik et al. 2006). Furthermore, it accounts for the greatest proportion of total variance in the mean sea level field and its structure is similar to the 2nd EOF of SSHA. This mode was also found to be significantly correlated to SSHA at the Greenland and Norwegian continental shelves, explaining there about 10 - 15% of variance (not shown). Furthermore, some weak significant positive correlations were obtained for this mode and SSHA in the central Nordic Seas, but the explained variance was found to be less than 10% of the SSHA variance and it corresponds to a scattered pattern along a few tracks in the SSHA data (not shown). On the other hand, much stronger negative correlations were obtained in the central Nordic Seas, Fram Strait and a region north and east of Svalbard for the 1st PC of the seasonally filtered mean sea level pressure and the filtered SSHA. Furthermore, positive significant correlations were found in the Barents Sea and along the continental shelf of Norway. The 1st PC of the filtered mean sea level pressure can explain locally about 10-15% of the filtered SSHA variance in the areas of the significant correlation.

The second EOF of mean sea level pressure shows antiphase oscillations between the eastern and western parts of the region. It has two centres; one located over northern Norway, and the second located over the Iceland and Irminger Seas. Jahnke-Borneman and Brummer (2009) described this pattern as the Iceland Lofoten Difference (LID) because it is caused by the atmospheric pressure difference over the Iceland and Lofoten regions. Their study found that this pattern produces changes in the atmospheric meridional mass transport, which affects the surface air temperature in the Nordic Seas with maximum of -7K in the north-western Nordic Seas and a wide region along the coast of Greenland. Furthermore, they have argued that the LID causes changes in sea ice export through Fram Strait and can explain about 20% of the sea-ice extent variability. The 2nd EOF of mean sea level pressure explains about 9.6% of variance in the unfiltered data and almost 17% in the seasonally filtered data. This implies that the mode is more important at other frequencies than the annual. Its PC shows a negative trend in mean sea level pressure in the first two years of the record and a recovery after that period. Moderate but significant positive correlations (R=0.35) were found for the 2nd PC of the seasonally filtered mean sea level pressure and the filtered SSHA in the central Nordic and Barents Seas and a region located to the north and east of Svalbard. The mode can explain locally up to 15% of the filtered SSH variance in these regions.

The third EOF of mean sea level pressure shows antiphase oscillations between the north-western and south-eastern regions of the Nordic Seas. This mode is therefore responsible for the atmospheric zonal mass transport. Its PC is more important on the semi-annual timescales. The mode is responsible for 7.5% of total variance in the unfiltered field and about 12% in the seasonally filtered field. However, no significant correlations were found between this mode and SSHA.

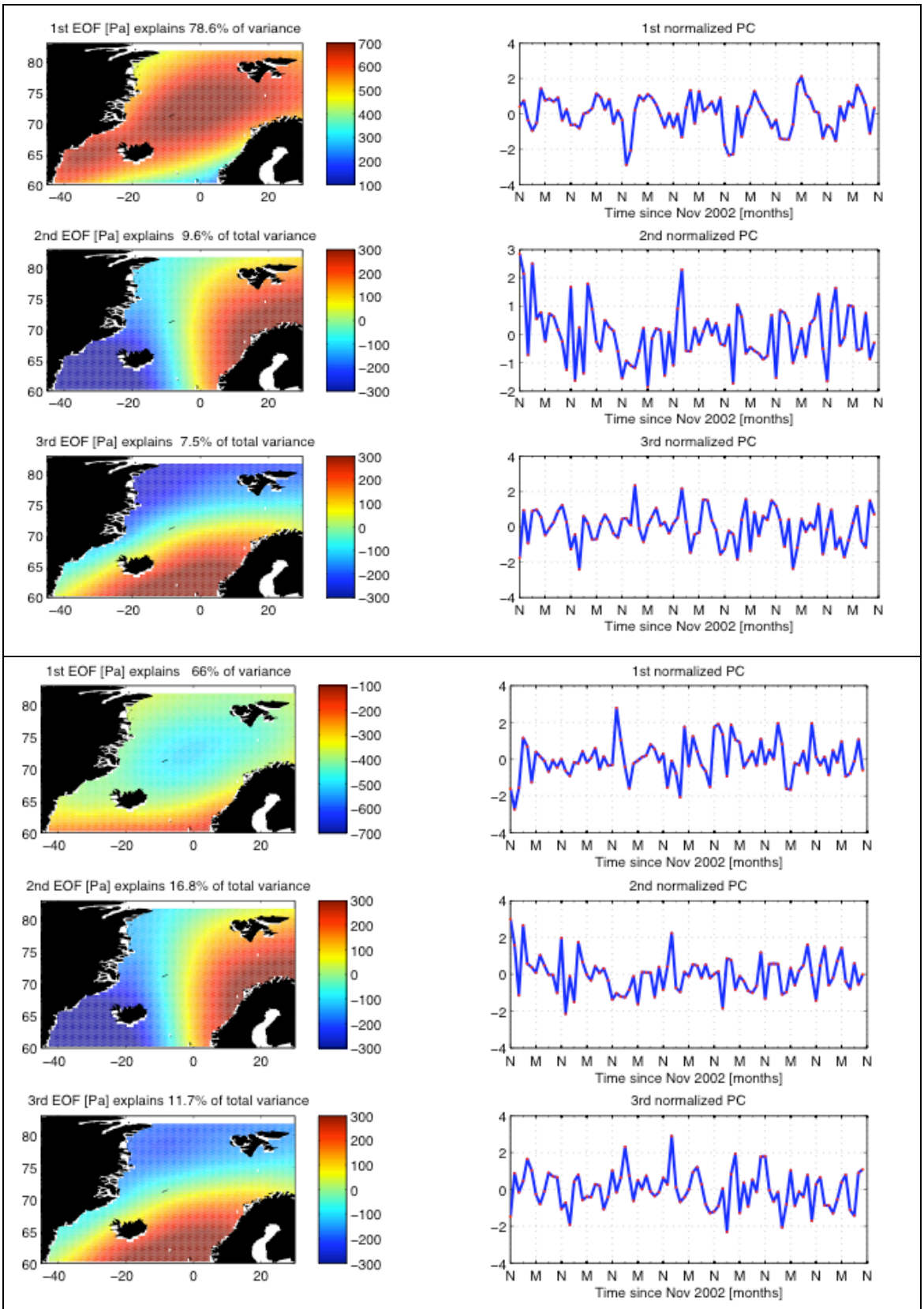

Figure 4.17. The first three EOFs of mean sea level pressure: their spatial patterns (left) [Pa] and their time series (right). Top: EOFs of unfiltered data; bottom: EOFs of seasonally filtered data.

Zonal Wind Stress [Nm^{-2}]

The first six EOFs of the zonal wind stress were found to be significant according to the results of Monte Carlo simulations for unfiltered and filtered cases. The first three PCs of the unfiltered data oscillate at the annual frequency and account for the major part of the total variance (about 78.2%). The modes did not change their patterns when the seasonal cycle was removed prior to the EOF calculation (Figure 4.18). The first EOF accounts for 52.2% (54.3% for the filtered case) of the total variance and shows oscillations in zonal wind stress in the area to the South of 70^0N. The mode is positively correlated with SSHA in the central Nordic Seas and to the north of Svalbard and negatively correlated along the Norwegian continental shelf, where it can explain 5-10% of the total variance. On the other hand, the seasonally filtered mode is negatively correlated to the filtered SSHA in the central Nordic Seas, north of Svalbard and north-west of Fram Strait. It can explain up to 20% of the filtered SSHA variance in the Greenland Sea and about 10% in the other regions that significantly correlated with the sea level variability.

The 2nd EOF accounts for 15.0% and 17.1% of total variance for the unfiltered and filtered case respectively. The mode shows an anti-phase relationship between south-eastern and north-eastern regions of the Nordic Seas. The 2nd PC of the unfiltered (filtered) zonal wind stress is negatively (positively) correlated with unfiltered (filtered) SSHA in the central Nordic and Barents Seas where it can explain about 10% of the SSHA variance.

The 3rd EOF of the zonal wind stress accounts for 5.9% and 7.2% of the total variance for the unfiltered and filtered fields. It is responsible for strong annual oscillations that have a centre in the Denmark Strait and Iceland Sea and are in the antiphase relationship with the zonal wind stress at the continental shelf of Norway. The mode is negatively correlated along the Norwegian and Greenland shelves and in the region located to the North of Fram Strait (North of 80^0N and from 0^0 to 8^0E). The mode of the seasonally filtered zonal wind stress is not significantly correlated with the filtered SSHA. The three EOFs show that the variability in the zonal wind stress occurs mainly in the southern and north-eastern region of the Nordic Seas. Figure 18 shows that zonal wind stress does not vary a lot at the Greenland continental shelf, Fram Strait and Greenland Sea.

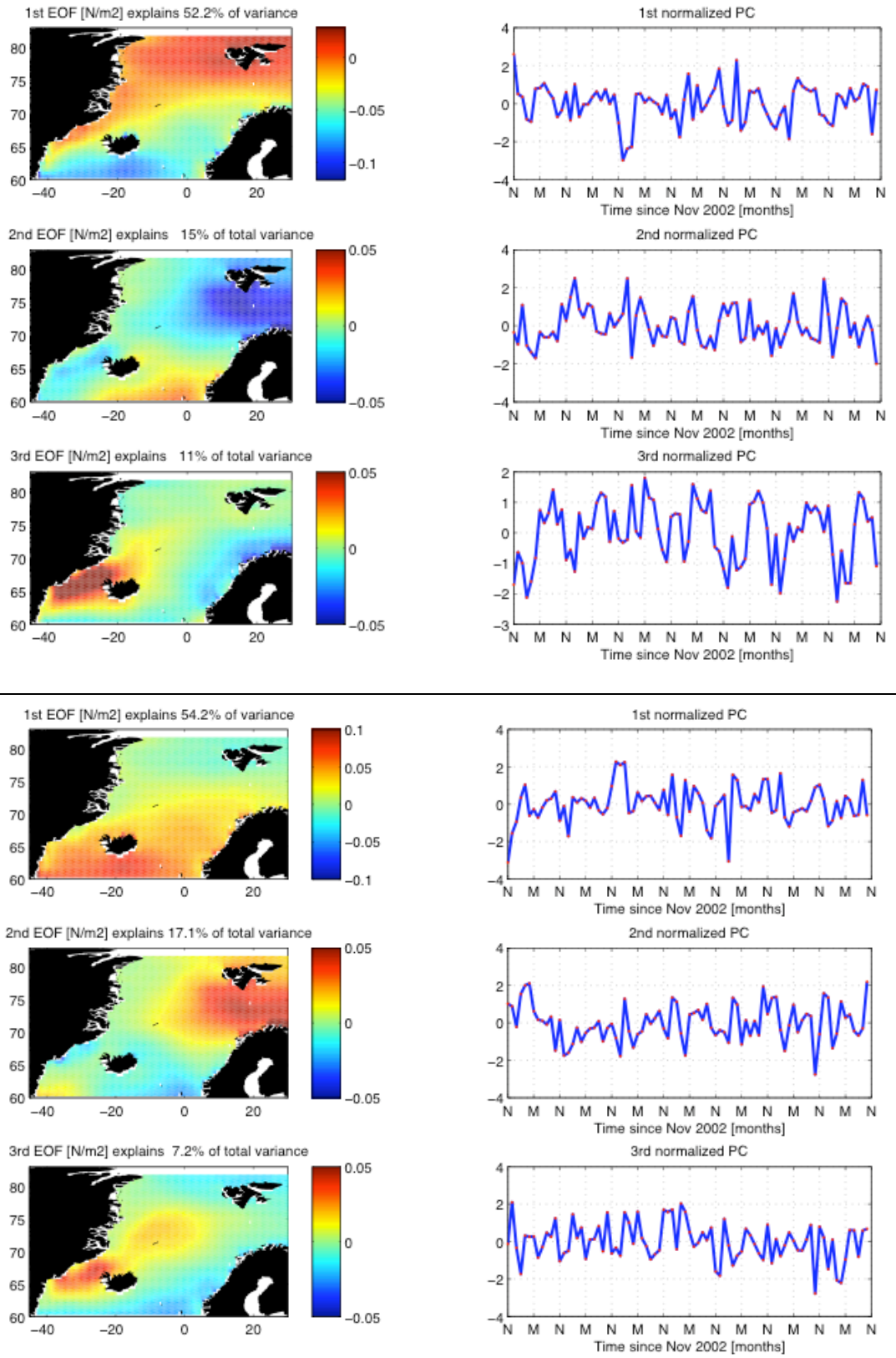

Figure 4.18. The first three EOFs of zonal wind stress: their spatial patterns (left) [Nm^{-2}] and their time series (right). Top: EOFs of unfiltered data; bottom: EOFs of seasonally filtered data.

Meridional wind stress [Nm^{-2}]

The first six EOFs of meridional wind stress are significant according to the Monte Carlo simulations for unfiltered and filtered cases. All the three first PCs of the unfiltered data oscillate at the annual frequency and account together for a major part of the variance (79.2%). The modes almost have not changed their patterns and time series when the seasonal cycle was removed prior to the EOF calculation (Figure 4.19). The first EOF accounts for 38.9% (46.8% for the filtered case) of the total variance and shows oscillations in the central Nordic Seas that get smaller away from the centre. It is significantly correlated with SSHA in the central Nordic Seas (negative correlation) and along Greenland coast (positive correlation) where it explains up to 12% of SSHA variance. The1st PC of the seasonally filtered meridional wind stress is negatively correlated to the filtered SSHA in the eastern Barents Sea where it can explain about 10% of SSH variance.

The 2nd EOF accounts for 29.4% and 17.3% of total variance for the unfiltered and filtered case respectively. The mode shows the anti-phase relationship between southeastern and northwestern regions of the Nordic Seas. It is significantly correlated with the SSHA in the central Nordic Seas (negative correlations) and along the Greenland and Norwegian continental shelves (positive correlations) explaining locally about 15% of SSHA variance. If considering frequencies other than annual, the 2nd PC of the filtered meridional wind stress is positively correlated with the filtered SSHA in the central Nordic Seas explaining up to 10% of SSH variance.

The 3rd EOF of meridional wind stress accounts for 10.9% and 12.2% of the total variance for the unfiltered and filtered case and it is responsible for antiphase oscillations in meridional wind stress between Irminger and Barents Seas and northern and southeastern regions of Nordic Seas (Figure 4.19). The mode is negatively correlated in the Greenland Sea where it can explain about 8% of the unfiltered SSH variance and up to 20% of the filtered variance in the Greenland Sea.

The rest of the significant EOF modes of meridional wind stress account for 12.4% of the unfiltered meridional wind stress and 14.1% of the filtered SSHA. From the rest

significant EOFs of meridional wind stress, only the 6th PC of the filtered meridional wind stress is significantly correlated to the filtered SSHA. The correlations are negative for the unfiltered fields and positive for the filtered variables. The relationship occurs in the ice-covered regions at the eastern Greenland continental shelf and a region associated with the West Spitsbergen Current located north of 73^{0}N (not shown).

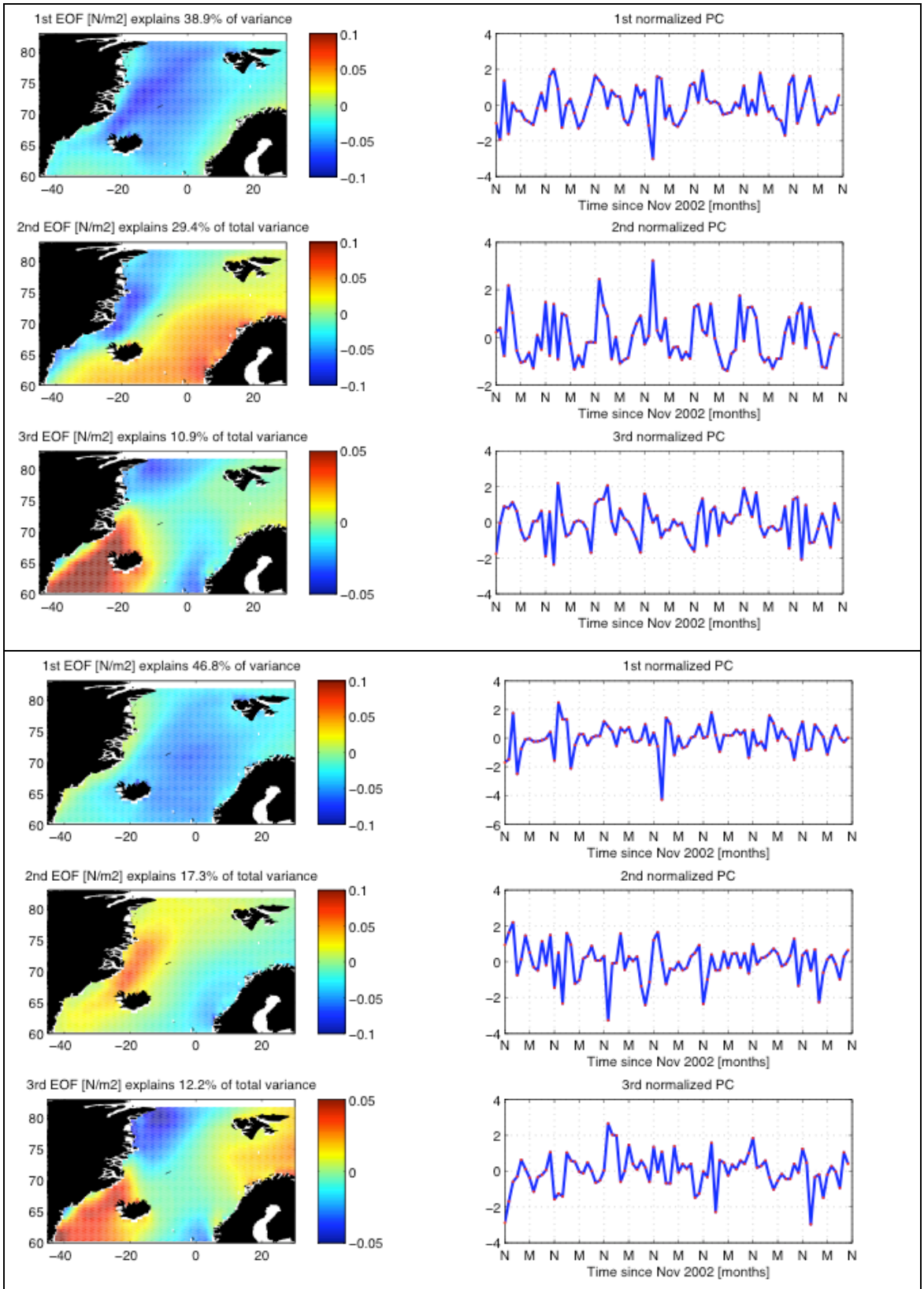

Figure 4. 19. The first three EOFs of meridional wind stress: their spatial patterns (left) [Nm^{-2}] and their time series (right). Top: EOFs of unfiltered data; bottom: EOFs of seasonally filtered data.

Wind Stress Curl [Nm^{-3}]

The Monte Carlo simulations showed that the first twelve EOFs of wind stress curl are significant. There is a difference in the pattern and time series between the EOFs of unfiltered and filtered data. The first EOF of the seasonally filtered wind stress curl is similar to the 2nd EOF of the unfiltered data (Figure 4.20). It accounts for 14.5% and 18.9% of variance in the unfiltered and filtered data respectively. The mode oscillates at the continental shelf of Greenland where the amplitudes are negative. Positive amplitudes for this mode are found in the central Nordic Seas and southern Greenland regions. No significant correlations were found for this mode and SSHA when the seasonal cycle was present. However, significant negative correlations were found for this mode and the filtered SSHA in the central Nordic Seas, Fram Strait, and a region north and east of Svalbard (not shown). Locally, the 1st PC of the filtered wind stress curl can explain about 10% of variance in the filtered SSHA. Furthermore, it was found that the first three PCs of the filtered wind stress curl are significantly negatively correlated in the central Nordic Seas where each can explain about 10% of the total variance in the filtered SSHA.

The 1st EOF of the unfiltered wind stress curl accounts for 23.1% of total variance and shows the antiphase oscillations in wind stress curl at the annual frequencies over a wide region stretching from 75^0N at the Greenland continental shelf to the east, reaching Fram Strait via Greenland and Iceland Seas (Figure 4.20). The 1st PC of the unfiltered wind stress curl is significantly correlated (at 95% confidence level) to the unfiltered SSHA in the central Nordic Seas (positive correlation), the region north of Svalbard (positive correlation) and along the Norwegian and Greenland coasts (negative correlation) and can explain locally about 25% of the SSHA variance.

The 3rd EOF of wind stress curl accounts for 13% of the total variance in both scenarios (filtered and unfiltered) and also has similar patterns and time series. It shows anti-phase oscillations in wind stress curl at the borders of Nordic Seas and at the Greenland and Norwegian continental shelves. The mode is not significantly correlated with SSHA if the seasonal cycle is not filtered out from the fields before EOF analysis. Significant negative correlations between the 3rd PC of the filtered wind stress curl and the filtered

SSHA occur in the central Nordic Seas and explain there about 10% of the filtered SSHA variance.

The higher modes of variability account for 10.2%, 5.7%, 4.6% of total variance for the 4^{th},5^{th} and 6^{th} EOF of unfiltered wind stress curl and 9.9%, 5.9%, 4.0% for the EOFs of seasonally filtered data. The significant correlations between the unfiltered SSHA and PCs of the unfiltered wind stress curl were only found for PC1 of wind stress curl and SSHA (if taking into account the effective number of degrees of freedom of the two variables). On the other hand, significant correlations were found for the first three PCs of the seasonally filtered wind stress curl and the filtered SSHA in the central Nordic Seas. Furthermore, significant positive significant correlations were found for the 6^{th} PC of the filtered wind stress curl and the filtered SSHA at the Greenland continental shelf and in the Barents Sea, explaining locally about 10% of the filtered SSHA variance.

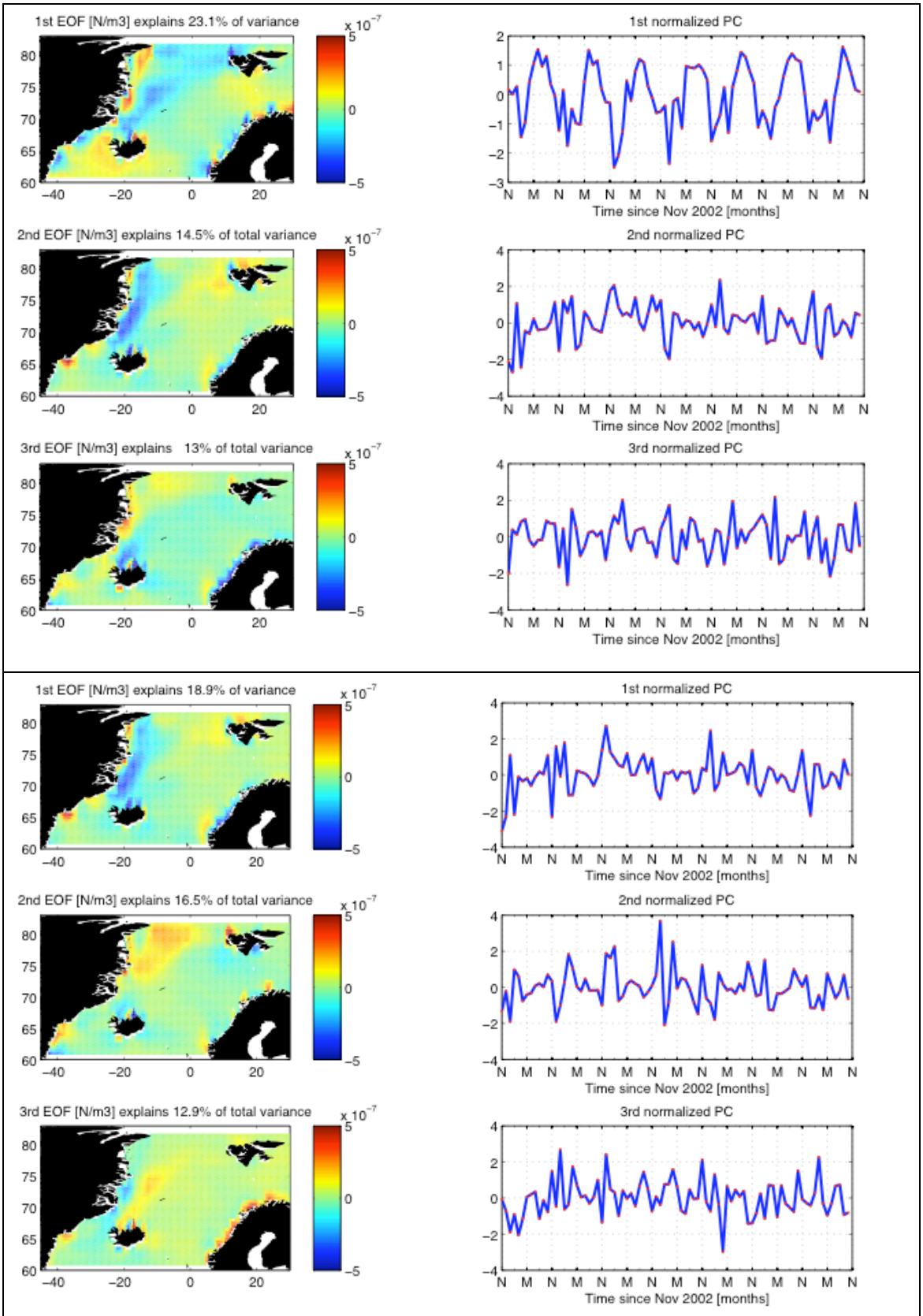

Figure 4.20.The first three EOFs of wind stress curl: their spatial patterns (left) [Nm^{-3} *100] and their time series (right). Top: EOFs of unfiltered data; bottom: EOFs of seasonally filtered data.

Heat flux [Wm^{-2}]

The first EOF of heat flux accounts for a major part of the total variance: 77.5% and 58.1% for the unfiltered and filtered fields. Therefore the greatest variability in the heat flux corresponds to the in-phase oscillations of the whole basin with maximum amplitudes occurring east of the east Greenland continental shelf, in the deep basins and in the Barents Sea. This dominant mode of variability shows oscillations at annual and higher frequencies (Figure 4.21, top). The 1st PC of the unfiltered heat flux is negatively correlated with SSHA in the central Nordic Seas and positively correlated with SSHA along the coast of Greenland, north of 65^0N, and to the North of Fram Strait. It can explain locally about 15% of the total variance in the unfiltered SSHA. The 1st PC of the seasonally filtered heat flux is not significantly correlated with the filtered SSHA.

The 2nd EOF of heat flux accounts for only 5.5% of variance in the unfiltered case and 11.6% of variance for the filtered case. It shows antiphase oscillations between the Barents Sea and Irminger Sea and the area associated with the sea-ice edge. This mode does not show any oscillations at annual frequency and the removal of the seasonal cycle prior to determining the EOFs makes this mode more important, suggesting this mode plays a role at frequencies other than annual. The 2nd PC of the unfiltered heat flux is negatively correlated with sea level variability in the central Nordic seas and positively correlated at the Norwegian shelf explaining there from 5-10% of the total SSHA variance. On the other hand, the 2nd PC of the seasonally filtered heat flux is positively correlated with the filtered SSHA in the central Nordic Seas, north of Fram Strait and Svalbard, and east of Svalbard.

The third EOF of heat flux accounts for only 4.6% and 8.7% (unfiltered and filtered) and it is responsible for the antiphase oscillations between the Fram Strait and central Nordic Seas. The third PC of heat flux is positively correlated with the SSHA in the Irminger Sea, where it can explain 10% of the SSH variance. On the other hand, the 3rd PC of the filtered heat flux is negatively correlated with the filtered SSHA along continental shelf of Norway and the Barents Sea.

The results of Monte Carlo simulations indicated that the first six and eight modes are significant at 95% confidence level for the unfiltered and filtered scenarios respectively. However, the rest of the significant modes (3-8) account only for a small fraction of the total variance, about 6% for the unfiltered case and 18% for the filtered case and therefore are not discussed here.

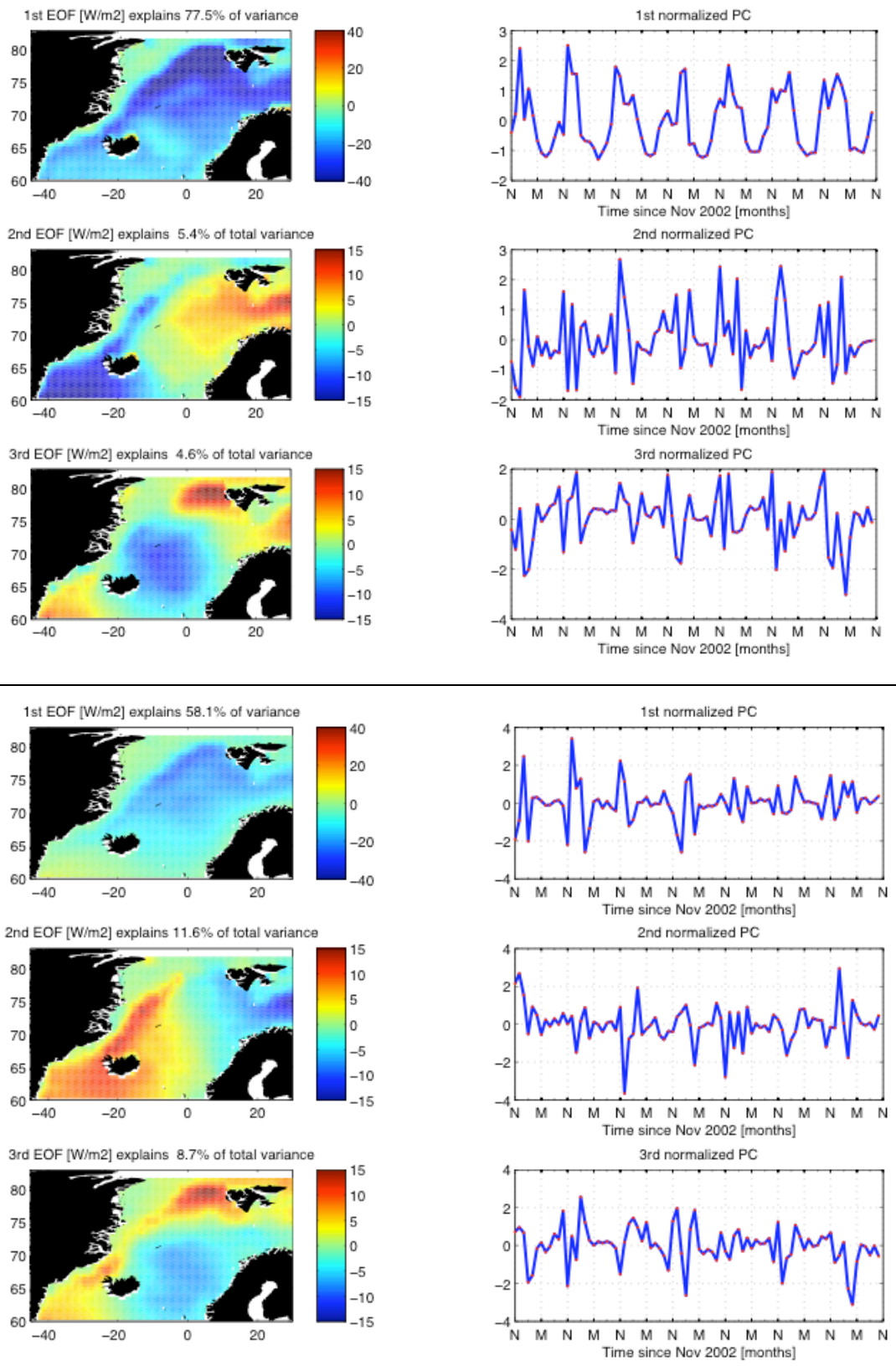

Figure 4. 21.The first three EOFs of heat flux: their spatial patterns (left) [Wm^{-2}] and their time series (right). Top: EOFs of unfiltered data; bottom: EOFs of seasonally filtered data.

Evaporation [m]

The 1st EOF of evaporation has a very similar pattern to the 1st EOF of heat flux and describes in-phase oscillations of the whole Nordic Seas with almost zero amplitudes in the ice-covered regions. The mode has a strong seasonal cycle and accounts for 75.9% of total variance (Figure 4.22 top). It is positively correlated to the SSHA in the central Nordic Seas and negatively correlated along the Greenland continental shelf where it can explain about 15% and 20% respectively (not shown). The structure of the mode changes in the Irminger Sea after the seasonal cycle removal and the mode describes oscillations in the central Nordic Seas and Barents Sea and accounts for 47% of the total variance in the filtered evaporation. The 1st PC of the filtered evaporation is positively correlated with the filtered SSHA in the Barents Sea and in the region to the North-East of Svalbard (not shown).

The 2nd and 3rd EOFs have very similar patterns to the corresponding modes of heat flux. The 2nd EOF of evaporation shows antiphase oscillations between the central and eastern Nordic Seas and Irminger Sea. The mode accounts for 7.1% and 19.1% of the total variance in unfiltered and filtered data. However, only the 2nd PC of the filtered evaporation shows significant correlations to the filtered SSHA. The correlations are positive in the central Nordic Seas and in the region to the north of 80^0N and to the east of Svalbard. The mode can explain locally about 10% of the filtered SSHA variance.

The 3rd EOF of evaporation explains the variability that is due to antiphase oscillations between the Norwegian Basin and the rest of the Nordic Seas. Again, zero amplitude was found in the ice-covered regions. Its time series show an event of higher (or lower) than normal evaporation from November 2008 to July 2009. The mode accounts for 4.7% and 9.9% of the total variance in the unfiltered and filtered field. Only the 3rd PC of the filtered evaporation is significantly correlated with the filtered SSHA. Positive correlations were found along the Greenland and Norwegian continental shelves, where about 10% of the variance could be explained in the filtered SSHA data. It was found that five and ten modes are significant at 95% confidence level for the unfiltered and filtered fields according to the Monte Carlo simulations. Each of the 4-6 filtered PCs of evaporation accounts for more than 2% of the total variance in the filtered SSHA. The 4th PC is negatively correlated to the filtered SSHA in the Greenland and Iceland Seas and along the Norwegian and Greenland continental shelves. It explains about 15% of

variance in the Greenland Sea and about 10% of SSH variance in the other areas. The 5th and 6th PCs of the filtered evaporation are also significantly correlated to the filtered SSHA at the Greenland Continental shelf (positive correlations), where they explain about 10% of the total variance in the filtered SSHA.

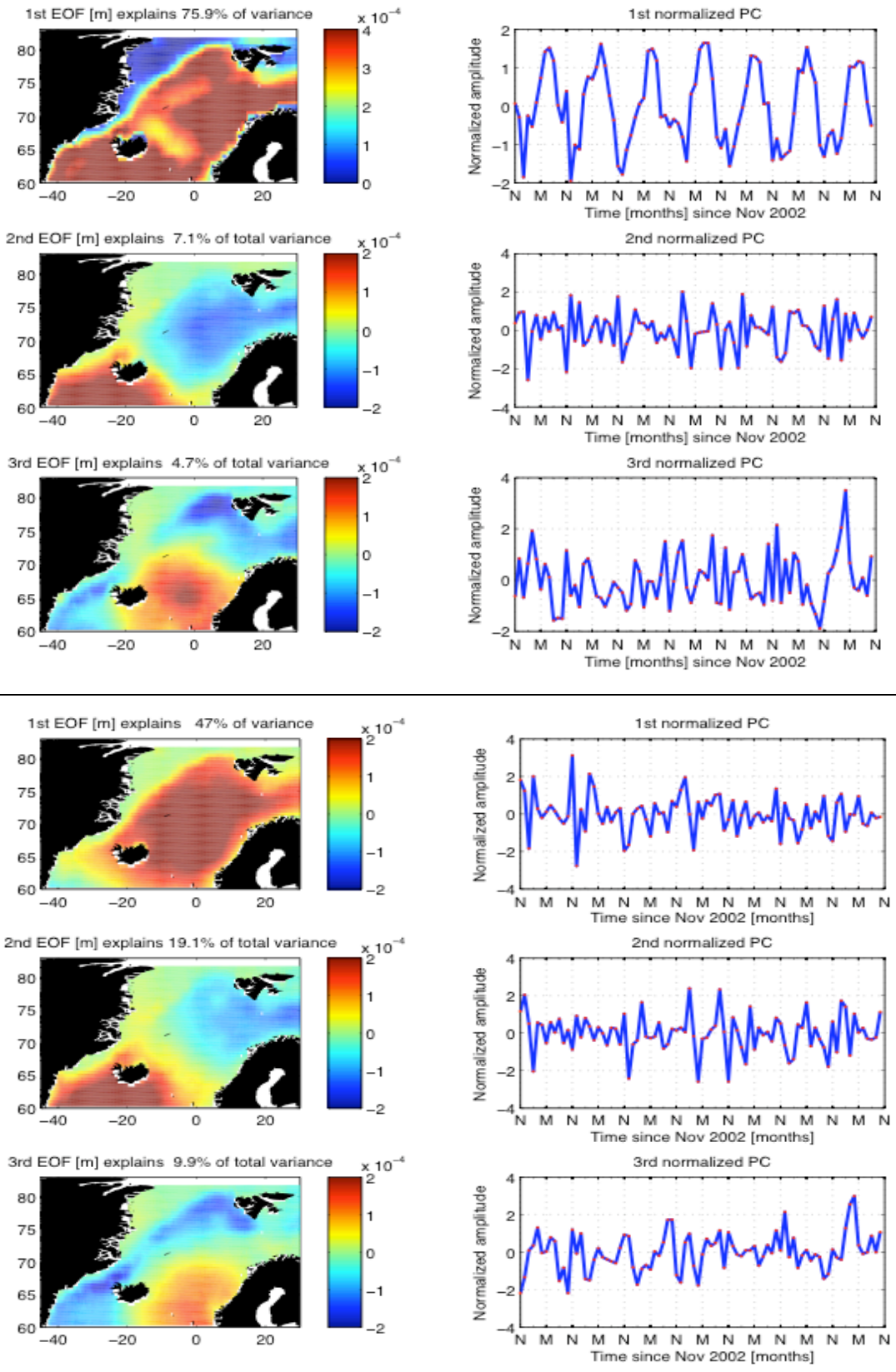

Figure 4. 22. The first three EOFs of evaporation: their spatial patterns (left) [m] and their time series (right). Top three: EOFs of unfiltered data; bottom three: EOFs of seasonally filtered data.

Precipitation [m]

The first EOF of precipitation accounts for 51.8% of total variance and it is very similar to the 1st EOF of heat flux and freshwater flux. It is responsible for the in-phase oscillations of precipitation in the whole Nordic Seas that have the largest amplitudes close to the southern (south of 70^0N) coasts of Greenland and Norway. This mode varies mainly at the annual frequencies and for the second case, where the seasonal cycle was removed prior to the EOF calculation, its importance decreases to 33% of the total filtered variance (Figure 4.23). The 1st PC is positively correlated with SSHA in the shallow regions of the Nordic Seas: continental shelves of Greenland and Norway, Barents Sea, a region North of Fram Strait. The mode can explain locally in these areas up to 20% of the SSH variance.

The 2nd EOF accounts for 13.5% of variance in the unfiltered data. The mode is responsible for anti-phase oscillations between the Irminger Sea and the rest of the Nordic Seas and varies at the other frequencies than annual. This mode becomes the most important one when the seasonal cycle is removed prior to the EOF calculation and accounts for 25.3% of total variance in the filtered data. The 1st PC of the seasonally filtered precipitation is negatively correlated to the filtered SSHA in the central Nordic Seas and a region to the north and east of Svalbard. It can explain locally about 10% of the filtered SSHA variance in these regions.

The 2nd mode of the seasonally filtered data describes the variability in the Denmark Strait and Irminger Sea and it is responsible for 17% of the total variance in the filtered data. It is positively correlated with the filtered SSH at the Norwegian continental shelf and can explain there about 10% of the total filtered SSHA variance.

The 3rd mode shows antiphase oscillations between a small region located to the east of south-eastern coast of Greenland and the rest of the Nordic Seas. It accounts for 6.7% and 11.7% of total variance in unfiltered and filtered data respectively. No significant correlations were found for this mode and unfiltered/filtered SSHA. According to the Monte Carlo simulations 6 and 10 EOFs of unfiltered and filtered data are significant at 95% confidence level. However, no significant correlations were found for these modes and SSHA.

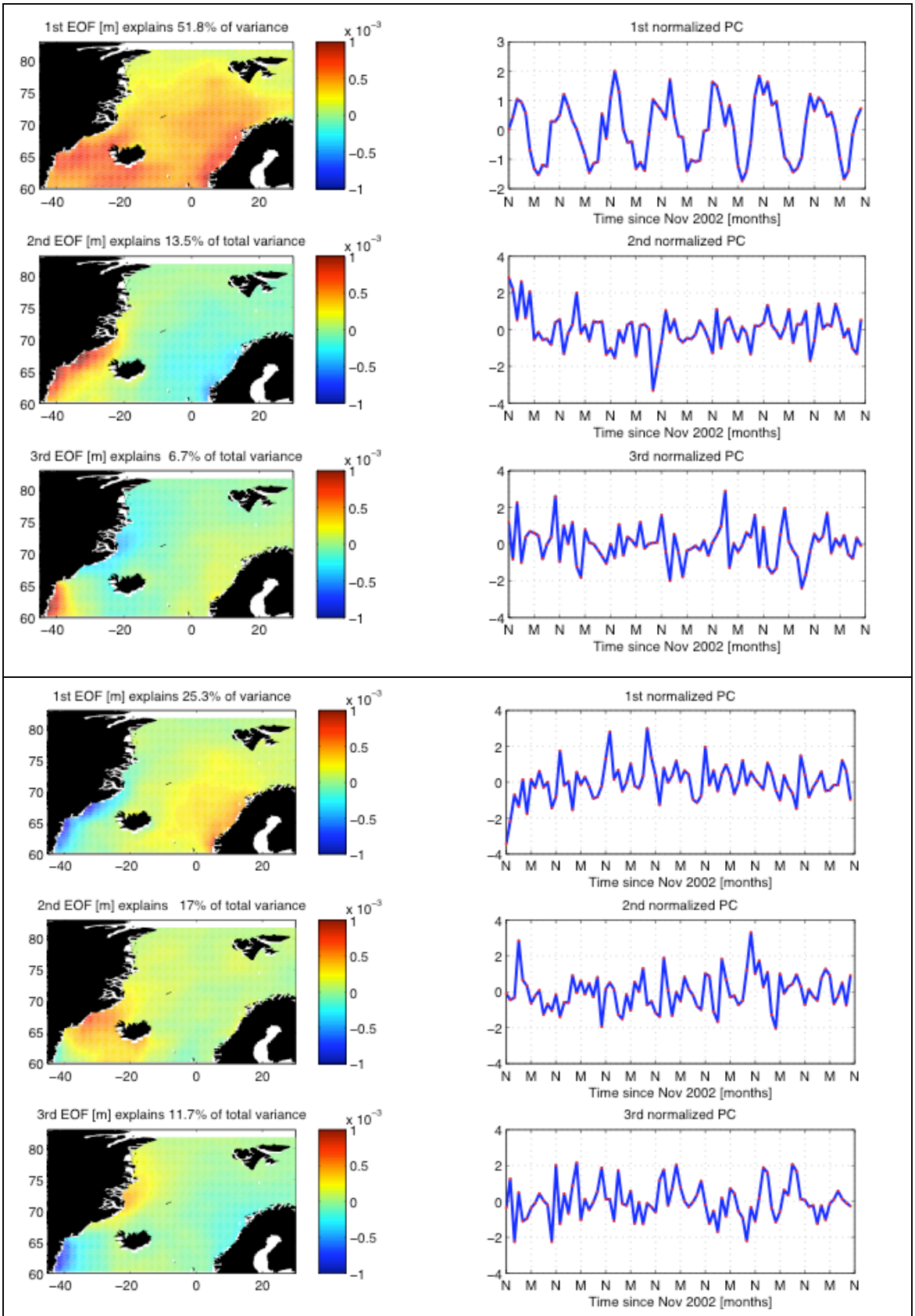

Figure 4. 23. The first three EOFs of precipitation: their spatial patterns (left) [m] and their time series (right). Top: EOFs of unfiltered data; bottom: EOFs of seasonally filtered data.

Freshwater flux [kg s^{-1} m^{-2}]

The 1st EOF of freshwater flux accounts for a major part of the total variance (69.9%). It is very similar to the 1st EOF of heat flux and therefore also shows in-phase oscillations of the whole Nordic Seas in the ice-free regions. This mode varies mainly at annual frequency, but even after the removal of the seasonal cycle prior to the analysis, this mode still contributes a large part of variance (32.7%) and it is also the most important at frequencies other than annual (Figure 4.24). The 1st PC of freshwater flux is positively correlated to the SSHA along Greenland and Norwegian continental shelves where it can explain 20% (west) and 15% of the total SSH variance. On the other hand, the same PC for the seasonally filtered freshwater flux was found to be positively correlated to the filtered SSH in the central Nordic Seas, and a region east and north of Svalbard.

Similarly to the 2nd EOF of heat flux, the 2nd EOF of the freshwater flux shows anti-phase oscillations between the Irminger Sea and the rest of the Nordic Seas. This mode accounts for 8% and 15.5% of total variance in unfiltered and seasonally filtered data. Only the 2nd PC of the filtered freshwater flux is significantly positively correlated to the filtered SSH at the Norwegian continental shelf, explaining locally less than 10% of the filtered SSH variance.

The 3rd EOF of freshwater flux shows also anti-phase oscillations in freshwater flux between a wide region located north of Norway and the rest of the Nordic Seas. The mode is responsible for 4.5% and 10.8% variance in the unfiltered and filtered data. Only the 3rd PC of the seasonally filtered freshwater flux is significantly and negatively correlated to the filtered SSH, explaining about 10% of variance there.

According to the Monte Carlo simulations only 5 and 6 modes are significant at 95% confidence level for the unfiltered and filtered cases. The rest of the significant modes, not described here, make up in total for 4.9% and 15.7% of total variance in unfiltered and filtered data respectively.

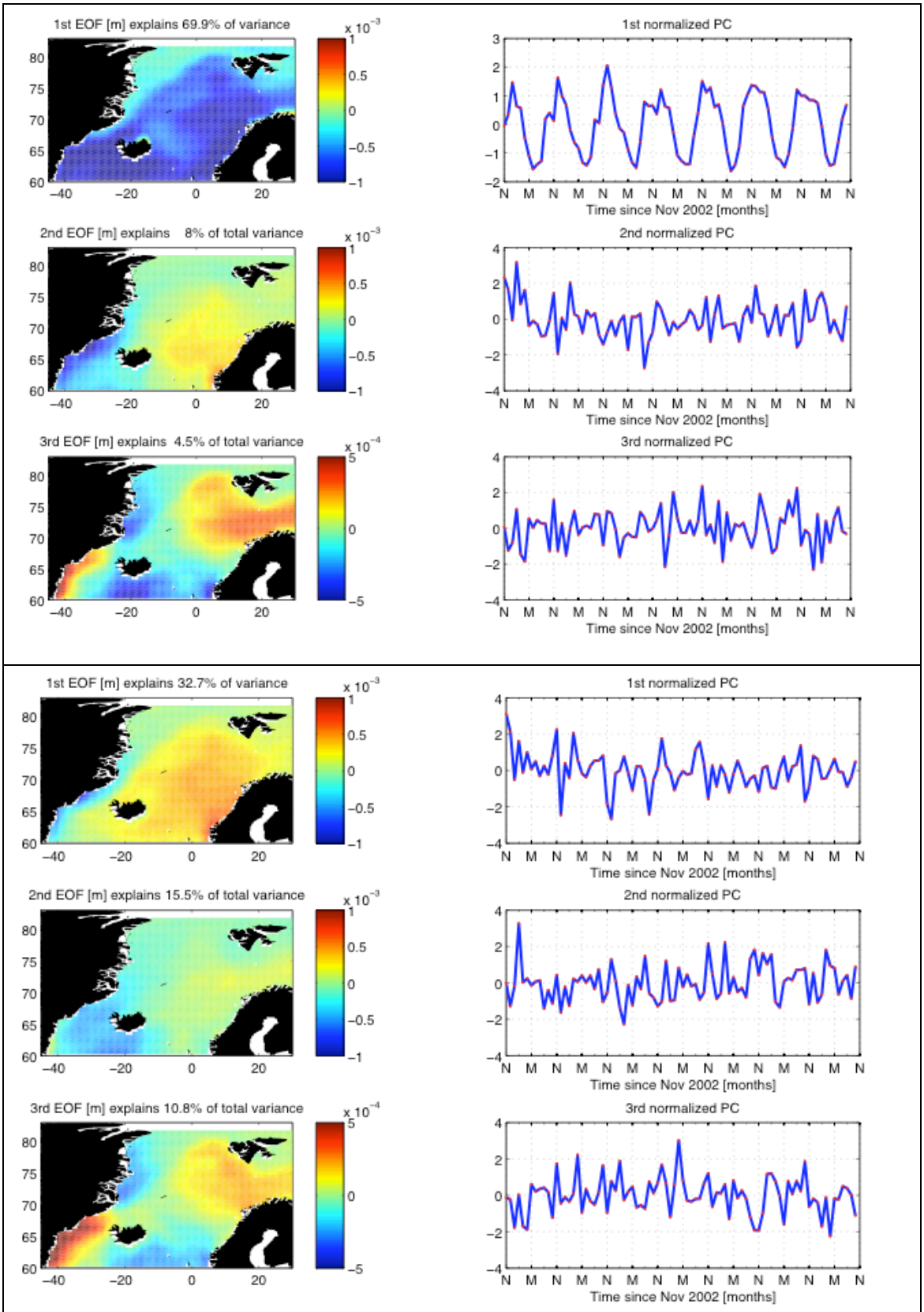

Figure 4.24. The first three EOFs of freshwater flux: their spatial patterns (left) [m] and their time series (right). Top: EOFs of unfiltered data; bottom: EOFs of seasonally filtered data.

4.3.2 Relationships between Sea Level and Atmospheric Fields

This section explores possible links between sea surface height and the other atmospheric reanalysis products using correlation coefficients calculated for the corresponding principal components. The significance of the correlations is checked using Sciremammano's (1979) method that takes into account autocorrelation functions of both variables. There is a more detailed description of the method in Section 4.4.2. A number of principal components have the seasonal cycle present in their time series. This seasonal cycle can affect the correlation and mask the relationship at other frequencies. On the other hand, correlations for the unfiltered fields can reveal if there is any relationship between the variables. Therefore, for each pair of fields, two correlations were calculated: one for the monthly data and the second for the seasonally filtered fields.

In the previous chapter the relationships between the SSH and the North Atlantic and Arctic Oscillations were analyzed. Also a number of studies (e.g. Dickson et al., 2000) showed that the large-scale atmospheric modes of variability like the North Atlantic and Arctic Oscillations affect a number of other processes connected to the fields investigated here. For example, wind speed and direction are a direct response to the NAO and AO and therefore all the wind fields investigated here could be affected by NAO (wind stress curl and both wind stress components). On the other hand, also heat and freshwater fluxes (therefore also evaporation and precipitation) can be affected by changes in the atmospheric pressure and wind fields. This section widens the analysis of the previous chapter to find out which fields connected to the NAO or AO could affect SSHA modes of variability. Therefore, correlations between the principal components of the atmospheric fields and AO and NAO indices are analysed to check for the links between the atmospheric principal components and the North Atlantic and Arctic Oscillations. The monthly NAO and AO indices were obtained from the Climate Research Unit, University of East Anglia (NAO) and National Oceanic and Atmospheric Administration (AO), and are used as proxies for the North Atlantic and Arctic Oscillation. The results of the analysis are presented in Table 4.1.

Relationship between the Atmospheric Fields and NAO and AO indices

The analysis showed that the 1st PC of mean sea level pressure is strongly affected by the NAO on seasonal to interannual timescales. A similar relationship was found for the 1st PC of wind stress curl but only on seasonal timescales. This relationship was expected because the 1st EOF of mean sea level pressure corresponds to the NAO oscillation pattern and winds are the result of pressure gradient in the area and therefore show similar structure and significant correlations with the NAO Index. The 1st PC of mean sea level pressure is also affected strongly by the Arctic Oscillation especially on the periods other than the annual. Principal components of meridional and zonal wind stresses are also strongly correlated to the NAO and AO indices. Particularly, the 2nd PC of meridional wind stress and the 1st and 3rd PCs of zonal wind stress are moderately correlated with both indices. The three most important EOFs of wind stress curl are not correlated to NAO and AO indices at other frequencies than the annual and only the 1st EOF is significantly correlated to NAO at the annual frequency. This could suggest that the atmospheric pressure changes caused by the NAO and AO are only important for the wind stress curl variability at the seasonal frequency and are responsible for about 20% of wind stress curl variance (the variance explained by the 1st EOF). There were no other significant correlations between the significant EOFs of wind stress curl and NAO and AO indices except the 6th EOF (explains about 6% of wind stress curl variance) that is strongly correlated to both the indices at the annual period and the 5th and 6th EOF that are correlated to AO index at frequencies other than the annual (R=0.47, R=0.48 significant at 99% confidence level) and explain together about 16% of the seasonally filtered wind stress curl variance.

The first EOFs of evaporation and heat flux were found to be uncorrelated with NAO and AO indices even considering lagged correlations up to 36 months. The 1st EOF of freshwater flux is also not correlated to either index if the seasonal cycle is present but becomes significant if considering the seasonally filtered data. On the other hand, significant correlations were found for the 2nd PC of heat flux and NAO and AO but also with the 3rd PCs of heat flux and AO on the other periods than the annual (Table 4.1). This means that the 2nd and 3rd EOFs of the heat flux could be driven by AO variability at annual (2nd EOF) and other periods. The three most important EOFs of freshwater flux are also weakly correlated to the NAO or AO indices and the

correlations are stronger when considering other frequencies than the annual. The first two EOFs are significantly correlated to the AO index at other frequencies than the annual, whereas the 3rd EOF is significantly correlated to the NAO index at all frequencies. It is also not surprising that precipitation is correlated to the NAO and AO indices at annual frequency (PC1) but this relationship is even stronger if considering seasonally filtered data (PC1 and PC2). On the other hand, evaporation is only weakly correlated to AO Index at all frequencies (PC2) and for the seasonally filtered case (PC3).

Similarities to the 1st EOF of SSHA

It was found that only the 2nd PC of zonal wind stress is significantly correlated to the 1st PC of SSHA when considering the unfiltered data. The reason for this relationship might be the similar phase of the annual cycle in both PCs. However, the same correlation for the seasonally filtered data suggests the relationship occurs at a different frequency. This mode of SSHA variability is also strongly correlated to the wind stress curl (all the 3 PCs of wind stress curl) and wind stress at frequencies other than annual (3rd PC of meridional wind stress and 1st and 2nd PC of the zonal wind stress). It is not surprising that it is also correlated to the PCs of the other atmospheric fields that are correlated to NAO and AO indices (PC2 of heat flux, PC3 of freshwater flux and PC2 & 3 of evaporation). However, the mode itself does show a weak relationship to the NAO index when considering the annual frequency but it is not correlated to NAO and AO indices or any PCs of mean sea level pressure at frequencies other than annual. This suggests that the mode is mainly an effect of the wind forcing, and that some other fields connected to the wind via NAO or AO might also play a minor role in the forcing of this SSHA mode.

Similarities to the 2nd EOF of SSHA

The 2nd mode of SSHA variability is significantly correlated to a large number of other atmospheric EOFs. The correlations are strongest for the unfiltered data suggesting in-phase relationship between this SSHA mode and other PCs. Generally the strongest correlations are found for the 2nd EOF of SSHA and the most important PC of an atmospheric field that is also related to the NAO index. The 2nd PC of SSHA is also weakly, but significantly, correlated to the NAO and AO indices and even stronger correlations were found for the 2nd PC of SSH and PC1 and 2 of the mean sea level

pressure. The significant correlations imply the role of the atmospheric pressure forcing of this mode. It is also not surprising that significant correlations are found for the 2nd PC of SSHA and the wind fields that are also correlated to NAO and AO indices. High correlations confirm a strong relationship with all wind fields but the strongest with the 1st PC of wind stress curl. This supports our conclusions from the previous chapter that the 2nd EOF of SSHA is a response to the NAO-related wind forcing.

Similarities to the 3rd EOF of SSH

The 3rd PC of SSHA is correlated weakly with the NAO index but stronger correlations are found when correlating with the 1st and 2nd PC of mean sea level pressure. This suggests that the 3rd EOF of SSHA could also be forced by the NAO-related wind changes. The correlations indicate that this mode could be a result of different processes depending on the considered frequency. For example, the mode is correlated to the 2nd PC of meridional wind stress but after the seasonal cycle was removed, the mode only shows correlations to the 1st PC of meridional wind stress. Also other correlations show that this mode could be forced by the NAO mainly at the annual frequency (Table 4.1).

Modes	*PC1 SSH*	*PC2 SSH*	*PC3 SSH*	*NAO index*	*AO index*
PC1 MSLP	-0.02/-0.21	**0.69/-0.50**	***0.37*/-0.24**	**-0.59/0.66**	**-0.61/0.81**
PC2 MSLP	-0.10/0.25	0.14/**0.39**	**-0.35/-0.26**	**0.28/0.32**	-0.02/0.05
PC3MSLP	-0.11/-0.06	0.08/-0.03	0.11/-0.13	***-0.22*/-0.27**	0.01/-0.05
PC1 WSC	-0.31/***-0.31***	**0.71/-0.45**	***0.39***/0.06	**-0.44**/-0.14	***-0.27***/0.14
PC2 WSC	0.15/-**0.30**	***-0.20/-0.22***	***0.24*/-0.39**	-0.16/0.16	0.08/0.15
PC3 WSC	-0.01/***-0.28***	-0.03/***-0.25***	-0.15/0.01	-0.05/0.14	0.14/-0.06
PC1 MWS	0.21/-0.10	**-0.42**/***-0.20***	0.20/**0.37**	0.03***/-0.21***	0.08/-0.07
PC2 MWS	0.18/***0.21***	**-0.63**/**0.42**	**-0.43**/0.08	**0.51/-0.47**	**0.34/-0.37**
PC3 MWS	0.15/-**0.34**	-0.20//-**0.45**	0.03/-0.11	-0.09/-0.02	0.07/0.18
PC1 ZWS	-0.21/-**0.39**	**0.47/-0.44**	***0.26*/*-0.18***	***-0.24***/0.14	**-0.45/0.44**
PC2 ZWS	**0.36/0.36**	-0.22/0.18	-0.10/0.09	***0.23***/-0.05	0.05/0.04
PC3 ZWS	0.02-0.03	***0.46***/0.13	0.18/0.01	**-0.41/-0.55**	-0.24/-0.59
PC1 HF	0.29/0.02	***-0.62***/-0.10	-0.03/**0.30**	0.16/-0.08	0.06/0.02
PC2 HF	0.12/**0.32**	**-0.40**/**0.49**	-0.21/0.10	**0.43/0.43**	**0.35/-0.31**
PC3 HF	-0.08/-0.20	0.00/0.03	0.07/-0.07	-0.24/-0.16	-0.13/-**0.42**
PC1 FF	0.05/0.15	**-0.79/0.53**	-0.27/-0.16	0.30/0.11	0.23/-**0.34**
PC2 FF	0.03/0.11	0.05/-0.12	-0.19/-0.14	0.21/0.13	-0.05/**0.39**
PC3 FF	-0.08/***-0.27***	-0.19/-0.20	-0.16/-0.13	**0.38/0.45**	***0.28***/0.03
PC1 PREC	-0.06/-0.22	**-0.77/0.61**	***-0.36***/-0.10	***0.36***/0.09	***0.31*/0.43**
PC2 PREC	0.05/0.15	-0.08/-0.10	-0.10/-0.13	0.04/**0.43**	-0.21/**0.37**
PC3 PREC	0.02/-0.06	-0.01/-0.02	0.10/-0.10	***-0.24***/0.09	-0.13/-0.09
PC1 EVA	-0.21/0.08	**0.72**/***0.21***	0.14/-0.21	-0.20/0.16	-0.01/-0.01
PC2 EVA	-0.07/**0.23**	**0.20/0.26**	**0.26**/0.17	-0.45/-0.41	**-0.29/-0.29**
PC3 EVA	0.09/***0.24***	-0.15/-0.20	0.01/-0.01	0.20/0.30	0.13/**0.37**
NAO index	***0.27***/-0.09	***-0.26***/-0.12	***-0.28/-0.26***	1	**0.61**/
AO index	0.03/0.03	***-0.27*/-0.31**	-0.12/-0.13	**0.61**/	1

Table 4. 1. Correlation coefficients (R) between the first three EOFs of SSHA and the three most important EOFs of the atmospheric fields: mean sea level pressure (MSLP), wind stress curl (WSC), meridional and zonal wind stress (MWS and ZWS), evaporation (EVA), precipitation (PREC), freshwater flux (FF). For each pair two correlations are reported: for the raw unfiltered fields (left) and seasonally filtered data (right). Significant correlations are marked with a bold face; the italic bold face indicates correlations significant at 95%, and bold only significant at 99%. The significance level was calculated for each correlation using Sciremammano (1979) large-lag standard error method (See Section 4.4.2). Mean sea level

pressure (MSLP), wind stress curl (WSC), meridional and zonal wind stress (MWS and ZWS), evaporation (EVA), precipitation (PREC), freshwater flux (FF)

4.3.3. Summary

The atmospheric modes of variability and their relationship to the modes of variability of sea surface height were explored in this section. Strong and moderate correlations between the atmospheric and sea level modes of variability can suggest which of the atmospheric fields are linked to particular SSHA modes. The results of the analysis indicated that the 1st EOF has the strongest linkage to the fields related to the wind stress. The significant correlation for the unfiltered case was only found for the 1st PC of SSHA and 2nd PC of the zonal wind stress suggesting that the annual frequencies of both PCs have the same phase. The significant correlation to the NAO Index also showed that this mode is related to the NAO at the annual frequency. On the other hand, for the other frequencies zonal wind stress still shows the strongest correlations with the 1st PC of SSHA but also strong correlations are found for all the first three PCs of wind stress curl and the two most important PCs of meridional wind stress. Also moderate correlations between the 1st PC of SSH and PC2 of heat flux indicate a link between these fields. However, no significant correlations were found between NAO/AO index or any PCs of the mean sea level pressure and the 1st EOF of the filtered SSHA.

Much stronger correlations were found for the various atmospheric PCs and the 2nd PC of SSHA, especially for the unfiltered case. Very strong correlations with the 1st PC of mean sea level pressure indicate that this mode shows a response of sea level to the NAO forcing. Strong correlations between the 2nd PC of SSH and other PCs of various fields, that are also related to NAO, confirm this conclusion. The relationship does not only occur at the annual frequencies but it is strong when considering seasonally filtered data. The 3rd PC of SSHA has the strongest relationship with the 2nd PC2 of meridional wind stress but only when the annual cycle is present in both fields. Because this PC is also correlated to NAO, and the 3rd PC of SSH is also correlated to the 1st PC of mean sea level pressure and the NAO index, we can conclude that this mode is also a result of the NAO forcing, especially at the annual frequency. At the other frequencies, the mode shows also a moderate relationship to the 1st PC of heat flux, which does not show any significant correlations to NAO. This means that this mode could not only be a response of sea level to the NAO and wind forcing but also to a local heat flux.

4.4. Maximum Covariance Analysis

To better study and confirm the relationships between the sea level and the atmospheric fields, which were described in previous section, Maximum Covariance Analysis (MCA) is used to find only those modes of behavior where the variations in the fields are strongly coupled. The aim of MCA analysis is to extract, from the cross-covariance matrix of the two fields, pairs of spatial patterns that explain as much as possible of the mean-squared temporal covariance between these two fields. The obtained spatial pattern multiplied by its time expansion coefficient defines an MCA mode. The modes are ordered according to the fraction of squared covariance (FSC) explained by them and the strength of coupling between the fields is described by the correlation coefficient ***R*** between the time expansion coefficients of each MCA pair. In the MCA the length of the observations of both fields should be the same but the time of the observations could be different (for example with some lag). On the other hand, the spatial dimension can be different for the two fields. The obtained patterns are spatially orthogonal but their time series are not uncorrelated, as in case of EOFs.

4.4.1 Method

Singular value decomposition (SVD), also called Maximum Covariance Analysis (MCA) is used to isolate patterns of coupled variability between two different fields that are sampled simultaneously. MCA finds optimally coupled spatial structures by maximizing the covariance between various possible patterns (Bretherton, 1992). The two fields *a(t)* and *b(t),* designated right and left, have time varying expansion coefficients:

$a(t) = u \cdot x(t)$

$b(t) = v \cdot y(t)$

where *u* and *v* are the left and right singular vector that are describing spatial patterns of the co-variability and *x(t)* and *y(t)* are their time series.

The cross-covariance is matrix for the two fields is therefore:

$\text{Cov}[a,b] = \mathbf{u}^T < \mathbf{y}\mathbf{x}^T > \mathbf{v}$

A singular value decomposition (SVD) of $\mathbf{C_{xz}}$ will produce the optimal left and right patterns of the left and right data fields.

$$\text{SVD}[\mathbf{C_{yx}}] = \mathbf{U}\mathbf{D}\mathbf{V}^T$$

Where **U** is the matrix of orthogonal left singular vectors, **V** is the matrix of orthogonal right singular vectors and **D** is the diagonal matrix of singular values, ordered from highest value to lowest value of their squared covariance fraction (SCF). These singular values are the associated covariances of the left and right singular vectors (Bretherton, 1992). The leading eigenvectors, **U** and **V**, are the spatial fields that explain the most coupled variance and succeeding eigenvectors are subject to orthogonality. The corresponding time series may be temporally correlated. However, even if the modes are perfectly linearly coupled, the SVD may only approximately identify the coupling (Cherry, 1996). The exact method of MCA analysis used in this study is the same as in Bjornson and Venegas (1997).

4.4.2 Significance of SVD Results

The statistical significance of the results can be assessed by comparing correlation coefficient R, squared covariance (SC), SCF or cumulative squared covariance fraction (CSCF) with the corresponding value obtained from SVD analysis calculated on the same fields but with one field which has its temporal order scrambled. Monte Carlo simulations have been used broadly for SC significance tests in order to study the significance of SVD results (Wallace et al., 1992; Bjornsson & Venegas, 1997, Venegas et al., 1997). If the two fields have different spatial sizes (number of grid points), the SC should be normalized by dividing it by the product of the spatial sizes of the two fields. In the Monte Carlo simulations, the field that is chosen to be randomly permuted in time should have a smaller month-to-month autocorrelation of the two fields. The simulations are repeated at least 100 times, each time keeping the values of total squared covariance (TSC) and SC of each SVD mode. The SC value from the original data is significant at the 95% level if it is not exceeded more than 5 times during the simulations.

Another method of assessing the significance of the SVD results is to calculate a significance level for the correlation coefficient between the two expansion time coefficients of each mode. The autocorrelation in the data and its length affects the number of degrees of freedom, which affects the significance of $\boldsymbol{R}$. The shorter the decorrelation time scale, the more degrees of freedom have the data and the lower the significance level. The method of Sciremammano (1979) is used in this study to measure the significance level of $\boldsymbol{R}$ obtained from SVD analysis. This method takes into account the autocorrelation of the two time series involved in the calculation of $\boldsymbol{R}$. The large-lag standard error σ between the two time series $\boldsymbol{A(t)}$ and $\boldsymbol{B(t)}$ is calculated from:

$$\sigma^2 = n^{-1} \sum_{i=-M}^{M} C_{AA}(it) C_{BB}(it)$$

Where $\boldsymbol{C_{AA}}$ and $\boldsymbol{C_{BB}}$ are autocorrelation functions of $\boldsymbol{A(t)}$ and $\boldsymbol{B(t)}$, $\boldsymbol{n}$ is the length of both time series, $\boldsymbol{M}$ is large compared to the lag at which $\boldsymbol{C_{AA}}$ and $\boldsymbol{C_{BB}}$ are zero. For time series with at least 10 degrees of freedom the 95% and 99% significance level corresponds to: $\boldsymbol{C_{95}}=2\sigma$ and $\boldsymbol{C_{99}}=2.6\sigma$ (Sciremammano, 1979).

4.4.3. Presentation of the Results.

Each SVD mode consists of two spatial patterns, one for each field (left and right). There are four ways to plot the results of SVD, which hold for the first (left) and second (right) field:

1. Plot singular vectors of the patterns.

This is usually difficult to interpret physically and therefore not used in the literature and in this study.

2. Plot each pattern as a *homogeneous correlation map*, defined as correlation coefficient $r[A(t), a_k(t)]$ between the grid point values of the first (left) field $A(t)$ and the ***k-th*** time expansion coefficient of the left SVD pattern $a_k(t)$. This plot indicates the geographical location of high covariance between original data and its SVD pattern.

3. Plot each pattern as a *heterogeneous correlation map*, defined as correlation coefficient $r[A(t), b_k(t)]$ between the grid point values of the first (left) field $A(t)$ and ***k-th*** time expansion coefficient of the right SVD pattern $b_k(t)$. This plot shows how well the grid points in the left field can be predicted from the ***k-th*** SVD mode of the right field.

4. Plot *homogeneous regression map*, defined as *homogeneous correlation map* (see no. 2) multiplied by the temporal standard deviations of the original data at each grid point. This plot shows a typical magnitude of the SVD mode in the original data.

The above methods (2-4) are often used in the literature to describe the results of SVD analysis. In this study *homogenous regression maps (no.4)* and *heterogeneous correlation maps (no.3)* are chosen to represent the SVD results. Both methods provide useful information about the co-variability of the fields.

The results of SVD analysis are described below in eight sections analyzing each pair of fields separately. In each subsection the homogenous regression maps are used to present the SVD modes in real units and heterogeneous correlation maps are used to present the co-varying locations between the fields that can be predicted from the other field. Furthermore, each section consists of three tables where SVD statistics are

described and the correlations between the SVD modes and EOFs of the separate fields are examined.

4.4.4. Results of Monte Carlo Significance Tests.

The Squared Covariance Fraction (SCF) and correlation coefficient between the left and right expansion time coefficients are an indirect measure of the relationship between the two fields. However, they are only meaningful when they are associated with a significant Squared Covariance (SC) (Wallace et al., 1992). The significance of the SVD analysis was assessed using 100 Monte Carlo simulations of SC (see section 4.5.2) for each pair of fields by randomly permuting ECMWF fields and keeping the order of SSHA unchanged. The atmospheric fields were chosen for scrambling because they have a shorter "memory" (decorrelation time scale) that is maximally equal to three months (this was estimated from the mean autocorrelation function). Also in the previous studies (e.g. Wallace et al., 1992, Czaja et al. 1999, Martin et al. 2010) these fields were usually randomly permuted to check the significance of SVD results. Because randomly reordering removes the temporal autocorrelation from the time series of one field the statistical significance could be overestimated. The SC was normalized by dividing by the product of the number of grid points in each field (MxN); then Squared Covariance (SC) of each simulation was compared to the normalized SC of the original SVD mode. In the case of seasonally filtered data, the method of Czaja et al. (1999) was used. This method is exactly the same as for the unfiltered data except that only years of the scrambled field are randomly permuted and the order of months remains unchanged. This method does not disturb month-to-month autocorrelation and therefore provides more accurate estimation of the SVD mode significance.

The results of Monte Carlo simulations indicated that almost all the first SVD modes are significant at 95% confidence level except for the seasonally filtered heat flux. Also most of the 2nd SVD modes are significant except precipitation and the filtered ZWS, FF. Furthermore, only three from all 3rd SVD modes are not significant: the filtered MSLP, ZWS and precipitation. The situation changes for the 4th SVD mode, the simulations revealed that most of the modes are not significant and only four are at the 95% confidence level: the filtered mean sea level pressure, wind stress curl, meridional wind stress and unfiltered evaporation. The 5th SVD is only significant in the case of seasonally filtered WSC, MWS and evaporation. None of the insignificant modes will be discussed in the remainder of this section.

Fields svd	*SSH-MSLP*		*SSH-WSC*		*SSH-MWS*		*SSH-ZWS*		*SSH-HF*		*SSH-FF*		*SSH-PREC*		*SSH-EVAP*	
	U	**F**	**U**	**F**	**U**	**F**	**U**	**F**	**U**	**F**	**U**	**F**	**U**	**F**	**U**	**F**
1	**0**	**0**	**0**	**0**	**0**	**5**	**0**	**0**	**0**	29	**0**	**1**	**0**	**0**	**0**	**2**
2	**5**	**2**	**0**	**1**	**1**	**0**	**0**	10	**4**	**0**	**2**	7	37	9	**0**	**0**
3	**0**	6	**0**	**1**	**1**	**2**	**0**	45	**0**	**0**	**0**	**3**	**0**	50	**2**	**0**
4	10	**0**	**0**	**2**	**4**	**0**	47	47	8	9	9	19	12	24	**0**	20
5	8	27	45	**0**	8	**0**	12	42	24	15	15	24	15	40	8	**1**
6	27	30	28	20	12	38	30	31	32	20	27	35	16	44	9	12

Table 4.2. Results of 100 Monte Carlo simulations of the SVD squared covariance presented as a number of SC simulated values exceeding the real SC obtained from MCA. The modes that are significant at 95% confidence level are in bold face. The results are presented for the unfiltered (U) and seasonally filtered fields (F) for the pairs consisting SSHA and the following atmospheric fields: mean sea level pressure (MSLP), wind stress curl (WSC), meridional and zonal wind stress (MWS and ZWS), evaporation (EVA), precipitation (PREC), freshwater flux (FF).

4.4.5 Results of the SVD Analysis.

The results of the MCA are illustrated for each pair of fields in three figures. The first one presents the coupled modes in real units (homogeneous regression maps). The second figure illustrates the co-varying locations between the fields that can be predicted from each other (heterogeneous correlation map). Finally, the third figure shows time expansion coefficients for each pair of MCA patterns.

The results for each pair of fields are then summarized in three tables. In the first one, the squared covariance fraction (SCF), the cumulative squared covariance fraction (CSCF) and correlation coefficient (R) are summarized for each coupled mode. The next table shows how much of the variance can be explained by left and right modes in the corresponding left and right field (homogeneous variance). It also shows how well a right/left MCA mode predicts the variance of the other field (heterogeneous variance). Finally, the last table checks how well the MCA modes correspond to the PCA modes described in section 4.3.

Sea Surface Height and Mean Sea Level Pressure

All significant right SVD modes can predict 10.6% and 9.5% of variance in SSH data. The results of the MCA show some interesting relationships between the fields and mainly indicate that the 2nd EOF of SSHA is coupled with the 1st EOF of mean sea level pressure. This relationship is significant at all frequencies. There is also less important coupling between the 1st EOF of SSHA and the 2nd EOF of mean sea level pressure that is significant at frequencies other than annual. A more detailed description of the results follows, where each mode of variability is discussed separately.

Mode 1

The 1st SVD mode of SSHA and mean sea level pressure explains 91.1% and 79.7% of covariance between the two unfiltered and filtered fields respectively (Table 4.3). The left pattern is characterized by the increased sea level of about 10 cm in SSHA at the Eastern and Western continental shelves, and is highly correlated with mean sea level pressure ($R \approx 0.6$). It also shows a 5 cm depression in SSHA in the central Nordic Seas that is also moderately correlated with mean sea level pressure (Figures 4.25 & 4.26). High correlations between the left and right modes indicate strong coupling on the seasonal and other frequencies (Table 4.3).

The square of the spatial mean of the homogeneous correlation indicates that the left field explains about 9% of variance in the unfiltered SSHA data and the right field can predict about 5% of variance in the unfiltered SSHA (Table 4.4); That is more than half of the variance explained the left field. If we consider the filtered case where the left mode accounts for 17.6% of the total variance in the unfiltered data, the right field can predict only 5% of the total variance in the filtered SSHA data. Therefore, more than 50% can be predicted from mean sea level pressure when the seasonal cycle is present in both data sets but only 30% when the seasonal cycle is filtered out. On the other hand, the right field explains high percentage of variance in the mean sea level pressure (78%) and can be well predicted from SSHA (48% of variance explained).

The structure of the left SVD mode is associated with the 2nd EOF the sea surface height and the correlation between the two is very high and significant at 99% confidence level for the unfiltered and filtered case (Tables 4.3, 4.5). Therefore we can conclude that the

1st SVD mode of mean sea level pressure can predict more than 50% of variability of the 2nd EOF of SSH if the unfiltered data is considered. The right mode is significantly positively correlated with SSH along continental shelves of Greenland and Norway. It can locally predict about 15% of SSHA variance in these regions. For the seasonally filtered case, the right SVD SSHA mode is now significantly correlated with the 1st and the 2nd EOF of SSH suggesting this mode is a mixture of the two and only up to 30% of variance in this mode can be predicted by the 1st SVD of mean sea level pressure. The right SVD mode is negatively correlated with SSHA in the central Nordic Seas and positively along Norwegian coast, south of 70^0 N. It can predict about 10% of the filtered SSHA variance in these regions.

On the other hand the right pattern of the SVD mode is almost the same as the 1st EOF of MSLP, and the correlation coefficient confirms this relationship. The correlation coefficient between the left and right time coefficients suggests that mean sea level pressure leads SSH simultaneously and at 1-month lag.

Mode 2

The 2nd SVD mode of SSHA and mean sea level pressure explains 5.1% of the co-variability between the two unfiltered fields and shows a significant simultaneous relationship between its time expansion coefficients (Table 4.3). Its left structure indicates high similarity to the 1st EOF of SSHA and the right one to the 2nd EOF of mean sea level pressure (Figure 4.1, Table 4.5). The right mode can predict about 4% of variance in the unfiltered SSH (Table 4.4); that is about 11% of variance accounted for the left mode. The heterogeneous correlation map (Figure 4.26) shows significant correlations along the Norwegian continental shelf and in the Barents Sea ($|R| > 0.33$ at 95% confidence level) (Figure 4.2).

The same left mode, obtained for the seasonally filtered fields, accounts for 14.6% of SSHA variance, and about 2% of SSHA variance can be predicted from the 2nd right mode. The correlation between the left and right mode increases from 0.39 to 0.66 after the seasonal cycle removal suggesting a strong coupling at frequencies other than annual. Also the right mode is now significantly and positively correlated in the central Nordic Seas and in the whole eastern side of the Nordic Seas.

In conclusion, the 2nd left mode corresponds to the 1st EOF of SSHA and the 2nd right mode corresponds to the 2nd mean sea level pressure EOF. The MCA shows that the two modes are coupled but only a very small fraction of the variance explained by the 1st SSHA can be predicted from the 2nd mean sea level pressure EOF: 11% and 15%.

Mode 3

According to the results of Monte Carlo simulations only the 3rd SVD mode for the unfiltered fields is significant at 95% confidence level. This mode explains only about 2.1% of co-variability between the two fields. The 3rd left pattern is strongly correlated (R=0.86) to the 1st EOF of SSHA and accounts for 29% of variance in the filtered SSHA data (Figure 4.1, Table 4.3). The two time expansion coefficients show simultaneous moderate correlation (Table 4.3). The heterogeneous correlation maps (Figure 4.26) indicate significant correlation only along the southern coast of Greenland, from 65^0N to 70^0N. The coupling between the left and right mode occurs only for at the annual frequency and it is very weak. Only 1% of SSHA variance can be predicted by the 3rd right mode. That accounts only for 5% of the variance explained by the left mode.

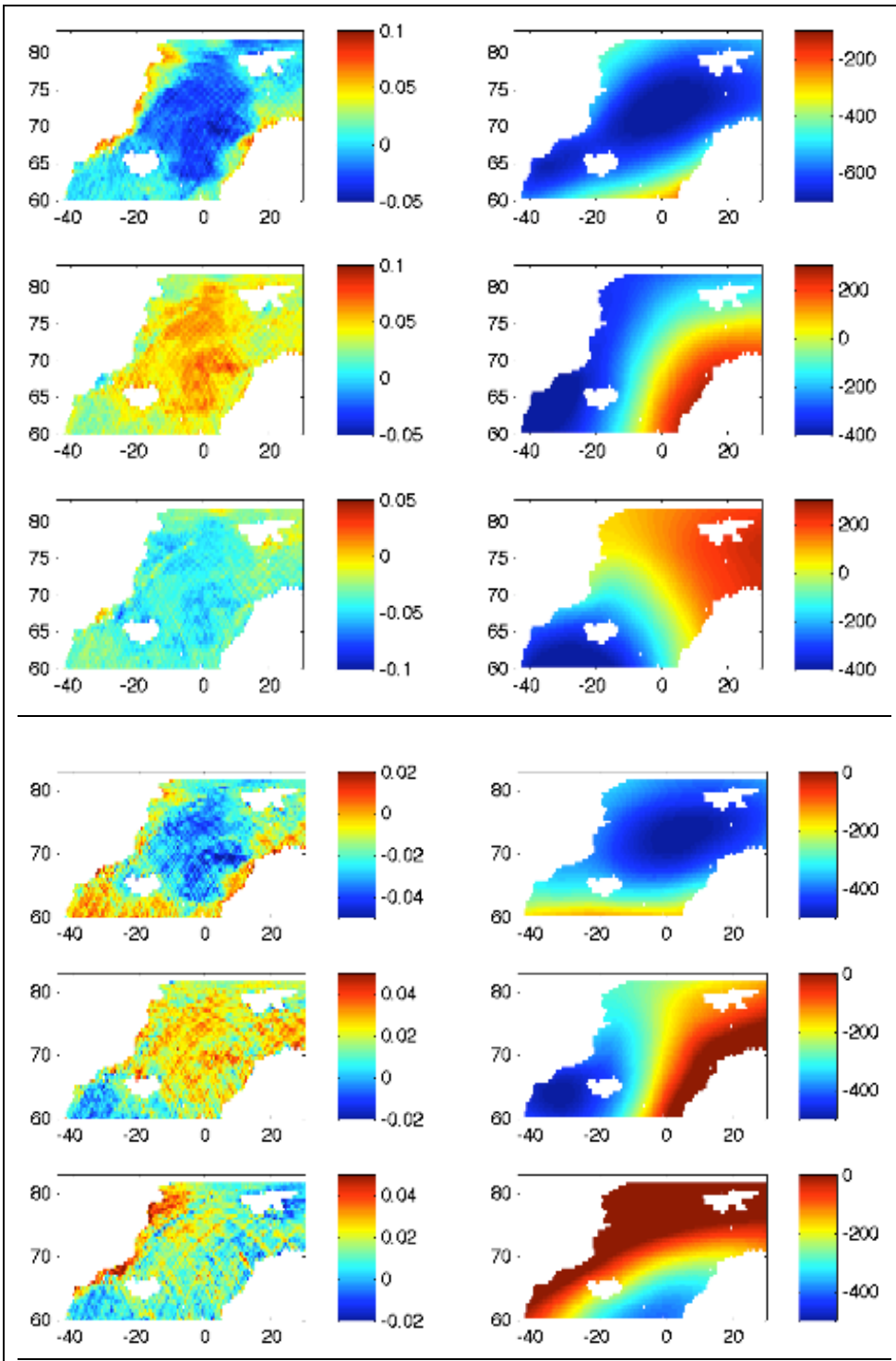

Figure 4.25.The three most important MCA coupled modes presented as homogenous regression maps of SSHA [m] (left) and mean sea level pressure (right) [Pa] for the unfiltered (top 3) and seasonally filtered fields (bottom 3).

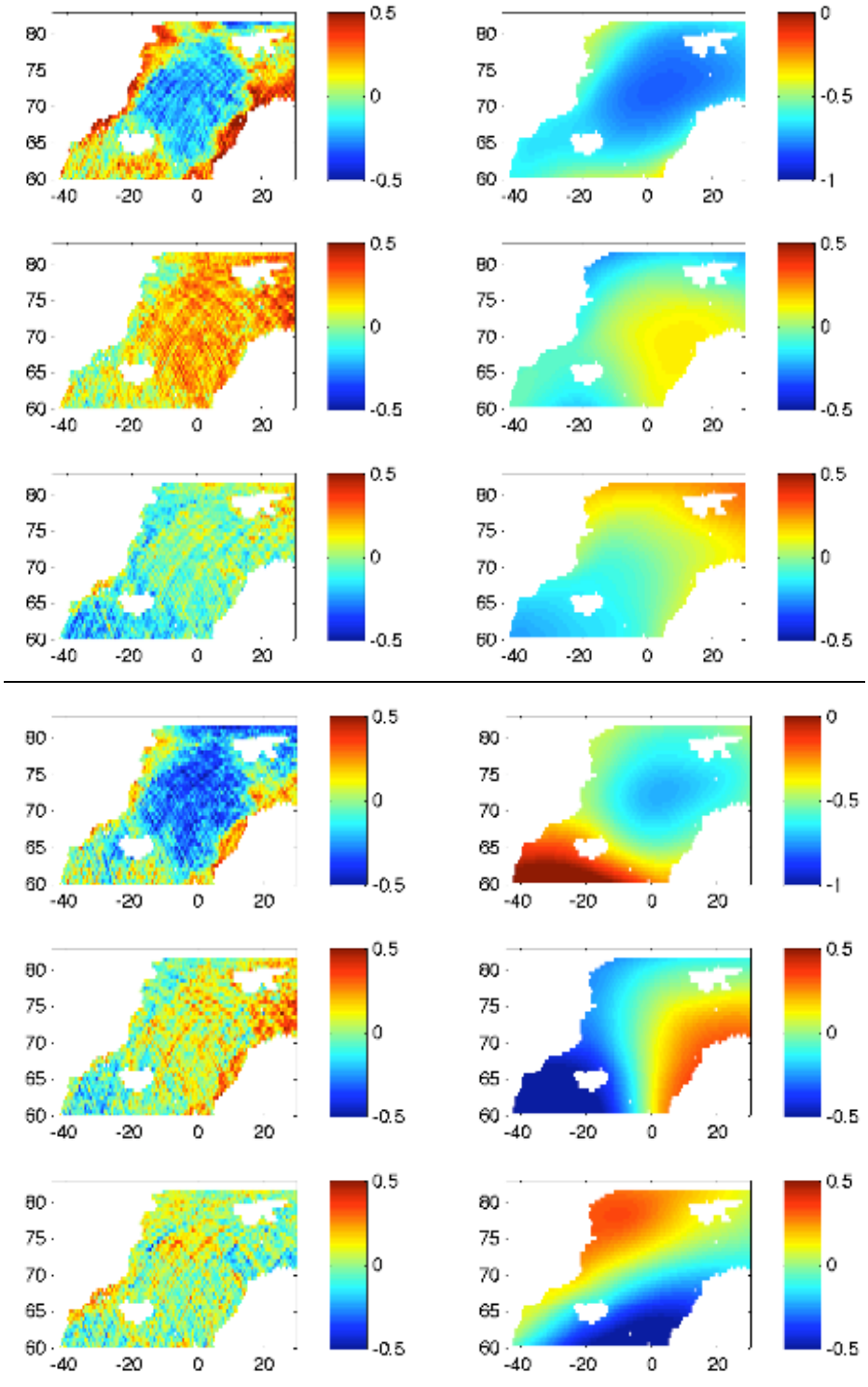

Figure 4.26.The 3 most important coupled MCA modes presented as heterogeneous correlation maps of the unfiltered (top 3 rows) and filtered (bottom 3 rows) mean sea level pressure (right) and SSHA (left). The colour scale represents a correlation coefficient $r[A(t), a_k(t)]$ between the grid points of original data (left and right fields) and time expansion coefficients of corresponding SVD modes of the other field (right and left) and R∈ (-1,1).

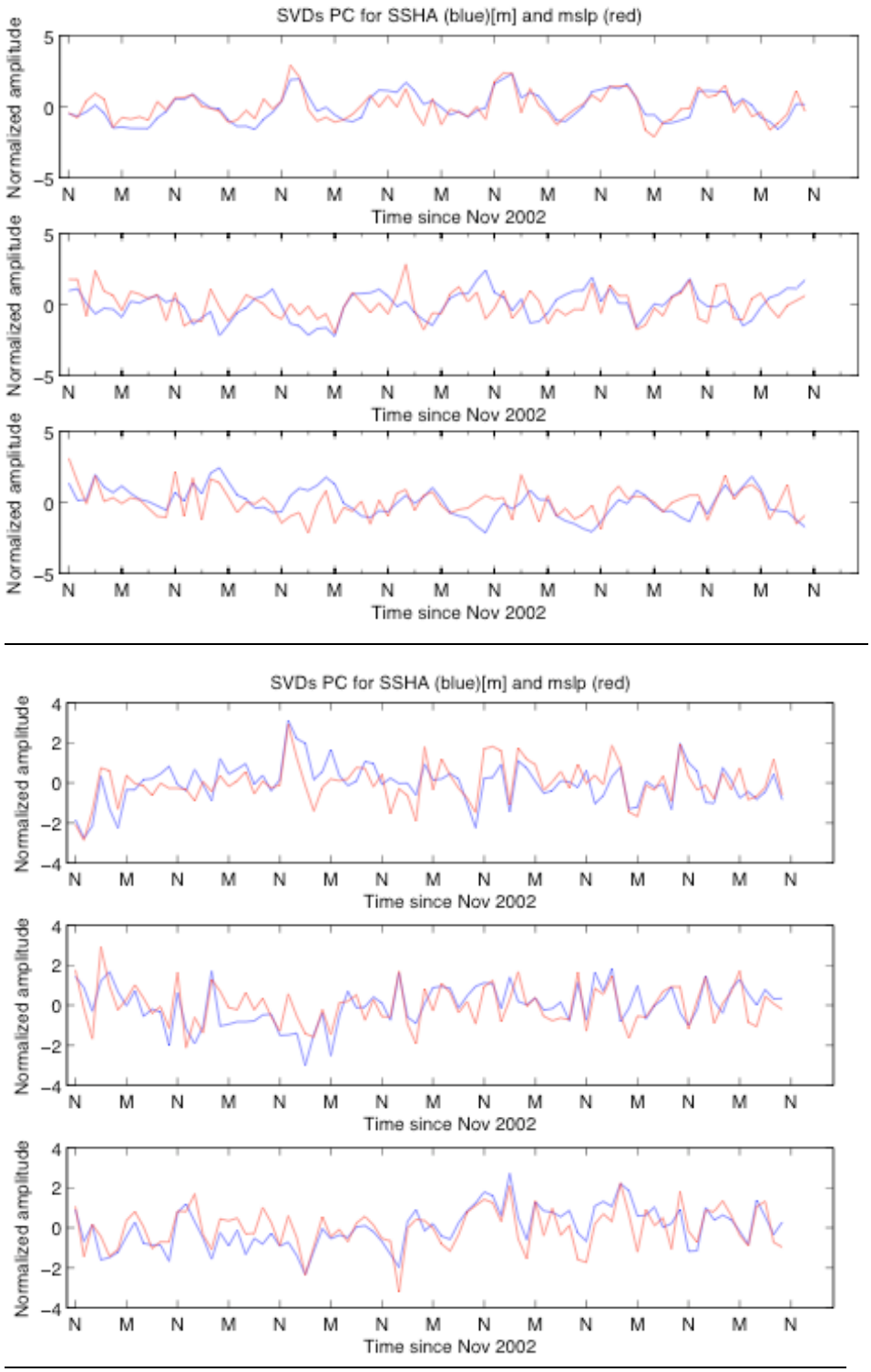

Figure 4.27. Normalized time series of the first three most important MCA coupled modes of the unfiltered (top 3) and filtered (bottom 3) SSH (blue) and mean sea level pressure (red).

Mode (k)	SCF (%)	CSCF(%)	R(ak(t),bk(t))
SVD1	91.1/79.7	91.1/79.7	0.79/0.68
SVD2	5.1/12.7	96.2/92.4	0.39/0.66
SVD3	2.1/4.7	98.3/97.1	0.48/0.74
SVD4	1.1/2.2	99.4/99.3	0.44/0.51
SVD5	0.4/0.3	99.8/99.6	0.78/0.66
SVD6	0.0/0.2	99.8/99.8	0.83/0.79

Table 4.3. Results of the MCA analysis for 6 most important coupled modes of variability of SSHA and mean sea level pressure. The columns present squared covariance fraction, cumulative squared covariance fraction and correlation coefficient for each coupled mode of variability obtained for the unfiltered (right) and seasonally filtered fields (left).

Mode [k]	HomoVar [%] SSH	HomoVar [%] MSLP	HetVar [%] SSH	HetVar [%] MSLP
1	8.8/17.6	77.5/64.8	4.9/5.3	47.9/28.0
2	37.3/14.6	11.8/29.9	4.2/2.2	1.0/8.6
3	28.8/8.1	8.5/13.4	1.5/1.4	1.7/6.7
4	28.8/17.2	8.5/8.1	1.1/2.0	0.9/0.9
5	4.1/7.9	6.9/3.8	1.0/1.1	1.4/0.4
6	1.7/3.8	3.1/2.6	0.7/1.0	0.4/0.5

Table 4.4. Variance explained by the 6 most important MCA coupled modes of variability for SSH and mean sea level pressure for the unfiltered (left) and seasonally filtered fields (right). HomoVar informs how much of the left/right field the variance explained by the left/right SVD mode. HetVar is the amount of variance in the left/right field predicted from the right/left SVD mode (from the other field).

Left (SSH) SVD Modes	**PC1 (SSH)**	**PC2 (SSH)**	**PC3 (SSH)**
1	0.13/-**0.75**	**-0.97**/**-0.62**	-0.15/-0.11
2	**-0.98/0.75**	0.03/0.18	-0.11/-**0.37**
3	**0.86**/**0.55**	0.11/-0.23	-0.26/0.26

Right (MSLP) SVD modes	**PC1 (MSLP)**	**PC2 (MSLP)**	**PC3 (MSLP)**
1	**-1/1**	-0.01/-0.14	-0.01/0.02
2	-0.21/0.52	**0.81/0.85**	0.74/-0.01
3	-0.02/0.13	**0.83**/-0.07	-0.54/-**0.98**

Table 4.5.Correlation coefficients between the fist three most important SVD coupled modes and principal components of sea surface height (SSH) and mean sea level pressure (MSLP). Numbers in bold indicate that the correlations are significant at 99% confidence level.

Sea Surface Height and Zonal Wind Stress

The first MCA mode for the unfiltered fields accounts for 78.5% of the total squared covariance, while the second and third modes account for 13% and 5.1%, respectively. On the other hand, about 84% of the total squared covariance is explained by the first seasonally filtered coupled mode and the rest are insignificant. All three coupled modes explain mainly the coupling between the 1st EOF of SSHA and the 1st and 2nd EOF of zonal wind stress. In total all significant right modes can predict about 11.6% of unfiltered SSH variance and 8.3% of the filtered SSHA variance.

Mode 1

The coupled mode indicates that when SSHA is positive in the central Nordic Seas the zonal wind stress anomaly is negative south of Iceland and positive in the Fram Strait and around Svalbard. A very similar coupled mode was also obtained for the seasonally filtered fields but now also SSHA at the Greenland continental shelf is positive. The heterogeneous correlation maps obtained for the unfiltered and filtered fields indicate that the right mode explains most of the variance at frequencies other than annual. For the unfiltered fields about 7.4% of SSHA variance can be predicted by the right mode. That is about 20% of the variance explained by the left mode itself. The right time expansion coefficient is positively correlated with SSHA in the central Nordic Seas (Figure 4.29) and can explain about 20% of SSHA variance in the Greenland Sea and about 15% in the other gyres.

When considering the seasonally filtered mode, about 8.3% of the total filtered SSHA variance can be predicted by the right mode, mainly in the deep basins. That consists of almost 40% of variance that is explained by the left mode (Table 4.7). The left mode is strongly correlated to the 1st EOF of SSH and the right mode to the 1st EOF of zonal wind stress (Table 4.8). The right time expansion coefficient is positively correlated with the filtered SSHA in the central Nordic Seas, Fram Strait and the region located to the north and east of Svalbard (Figure 4.29). The right mode can explain locally about 30% of the filtered SSHA variance in the Greenland Sea and 15% in the other deep gyres.

Mode 2

The 2nd coupled SVD modes indicate that when SSHA is negative everywhere in the Nordic Seas, the zonal wind stress anomaly is also negative everywhere except in Denmark Strait and at the continental shelf of Greenland. A similar mode was obtained for the seasonally filtered fields but after the removal of the seasonal cycle the SSHA changed sign to negative at the continental shelf of Greenland and in the Barents Sea. Heterogonous correlation maps (Figure 4.29) indicate that most of the variability in the SSHA can be predicted locally by the right mode in the Barents Sea (about 15% of the unfiltered and seasonally filtered SSHA). The right expansion coefficient is negatively correlated to the SSHA at the Norwegian and Greenland continental shelves and in the Barents Sea.

The left mode accounts for about 31.5% of total variance in the unfiltered SSHA data (Table 4.7). The right mode can predict about 3% of variance in the unfiltered SSHA, which accounts for 9% explained by the corresponding left mode (Table 4.7). The left mode is strongly correlated with the 1st EOF of SSHA and the right to the 1st and 2nd EOFs of zonal wind stress (Table 4.8).

Mode 3

The 3rd MCA mode shows that when negative SSHA occurs along the Greenland and Norwegian continental shelves the positive zonal wind stress anomaly occurs in the Denmark Strait and in the Irminger and Greenland Seas (Figure 4.28). The left mode accounts for 5% of total variance in the unfiltered SSHA data and is moderately correlated to the 2nd EOF of SSH (Tables 4.7, 4.8). The coupling between the unfiltered time expansion coefficients is strong (Table 4.6) but the right expansion coefficient is not significantly correlated to the SSHA (Figure 4.29).

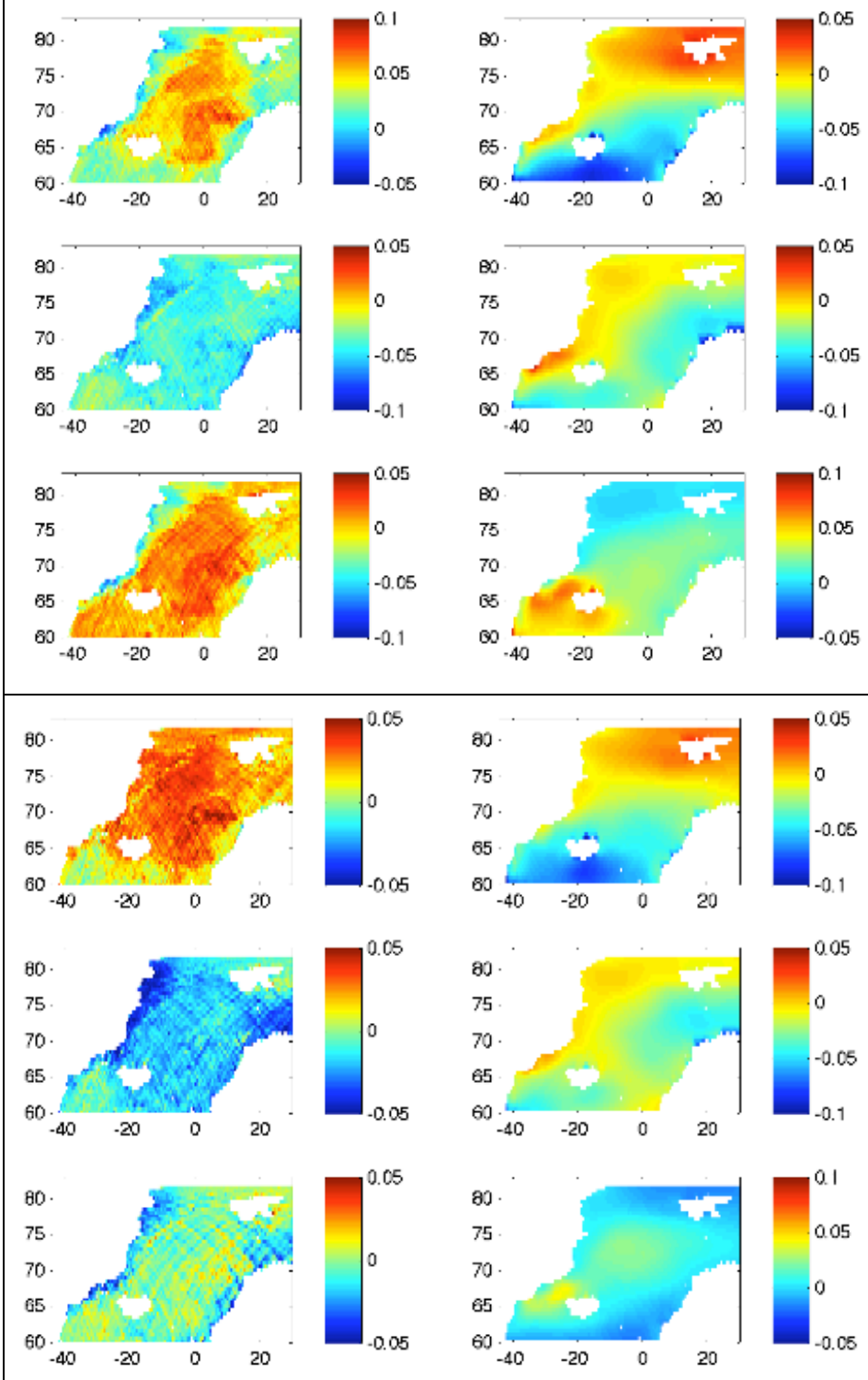

Figure 4.28. The three most important MCA coupled modes presented as homogenous regression maps of SSHA [m] (left) and zonal wind stress [Nm^{-2}] (right) for the unfiltered (top 3) and seasonally filtered fields (bottom 3).

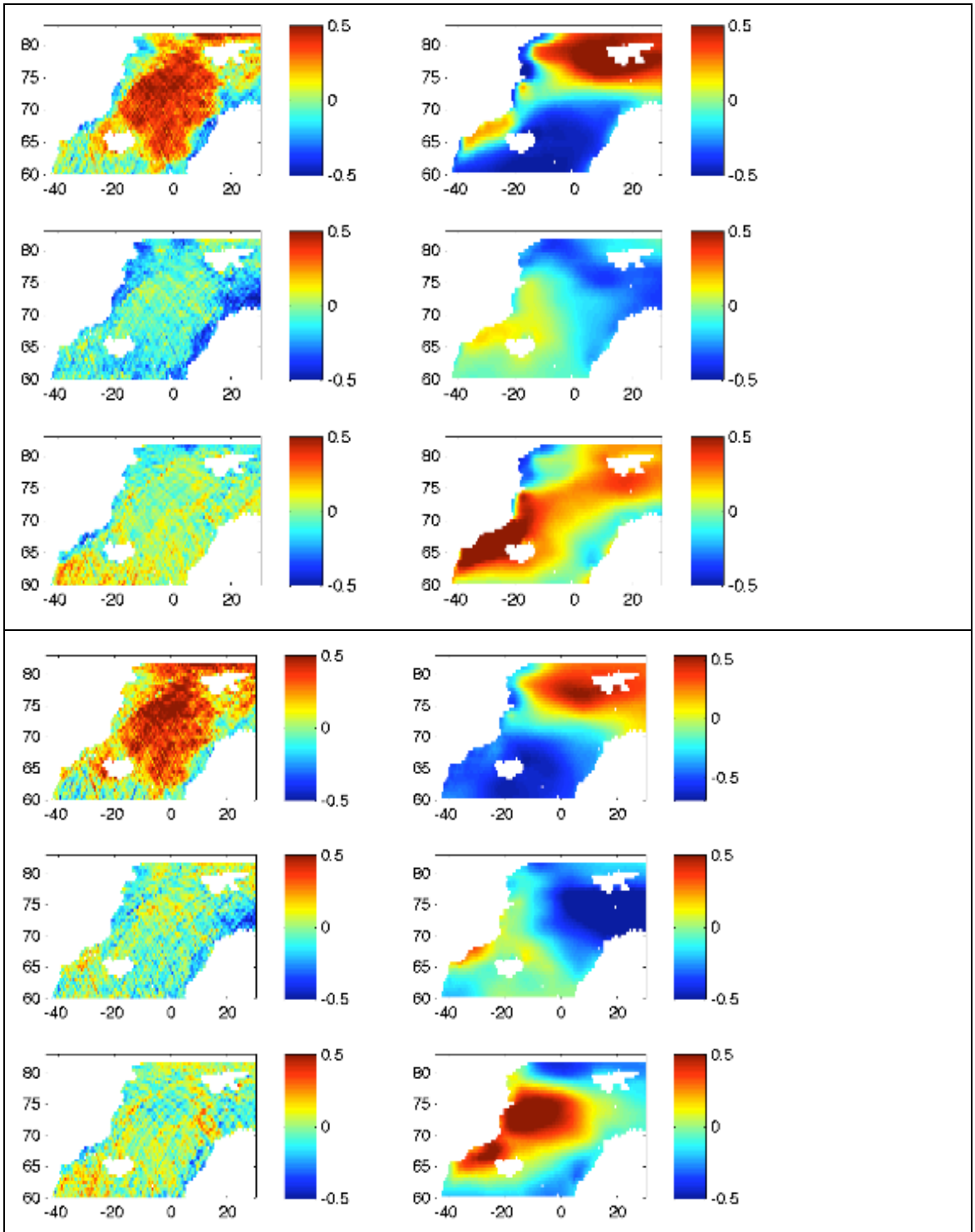

Figure 4. .29. The 3 most important coupled MCA modes presented as heterogeneous correlation maps of the unfiltered (top 3 rows) and filtered (bottom 3 rows) zonal wind stress (right) and SSHA (left). The colour scale represents a correlation coefficient $r[A(t), a_k(t)]$ between the grid points of original data (left and right fields) and time expansion coefficients of corresponding SVD modes of the other field (right and left) and R∈ (-1,1).

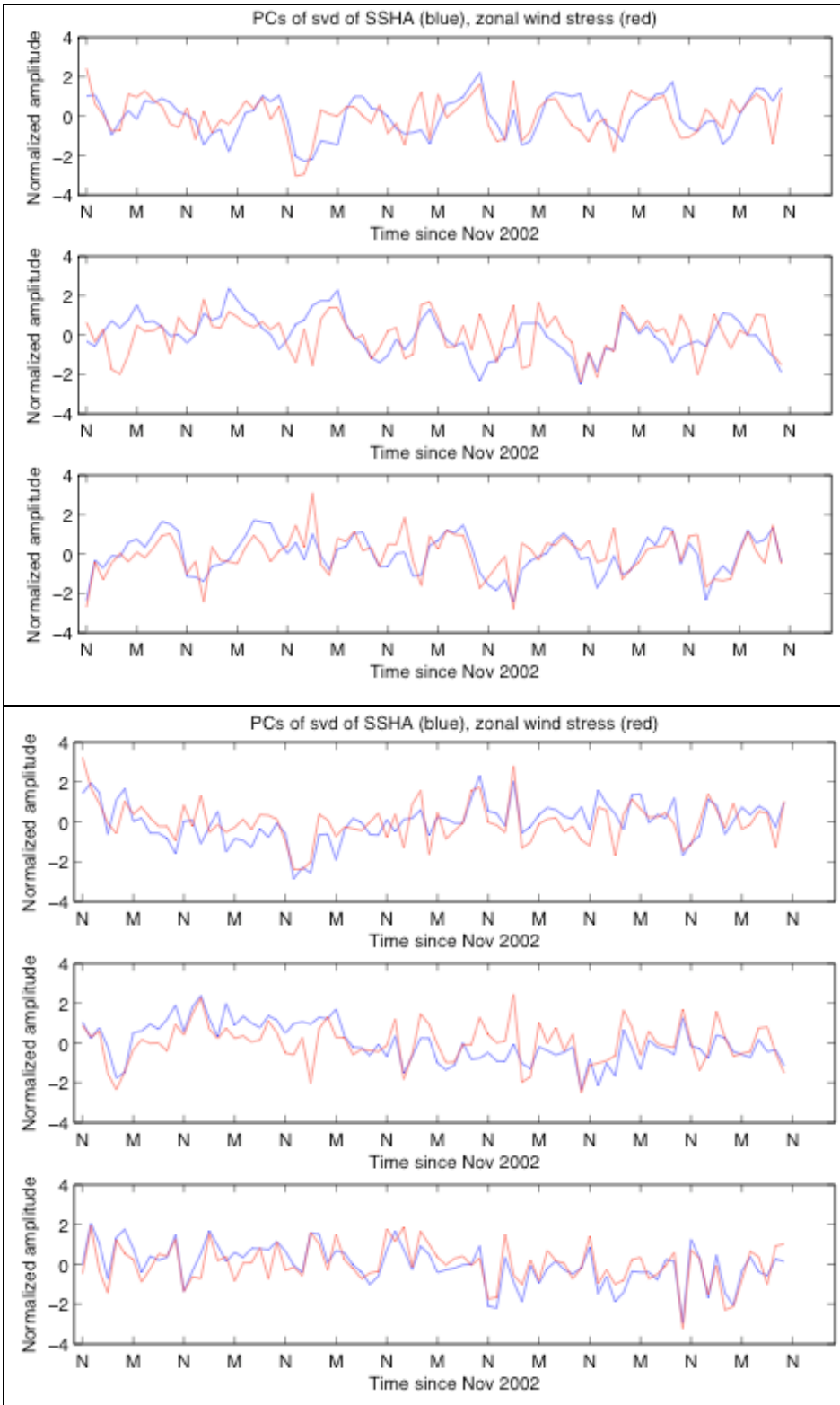

Figure 4. 30**.** Normalized time series of the first three most important MCA coupled modes of the unfiltered (top 3) and filtered (bottom 3) SSH (blue) and zonal wind stress (red).

Mode (k)	SCF (%)	CSCF(%)	R(ak(t),bk(t))
SVD1	78.5/84.1	78.5/84.1	0.58/0.67
SVD2	13.0/9.3	91.5	0.42
SVD3	5.1/2.6	96.6	0.80
SVD4	1.4/2.1	98.0	0.79
SVD5	1.2/1.0	99.2	0.53
SVD6	0.6/0.7	99.8	0.70

Table 4.6.Results of the MCA analysis for 6 most important coupled modes of variability of SSHA and zonal wind stress. The columns present squared covariance fraction, cumulative squared covariance fraction and correlation coefficient for each coupled mode of variability obtained for the unfiltered (right) and seasonally filtered fields (left).

Mode [k]	HomoVar [%] SSH	HomoVar [%] ZWS	HetVar [%] SSH	HetVar [%] ZWS
1	32.5/21.8	35.7/38.0	7.4/8.3	13.1/16.9
2	31.5/13.5	23.8/27.1	3.0/1.7	3.8/9.6
3	5.0/3.4	23.3/12.2	1.2/1.4	8.1/7.2
4	7.3/8.6	11.0/6.4	0.9/1.3	6.7/2.9
5	22.5/7.9	7.5/5.1	0.9/1.6	2.0/2.5
6	6.8/1.9	4.3/6.1	0.8/0.8	2.8/4.0

Table 4.7.Variance explained by the 6 most important MCA coupled modes of variability for SSH and zonal wind stress for the unfiltered (left) and seasonally filtered fields (right). HomoVar informs how much of the left/right field the variance explained by the left/right SVD mode. HetVar is the amount of variance in the left/right field predicted from the right/left SVD mode (from the other field).

Left SVD Modes (SSH)	**PC1 (SSH)**	**PC2 (SSH)**	**PC3 (SSH)**
1	**-0.89/0.93**	0.42/0.35	0.07/0.07
2	**0.89/-0.76**	0.43/0.27	0.06/0.04
3	-0.13/-0.21	**0.62/0.42**	-0.02/-0.03

Right SVD Modes (ZWS)	**PC1 (ZWS)**	**PC2 (ZWS)**	**PC3 (ZWS)**
1	**0.96/-0.98**	-0.25/0.19	0.07/0.00
2	**0.57/-0.55**	**0.67/-0.83**	**0.44**/0.07
3	**-0.63**/0.13	**-0.40**/0.16	**0.65/0.96**

Table 4.8.Correlation coefficients between SVD modes and principal components of sea surface height (SSH) and zonal wind stress (ZWS). Numbers in bold indicate that the correlations are significant at 99% confidence level.

Sea Surface Height and Meridional Wind Stress

The first MCA mode for the unfiltered fields accounts for 78% of the total squared covariance, while the second and third modes account for 12.8% and 5.1%, respectively. On the other hand, about 55%, 26% and 8% of the total squared covariance is explained by the first three seasonally filtered coupled modes. All three coupled modes explain mainly the coupling between the 1st EOF of SSHA and the 1st and 2nd EOF of meridional wind stress. In total all significant right modes can predict about 13.3% of unfiltered SSHA variance and 12.7% of the filtered SSHA variance.

Mode 1

The coupled SVD modes indicate that when SSHA is positive at the Greenland Continental Shelf the meridional wind stress anomaly is negative, suggesting that more northerly winds occur. The opposite relationship was found at the Norwegian continental shelf, where the positive SSHA occurs at the same time as the positive meridional wind stress anomaly, which is associated with more southerly winds. The right expansion coefficient is negatively correlated with the SSHA in the central Nordic Seas and positively correlated along the coasts of Greenland and Norway (Figure 4.32), where about 20% of SSHA variance can be explained by the right mode.

A quite different coupled mode was obtained for the seasonally filtered fields. When negative SSHA occurs in the central Nordic Seas, weaker and more northerly winds occur, which is demonstrated as negative meridional wind stress anomaly in Figure 4.31. At the borders of the Nordic Seas, the SSHA is almost zero together with meridional wind stress anomaly. The right time expansion coefficient is negatively correlated with the filtered SSHA in the central Nordic Seas, Barents Sea and in the region to the north and east of Svalbard (Figure 4.32) and explains there about 10% of the filtered SSHA variance. The heterogeneous correlation maps obtained for the unfiltered and filtered fields indicate that the right mode explains most of the left mode's variance at the annual frequency (Figure 4.32). For the unfiltered fields about 9% of the unfiltered SSHA variance can be predicted by the right mode (Table 4.10). That is almost 30% of variance explained by the left mode itself. When considering the seasonally filtered mode, about 5% of the filtered SSHA variance can be predicted by the right mode (Table 4.10), mainly in the central Nordic Seas (Figure 4.32). That

consists of about 25% of variance that is explained by the left mode. The left mode is strongly correlated to the 1st EOF of SSHA and the right mode to the 1st and 2nd EOF of the meridional wind stress.

Mode 2

The 2nd coupled mode indicates that when SSHA is positive in the Nordic Seas the meridional wind stress anomaly is also positive everywhere, except for a region close to the coast of Greenland. A similar mode was obtained for the seasonally filtered fields but now positive meridional wind stress corresponds to negative SSHA in the deep basins. The heterogeneous correlation maps indicate that most of the variability in the SSHA can be predicted by the right mode along the Norwegian continental shelf and in the Barents Sea, where the right time expansion coefficient is positively correlated with SSHA and can explain about 10% of the filtered and unfiltered SSHA. The left mode accounts for about 26% and 14% of total variance in the unfiltered and filtered SSH data respectively. The right mode can predict about 1.6% and 2.2% of variance in the unfiltered and filtered SSH, which accounts for 6% and 15% accounted by the corresponding left mode. The left mode is strongly correlated with the 1st EOF of SSH and the right to the 1st and 2nd (only at the annual frequency) EOFs of meridional wind stress.

Mode 3

The 3rd MCA mode shows that when negative SSHA occurs along the Greenland continental shelf the positive meridional wind stress anomaly occurs in the Denmark Strait and in the Irminger and Greenland Seas. The left mode accounts for 32.2% of total variance in the unfiltered SSH data and is strongly correlated to the 1st EOF of SSH. The right time expansion coefficient is negatively correlated with the unfiltered SSHA at the Greenland continental shelf, where it can explain about 10% of the monthly SSHA variance.

The coupling between the unfiltered time expansion coefficients is weak and becomes stronger when seasonal cycle is removed prior to the MCA (Table 4.9). The left MCA mode of the filtered fields accounts for 12.5% of total variance in the filtered SSHA and the right mode can predict about 12% of it (Table 4.10).

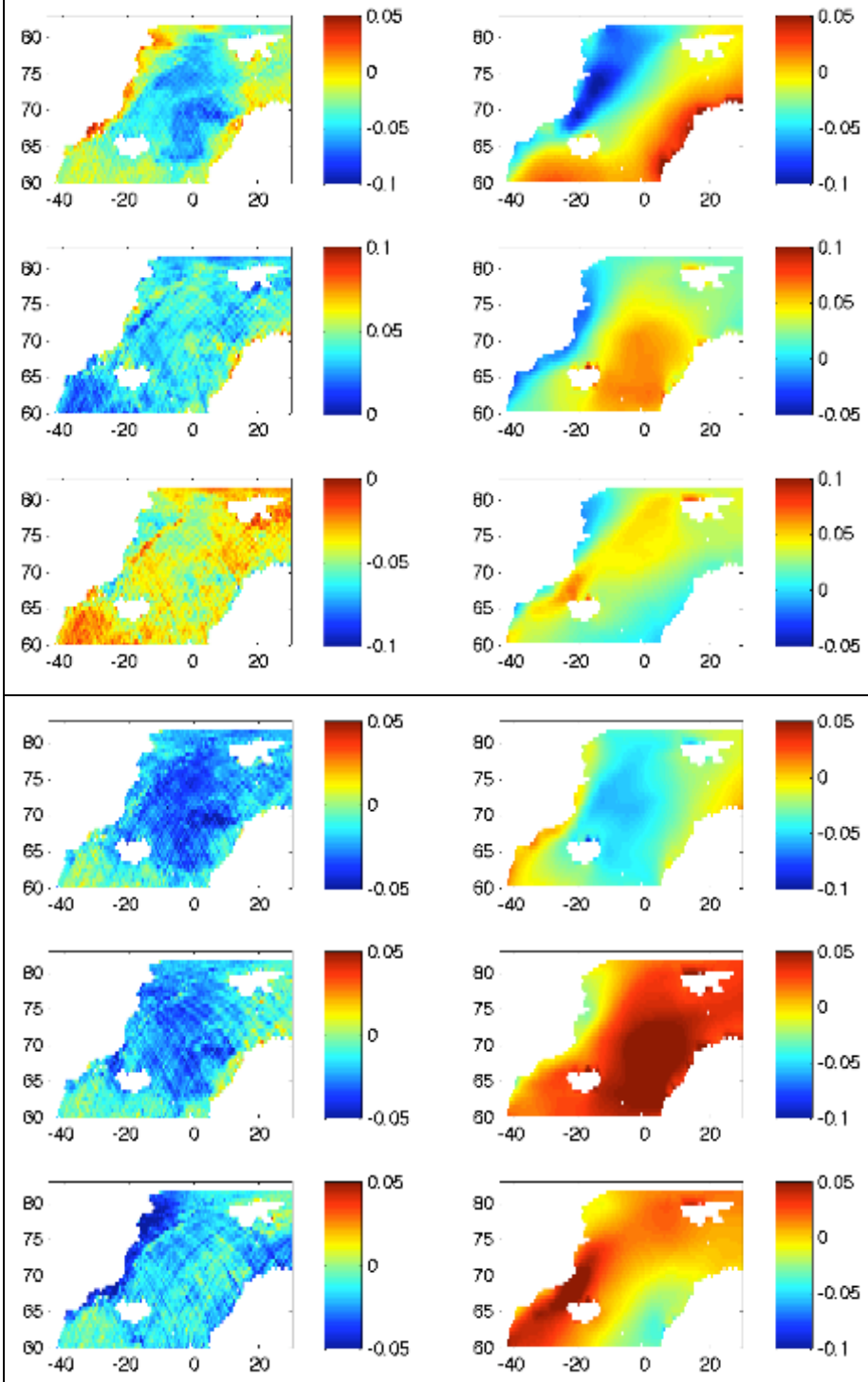

Figure 4. 31.The three most important MCA coupled modes presented as homogenous regression maps of SSHA [m] (left) and meridional wind stress [Nm^{-2}] (right) for the unfiltered (top 3) and seasonally filtered fields (bottom 3).

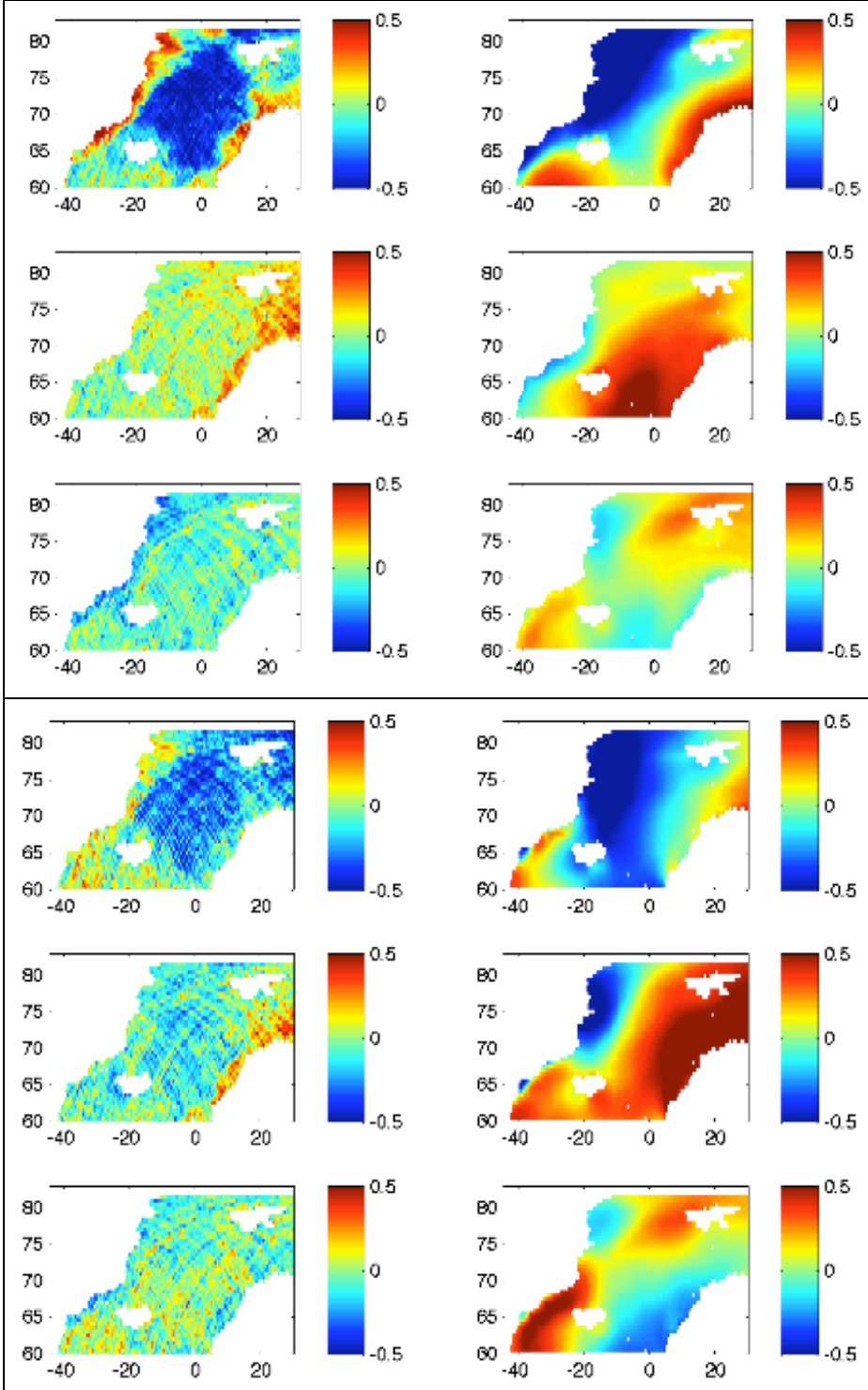

Figure 4.32.The 3 most important coupled MCA modes presented as heterogeneous correlation maps of the unfiltered (top 3 rows) and filtered (bottom 3 rows) meridional wind stress (right) and SSHA (left). The colour scale represents a correlation coefficient $r[A(t), a_k(t)]$ between the grid points of original data (left and right fields) and time expansion coefficients of corresponding SVD modes of the other field (right and left) and R∈ (-1,1).

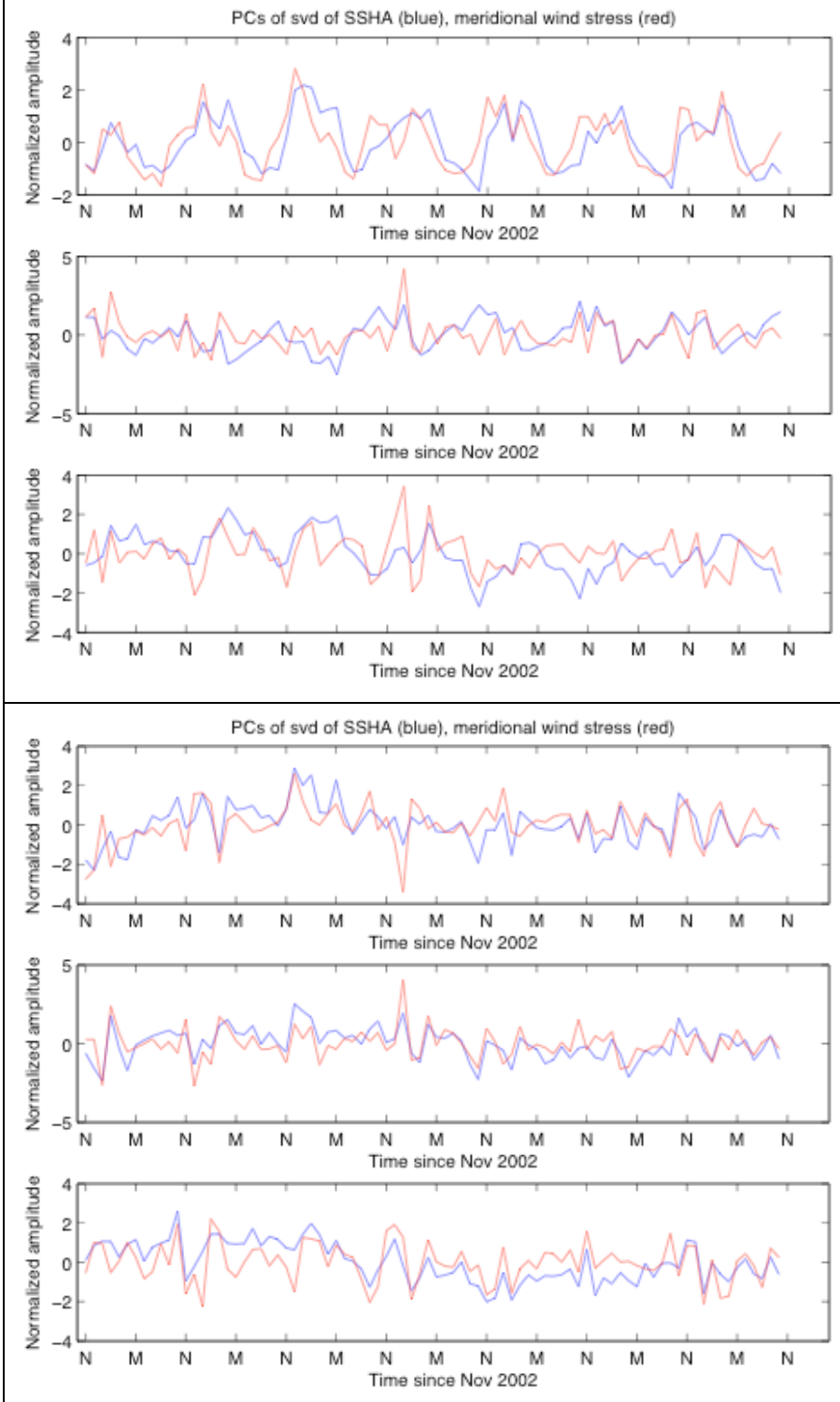

Figure 4.33. Normalized time series of the first three most important MCA coupled modes of the unfiltered (top 3) and filtered (bottom 3) SSH (blue) and meridional wind stress (red).

Mode (k)	SCF (%)	CSCF(%)	R(ak(t),bk(t))
SVD1	78.0/54.9	78.0/54.9	0.71/0.63
SVD2	12.8/26.0	90.8/80.9	0.48/0.65
SVD3	5.1/8.5	95.9/89.4	0.36/0.59
SVD4	2.2/6.1	98.1/95.5	0.71/0.62
SVD5	1.1/3.1	99.2/98.6	0.51/0.58
SVD6	0.6/1.1	99.8/99.7	0.79/0.84

Table 4.9.Results of the MCA analysis for 6 most important coupled modes of variability of SSHA and meridional wind stress. The columns present squared covariance fraction, cumulative squared covariance fraction and correlation coefficient for each coupled mode of variability obtained for the unfiltered (right) and seasonally filtered fields (left).

Mode [k]	HomoVar [%] SSH	HomoVar [%] MWS	HetVar [%] SSH	HetVar [%] MWS
1	29.5/19.9	27.0/37.3	9.3/5.4	12.7/11.1
2	26.6/14.4	37.4/40.3	1.6/2.2	7.3/13.8
3	32.2/12.5	28.0/13.8	1.6/1.5	1.7/4.6
4	10.8/11.6	10.0/9.5	0.8/1.8	5.0/3.3
5	23.2/12.8	7.7/8.6	1.3/1.8	1.1/1.8
6	2.0/2.1	4.2/3.8	0.9/1.0	1.8/2.2

Table 4.10. Variance explained by the 6 most important MCA coupled modes of variability for SSH and meridional wind stress for the unfiltered (left) and seasonally filtered fields (right). HomoVar informs how much of the left/right field the variance explained by the left/right SVD mode. HetVar is the amount of variance in the left/right field predicted from the right/left SVD mode (from the other field).

Left SVD Modes (SSH)	**PC1 (SSH)**	**PC2 (SSH)**	**PC3 (SSH)**
1	**0.83/-0.85**	**-0.54/-0.48**	-0.03/0.12
2	**-0.81/-0.73**	-0.35/-0.26	-0.37/-0.44
3	**0.91/-0.73**	0.34/0.43	-0.14/-0.11

Right SVD Modes (MWS)	**PC1 (MWS)**	**PC2 (MWS)**	**PC3 (MWS)**
1	**0.73/0.88**	**0.66/-0.33**	0.11/**0.33**
2	**-0.71/-0.87**	**0.69/-0.39**	-0.07/**0.29**
3	**-0.71**/-0.12	0.12/**0.80**	0.34/**0.53**

Table 4.11. Correlation coefficients between SVD modes and principal components of sea surface height (SSH) and meridional wind stress (MWS). Numbers in bold indicate that the correlations are significant at 99% confidence level.

Sea Surface Height and Wind Stress Curl.

All significant right SVD modes of WSC can predict 19.1% and 18.2% of the total variance in the unfiltered and filtered SSH data respectively. The results indicate that about 30% of variability explained by the 1st EOF of SSHA can be predicted from the 1st EOF of WSC (Tables 4.13, 4.14). For the seasonally filtered modes, the left SVD field, which consists of the rotated 1st and 2nd EOFs of WSC, can predict about 50% of the 1st EOF SSHA variance. The 2nd SVD mode also shows relationships between the 1st EOF of SSHA and the 1st and 2nd EOF of WSC that occurs at the borders of the Nordic Seas on the annual timescales and also at the Greenland continental shelf for the other timescales. There exists a phase lag of 7 months between the 1st and 2nd SVD right modes and 8 months for the 1st and 2nd left fields. Therefore the 1st right SVD mode is correlated on the annual frequency with the SSHA in the central Nordic Seas and the 2nd with the SSHA at the borders of the Nordic Seas. In total, about 50% of the 1st EOF unfiltered SSHA variability can be explained by the first two SVD right modes.

Considering the seasonally filtered fields the first two right SVD modes are not correlated with each other but the left are significantly correlated at 8 months lag (R=-0.48, at 95% confidence level). All the first three SVD right modes are significantly correlated to the NAO index at 99% confidence level (not shown). The left modes are also significantly correlated to the NAO index but with a lower significance level (95%). Only the 2nd left SVD mode of the unfiltered SSHA was found to be uncorrelated to the NAO Index.

<u>Mode 1.</u>

The 1st SVD mode of SSHA and wind stress curl explains 73% of the squared covariance between the two fields for the unfiltered data and 63% for the filtered fields. The left pattern of the unfiltered fields is characterized by the oscillations between the deep basins (with a negative amplitude in SSHA of about 10cm) and the boundaries of the basin where the amplitudes reach 5cm at the Greenland continental shelf (Figure 4.34). However, the significant correlations between the SSHA timeseries and the expansion coefficient of the right SVD mode (|R|>0.49 significant at 95% confidence level) are found only to the north of Svalbard and in the interior of the Nordic Seas in four deep basins: the Greenland Sea, Iceland Sea, Norwegian Basin and Lofoten Basin

(Figure 4.35). The right mode can explain locally up to 30% of the unfiltered SSHA variance in the central Nordic Seas. The left SVD mode is very similar to the 1st EOF of SSHA at all frequencies and the right SVD mode is related to the 1st EOF of wind stress curl (Table 4.14).

The square of the spatial mean of the homogeneous correlation map indicates that the left unfiltered field explains 32% of variance in the SSH data (similarly to the 1st EOF of SSHA) and the unfiltered right field can predict about one third of it (Table 4.13). On the other hand, the right field explains a high percentage of variance in the wind stress curl (22%). This suggests that the 1st EOF of wind stress curl could be responsible for forcing the 1st EOF of SSHA. It was found that that the 1st right SVD mode (wind stress curl) leads the 1st SVD left mode (sea level) simultaneously and with a 1-month lag for the unfiltered data and this simultaneous relationship becomes stronger for the seasonally filtered data (Table 4.12). The left filtered SVD mode shows about 5 cm oscillations in the deep basins and smaller, but of the same sign, oscillations at the northern Greenland continental shelf. In total about 50% of the variability explained by the left mode can be predicted from the right mode when considering frequencies other than annual. The 1st right SVD mode of the filtered wind stress curl is negatively correlated with the filtered SSHA in the CENTRAL NORDIC Seas, Barents Sea, Fram Strait and the region located to the North and East of Svalbard. It explains about 30% of the filtered SSH variance in the Greenland Sea and about 20-25% in the other areas that are significantly correlated with the SSHA.

Mode 2

The 2nd SVD mode explains about 13% of co-variability between wind stress curl and SSHA and shows a significant simultaneous relationship between its time expansion coefficients (Table 4.12). For the unfiltered fields the relationship was found also at -1,-2 and -3 month lags. The right SVD mode can predict about 6.1% of variability in the unfiltered SSHA that is about 20% of the left mode. Regionally, the right mode is significantly and positively correlated with the SSHA in the Barents Sea and at the borders of the Nordic Seas: the continental shelves of Norway and Greenland where it can explain about 25% of the local variance (Figure 4.35). On the other hand, significant correlations between the seasonally filtered right mode and SSHA were

found for the Greenland continental shelf only (Figure 4.35), explaining locally 10-15% of the filtered SSHA variance.

The 2nd left SVD pattern indicates also a high similarity to the 1st EOF of SSHA that describes in-phase oscillations in the whole Nordic Seas with the greatest amplitudes at the borders of the Nordic Seas for the unfiltered fields and at the Greenland continental shelf for the filtered fields. The 2nd right unfiltered mode is similar to the 1st and 2nd EOF of wind stress curl (Figure 4.34, Table 4.14).

Mode 3

The 3rd SVD mode explains only about 5.6 % and 8.6% of co-variability between the two unfiltered and filtered fields. The 3rd right pattern is very similar to the 2nd EOF of wind stress curl and can predict about 1.5% of variability in the SSHA (Figure 34, Table 4.13). The left mode has a moderate relationship to the 2nd and 3rd EOF of SSHA at the annual frequencies but is more similar to the 1st EOF of SSHA when considering seasonally filtered data (Table 4.14). The left mode describes oscillations in SSHA at the northern continental shelf of Greenland, the region that is also covered by sea-ice. This mode accounts for about 10% of the total variance in the SSHA data (unfiltered and filtered). The right mode shows oscillations in wind stress curl between a narrow region to the north of Denmark Strait. The mode changes when seasonality is removed prior to the MCA and explains the antiphase relationship between two narrow regions located to the north of Iceland and along the northern continental shelf of Greenland. The wind stress curl right mode can explain up to 16% of SSHA variance described by the left mode for the seasonally filtered case.

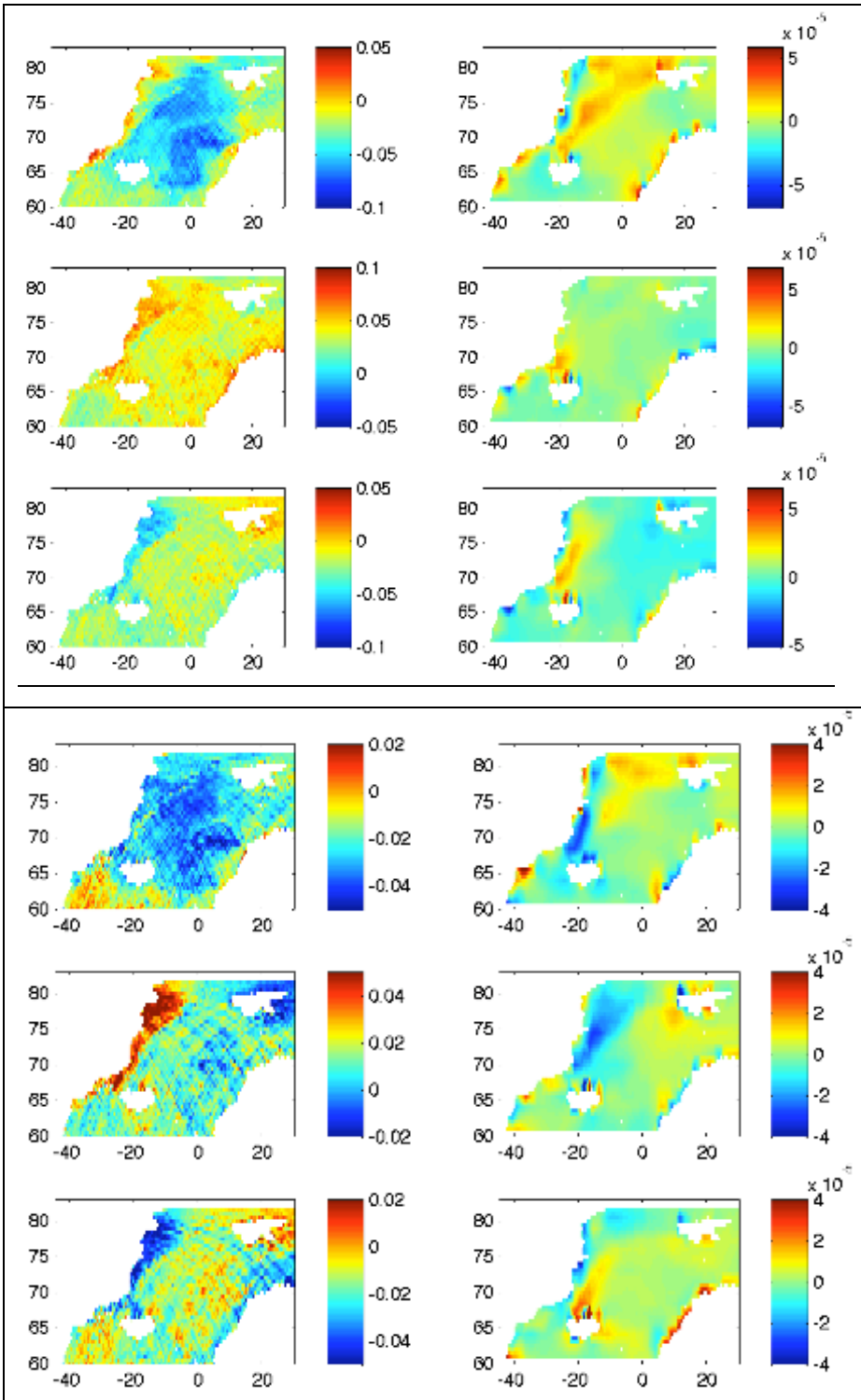

Figure 4.34.The three most important MCA coupled modes presented as homogenous regression maps of SSHA [m] (left) and wind stress curl [Nm^{-3}] (right, multiplied by 100) for the unfiltered (top 3) and seasonally filtered fields (bottom 3).

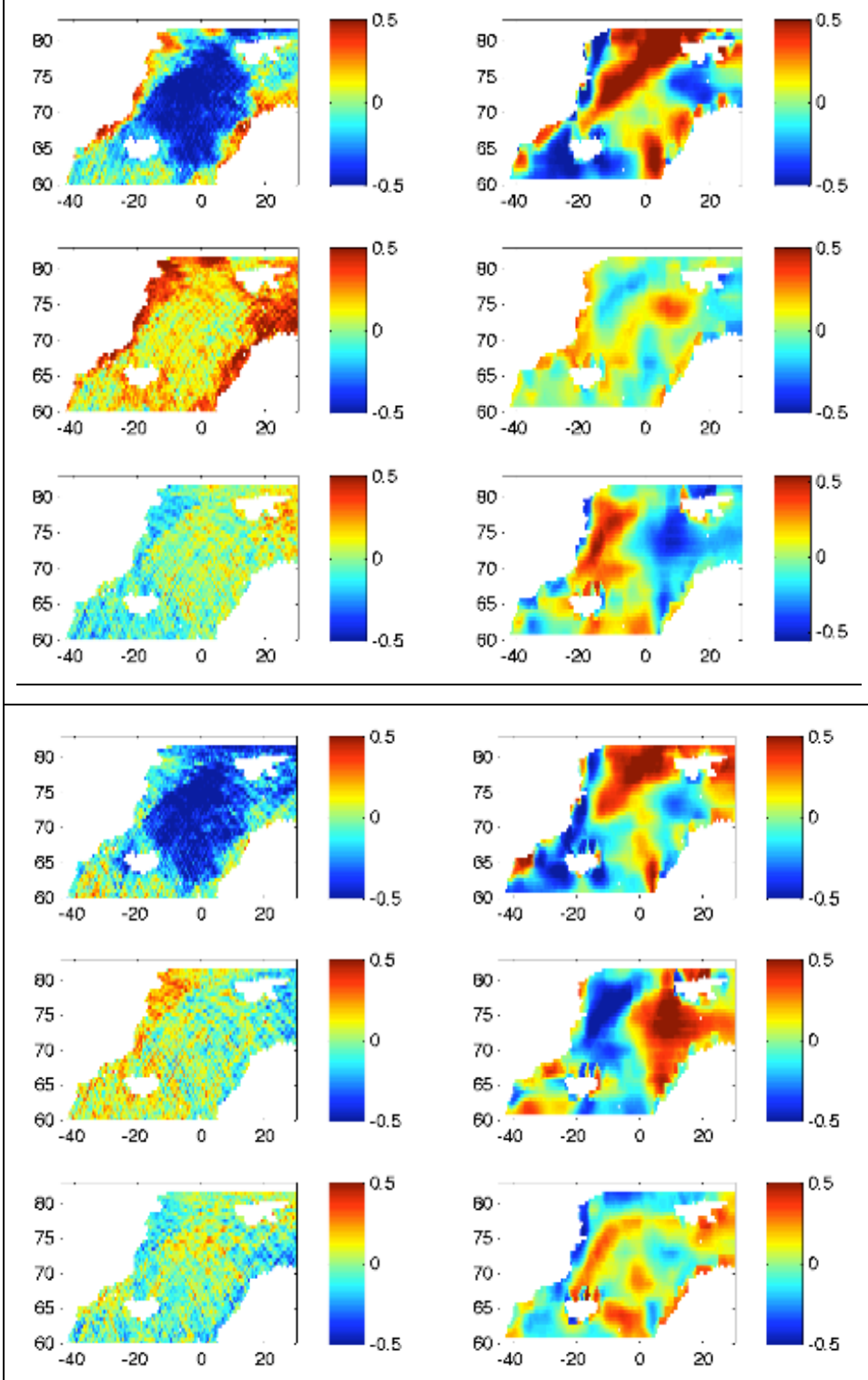

Figure 4.35.The 3 most important coupled MCA modes presented as heterogeneous correlation maps of the unfiltered (top 3 rows) and filtered (bottom 3 rows) wind stress curl (right) and SSHA (left). The colour scale represents a correlation coefficient $r[A(t), a_k(t)]$ between the grid points of original data (left and right fields) and time expansion coefficients of corresponding SVD modes of the other field (right and left) and R∈ (-1,1).

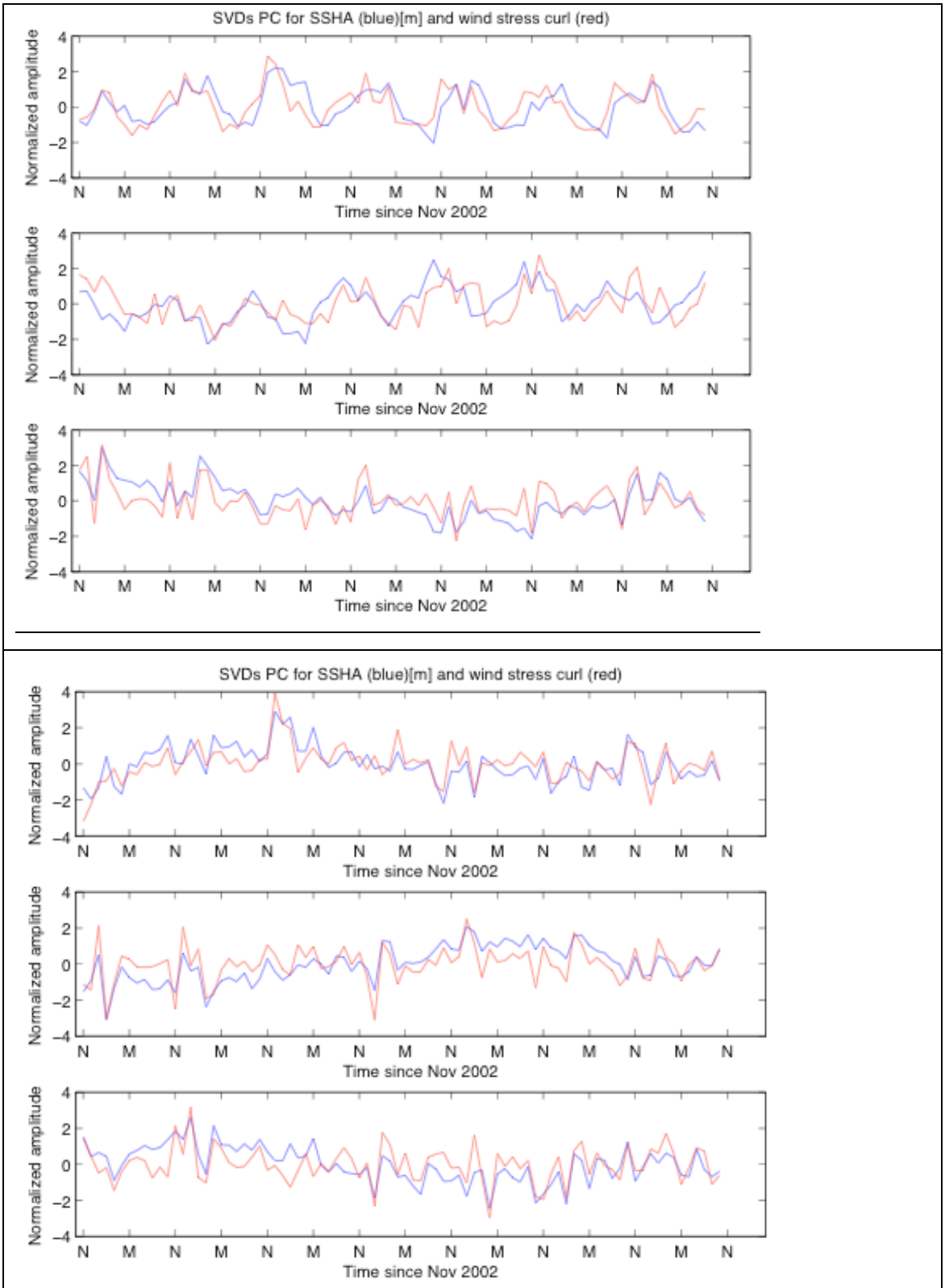

Figure 4.36. Normalized time series of the first three most important MCA coupled modes of the unfiltered (top 3) and filtered (bottom 3) SSH (blue) and wind stress curl (red).

Mode (k)	SCF (%)	CSCF(%)	R(ak(t),bk(t))
SVD1	73.0/62.9	73.0/62.9	0.71/0.76
SVD2	13.2/13.5	86.2/76.4	0.56/0.69
SVD3	5.6/8.6	91.8/85.0	0.68/0.65
SVD4	4.0/6.5	95.8/91.5	0.77/0.63
SVD5	2.5/5.5	98.3/97.0	0.74/0.81
SVD6	1.5/2.6	99.8/99.6	0.78/0.77

Table 4.12. Results of the MCA analysis for 6 most important coupled modes of variability of SSHA and wind stress curl. The columns present squared covariance fraction, cumulative squared covariance fraction and correlation coefficient for each coupled mode of variability obtained for the unfiltered (right) and seasonally filtered fields (left).

Mode [k]	HomoVar [%] SSH	HomoVar [%] WSC	HetVar [%] SSH	HetVar [%] WSC
1	31.6/22.1	20.8/12.9	10.6/11.3	10.8/7.8
2	31.6/8.6	6.9/14.6	6.1/1.9	1.6/8.0
3	11.3/10.4	11.7/8.8	1.4/1.7	5.7/3.2
4	6.0/9.8	9.1/8.4	1.0/1.9	5.2/3.0
5	8.3/3.1	7.9/6.6	0.8/1.4	4.7/4.2
6	6.7/5.6	4.7/6.7	0.9/1.3	2.8/3.8

Table 4.13. Variance explained by the 6 most important MCA coupled modes of variability for SSH and wind stress curl for the unfiltered (left) and seasonally filtered fields (right). HomoVar informs how much of the left/right field the variance explained by the left/right SVD mode. HetVar is the amount of variance in the left/right field predicted from the right/left SVD mode (from the other field).

Left SVD Modes (SSH)	**PC1 (SSH)**	**PC2 (SSH)**	**PC3 (SSH)**
1	**0.88/-0.94**	-0.47/-0.33	-0.06/-0.04
2	**-0.89/0.54**	-0.43/**-0.56**	-0.05/**0.37**
3	0.47/**-0.63**	0.46/0.45	-0.52/**0.36**

Right SVD Modes (WSC)	**PC1 (WSC)**	**PC2 (WSC)**	**PC3 (WSC)**
1	**-0.97/0.74**	0.21/**0.53**	0.01/**0.38**
2	-0.45/**0.70**	**-0.42**/**-0.65**	0.09/-0.01
3	-0.25/-0.27	**-0.93**/**-0.56**	-0.07/**0.74**

T able 4.14. Correlations coefficients between SVD modes and principal components of sea surface height (SSH) and wind stress curl (WSC). Numbers in bold indicate that the correlations are significant at 99% confidence level.

Sea Surface Height and Heat Flux

The significant SVD right modes can predict 17.9 % of SSHA variability in the unfiltered data and 9% in the seasonally filtered SSHA. Therefore most of the coupling between the two fields occurs at the annual frequency. The results of SVD show that heat flux explains most of the variability described by the 1st EOF of SSHA.

Mode 1

Only the 1st SVD of the unfiltered data is significant according to Monte Carlo simulation results. It explains 94.5% of the squared covariance between the two fields. The left pattern is characterized by the oscillations at annual frequency in the deep basins and it is similar to the 1st EOF of SSHA. The right time expansion coefficient is positively correlated with SSHA in the central Nordic Seas and to the north of Svalbard and negatively correlated along the coast of Greenland (Figure 4.38), where the right mode can explain locally about 15% of the SSHA variance. The square of homogeneous correlation indicates that the left field explains 31% of variance in the SSHA data (similarly to the 1st EOF of SSHA) and the right field can predict about one quarter of it (Table 4.16). On the other hand the right field explains a high percentage of variance in the heat flux (55%). The structure of the left SVD mode is very similar to the 1st EOF of sea surface height and the right mode is very similar to the 1st EOF of heat flux (Figure 4.37, Table 4.17). The lagged correlations indicate that the strongest link between left and right mode occur when SSH lags heat flux at 1 month.

Mode 2

The 2nd SVD mode between unfiltered SSH and heat flux explains 3.8% of co-variability and shows a significant simultaneous relationship at the annual frequencies between the two time expansion coefficients (Table 4.15). Its left structure indicates high similarity to the 1st EOF of SSHA and the right one to the 2nd and 3rd EOF of heat flux (Figure 4.37, Table 4.17). The heterogeneous correlation indicates that almost 9% of variance in SSHA data can be predicted from the right field (Table 4.16). The heterogeneous correlations maps show significant positive correlations in shallow regions of the Nordic Seas: Greenland and Norwegian continental shelf, Irminger and Barents Seas ($|R| > 0.48$ at 95% confidence level) (Figure 4.38). The right mode can

explain in these regions about 20% of the SSHA variance. The relationship is the strongest when sea level occurs 1 month before the heat flux (R=0.76).

Considering seasonally filtered data, the 2nd SVD mode explains 31.2% of co-variance between the two fields. The left field is still very similar to the 1st EOF of SSHA and the right is now similar to the 2nd EOF of seasonally filtered heat flux. The left mode accounts for 21.9% of variance in the filtered SSHA, from which 27% of it can be predicted from the right mode, mainly in the deep basins. However, the amplitudes of the left mode are very small with the mean amplitudes of about 3 cm in the central Nordic Seas, which reach the maximum of about 5 cm in the Lofoten Basin. The right mode of the seasonally filtered heat flux is positively correlated with the filtered SSHA in the central Nordic Seas and explains there about 12% of the filtered SSHA variance.

Mode 3

The 3rd SVD mode explains only about 1 % of co-variability between the two unfiltered fields. The 3rd right pattern is strongly correlated with the 2nd EOF of heat flux and can predict about 1% of variance in the SSHA. That is about 8% of the homogeneous variance explained by the left field in the SSHA data. The left field of this mode has a moderate relationship to the 1st and 3rd EOF of SSHA and corresponds to the small (4 cm) oscillations in the Greenland and Norwegian Seas (Figure 4.37). The two time expansion coefficients show a simultaneous and significant correlation equal to 0.69 that is also significant at 99% when heat flux leads SSH with 1-month lag. The heterogeneous correlation map (Figure 4.38) shows significant correlation between SSHA data and the 3rd right expansion coefficient in the Vøring Plateau and the southern Barents Sea (|R|> 0.22 and at 95% confidence level).

For the seasonally filtered fields the 3rd mode explains about 11% of their co-variance. The left mode is more similar to the 1st and 2nd EOF of SSHA and shows oscillations with magnitudes of about 6-8 cm at the eastern Greenland continental shelf that are in an anti-phase relationship with the rest of the Nordic Seas. This mode can explain that part of the 1st EOF of the seasonally filtered SSHA that is located at the Greenland continental shelf, explaining there about 10% of the filtered SSHA variance. It indicates that when a positive heat flux anomaly occurs at the western border of the Nordic Seas the sea level is lower than the mean (negative SSHA) and vice versa; when a negative

heat flux occurs with a magnitudes reaching 10 Wm^{-2} the sea level increases by 8 cm at the Greenland continental shelf (positive SSHA). This mode might be connected to the sea-ice but it does not describe melting and freezing, which would cause a positive correlation between the right field and the SSHA (Figure 4.38). Most of the variance in the filtered SSHA can be predicted by the right mode in the southern Barents Sea and along continental shelves of Greenland and Norway. The right mode can predict 3.1% of variance in the filtered SSHA that accounts for up to 23% of variance explained by the left mode.

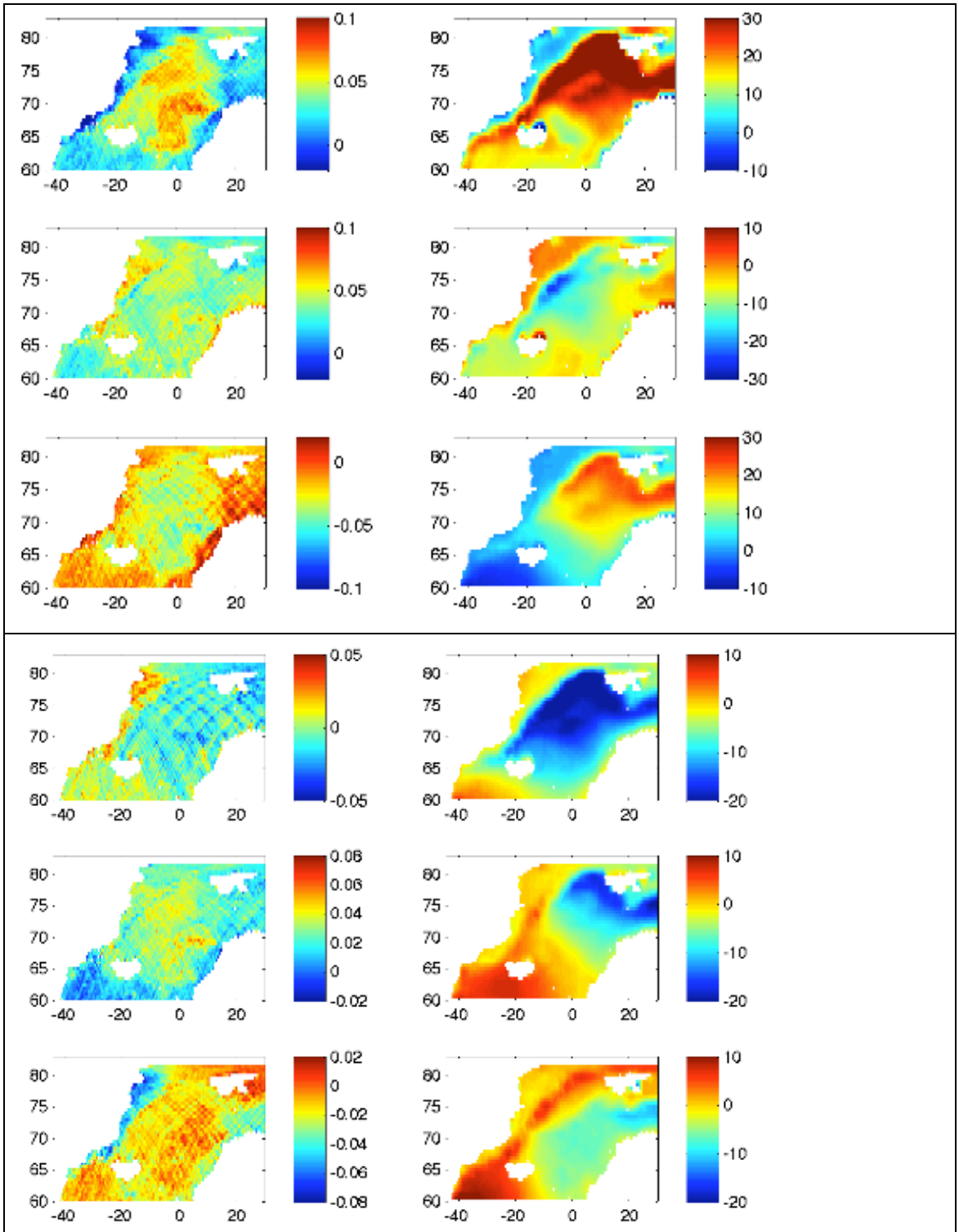

Figure 4.37. The three most important MCA coupled modes presented as homogenous regression maps of SSHA [m] (left) and heat flux [Wm^{-2}] (right) for the unfiltered (top 3) and seasonally filtered fields (bottom 3).

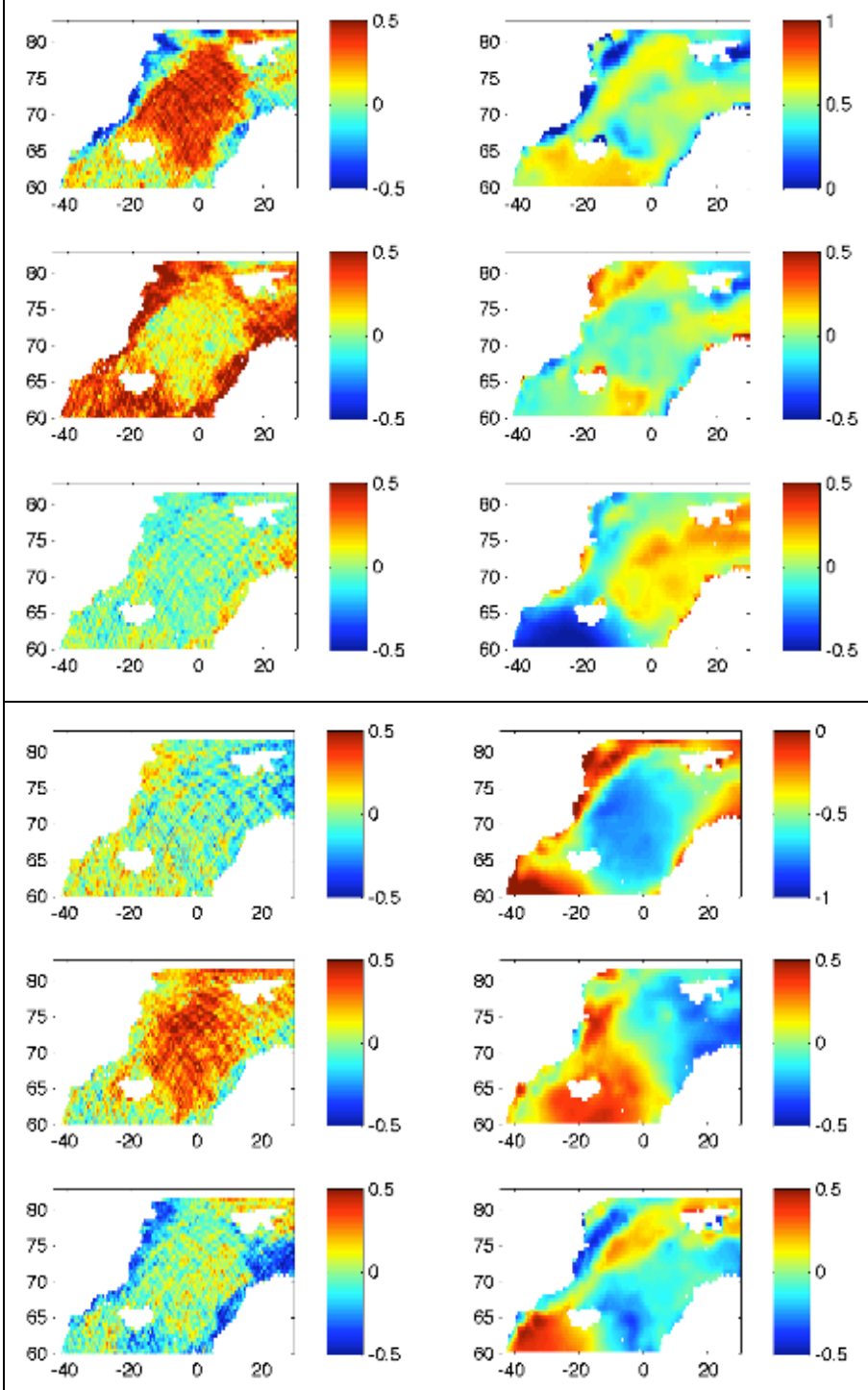

Figure 4.38. The 3 most important coupled MCA modes presented as heterogeneous correlation maps of the unfiltered (top 3 rows) and filtered (bottom 3 rows) heat flux (right) and SSHA (left). The colour scale represents a correlation coefficient $r[A(t), a_k(t)]$ between the grid points of original data (left and right fields) and time expansion coefficients of corresponding SVD modes of the other field (right and left) and R∈ (-1,1).

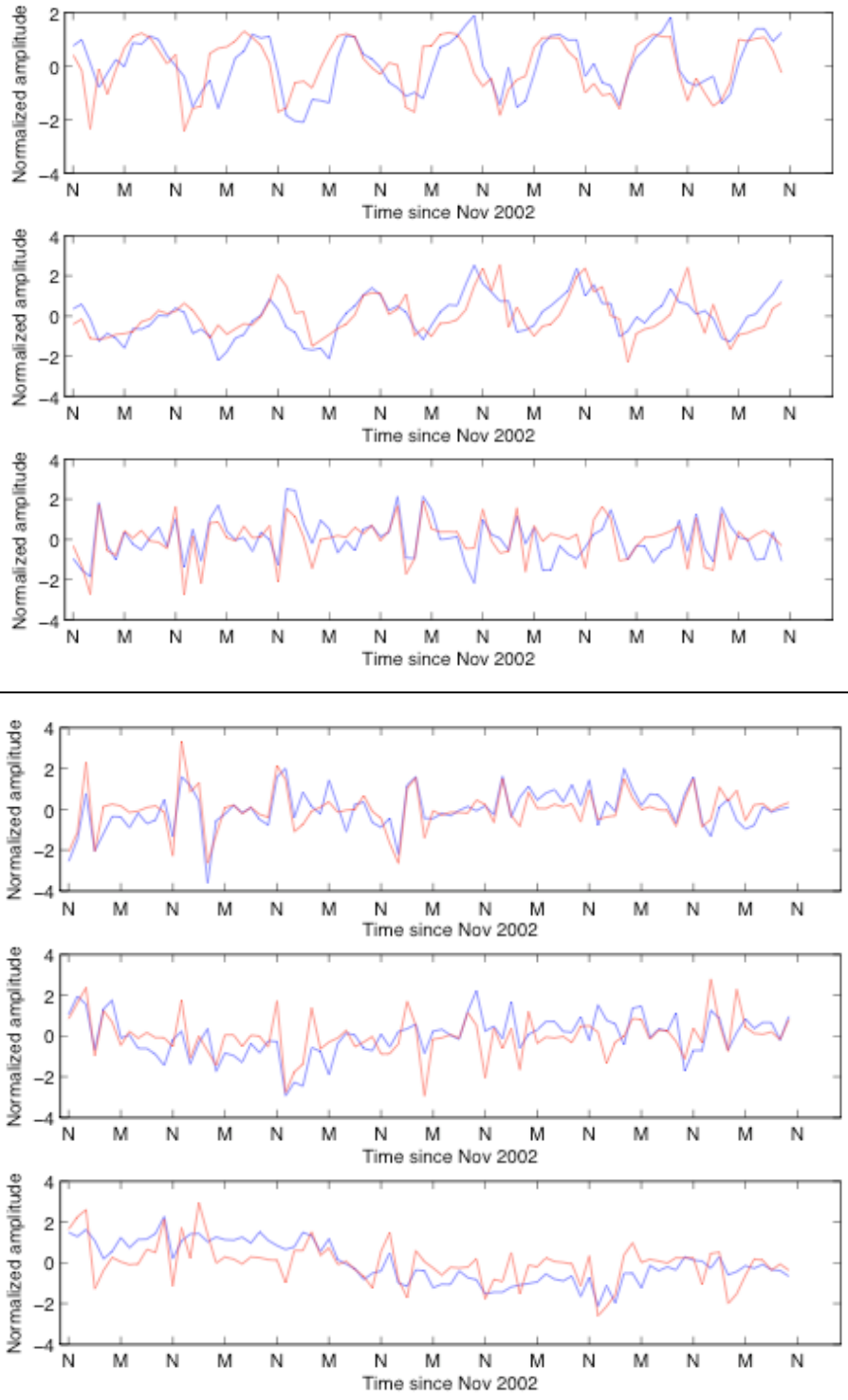

Figure 4.39. Normalized time series of the first three most important MCA coupled modes of the unfiltered (top 3) and filtered (bottom 3) SSH (blue) and heat flux (red).

Mode (k)	SCF (%)	CSCF(%)	R(ak(t),bk(t))
SVD1	94.5/48.3	94.5/48.3	0.62/0.78
SVD2	2.8/31.2	97.3/79.5	0.65/0.59
SVD3	1.0/11.2	98.3/90.7	0.69/0.64
SVD4	0.8/4.3	99.1/95.0	0.77/0.66
SVD5	0.3/2.8	99.4/97.8	0.77/0.76
SVD6	0.2/1.9	99.6/99.7	0.77/0.84

T able 4.15. Results of the MCA analysis for 6 most important coupled modes of variability of SSHA and heat flux. The columns present squared covariance fraction, cumulative squared covariance fraction and correlation coefficient for each coupled mode of variability obtained for the unfiltered (right) and seasonally filtered fields (left).

Mode [k]	HomoVar [%] SSH	HomoVar [%] HF	HetVar [%] SSH	HetVar [%] HF
1	30.6/4.7	64.4/44.0	7.6/1.8	25.9/28.2
2	32.5/21.9	12.1/16.1	9.3/6.0	1.4/4.6
3	12.4/13.0	17.5/11.7	1.0/3.1	4.1/3.5
4	10.3/8.5	5.5/9.8	1.3/1.4	3.5/3.8
5	2.3/7.0	4.0/6.9	0.8/1.4	2.1/3.3
6	3.5/2.8	7.7/4.8	1.2/1.4	1.8/3.2

T able 4.16. Variance explained by the 6 most important MCA coupled modes of variability for SSH and heat flux for the unfiltered (left) and seasonally filtered fields (right). HomoVar informs how much of the left/right field the variance explained by the left/right SVD mode. HetVar is the amount of variance in the left/right field predicted from the right/left SVD mode (from the other field).

Left SVD Modes (SSH)	**PC1 (SSH)**	**PC2 (SSH)**	**PC3 (SSH)**
1	**-0.86**/-0.14	0.51/**-0.52**	0.01/**0.49**
2	**-0.91/0.94**	-0.41/0.32	-0.02/0.09
3	**0.53/-0.72**	-0.28/0.64	**-0.37**/0.02

Right SVD Modes (HF)	**PC1 (HF)**	**PC2 (HF)**	**PC3 (HF)**
1	**-1/1**	-0.03/-0.08	0.01/0.02
2	0.35/**0.44**	**0.34/0.86**	**0.41**/-0.23
3	-**0.48**/0.16	**0.86/0.46**	-0.10/**0.76**

Table 4. 17. Correlations coefficients between SVD modes and principal components of sea surface height (SSH) and heat flux (HF). Numbers in bold indicate that the correlations are significant at 99% confidence level.

Sea Surface Height and Evaporation

All fluxes in the ERA Interim dataset are defined to be positive downward. Therefore evaporation is normally negative and only when condensation occurs, over ice or very cold sea, it could be positive. Therefore more negative evaporation causes sea level to drop and therefore should be positively correlated with SSHA. In the MCA the temporal mean is removed prior to the analysis and the results are shown as anomalies relative to the mean. Therefore, negative anomalies mean that there was more evaporation than the mean and positive anomalies mean that there was less, when compared to the 2002-2009 time average. The first MCA mode for the unfiltered fields accounts for 92% of the total squared covariance, while the second and third modes account for 5.4% and 1.1%, respectively. On the other hand, about 51.6%, 25.9% and 14.2% of the total squared covariance is explained by the first three seasonally filtered coupled modes. All three coupled modes explain mainly the coupling between the 1st EOF of SSHA and the 1st and 2nd EOF of evaporation. In total all significant right modes can predict about 21.8% of unfiltered SSH variance and 8.3% of the filtered SSH variance.

Mode 1

The coupled mode indicates that when SSHA anomaly is positive in the central Nordic Seas, positive evaporation occurs (less evaporation). On the other hand, when SSHA is negative at the borders of the Nordic Seas the evaporation anomaly is positive or zero. The opposite coupled modes were obtained for the seasonally filtered fields where the negative SSHA anomaly is associated with a negative evaporation (more evaporation) anomaly in the whole Nordic Seas except the ice-covered ocean (Figure 4.40). The heterogeneous correlation maps obtained for the unfiltered and filtered fields indicate that the right mode explains most of the variance at the annual frequency. Also the strongest coupling occurs for the unfiltered MCA modes (Table 4.18). For the unfiltered fields about 6.8% of variance can be predicted by the right mode (Table 4.19). That is about 25% of variance explained by the left mode itself. The right mode is significantly and positively correlated with the monthly SSHA in the central Nordic Seas and negatively correlated along the Greenland continental shelf. It can explain about 20% of the SSHA variance along the Greenland coast and about 15% in the central Nordic Seas (Figure 4.41).

When considering the seasonally filtered mode, about 3.4% of the total filtered SSHA variance can be predicted by the right mode (Table 4.19). That consists of almost 18% of variance that is explained by the 2nd SVD left mode itself. The left unfiltered mode is strongly correlated to the 1st and 2nd EOF of unfiltered SSHA and the right unfiltered mode to the 1st EOF of evaporation (Table 4.20). Considering seasonally filtered data the left mode is strongly correlated with the 1st EOF of SSHA but significant heterogeneous correlations between the 1st right mode and SSHA are found mainly in the Barents Sea and a region located to the north and east of Svalbard (Figure 4.41).

Mode 2

The 2nd MCA coupled mode indicates that when SSHA is positive everywhere in the Nordic Seas, the evaporation anomaly is negative (more evaporation) or zero in the same area (Figure 4.40). A very similar mode was also obtained for the seasonally filtered fields. The heterogeneous correlation maps for the unfiltered data indicate that most of the variability in the SSHA can be predicted by the right mode in the shallow regions of the Nordic Seas (Figure 4.41). The left mode accounts for about 35.7% of total variance in the unfiltered SSHA data. The right mode can predict about 13% of variance in the unfiltered SSHA, which accounts for 36% explained by the corresponding left mode. The left mode is strongly correlated with the 1st EOF of SSH and the right is moderately correlated with the 1st EOF of evaporation (Table 4.20).

The heterogeneous correlation maps for the seasonally filtered data indicate that most of the variability in the SSHA can be predicted by the right mode at the northern continental shelf of Greenland where the right expansion coefficient is significantly and positively correlated with the filtered SSHA (Figure 4.41). The right expansion coefficient can locally explain about 8% of the filtered SSHA variance at the northern Greenland continental shelf. The left mode accounts for about 20.1% of total variance in the filtered SSHA data (Table 4.19). The right mode can predict about 2.6% of variance in the filtered SSHA, which accounts for 13% explained by the corresponding left mode. The left mode is strongly correlated with the 1st EOF of SSH and the right to the 1st and 2nd EOFs of evaporation (Table 4.20). Significant positive correlations were found between the right seasonally filtered mode and the filtered SSH at the northern Greenland continental shelf (Figure 4.41).

Mode 3

The 3rd MCA mode shows that when negative SSHA anomaly occurs along the Greenland and Norwegian continental shelves, the positive evaporation anomaly (less evaporation) occurs in the Irminger Sea and negative anomaly (more evaporation) in the central and eastern Nordic Seas (Figure 4.40). The left mode accounts for only 2% of total variance in the unfiltered SSHA data and is moderately correlated to the 3rd EOF of SSH (Tables 4.18, 4.20). The coupling between the unfiltered time expansion coefficients is strong but decreases for the seasonally filtered fields (Table 4.18). The filtered left field explains about 10% of total variance in the filtered SSHA and is correlated with the 2nd EOF of SSHA (Tables 4.18, 4.20). The right field can explain 2.3% of total variance in the filtered SSH mainly at the continental shelf of Norway and the Barents Sea (Figure 4.41).

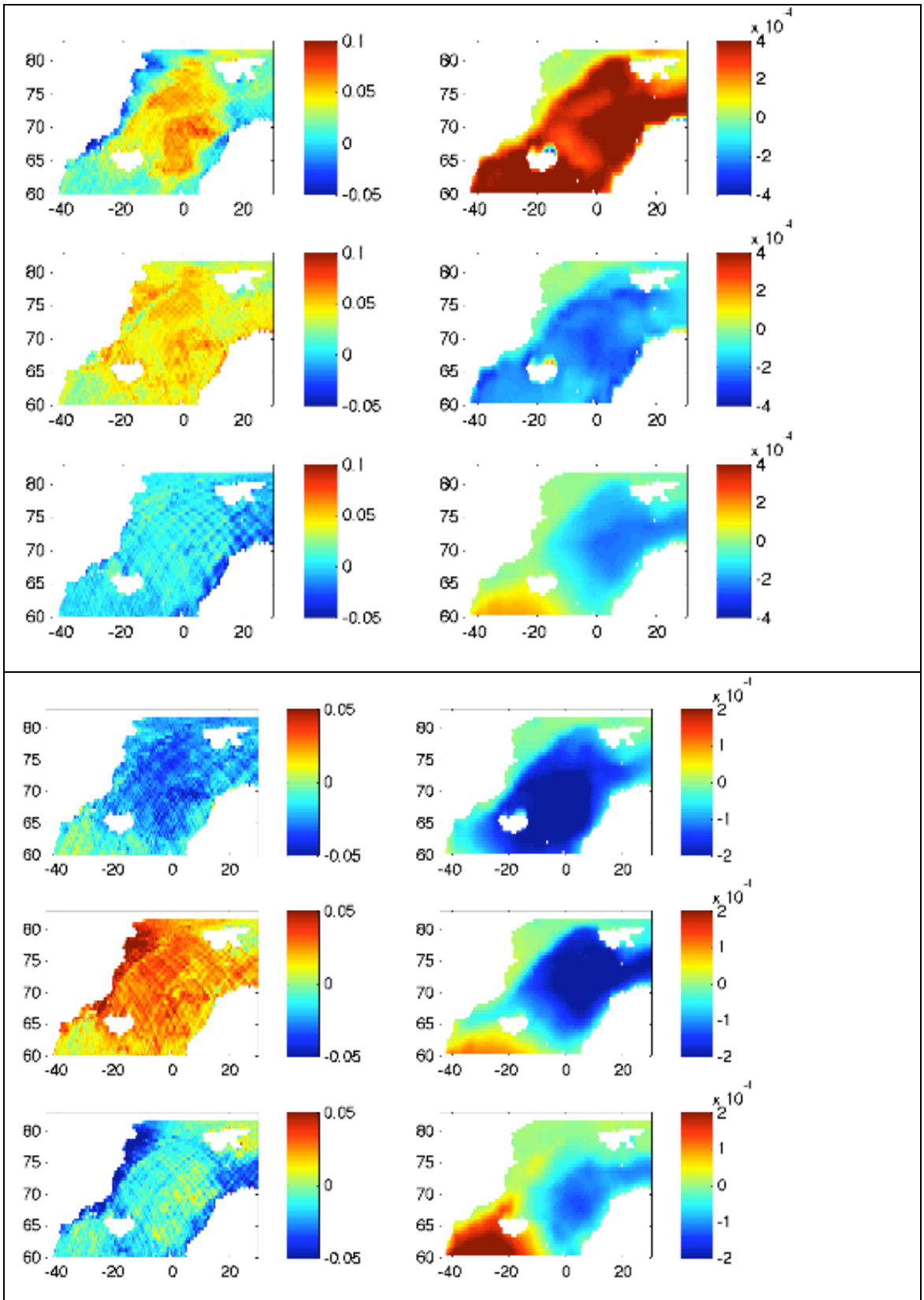

Figure 4. 40. The three most important MCA coupled modes presented as homogenous regression maps of SSHA [m] (left) and evaporation [m] (right) for the unfiltered (top 3) and seasonally filtered fields (bottom 3).

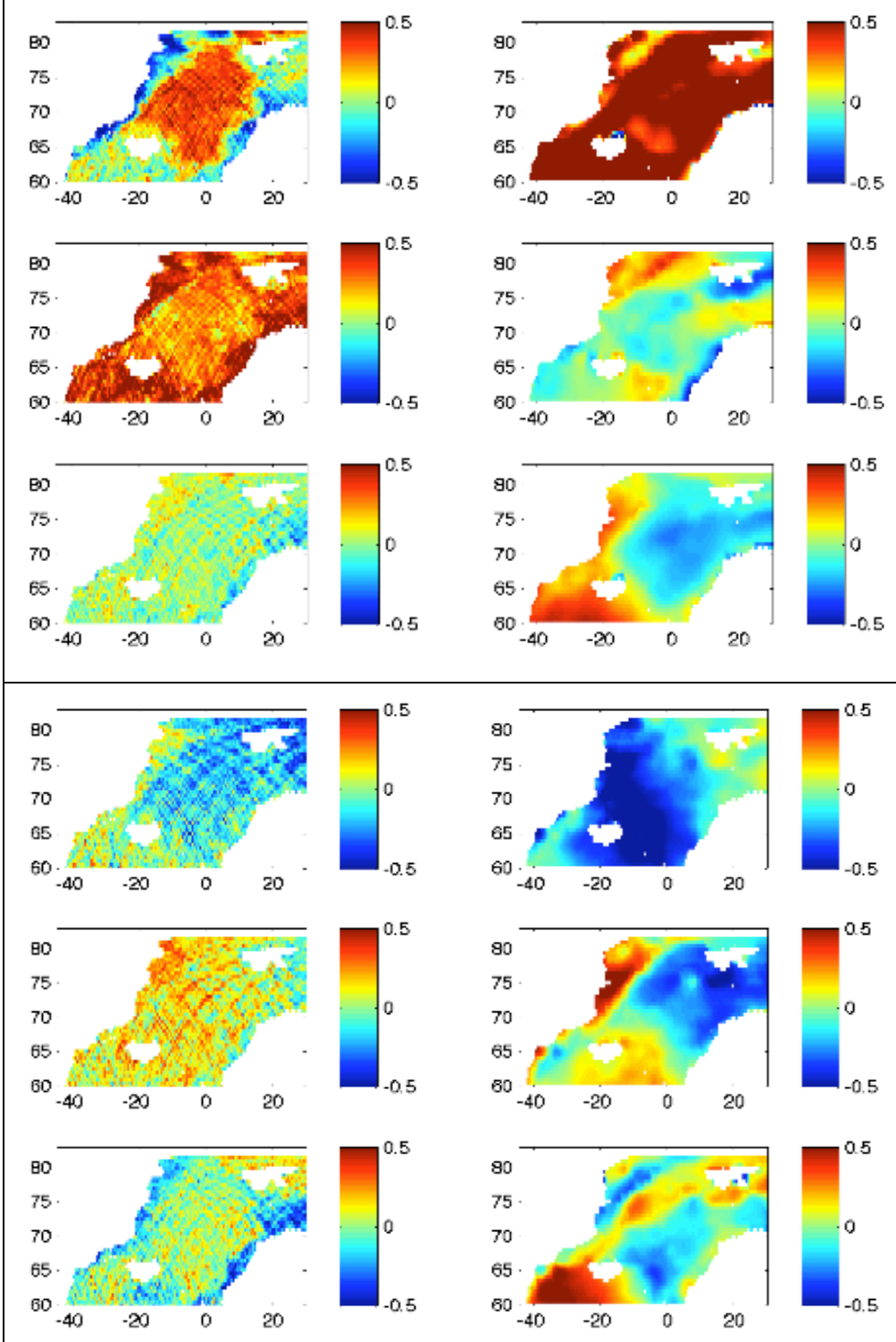

Figure 4. 41. The 3 most important coupled MCA modes presented as heterogeneous correlation maps of the unfiltered (top 3 rows) and filtered (bottom 3 rows) evaporation (right) and SSHA (left). The colour scale represents a correlation coefficient $r[A(t), a_k(t)]$ between the grid points of original data (left and right fields) and time expansion coefficients of corresponding SVD modes of the other field (right and left) and R∈ (-1,1).

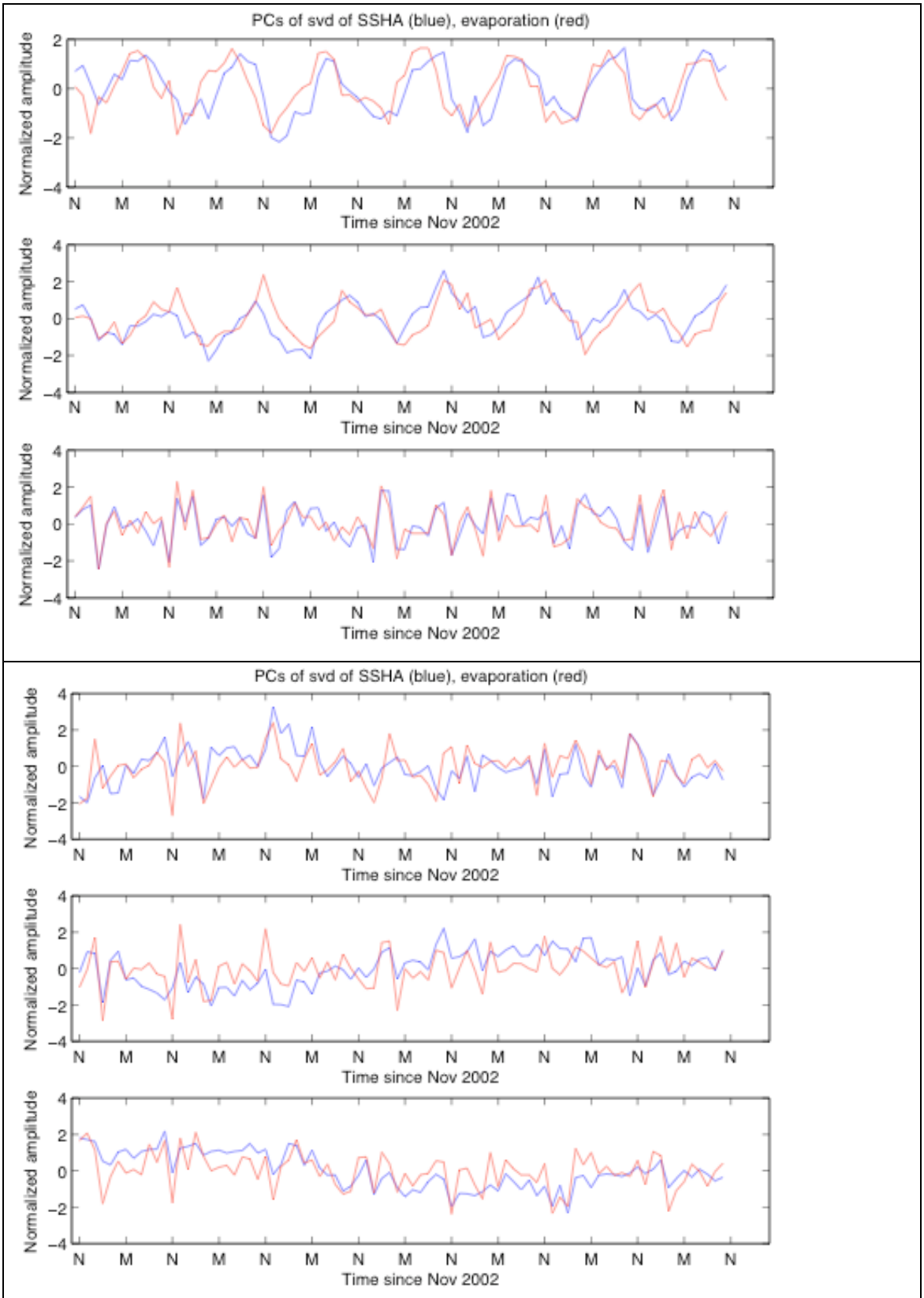

Figure 4.42. Normalized time series of the first three most important MCA coupled modes of the unfiltered (top 3) and filtered (bottom 3) SSH (blue) and evaporation (red)

Mode (k)	SCF (%)	CSCF(%)	R(ak(t),bk(t))
SVD1	92.0/51.6	92.0/51.6	0..70/0.57
SVD2	5.4/25.9	97.4/77.5	0.67/0.48
SVD3	1.1/14.2	98.5/91.7	0.79/0.64
SVD4	0.7/3.7	99.2/95.4	0.77/0.66
SVD5	0.3/2.8	99.5/98.2	0.78/0.70
SVD6	0.2/1.4	99.7/99.6	0.76/0.82

Table 4.18. Results of the MCA analysis for 6 most important coupled modes of variability of SSHA and evaporation. The columns present squared covariance fraction, cumulative squared covariance fraction and correlation coefficient for each coupled mode of variability obtained for the unfiltered (right) and seasonally filtered fields (left).

Mode [k]	HomoVar [%] SSHA	HomoVar [%] EVAPORATION	HetVar [%] SSHA	HetVar [%] EVAPORATION
1	24.5/19.3	65.2/35.0	6.8/3.4	30.8/11.1
2	35.7/20.1	21.8/29.5	13.0/2.6	1.9/5.9
3	2.1/10.1	9.8/12.4	0.9/2.3	3.7/4.1
4	6.4/9.6	7.1/8.6	1.1/1.4	3.1/3.2
5	3.6/5.0	4.1/9.3	0.7/1.4	2.6/2.8
6	3.7/2.9	6.2/3.0	1.3/1.4	1.0/1.9

Table 4.19. Variance explained by the 6 most important MCA coupled modes of variability for SSH and evaporation for the unfiltered (left) and seasonally filtered fields (right). HomoVar informs how much of the left/right field the variance explained by the left/right SVD mode. HetVar is the amount of variance in the left/right field predicted from the right/left SVD mode (from the other field).

Left SVD Modes (SSH)	**PC1 (SSHA)**	**PC2 (SSHA)**	**PC3 (SSHA)**
1	**-0.73/-0.84**	**0.68/-0.41**	0.04/0.11
2	**-0.96/0.94**	-0.26/-0.12	-0.02/0.17
3	-0.03/-**0.59**	0.18/**0.69**	**0.58**/0.18

Right SVD Modes (EVA)	**PC1 (EVA)**	**PC2 (EVA)**	**PC3 (EVA)**
1	**1/-0.94**	0.03/-0.31	-0.01/-0.06
2	-0.52/-**0.76**	0.08/**0.57**	-0.18/0.23
3	-0.25/-0.24	**0.96**/**0.73**	-0.04/-**0.59**

T able 4.20. Correlation coefficients between SVD modes and principal components of sea surface height (SSH) and evaporation (EVA). Numbers in bold indicate that the correlations are significant at 99% confidence level.

Sea Surface Height and Precipitation

According to the results of Monte Carlo significance tests (Section 4.4.2) only the first MCA mode of SSHA and precipitation is significant when considering unfiltered and seasonally filtered fields. The results indicated that also the 3rd mode of the unfiltered fields is significant but due to the low covariance and variance explained by this mode, this mode will not be described here. The first MCA mode for the unfiltered fields accounts for 88.1% of the total squared covariance, while for the seasonally filtered fields the mode accounts for 63.2% of the total squared covariance. In total about 6% of SSHA variance can be predicted by the 1st right mode.

Mode 1

The coupled SVD modes for the unfiltered fields indicate that when SSHA is negative in the central Nordic Seas the positive precipitation anomaly (more precipitation) occurs in the same area. On the other hand, the positive SSHA is associated with a large positive precipitation anomaly close to the coasts of Greenland and Norway (Figure 4.43). The right expansion coefficient is positively correlated with the monthly SSHA at the continental shelves of Greenland and Norway where it can explain locally about 15-20% of the SSHA variance (Figure 4.44).

A very similar coupled mode was also obtained for the seasonally filtered fields but with a positive SSHA occurring in the central Nordic Seas, which is associated with almost zero precipitation in the same region. On the other hand, close to zero SSHA at the borders of the Nordic Seas is associated with a positive precipitation anomaly at the southern Greenland continental shelf and negative precipitation at the coast of Norway (Figure 4.43). The right time expansion coefficient (Figure 4.45) is positively correlated with the filtered SSHA in the central Nordic Seas and in the region to the north and east of Svalbard (Figure 4.44). It can locally explain in these regions about 15% of the filtered SSHA variance.

The coupling between the modes is strong at the annual frequency and moderate at other frequencies (Table 4.21). For the unfiltered fields about 5.7% of variance can be predicted by the right mode (Table 4.22). That is about 55% of variance explained by the left mode itself. When considering the seasonally filtered mode, about 5.5% of the total filtered SSHA variance can be predicted by the right mode (Table 4.22). That consists of 30% of variance that is explained by the left mode. The left mode is strongly correlated to the 2nd EOF of the unfiltered SSHA and the right mode to the 1st EOF of

the unfiltered precipitation (Table 4.23). The filtered left field is also correlated with the 1st and 2nd EOF of the filtered SSHA (Table 4.23).

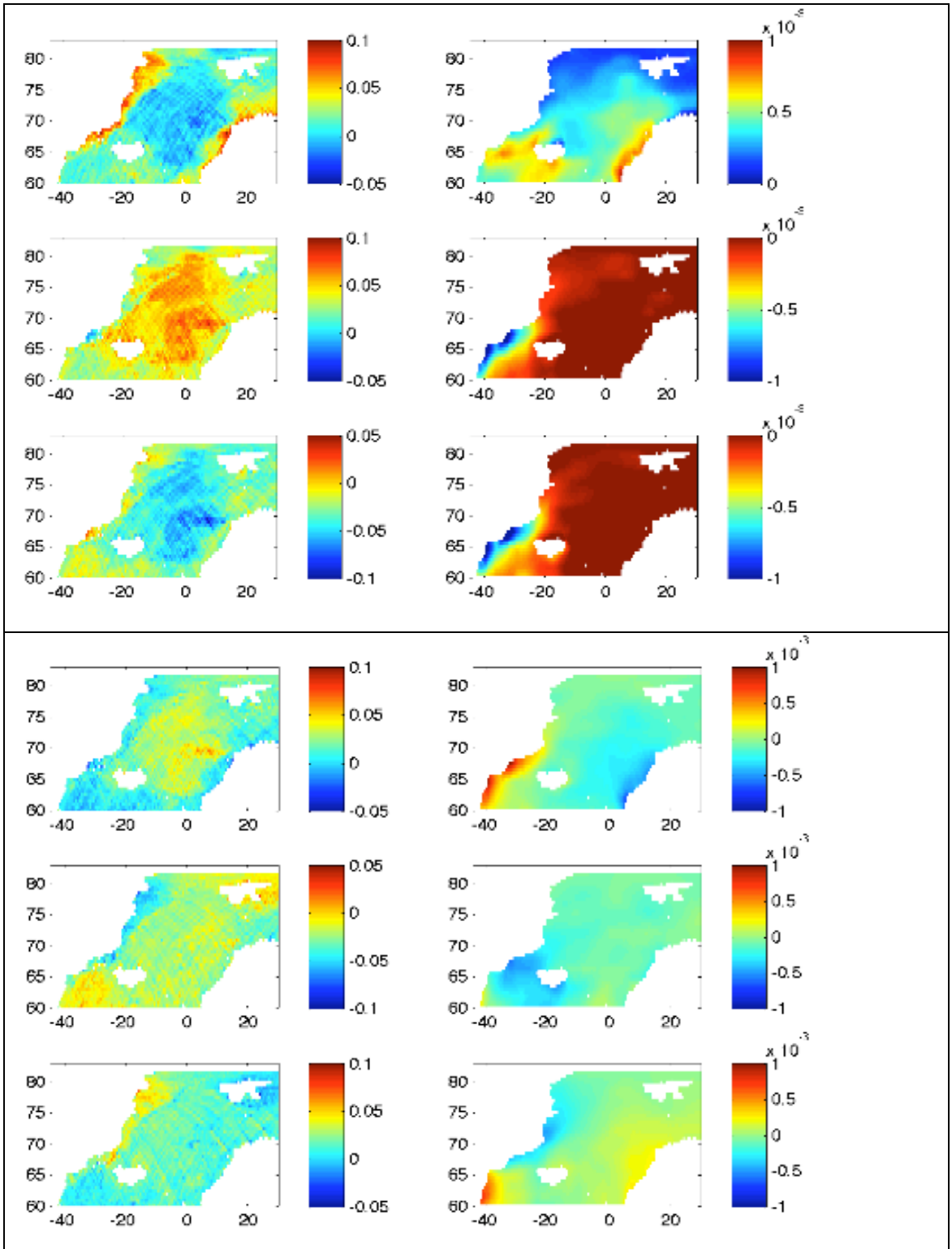

Figure 4.43. The three most important MCA coupled modes presented as homogenous regression maps of SSHA [m] (left) and precipitation [m] (right) for the unfiltered (top 3) and seasonally filtered fields (bottom 3).

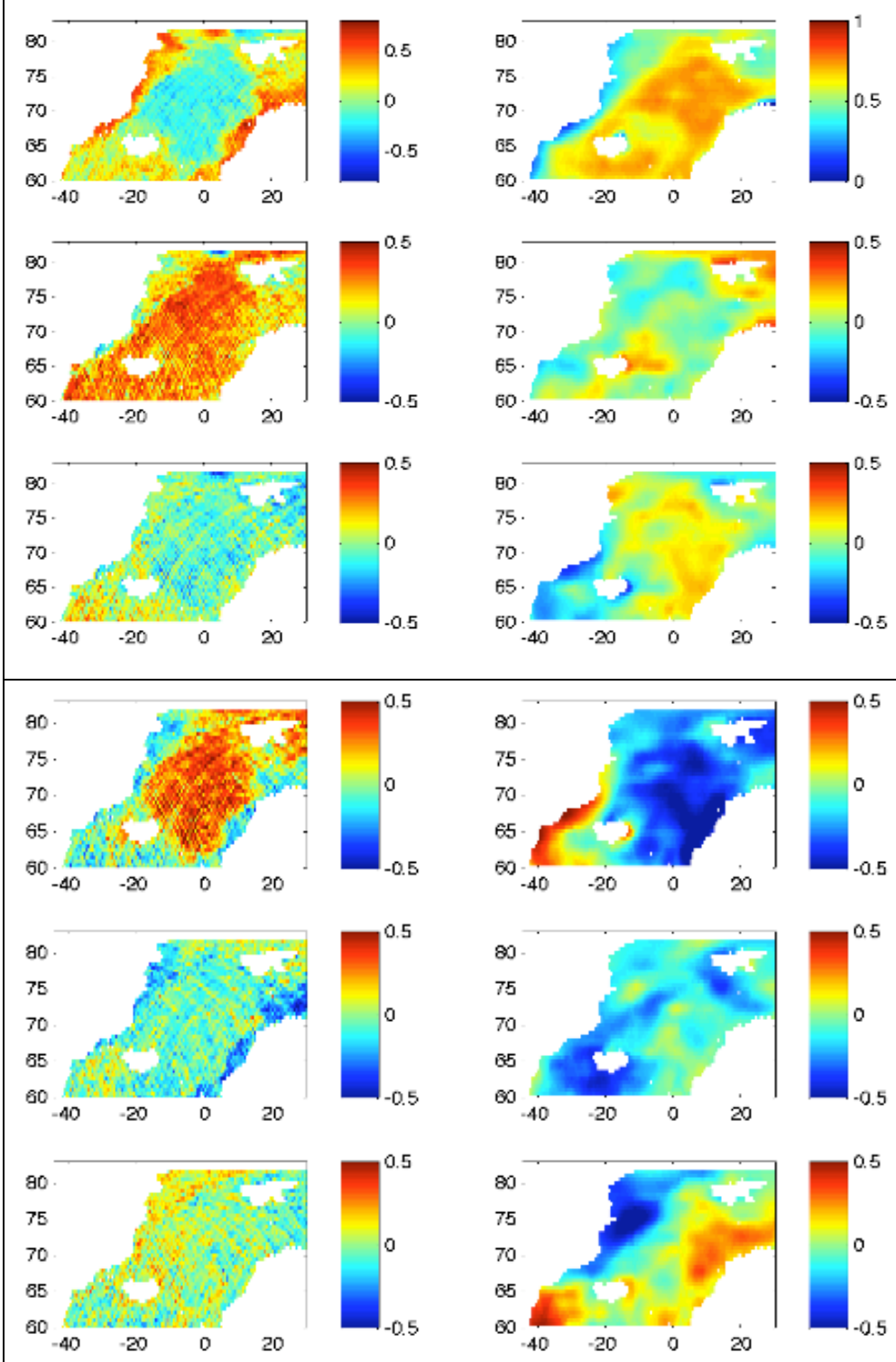

Figure 4.44.. The 3 most important coupled MCA modes presented as heterogeneous correlation maps of the unfiltered (top 3 rows) and filtered (bottom 3 rows) precipitation (right) and SSHA (left). The colour scale represents a correlation coefficient $r[A(t), a_k(t)]$ between the grid points of original data (left and right fields) and time expansion coefficients of corresponding SVD modes of the other field (right and left) and R∈ (-1,1).

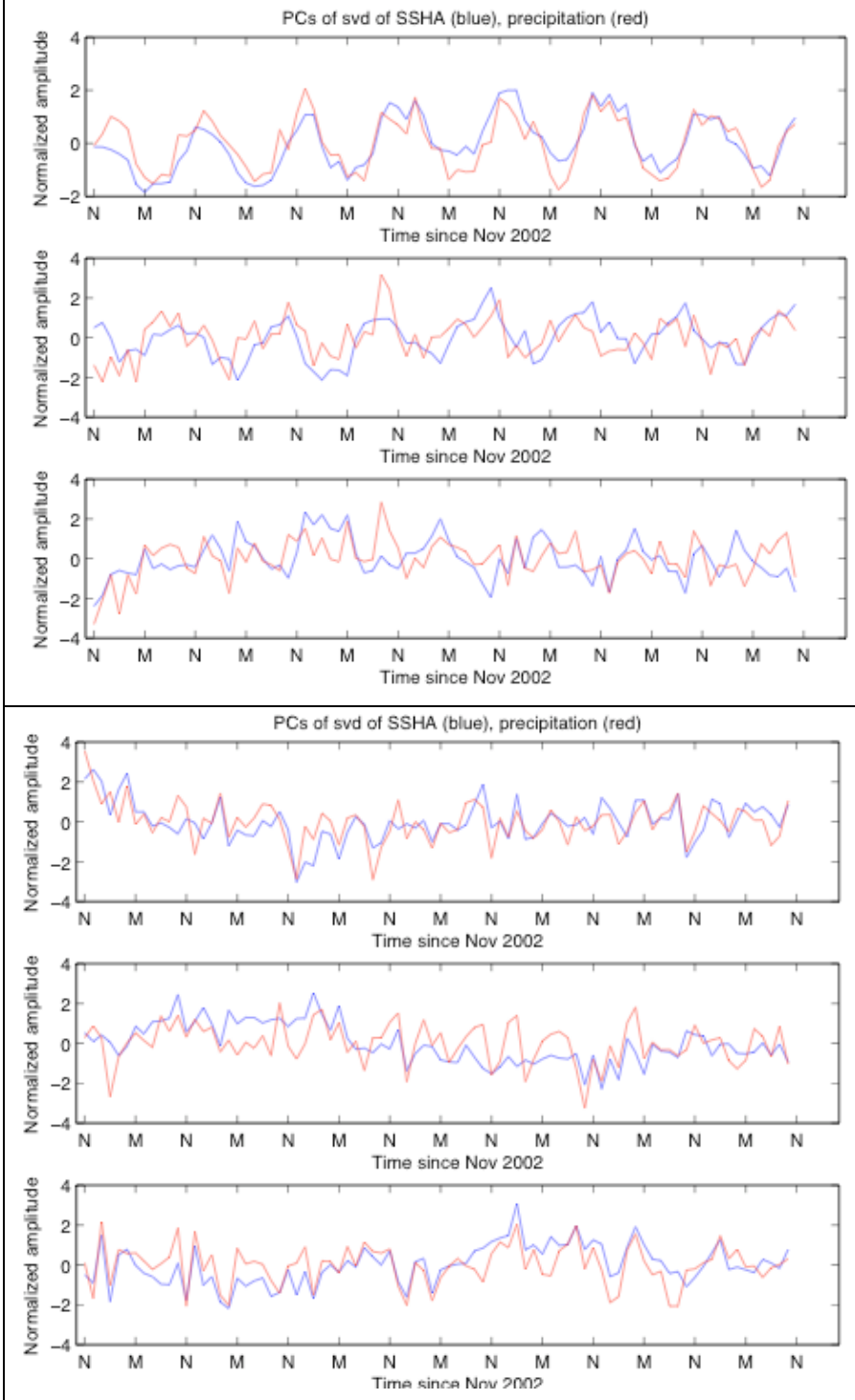

Figure 4.45. Normalized time series of the first three most important MCA coupled modes of the unfiltered (top 3) and filtered (bottom 3) SSH (blue) and precipitation (red).

Mode (k)	SCF (%)	CSCF(%)	R(ak(t),bk(t))
SVD1	88.1/63.2	88.1/63.2	0.84/0.69
SVD2	5.6/17.4	93.7/80.6	0.44/0.50
SVD3	3.4/7.3	97.1/87.9	0.48/0.69
SVD4	1.3/5.3	98.4/93.2	0.78/0.76
SVD5	0.8/3.4	99.2/96.6	0.79/0.71
SVD6	0.5/3.0	99.7/99.6	0.82/0.57

Table 4.21 Results of the MCA analysis for 6 most important coupled modes of variability of SSHA and precipitation. The columns present squared covariance fraction, cumulative squared covariance fraction and correlation coefficient for each coupled mode of variability obtained for the unfiltered (right) and seasonally filtered fields (left).

Mode [k]	HomoVar [%] SSH	HomoVar [%] PREC	HetVar [%] SSH	HetVar [%] PREC
1	10.4/17.2	52.4/21.8	5.7/5.5	37.8/9.7
2	37.7/17.5	5.2/15.3	6.2/2.0	1.0/3.5
3	27.5/9.7	6.1/9.1	1.3/1.2	1.5/4.4
4	5.1/8.2	5.5/8.1	0.8/1.5	3.5/4.9
5	6.7/8.2	5.0/7.3	0.9/1.3	3.5/3.4
6	2.2/13.2	5.2/4.0	0.7/1.3	3.6/1.5

T able 4.22. Variance explained by the 6 most important MCA coupled modes of variability for SSH and precipitation for the unfiltered (left) and seasonally filtered fields (right). HomoVar informs how much of the left/right field the variance explained by the left/right SVD mode. HetVar is the amount of variance in the left/right field predicted from the right/left SVD mode (from the other field).

Left SVD Modes (SSH)	**PC1 (SSH)**	**PC2 (SSH)**	**PC3 (SSH)**
1	-0.29/**0.72**	**-0.94/0.67**	-0.13/0.06
2	**-1/-0.88**	0.07/0.31	0.02/0.12
3	**0.83/0.63**	-0.20/-0.23	0.19/**0.26**

Right SVD Modes (PREC)	**PC1 (PREC)**	**PC2 (PREC)**	**PC3 (PREC)**
1	**1/1**	-0.04/0.04	-0.02/-0.04
2	-0.14/-0.12	**-0.83/-0.98**	-0.15/0.03
3	-0.14/0.13	**-0.97**/-0.16	-0.03/-**0.97**

Table 4. 23Correlation coefficients between SVD modes and principal components of sea surface height (SSH) and precipitation (PREC). Numbers in bold indicate that the correlations are significant at 99% confidence level.

Sea Surface Height and Freshwater Flux

The first three SVD right modes can predict 21.2 % of variance in the unfiltered SSHA and only 6.1 % of variance in the seasonally filtered SSHA. The coupling between the two fields is mainly between the first two most important EOFs of the two fields and occurs mainly at the annual frequency. Therefore, one can argue that the local freshwater flux can be important for forcing the seasonal cycle of SSHA but its role in causing SSHA variability at other frequencies than annual is very small.

Mode 1.

The 1st SVD mode of unfiltered SSH and freshwater flux explains about 91% of the squared covariance between the two fields. The left pattern is characterized by the oscillations between the deep basins (with an amplitude in SSHA of 8 cm) and the boundaries of the basin, higher at the Greenland continental shelf (amplitude = 6 cm) and lower at the Norwegian shelf (4 cm). This mode is similar to the 2nd EOF of SSHA what was confirmed by a high correlation between the SVD left time expansion coefficient and the 2nd PC of SSHA (Table 4.24). The left mode also explains similar amount of variance in the SSHA (10%). The right field can predict about 6% of SSHA variance, which is about 50% of variance explained by the left mode (Table 25). The right mode is almost the same as the 1st EOF of freshwater flux and accounts for 65% of variance (Tables 4.25, 4.26). The coupling between the left and right modes is strong and occurs mainly at annual frequencies for the unfiltered fields. This relationship is weaker but significant at 99% for the freshwater flux occurring at 1-month lag (not shown). The right time expansion coefficient is significantly negatively correlated with SSHA along continental shelves of Norway and Greenland (Figure 4.47), where it can explain about 17% of the total SSHA variance.

Considering the seasonally filtered fields, the 1st SVD mode explains 62% of co-variance between the two filtered fields. The left field accounts for 16% of variance in the filtered SSHA and is moderately correlated to the 1st and 2nd EOF of filtered SSHA (Table 4.26). The right mode is almost the same as the 1st EOF of the filtered freshwater flux and can explain 4.7% of variance in the filtered SSHA, which accounts for about 30% of variance explained by the left mode itself. The 1st right time expansion coefficient is negatively correlated to the filtered SSHA in the central Nordic Seas and

north and east of Svalbard (Figure 4.47), where it explains about 10% of the filtered SSHA variance.

To sum up, the 1st EOF of freshwater flux can predict up to 50% of the 2nd EOF SSHA variance for the unfiltered data and 30% of the 1st SVD left mode that is strongly correlated with 1st and 2nd EOF of filtered SSHA.

Mode 2

According to Monte Carlo simulations only the 2nd unfiltered mode is significant and therefore only this mode will be further described.

The 2nd SVD mode between SSH and freshwater flux explains 4.5% of co-variability between the fields and shows a simultaneous relationship at annual frequency between its time expansion coefficients (Figure 4.48, Table 4.24). Its left structure indicates a strong similarity to the 1st EOF of SSHA and the right one is weakly related to the 2nd EOF of freshwater flux and explains about 6% of its variance (Tables 25, 26). The left mode describes oscillations of the SSHA over the whole Nordic Seas with the largest amplitudes occurring in the central Nordic Seas and in the ice-covered regions (Figure 4.46). The coupling occurs between the negative freshwater flux (more freshwater input) along the Norwegian coast and central Nordic Seas and positive freshwater flux anomaly (less freshwater input) in the Barents, Greenland and Irminger Seas.

The right mode can predict about 14% of variance in SSHA data, which accounts for 30% of variance explained by the left field (Table 4.25). Most of the variance can be predicted in the Fram Strait and Greenland Sea, southern Barents Sea and south of Iceland (Figure 4.47). The right time expansion coefficient is negatively correlated with the SSHA in these regions and can explain there about 15% of SSHA variance (Table 4.24, Figure 4.48).

Mode 3

The 3rd SVD mode explains only about 1 % of co-variability between the two unfiltered fields and 9% of co-variance for the seasonally filtered fields. The 3rd left pattern is weakly correlated with 1st and 3rd EOF of SSHA and explains about 9% of variability in the unfiltered and filtered SSHA (Figure 4.48, Table 4.24).

The right field of this mode has a significant relationship with the 2nd EOF of freshwater flux data and explains 2.4% of variance in the unfiltered right field and 7.5% in the filtered right field (Table 4.25). The right mode describes anti-phase oscillations between the narrow region located at the continental shelf of Greenland and the rest of the Nordic Seas. It can predict on average about 1% of SSHA variance. However, no significant point-to-point correlations were found between the right time expansion coefficient and SSHA (Figure 4.47).

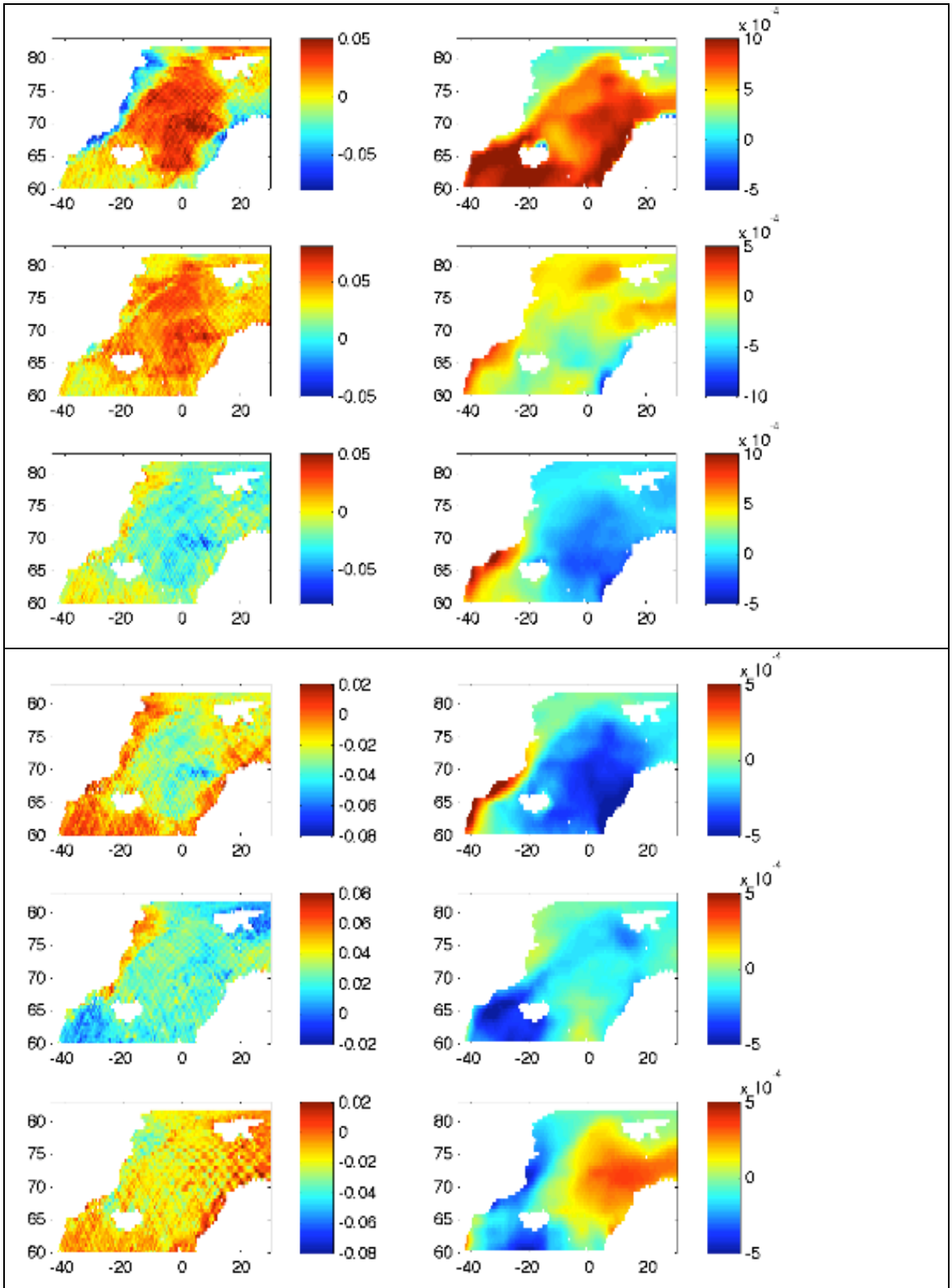

Figure 4.46. The three most important MCA coupled modes presented as homogenous regression maps of SSHA [m] (left) and freshwater flux [m] (right) for the unfiltered (top 3) and seasonally filtered fields (bottom 3).

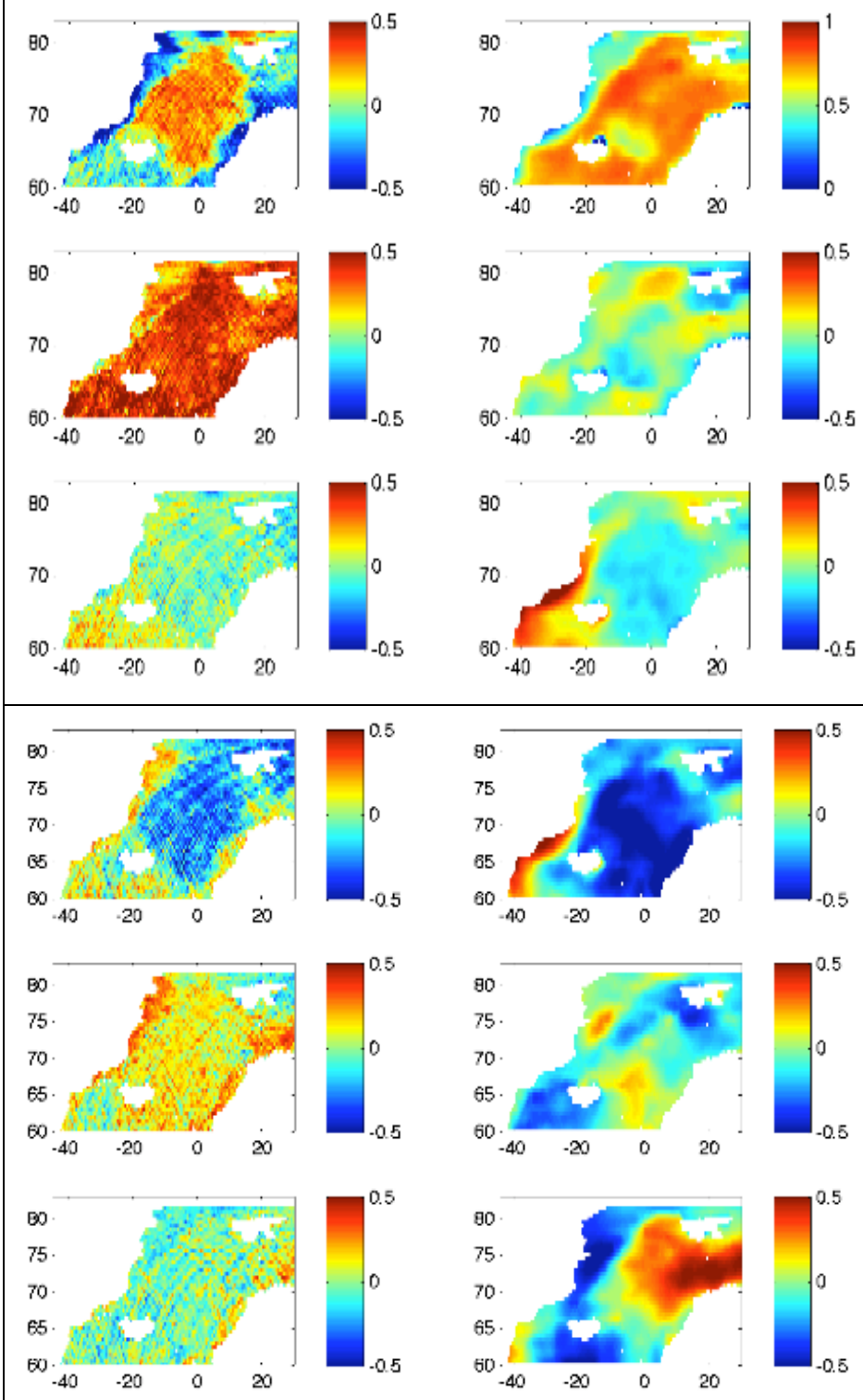

Figure 4.47. The 3 most important coupled MCA modes presented as heterogeneous correlation maps of the unfiltered (top 3 rows) and filtered (bottom 3 rows) freshwater flux (right) and SSHA (left). The colour scale represents a correlation coefficient $r[A(t), a_k(t)]$ between the grid points of original data (left and right fields) and time expansion coefficients of corresponding SVD modes of the other field (right and left) and R∈ (-1,1).

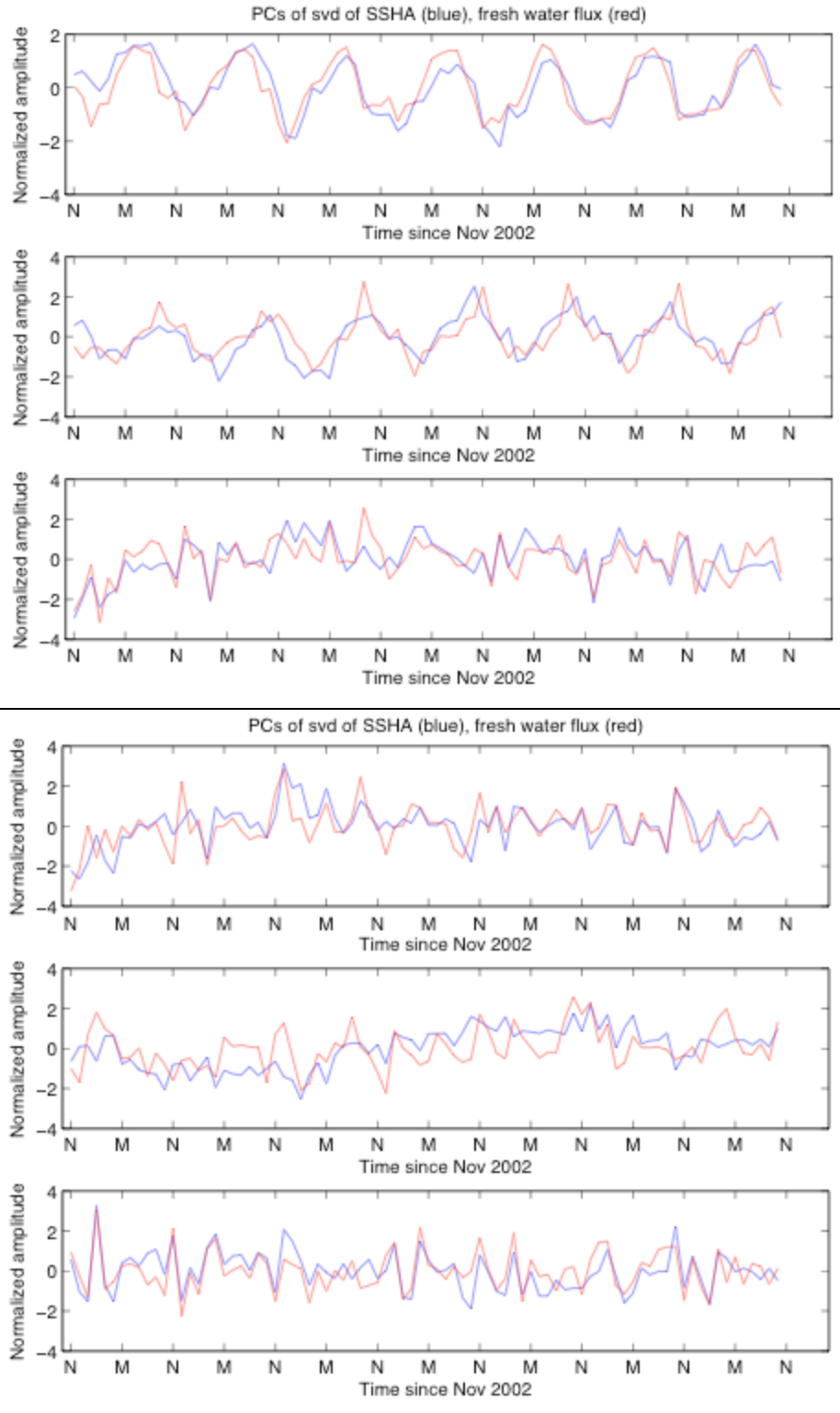

Figure 4.48.. Normalized time series of the first three most important MCA coupled modes of the unfiltered (top 3) and filtered (bottom 3) SSH (blue) and freshwater flux (red).

Mode (k)	SCF (%)	CSCF(%)	R(ak(t),bk(t))
SVD1	92.3/62.1	92.3/62.1	0.84/0.67
SVD2	4.5/17.1	96.8/79.2	0.64/0.49
SVD3	1.5/9.4	98.3/88.6	0.72/0.72
SVD4	0.7/5.1	99.0/93.7	0.68/0.84
SVD5	0.4/3.2	99.4/96.9	0.84/0.60
SVD6	0.3/2.8	99.7/99.7	0.70/0.75

T able 4.24. Results of the MCA analysis for 6 most important coupled modes of variability of SSHA and freshwater flux. The columns present squared covariance fraction, cumulative squared covariance fraction and correlation coefficient for each coupled mode of variability obtained for the unfiltered (right) and seasonally filtered fields (left).

.

Mode [k]	HomoVar [%] SSH	HomoVar [%] FF	HetVar [%] SSH	HetVar [%] FF
1	10.3/16.2	64.6/30.2	5.9/4.7	46.5/12.2
2	37.8/19.5	5.8/14.3	14.2/2.8	1.1/2.7
3	9.2/8.9	5.1/16.1	1.1/1.4	2.4/7.6
4	14.1/3.0	5.5/8.1	0.9/1.5	2.4/6.2
5	1.7/11.8	3.4/6.8	0.8/1.4	3.0/1.5
6	6.9/7.6	3.0/5.6	1.1/1.3	0.8/3.4

Table 4. 25. Variance explained by the 6 most important MCA coupled modes of variability for SSH and freshwater flux for the unfiltered (left) and seasonally filtered fields (right). HomoVar informs how much of the left/right field the variance explained by the left/right SVD mode. HetVar is the amount of variance in the left/right field predicted from the right/left SVD mode (from the other field).

Left SVD Modes (SSH)	**PC1 (SSH)**	**PC2 (SSH)**	**PC3 (SSH)**
1	-0.25/-**0.68**	**0.96/-0.71**	0.10/-0.01
2	**-0.99/0.94**	-0.05/-0.26	-0.03/-0.01
3	**0.43/-0.56**	-0.18/-0.03	**0.46/-0.39**

Right SVD Modes (FF)	**PC1 (FF)**	**PC2 (FF)**	**PC3 (FF)**
1	**-1/1**	0.01/0.01	-0.01/0.17
2	0.18/-0.32	**-0.36/0.75**	0.48/-0.52
3	-0.06/**0.35**	**-0.99/0.75**	0.05/**0.56**

Table 4. 26. Correlation coefficients between SVD modes and principal components of sea surface height (SSH) and freshwater flux (FF). Numbers in bold indicate that the correlations are significant at 99% confidence level.

4.4.6 Summary

The results of the MCA indicated that various atmospheric fields are coupled to SSHA. The coupling is the strongest when seasonal cycle is present in all fields and some fields are able to predict about 20% of total variance in the unfiltered SSHA. The fields that can explain about 20% of total variance in the unfiltered SSHA are wind stress curl, freshwater flux and evaporation. The wind stress curl is coupled mainly with the 1st EOF of SSHA and can also predict a large proportion of the variance of this field when the seasonal cycle is removed prior to MCA. On the other hand, freshwater flux and evaporation can explain a large proportion of variance in the 2nd EOF of SSHA but mainly at the annual frequency. Heat flux is able to predict about 18% of total unfiltered SSHA variance and the rest of the fields can only explain about 10% of the SSHA variance or less. Furthermore, these fields explain most of the variance associated with the 1st EOF of SSHA at the annual frequency except the meridional wind stress and precipitation that can also explain some variance in the 2nd EOF of SSHA. It was found that the 2nd EOF of SSHA is strongly coupled at annual frequencies with mean sea level pressure, freshwater flux and precipitation. The coupling is still significant at frequencies other than annual. This suggests that the 2nd EOF of SSHA is a result of the atmospheric forcing that is associated with the NAO variability.

Considering the results of MCA on the fields with their seasonal cycle removed, the best performers in explaining SSHA variance were the atmospheric fields connected to the winds. Particularly, wind stress curl is able to predict about 18% of the total variance in the filtered SSHA and the meridional wind stress is able to explain about 13% of the total seasonally filtered SSHA variance. The wind stress curl and meridional wind stress can explain most of the variance associated with the 1st EOF of SSHA. Both fields are able to explain a significant part of variance in the central Nordic Seas. On the other hand, wind stress curl also can predict a large part of SSHA variance at the Greenland continental shelf and the meridional wind stress component can predict a large part of the variance at the Norwegian continental shelf and the southern Barents Sea. The meridional wind stress can also explain some variance associated with the 2nd EOF of SSHA. The remaining modes can explain less than 10% of total variance in the seasonally filtered SSHA. Mean sea level pressure and heat flux can explain about 9% of the total variance in the filtered SSHA, which is mainly associated with 1st EOF of the filtered SSHA variance (mean sea level pressure and heat flux) and the 2nd EOF of

the filtered SSHA (only heat flux). The remaining fields can only explain 8% or less of the total filtered SSHA variance and are important in the smaller and localized regions.

The results showed that the 3rd EOF of SSHA is coupled only with three other fields: wind stress curl, freshwater flux and heat flux. The 2nd EOF of freshwater flux is coupled with the 3rd EOF of SSHA at all frequencies and can predict about 20% of variance in the narrow region at the Norwegian continental shelf and the southern Barents Sea. Also heat flux can explain a similar part of variance in SSHA in the same area but only at annual frequency. On the other hand, the first two EOFs of wind stress curl are coupled with the 3rd EOF of SSHA at other frequencies than the annual and can predict about 20% of the local SSHA variance in the ice-covered regions at the Greenland continental shelf. Furthermore, a large proportion of the local filtered SSHA variance can be predicted along the Norwegian continental shelf using the rotated 2nd and 3rd EOF of wind stress curl. The above results suggests that the 3rd EOF of SSHA could be influenced by the wind stress curl, which affects SSHA at the eastern and western boundaries of the Nordic Seas, and heat and freshwater fluxes, which affect mainly the eastern boundary. Furthermore, that coupling between SSHA and these three other fields occurs at all frequencies except heat flux, which contributes only to the annual SSHA variability.

To sum up, the MCA showed that the first three modes of SSHA variability could be the effect of wind forcing mainly with other atmospheric fields contributing also to some of their variability. Particularly, the results of MCA indicate that the 1st EOF of SSHA is a basin response to the Ekman pumping and heat loss. The 2nd EOF of SSHA is a large-scale basin-coherent response to the atmospheric forcing associated with the NAO mode and the 3rd EOF of SSHA is an effect of Ekman pumping and freshwater fluxes.

Canonical Correlation Analysis

There exist many methods that could be used to check the spatial and temporal patterns of coupling between SSH and other atmospheric fields. A number of studies (Bretherton et al. 1992, Cherry 1996, Wallace et al. 1991) have compared different statistical methods and described their limitations. This study has followed their suggestions and therefore other methods were checked to investigate the robustness of the results. Therefore, Canonical Correlation Analysis (CCA) was also applied to the fields. The

main difference between CCA and MCA is that the former investigates the correlations between the fields instead of co-variances (Hotelling, 1936). The CCA could not be used directly on the data in this study because the spatial dimension was much bigger than the temporal. Therefore, the method suggested by Barnett and Preisendorfer (1987) was used. This can improve the results due to removal of noise in the data by using only a limited number of principal components obtained for the two fields. However, there is no quantitative method to determine how many PCs should be used and our test shows that some of the results are sensitive to the number of PCs used as an input to CCA. Therefore, the MCA method is technically easier to use than CCA due to the orthogonality of the patterns, and because its application requires fewer subjective decisions. The results of CCA were very similar to for MCA results but sometimes the order of the modes was reversed because the CCA outputs the most important modes as the ones that have the strongest temporal correlations but do not necessarily explain a significant amount of covariance between two fields. Also a number of studies that used both methods to investigate the coupling between atmospheric fields found that the two methods give very similar results but often with reversed order (Bretherton et al. 1992, Wallace et al. 1992). Because the results of the two methods were almost the same, only the MCA results were presented in this chapter.

4.5. Discussion

We begun the investigation into the possible local atmospheric forcing that may caused SSHA variability in the Nordic Seas from the analysis of the annual cycle of the atmospheric fields and point-to-point correlation patterns (Section 4.2). The results showed that the annual cycle is the largest contributor (more than 50%) to the total variance of freshwater flux, evaporation and heat flux. Also for the precipitation and mean sea level pressure the seasonal cycle can explain about 40% of their variability, whereas for the wind stress and wind stress curl it only explains about 15% of the total variance because the wind is more localized in comparison to the other air-sea fluxes. The analysis has showed that the winter in the Nordic Seas is characterised by the minimum in the mean sea level pressure, maximum wind strength, maximum heat loss and evaporation and maximum precipitation and freshwater input. The timing of the maximum is quite similar for the different atmospheric fields and only differs slightly, by 1-2 months. Furthermore, there are some spatial differences in the phase of the annual cycle, which are also about 1-2 months. Comparing the seasonal cycle of SSHA to the other fields, one can notice that the maximum sea level in the SSHA occurs 1-2 months later in the central Nordic Seas than the maximum heat flux (heat gain by the ocean) and one month after the weakest winds occur in the same area. The maximum heat loss and wind stress are also the most important for the time of SSHA minimum in the central Nordic Seas because they both cause sea level to decrease. On the other hand, due to the presence of land, the response of the SSHA to the local wind forcing causes the maximum in the SSHA to occur almost in the same time as the maximum wind strength along the coast of Greenland and Norway and in the Barents Sea. The phase of the SSHA at the borders is therefore very similar to the phase of the wind stress, which causes downwelling and sea level increase close to the coasts. Furthermore, along the continental slope of Greenland the peak in the anticyclonic wind occurs at the same time and causes sea level rise due to the convergence. The similarity between the phases of the atmospheric fields and SSHA suggests that the ocean responds simultaneously or with 1-2 months lag to the seasonal atmospheric forcing and therefore its response is mainly barotropic.

The spatial correlations between the SSHA and other fields support the preceding analysis of the seasonal cycle and proved that there exists a relationship between all the

atmospheric fields and SSHA not only at the annual period. They also provided three new suggestions that are based on the correlation patterns, but only if they were supported by the hypothesis described in section 4.1. These new suggestions are only based on the correlations between the atmospheric fields and SSHA, and the expectations, which are the consequence of the theoretical arguments described in Section 4.1. Therefore, the results can be used only as suggestions and are not proved. The first of the important suggestions provided by the analysis of Section 4.2.2 is that heat flux is important for the SSHA variability in the ice-covered regions and in the central Nordic Seas at all timescales. The second suggestion is that precipitation and freshwater input can be important for the annual cycle of SSHA along the Norwegian continental shelf and in the central Nordic Seas for SSHA variability at other periods than the annual. The third suggestion based on the correlation analysis is that the wind stress curl could be the most important for the SSHA variability along the ice edge and at the northern Greenland continental shelf where the anticyclonic winds causes downwelling and sea level rise seasonally but also at the other periods.

To sum up, the first part of Section 4.2 described the seasonal cycles of the atmospheric fields and showed how they may affect the local SSHA. The second part of Section 4.2 showed that significant relationships exist for the all atmospheric variables and SSHA variability and identified the most likely atmospheric fields that may play an important role for the SSHA in the certain regions of the Nordic Seas. In Section 4.3 each atmospheric field was divided into modes of variability, which could be responsible for the different atmospheric processes. The three most important atmospheric modes were then correlated to the SSHA and its significant EOFs. The aim of the section was to suggest possible atmospheric forcing mechanisms that may cause the variability associated with each significant EOF of SSHA. The results indicated that the 1st EOF of SSHA has a weak, but significant, correlation to the wind stress and its curl. The mode was only correlated to the 1st EOF of the zonal wind stress when the seasonal cycle was present and for the seasonally filtered fields moderate (about 0.3) correlations were found for the three most important wind stress curl EOFs and the 2nd and 3rd EOF of the meridional wind stress. This mode can be also weakly related to the atmospheric forcing associated with the NAO but only when considering its seasonal cycle. Much stronger correlations were found for the 2nd EOF of SSHA and the atmospheric modes of variability. The strongest relationship was found for the 2nd EOF of SSHA and the 1st

EOF of the mean sea level pressure, which represents the Icelandic Low that is strongly associated with the NAO. Also very strong correlations were found for the 2nd EOF of SSHA and the 1st EOF of wind stress, especially when considering the EOFs of the unfiltered fields. This strong relationship indicates that the 2nd mode of SSHA could be forced by wind forcing caused by the changes in the atmospheric pressure that are in turn caused by the large-scale atmospheric variability described as the NAO. These findings are in agreement with the earlier results described in Chapter 3. Furthermore, the 2nd EOF of SSHA was found to be significantly correlated to those EOFs, which are also correlated to NAO and AO index. Finally, the analysis of the Section 4.3 pointed out that the 3rd EOF of SSHA can be also influenced by the NAO but did not designate any particular atmospheric field that could be responsible for this forcing.

The results of the PCA, which were described in Section 4.3, were constrained by the orthogonality of the modes and distinguished only those modes of variability that were the most important for a given field but could not identify the coupling between many fields. In effect the correlations between the atmospheric EOFs and the EOFs of the SSHA were often weak, and in effect could mask the relationship between the sea level and the air-sea fluxes. Furthermore, when analysing the EOFs of the atmospheric variables we have noticed that some less significant modes could be also significantly correlated to the SSHA (i.e. the 6th EOF of the wind stress curl), which implies that these modes could also be important for the SSHA variability. Therefore, the analysis of the coupling was supported by two other statistical methods: MCA and CCA, which are able to identify the modes that simultaneously co-vary in time (Bretherton et al., 1992). The resultant pair of modes often consisted of the few leading rotated EOFs of those two fields and showed the stronger relationship (correlation) between their time series when compared to the correlations between their leading EOFs (Section 4.3). The MCA results, described in Section 4.4, are in agreement with the earlier results of Sections 4.2 and 4.3 but provide new information about the coupling of the seasonally filtered data and the 3rd EOF of the unfiltered SSHA. Furthermore, the results of the MCA identified the modes of co-variability that are able to explain more variance in the SSHA when comparing to the earlier methods (Sections 4.2, 4.3). In the remainder of this section, the results of the MCA are discussed and compared to the existing theory, model results and *in situ* observations.

According to Sverdrup theory (Sverdrup, 1947), divergences caused by the wind stress curl are balanced by the transport across constant f/H contours, where f is the Coriolis parameter and H is the depth of the ocean. This flow should be balanced by a return flow along the western boundary (Stommel, 1948) but the theory does not hold in basins with closed f/H contours such as the Nordic Seas (Jenkins and Bye, 2006). Previous studies (Legutke et al., 1991) have reported that the fluctuations in such regions are trapped by the closed topography system. The model of Isachsen et al. (2003) revealed that the surface Ekman convergences/divergences spin up the gyres that are closed by the f/H isolines until the divergence in the bottom Ekman layer balances the mass flux convergence of the surface Ekman layer. This was also confirmed by the comparison of the modelled results with surface drifters (Nost and Isachsen, 2003) where the flow velocity was found to be a function of f/H, and it was found that the Ekman pumping drives also the bottom flow. The more recent observations of Voet et al. (2010) indicated that also the mid-depth mean circulation is coupled to the topography, at least in the central Nordic Seas. The reason for this could be a weak stratification in the gyres and a strong annual wind forcing associated with the NAO (Voet et al., 2010). The 1st EOF of the unfiltered SSHA also describes the surface circulation in the central Nordic Seas that spins up annually. The mode shows a strong dependence of the surface circulation on the bathymetric contours and therefore indicates the importance of strong topographic steering in the central Nordic Seas. The Coriolis parameter varies little in the Nordic Seas, thus the f/H contours can be approximated by the depth contours. The statistical analysis confirmed that the 1st EOF of the unfiltered SSHA describes a barotropic response of the gyres to the local wind forcing, at least, considering the annual frequency. Therefore, our results agree with the theory and the earlier *in situ* observations in the area. The Sverdrup balance describes the potential vorticity that is balanced by the wind stress curl and ignores the effect of topography on the flow. The balance is set up by Rossby waves propagating from the eastern boundary. Firstly, the fast barotropic waves propagate and set up an interior flow, then the 1st baroclinic Rossby waves set up the flow more slowly above the thermocline, and the higher baroclinic modes propagate slower and are important in the thinner layers close to the ocean surface (e.g. Young et al., 1981). If the topography is included into these theoretical considerations the final effect of this process can be described as the Sverdrup balance as long as the 1st baroclinic Rossby waves propagate faster than the current. However, in the high latitudes the 1st baroclinic Rossby waves propagate much

slower, with a speed of about 1 cms^{-1} (Killworth et al., 1997) and therefore the Sverdrup balance would fail because of the flow interactions with the bottom topography. This argument explains why the SSHA in the Nordic Seas is strongly related to the bathymetry contours (e.g. the 1st and 2nd EOF). This reasoning can be further supported by the model results of Hughes and de Cuevas (2001) from the Southern Ocean that showed that when sloping topography is present, the dominant balance is obtained between the wind stress curl and the bottom pressure torque. They argue that the dominance of the bottom pressure torque in the Southern Ocean over viscous and nonlinear terms results in flow along f/H contours and is therefore more barotropic. The observed SSHA variability that is strongly influenced by the topography suggests that the bottom pressure torque also dominates over the viscous and nonlinear terms in the Nordic Seas.

The situation is not apparent when considering the 1st EOF mode of the seasonally filtered SSHA. Firstly, the atmospheric fields are not as energetic at other frequencies and therefore may be inaccurate. Secondly, the 1st EOF of the filtered SSHA describes not only the circulation in the central Nordic Seas but also the currents at the Greenland continental shelf. Most of the seasonally filtered variance associated with the 1st EOF explains SSHA variability in the Greenland gyre and at the northern Greenland continental shelf. The results of the Maximum Covariance Analysis suggest that the coupling between the 1st EOF of SSHA and wind stress curl is even stronger for the seasonally filtered case but mainly in the central Nordic Seas (see Figure 4.35, top left). Also the model results of Isachsen (2003) support our findings about the importance of the wind forcing on monthly and longer scales in the Greenland and Norwegian Seas.

In order to explain the part of the 1st EOF of the seasonally filtered SSHA located at the Greenland continental shelf, one needs to take into account the sea-ice presence, which also could affect some fluxes. All the fluxes in the ECMWF Era Interim dataset are positive downward, which in the case of heat flux, means the ocean gains heat from the atmosphere. However, in the MCA all the mean fields are removed prior to the analysis and we should think about positive heat flux anomalies relative to the mean field. The MCA shows that the positive heat flux anomaly at the Greenland continental shelf (more heat is gained by the ocean or less heat is lost by the ocean) is coupled to the negative SSHA in the same area (3rd SVD mode, Figure 31). This does not agree with

our expectations because the sea level should increase with the increasing heat flux due to the thermal expansion of the water column above the thermocline. This coupling can only be physically interpreted by the sea-ice formation process that reduces the heat-flux between the atmosphere and the ocean. Therefore, the mode cannot explain SSHA variability associated with the 1st EOF of SSHA at the Greenland continental shelf because it shows that SSHA variation due to the ice-formation drives the heat flux variability. However, it confirms that the sea-ice processes are important for the SSHA variability in the region.

The MCA also revealed that an anomalous negative wind stress curl (less cyclonic or more anticyclonic), spreading from the north of Iceland along the Greenland continental shelf, is locally coupled with the higher than normal sea level reaching about 4 cm. The coupling was described by the left mode consisting of the first three rotated EOFs of the filtered SSHA, and by the right mode that was a mixture of the two first EOFs of wind stress curl. The time expansion coefficient of the right MCA mode was found to be significantly correlated to the NAO index ($R=-0.35$, $p<0.01$). It could be argued that this MCA mode could be also related to the sea-ice transport because its dynamics are mainly attributable to the winds rather than the ocean currents (Dickson et al., 1988, Tremblay and Mysak 1998, Fang and Wallace 1994). Furthermore, the drag coefficient between the atmosphere and ice is much larger than for the atmosphere and ocean, and ice export from the Arctic is dependent on the Ekman transport (Saenko et al. 2002). Many previous studies also found that the sea-ice export through Fram Strait is driven by a large scale atmospheric pressure forcing such as NAO and AO (Kwok and Rothrock, 1998, Fang and Wallace, 1994) but this relationship depends also on the NAO phase (Schmidt and Hansen, 2003). A similar SVD mode, which is correlated to the |NAO index, was also obtained for the unfiltered fields. It was shown that more cyclonic winds spreading northwards from the north of Denmark cause a lower than normal sea level at the Greenland continental shelf (Figure 4.34, SVD mode 3).

The MCA analysis confirms the conclusions from Chapter three about the forcing of the 2nd EOF of SSHA. The forcing mechanisms of this mode could be explained by the annual variation in the pressure field which causes cyclonic winds that depress sea level in the central Nordic Seas (negative SSHA) but increase sea level at the borders of the Nordic Seas (positive SSHA), at the continental shelves of Greenland and Norway

(Figure 4.25). In fact, the 2nd EOF of SSHA has a similar pattern to the phase of the annual harmonic described in Chapter 3. The correlation coefficient for the unfiltered 1st left and right SVD mode (SSHA and mean sea level pressure) is 0.79 and the right field can predict 5% of the SSHA variance, that is 50% of the variance explained by the 2nd EOF of SSHA itself. The 1st EOF of freshwater flux is coherent with the mean sea level pressure and the NAO index at the annual frequency and therefore it is also strongly coupled with the 2nd EOF of the SSHA. It can explain 6% of the unfiltered SSHA variance, which means it explains about 60% of variance explained by the 2nd EOF of SSHA.

However, the MCA does not clearly indicate which fields are coupled to the 2nd EOF of the seasonally filtered SSHA at frequencies other than annual. A number of left modes were correlated to the 2nd EOF of SSHA but also to the 1st EOF of the filtered SSHA. This suggests that the coupling between SSHA and the other fields occurs for a left mode consisting of the two rotated EOFs of seasonally filtered SSHA. For example, the strongest coupling between the mean sea level pressure and SSHA occurs for the right mode describing the NAO-related variability (1st EOF of mean sea level pressure) and a left mode that is a mixture of the 1st and 2nd EOF of SSHA. The right mode of the mean sea level pressure can predict in total 5.3% of the unfiltered SSHA variance, mainly in the central Nordic Seas and at the continental shelf of Norway. A similar amount of variance in the unfiltered SSHA can be predicted by the meridional wind stress (5.4%) with a significant contribution in the central Nordic Seas (Figure 4.32, 1st left mode). The left mode is more similar to the 1st EOF of SSHA but it is also moderately correlated with its 2nd EOF. The MCA results also showed that the 1st EOF of precipitation, which is also correlated to NAO index, is strongly coupled to the left SSHA mode consisting of the rotated 1st and 2nd EOFs of SSHA. The right mode explains a very similar amount of variance (5.5%) to all the other fields coupled to the 2nd EOF of SSHA at other frequencies than the annual, which were described above. The right mode of precipitation can predict most of the variance in the shallow regions of the Nordic Seas: at the Greenland and Norwegian shelf and in the Barents Sea. The results of the MCA analysis are in agreement with the results described before in Section 4.3, which also show the coupling between the 2nd EOF of SSHA and various atmospheric EOFs that are correlated to the NAO Index, not only at the annual frequency. However, the MCA has clarified this relationship by showing that the

coupling is the strongest for SSHA and the following four fields: mean sea level pressure, meridional wind stress, precipitation and freshwater flux. The MCA also showed that the strength of the coupling depends on the region. For example, meridional wind stress and freshwater flux explain a significant proportion of variance in the SSHA in the central Nordic Seas but mean sea level pressure and precipitation are important in the shallow waters: at the Greenland and Norwegian continental shelf and in the Barents Sea.

The in situ velocity observations of Ingvaldsen et al. (2002) showed that the inflow to the Barents Sea is controlled by the Ekman transport associated with the strength and direction of the local winds and is mainly barotropic. The 2nd EOF shows the same behaviour in the Barents Sea that is characterised by the sea level oscillations with a strong annual component suggesting it is also mainly wind driven. Also a number of studies (Mauritzen et al. 2006, Nielsen et al. 2003) showed that the strength of the inflow of the Atlantic water into the Nordic Seas is driven by the large-scale atmospheric pressure systems like the NAO. Various other in situ observations show strengthening of the circulation during the winter in the boundary currents (Woodgate at al. 1999, Fahrbach et al. 2001 for EGC; and Skagseth and Orvik 2002, Orvik et al. 2003, Mork and Skagseth, 2005 for NwAC) and central Nordic Seas (Poulain et al. 1996, Orvik and Niller 2002, Jakobsen et al. 2003, Voet et al. 2010).

The 3rd EOF of SSHA, described in detail in the previous chapter, shows the antiphase oscillation in the sea level between Belgica Bank (northern shelf of Greenland) and the eastern boundary of the Nordic Seas: an area to the east of Svalbard and along the Norwegian continental shelf. The 3rd PC of SSHA has a clear seasonal cycle but also substantial variability at 4 month period and a low frequency trend from the beginning of the record until August 2008. At the western boundary, the sea level increases gradually and decreases at the eastern side of the basin. A similar increasing trend was also found in the monthly AO and NAO winter indices. The preliminary analysis of correlations in Section 4.3 showed that this mode is significantly correlated to the NAO index. It is also significantly correlated to the 2nd EOF of mean sea level pressure, that is responsible for sea-ice transport (Jahnke-Borneman and Brummer, 2009). Even higher correlations were found for this mode and the 2nd EOF of meridional wind stress that is also strongly correlated to the NAO index (Section 4.3.2). The obtained relationships

suggest that this mode can be related to the sea-ice presence at the western boundary and its transport through the Fram Strait. It is known that evaporation is reduced to almost zero in the ice-covered ocean and significant correlations obtained for the 3rd EOF of SSHA and the 2nd EOF of evaporation confirm that the 3rd mode of SSHA can be related to sea-ice presence at the annual frequency. The MCA analysis has pointed out that this mode is also moderately coupled (R=0.72) to the 2nd EOF of the local freshwater flux. This means that more freshwater input (positive anomaly) causes a higher sea level at the Belgica Bank (positive SSHA) and more freshwater output occurring at the same time in the central Nordic Seas causes negative SSHA. After the removal of the seasonal cycle the pattern is more similar to the 3rd EOF of the unfiltered SSHA (Figure 4.34) that is coupled with a negative freshwater flux anomaly along the Norwegian shelf and in the Barents Sea (negative SSHA, -2cm) and a positive freshwater flux at the Belgica Bank (positive SSHA, 3cm).

Errors and limitations of the ECMWF dataset

The errors in the ECMWF reanalysis products could affect the analysis by hiding coupling that is important but is not resolved by the atmospheric fields. For example, heat flux in the model is obtained with a basic treatment of sea-ice with a very low resolution and only two categories of sea-ice: 0 and 100% concentration of ice. Oshima (2003) found that this treatment considerably underestimates the winter heat loss in the ice-covered ocean. On the other hand, a small change in the ocean heat flux affects greatly sea-ice thickness and formation and melting that affects SSHA and currents (Kwok et al., 2008). Advection of heat is also not represented in the statistical analysis. Furthermore, increased river discharge in the spring (Jones et al. 2008, Rabe et al. 2009) could also have an effect on the sea level but is unrepresented in this analysis.

Limitations of the statistical methods

The two statistical methods used in this chapter to describe the coupled modes of variability between the sea level and various air-sea fluxes (MCA and CCA) have common drawbacks because CCA is actually a weighted MCA (Cherry, 1996). It was argued in the past that temporally autocorrelated (not independent) time series could produce spurious patterns in CCA (Kendall, 1975) and in MCA (Cherry, 1996). Furthermore, the patterns could be a result of the mathematics rather than caused by a geophysical coupling (Cherry, 1996). Because of the orthogonality constraint and the

maximization procedure, the MCA can identify the coupling only in special circumstances and therefore could produce misleading results for other cases (Sardeshmukh, 1995). In order to trust the results of MCA, the transformation (coupling) linking the two fields must be orthogonal and the covariance matrix of either field must be the identity matrix (the spatial grids should be uncorrelated with each other). In fact we should consider MCA as the method that isolates the most frequently occurring patterns for the two fields (Cherry, 1996). Following Cherry (1996) who has investigated when the MCA produces the real coupled modes, we can believe the results if the coefficient time series of the two fields are highly correlated and project strongly on the leading EOFs of both fields. In this study these criteria were fulfilled (see a summary of the statistics for each pair of fields in tables) and therefore it can be argued that MCA results are useful in identifying the physical coupling. To further investigate the dependence on the grid size, the MCA was repeated on the fields with the increased grid size (3^0 longitude x 1.5^0 latitude) and very similar coupled modes were obtained. However, some of the atmospheric fields are dominated by a single EOF that explains a major part of its variance, which means that pattern also occurs the most frequently (Section 4.3.1). For example, the 1st EOFs of the unfiltered mean sea level pressure, heat and freshwater fluxes and evaporation explain more than 70% of the total variance of these fields. A large proportion of this variance is the seasonal cycle (Section 4.2.1), so the 1st EOFs of the same seasonally filtered fields explain much less variance. If one of those fields is dominated by a single EOF, the results of the MCA will be affected by it. Therefore, the 1st right mode of the MCA could be the same as the dominant EOF because it occurs most frequently. However, it does not mean that the two patterns are strongly related to each other, or there is a physical causality between them. Due to the drawbacks of the MCA analysis other statistical methods were also used (Sections 4.2, 4.3).

Steric contribution to the SSHA

The annual variability of SSHA can be divided into several components (Gill and Niller, 1973). A part of the annual signal is caused by a thermal expansion of seawater above the thermocline due to a local heating and advection (steric height). This could be further divided into the advection term and change of the sea level caused by the buoyancy forcing that could be an effect of net heat and freshwater fluxes. Mork and Skagseth (2005) showed that the changes in sea level due to the steric contribution

account for about 40% of the annual signal. This was found to be mainly caused by the local net heat flux (60% of the total steric height variance) but the steric contribution to the currents was found to be very small and reached 0.3 cm/s in the case of the NwAC (Mork and Skagseth, 2005). It was not the aim of this study to investigate the steric height contribution to the annual SSHA signal. This has already been done for most of the area (Mork and Skagseth, 2005) and it could be improved in the ice-covered part of the Nordic Seas with our SSHA data but only if a better heat flux product is used with a representation of the ocean-ice heat flux. All the reanalysis products treat heat flux in the ice-covered seas as the atmosphere-ice heat flux but the greatest contribution, from ocean-ice heat flux, is missed. The errors in the heat flux are around 15% in the ocean (Godoy et al., 1998) but much greater in the ice-covered part of the ocean. This results in the signal of interest being comparable to the error term in the ice-covered ocean. The steric contributions to the SSHA were not removed prior to the statistical analysis and some of the coupling that was found by the MCA could be explained by the steric height variability. However, Mork and Skagseth (2005) showed that this contribution is only a small part of the signal that occurs only at the annual frequency, and we expect this contribution to be even smaller in the ice-covered ocean because the seawater temperature differences are small there.

We have only analyzed the local sea level response that is driven at the same time or at a very close lag of 1-2 months. We have not investigated the correlations for longer lags (greater than 15 months) because the SSHA time series are too short (84 months). The remote forcing that could also drive sea level variability was not investigated here. The statistical analysis that was applied here only provided clues for the possible forcing mechanisms of sea level variability in the Nordic Seas. In order to properly describe the driving mechanisms of sea level one needs to use a numerical model and this analysis could be expanded in the future with the help of numerical model. However, it was demonstrated that the MCA and EOF analysis provided useful clues about the possible forcing mechanisms (e.g. wind forcing) that have been confirmed in numerical models (Isachsen et al. 2003) and *in situ* observations (Ingvaldsen et al, 2002).

4.6. Conclusions

We began the investigation of the relationship between sea level variability and various important atmospheric variables from the analysis of the seasonal cycle. The major motivation was to provide the explanation for the different phase of SSHA between the central Nordic Seas and its boundaries. The similarity between the phases of the atmospheric fields and SSHA suggested that the ocean responds simultaneously or with 1-2 months lag to the seasonal atmospheric forcing and therefore its response is mainly barotropic. The timing of the sea level maximum in the central Nordic seas occurs 1 month after the local weakest winds and 2 months after the maximum heat gain by the ocean occurs in the same area. The presence of land changes the ocean response to the wind. The maximum SSHA occurs simultaneously with the maximum wind strength along the coasts of Greenland and Norway and in the Barents Sea. This can be explained by the Ekman theory because the local wind stress along the coast causes downwelling there that in effect causes a local sea level rise close to the shore. Furthermore, an anticyclonic wind that occurs along the northern shelf of Greenland causes convergence and therefore the local sea level rise. It was found that the timing of the maximum wind stress curl is the same as the timing of the local SSHA at the northern Greenland continental shelf.

The aim of this chapter was to provide some possible explanation of the sea level variability in the Nordic Seas from October 2002 to November 2009. The analysis described in the previous chapter showed that most of the variability in the SSHA was found to be associated with the first three EOFs of SSHA (about 50%). Therefore, in this chapter we have decided to explain the variability associated with these three EOFs. The relationship between sea level variability and various ECMWF atmospheric fields was investigated by regressing the EOFs of the atmospheric fields onto sea level data and also by correlating the corresponding EOFs to the three first EOFs of SSHA (Section 4.3). Furthermore, the relationship was further investigated using the MCA and CCA (Section 4.4). All the statistical methods showed that wind forcing plays the major role in driving the first three EOFs of SSHA and can explain also a large percentage of variance in the SSHA at annual and other frequencies. It was found that wind stress curl could explain most of the variance accounted by the 1st EOF of SSHA. Therefore, one

can argue that the central Nordic Seas spin up/down at the same time as the wind stress curl is strengthening/weakening, which indicates a barotropic response to the wind forcing in the area. The strongest forcing of this mode occurs annually but other frequencies are also important in the central Nordic Seas and at the Greenland continental shelf where the sea-ice is present. It was found that the sea level variability that was described by a 2nd EOF of SSHA is driven/influenced by the NAO-related atmospheric forcing at the annual and other frequencies. This mode of sea level variability was found to be significantly correlated to the mean sea level pressure and precipitation at all frequencies. Furthermore, this mode was also correlated to the other fields, which were also correlated to the NAO Index. The results suggest that the 3rd EOF of SSHA can be described as a response of the ocean to the wind stress curl, which affects SSHA at the eastern and western boundaries of the Nordic Seas, and heat and freshwater fluxes, which affect mainly the eastern boundary. Furthermore, the coupling between the 3rd EOF of SSHA and the other fields (wind stress curl, freshwater and heat fluxes) occurs at all frequencies except heat flux, which contributes only to the annual SSHA variability. The results of the statistical analysis are in agreement with the earlier *in situ* observations in the Nordic Seas (Woodgate at al, 1999, Fahrbach et al. 2001 for EGC and Skagseth and Orvik 2002, Orvik et al. 2003, Mork and Skagesth,, 2000, Poulain et al. 1996, Orvik and Niller 2002, Jakobsen et al. 2003, Voet et al. 2010) and recent modelling studies (Isachsen et al. 2003, Mauritzen et al. 2006, Nielsen et al. 2003). The results described in the previous two chapters show that sea level and therefore the ocean circulation varies greatly on the seasonal timescales. The currents strengthen during the winter, which is mainly the effect of the seasonal wind forcing related to the centre of the low atmospheric pressure – the Icelandic Low. The wind stress strengthens the circulation in the central Nordic Seas but also the main boundary currents: EGC, NwAC, WSC, this was previously observed by the mooring arrays (Farhbach et al. 2001, Schauer et al. 2004, De Steur et al. 2009) and surface drifters (Voet et al. 20100). The results of this chapter also show the importance of the atmospheric forcing that is related to the atmospheric pressure mode of variability, the North Atlantic Circulation, for the sea level variability. The results indicated that the air-sea fluxes affected by the wind variability induced by the NAO cause the other air-sea fluxes to change and this has its signature in the SSHA and therefore also affect the circulation in the area. Previously, the importance of NAO-related atmospheric forcing was observed for the branch of the NwAC (Orvik et al. 2003) and Barents Sea (Dickson

et al. 2000). We have also found that the major part of the SSHA variability is influenced by the bottom topography. This suggests the barotropic response of the ocean to the local wind forcing and was proved by the barotropic model of Isachsen et al. (2003) and Isachsen and Niiler (2003). The simultaneous correlations with the wind stress and wind stress curl explain therefore the greatest percentage of variance in the SSHA data when comparing with the other air-sea fluxes (Section 4.4).

The statistical analysis cannot prove that a particular atmospheric process forces the sea level variability. However, the statistical analysis can indicate which atmospheric fields are important and how much variance they explain in the SSHA variance. This information can be used in the future in the model studies to test these relationships and can help to explain the mechanisms that control the sea level variability in the Nordic Seas. Due to the limited time framework of this PhD it was not possible to investigate the obtained results with a numerical model but it can be done in the future.

CHAPTER 5: SURFACE CIRCULATION IN THE NORDIC SEAS AND TRANSPORTS OF THE EAST GREENLAND CURRENT.

5.1 Introduction

The main aim of this chapter is to infer and characterize the transport variability of the East Greenland Current along its path from the north of Fram Strait (80.5^0N) to north of Denmark Strait (69^0N), with a focus on the seasonal and interannual variability in 2002-2009. The altimetry data from the ice-covered ocean provides the framework for this chapter and makes possible to describe the spatial and temporal transport variability of the EGC for the first time over such a large area. The analysis begins with the calculation of the surface currents in the entire Nordic Seas (Section 5.2). In order to calculate the transports one needs to know how the velocity of the current changes with depth, along its path – the vertical structure of the current. Due to the lack of appropriate long-term *in situ* measurements numerical model output was used to obtain the vertical structure of the current velocity (See Chapter 2). In Section 5.3 the numerical model is validated against the observations. The model's SSHA is compared to the remotely sensed SSHA and In the same section the model transport variability at 75^0N is compared to the mooring observations of Woodgate et al. 1999. The method of the transport estimation is described in detail in Section 5.4. The results are presented and discussed respectively in Sections 5.5 and 5.6. Finally, the conclusions are presented in Section 5.7.

5.2 Surface circulation in the Nordic Seas

Surface currents were calculated assuming the geostrophic balance and using equation 1.1 with forward difference of the SSHA. The calculation of the velocity field requires differentiation of the SSHA. Therefore any noise in the SSHA is amplified in the velocity maps. Temporal averaging of data reduces the noise and makes the velocity field less noisy, which improves the quality of the maps. Therefore in this chapter we focus on the mean seasonal cycle and annual averages of the velocity field. The results are presented on the 0.5^0x1^0 grid as the monthly averaged velocities for the 7-year long time period (mean seasonal cycle) and the annually averaged velocities. Additionally to the velocity maps, the SSHA used for the velocity calculation, is presented in the same figure. Each map of the mean seasonal cycle (Figures 5.1-5.12) illustrates the temporal average of the 7 months (i.e. 7 Januaries) and each annual average is a temporal average of the 12 subsequent calendar months from November to October (Figures 5.13-5.19). The velocities that have their magnitude smaller than 1 cm s^{-1} are not presented.

This section is ordered as follows; Firstly the mean seasonal cycle of the surface circulation is presented. Then the annually averaged anomalous surface currents are described. Finally, the mean eddy kinetic energy (EKE) in 2002-2009 is characterized and compared to the previous observations.

Seasonal cycle of the anomalous surface currents in the Nordic Seas

The mean seasonal cycle of the velocity field is shown in Figures 5.2-5.13 together with the corresponding SSHA field. The figures show the anomalous velocity field – the currents that are referenced to the mean circulation over the 7-year long period. Therefore, the interpretation of the circulation variability needs to be done in reference to the mean surface circulation in that region, which is presented again in this chapter in Figure 5.1. Generally, the currents are stronger in the winter and weaker in the summer. The strengthening of the currents begins in August and continues until February. The greatest velocities and the greatest variability occur along the northern Greenland shelf and are associated with the East Greenland Current and the shelf circulation. The anomalous velocities reach about 10 cm s^{-1} in August and February in the ice-covered regions along the northern Greenland shelf. The velocities of the NwAC and WSC reach the minimum in the same time as the EGC, in June/July and the maximum in January. EGC was stronger in August and September but the shelf circulation was weaker in the

same time. However, from October until March the EGC and the currents at the Greenland shelf are stronger. It was found that the EGC was the strongest from December to February to the south of 74°N and from January to March to the north of 74°N. The East Icelandic Current (EIC) was the weakest in March and the strongest in October. The significant seasonal cycle was also observed in the central Nordic Seas, which speed up during the winter. This is in agreement with the recent observations of Voet et al. (2010) who showed that the velocities in the GIN Seas varied from 1cms^{-1} to 4cms^{-1} in 2001-2009. However, their results also showed that in some basins (e.g. Iceland Plateau) the seasonal cycle was very small and therefore could be impossible to detect with the altimetry.

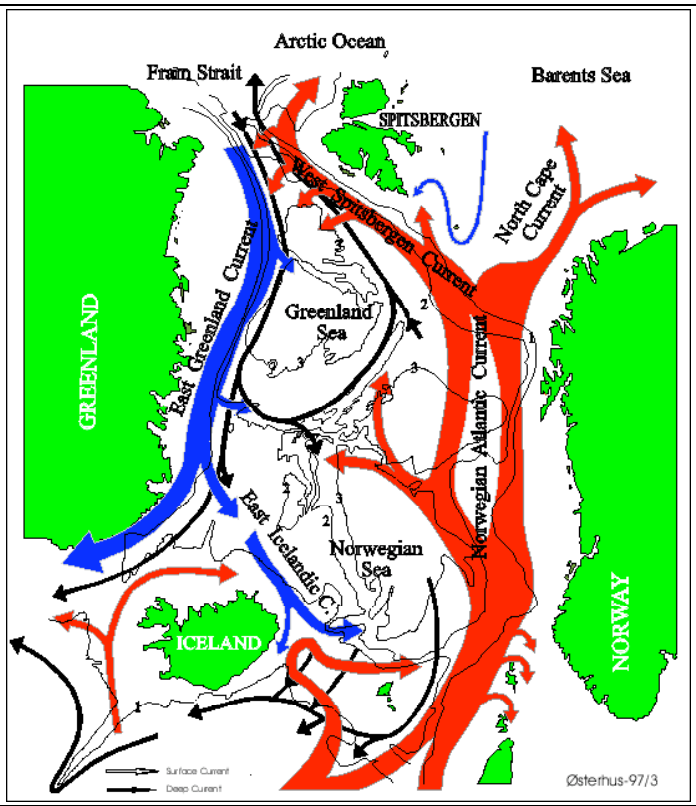

Figure 5. 1. Surface circulation in the Nordic Seas (in blue and red). Warm and saline Atlantic water is marked in red. Cold and fresh water transported from the Arctic by the East Greenland Current is marked in blue. (Source: Eliasen et al., 2000)

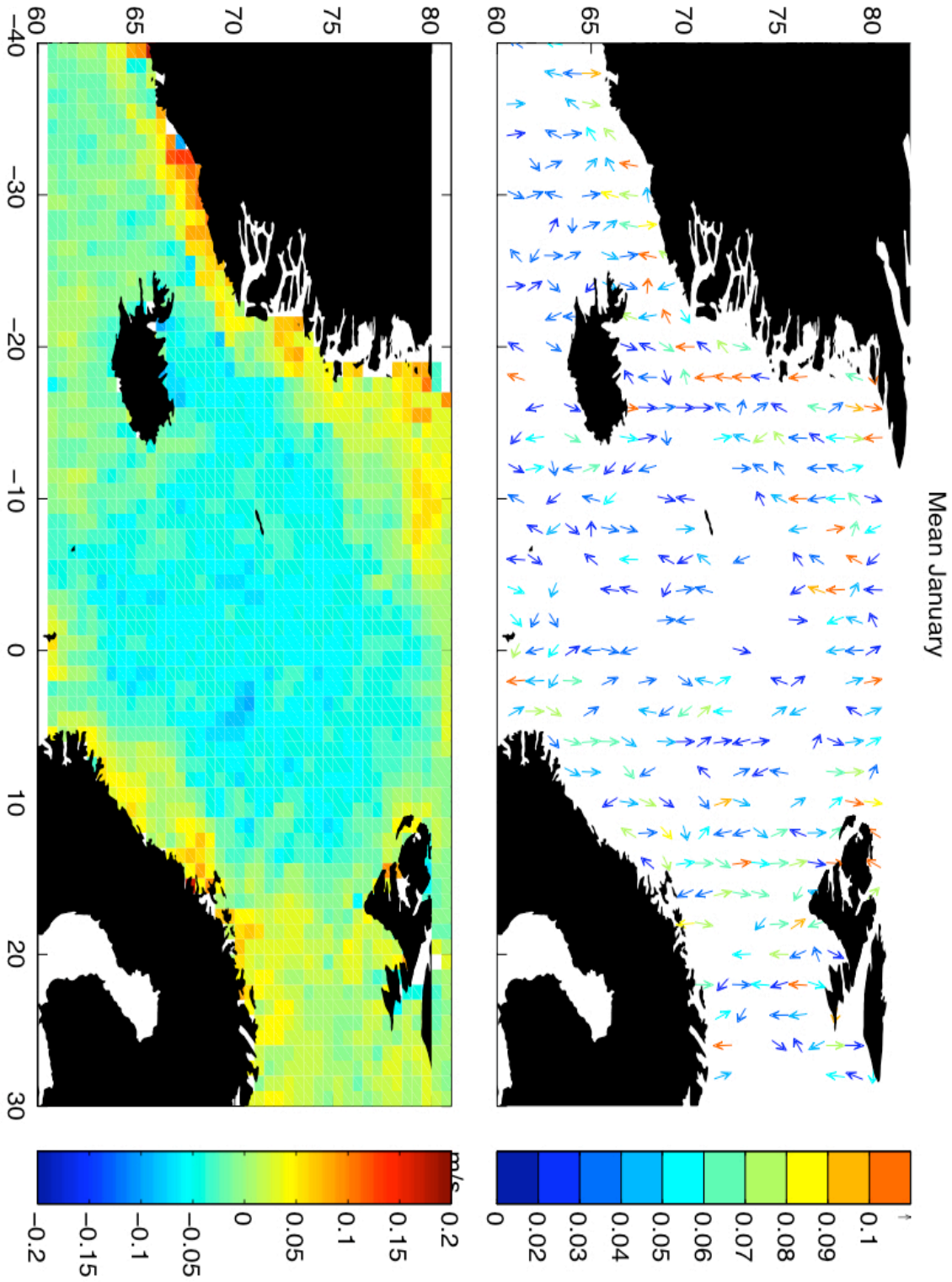

Figure 5.2 Mean (2003-2009) SSHA (m) and the anomalous surface currents (ms^{-1}) in January.

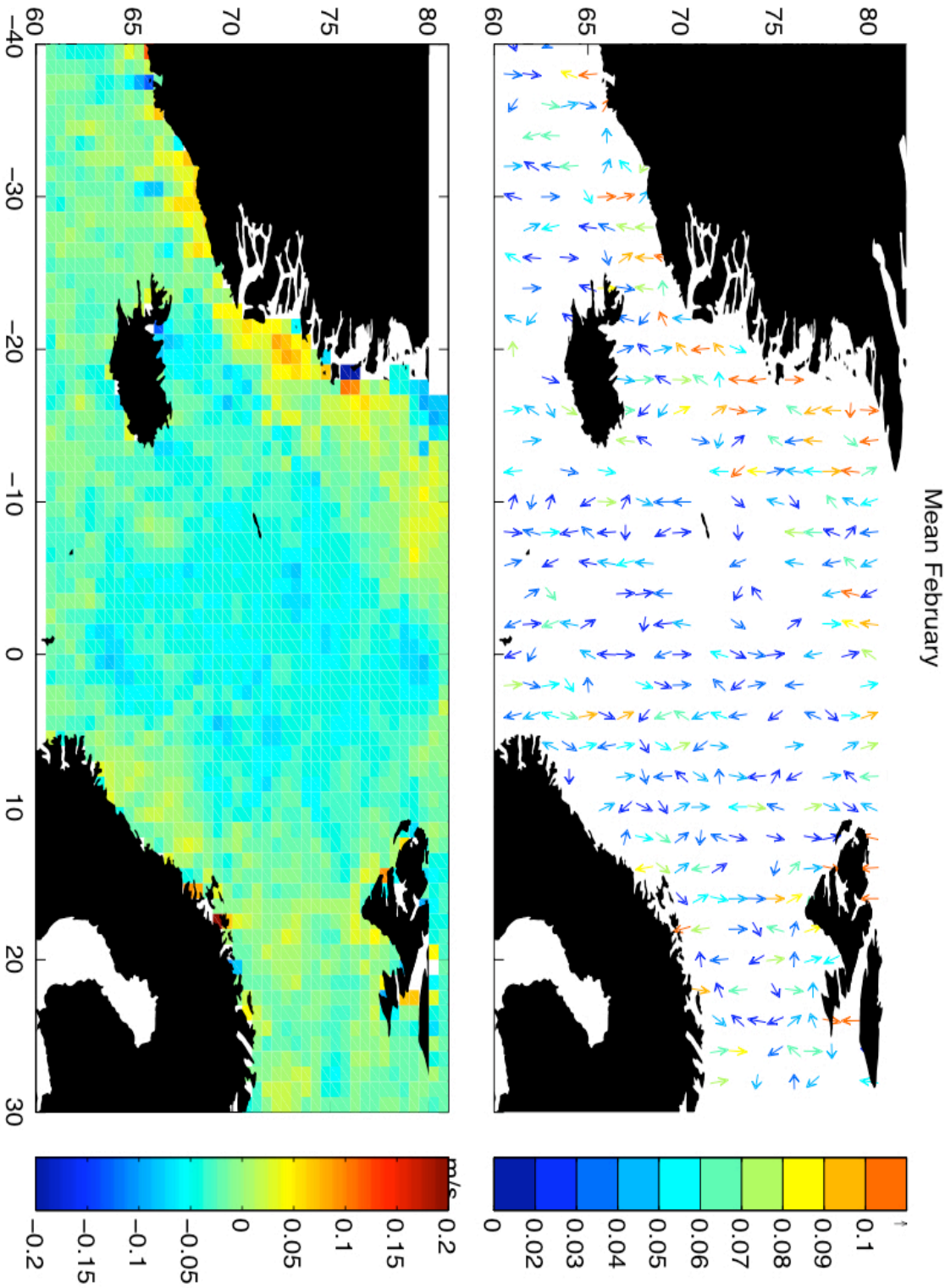

Figure 5.3. Mean (2003-2009) SSHA (m) and the anomalous surface currents (ms^{-1}) in February.

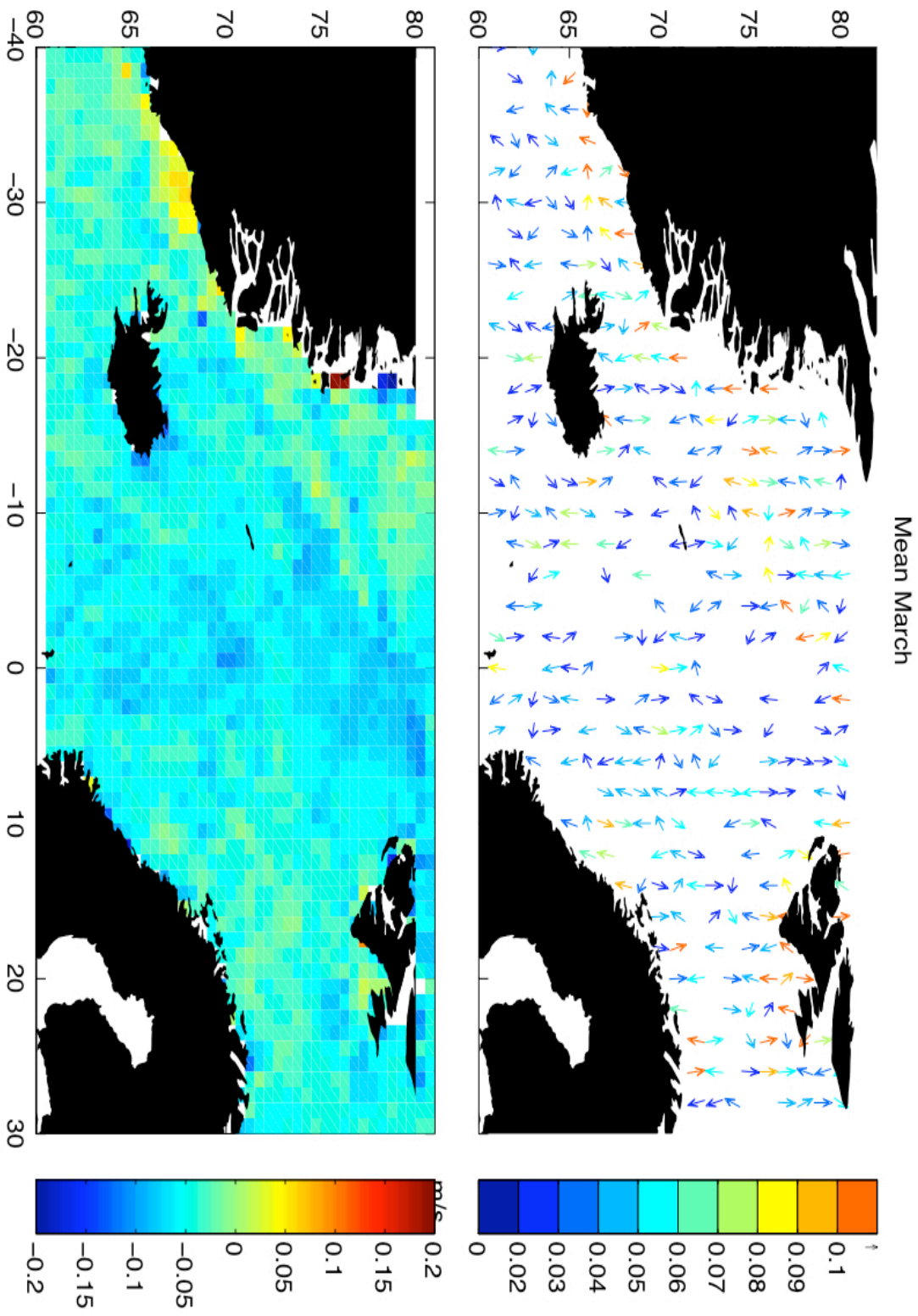

Figure 5.4. Mean (2003-2009) SSHA (m) and the anomalous surface currents (ms^{-1}) in March.

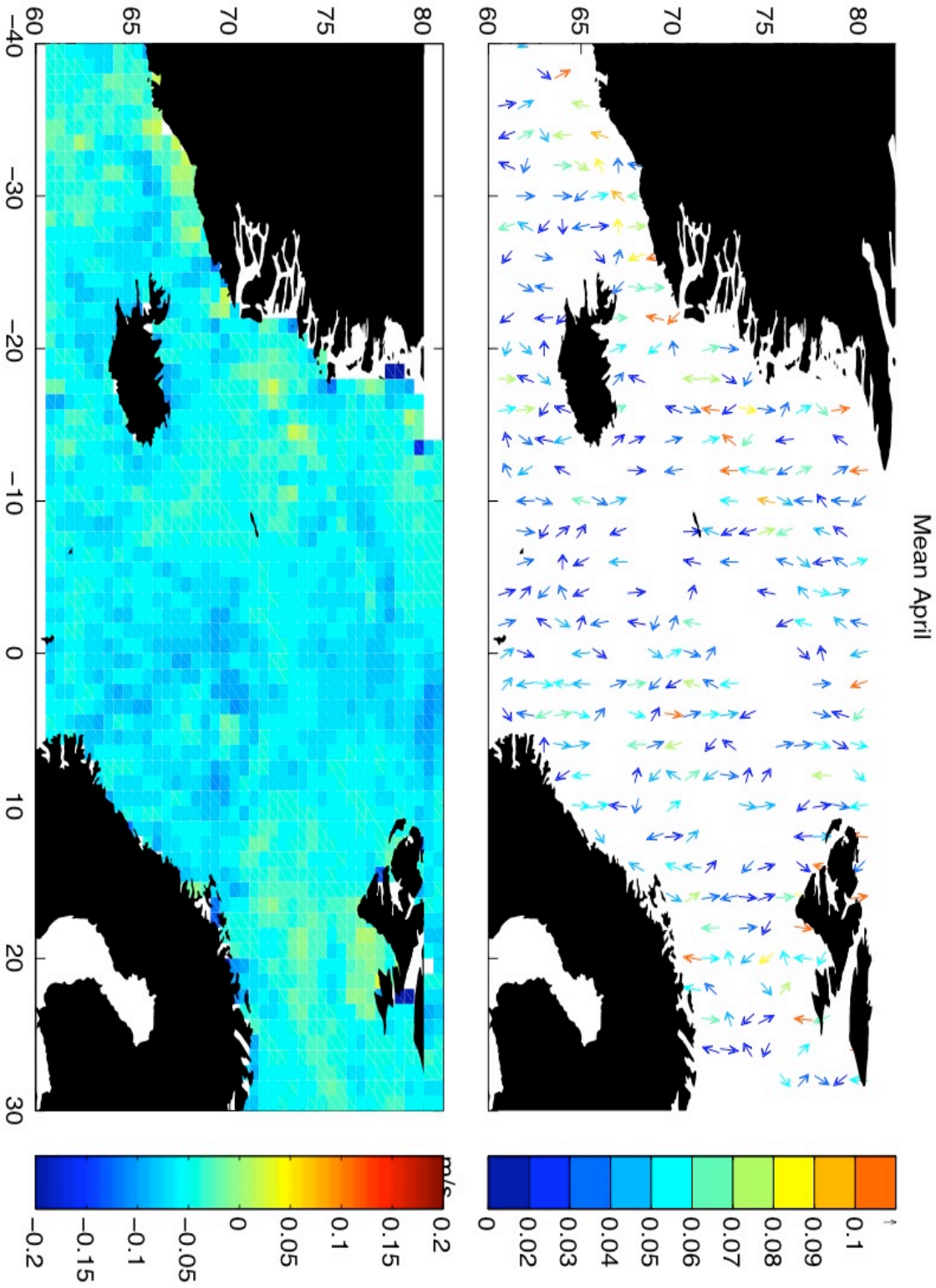

Figure 5.5. Mean (2003-2009) SSHA (m) and the anomalous surface currents (ms^{-1}) in April.

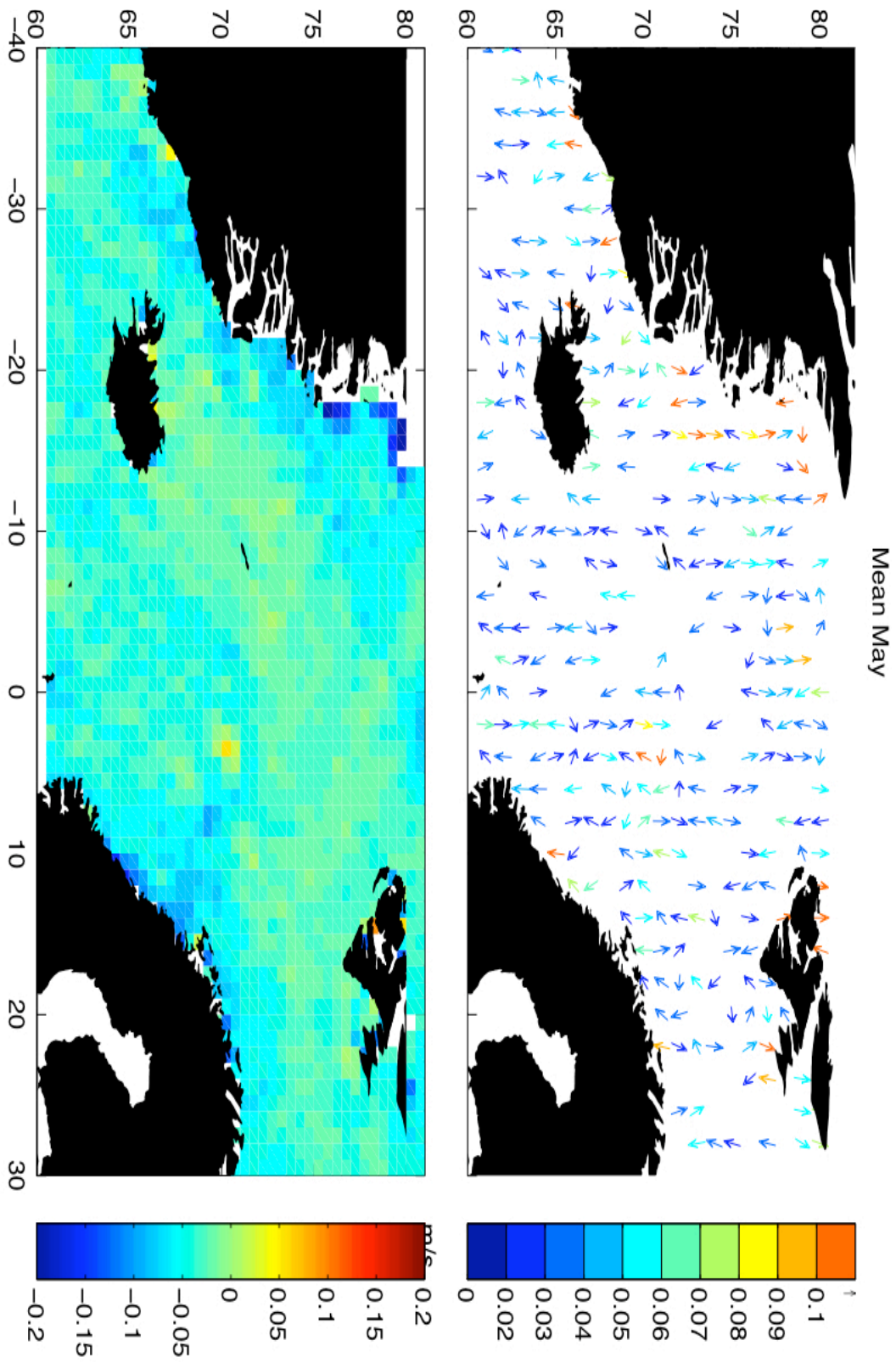

Figure 5.6 Mean (2003-2009) SSHA (m) and the anomalous surface currents (ms^{-1}) in May.

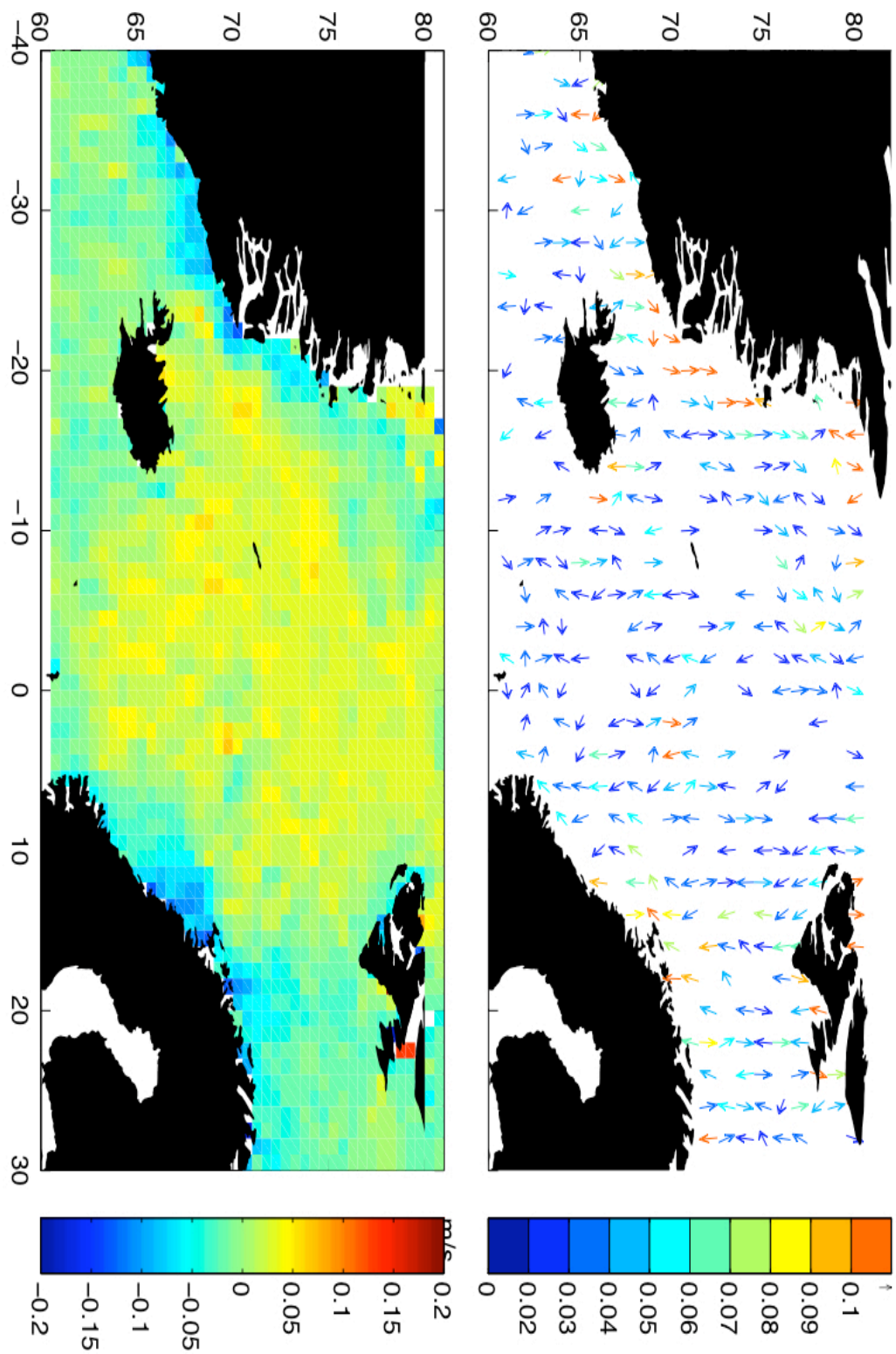

Figure 5.7. Mean (2003-2009) SSHA (m) and the anomalous surface currents (ms^{-1}) in June.

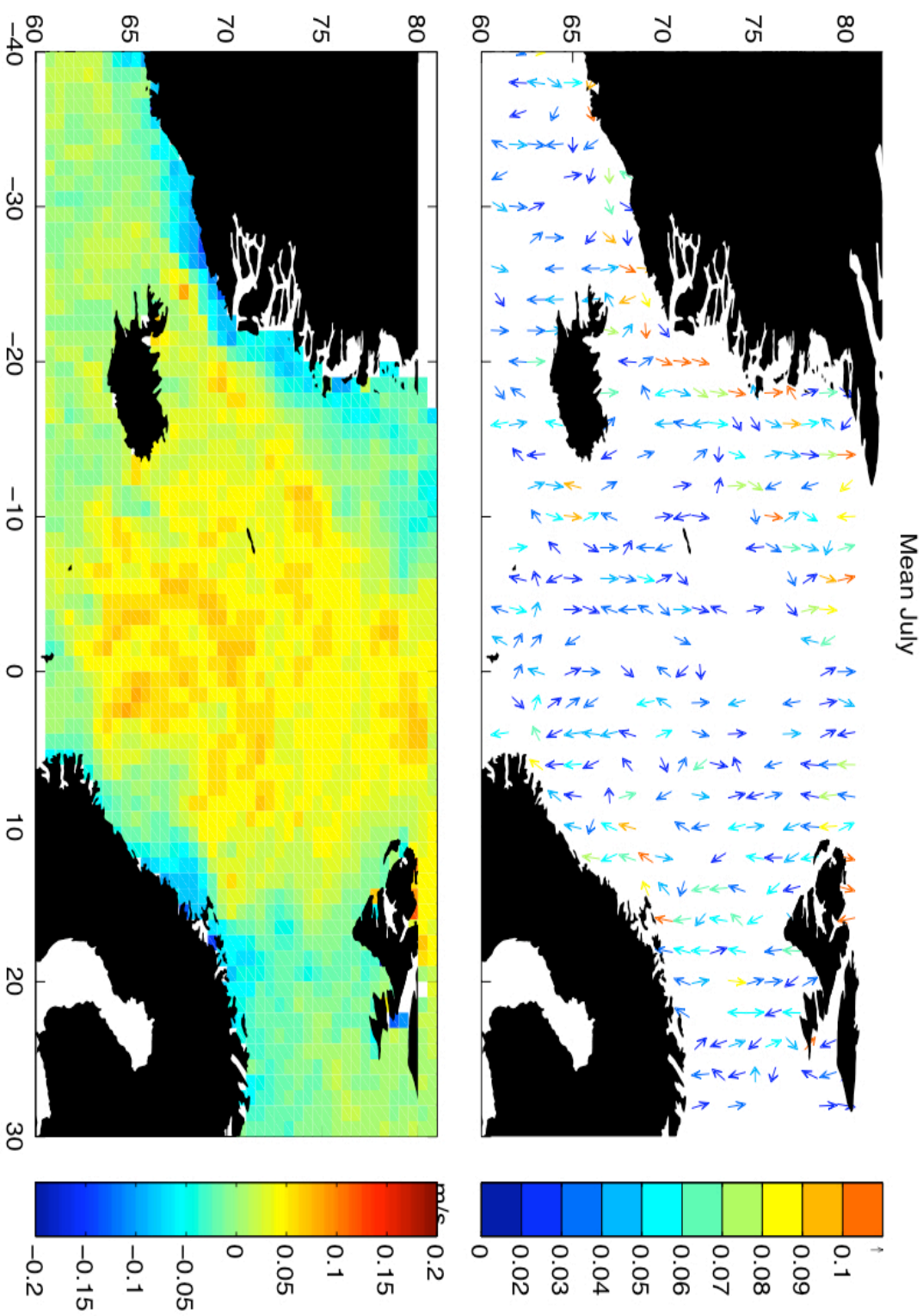

Figure 5.8 Mean (2003-2009) SSHA (m) and the anomalous surface currents (ms^{-1}) in July.

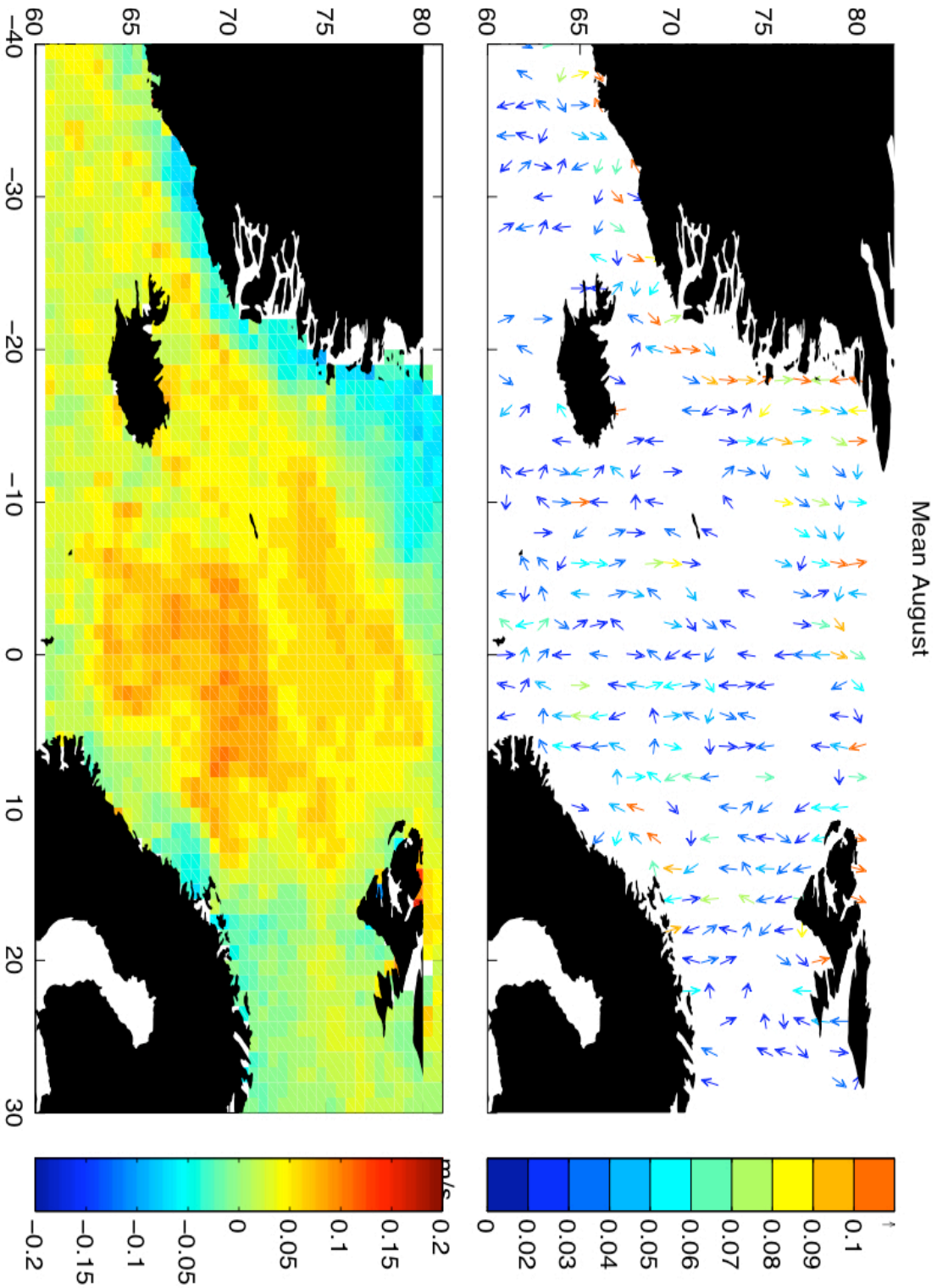

Figure 5.9. Mean (2003-2009) SSHA (m) and the anomalous surface currents (ms^{-1}) in August.

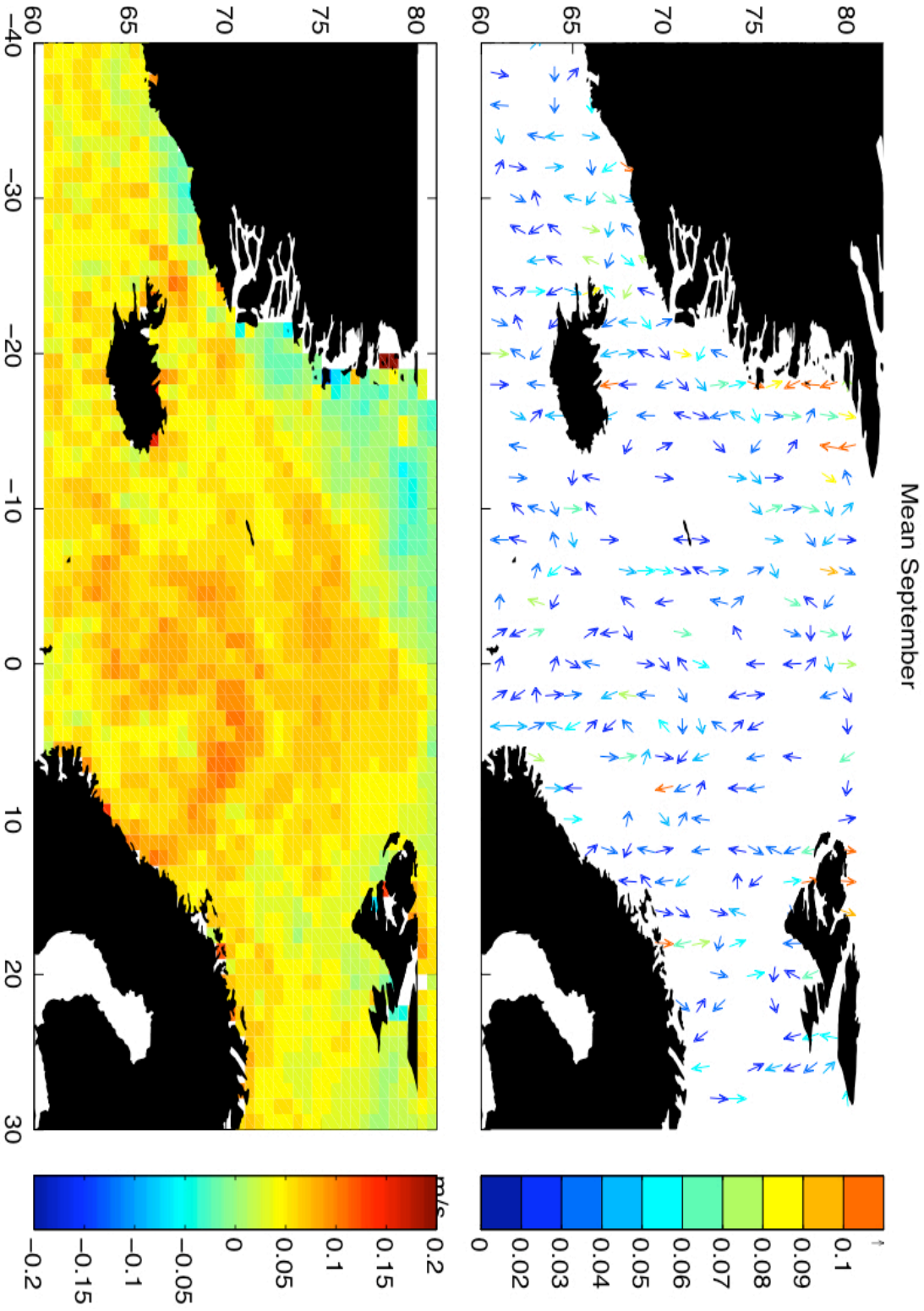

Figure 5.10 Mean (2003-2009) SSHA (m) and the anomalous surface currents (ms^{-1}) in September.

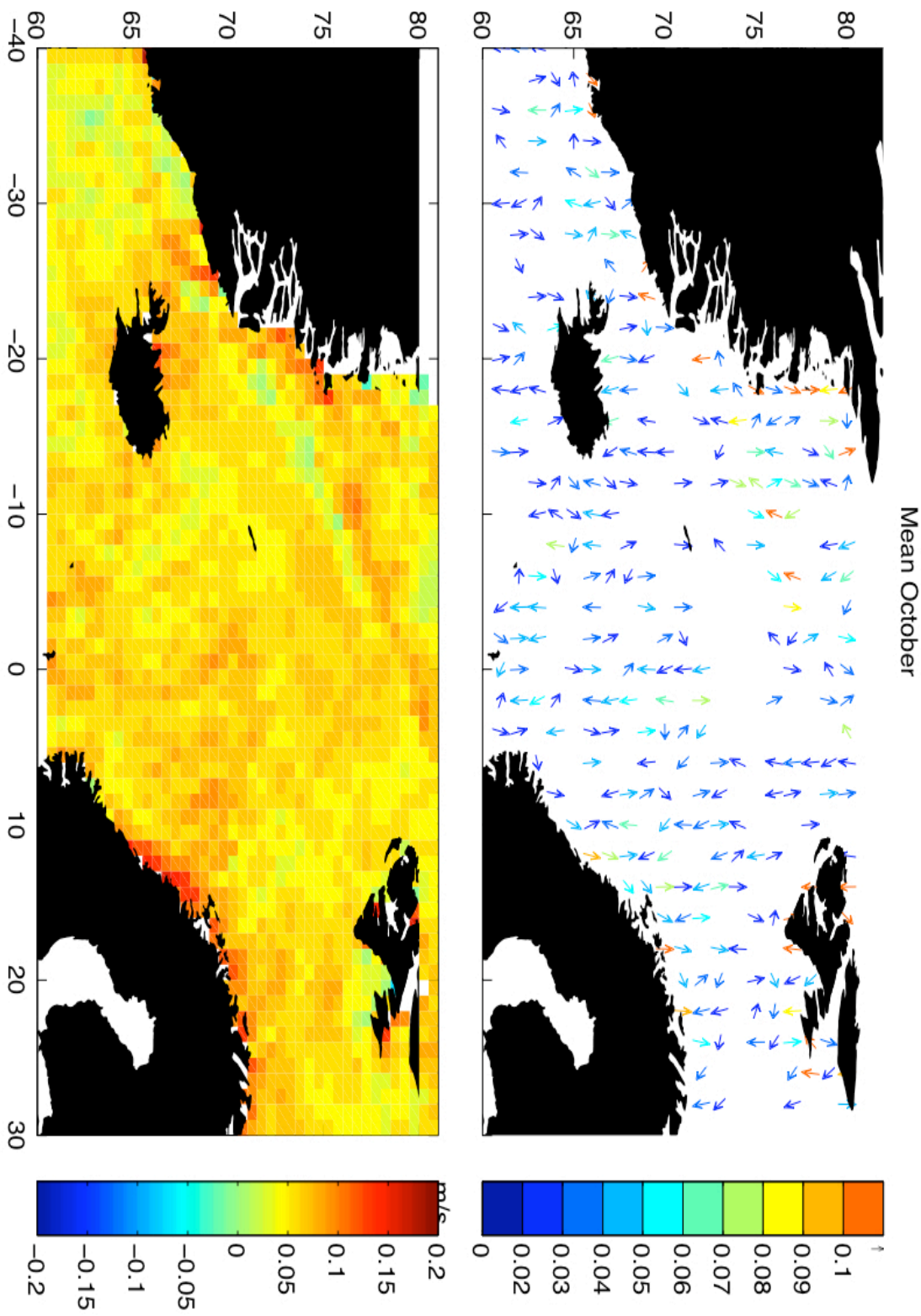

Figure 5.11. Mean (2003-2009) SSHA (m) and the anomalous surface currents (ms^{-1}) in October.

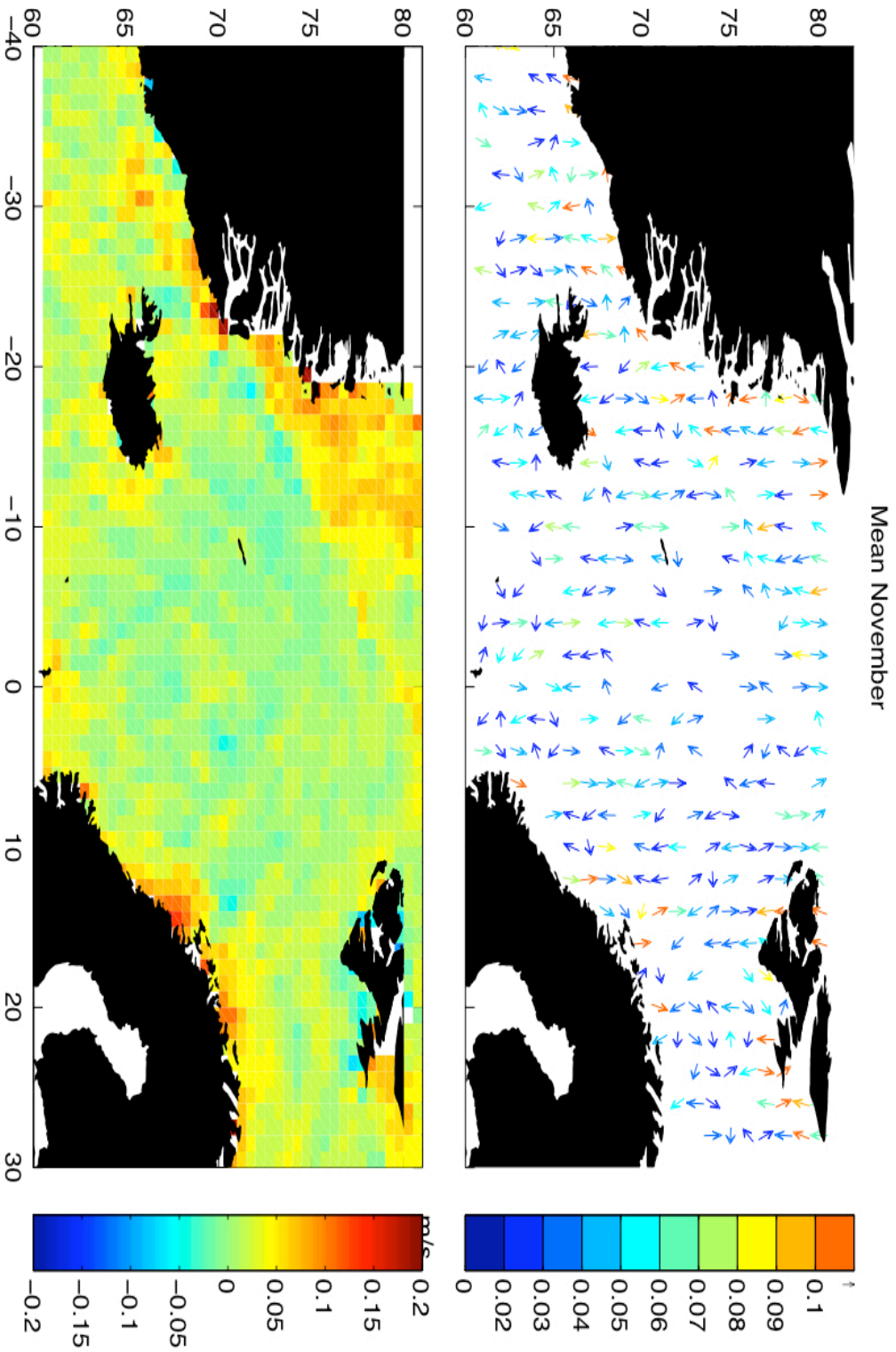

Figure 5.12 Mean (2002-2009) SSHA (m) and the anomalous surface currents (ms^{-1}) in November.

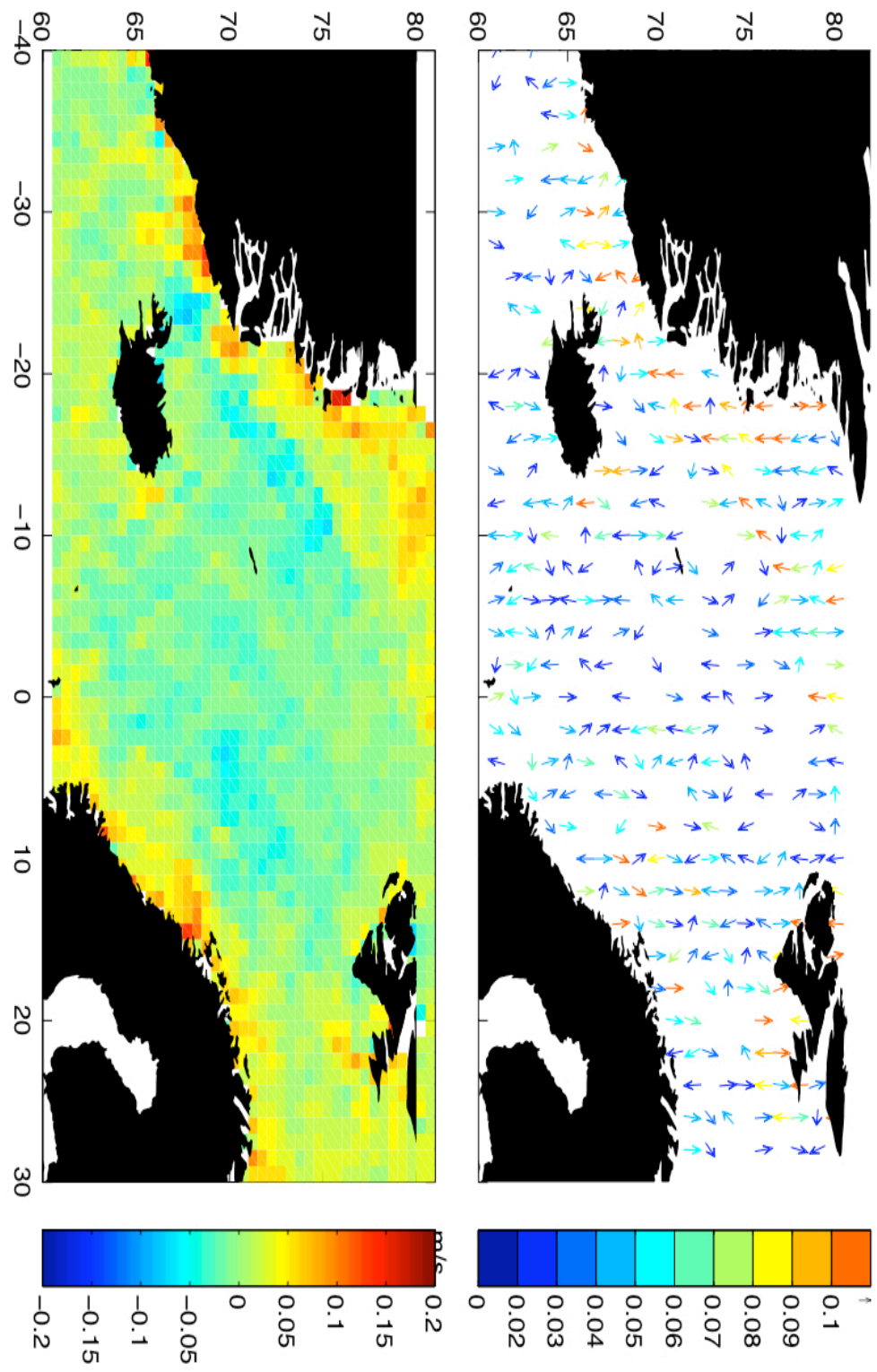

Figure 5.13. Mean (2002-2008) SSHA (m) and the anomalous surface currents (ms^{-1}) in December.

Interannual variability of the surface circulation in the Nordic Seas

The annually averaged surface velocities are shown in Figures 5.14-5.20 as the anomalous velocities with the reference to the mean velocity field over the analyzed time period. Each map corresponds to the temporal average of the currents over one year: November until October and therefore represents the yearly anomalous surface currents (centered on April).

The first year of the record is characterized by the weaker circulation in the whole area except the shelf circulation along the northern coast of Greenland where the current is stronger by about 2-5 cm s^{-1}. The 1st year of the record is also characterized by the two centers of the high SSHA located in the Norwegian and Lofoten Basins and much weaker currents in those basins by about 4 cm s^{-1}. The circulation during the 2nd year of the record (November 2003 – October 2004) continued to be weaker than average especially when considering the EGC. The surface currents in the other regions of the Nordic Seas had similar magnitude to the time mean circulation. The circulation became stronger in the 3rd year of the record (November 2004- October 2005) by about 2-4 cm s^{-1} in the NwAC and 2-6 cm s^{-1} in the EGC. Furthermore, the deep gyres speeded up by about 1-3 cm s^{-1}. The annual mean of the velocity field from November 2005 to October 2006 was characterized by the stronger than average EGC with velocity anomalies reaching about 3-5 cm s^{-1} and slightly stronger WSC (2-3 cm s^{-1}). In the 5th year of the record the EGC speeded up and reached its maximum in the investigated time period. The corresponding SSHA field was the greatest in the ice-covered regions and much lower elsewhere.

The annually averaged velocity form November 2007 to October 2008 was characterized by the stronger velocities of the EGC with the peak values of about 6-7 cm s^{-1} in the Fram Strait and at 67-68^{0}N. On the other hand, the WSC was slightly weaker in the Fram Strait by about 2-3 cms^{-1} but the velocities in the southern part of the NwAC were stronger by about 3-5 cm s^{-1}. During the last year of the record the strongest currents occurred at the Greenland continental shelf. Furthermore, the circulation in the Irminger Sea was the strongest in the considered 7 years but the rest of the region had the current speeds similar to the time mean circulation.

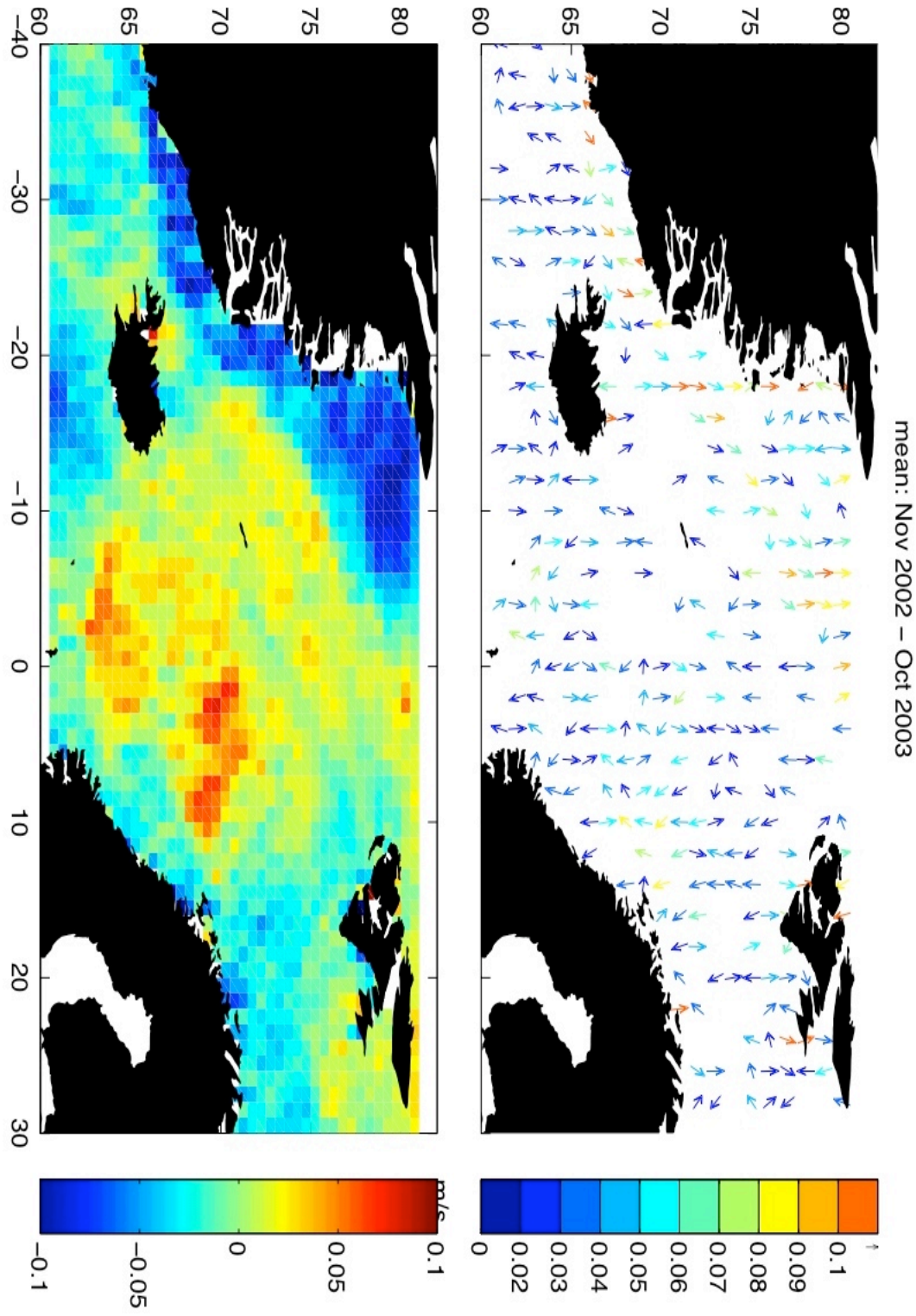

Figure 5.14. Mean SSHA [m] and the anomalous surface currents (ms^{-1}) from November 2002 to October 2003.

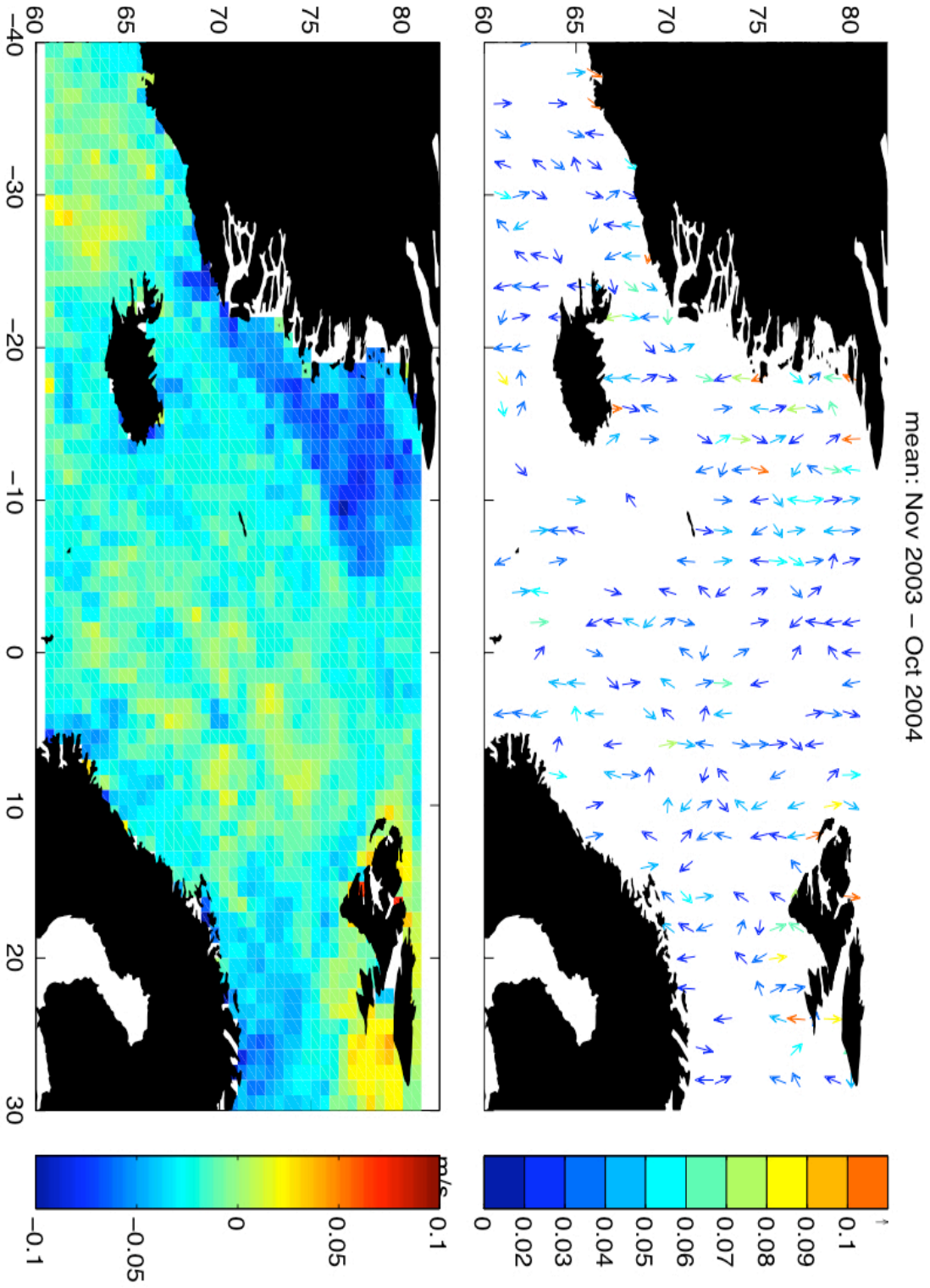

Figure 5.15 Mean SSHA [m] and the anomalous surface currents (ms^{-1}) from November 2003 to October 2004.

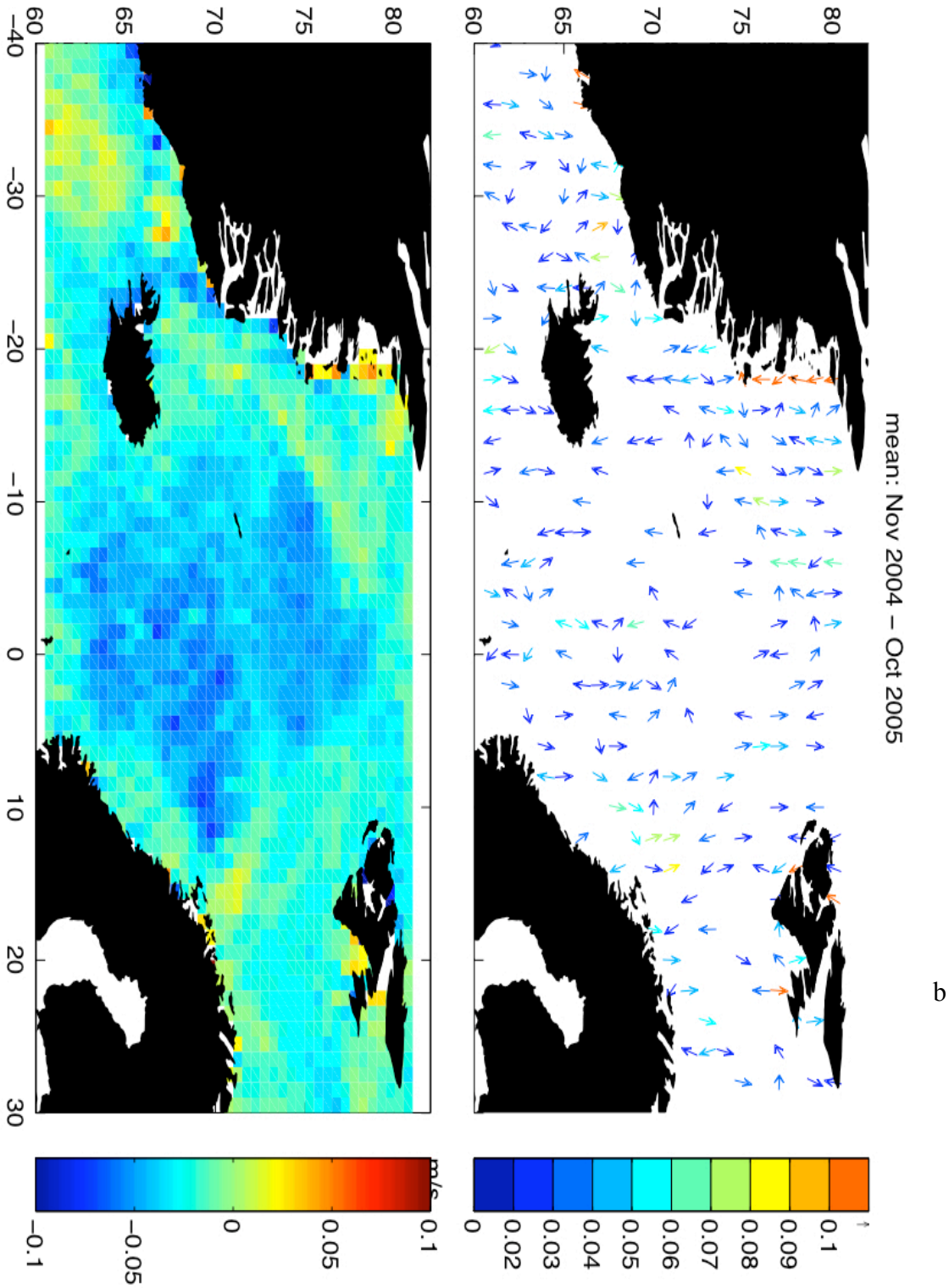

Figure 5.16. Mean SSHA [m] and the anomalous surface currents (ms^{-1}) from November 2004 to October 2005.

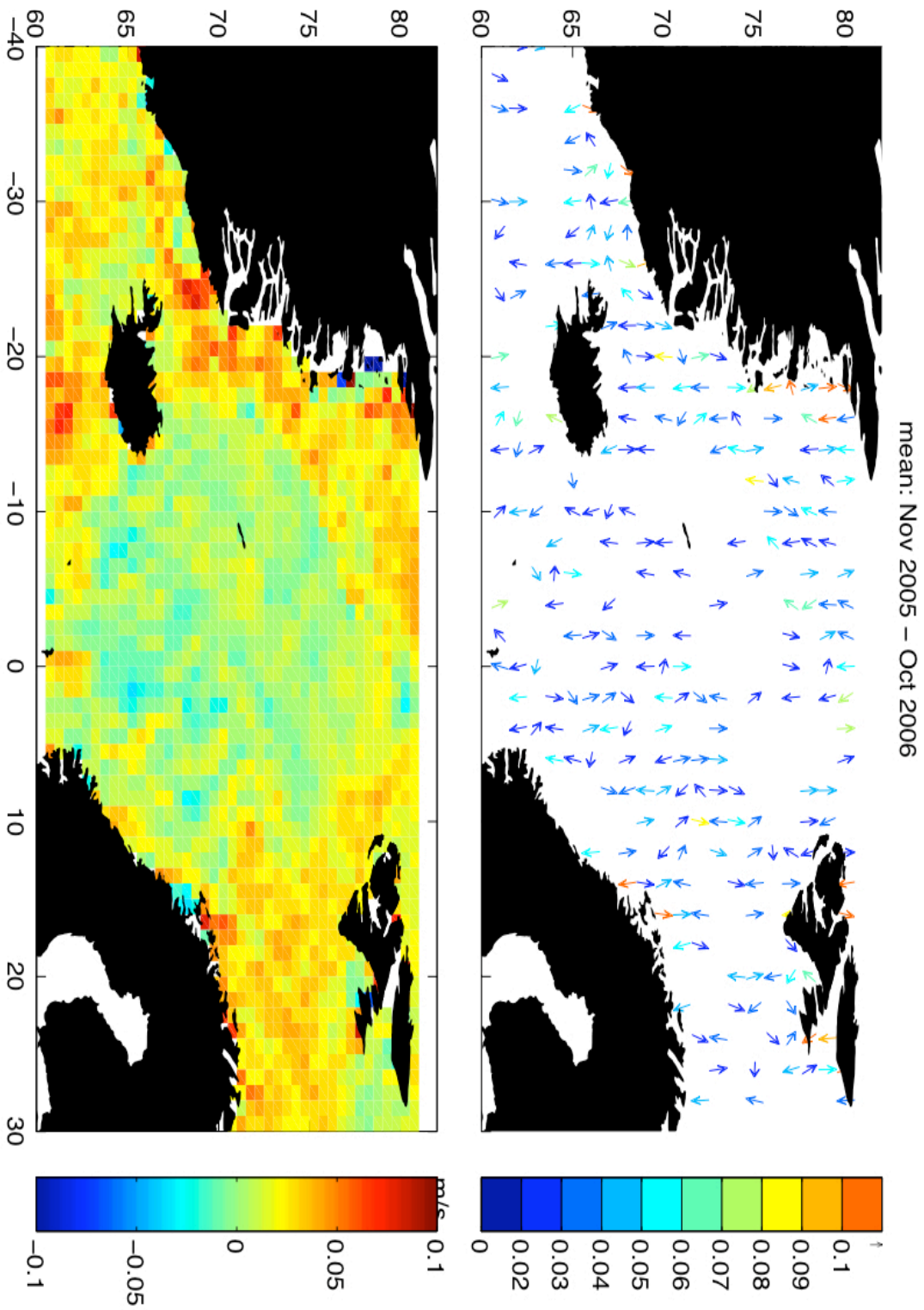

Figure 5.17. Mean SSHA [m] and the anomalous surface currents (ms^{-1}) from November 2005 to October 2006.

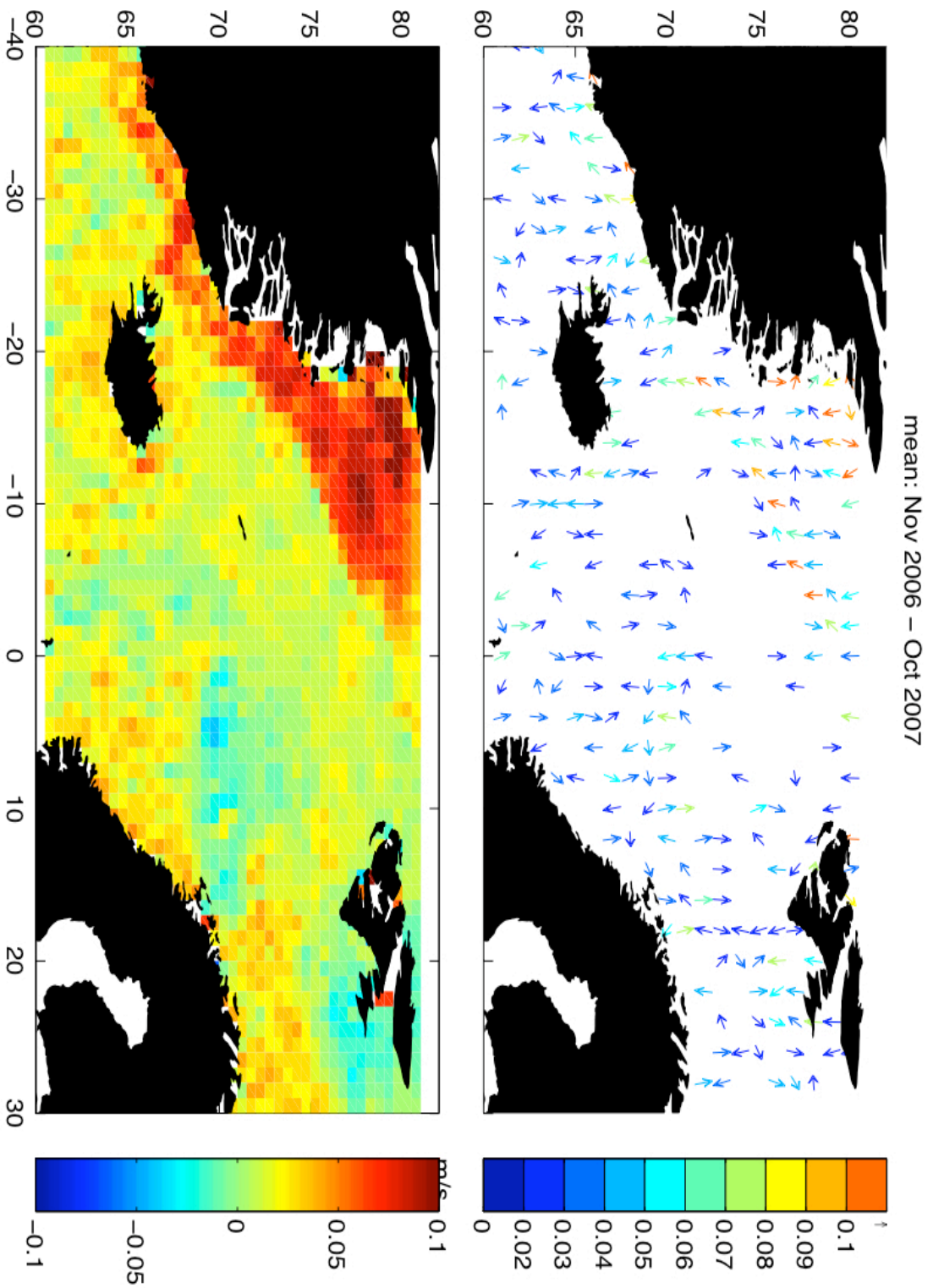

Figure 5.18. Mean SSHA [m] and the anomalous surface currents (ms^{-1}) from November 2006 to October 2007.

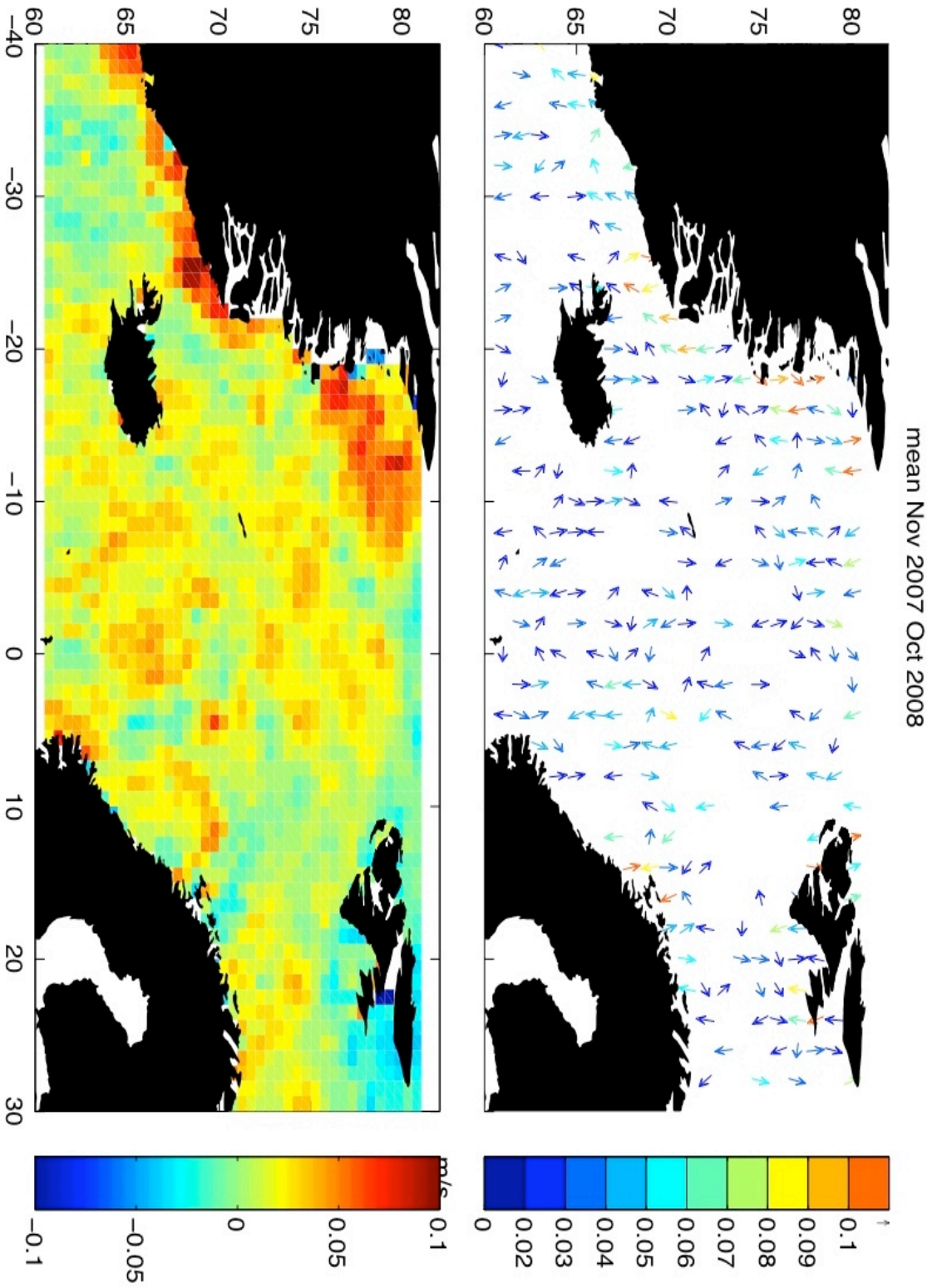

Figure 5.19. Mean SSHA [m] and the anomalous surface currents (ms^{-1}) from November 2007 to October 2008.

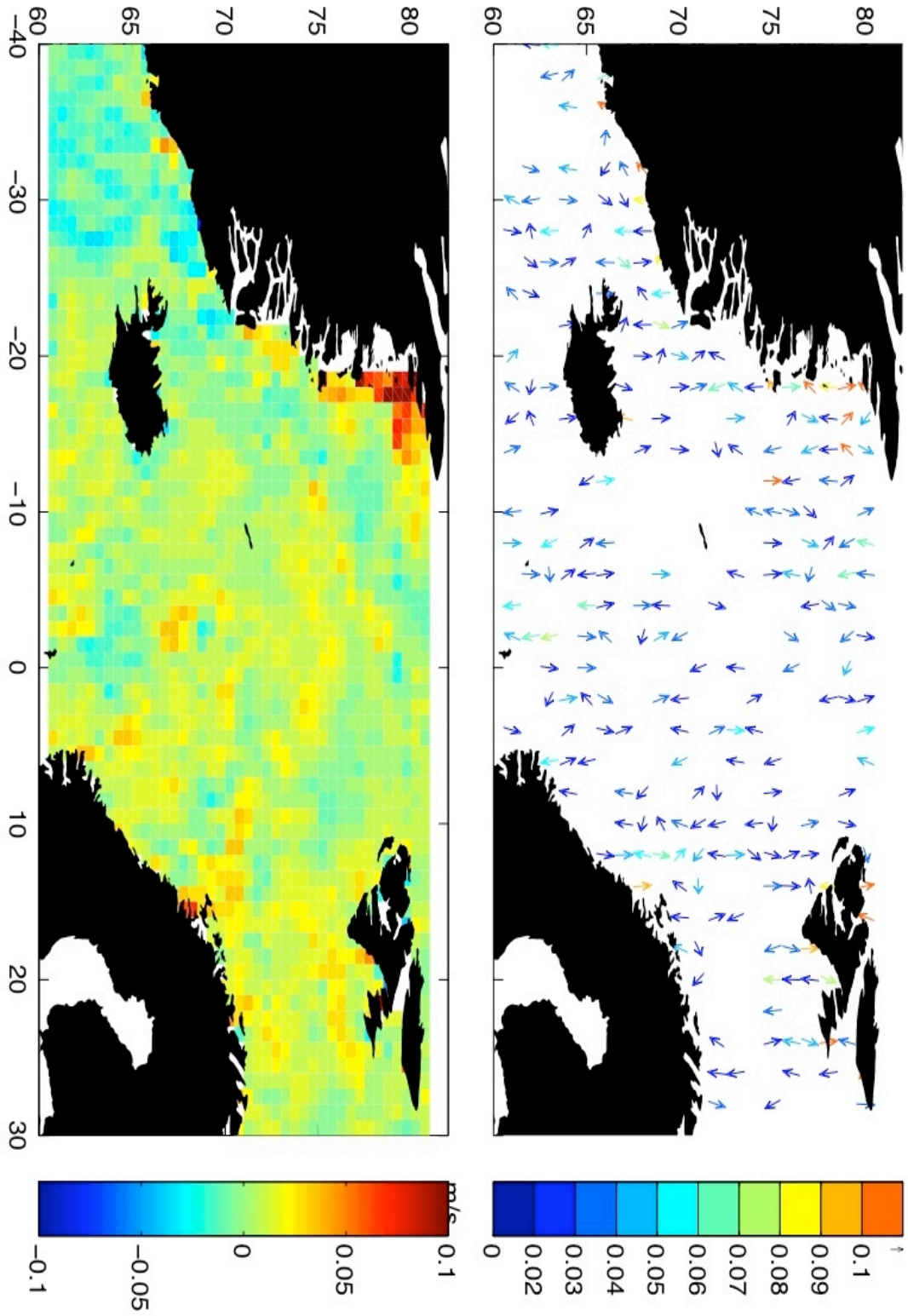

Figure 5.20. Mean SSHA [m] and the mean anomalous surface currents (ms^{-1}) from November 2008 to October 2009.

Eddy Kinetic Energy (EKE)

The satellite altimetry SSHA allowed to calculate the average EKE using:

$$EKE = \frac{1}{2}\left(\left\langle U'^2 \right\rangle + \left\langle V'^2 \right\rangle\right) \qquad \text{EQ. 5.1}$$

Where $\left\langle U'^2 \right\rangle$ and $\left\langle V'^2 \right\rangle$ are the anomalous zonal and meridional components of the geostrophic surface currents obtained using equation 1.1 averaged over the analyzed period. The EKE was calculated on the three different grids: 2^0x1^0, 1^0x0.5^0 and 0.5^0x0.5^0. We are interested in the EKE because oceanic eddies can shape the mean flow and therefore affect the circulation (Thompson et al. 2008, 2010). Furthermore, the lateral eddy mixing is proportional to EKE and often more energetic than the mean current energy, which makes it a significant driving source for the mean current (Richardson, 1983). The obtained EKE is shown in Figure 5.21. The lowest resolution map shows larger EKE along the Greenland coast and at the Greenland continental shelf. Furthermore, the increased EKE is visible in the centre of the Lofoten Basin and along the Norwegian shelf. The higher resolution maps (grid 1^0x0.5^0 and 0.5^0x0.5^0) better resolve the regional variability and show increased EKE along the coasts, which could be also caused by the greater errors in the altimetry data close to the land. The greatest EKE can be also observed along the ice-edge and along the eastern continental slope of Greenland (200-400 cm^2s^{-2}), near Denmark Strait, in the Lofoten Basin (up to 250 cm^2s^{-2}) and to the south of Svalbard (350 cm^2s^{-2}). Furthermore, enhanced values of EKE occur along the Norwegian shelf and Iceland-Faroe Ridge. Very similar spatial patterns of EKE were recently obtained using surface drifters by Koszalka et al. (2011). However, their results described EKE patterns in the ice-free part of the Nordic Seas thus over a much shorter time period (2 years). The good agreement between the two different methods of EKE estimations in the ice-free regions shows that altimetry provides a good tool for studying EKE and suggests that the EKE estimation in the ice-free regions can be also correct. Johannessen et al. (1987) also observed, using the satellite and aircraft photography combined with the temperature-salinity vertical profiles, an intensified mesoscale activity to the east of the EGC between 78°N and 81°N in the marginal ice zone during summer. They have reported the EKE that was twice as much as the kinetic energy of the mean flow and suggested that eddies might contributed to the ice melting. The abundance of the mesoscale eddies was also observed in the Fram Strait and to the north of Svalbard along the ice-edge by Johannessen et al. (1983) and Johannessen et al. (1987) who argued that eddies were

induced by the barotropic instability forced by the wind stress and sea-ice motion. These previous studies agree well with the results obtained by the altimetry in the ice-covered regions. However, our results suggests the enhanced EKE is general to the ice-edge area that often coincides with the eastern Greenland continental shelf.

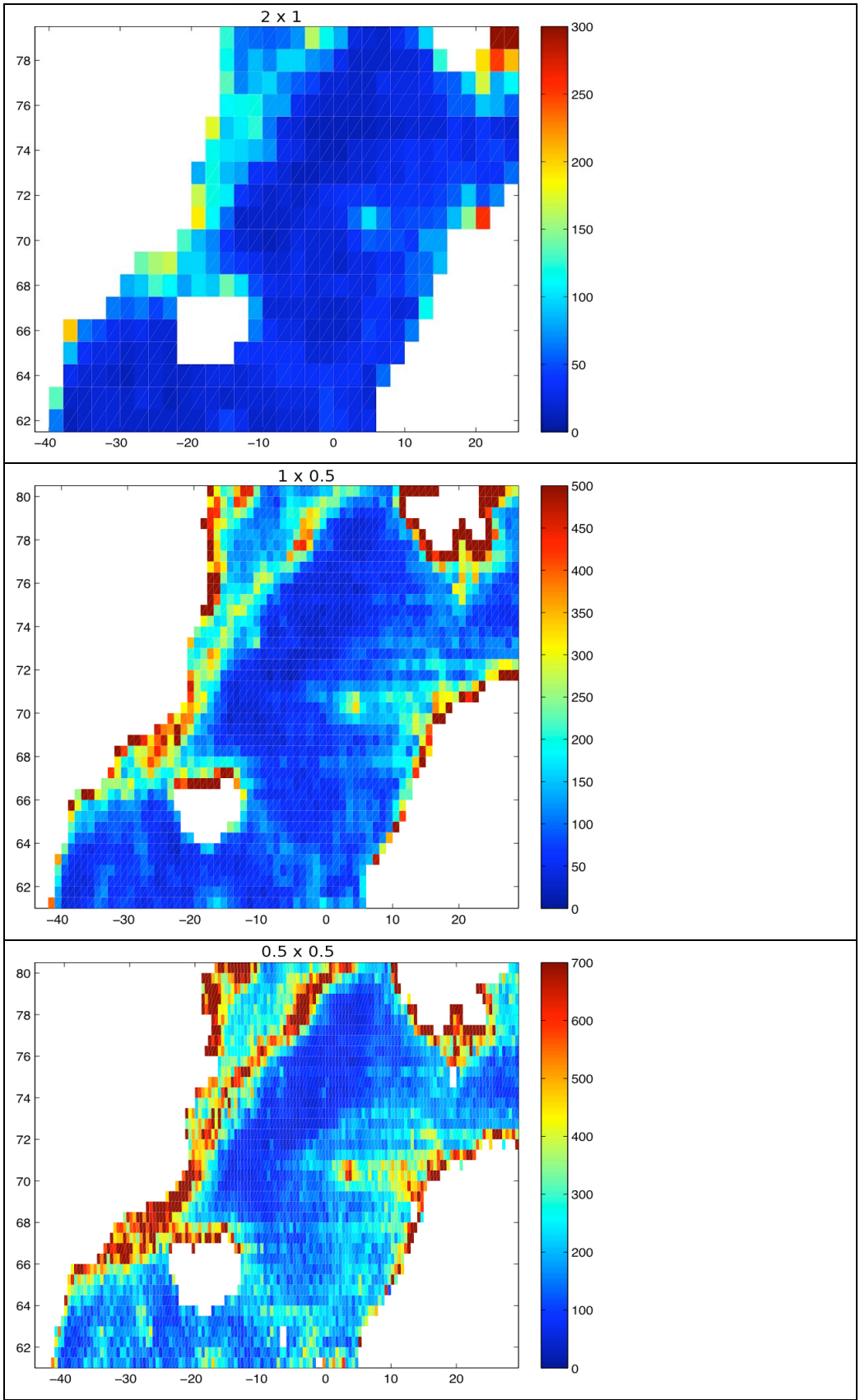

Figure 5.21. Mean EKE calculated for different spatial resolutions [m^2s^{-2}]

5.3 Model validation

Since long-term *in-situ* measurements of the EGC velocity do not exist, we use the model output from NEMO, the numerical ocean model (Chapter 2, Section 2.4) to obtain the vertical structure of the EGC. However, firstly we must be sure that the model output can approximate adequately the real ocean. Therefore in this section the model SSHA is compared to the altimetric SSHA and the model transports at 75^0N are compared to the mooring observations previously described by Woodgate et. al. (1999).

5.3.1.Model SSHA vs. remotely sensed SSHA

In order to compare the observed and modelled SSHA, we use model output from the NEMO model from November 2000 until October 2007. The model output was interpolated on the 0.5^0x0.5^0grid in order to compare with the remotely sensed SSHA. The two datasets of SSHA have a 4-year long overlapping period from November 2002 until October 2007. The temporal variability in the model SSHA data is described as a standard deviation calculated for each grid point in the 7 year long time period and is shown in Figure 5.22. It can be seen that the maximum variability occurs along the coast of Norway and can be associated with the Norwegian Coastal Current. This was also observed by the remotely sensed SSHA (Chapter 3, Figure 3.2) but its standard deviation had about 3 cm greater amplitude in the area. The model SSHA also shows high variability along the southern Greenland coast that may be associated with the southward-flowing freshwater jet called East Greenland Coastal Current (EGCC) (Bacon et. al, 2002). However, the EGCC could not be observed by the altimetry due to unavailability of accurate SSHA close to the coast. The model SSHA also shows higher variability in the GIN Seas as was also observed by the altimetry. Generally, when comparing the observed with the modelled SSHA the agreement between the datasets is good but the modelled SSHA has much smaller variability (30% of the observed). This may be caused by the simplified model dynamics; for example suppressed mesoscale eddies due to the limited model resolution. The modelled variability along the Greenland continental shelf is also much smaller with the amplitude of the standard deviation of about 40% of the observed values. This can be caused by the limited sea-ice dynamics that is greatly simplified by the model.

The next step in the assessment is the comparison of the seasonal cycle of the observed and modelled SSHA. The mean seasonal cycle of the modelled SSHA is shown in Figure 5.23. The sea level is high at the borders of the Nordic Seas and lower in the central Nordic Seas in the winter (October-February). During the spring (March-May) the sea level is almost the same in the whole region and gradually increases from May in the central Nordic Seas. This large-scale SSHA seasonal variability is in agreement with the altimetry observations (Chapter 3, Figure 3.1). The phase of the annual cycle of the modelled SSHA is also very similar to the observations (Figure 5.24) and shows that the highest sea level occurs in August and September in the central Nordic Seas and during the winter (November and December) at the eastern and western borders. However, the amplitudes of the modelled SSHA annual harmonic are 50% smaller in the GIN Seas. In the rest of the Nordic Seas the amplitudes of the annual harmonic of the modelled SSHA have similar values (Compare Figures 5.24 with 3.5). Therefore, we can conclude that the annual cycle of the SSHA is well represented in the model. This argument was further confirmed with the point-to-point correlations of the two SSHA data sets (Figure 5.25), which indicate significant correlations in the whole area except a few regions: the ice-edge, a region to the southwest of Svalbard, Belgica Bank and a narrow region adjacent to the southern Greenland coast. The correlations between the seasonally filtered SSHA data were weaker but significant in the GIN Seas, Barents Sea and a region located to the north of Fram Strait and Svalbard.

The variability of the modelled SSHA was also investigated with the Empirical Orthogonal Functions and the results of the analysis are presented in Figure 5.26. The 1st EOF of the modelled SSHA explains 54% of the total variance and describes the in-phase oscillations of the whole Nordic Seas with the largest amplitudes observed along the Greenland and Norwegian coasts, the regions associated with the freshwater flow. The 2nd EOF explains about 15% of the modelled SSHA variance and describes the antiphase oscillations between the deep basins and the borders of the Nordic Seas. The oscillations have the greatest amplitudes at the eastern border. The 3rd EOF of the modelled SSHA explains 6% of the total variance and describes antiphase oscillations between the Irminger Sea/Greenland Continental Shelf and the rest of the Nordic Seas. All the first three EOFs of the modelled SSHA explain together 75% of the total variance and show oscillations mainly with the annual frequency. Only the 2nd EOF's spatial structure is similar to the observed EOFs described in Chapter 3. However, the

timeseries of the first three EOFs are very similar to each other (Figure 5.26). This could be due to the good representation of the modelled SSHA annual cycle, its similar phase and amplitude. The differences in the spatial patterns could be caused by the annual variability that is more important in the coastal areas in the model (Figure 5.24) but much less important in the observed data (Chapter 3, Figure 3.5). The removal of the seasonal cycle from the modelled SSHA makes the spatial patterns more similar to the EOFs obtained for the measured SSHA (Figure 5.27). The 1st EOF of the filtered modelled SSHA explains 39% of its variance and describes the oscillations of the deep gyres. It shows similar trend in its time series to the trend observed in the 1st EOF of the filtered altimetric SSHA. The 2nd EOF of the modelled SSHA explains about 11% of the total variance and describes antiphase oscillations of the central Nordic Seas and its borders. The spatial pattern and its time series are very similar to the 2nd EOF of the observed SSHA. The 3rd EOF of the modelled SSHA explains 7% of its variance and describes antiphase oscillations between the western and eastern parts of the Nordic Seas.

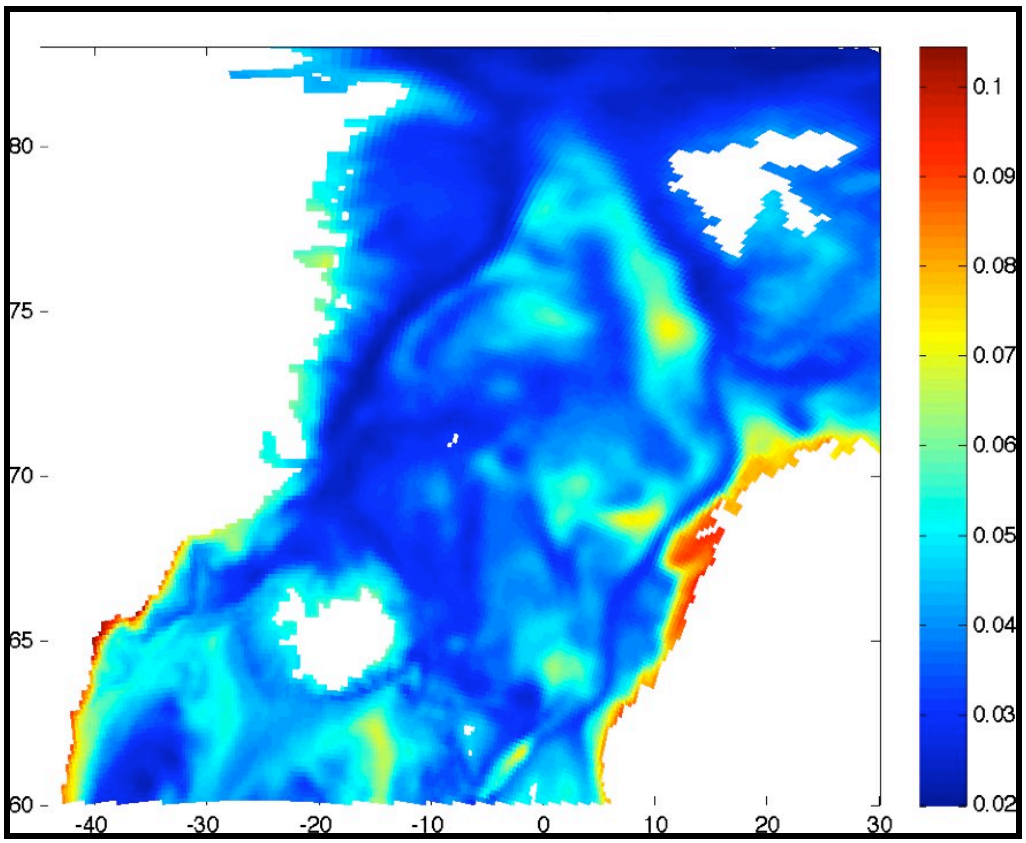

Figure 5.22. Standard deviation [m] of the NEMO SSHA from 2000 to 2007.

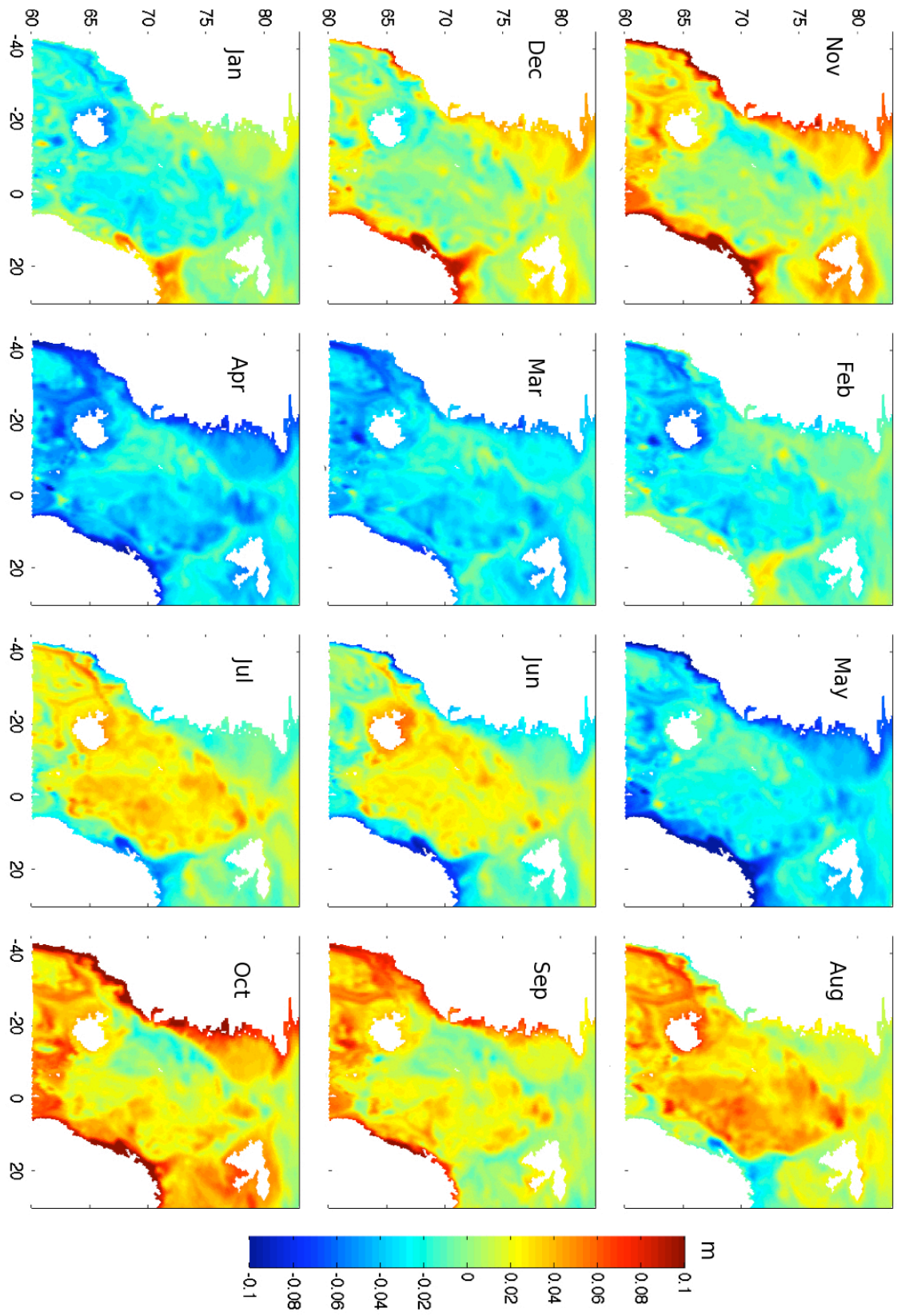

Figure 5.23Mean Seasonal Cycle of SSHA in the NEMO model in 2000 - 2007.

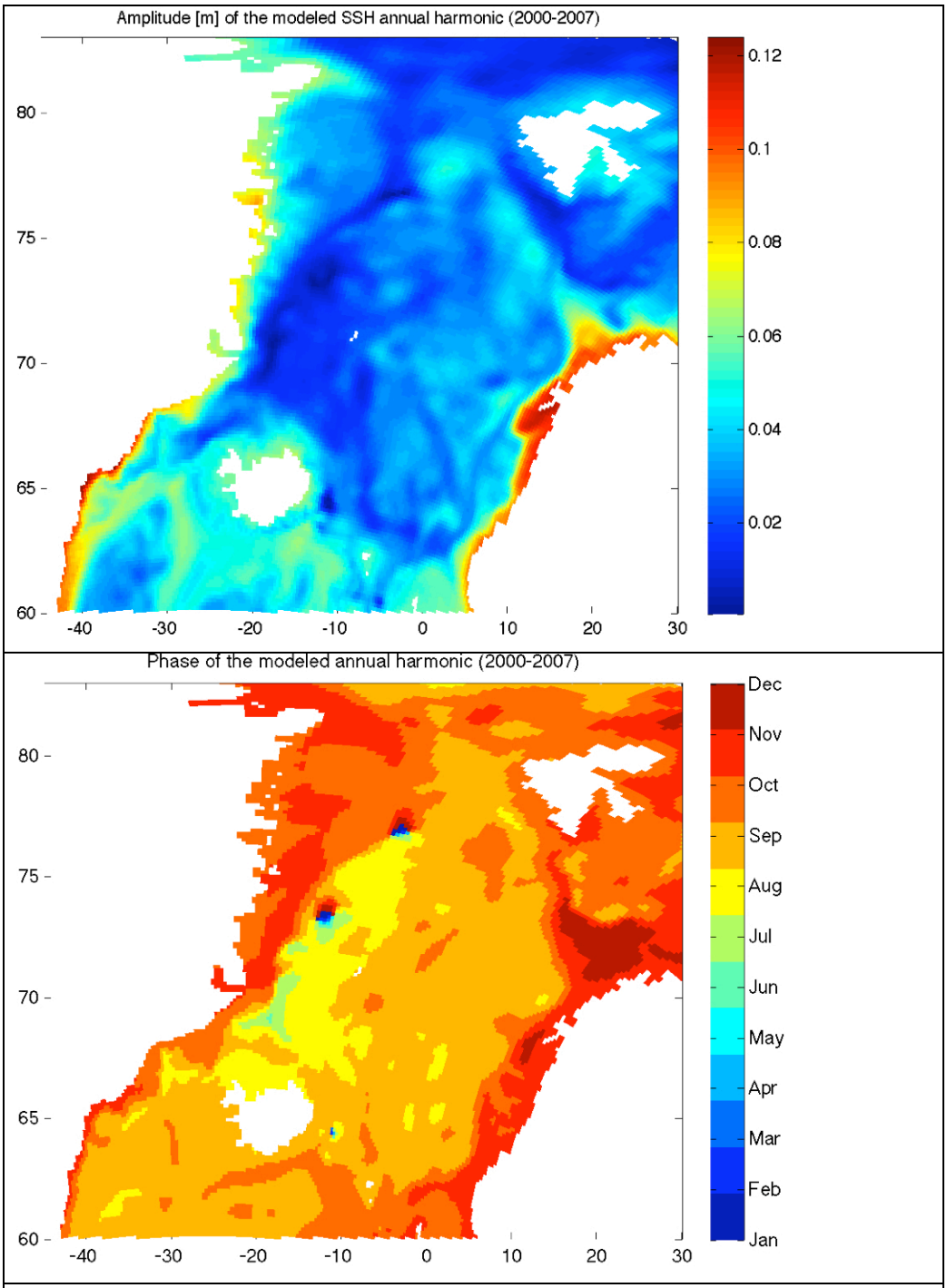

Figure 5.24. Amplitude [m] and phase of the SSHA seasonal cycle (2000-2007) in the NEMO model.

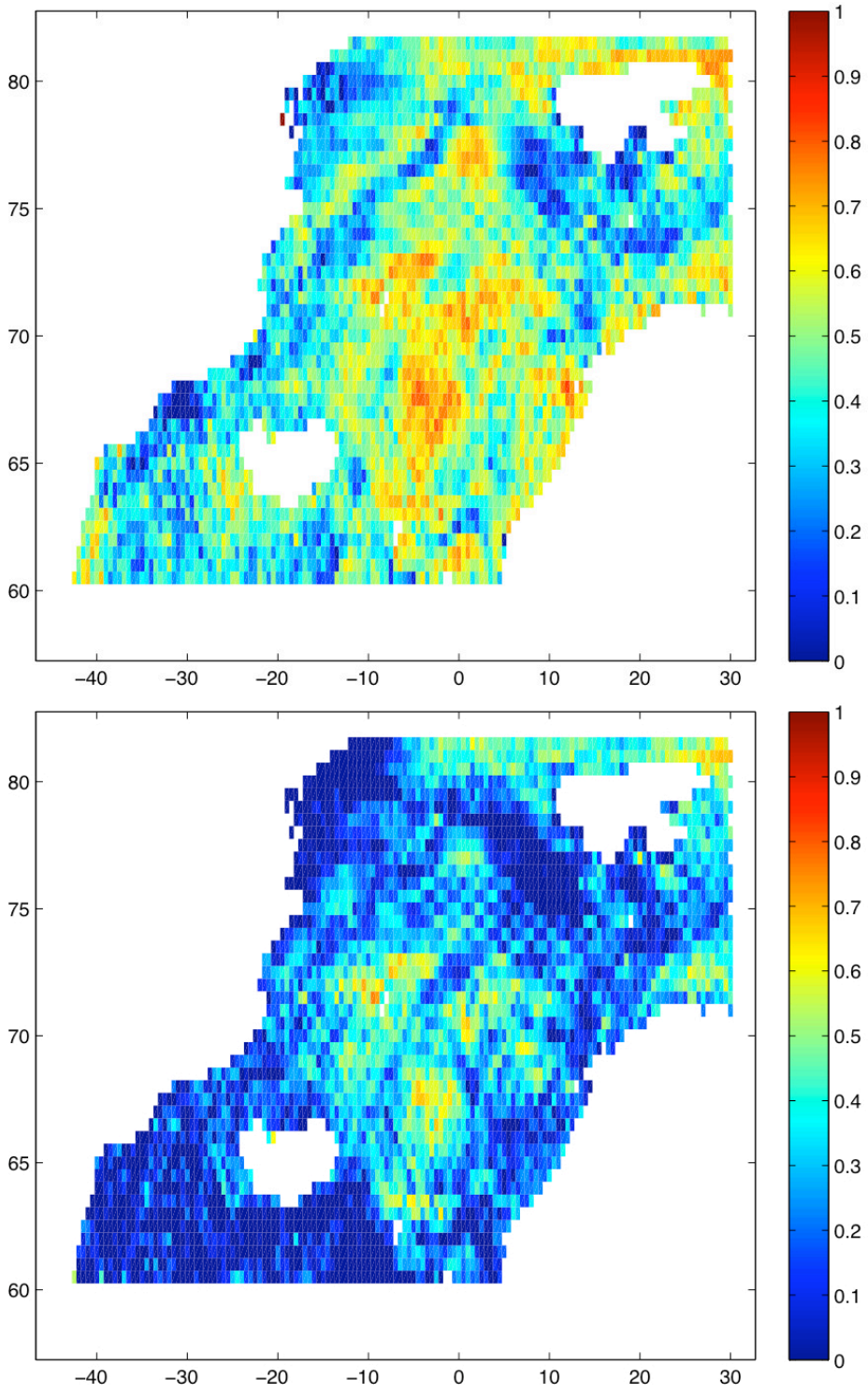

Figure 5.25 Correlation coefficient for the NEMO SSHA and Envisat SSHA for the whole data (top) and seasonally filtered data (bottom).

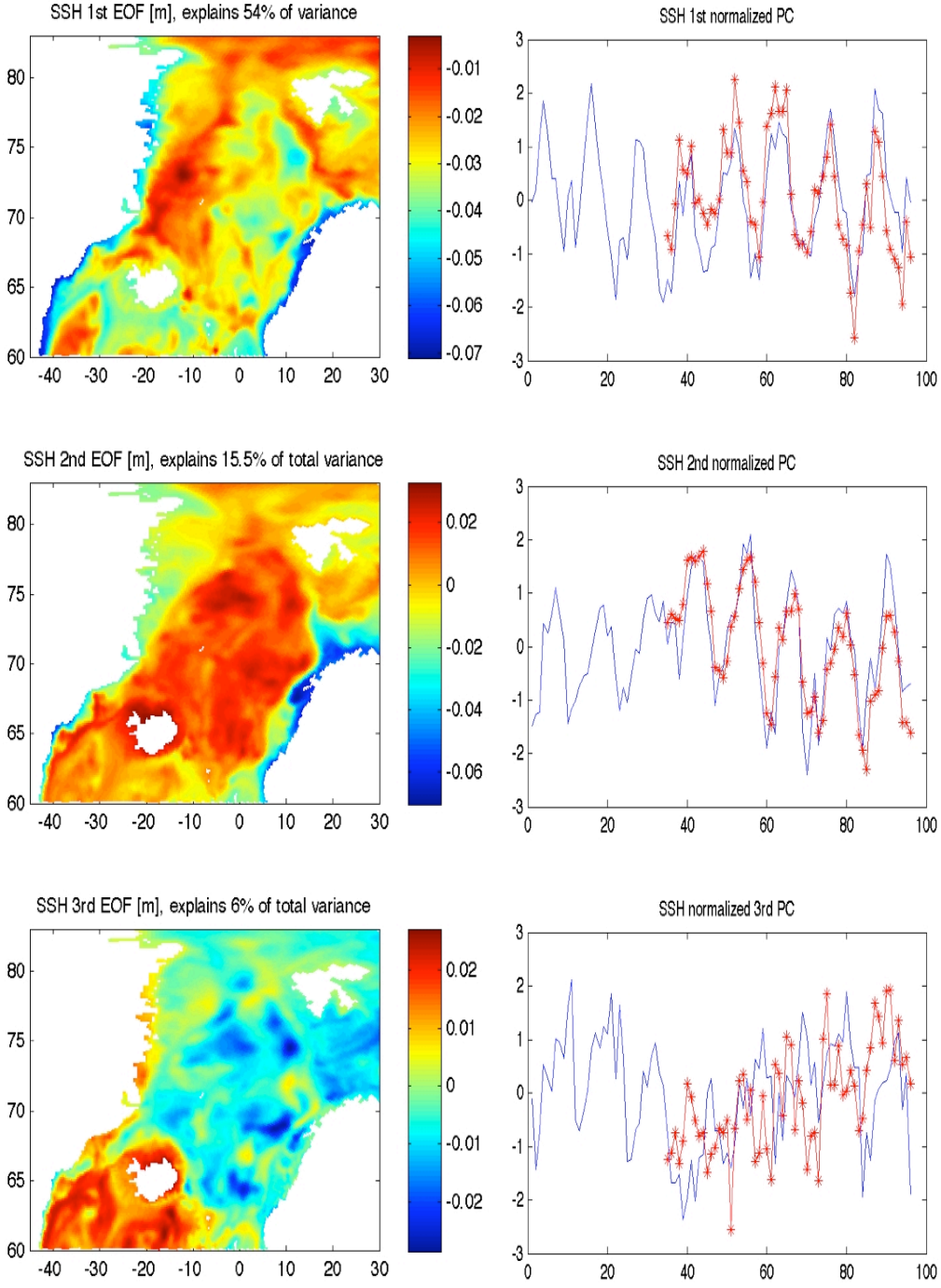

Figure 5.26. EOFs of the NEMO SSHA- comparison with the remotely sensed PCs of SSHA (right) in red.

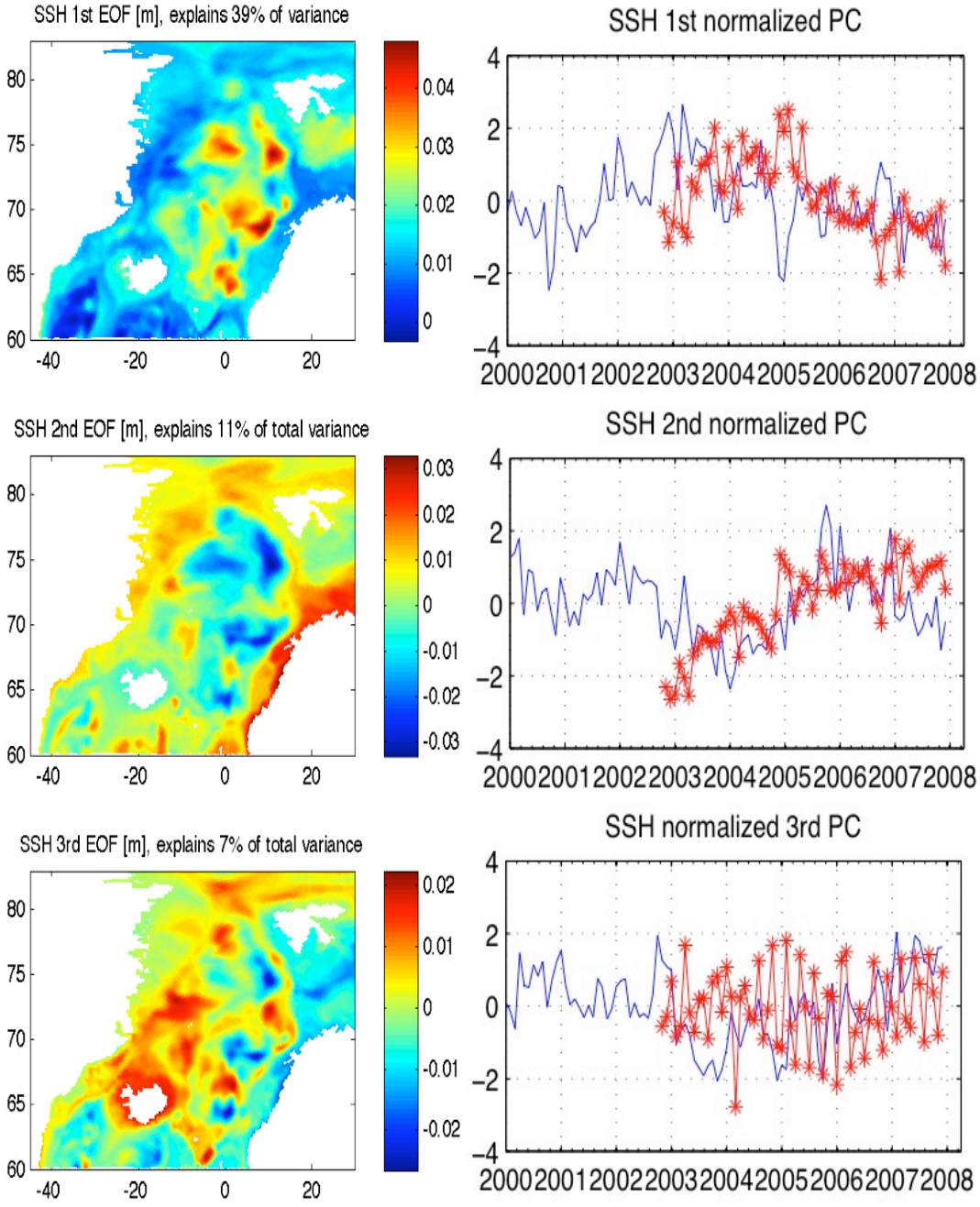

Figure 5.27. EOFs of the seasonally filtered NEMO SSHA- comparison with the remotely sensed PCs of SSHA (right) in red.

5.3.2. Model transport at 75^0N- comparison with a mooring array.

In this section the model velocity and transport of the EGC is compared to the mooring observations located at 75^0N that were described by Woodgate et al. (1999). The same time period is used for the comparison: August 1994- July 1995. The annually/monthly averaged transports and meridional velocities of the EGC are compared to the mooring observations. The cross-section of the annually averaged meridional velocity is shown in Figure 5.28. The core of the modelled EGC lies over the continental slope at depths from 1000m-3400m. The current is located between 9^0W-12^0W and its velocity is the strongest at the surface and decreases with depth. The current is also strong (annual mean northward velocity= 6-10 cm s^{-1}) close to the seabed where the maximum depth reaches 1000-1500m (Figure 5.28). The modelled EGC at 75^0N is shifted about 30km to the west when comparing with the mooring observations but this could be caused by the shifted location of the model section due to the model grid resolution and not exactly the same orientation of the cross section. However, the core of the current is located in the similar location at the continental slope in very similar depths (1-3km) as the observations of Woodgate et al (1999) suggest. The mean northward velocity profile is also very similar as measured previously but show greater velocities very close to the surface (this could not been observed by the mooring array due to the limited vertical resolution) and lower velocities observed next to the bottom (about 4 cm s^{-1} comparing to about 8 cm s^{-1} measured). In the deepest waters the current is much weaker and its velocity decreases almost to zero at the eastern edge of the section. This is consistent with the mooring observations but the sparse horizontal resolution of the mooring array makes the comparison hard in the deeper part of the section.

Time series of cross section of the monthly mean northward velocity are shown in Figure 5.29. The modelled current has strong seasonal variations; it is the strongest during winter (December to March) and the weakest in the summer (May-July). The greatest velocities occur at the surface in January and exceed 20 cm s^{-1}, which is consistent with the previous observations of Woodgate et al. (1999). The core of the current is located more to the east between 500-1000m depths during almost all the seasons, except winter. In November, June and July the current has two cores: one at the sea surface and another at depths from 500-1000m located more to the west. Two cores were also observed by the mooring array *in situ* in August and January but they were

both the strongest at the sea surface. The modelled EGC is therefore more coherent when comparing to the previous observations of Woodgate et al. (1999), but shows similar seasonal variations of the current with depth. To adequately compare the modelled current with the real one, the depth-averaged northward velocities are compared. The results are shown as a time-distance plot in Figure 5.30 and show the strengthening of the current in the winter and in the autumn (September until November) closer to the Greenland continental shelf. The comparison with Figure 6 of Woodgate et al. (1999) reveals that the two plots are quite similar especially at the central and the eastern parts but the observed depth-averaged velocities are greater in the shallow depths. The transports of EGC were calculated using the mean section velocity and the same area as in Woodgate et al. (1999). The time series of the mean section velocity and the corresponding transports are shown in Figure 5.31. For the whole cross section (180km) the largest transports of about 35 Sv were found in January and the weakest were obtained from May to November (15 Sv).

Woodgate et al. (1999) observed similar seasonal amplitudes of the EGC transport but found dual peaks in their time series that occurred in January and March. They argued that the large seasonal cycle of the transport observed by the mooring array is mainly caused by the barotropic response of the ocean to the local wind forcing. Furthermore, they showed that the dual peaks observed could be caused by the dual peaks in the local wind stress that occurred in the same months. However, the wind stress could not explain the annual mean and therefore the authors suggested the transport consists of the two parts: seasonally wind driven, which is confined to the Greenland gyre (70%) and thermohaline-driven, which shows little seasonal variations (30%).

The transports of the modelled EGC across the section located at 75^0N are compared to the mooring observations in Table 5.1. The two estimates of transports agree quite well with each other when considering the whole cross section (180 km). The differences fall within the limits of the error bars estimated by Woodgate et al. (1999). The model mean annual transport in 1994-1995 is weaker when compared to the mooring observations over the two smaller cross sections that are located between 14^0W and 10^0W and 14^0W and 9^0W. This is probably caused by the inaccurate model bathymetry and a shifted location of the core of the current, which is about 20km to the east when comparing with the mooring observations.

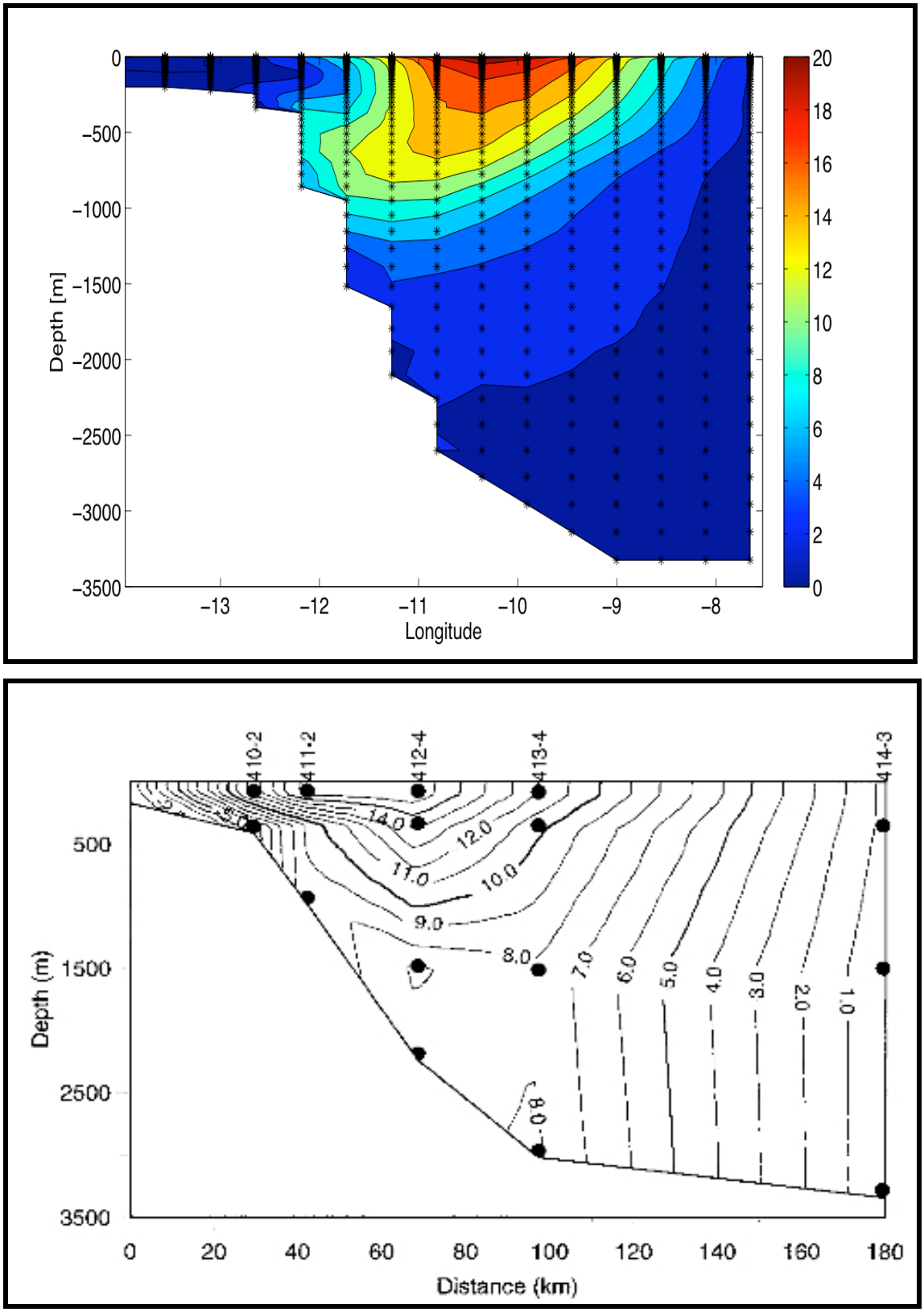

Figure 5.28 Cross section at 75^0N from 140W (left) to 7.5^0W (right) showing annual mean (August 1994-July 2005) meridional velocity (positive southward) in cm/s and the same cross-section obtained from Woodgate et al. (1999, bottom).

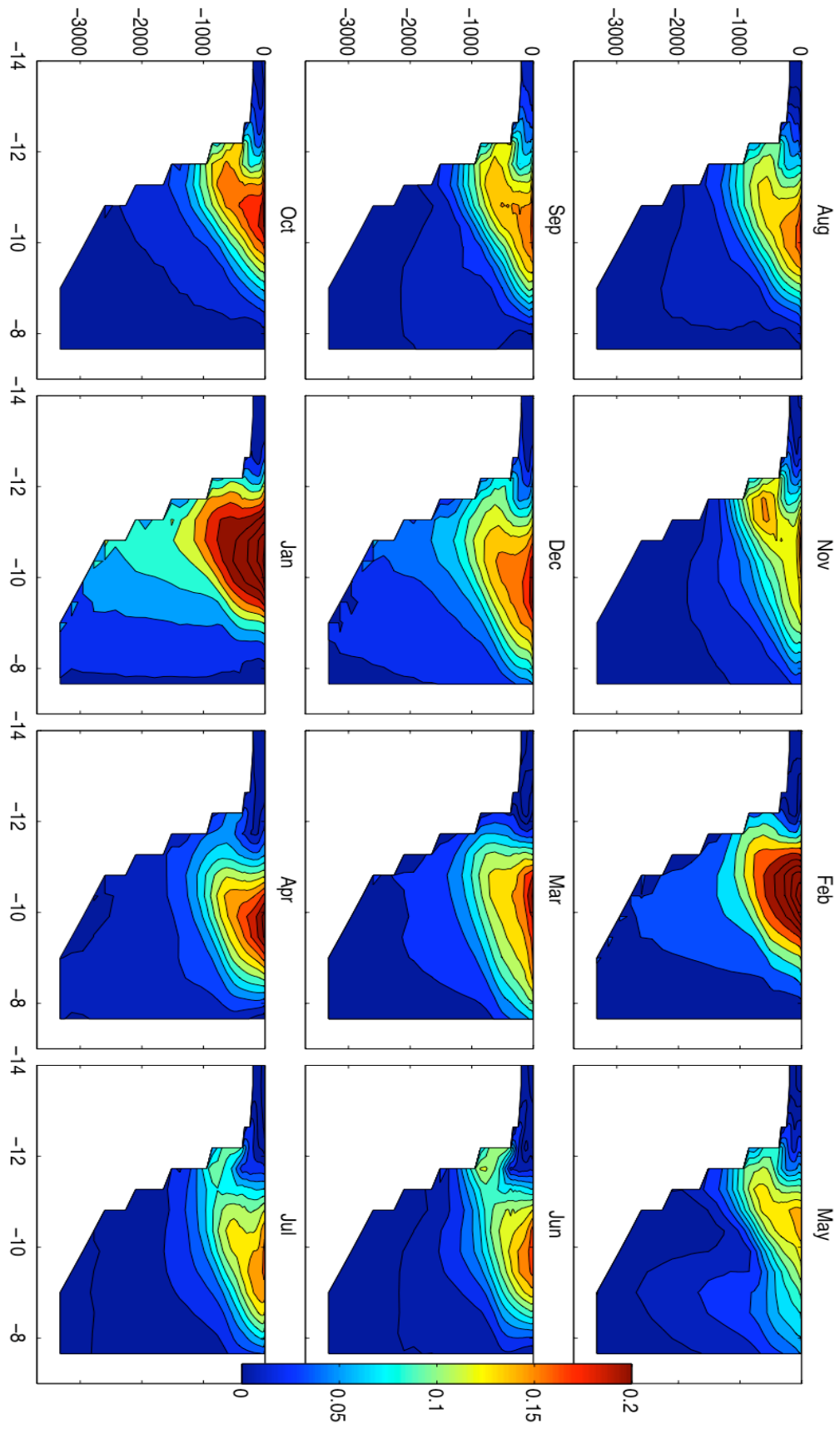

Figure 5.29 Series of cross sections (as in Figure 5.26) of monthly averaged meridional velocity across 75^0N from the NEMO model output.

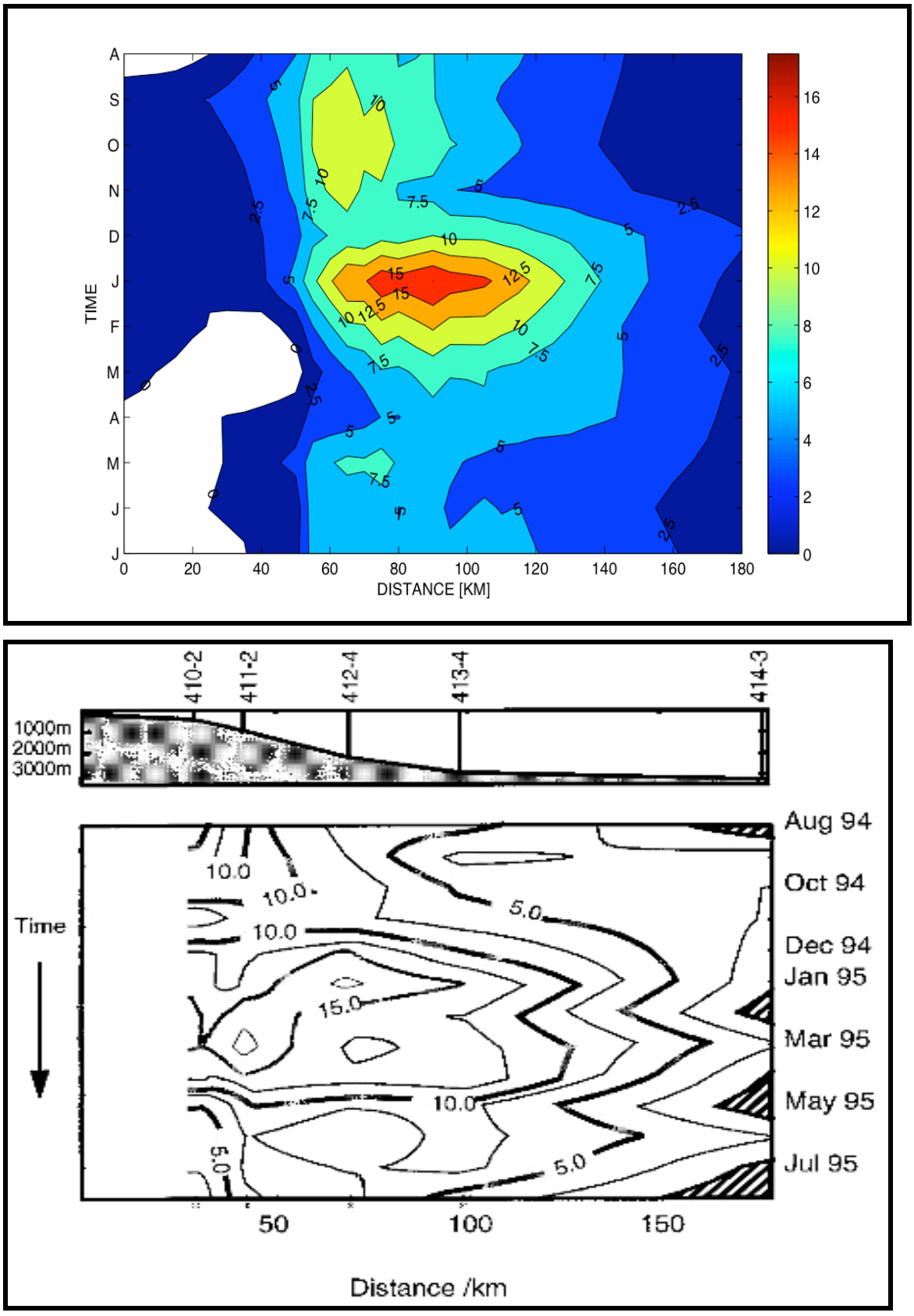

Figure 5.30 Hovemoller diagram of the depth-averaged monthly values of meridional velocity (positive southwards) in cms^{-1} for the cross-section located at 75°N and 14°W-7.5°W and the same section obtained by Woodgate et al. (1999, bottom).

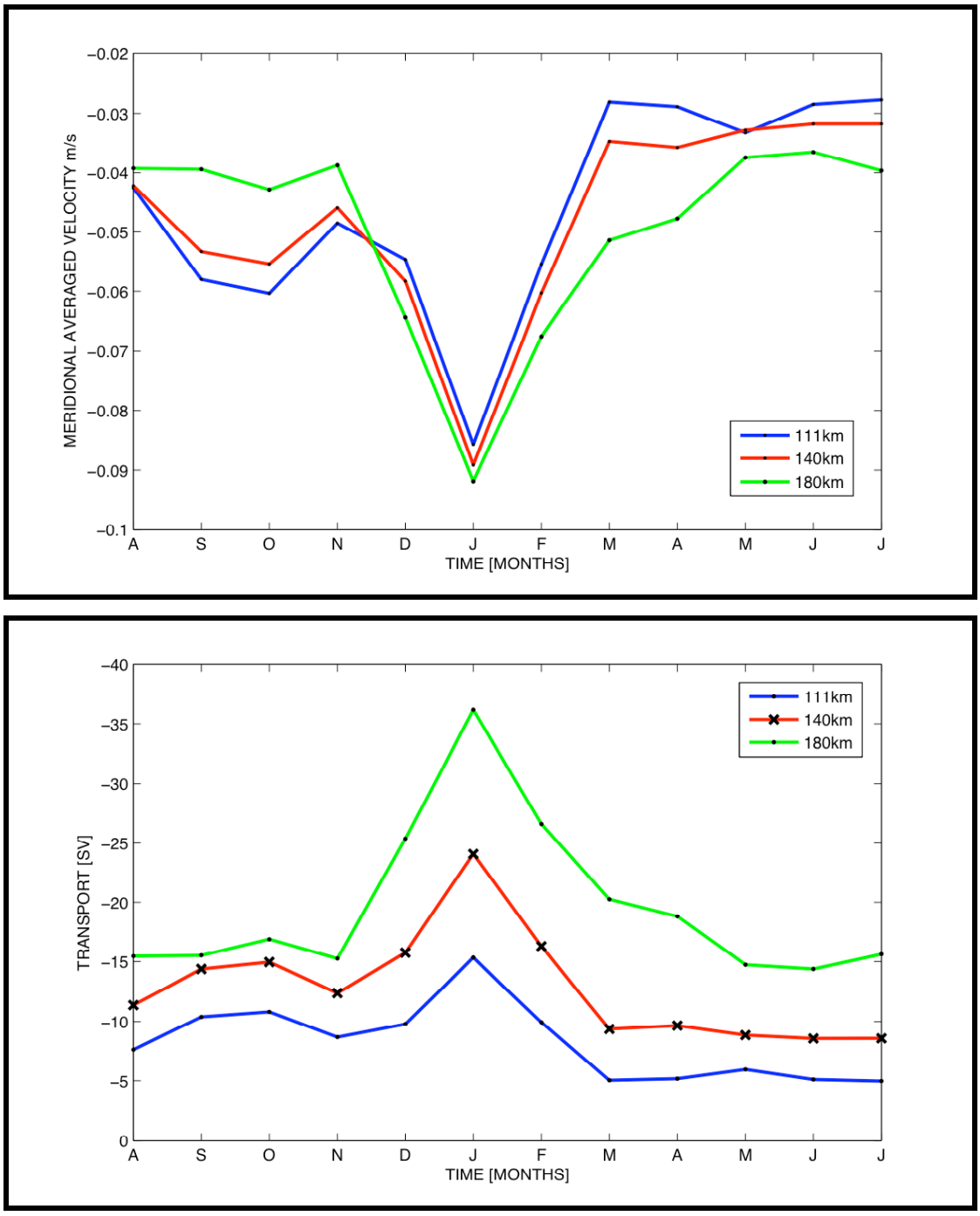

Figure 5.31 Time series of the cross-section mean northward velocity (top) and total transport (bottom) calculated for 111 km, 140 km and 180 km.

	Transport integrated from 14^0W out to		
	111 km~ 10^0W (area=179 km^2)	140 km ~ 9^0W (area =270 km^2)	180 km ~ 8^0W (area=394 km^2)
Annual mean transport [Sv]	**13** (16±2)	**17** (25±4)	**20** (21±3)
Range of seasonal cycle [Sv]	**5-15** (9-27±3)	**8-24** (11-37±5)	**14-36** (14-41±7)

Table 5.1. Comparison of the modelled (bold) and observed transports of the EGC (August 1994-July 1995) for the section located at 75^0N.

5.4 What vertical mode of variability of the EGC does the altimeter reflect?

Sea level measured by an altimeter contains signatures of many ocean processes that are related to the barotropic and baroclinic changes in the ocean circulation. Some attempts have been made to relate SSHA and the interior of the ocean in the low and mid latitudes (5°- 60°). Stammer (1997) has observed that the length scale of zero-crossing of the spatial autocorrelation function of SSHA was proportional to the first Rossby radius of deformation. This suggests that the first-mode processes dominate SSHA variability. Furthermore, an analysis of data from moored current meters led Wunsch (1997) to the conclusion that the near-surface flow field in the interior ocean is primarily baroclinic and that barotropic contributions become important only in the recirculation regime of boundary currents (note that high-latitude regions were not adequately sampled). Numerical simulations also confirmed the above observations. The numerical model simulations of Smith and Vallis (2001) showed for the stratification with a thermocline that the baroclinic mode dominated the barotropic mode. On the other hand, recent results of Lapeyre (2009) showed that the surface mode is important in most of the Atlantic and dominates in the Gulf Stream and the North Atlantic Current. In consequence, the geostrophic velocities measured by the altimeter are most of the time due to the surface mode, and not to the first baroclinic mode (Lapeyre, 2009). The surface mode was defined by Lapeyre et al. (2009) by decomposing the streamfunction into the vertical modes with the surface boundary

condition and therefore the mode is a combination of the baroclinic and the barotropic modes and particular contribution to the mode depend on the spatial scales considered.

The vertical structure of the circulation depends on the vertical stratification and on the Coriolis parameter (Wunsch, 1982). The high-latitude seas are weakly stratified and the Coriolis parameter is quite large, which should make the circulation more barotropic (Guinehut et al., 2006). The relationship between the SSHA and the ocean interior was not explored well in the high latitude regions and the Nordic Seas due to few data available. Furthermore, in the ice-covered seas the relationship was not examined due to a lack of satellite data. In order to determine the nature of velocity variability calculated from SSHA, and transport anomalies derived from surface velocity anomalies, the sea surface height measured by the altimeter must be compared to the in situ velocity observations or a model output.

Barotropic transport is defined as a depth integrated bottom velocity, which is aligned with the depth contours in the Nordic Seas (Woodgate et al., 1999, 2001, Fahrbach et al., 2001). Recent findings of Aaboe et al. (2009) suggest that at least 60% of the barotropic transport in the West Spitsbergen Current has been transformed along the Arctic shelf into baroclinic flow when reaching northern Fram Strait. Further downstream, from Fram Strait towards the Greenland Sea at 75°N, the transport of EGC becomes more barotropic (Schlichtholtz, 2007, Aaboe et al., 2009). Lettmann and Olbers (2005) showed for the Antarctic Circumpolar Current (ACC) that the variability of ACC transport can be dominated by the barotropic mode over short temporal scales (less than a year) and that baroclinic modes are more important for the longer time scales. Can similar variability of the EGC be observed? Which periods in the EGC transport variability are dominated by the barotropic and baroclinic modes? These questions will be investigated in the next subsections using the NEMO model output (See Chapter 2 for description).

5.4.1. Coherence between EGC surface velocity and velocities at other depths.

In Section 5.3.2 the model transports of the EGC through the section located at 75^0N were compared to the mooring observations described by Woodgate et al. (1999). Therefore the investigation of the vertical structure of the EGC begins with the examination of the vertical structure of the EGC at the core of the current located at 75^0N and 10.82^0W. The power spectral density of the velocity magnitude at this location shows that the most energetic flow occurs at semi-annual, annual and longer periods (Figure 5.32). The squared coherence for the surface velocity anomaly and the deeper velocities shows significant coherence for the top 1000m-thick layer and for all periods (Figure 5.32). The significant coherence was found also for the whole water column for the most energetic periods: 4, 6, 12 months (Figure 5.33). This is a sign of the barotropic ocean response at these periods to the local wind forcing. Furthermore, significant coherence was found in the top 1500m-thick layer for periods from 1.2 to 2.2 years and in the top 2000m-thick layer for periods from 3.1-4.8 years. The high coherence reported for the longer periods was caused by the increasing trend of the velocity anomaly in the top 1000m of the water column but no trend was found in the deeper part of the water column. A similar trend was also observed in the barotropic velocity (Figure 5.37), which suggests that the current in the top 1000m is mainly depth-independent. The significant values of the squared coherence were found for the most energetic periods, and for the periods when low coherence occurs there is little energy (Figure 5.32).

The coherence between the surface velocity and the velocities at other depths was also calculated for the whole Nordic Seas and for different periods ranging from semi-annual to decadal. For the short periods (up to 4 months) the coherence in the EGC is significant only in the top 200 m of the water column. In the deeper regions, along the EGC, the significant coherence was only found for the EGC part adjacent to the Greenland gyre (See Appendix). For the annual period the significant values of coherence were found in the whole water column in the broad region from Fram Strait to the north of Denmark Strait along the EGC (Figure 5.34). Similar patterns of the squared coherence were found for the semi-annual and decadal periods. However, for periods longer than the annual but shorter than the decadal the significant coherence was found mainly in the top 1000m-thick layer in the Fram Strait and in the region

along the EGC where the Greenland gyre recirculates (Appendix). The high coherence that was found in the whole water column along the EGC occurs at the same periods as the wind forcing and suggests the ocean response at semi-annual, annual and decadal frequencies is mainly barotropic (Figure 5.35). To sum up, the coherence maps indicated a barotropic response of the EGC when the wind forcing occurs in the model with periods of 6 and 12 months, and 10 years. For the other periods the baroclinic response becomes important, however significant coherence was observed for these periods in the top 1000m of the water column along the EGC, from the Fram Strait to the Denmark Strait.

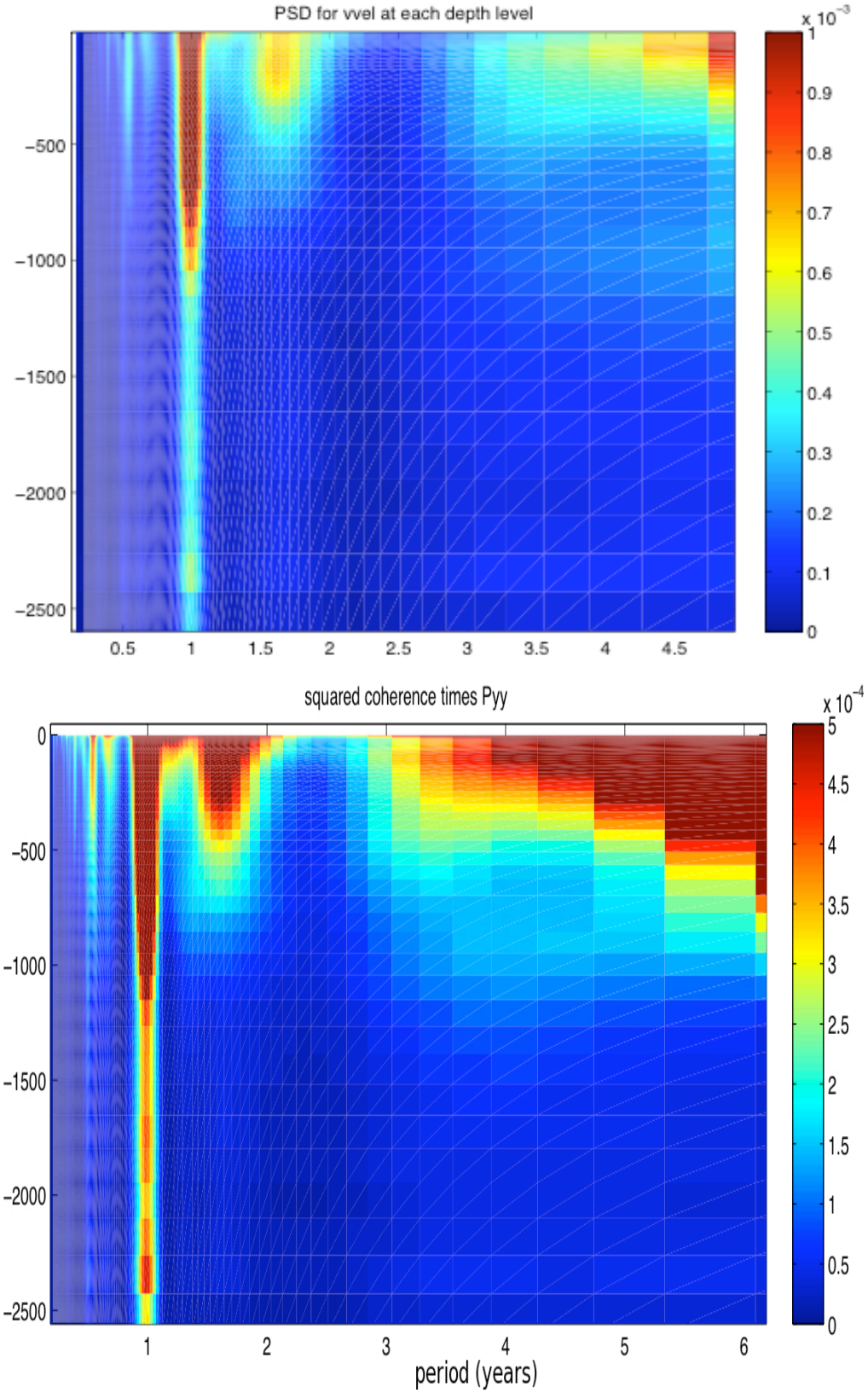

Figure 5.32. Power spectrum density (PSD) of the meridional velocity (top) and PSD of the meridional velocity component multiplied by the squared coherence between the surface velocity and the velocity at other depths (bottom) at the core of EGC at 75°N, 10.8°W.

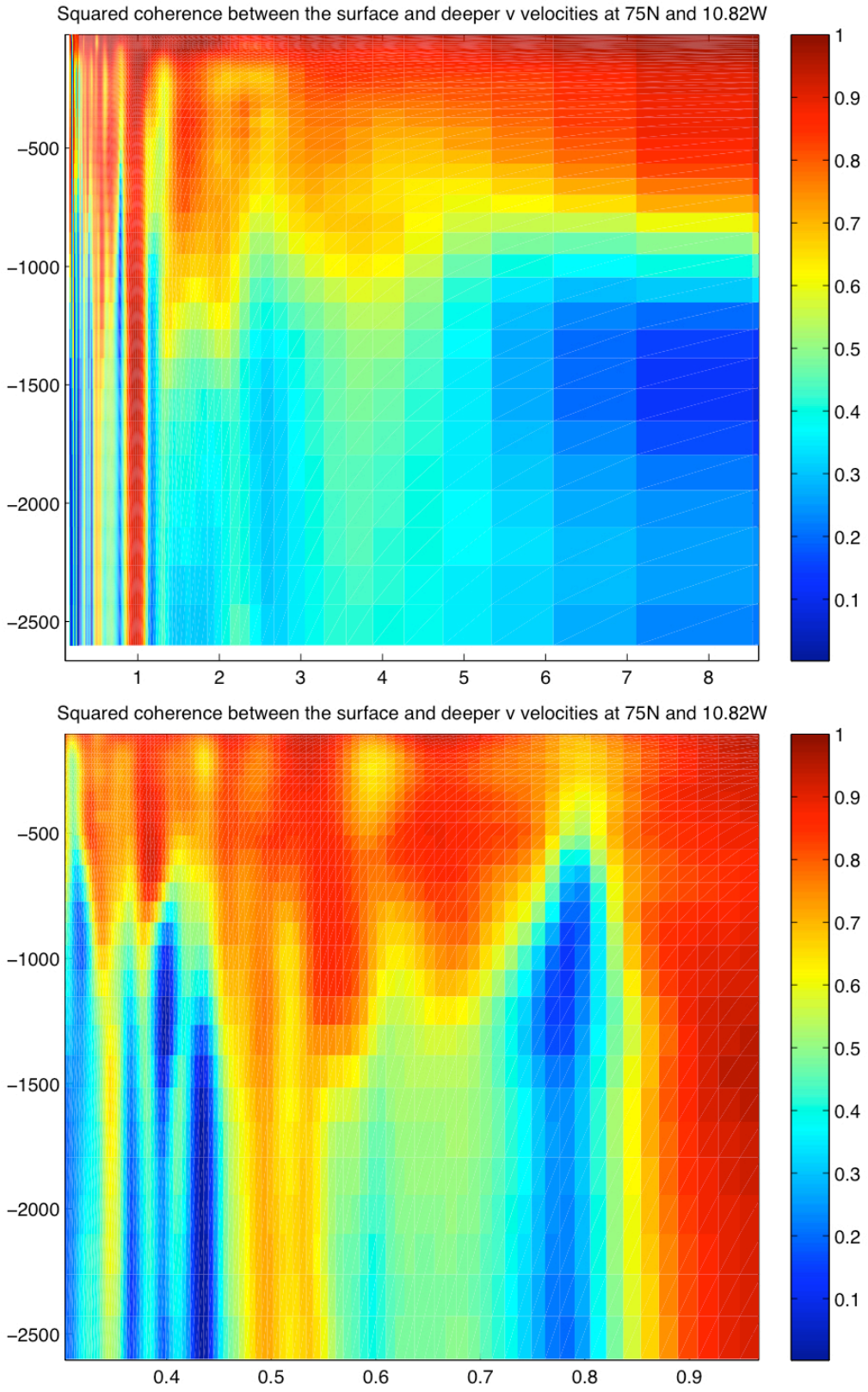

Figure 5.33 Squared coherence for the surface velocity and velocity at other depths in the core of the EGC at 75^0N and 10.8^0W for different periods (x-axis).

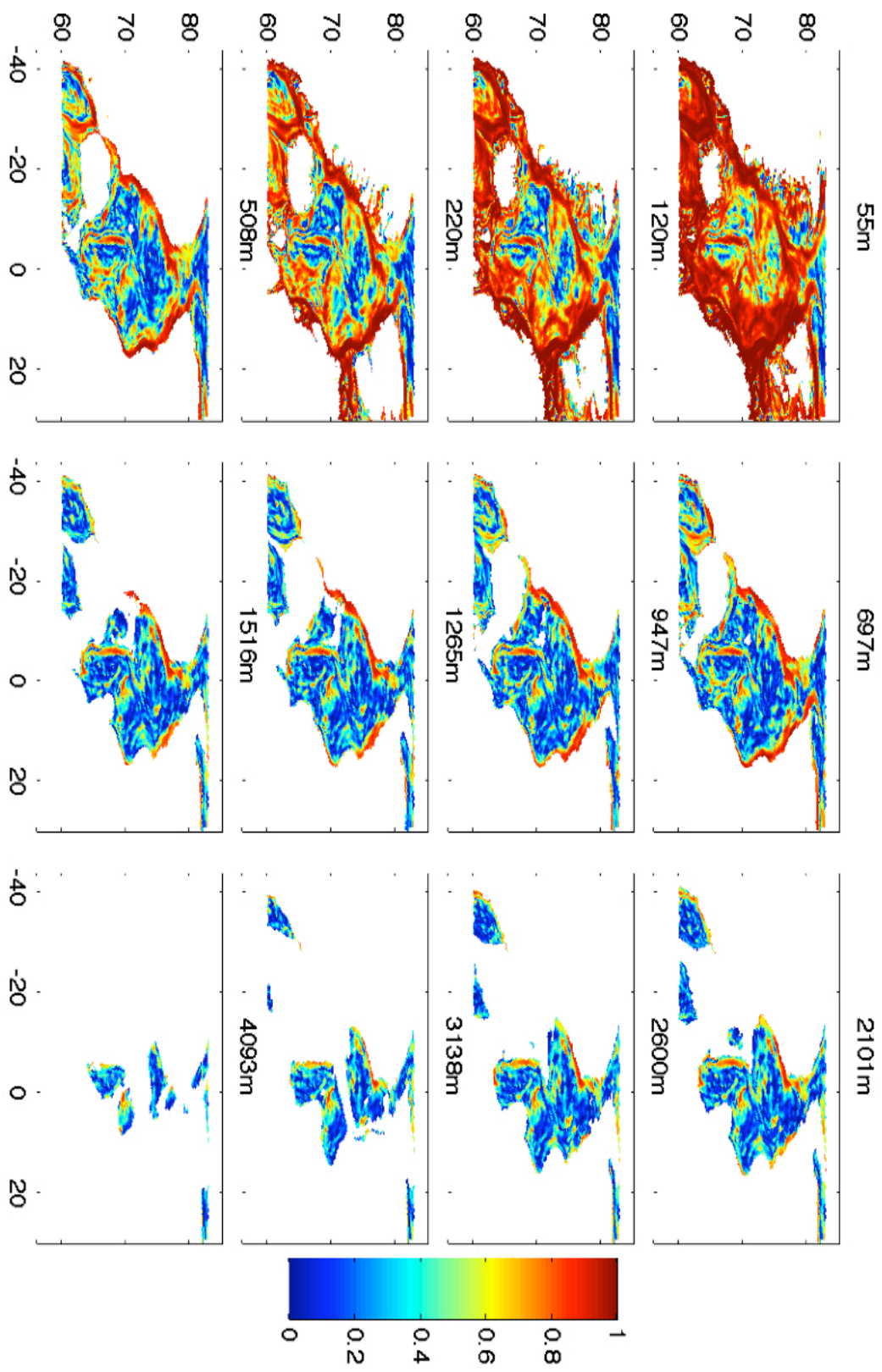

Figure 5.34. Squared coherence for the surface velocity and velocity at other depths for the whole Nordic Seas at the annual period.

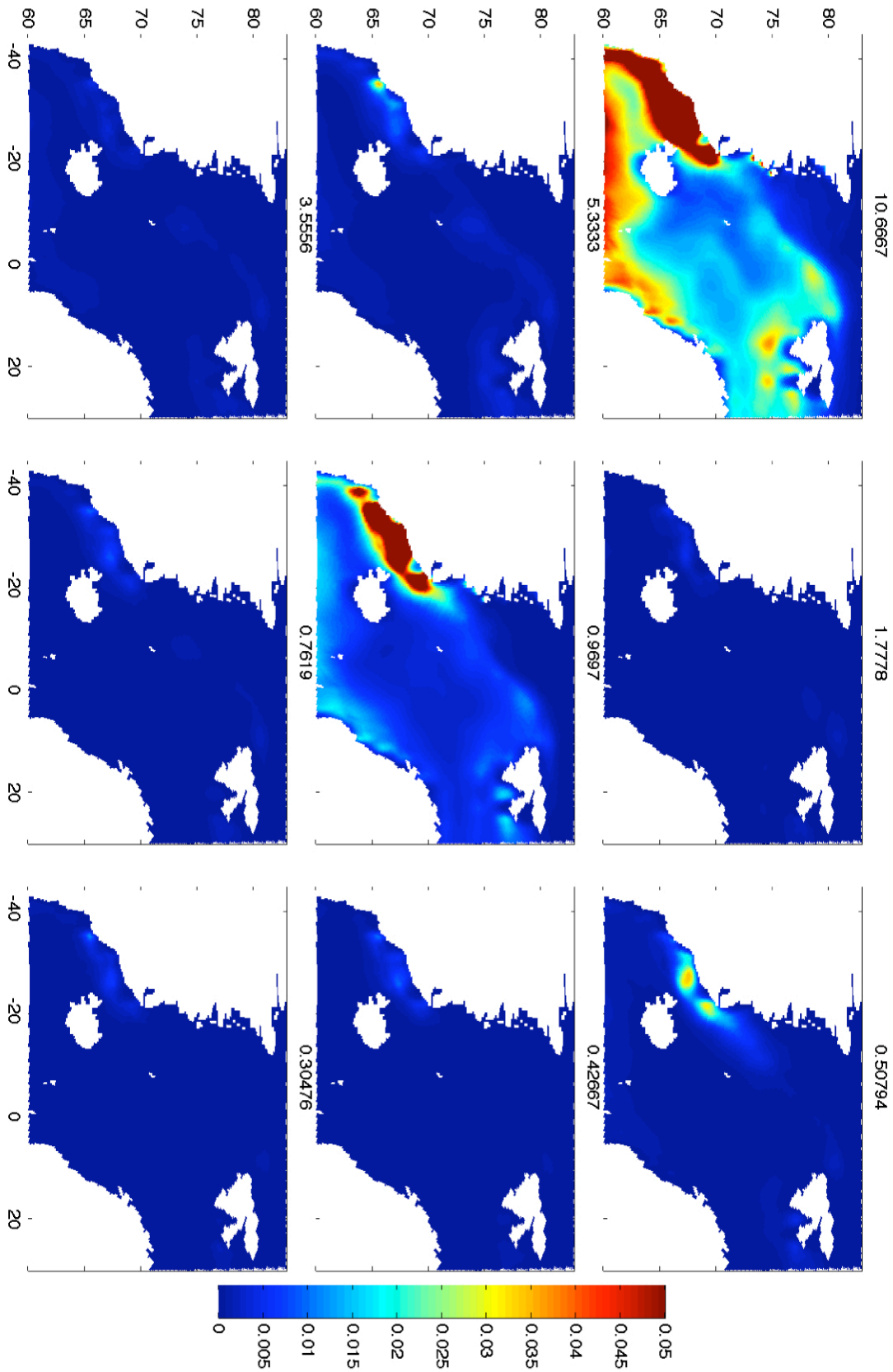

Figure 5.35 Power Spectrum density of the surface wind stress in the Nordic Seas for periods from decadal to inner-annual.

5.4.2. Vertical structure of the EGC velocity

Core of the EGC at 75^0N

The velocity structure of the model EGC at 75^0N can be characterized by the greatest velocities (16 cms^{-1}) close to the sea surface, decreasing with depth and reaching an almost constant value of 13 cm s^{-1} in depths ranging from 300 m to 700 m (Figure 5.36). The current is weaker below 800 m and its magnitude decreases gradually from 12cms^{-1} to about 4 cm s^{-1} at 1500m. Below 1500 m the decrease is slower and the velocities reach here about 1.5-4 cm s^{-1}. The top 200 m of the water column have the greatest velocities and also the greatest variability, which could be caused by Ekman layer dynamics (Figure 5.36). In the layer located in the middle of the water column (200-1000m) the variability decreases gradually with depth with standard deviation (SD) of the current speed reaching 6 cm s^{-1} at 200m and 1.8 cm s^{-1} at 1000 m. In the waters deeper than 1000 m the SD of the current velocity has almost constant value of about 1.5 cm s^{-1}. Generally, one can describe the modelled EGC at 75^0N as a surface intensified current that has the greatest velocities, transport and variability in the top 1000m of the water column. However, how much variance can be explained by the barotropic and baroclinic vertical modes? The barotropic (depth integrated) velocity can explain about 74% of the total variance of the velocity magnitude over 40 years. Its magnitude increased with time by about 8cm s^{-1} from 1986 to 1993, which may be caused by the model drift. In the 40-year long period, the greater variability of barotropic velocity was observed from 1993 to 2007 and the barotropic current reached two local maxima of 27 cm s^{-1} in January 1995 and November 2005 (Figure 5.37). Its power spectrum shows high energy at semi-annual, annual and longer periods and it is greater than for the baroclinic velocity except for the monthly periods (Figure 5.38). The barotropic velocity also explains most of the variance in the top 1000 m of the water column and only about 30% in the deeper waters (Figure 5.37). However, the variability is much smaller deeper than 1km and therefore the barotropic velocity explains the majority of the variance in the whole water column.

The EOF analysis performed on the monthly vertical profiles of the speed anomaly (covariance matrix of the size equal to time (40years x 12 months) and depth levels (75)) indicated that the 1st EOF of the speed anomaly explains 94% of the total velocity

variance and consists of the barotropic and the 1st baroclinic mode and oscillates very similarly to the barotropic velocity (Figure 5.40). The correlation between the 1st PC and the barotropic velocity time series is 0.997 and therefore the barotropic mode explains 99.42% of the 1st PC variance. Also the surface velocity is strongly correlated to the barotropic mode (R=0.97) and explains 94% of its variance.

Direction of the EGC current at 75°N

The model results showed that the current direction during the 40-years period analyzed was generally uniform with depth and the current flowed mainly south-westerly along isobaths (Figure 5.39). There are few exceptions that occurred in the 1000 m thick layer above the seabed when the current changed direction to the opposite (northerly). However, if we only consider the anomalies from the mean, the velocity components of the anomalous velocity have the same sign during the whole period analyzed in the whole water column. The uniform direction of the current and large variance explained by the surface velocity provide a satisfactory evidence that the surface velocity can be used to accurately describe the velocity variability at other depths.

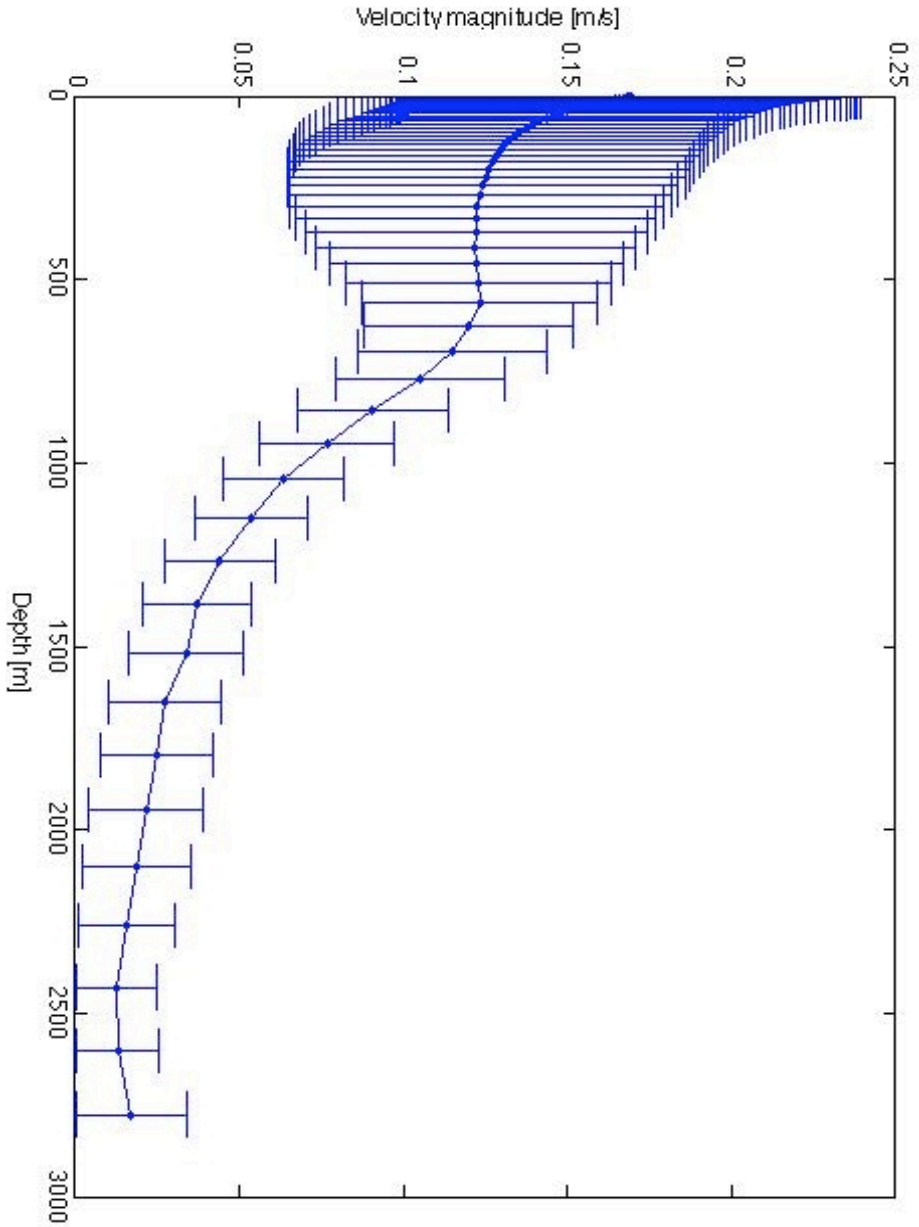

Figure 5.36 Mean (1968-2007) profile of the model EGC speed at 75°N 10.8°W and its standard deviation plotted as an error-bar.

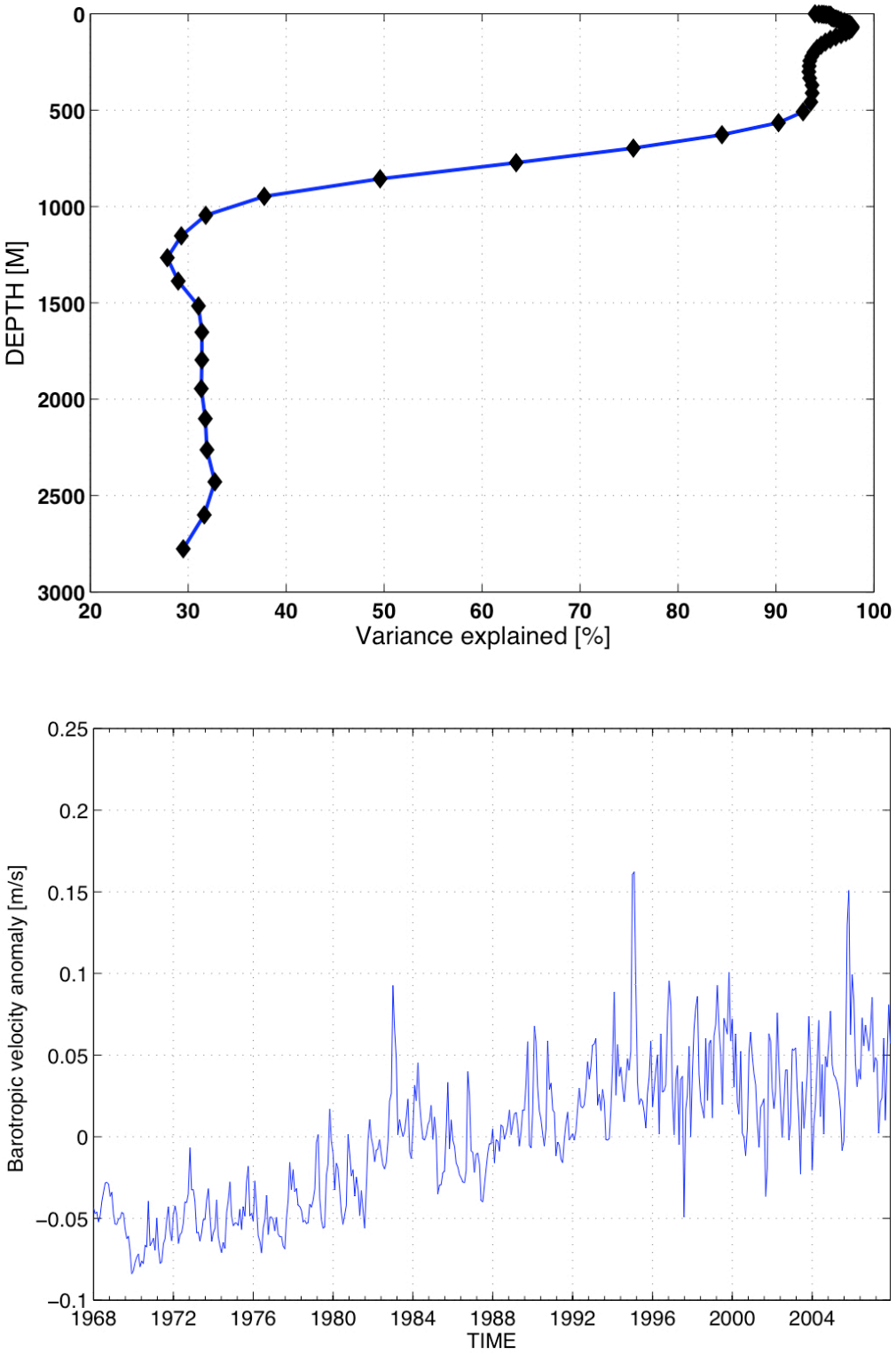

Figure 5. 37 Barotropic velocity time series from January 1968 to December 2007 (bottom) and the % of the variance explained at every model depth level (top).

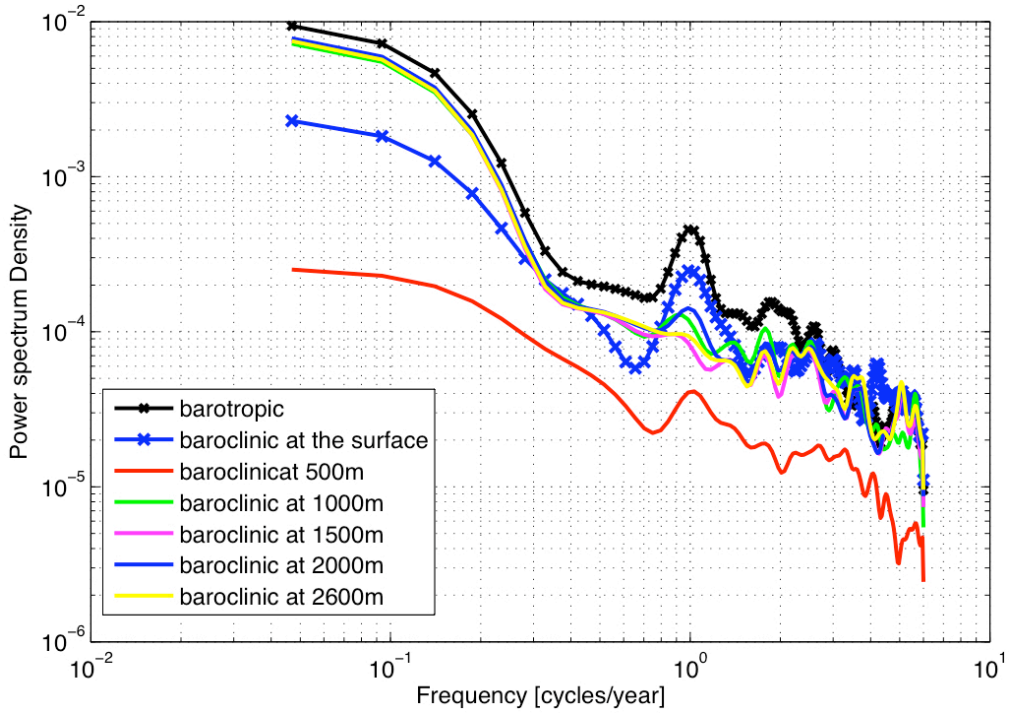

Figure 5.38 Power spectrum density of the barotropic velocity (black) and the baroclinic velocity at different depth levels.

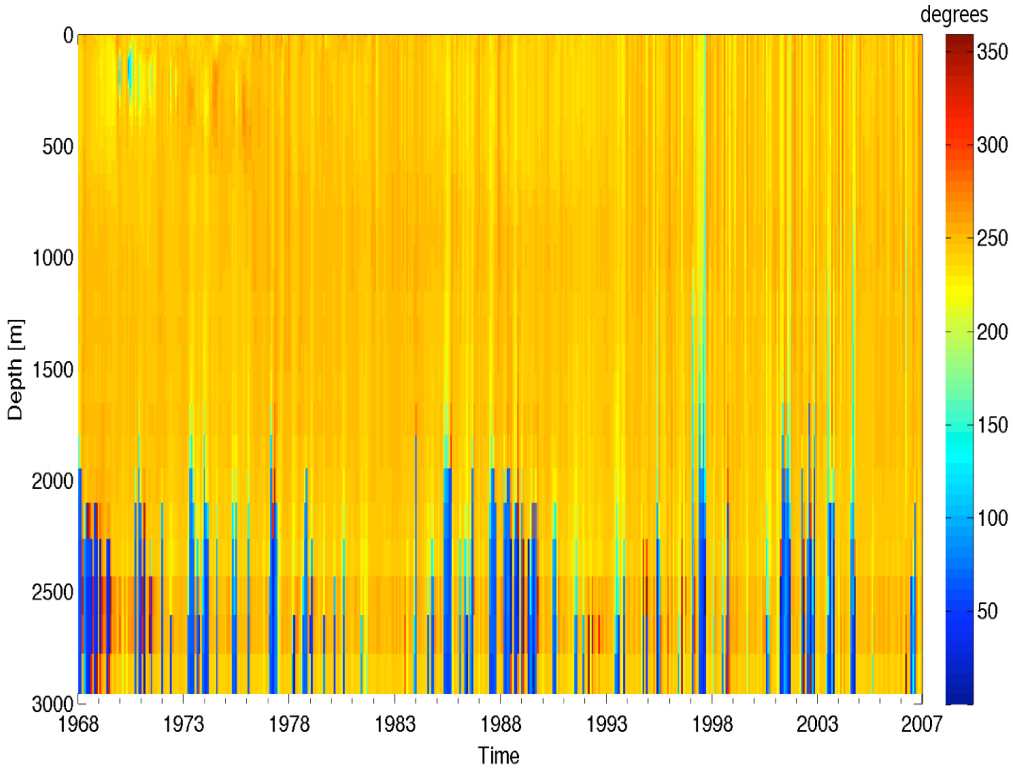

Figure 5.39 Direction of the EGC current at 75°N (degrees, contraclockwise from East).

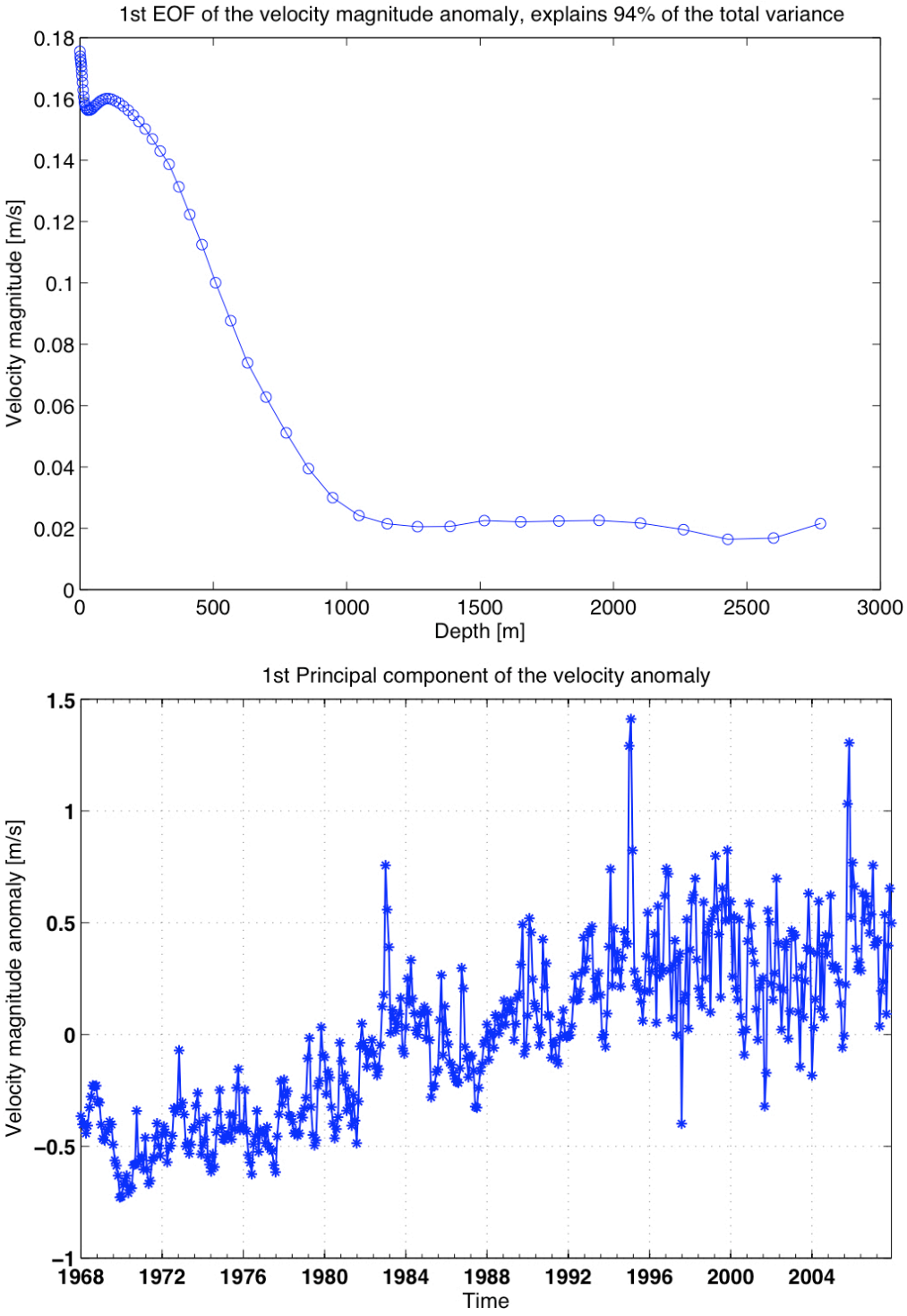

Figure 5.40 . The 1st vertical EOF of the EGC speed anomaly at 75°N 10.8°W.

Changes of the EGC vertical structure along the path of EGC

In this section the vertical structure along the current path is examined and the following question is answered: Is the structure of the EGC coherent along its path in the Nordic Seas?

Firstly, we need to define EGC in the model grid. The EGC was defined in the model as the long-term (40-years) averaged current flowing along the continental slope of the eastern Greenland in the southerly direction at all depths (Figure 5.41). The points with the mean velocity magnitude greater than $2.2 cms^{-1}$ at the surface and with the negative meridional velocity component (southward flow) were chosen to define the EGC (Figure 5.41). The current has the greatest variability on its north-eastern edge, in the Fram Strait and in the vicinity of the Greenland Gyre (Figure 5.42).

The greatest variability occurs in the top 1km of the water column for all EGC grid points. Furthermore, the large variability was found in the whole water column in the southern part of the EGC from 69°N to 72°N and in the Greenland Sea from 75°N to 78°N. The anomalous surface velocity magnitude was found to be significantly correlated with the velocities from other depths along the EGC path from 69°N to 78.5°N and only for the depths between 500-1000m to the north of 79°N (Figure 5.43). However, the anomalous surface along-slope velocity component showed similar correlations but the insignificant correlations were shifted northerly from 80°N to 83°N. The barotropic velocity anomaly is highly correlated with the surface velocity along the path of the EGC from 83°N to 69°N. It explains more than 50% of velocity variance in the top 1000 m of the water column almost everywhere except the northern part of the EGC (north of 78°N) where it explains only 30% (Figure 5.44). The surface velocity anomaly is significantly correlated with the velocities at other depths except a region located to the north of 80°N where the velocities of the intermediate layer (200-500m) and the layer next to the seabed (deeper than 1500m) are not significantly correlated with the surface velocity (Figure 5.43). This suggests that the surface velocity anomaly can be used to model the velocities at other depths within the water column. Very similar correlations were also found for the barotropic velocity and the velocities at other depths. The coherence estimates showed that only for the annual period the coherence between the surface velocity and the velocities at the depths is large in the

region to the north of 80°N, whereas for the region located to the south of 80°N there are also other periods when the surface velocity has a significant coherence with the velocities in the deeper part of the water column (Appendix).

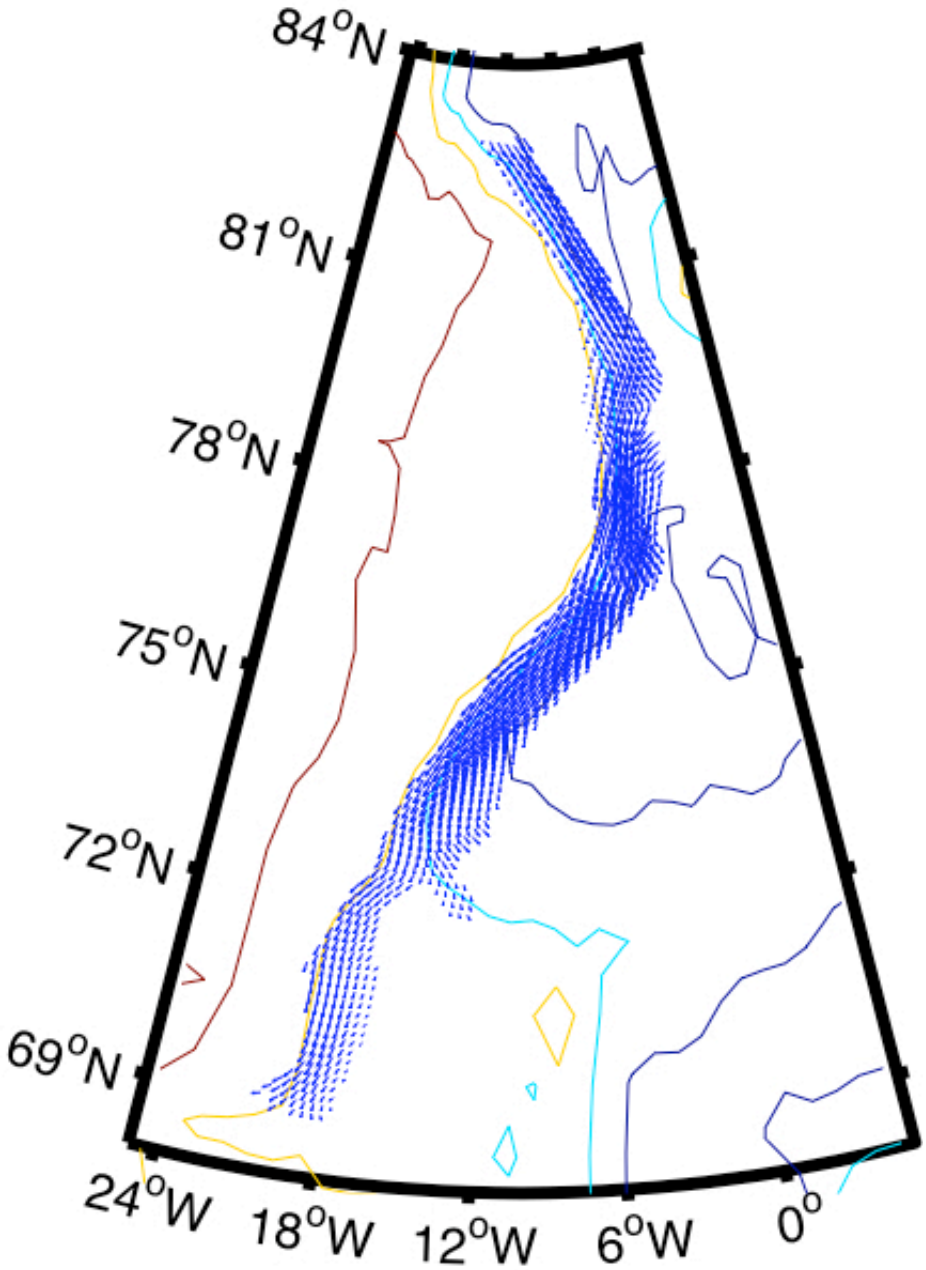

Figure 5.41. EGC defined in the NEMO model: mean surface velocity is plotted in blue as arrows over the bathymetric contour (plotted in color from 0 to 3km by every 1km).

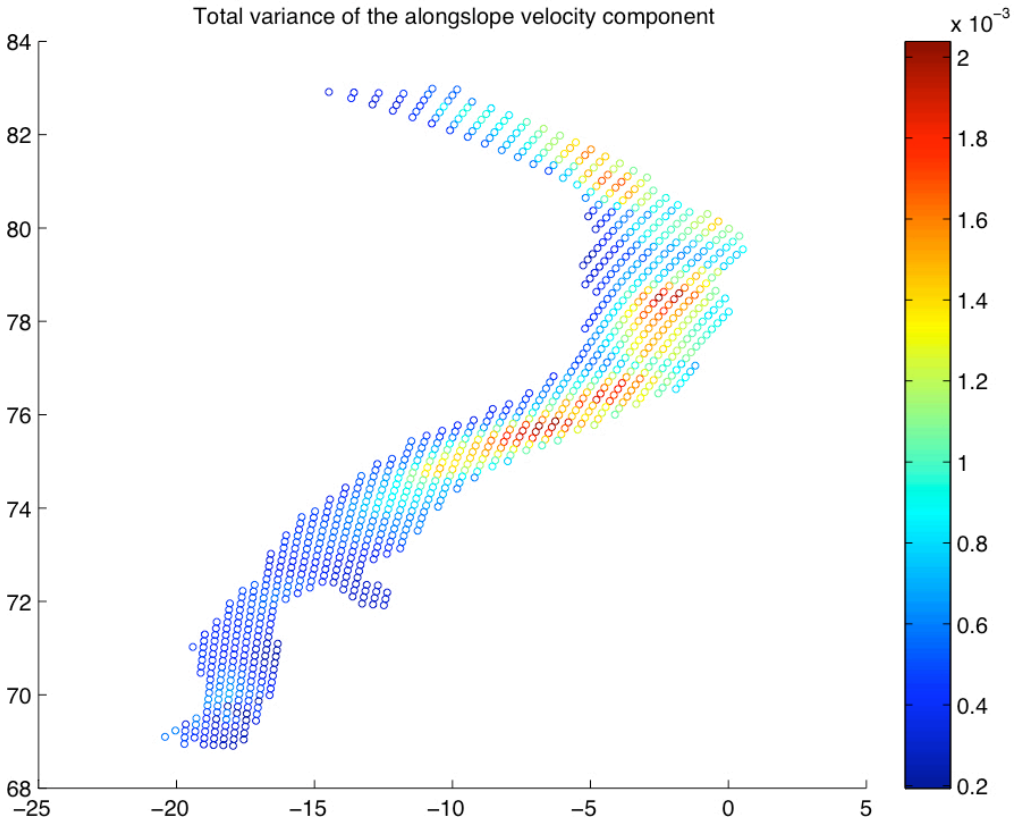

Figure 5.42. Total variance of the along-slope velocity component [m^2s^{-2}].

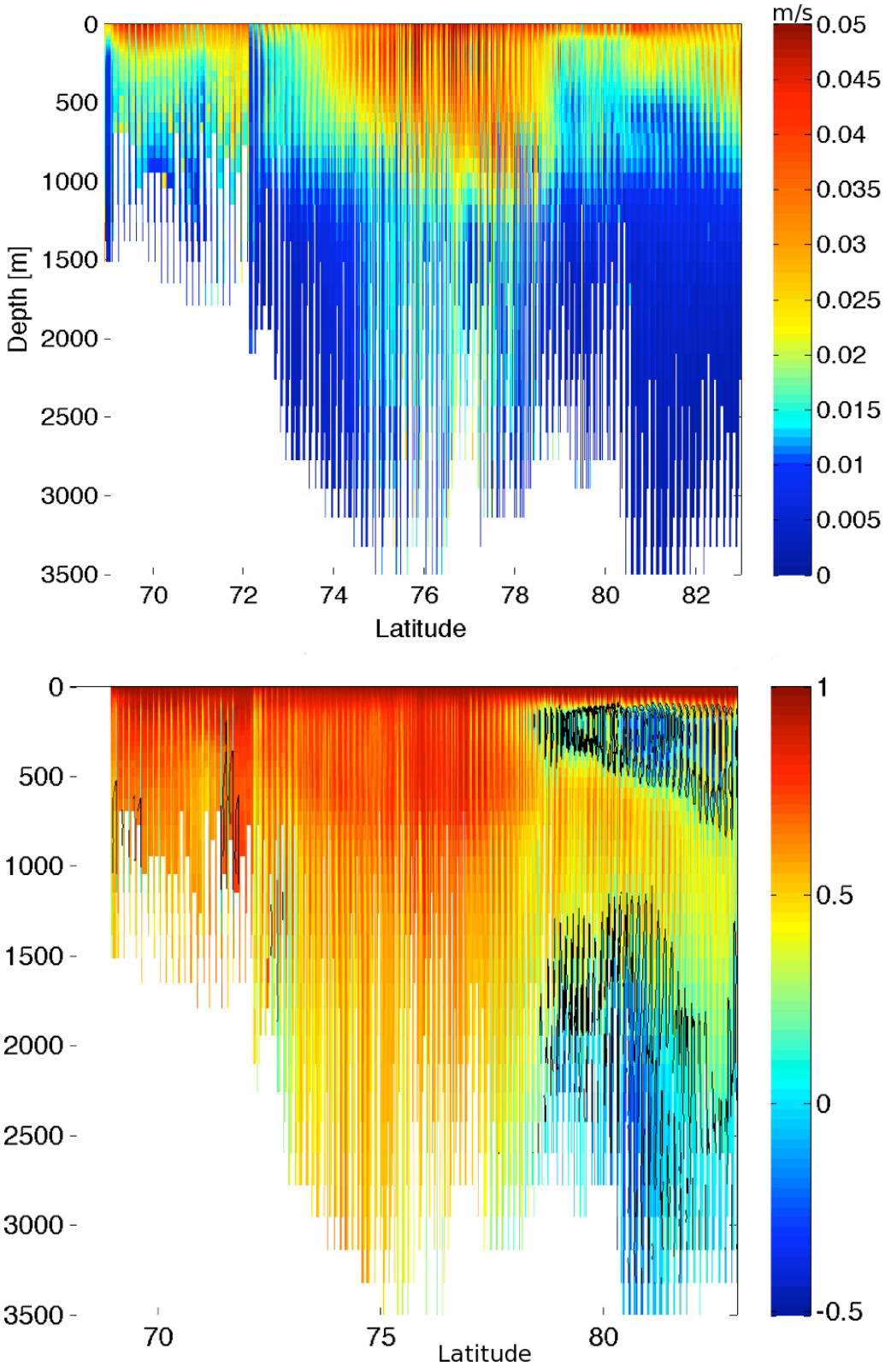

Figure 5.43 Standard deviation of the speed anomaly ([ms^{-1}], top) and the Pearson correlation coefficient for the surface speed anomaly and the speed velocity anomaly at other depths in the EGC (bottom).

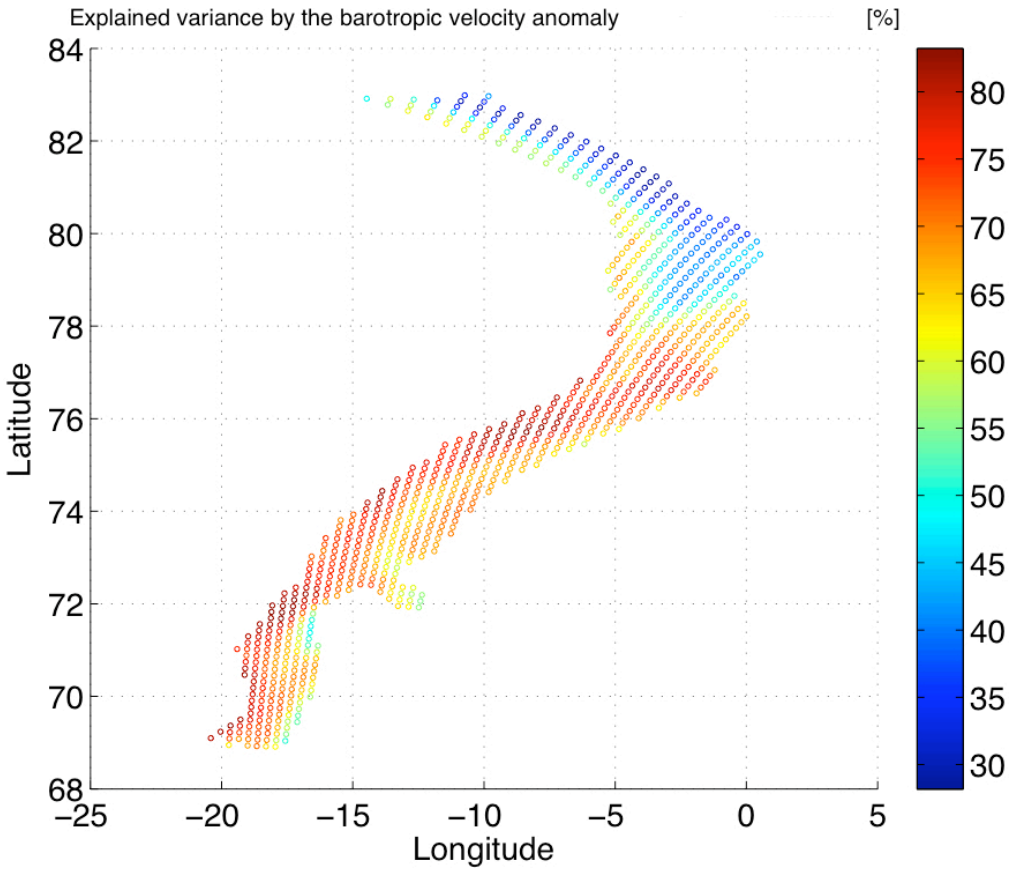

Figure 5.44 Explained variance [%] by barotropic velocity anomaly (depth averaged) along the EGC.

5.5 Method of the EGC transport calculation.

How well can vertical structure be modelled as a function of the surface velocity?

In the previous section the vertical structure of the EGC was investigated and the model output suggested that the surface velocity could be used to describe the velocities at other depths along the path of EGC from 80°N to 69°N. Two methods will be used to calculate the anomalous transports of the EGC. If one assumes the altimeter sees mainly the barotropic velocity, the surface velocity anomaly can be translated into the barotropic velocity by propagating the surface geostrophic velocity to the bottom, or to a certain depth level (e.g. 1000 m where the coherence is large)- Method 1. The 2nd method takes into account the variation of the velocity with depth and is described below.

The profile of the velocity anomaly changes with depth. Therefore, the surface velocity anomaly was subtracted from each velocity anomaly profile, for each month (time step) and every model grid point. This was done for the along-slope velocity anomaly component. The vertical structure of the resulting velocity anomaly was modelled by performing the EOF analysis for each EGC location. The EOF analysis was executed for all EGC locations (Figure 5.41) and over 40 years of the model run and therefore it was assumed that the obtained vertical structure (1st EOF) is typical for any time period considered. The 1st vertical EOF of the along-slope component described on average 84% of the velocity variance over 40-year long time period. Because the subtracted surface velocity anomaly was well correlated with the barotropic velocity anomaly (Section 5.4.2), the 1st EOF is equivalent to the 1st baroclinic mode of the velocity. The 1st PC describes the variation of the vertical mode with time and was well correlated with the surface velocity anomaly. Therefore, in order to model the velocity anomaly that remained after the subtraction of the surface velocity, one can use the product of the 1st EOF velocity structure and its PC at each location (grid point). The 1st PC can be obtained from a regression model consisting of the product of the regression coefficient (A) and the surface velocity (V) time series:

$$V_{(longitude,latitude,depth,time)} = 1^{st}EOF_{(longitude,latitude,depth)} \times 1^{st}PC_{(longitude,latitude,time)}$$
$$1^{st}PC_{(longitude,latitude,time)} = \left(A_{(long,lat)} \times V_{(longitude,latitude,0,time)}\right) \quad \text{EQ.5.2}$$

The above model was further simplified by using the mean shape of the 1st EOF and mean slope (A) over the entire region of the EGC. Tests were also performed to check how much difference this approximation makes, and if the region is divided into 2 smaller areas with division at 78°N. However, the differences between the different approximations were very small (less than 3%) and using the mean slope and velocity structure function explained on average 66% of the along-slope velocity variance. The averaged 1st EOF was zero at the surface and decreased with depth. Therefore, the 2nd method to obtain the anomalous EGC transports is to use the surface velocity anomaly calculated from the SSHA (Section 5.2), the mean model velocity structure function and the mean regression coefficient:

$$V_{(x,y,z,t)} = V_{(x,y,0,t)} - \left(\left|1^{st}\, EOF_{(z)}\right| \times \left(|A| \times V_{(x,y,0,t)}\right)\right) \qquad \text{EQ. 5.3}$$

Where V is a magnitude of a velocity anomaly (or along-slope component of the velocity), x is the longitude, y is the latitude, z is a depth and t is time. This structure function consists of the vertical modes: the barotropic and the 1st baroclinic.

The transport was calculated as follows:

1. In order to define the EGC, the mean current was calculated for the NEMO output (40-years) and interpolated to the same grid as the surface velocity obtained from the altimetry. The EGC was defined as the current flowing southward along the eastern continental slope of Greenland. Only those grid points were classified as the part of EGC that have their average transports per 1km greater than 0.025Sv and transports per one degree of longitude 1Sv (Figure 5.45).

2. The surface velocity anomaly was interpolated to the seabed at each grid point of the defined EGC to calculate the barotropic transport (assuming altimeter sees mainly the barotropic transport or most of the transport in that layer is mainly barotropic) – Method 1.

3. The surface velocity anomaly was interpolated to the seabed at each grid point of the defined EGC using the model mean structure function (1st EOF) and equation 5.3- Method 2.

4. The anomalous transport ϕ at each grid point was calculated using:

$$\phi\left[\frac{m^3}{s}\right] = \sqrt{u^2 + v^2}\left[\frac{m}{s}\right] \times \cos\theta \times layer_{thickness}[m] \times grid_{length}[m] \quad \text{EQ. 5.4}$$

where u is a zonal component of velocity anomaly, v is a meridional component of the velocity anomaly and θ is the angle from the South direction (the transports are perpendicular to the grid which lies along constant latitude: east-west direction).

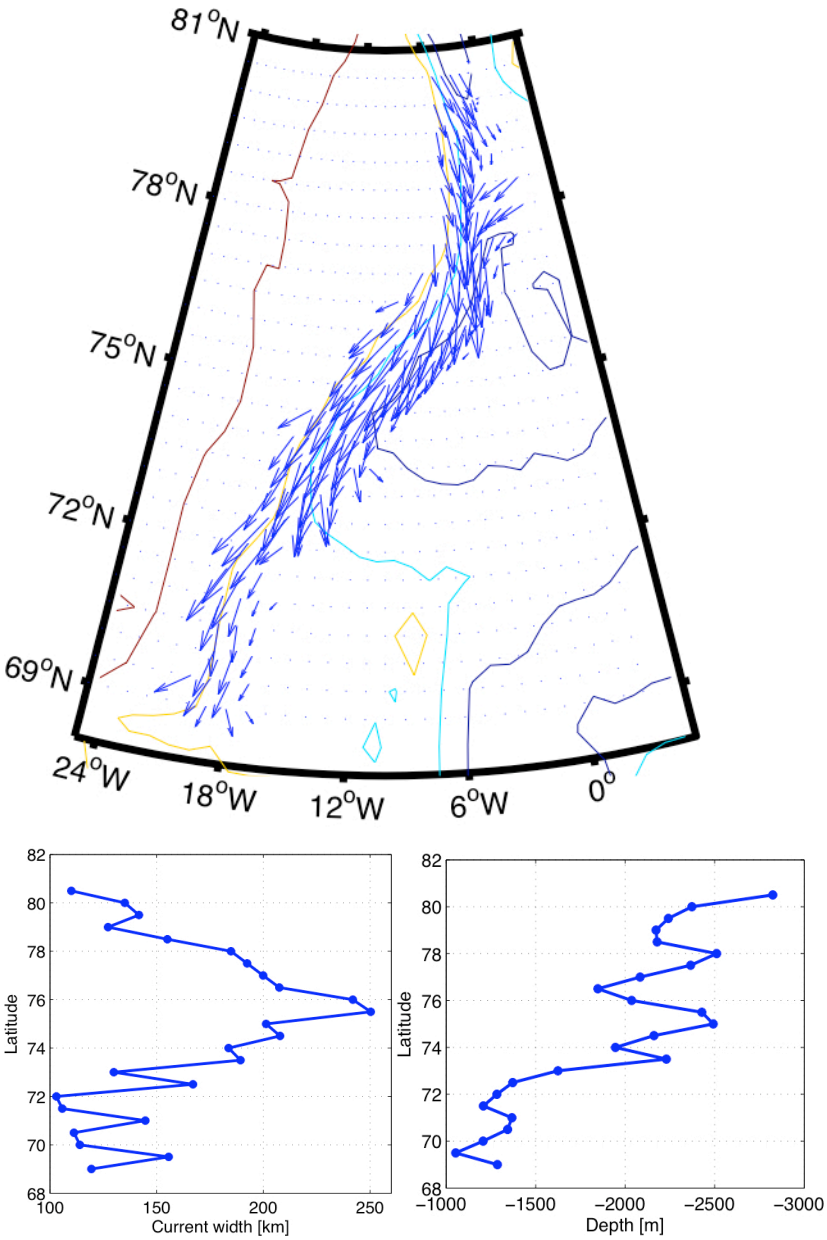

Figure 5 45. EGC defined in the NEMO model on the interpolated grid. Depth averaged current in 1986-2007 (top), its width and average depth of the interpolated bathymetry at each grid point.

5.5.1. Errors due to the method.

The aim of this section is to estimate the error of the transport variability when using the surface currents obtained in Section 5.2. The first part of the error is the error associated with the method of the transport calculation and therefore with the various assumptions made about the velocity structure along the path of the EGC from 80.5°N to 69°N. This error can be estimated by simulating the transports in the numerical model and examining the differences between the ‘‘true’’ model transport and the simulated transports. The simulated transport was estimated using two methods. The first assumed the surface velocity describes the barotropic velocity and the velocities at other depths have the same direction and magnitude as at the surface (Method 1). The second method assumed the velocity also can be described using the surface velocity (the same direction) but the velocities at deeper levels can be represented by the mean 1st vertical EOF of the velocity magnitude anomaly (different magnitude)- Method 2. The 2nd method therefore uses EQ. 5.3 to obtain the vertical velocity structure at each grid point. Because the altimetry data is 7-years long and the currents obtained from the SSHA are relative to the 7-year long mean of the circulation, the model and simulated transports were calculated for the 7 year long periods and the obtained transports are relative to the average transport in that time. The coherence plots (Appendix) showed already that the method of transport calculation would produce different errors for different periods (frequencies). The aim of this Chapter is to calculate the mean seasonal cycle of the EGC transport and the annually averaged transport from November 2002 to October 2009. Therefore, the simulations performed to estimate the errors due to the methods were done for the same frequencies: seasonal and inter-annual. The model run does not extend to 2009 and therefore other available 7-years long periods were used to simulate the transports of the EGC.

A) Mean seasonal cycle during 7-year long period

The mean seasonal cycle of the anomalous EGC transport for four different 7-year long periods is shown in Figure 5.46 (left). The greatest transports occurred from 1993-2007 in the Greenland Gyre (74°N-77°N) and in the Fram Strait (78-80.5°N). The transport of the EGC showed significant seasonal fluctuations along its path with the smallest range reaching a few Sverdrups at the northern and southern limit and about 15-18 Sv at 76°N (Figure 5.50). Generally the transports were stronger from November to April in the area to the north of 75°N and weaker during the rest of the year. In November the transports were stronger along the whole path of the current.

Transports obtained with Method 1

The simulated model transport, using the 1st method, shows similar seasonal variations to the 'true' model but with the larger amplitudes of the transport anomalies (Figure 5.46). The differences between the model and simulated transports are generally about 2 Sv or less except March-September mean seasonal cycle for 1979-1986 period in the area from 73°N to 76°N when the simulated transports are smaller by 2-4 Sv (Figure 5.49). The range of the mean seasonal cycle can also be well predicted with the method 1 and the differences between the two ranges are usually about 2-4 Sv (Figure 5.50). The simulated anomalies using method 1 are always more positive/negative when compared with the model transport anomalies. Therefore, method 1 overestimates the range of the mean seasonal cycle by about 2-4Sv. The 1st method performs better when the transport anomalies are greater, which suggests it performs better when the stronger atmospheric wind forcing occurs.

Transports obtained with Method 2

The results of the 2nd method of the transport estimation shows also similar patterns of the seasonal variability as the model 'true' transports but the simulated transport anomalies are much smaller, which makes the range of the mean seasonal cycle underestimated by about 50% (Figures 5.47 and 5.50). The 2nd method performs better to the south of 74°N where the errors due to the method are much smaller and generally less than 2Sv. This method greatly underestimates the transports in the vicinity of the Greenland Gyre but it identifies the location of the maximum range of the seasonal cycle quite well (Figure 5.50). The simulated mean seasonal cycle shows much smaller

spatial variation of the range when comparing to the model range. Therefore the transport anomalies obtained using method 2 are more coherent in space (Figure 5.50).

The previous sections showed that greatest proportion of the anomalous transport occurs in the top 1000m of the water column. This part of the water column is also significantly correlated with the surface velocity and therefore the two methods should produce smaller errors when comparing the simulated to the model transports in the top 1000m of the water column. The model and simulated transports in the top 1000m of the water column were calculated for the 4 different, 7-years long periods, using the same methods as for the whole water column. The resulting transports calculated using method 1 are shown in Figure 5.47. Again this method overestimates the amplitudes of the transport anomalies and the range of the mean seasonal cycle (Figures 5.47 and 5.51). However, the errors due to the method are always less than 2 Sv for any location and month and the ranges of the seasonal cycle are quite similar and usually differ by about 2 Sv or less. The 2nd method again underestimates the transport range in the top 1100m of the water column and produces much greater errors in the vicinity of the Greenland gyre (4Sv) when compared to method 1 (Figure 5.51).

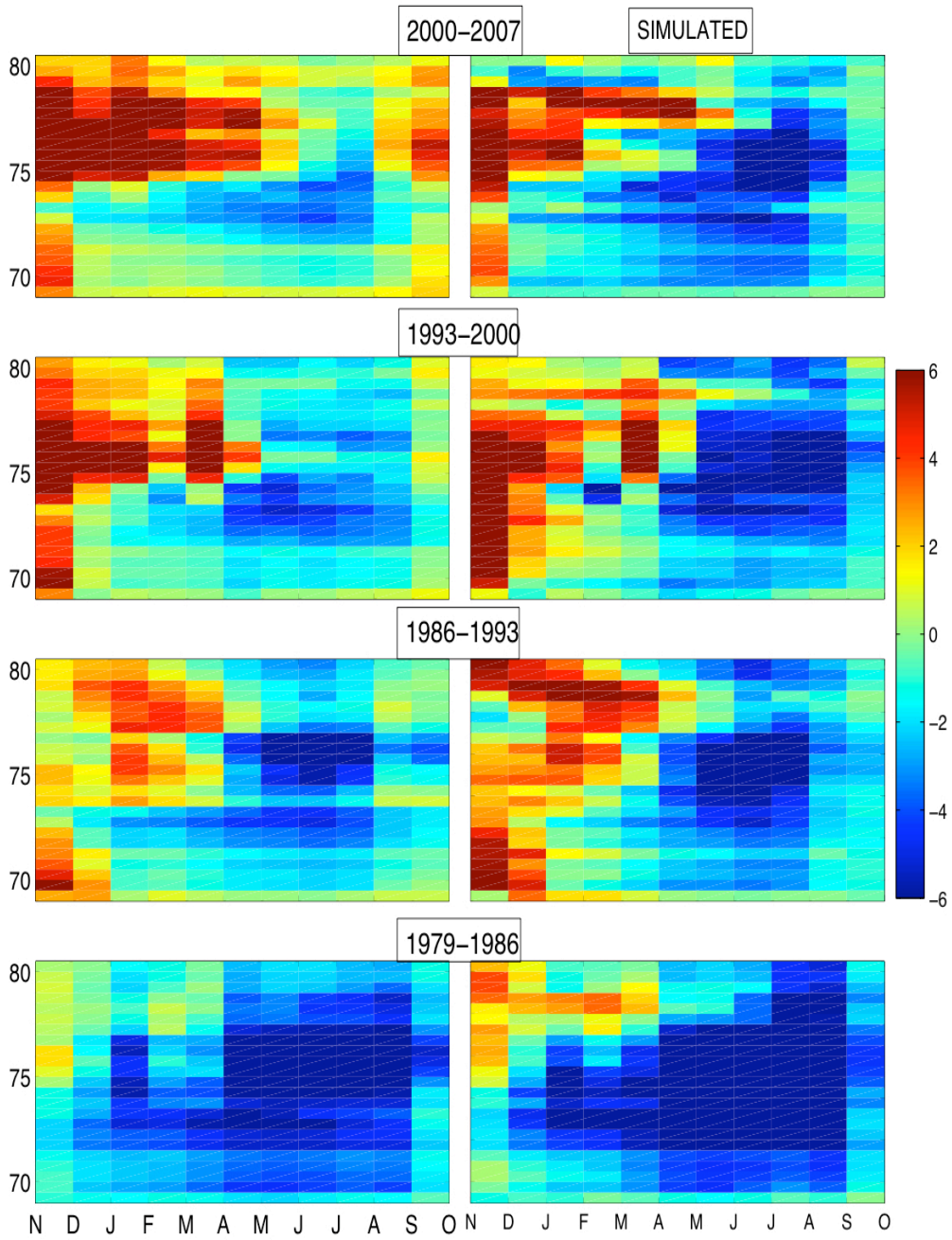

Figure 5.46 Full depth anomalous model transport [Sv] (left) and simulated anomalous transport [Sv] (right) obtained with Method 1.

SIMULATED: METHOD 1

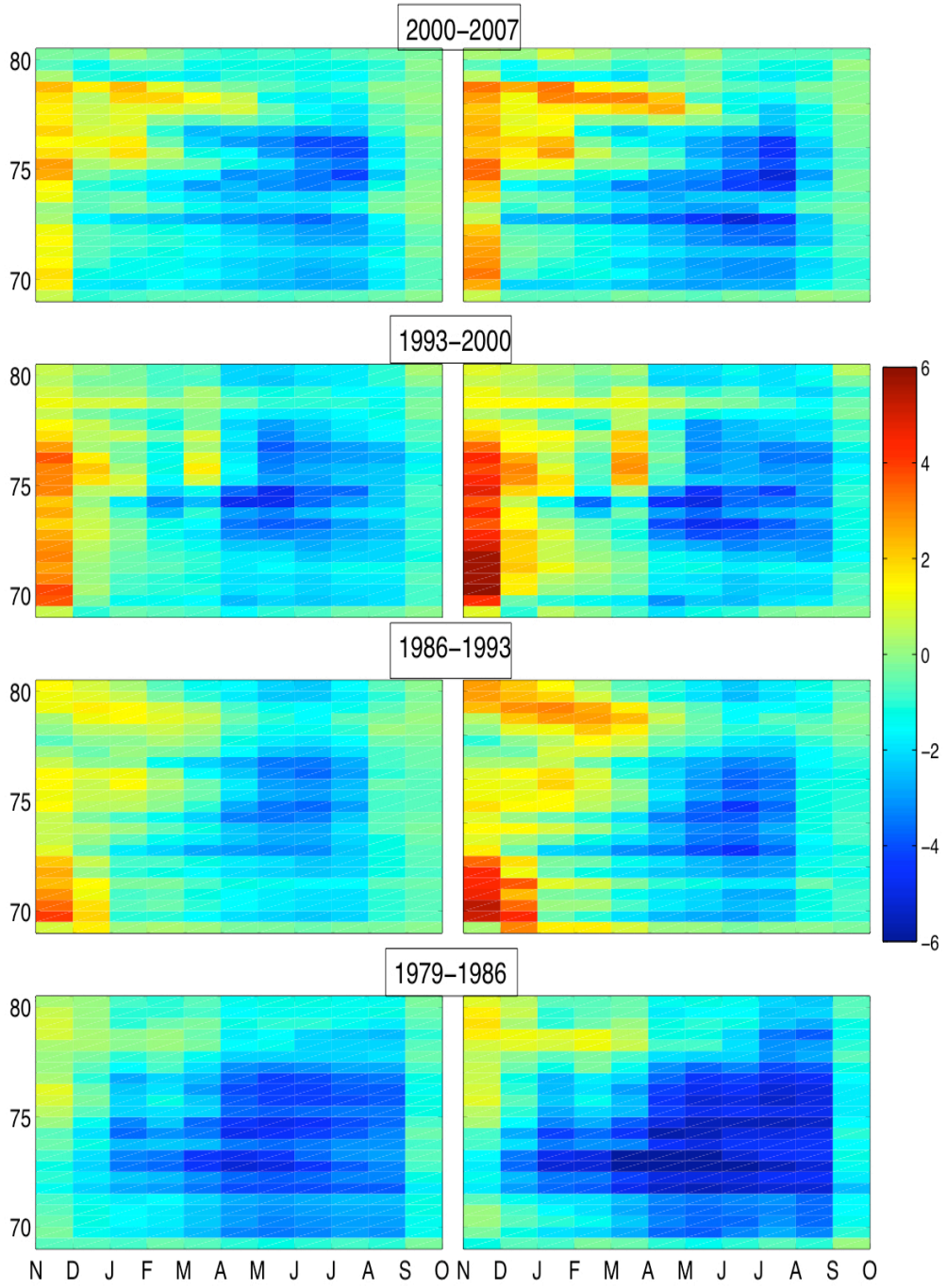

Figure 5.47. Top 1000m model transport [Sv] (left) and simulated transport [Sv] obtained with Method 1.

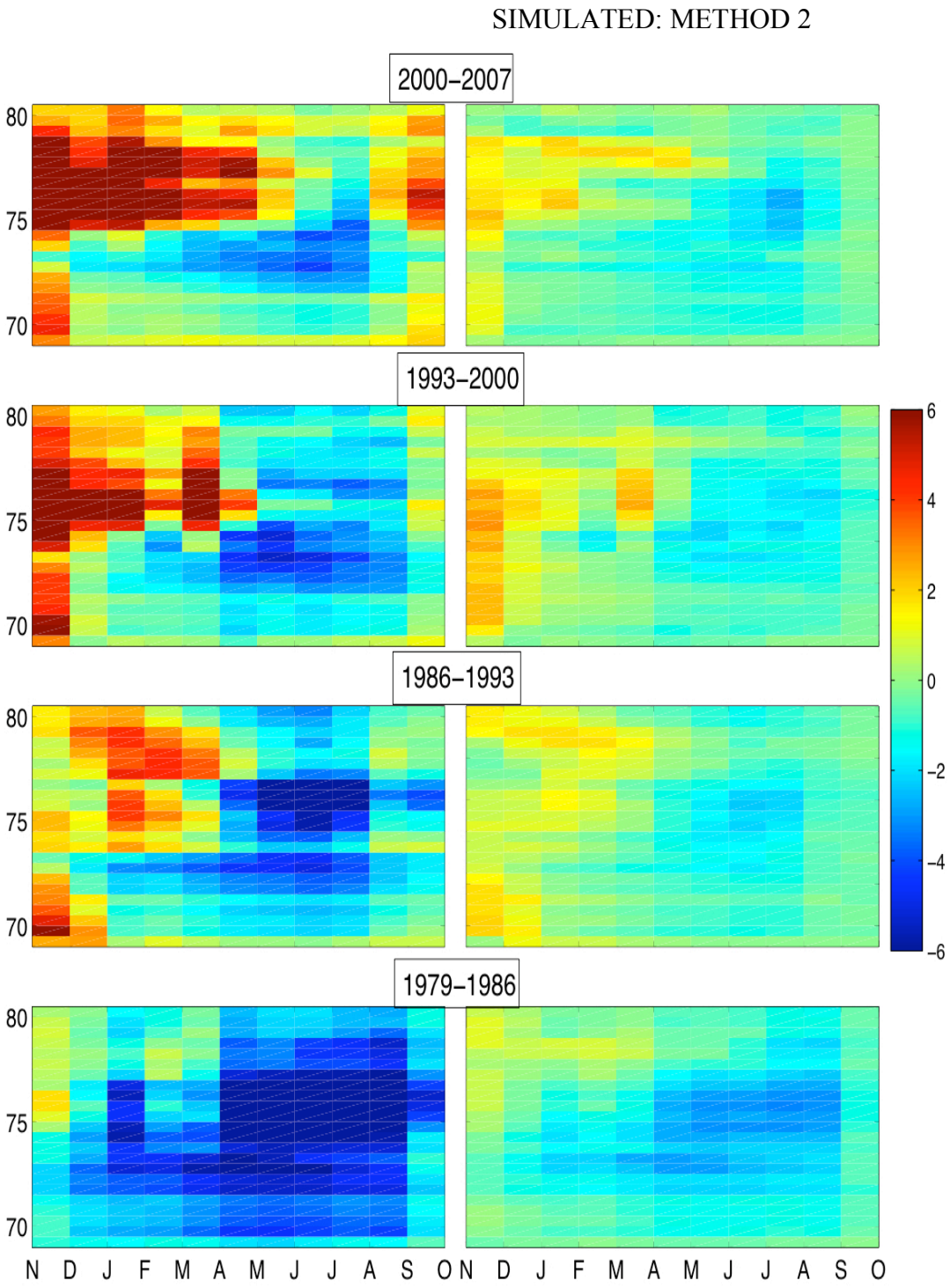

Figure 5.48 Full depth mean seasonal anomalous transport of the model [Sv] (left) and simulated anomalous transports [Sv] (right) obtained with Method 2.

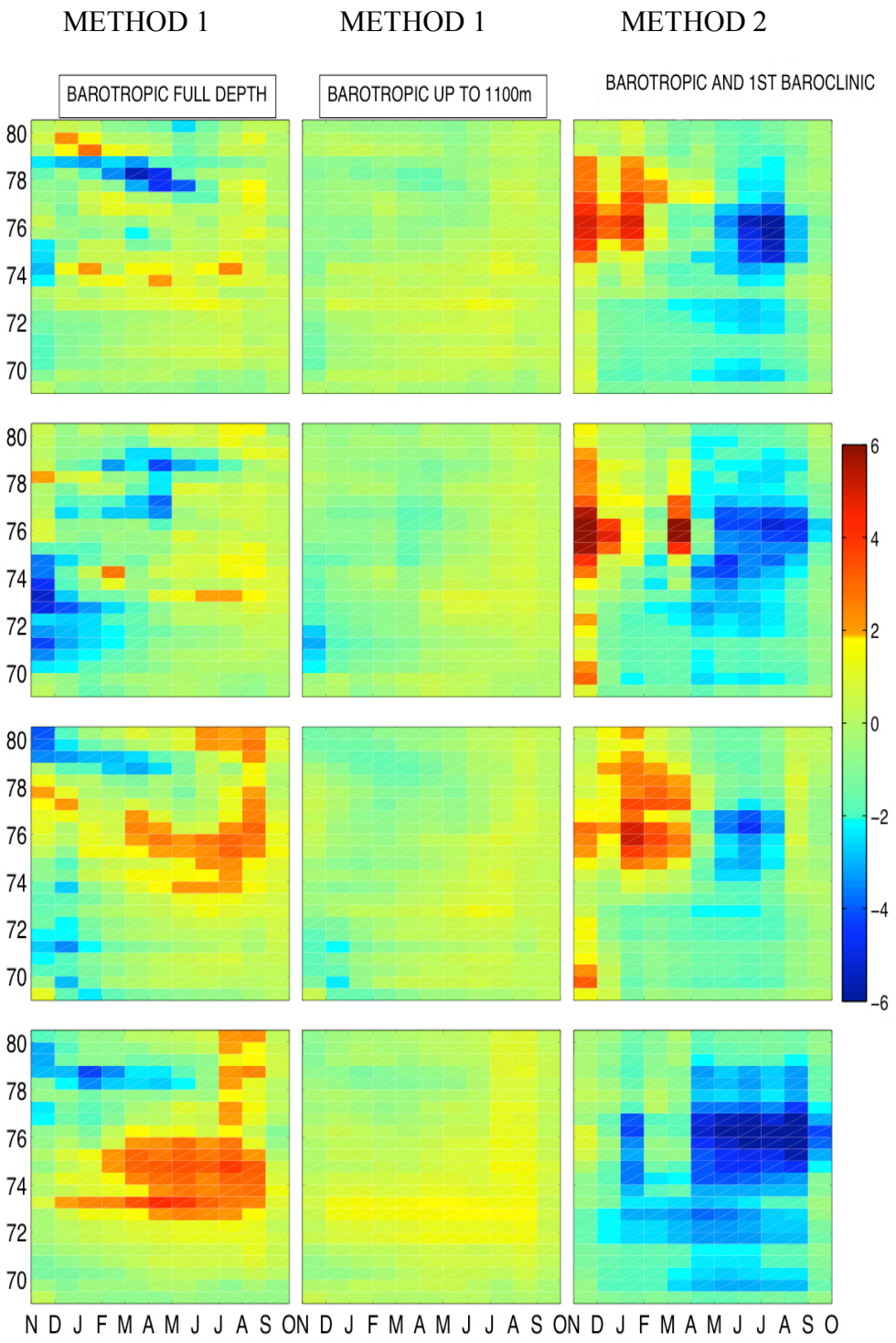

Figure 5. 49. Errors [Sv] due to the different method of transport calculation. Left: Full depth transports calculated with Method 1, middle-Top 1000m transports obtained with Method 1, right- full depth transports obtained with Method 2. Negative values means the simulated transports are greater than the model transports and positive values means the simulated transports are smaller than the model.

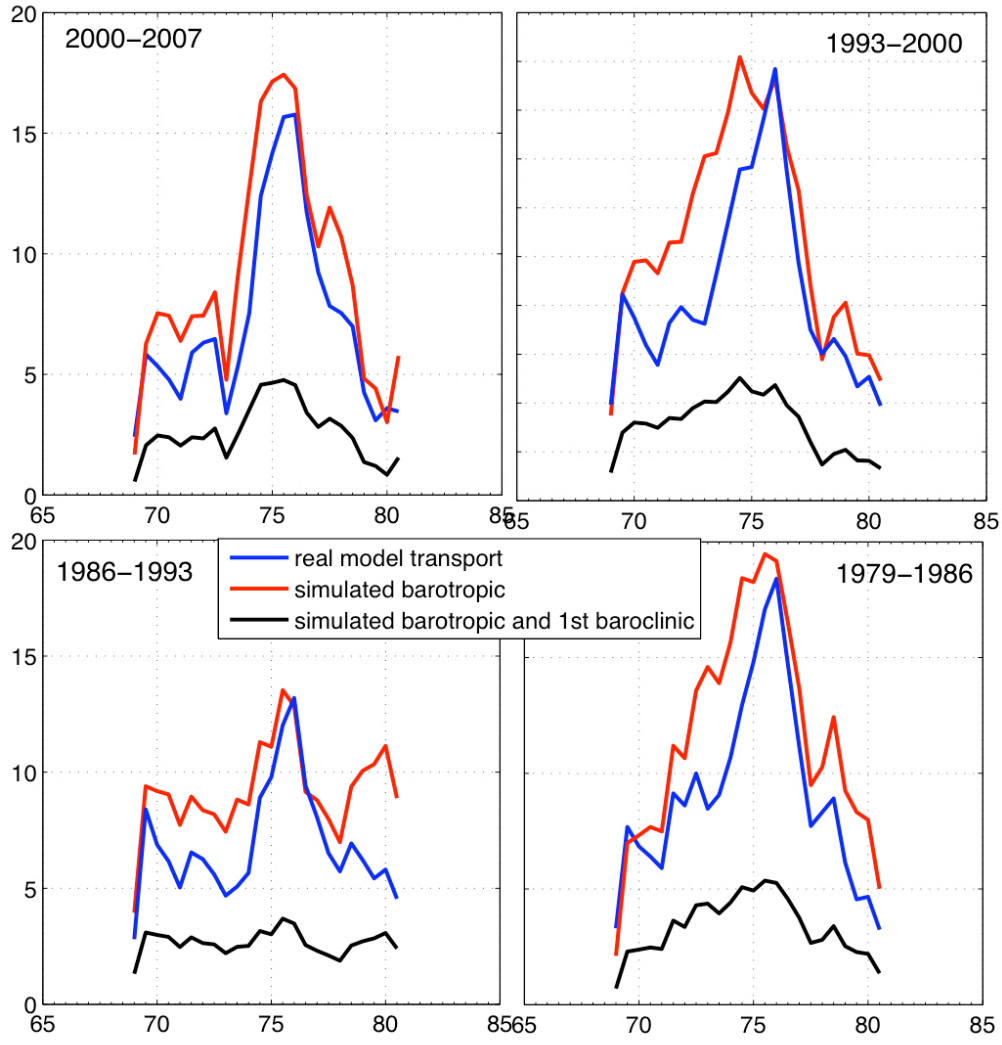

Figure 5. 50. Range [Sv] of the seasonal cycle of the full depth total transport for the true model transport (blue), simulated transport obtained with Method 1 (red) and transport obtained with Method 2 (black).

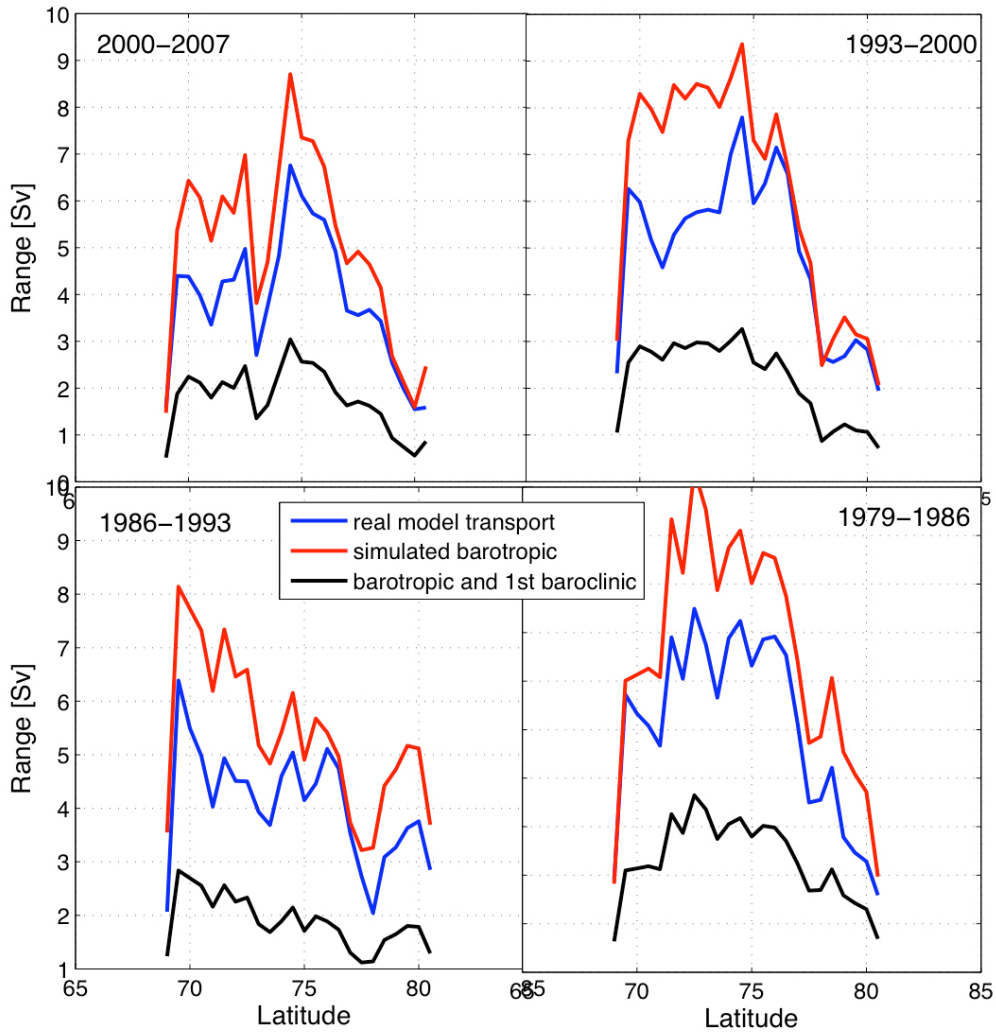

Figure 5. 51 Range [Sv] of the mean seasonal cycle of the EGC transport in the top 1000m of the water column: model transport (blue), simulated transport obtained with Method 1 (red) and transport obtained with Method 2 (black).

B) Annually averaged transport

The EGC transport showed large inter-annual variations during all four different time periods considered (Figure 5.52). The largest anomalies occurred in the last 7-years of the model run in the Greenland Gyre where the range of the variability reached about 30Sv (Figure 5.57). The maximum range of the transport always occurred at 76°N and rapidly decreased from this latitude to the south to 72.5°N and north to 78°N. At the southern and northern limit of the EGC (69°N and 80.5°N) the transport range was small and reached from 1 to 4 Sv.

Method 1

The simulated transport using Method 1 is shown in Figure 5.52. It can be seen that the transport variability is overestimated by this method and shows more positive/negative anomalies when comparing to the 'true' model transport variability. However, the spatial and temporal variability agrees quite well with the model transports. The simulated transports show strengthening and weakening of the circulation in the same time and location as the 'true' model transports. The range of the inter-annual transport variability can be well represented by the simulated model transports to the south of 76°N but north of this location the range can be overestimated by Method 1 by about 50% (Figure 5.57). However, the error depends on the time period considered. For example Method 1 greatly overestimated the transport range at 79.5°N and 73°N during 1979-1986 (Figure 5.57). This could be due to the quite small transports in this period and weaker wind forcing when compared to the other time periods considered.

Similar conclusions can be made from examination of the simulated transports in the top 1000m of the water column (Figure 5.54). However, this time the differences between the 'true' model transport and the simulated one are much smaller (Figure 5.56) and do not exceed 2 Sv. Also the range of the inter-annual transport variability can be better predicted if considering the top 1000m of the water column (Figure 5.58). The method identifies peaks in the transport range much better in the top 1000m of the water column and the range differences between the 'true' and simulated range are less (or equal) than about 2Sv. Again the greatest differences were observed for the 1979-1986 period.

Method 2

The simulated model transports with Method 2 have the same spatial and temporal variability as the 'true' model transport but the anomalies are less positive/negative and therefore the range of the variability is underestimated (Figure 5.53). During the three periods analyzed here (1979-2000) the simulated range of the transport was almost the same along the EGC path and did not show the maximum variability at the 76°N (Figure 5.57). Therefore the method has the largest error in the Greenland gyre where the barotropic transport becomes more important and also the greater transports occur. To the south and north of the Greenland gyre the method performs much better and the differences between the simulated and 'true' transports are about 2Sv or less (Figure 5.53, 5.57). Very similar transport variability was also observed for the transport simulated with Method 2 in the top 1000m of the water column. Even the ranges had the same shape as for the whole water column transports and did not show the maximum transport at 76°N (Figure 5.58). The differences between the full depth 'true' model and simulated transports were about 2 Sv except in the Greenland Gyre (Figure 5.55) and the errors were comparable with the one produced by Method 1. However, the errors associated with Method 2 are greater than for those obtained by Method 1 if only top 1000m of the water column is considered (Figure 5.57). This suggests that Method 1 performs better in simulating the transport in the top 1000m of the water column and Method 2 performs better in simulating the deeper transport except the Greenland gyre region where the transports are more barotropic.

However, a strong linear relationship was found between the range of the model transport and the range of the simulated transport. In the regression model all four simulation periods were taken into account. The model explained 83% of the total variance and indicated that the model range (Y) strongly depends on the simulated range (X) as: $Y=2.86X - 0.99$ Sv. This indicates the bias in the method 2, which should be corrected. When this linear regression model was applied to the simulated range the range was very similar to the range obtained with method 1. Also for the simulated transports it was found that the inter-annual model 'true' transport (Y) is linearly dependent on the simulated transport (X) with method 2: $Y=2.15X+0.17$ Sv ($R^2=0.78$). Therefore there is a bias in method 2 dependent on the strength of the true transport. This bias was probably caused by the different frequency of the simulated model when

compared with the original method, which was developed for the whole 40-year long period and frequencies from monthly to decadal. The Method 2 can be easily corrected for the bias and the results in the next section will be presented for the corrected Method 2.

Conclusions:

The anomalous EGC mean seasonal transport was calculated using two different methods, which were compared with the model mean seasonal cycle. This allowed the assessment of the methods and estimation of the errors produced by them. The 1st method, which used the surface velocity propagated to the sea bottom (or to 1000m), performed much better in simulating the seasonal transport variability than the 2nd method, that used EQ.5.3 to obtain a velocity profile at every grid point. The 1st method produced much smaller errors when considering the full depth transport and in the top 1000m of the water column. This is due to the fact that there exists large atmospheric wind forcing at the annual frequency, which produces a barotropic oceanic response. Therefore, the seasonal cycle can be well predicted by the surface velocity and Method 1.

The situation is quite different if one considers the annually averaged transports. For this frequency the transports are more baroclinic if compared with the seasonal transport variability. However, the results of the simulations has shown the inter-annual transport variability can be well predicted in the top 1000m of the water column with use of Method 1. The results indicated that Method 1 performs better in simulating the inter-annual transport variability in the top 1000m of the water column, whereas the 2nd method performs better (smaller total error) in simulating the full depth transport variability except the Greenland Gyre where Method 1 performs better.

SIMULATED: METHOD 1

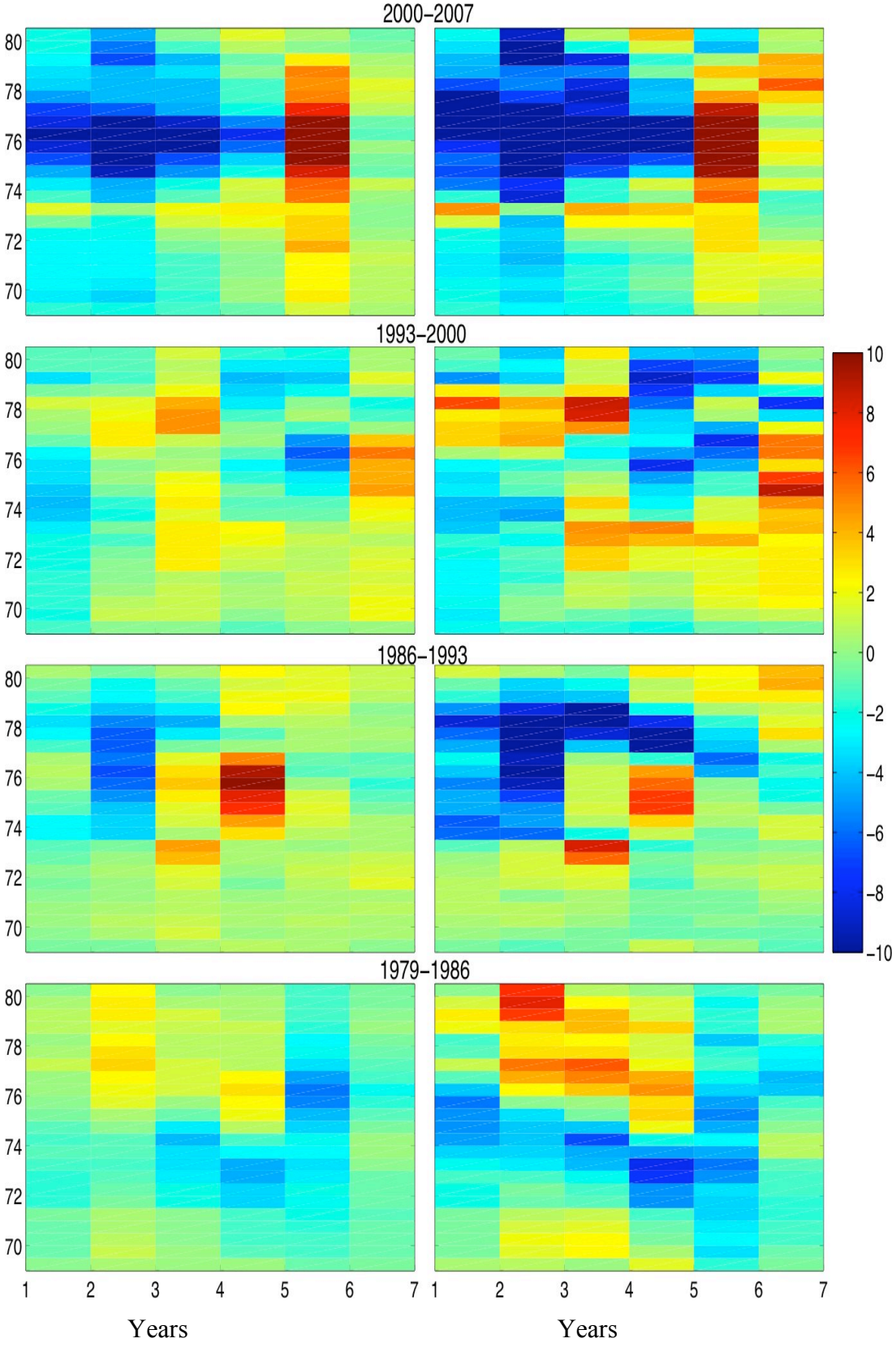

Figure 5. 52. Full depth annually averaged anomalous model transport [Sv] (left) and the same transport [Sv] obtained with Method 1.

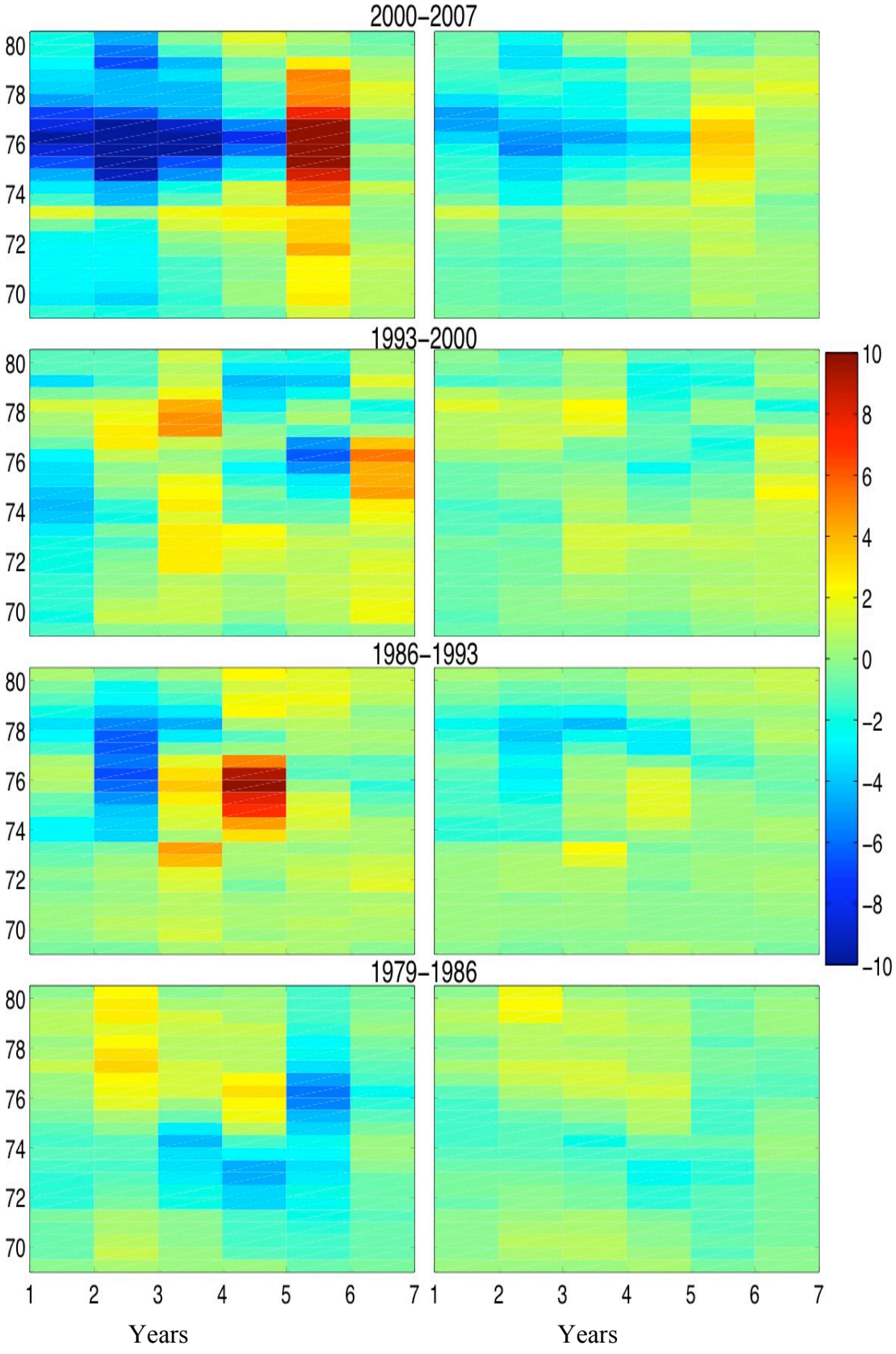

Figure 5. 53. Full depth annually averaged anomalous model transport [Sv] (left) and the same transport [Sv] obtained with Method 2.

SIMULATED: METHOD 1

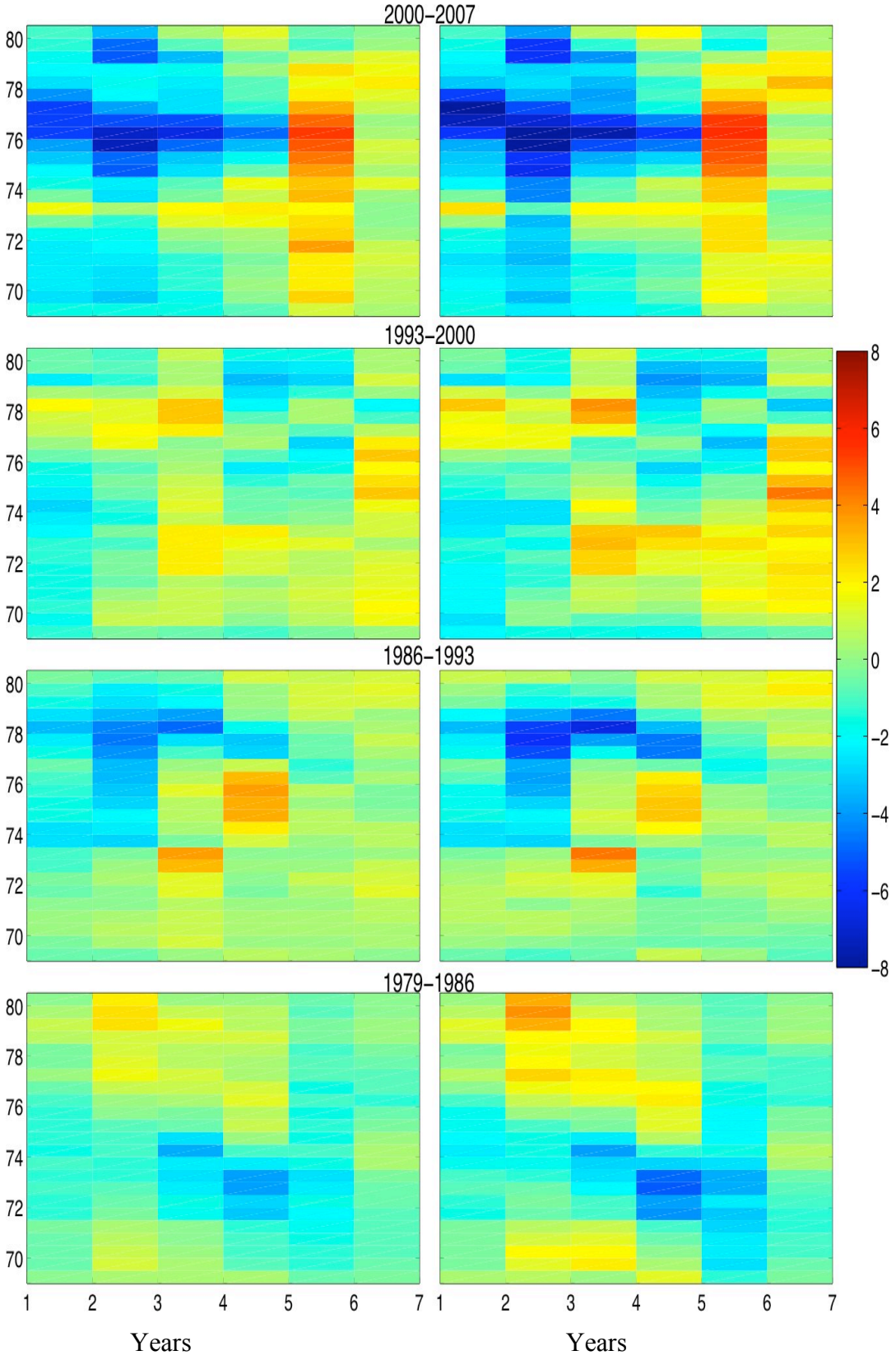

Figure 5. 54. Anomalous model transport [Sv] in the top 1000m of the water column (left) and simulated transport using Method 1 (right) [Sv].

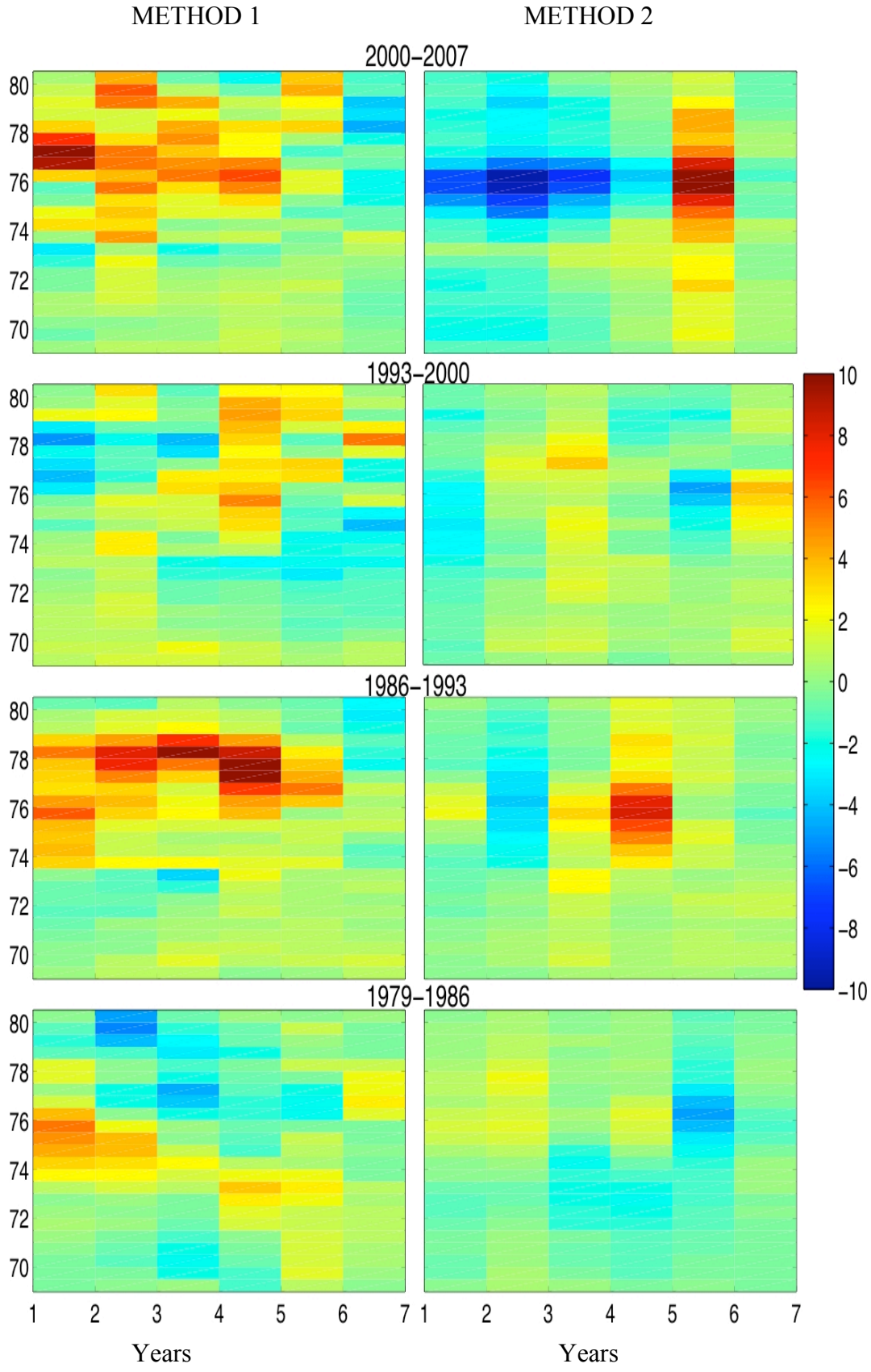

Figure 5. 55. Difference [Sv] between the NEMO model transport and simulated transport (Sv). Left- Method 1; Right- Method 2.

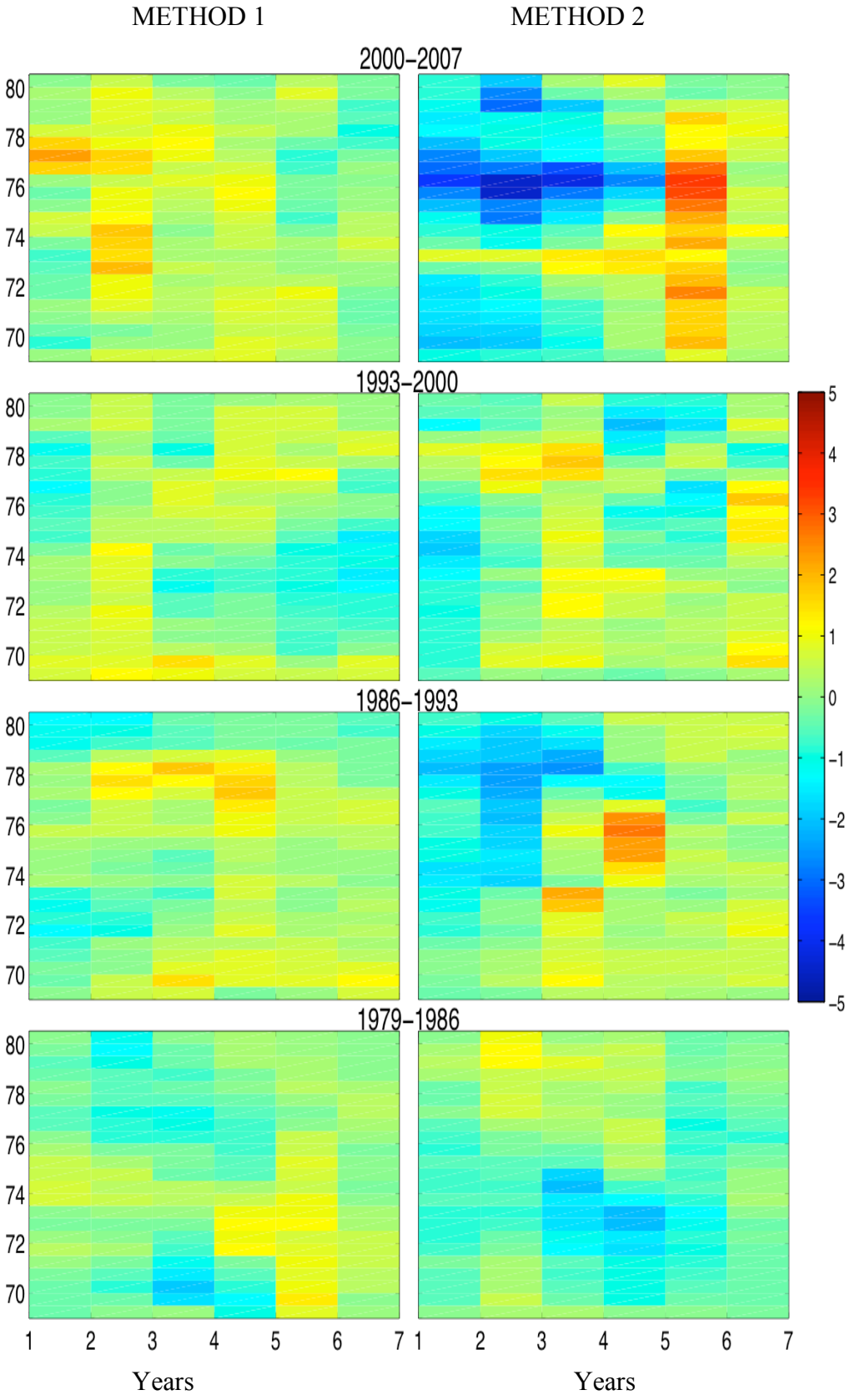

Figure 5. 56. Difference [Sv] between the model transport and simulated transports in the top 1000m of the water column Left-Method 1; Right- Method 2.

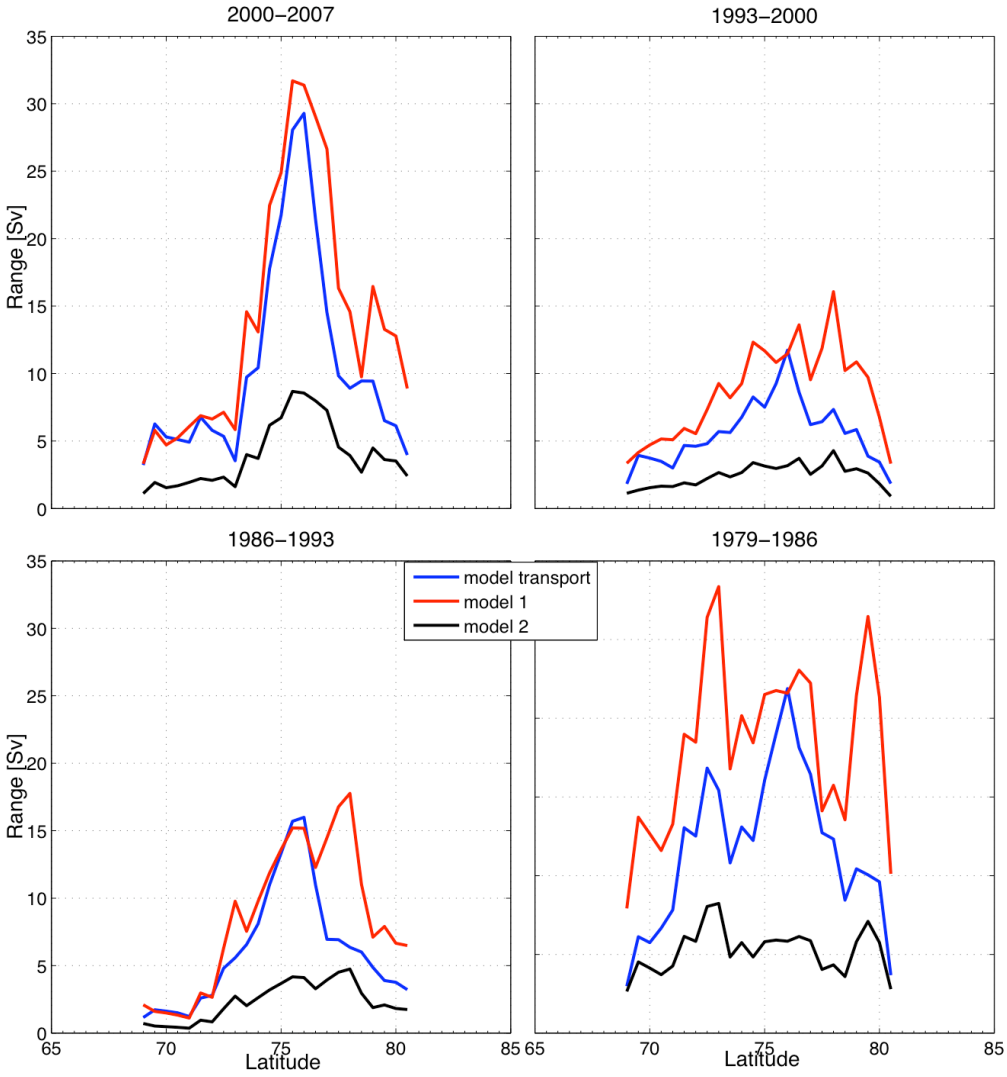

Figure 5. 57 Range [Sv] of the annually averaged full depth transport (Sv) during different 7-year long time periods. The model transport (blue), simulated transport obtained with Method 1 (red) and simulated transport obtained with Method 2 (black) are plotted against the latitude.

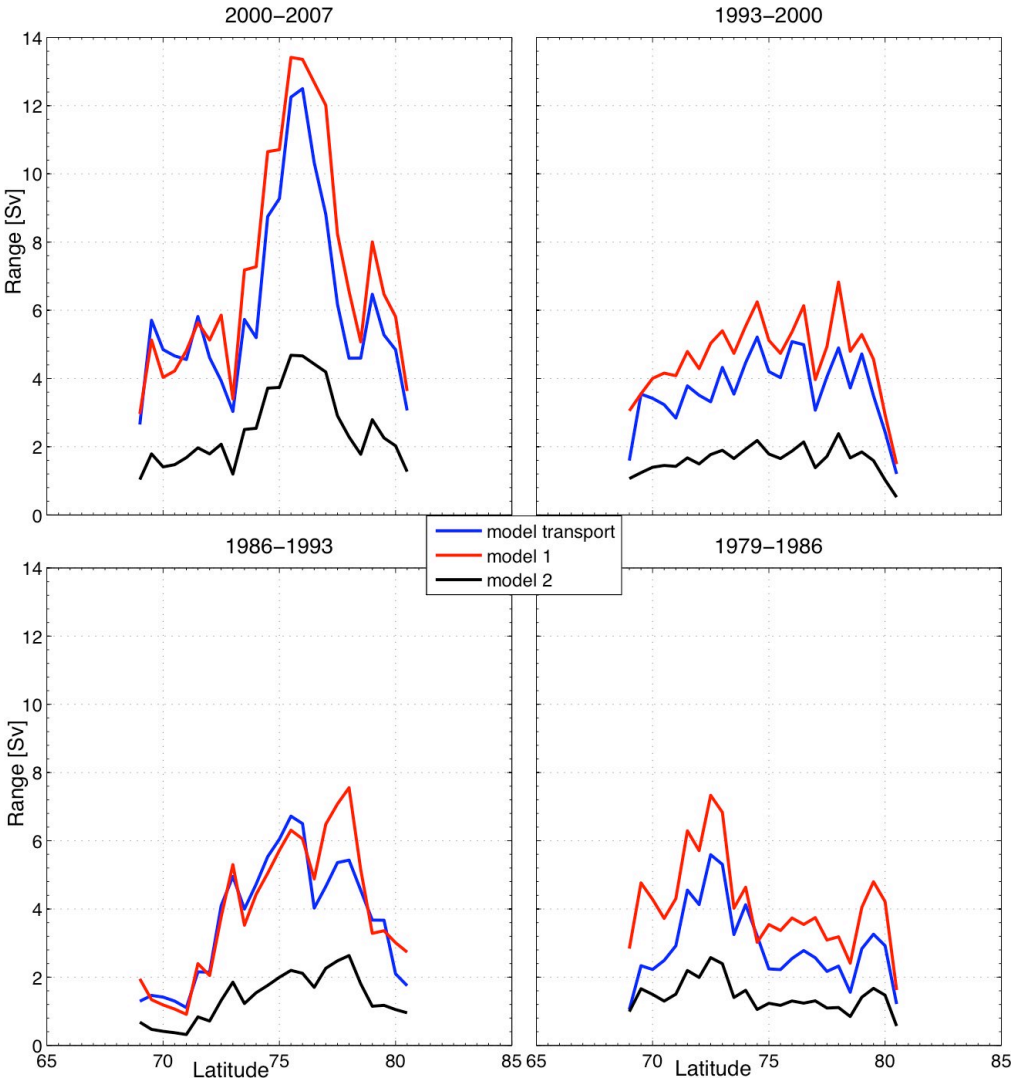

Figure 5. 58 Range [Sv] of the annually averaged transport in the top 1000m of the water column (Sv) during different 7-year long time periods. The model transport (blue), simulated transport obtained with Method 1 (red) and simulated transport obtained with Method 2 (black) is plotted against the latitude.

5.5.2. Total error in the transport estimation

The total error in the transport calculation consists of the error due to the method described above (i) and error in the surface velocity calculation (ii). The above statement is correct only when assuming that the model structure function adequately represents the real vertical structure function.

For the simulated transport that assumes the barotropic profile of the velocity, when the barotropic velocity is approximated by the geostrophic surface velocity, an error of 1cm s^{-1} in the surface velocity would produce an error in the transport estimation of about 1 Sv per 100 km width and 1km water depth. Considering the whole current width the resulting error has a minimum of 1.13Sv at 72°N and 2.75Sv at 75.5°N (Figure 5.59). The average depth of the current is always less than 2800m (80.5°N) and the maximum current width is 250km (75.5°N), which makes the upper limit of the transport error due to 1cm s^{-1} error in the surface velocity to be 6 Sv.

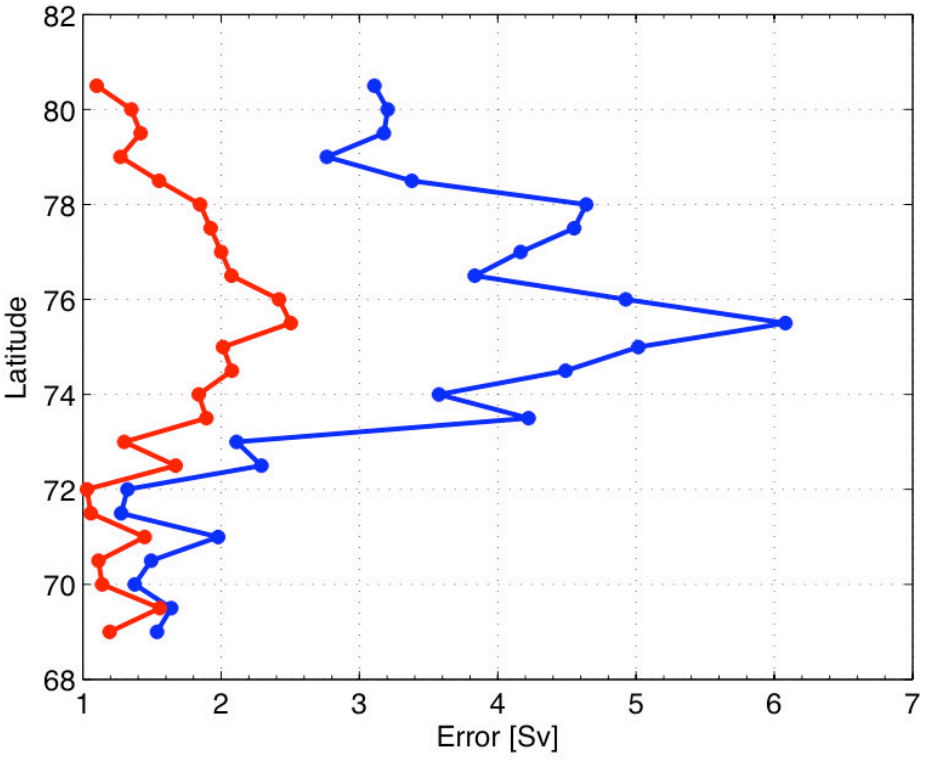

Figure 5. 59 Total errors produced by each 1cm s^{-1} surface velocity error in the transport estimation using method 1 in the top 1000m of the water column (red) and full depth (blue).

For the annually averaged transport estimated with method 2, the error of 1cm s^{-1} in the surface velocity produces maximum 2 Sv error in the total transport variability estimation over the entire width of the current in the top 1000m of the water column. Also the error of maximum 2Sv is produced when considering the full water depth except the Greenland Gyre region and Fram Strait (73.5°N-80°N) where the error is about 4Sv.

Summing up, the 1 cm s^{-1} error in the surface velocity produces smaller errors (1-2.5Sv) when estimating the transport in the top 1000m of the water column using Method 1. However, Method 2 performs much better when considering the full depth transports (2-4Sv vs. 1.2-6Sv). However, the total error is the product of the two errors and the previous section showed the error due to the method is smaller for Method 1 in the top 1100m of the water column when considering the seasonal and inter-annual transport variability and in full depth when considering only the seasonal variability.

The EOF analysis of the SSHA, described in Chapter 3, provided clues about the error estimate. Temporal averaging was performed to obtain the mean seasonal cycle of SSH (7 months averaged) and annual averages (12 months averaged) of the SSHA. This has further decreased the error for each grid-point. Furthermore, the more accurate Gaussian gridding was used with 100km width and 60km search radius. In order to check what is the noise level in these data the EOF analysis was performed on the seasonally and annually averaged SSHA. The results showed that only 2 modes of variability were important for each dataset and accounted for 78% of the total annually averaged variance and 86% of the seasonally averaged SSHA. The noise level was calculated from the remaining EOFs (3-7 and 3-12) as the standard deviation of the reconstructed SSHA. The average noise for the seasonally averaged SSHA in the EGC area was found to be about 1.4 cm with lower values (less than 1cm) located at 69°N and 73°N to 78°N. The noise level in the annually averaged SSHA was found to be about 1cm (0.7-1.14cm). Following Skagseth and Mork (2005) the error in the surface velocity was approximated by the error in the SSHA and therefore 1cm in the SSHA results in 1cms^{-1} error in the surface velocity. Therefore, in the next Section an error of 1cms^{-1} in the surface velocity is assumed to create the error bars for the range estimates.

5.6 Results

5.6.1 Mean seasonal cycle of the observed EGC transport anomaly from November 2002 to October 2009.

The mean seasonal anomalous transports of EGC were calculated using method 1 in the full water depth and in the top 1000 meters of the water column (Figure 5.60). Generally, the EGC transports were stronger than the average transport over the 7-year long period from November until April and weaker during the rest of the year. However, some spatial variability of the phase and magnitude of the seasonal cycle was observed. The southern part of the EGC (south of 72°N) flows over the mean depth of about 1km and the maximum transport occurs there from December (71.5-72°N) to February (south of 70°N). The Greenland gyre contributes to the EGC from about 77°N to 73°N (Figure 5.45) where also the average depth and width of the current is greater. This part of the EGC is characterized by the large range of the seasonal cycle with the maximum of 28± 6Sv v at 75°N and 17Sv±2.5Sv at 73.5°N in the top 1km of the water column (Figure 5.61). The location where the maximum seasonal transport occurs is different when comparing with the model results that indicated the maximum seasonal transport at 76°N. The strongest transports occurred during March from 73°N to 75°N and the weakest to the north of 77.5°N from August until November. The maximum in the transport occurred in December for 71.5°N-72°N, February/March for 73°N-80°N and 69.5-70°N and in May for 69.5°N and 80.5°N. The weakest transports occurred generally from July to October (72°N-80.5°N) except the southern part of the EGC (south of 71.5°N) where the weakest transport occurred in November (71.5°N and 69.5°N), March (69°N, 70°N) or May (70.5°N-71°N). The results suggest that the EGC over the analyzed period showed large seasonal fluctuations along its path, especially to the north of 71°N. Large amplitudes of the mean seasonal cycle were also found in the northern Fram Strait with the maximum range of about 30Sv±5Sv at 79.5°N and 19.5±2Sv for the transports in the top 1km of the water column. In Fram Strait (78-79°N) the range of the seasonal cycle was smaller: 19±5Sv and 11±2Sv in the top 1km of the water column. The smallest range was found to the south of 69.5°N and reached 5±2Sv. Generally, the ranges of the seasonal cycle were greater than for those found in the model (Section 5.4).

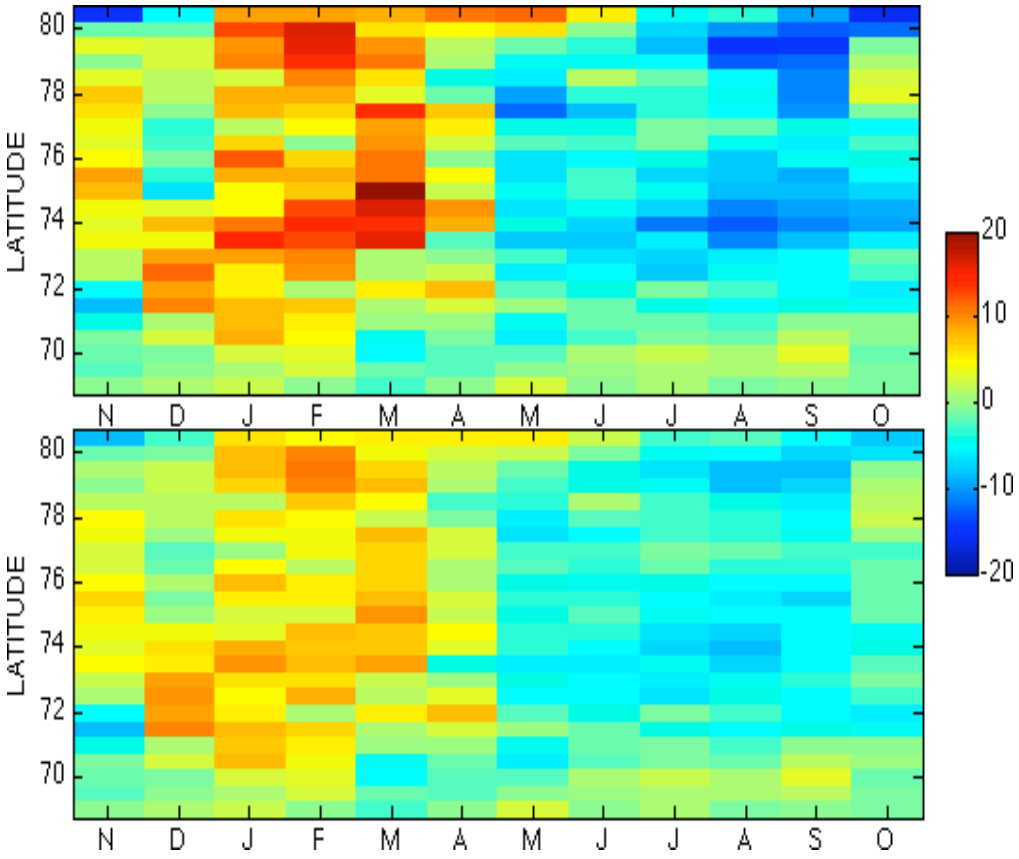

Figure 5. 60 The observed mean seasonal cycle of the anomalous EGC transports (Sv) for the full depth transports (top) and top 1km transports (bottom).

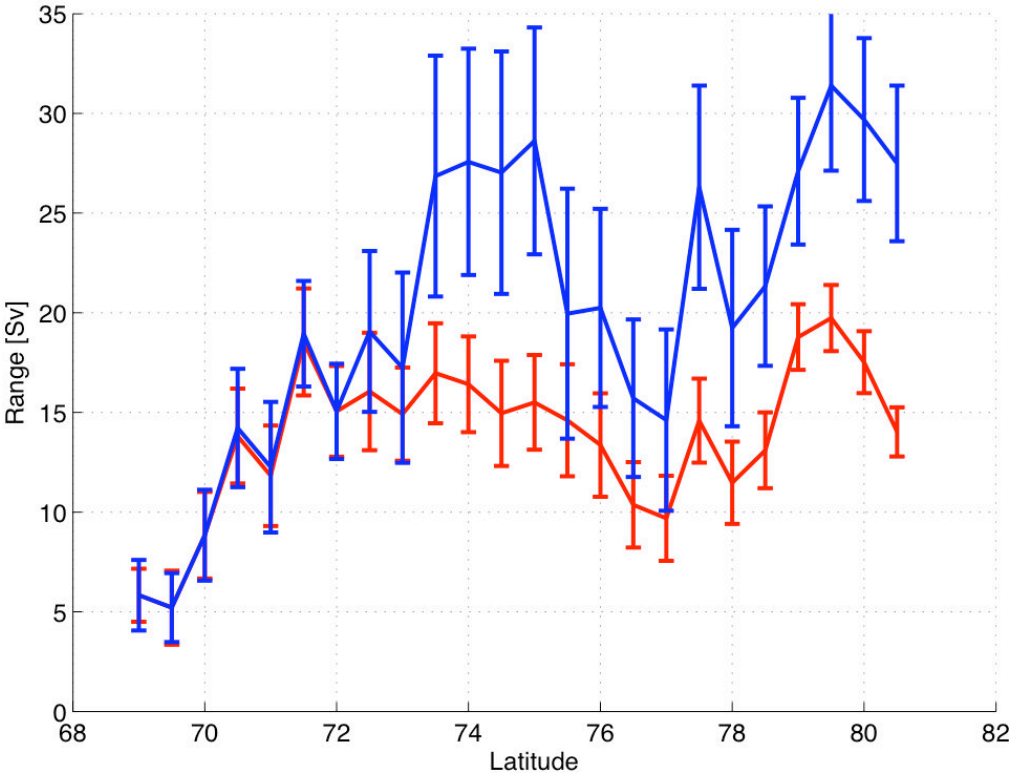

Figure 5.61 Range of the mean seasonal transport of the EGC for the full depth transports (blue) and top 1km transports (red).

5.6.2 Inter-annual variability of the observed EGC transport anomaly from November 2002 to October 2009.

The inter-annual transport variability was calculated using method 1 and 2 for whole water column (both methods) and the top 1km layer (Method 1). During the 1st year the transports were weaker and strengthen gradually in time reaching the maximum strength in 2007 (Figure 5.62). Then the transports weaken again and in 2009 reached the values close to the average. In the Greenland Gyre the maximum transports occurred in 2005. In the top 1km of the water column the spatio-temporal variability was the same and about 50% of the variability occurred. The 1st and 2nd method gave similar results and the differences between them are the greatest to the north of 77.5°N (~3Sv) with the maximum difference occurring at 80.5°N (3-6Sv). During the 7 years analyzed here, the annually averaged transports varied by at least 7.5±3Sv (77°N) when considering the top 1km transport and 9.5±4.5 Sv (76.5°N) for the full depth transport (Figure 5.63). Maximum variability occurred at 70.5° (range: 20±3 Sv) and 74.5 (range: 20±5 Sv)°N and to the north of 79°N (range: 22±5 Sv – 24±3 Sv). The top 1km transports showed similar spatial variability with the greatest ranges occurring at 70.5°N (18Sv±1.5) and 69.5°N (17±2 Sv). In the NEMO model also the range of the inter-annual variability can vary greatly and for the period 2000-2007 was the greatest at 76°N for the full depth transport (up to 30Sv) and the top 1km transport (13Sv) (Section 5.5.1). Figure 5.64 shows the annually averaged transports along the latitudinal bands as transports per degree of longitude. It indicates that the changes in the transport described earlier (Figure 6.62) are coherent along the whole width of the current and are not due to wrong definition of the current or the recirculation.

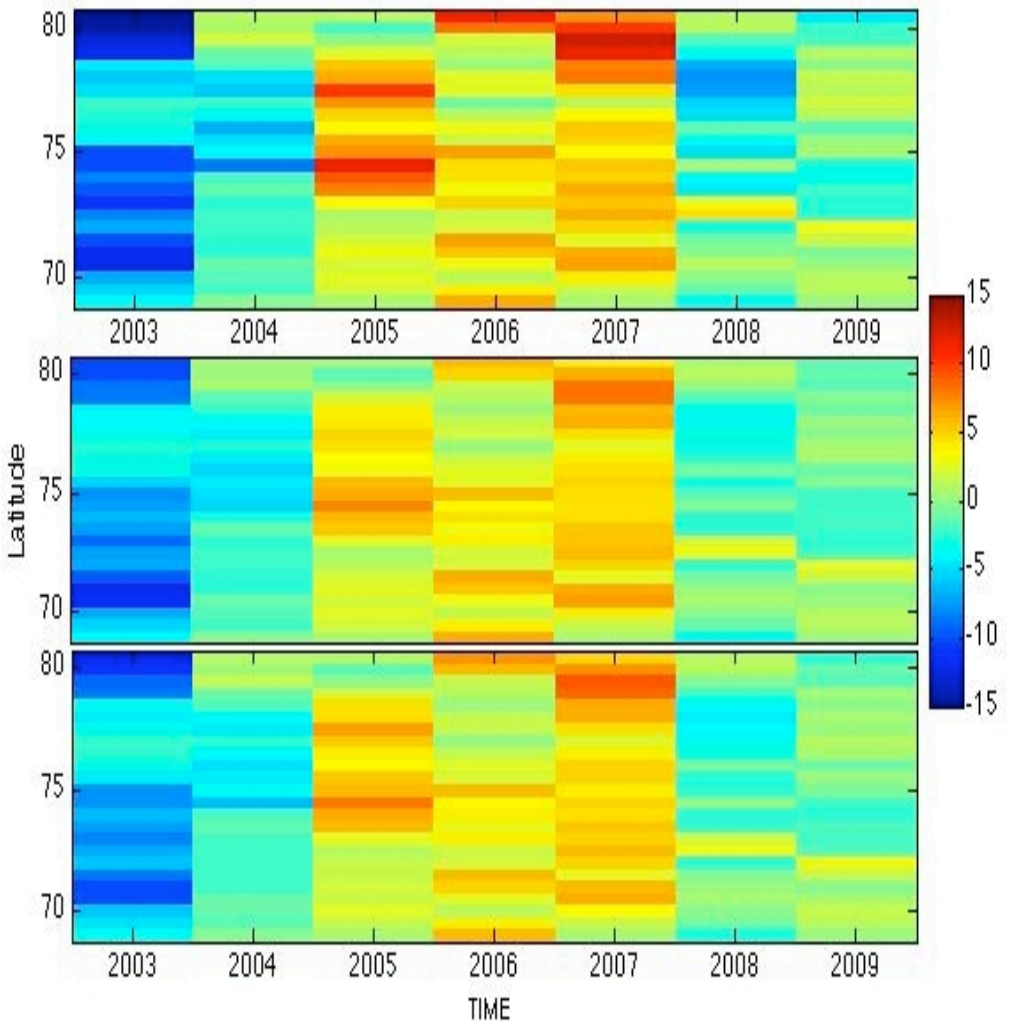

Figure 5. 62. The observed annually averaged anomalous EGC transports (Sv) for the full depth transports (top) and top 1km transports (middle) obtained with Method 1 and for the full depth transports obtained with Method 2 (bottom).

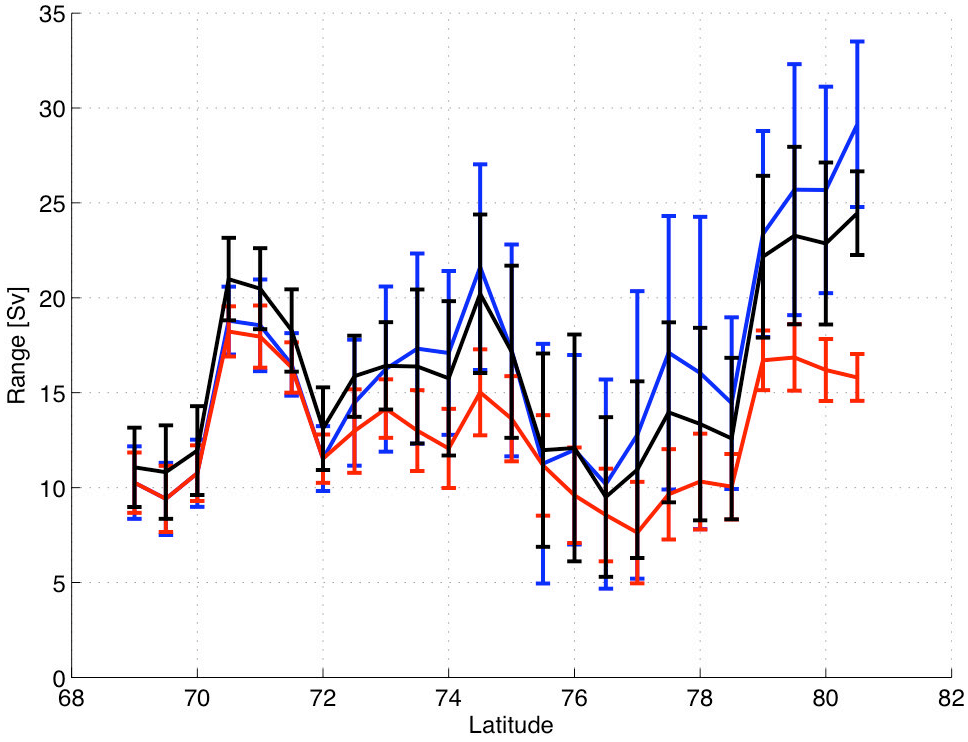

Figure 5. 63. Range [Sv] of the observed annually averaged transport of the EGC in the full water column (blue-Method 1, black-Method 2) and in the top 1km (red).

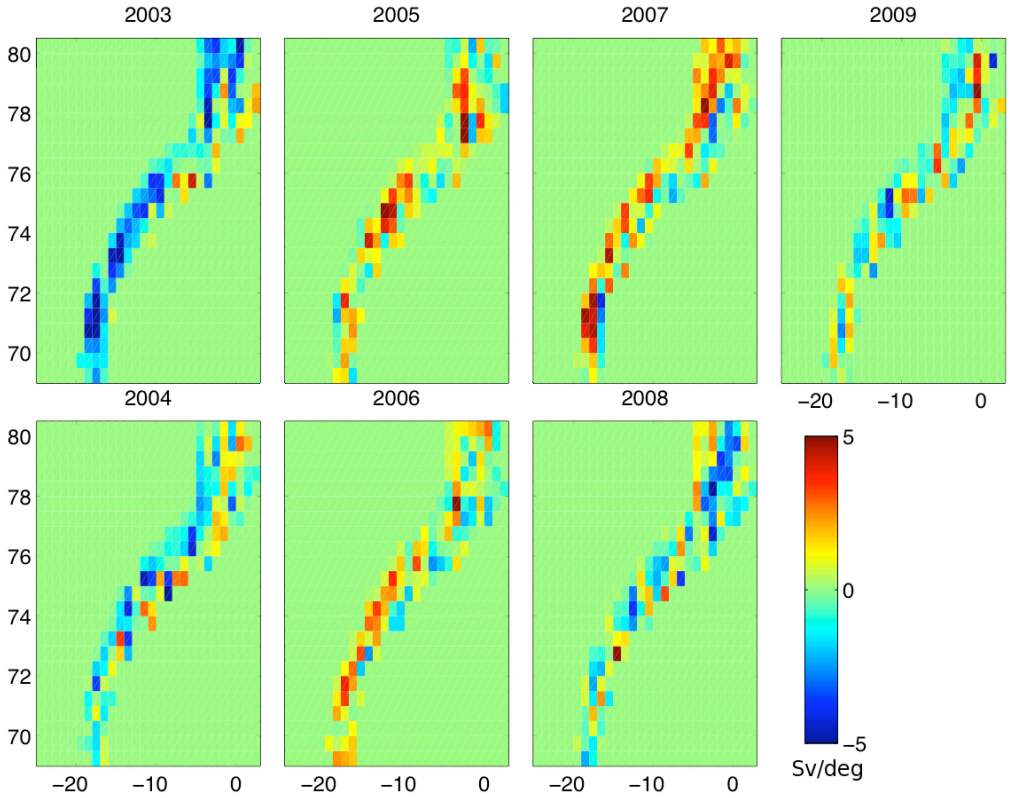

Figure 5. 64. Anomalous annually averaged full depth transport of EGC per degree of longitude (Sv/degree) obtained with Method 1.

5.7 Discussion

In this chapter the mean seasonal cycle and annually averaged surface currents in the Nordic Seas were described in 2002-2009. It was shown that the surface circulation in the whole area varied greatly seasonally and the maximum variability occurred on the Greenland continental shelf and along the east Greenland continental slope where the EGC flows. Generally the circulation was stronger in the winter (January to March) and weaker in the summer (July to September). It was already shown earlier in Chapter 4 that the seasonal cycle in the Nordic Seas is mainly caused by the barotropic response of the ocean to the wind forcing and to the local air-sea fluxes of freshwater and heat. The large seasonal variations of the major currents in the area had been already observed *in situ* for the NwAC, WSC and central Nordic Seas and in the EGC at 75°N (Fahrbach et al.2001, Morison 2001, Woodgate et al. 1999). However, no observations for the full year period had been done for the east Greenland shelf circulation and the EGC. The results also indicate the strengthening of the EGC and its transports from 2003 to 2007. The current maximum observed in 2007 may be caused by the strong wind forcing that occurred in 2007 and in effect was partly responsible for the Arctic sea-ice minimum and greater transport of the sea-ice from the Arctic to the Atlantic (Ogi et al., 2008). The observed inter-annual variability of EGC transport could be driven by the winds over the Arctic and Nordic Seas because the AO and NAO indices showed similar variability for the winter averaged data (January to March) (See Chapter 3). When the NAO was more positive the surface currents were stronger, which translated into greater EGC transports. This suggests the surface geostrophic currents obtained from altimetry and the transports of EGC were affected by the major atmospheric modes of variability and therefore showed similar behavior.

Transports at 75°N

The characteristics of the EGC change along its path from north to south. The transports of the current were measured previously and showed large barotropic transport in the Greenland Gyre (Aagaard and Coachman, 1968, Fahrbach et al.1995). The last measurements in this area have been done at 75°N in 1994-1995 (Woodgate et al., 1999) with results indicating a strong seasonal cycle with the range of 26±5 Sv for 140 km section width and 18±3 Sv for 111 km width. The comparison with the NEMO numerical model showed a good agreement between the observed and modelled transports at this location for the east-west section located between 14°W-8°W. It was shown in Sections 5.4 and 5.5 that the model transports could be well described at this location by the surface velocity assuming barotropic transports. The results described in the previous Section showed that the range of the mean seasonal cycle in 2002-2009 reached 28±6 Sv at 75°N (13°W-7°W) for the full depth transport and 15.5±2.5 Sv for the top 1km of the water column. These estimates agree well with the previous observations. Furthermore, the timing of the maximum and minimum transport is the same (March and September). Woodgate at al. have showed that the seasonal variations at these locations can be to a large extent explained by the local wind forcing (70%). The other part of the flow (30%) is probably buoyancy-driven and may not have a seasonal cycle (Woodgate et al., 1999). The previous comparison of the mooring observations over the 4 years (1991-1995) done also by Woodgate et al. (1999) did not indicate any significant (greater than 5Sv) inter-annual variability (Section 5.3.2). However, the estimation suffered from poor spatial and temporal coverage and assumed the same variability and velocity structure as in the year 1994-1995. The main weakness of this method was that the assumed velocity structure could not change its magnitude, which could cause substantial underestimation of the inter-annual variability. The other reason why any inter-annual variability was not previously observed could be the fact that the inter-annual variability was much smaller over this period (See results from the NEMO model, Figures 5.55 &5.56). However, the inter-annual variability was much greater for the other periods, which was confirmed in the numerical model. Section 5.4 also showed that the barotropic velocity had the greater variability after 1993. The annually averaged velocities described in Section 5.6.2 showed a strengthening of the EGC in time with the maximum current occurring at 75°N in 2005. Assuming the barotropic profile of the velocity and that the surface velocity approximates well the

barotropic velocity the resulting transport showed large inter-annual variability with the range of 13.5±3 Sv considering the transports in the top 1km of the water column and 17±6 Sv for the full depth transport. Therefore, the results indicate there is a significant inter-annual variability of the EGC at this location. One may suggest that may be an effect of a different location and width of the current used in this research. However, even though the current as defined here lies further east, the changes in the transport were observed over the entire current width (Figure 5.64).

The results are also exposed to many uncertainties. It is possible that the annually averaged surface velocity is not well correlated with the annually averaged velocities from other depths in the real ocean but currently no *in-situ* observations exist to prove or disprove it. However, the model exhibits many of the characteristics of the observed SSH variability and its velocity structure well compares with the previous observations (Section 5.2). Therefore the numerical model may well represent the ocean dynamics, which suggests the method used in this chapter to calculate the anomalous transports of the EGC is appropriate and the obtained results are accurate enough.

Transports at 78.5° N

The reported results at 78.5°N showed weaker transports at the beginning of the record (2003 and 2004) and stronger transports from 2005 to 2007. The transports rapidly decreased again in 2008 and reached the average value in 2009. The inter-annual variability of transports at 78.5°N agrees well with the mooring observations from the Fram Strait, which also showed the weaker transport of EGC in 2002-2003 and the later strengthening of the current with the maximum transport occurring in 2007 (De Steur et al., 2009). The range of the variability observed *in situ* from 2002 to 2007 was about 6.5±4 Sv and the range obtained by this study was 11±5 Sv. This indicates that the two results agree with each other within the error limit even when taking into account that the integration was done for a smaller distance (5°W-1°W instead of 6.5°W-1°W) and the averaging was done for a year starting in November instead of July. However, these differences can be the reason why our estimation of the inter-annual variability is slightly greater from the one reported earlier. In fact, even the *in situ* measurements confirmed that the transport is the greatest in March and our results are centered in March/April instead of December/January as for the values reported by De Steur et al. (2009). The mooring array located in the Fram Strait also observed a mean seasonal

cycle with the stronger transports occurring from October to April (6-9±3 Sv) and weaker from June to August (~4S±2 Sv). Therefore the measured range of the mean seasonal cycle in 1998-2008 was about 5Sv but the error associated with this range estimate is as high as the estimation itself, which makes any comparison hard to assess. Our estimation of the mean seasonal cycle also shows strengthening of the transports from October to March and weakening of the transports from June to September (at 78.5°N) but the range of the seasonal cycle is about 20±4 Sv for the full depth transport and 13±2 Sv for the top 1km transport. The error bars reported for these estimates do not take into account the inaccuracy of the numerical model because we did not have data for this location to assess how well the model agrees with the in-situ circulation. In fact such a comparison would be hard to perform due to the large errors in the mooring data. Furthermore, Fahrbach et al. (2001) showed that the monthly variability could be large with 16Sv transport difference observed between March and August. However, their results also showed this large variability does not occur every year and could be linked with the meridional shift of the recirculation in the Greenland Sea. Therefore, the reported range of the seasonal cycle could be right and in principle there are no reasons why we should disbelieve it.

Limitations

The transport estimates are subject to many uncertainties, which we tried to estimate earlier in this chapter. However, the model has its own limitations and therefore the circulation produced by the model could differ from the real oceanic circulation. Currently it is not possible to test the model in any different way to what we did. However, the lack of long-term EGC current measurements provided the main motivation for this research and makes this study interesting and significant.

The vertical structure of the current velocity was analyzed in Section 5.4 and showed the surface velocity is significantly correlated with the velocities at other depths almost in the whole area considered. Therefore, it was decided to use the surface velocity to describe the velocities at the other depths and calculate the transports. However, if we believe the model, the surface velocity is not well correlated with the velocities at other depths to the north of 80°N which should result in larger errors in that area when compared to the others and could make the transport estimates not reliable. Furthermore, many previous studies showed that the current is more baroclinic to the

north of Fram Strait and its baroclinicity decreases from the Fram Strait to the south, and reaches a maximum in the Greenland Gyre at about 75°N (Schlichtholtz, 2007, Aaboe and Nost, 2008, Aaboe et al., 2009) and therefore limits the application of the method to that region.

5.8 Conclusions

The analysis began from the investigation of the surface circulation in the Nordic Seas in 2002-2009. A significant seasonal cycle of the surface currents was observed with the strongest currents occurring in the winter and the weakest in the summer. However, some spatial differences were observed between the major surface currents of the Nordic Seas and it was found the greatest seasonal variability was associated with the Greenland shelf circulation and the EGC. In August and September the EGC strengthened but the shelf circulation was weaker than average. This changed from October to March, when the currents at the Greenland shelf and the EGC were stronger. It was observed that the NwAC and WSC were weakest in the same month as the EGC (June-July) but the maximum was reached in January. In contrast the EGC was the strongest from December to February to the south of 74°N and from January to March to the north of 78°N. The opposite occurred for the East Icelandic Current, which was the strongest in October and the weakest in March. The surface circulation also varied annually and was weaker in the two first years of the record (2003-2004) in the whole Nordic Seas except the Greenland shelf circulation, which was stronger than the average in 2004. The currents strengthened from 2005 to 2007 when the largest positive anomalies were observed along the EGC. In the same time the currents on the Greenland shelf weaken. In 2008 the EGC was still stronger than average together with the NwAC but the WSC was weaker or close to the average. In the last year of the record only the EGC to the north of 73°N was stronger than the average, and the currents in the remaining part of the Nordic Seas had their surface velocities close to the average value.

The remainder of this chapter focused on the EGC and its transport variability in 2002-2009. The method of the transport calculation was developed with the help of the numerical model output, which was first validated against the altimetric observations and in situ measurements located in EGC along the section at 75°N that were described by Woodgate et al (1999). The model results were generally in good agreement with the observations and proved that the numerical model output can be used to provide information about the EGC vertical structure. Two methods were developed to calculate the anomalous transports. The methods were simulated in the model to estimate the errors due to the method also the anomalous model transport was obtained for four 7-

years long periods in 1986-2007. The model showed large seasonal and inter-annual variability in the transports of the EGC with the largest variability occurring in the Greenland Gyre and its maximum is located at 76°N. However, the location of the greatest variability was different for the top 1km of the water column.

The aim of this chapter was to estimate the mean seasonal cycle and annually averaged anomalous transport of the EGC using the anomalous surface velocities obtained from the SSHA. The results showed that the EGC was stronger from November to April and weaker from may to October. The seasonal variability of the EGC was small to the south of 70°N but much greater for the other latitudes. The range of the seasonal cycle reached maximum of 28±6 Sv in the Greenland Gyre (73.5°-75°N), which is consistent with the model results. Large amplitudes of the seasonal cycle were also found to the north of Fram Strait where the maximum range was 30±5 Sv at 79.5°N. In the Fram Strait the range of the seasonal cycle was smaller (19±5 Sv). Generally the ranges for the mean seasonal cycle in 2002-2009 were greater than for any periods analyzed earlier in the model. The range of the seasonal cycle at 75°N was 28±6 Sv, which is similar when compared to the range reported by Woodgate et al. (1999). The anomalous EGC transport also showed large variability in the top 1km of the water column reaching values greater than 15Sv from 71.5°N to 74°N and to the north of 79°N.

The EGC transports showed strengthening from 2003 to 2007 and weakening in 2008 and 2009. Similar behavior was observed in Chapter 3 for the winter averaged NAO and AO indices, which suggests the inter-annual variability in 2002-2009 was driven to a large degree by the wind forcing associated with the two atmospheric modes of variability. The transports were compared to the transport estimates obtained from *in situ* mooring measurements at two locations: Greenland Sea (75°N) and Fram Strait (78.5°N). The variability of the EGC was quite similar at the two locations, which suggests our method of the transport estimation was correct. The study showed that EGC varies seasonally along its path, which was only observed before in the Greenland Gyre. Furthermore, the results suggest the wind forcing associated with the major atmospheric modes of variability has an effect on the annually averaged EGC transport and on its inter-annual variability. The results provide therefore new information about the variability of the EGC.

CHAPTER 6: CONCLUSIONS

CHAPTER 6: CONCLUSIONS

6.1 Overview

This chapter provides the summary of the thesis. The main conclusions are described here together with their implications. Furthermore, it provides recommendations for the future, which can develop the work done in this thesis.

The major contribution of this thesis is the inference and characterization of sea level variability and circulation in the whole Nordic Seas in 2002-2009. For the first time the variability of the surface currents was described in the ice-covered ocean of the Nordic Seas and over such a long record. The driving mechanisms causing this variability were also investigated using statistical analysis and the results provided insights into the most likely mechanisms causing the variability. Another important contribution of this thesis is the description of the transport variability of the EGC, which is the major current connecting the High Arctic with the Atlantic and is one of the main export routes for freshwater (liquid and solid) from the Arctic Ocean. This is the first study that has described EGC variability along its path (80°N-69°N) and over a period of time spanning several years.

Chapter 1 provided an introduction to the thesis, the main motivation behind the work undertaken and the main aims and objectives. Furthermore, it provided an overview of the Nordic Seas and gave a brief introduction to the subject of altimetry. In Chapter 2 the data and methods used in this thesis were described. The results were divided into three chapters, each one described a specific problem and the analysis that was performed to solve it. Chapter 3 described sea level variability in the Nordic Seas in 2002-2009. The forcing mechanisms that caused this variability were identified and assessed in Chapter 4. The variability of the surface circulation was described in Chapter 5. In Chapter 5 also the variability of the EGC transport along its path was explained.

The SSH measured by the satellite altimeter on board Envisat and processed by CPOM provided the framework and motivation for this thesis. Data were processed in a special

way by CPOM (See Chapter 2) and as a result the signal from the ice-covered part of the Nordic Seas was recovered. The data suffered from many uncertainties and a bias between the ocean and ice-covered part of the SSH signal. Therefore, the first step in this investigation was to develop a method for the bias removal. The subsequent analysis applied statistical methods to describe the variability of the SSHA: EOF, harmonic analysis etc. Possible explanations behind the variability were hypothesized and addressed in Chapter 4 by statistical analysis of the SSHA and air-sea and momentum fluxes (EOF, MCA, CCA, Pearson point-to-point correlations). Finally, the anomalous surface geostrophic currents were calculated from SSHA and the mean seasonal cycle and the inter-annual variability of the surface circulation was presented. The final aim of this thesis was the description of the EGC variability along its path using the previously obtained anomalous surface currents. However, to be able to calculate the transport one needs to know about the vertical structure of the current. The only possible (available) source of the information was the numerical ocean model (NEMO), which we used to analyze the vertical structure of the EGC and to develop a method of the transport calculation.

6.2 Main conclusions

The greatest variability in the SSHA over the Nordic Seas was observed along the Norwegian and East Greenland coasts, with the amplitude of SD reaching 15 cm (Figure 3.2) probably associated with the shelf circulation and coastal currents. Furthermore, large variability (SD<10 cm) was observed in the Norwegian and Greenland Seas and along the ice-edge extending from Svalbard to Greenland. Furthermore, the sea level in the coastal zones to the north of Iceland and south of Svalbard varied with amplitudes exceeding 10 cm in the analyzed 7 years. Large variability in SSH was also observed in the Lofoten Basin that could be caused by the high anticyclonic eddy activity observed in this region in the past (Rossby et al., 2009, Kohl et al. 2007). The EKE in 2002-2009 (Chapter 4) showed similar pattern as SD of SSHA. The greatest EKE was observed along the ice-edge (200-400 cm^2s^{-2}), in the vicinity of Denmark Strait, in the Lofoten Basin (up to 250 cm^2s^{-2}) and to the south of Svalbard (350 cm^2s^{-2}). Furthermore, greater values of EKE occurred along the Norwegian shelf and Iceland-Faroe Ridge. Very similar spatial patterns of EKE were recently obtained using surface drifters by Koszalka et al. (2011) but only in the open ocean. However, this study suggests that the

enhanced eddy activity is characteristic to the east Greenland ice-edge region. Therefore, the major contribution was the finding that the sea level varies greatly in the ice-covered part of the Nordic Seas and along the ice-edge.

Considering the interannual variability the greatest contributors to the variability were winter months (December, January, February) for the whole area but in October/November the variability was also high at the Greenland Continental Shelf. This shows that most measurements made in the western part of the Nordic Seas were taken in the least variable season (summer), which could, in effect, greatly underestimate the inter-annual variability because the annual mean would be especially sensitive to the winter changes. However, it was also found that the winter variability of sea level at the Greenland and Norwegian continental shelves is significantly correlated to the NAO index and the NAO can explain up to 80% of the winter SSHA variance at those locations. This is a very important finding because this can improve the existing knowledge about the inter-annual variability of the circulation in the region. At other seasons the wind forcing is weak and therefore no significant correlations were found for the NAO and SSHA, suggesting that other direct and indirect forcing mechanisms are important.

6.2.1 Seasonal variability

Sea level

It was found that the mean seasonal cycle was a large contributor to the variance of SSHA. The mean change in the variance over the whole Nordic Seas after removal of the mean seasonal cycle was 36%. The contributions of the mean seasonal cycle to the total variance differed regionally from 10% at the Greenland Continental Shelf and Barents Sea to 60-70% in the Greenland Sea. The EOFs of the monthly unfiltered SSH determined three important orthogonal independent modes of variability that oscillate with large annual and inter-annual frequencies. The three modes explained 49% of the total variance, and regionally up to 80% of the variance can be explained by the first 3 modes in the deep basins and at the Greenland continental shelf, demonstrating the importance of seasonal cycle at those locations.

- The 1st EOF (36%) described the SSHA oscillations in the central Nordic Seas with lower sea level in the winter and higher in the summer.

- The 2nd EOF (10%) explained oscillations of SSHA at the western and eastern borders of the Nordic Seas, which are in antiphase relationship to the deep basins.

- Finally, the 3rd EOF (3%) explained significant part of variance at the northern continental shelf of Greenland and showed that SSHA at the western and eastern boarders oscillates in the opposite phases. It also demonstrated that the long-term trend in SSHA at the western and eastern border is opposite and sea level increased with time at the west but decreased at the east.

Forcing

Correlations between the monthly NAO indices and EOFs of monthly SSH confirmed a strong relationship between the NAO and all the first 3 EOFs. However, this relationship does not exist for the seasonally filtered EOFs suggesting that the seasonality in NAO is strongly related to the seasonality of SSHA. Therefore, the statistical methods applied to SSHA and ECMWF atmospheric variables (Chapter 4) showed that wind forcing plays a major role in driving the first three EOFs of SSHA and can explain also a large percentage of variance in the SSHA at annual frequency. The similarity between the seasonal cycle phase of the atmospheric fields and SSHA suggested that the ocean responds simultaneously or with 1-2 months lag to the seasonal atmospheric forcing and therefore its response is mainly barotropic. The seasonal SSHA variability in the central Nordic Seas can be explained by the more cyclonic winds occurring in the central Nordic Seas during the winter that spin up the circulation also causing anomalous heat loss in the area. These two mechanisms cause sea level to decrease.

On the other hand, the maximum SSHA occurs during winter, simultaneously with the maximum wind strength along the coast of Greenland and Norway and in the Barents Sea. This response of sea level can be explained by the Ekman theory because the local wind stress blowing along the coast causes a local downwelling that in effect causes a local sea level rise close to the shore. Furthermore, an anticyclonic wind that occurs along the northern shelf of Greenland causes convergence and therefore the local sea level rise. It was found that the timing of the maximum wind stress curl is the same as the timing of the local SSHA at the northern Greenland continental shelf.

Surface Circulation

Because the sea level gradient translates into surface geostrophic currents the mean seasonal cycle of the anomalous surface circulation also shows the same variability, mainly characterized by the stronger currents in the winter and weaker in the summer. This seasonal variation was already observed *in situ* in many areas of the Nordic Seas (Woodgate et al. 1999, Fahrbach et al. 2001, Schauer et al. 2004, Voet et al. 2010). However, this study offers a broader view on the seasonal variability of the surface circulation in the Nordic Seas and provides an insight into spatial differences between different regions. Similarly to SSHA, the circulation in the ice-covered area shows large seasonal variability and the currents on the Greenland shelf reach a minimum in August and maximum in February. The minimum currents occur at the same time for the EGC and WSC and NwAC. The EGC is stronger from August/September but at the same time the Greenland shelf circulation is weaker. However, from October until March the EGC and shelf circulation are stronger. This different phase of the seasonal surface circulation was not observed before and provides new information about the circulation in the area.

EGC transports

This study contributed significantly to the knowledge about EGC. It described the mean seasonal cycle of the current along its path from the north of Fram Strait to the north of Denmark Strait. The results showed that EGC was stronger from November to April and weaker during the rest of the year. The greatest range of seasonal variability occurred in the Greenland gyre (73.5°N-75°N) reaching there 28±6Sv and to the north of Fram Strait (79°N-80.5°N) reaching there 30±5Sv. When considering only the top 1km of the water column the range of seasonal transports was the greatest to the north of Fram Strait at 79.5°N reaching 19.5±2Sv. The lowest seasonal variability of the EGC transport was observed to the south of 70°N with the range of 5±2Sv. Also a different time of the maximum transport was observed for different sections along constant latitude bands. In the Greenland gyre and Fram Strait the strongest transports occurred in February and March, whereas at the southern part (71.5-72°N) the maximum occurred in December. The weakest transports were observed from July to October to the north of 72°N and in November to the south of 72°N. The transports were compared to those observed previously by moorings at 75°N and 78.5°N and showed good

agreement with the previous estimates if the uncertainties of the two estimates are taken into account. The major contribution was the finding that the seasonal cycle is limited only to the Nordic Seas and does not contribute to the variability observed near Denmark Strait. Therefore, Nordic Seas act as a 'buffer' by limiting local seasonal variability from propagating further into the North Atlantic.

6.1.2 Inter-annual variability

Sea level

The removal of the seasonal signal does not change greatly the structure of the first two modes; the corresponding time series no longer have annual oscillations but the long-term trend is the same as for the unfiltered PCs. The response of the ocean to the local forcing is therefore similar at annual and other frequencies.

It was found that wind stress curl could explain most of the variance accounted for by the 1st EOF of SSHA. Therefore, one can argue that central Nordic Seas spin up/down at the same time as wind stress curl increases/decreases, which indicates a barotropic response to the wind forcing in the area. The strongest forcing of this mode occurs annually but other frequencies are also important in the central Nordic Seas and at the Greenland continental shelf where the sea-ice is present. Similar findings were obtained by Isachsen et al. (2003) who analyzed the barotropic model in the Nordic Seas.

It was found that the sea level variability that was described by a 2nd EOF of SSHA is driven/influenced by the NAO-related atmospheric forcing at the annual and other frequencies. This mode of sea level variability was found to be significantly correlated to the mean sea level pressure and precipitation at all frequencies. Furthermore, this mode was also correlated to the other fields, which were also correlated to the NAO Index.

The results suggest that the 3rd EOF of SSHA can be described as a response of the ocean to the wind stress curl, which affects SSHA at the eastern and western boundaries of the Nordic Seas, and heat and freshwater fluxes, which affect mainly the eastern boundary. Furthermore, the coupling between the 3rd EOF of SSHA and the other fields (wind stress curl, freshwater and heat fluxes) occurs at all frequencies, except heat flux, which contributes only to the annual SSHA variability.

Circulation

The study provided a description of inter-annual variability of the surface circulation in the whole Nordic Seas. The variability was not observed before in the ice-covered part of the Nordic Seas and therefore fills the gap in our knowledge about the circulation in the area. The study showed that surface currents in the Nordic Seas changed annually in 2002-2009. Generally, the currents were weaker in 2003 and strengthened in time reaching a maximum in 2007. However, not all the currents varied in the same way and spatial differences were also observed.

EGC transports

Significant strengthening of the annually averaged EGC transport was observed along its path from the 1st year of the record until 2007 when the maximum strength was reached. After that the current weakens and returned to the averaged strength in 2009. The only exception in this pattern was observed in the Greenland gyre where the maximum transport occurred in 2005. The observed variability could be caused by the winds blowing over the Nordic Seas associated with the NAO because the NAO winter averaged index showed similar interannual variability. This suggests that the winter variability of the EGC transports forced by NAO winds contributes significantly to the longer inter-annual variability and therefore affects the circulation over the longer periods than seasonal implying the baroclinic ocean response to the NAO wind forcing.

The range of the variability was about 10Sv or more along the whole path of the current. The smallest range was observed to the south of 70°N and from 75.5°N-78.5°N. Greater variability reaching about 20Sv was found in 70.5°-71°N, at 74°N and to the north of 79°N. The variability observed in the Fram Strait and to the north of it might be associated with the variability of the recirculation of Atlantic water, which was suggested in the past by Fahrbach et al. (2001). The increased variability observed between 70.5°N to 71°N could be associated with the Jan Mayen current.

6.3 Future work

This section presents how the study can be further developed to provide a better understanding of the circulation in the Nordic Seas. Firstly, the SSHA data set could be extended to 13 years record when including SSH collected by ERS-2 (1995-2006). This could not be done during this PhD due to limited time, and many technical issues, which need to be solved before connecting the two datasets. The starting aim of this project was to use Envisat and ERS-2 data and describe the SSHA variability during the longer period. However, when checking the quality of ERS-2 SSHA it was found that the noise level of this data is much greater than for Envisat. Furthermore, some corrections need to be calculated for the dataset; For example there was no sea state bias correction in the ocean data set. The use of ERS-2 data would extend the analysis of SSHA in the Nordic Seas to 13 years, which would help better identify the forcing mechanisms that influence the sea level variability and circulation in this region.

The ECMWF air-sea and momentum fluxes were also sensitive to large uncertainties due to the model physics and limited data assimilated in some areas and seasons (e.g. winter over sea-ice, Chapter 4). The largest errors were reported for the freshwater flux and precipitation (See Chapter 4), which makes it difficult to prove that these fluxes were responsible for the variability observed in SSHA. In order to confirm our findings about the driving mechanisms of SSHA experiments, experiments with a numerical model could be designed, run and analyzed.

In Chapter 5 EGC transport variability was calculated along its path from 80.5°N to 69°N. The calculation required a lot of assumptions and the numerical model output was used to approximate the vertical structure of the current and estimate the errors. It was assumed that the model approximates the real EGC velocity structure accurately, which does not have to be true everywhere along the path of EGC, even the transport variability and velocity structure agrees with the results of Woodgate et al. (1999) of the section located at 75°N. The structure function could be also checked in the Fram Strait (78°N) where the moorings were gathering current information over the last 10 years. This could not be done during this PhD because the data sharing problems between the institutions.

Finally, this PhD has proved that the SSHA measured in the ice-covered ocean and processed using Peacock and Laxon (2004) technique can be used for many oceanographic applications. It is recommended to use this technique in other regions to fill the gaps in our knowledge about the circulation in the ice-covered seas (e.g. Arctic and Antarctic).

The analysis described in this thesis suffers from a number of different uncertainties. Firstly, the SSH data used here is prone to many different errors (Chapter 2), which certainly contribute to its variability (Chapter 3) and obtained in Chapter 4 surface currents. During the analysis in Chapter 3 the total mapping error was estimated with the use of EOF. However, this is only the 'first' guess about the error in the SSH as it is known that the error budget of this type of data is hard to estimate. Therefore, it is recommended to identify the error sources in the SSHA data, especially for the data originating from the ice-covered part, which has a greater total error. Furthermore, the EOF analysis identifies statistical modes of the greatest variability, which could not be dynamical modes and cannot differentiate between the noise and dynamical signal (Chapter 4). Therefore, more research should be done on the error budget for the SSHA from the ice-covered seas. For this thesis. the total noise of the SSHA was estimated as the worst scenario (the upper level) for 18Hz data and using the EOFs for the girded product. However, information on the noise structure and particular contributors could help make the data more accurate, which would result in improving the transport estimation of the currents.

Using accurate mean dynamic topography (MDT) would make possible the estimation of absolute currents in the region. Currently the most accurate MDT product is provided by AVISO (AVISO, 2010). This product was checked during this PhD but it could not be used because it has too large error in the ice-covered part of the Nordic Seas and the absolute currents do not agree with our current knowledge about the circulation in the region.

Implications

The observed variability of the EGC can affect many physical processes in the ocean. The observed strengthening of the EGC in 2003-2009 could affect dense water formation process in the Nordic Seas and deep convection process occurring in the Greenland and Iceland Seas by providing enhanced freshwater flux into the region. This could increase the stratification of the water column and suppress dense water formation and therefore affect the global thermohaline circulation. Furthermore, the EGC provides part of the source waters to NADW and therefore the observed increased transports could affect the overflow through the Denmark Strait and affect the North Atlantic MOC. On the other hand, the results showed that the Nordic Seas trap a substantial part of EGC variability acting as a 'buffer' between the Arctic and the Atlantic Oceans, therefore any changes observed in the EGC require long time to propagate to the North Atlantic and further to the global ocean. The observed EGC variability also can affect the sea-ice transports through the Fram Strait and the North Atlantic and the model results suggested that this could also change the global MOC (Mauritzen and Hakkinen, 1997).

The study provided also new questions about the circulation in the Nordic Seas:

Why is the seasonal cycle of the EGC is limited to the Nordic Seas, and why does it not contribute to the variability observed further downstream in the Denmark Strait?

How are eddies in the Nordic Seas along the ice-edge generated? Is it local direct or indirect wind forcing that produces local instabilities? How do these eddies contribute to the observed variability? This could be investigated with a high-resolution coupled ocean-ice numerical model.

REFERENCES

Aaboe, S., and O. A. Nøst (2008), A diagnostic model of the Nordic Seas and Arctic Ocean circulation: Quantifying the effects of a variable bottom density along a sloping topography, *J. Phys. Oceanogr.*, 38, 2685– 2703, doi:10.1175/2008JPO3862.1.

Aaboe S, Nost O, Hansen E (2009) "Along-slope variability of barotropic transport in the Nordic Seas: Simplified dynamics tested against observations*." Journal of Geophysical Research,* 114(c3): C03009.

Aagaard, K., and E.C. Carmack (1989), The Role of Sea Ice and Other Fresh Water in the Arctic Circulation, *Journal of Geophysical Research*, *94* (C10), 14485 – 14498.

Aagaard, K., and L.K. Coachman (1968), The East Greenland Current north of Denmark Strait. Part I., *ARCTIC*, *21*, 181-200.

Alexandersson, H., T. Schmith, K. Iden, and H. Tuomenvirta, (1998). Long-term variations of the storm climate over NW Europe. *Global Ocean Atmos. Syst.,* 6**,** 97–120.

Ambaum, M.H.P., B.J. Hoskins, and D.B. Stephenson (2001), Arctic Oscillation or North Atlantic Oscillation? *Journal of Climate*, *14*, 3495-3507.

Anderson D.L.T and Killworth P.D, (1977) Spin-up of a stratified ocean with topography. *Deep Sea Research*, Vol. 24, pp 709-732.

Bacon, S., G. Reverdin, I. Rigor, and H. Snaith, (2001) A Freshwater Jet on the East Greenland Shelf, *Journal of Geophysical Research*, 107 (C7).

Bacon, S., P.G. Myers, B. Rudels, and D.A. Sutherland (2008) Accessing the inaccessible: buoyancy-driven coastal currents on the shelves of Greenland and eastern Canada. *Arctic-Subarctic ocean fluxes: Defining the role of the Northern Seas in climate*. Eds. Dickson, Meincke, and Rhines. Springer, 703–722.

Barnett and Preisendorfer (1987) Origins and levels of monthly and seasonal forecast skill for United States surface air temperature determined by canonical correlation analysis. *Monthly Weather Review*, vol. 115, pp. 1825-1850.

Barnier, B., G. Madec, T. Penduff, J. M. Molines, A. M. Treguier, J. Le Sommer, A. Beckmann, A., Biastoch, C. Boning, J. Dengg, C. Derval, E. Durand, S. Gulev, E. Remy, C. Talandier, S.Theetten, M. Maltrud, J. McClean, and B. De Cuevas (2006), Impact of partial steps and momentum advection schemes in a global ocean circulation model at eddy-permitting resolution, *Ocean Dyn.*, 56(5-6).
Barnston, A.G. and Livezey, R.E. (1987), Classification, seasonality and persistence of low-frequency atmospheric circulation patterns, Mon. *Wea. Rev., II5,* 1083-1126.

Bengtsson, L., V. A. Semenov, and O. M. Johannessen (2004), The early ntwentieth-century warming in the Arctic: A possible mechanism, *J. Clim.*,17, 4045–4057.

REFERENCES

Bersch, M., (1995) On the circulation of the northeastern North Atlantic. *Deep-Sea Research*, 42, 1583-1607.

Berry, D. I. and Kent, E. C. (2011), Air–Sea fluxes from ICOADS: the construction of a new gridded dataset with uncertainty estimates. International Journal of Climatology, 31: 987–1001.

Bjork G., Gustafsson B.G.,Stigebrandt A. (2001) Upper layer circulation of the Nordic seas as inferred from the spatial distribution of heat and freshwater content and potential energy. *Polar Research*, 20(2), 161-168.

Bjornsson H. and Venegas S.A (1997) A manual for EOF and SVD Analysis of Climatic Data. Report 97-1, *Centre for Climate and Global Change Research (CCGCR), Mc Gill University, Montreal*

Blindheim, J., V. Borovkov, B. Hansen, S.A. Malmberg, W.R. Turrell, and S. Østerhus, (2000) Upper layer cooling and freshening in the Norwegian Sea in relation to atmospheric forcing, *Deep Sea Research I*, *47*, 655 – 680.

Bonisch G.,Blindheim J.,Bullister J.L.,Schlosser P., Wallace D.W.R (1997) Long-term trends of temperature,salinity, density and transient traces in the central Greenland Sea. *Journal of Geophysical Research*, **102**, 18553-18571.

Bryden, H. L., and S. Imawaki. (2001). *Ocean heat transport, in Ocean Circulation and Climate*, edited by G. Siedler, J. Church and J. Gould, Academic Press, 455-474.

Bretherton, C.S., C. Smith, J.M. Wallace, (1992) An intercomparison of methods for finding coupled patterns in climate data. *J. Climate*, 5, 541-560.

Broecker, W. S., Peteet, D. M., and Rind, D., (1985) Does the ocean-atmosphere system have more than one stable mode of operation?, *Nature*, 315, 21–26.

Brown, G. S. (1977), The Average Impulse Response of a rough surface and its applications, *IEEE Trans. Antennas Propag.*, 25.

Bryden, H., H. Longworth and S. Cunningham, (2005) Slowing of the Atlantic meridional overturning circulation at 25_N. Nature, 438, 655–657.

Carmack, E. C., R. W. MacDonald, R. Perkin, F. A. McLaughlin, and R. J. Pearson (1995), Evidence for warming of Atlantic water in the southern Canadian Basin of the Arctic Ocean: Results from the Larsen-93 expedition, *Geophys. Res. Lett.*, 22, 1061–1064, doi:10.1029/95GL00808.

Cartwright, D.E., and R.J. Tayler (1971) New computations of the tide-generating potential, *Geophys.J.R.*, vol. 23, pp. 45-74.

Cartwright, D.E., and A.C. Edden, (1973) Corrected tables of tidal harmonics, *Geophys.J.R.*, vol. 33, pp. 253-264.

REFERENCES

Chelton D.B., Ries J.C., Haines B.J.,Fu L., Callahan P.S. (2001) Satellite altimetry. In *Satellite Altimetry and Earth Siences*, ed.Fu L. and Cazenave A., pp1-131. San Diego: Academic Press.

Cherry, S., (1997) Some comments on singular value decomposition analysis. *Journal of Climate*, vol. 10, pp. 1759-61.

Comiso, J. C., C. L. Parkinson, R. Gersten, and L. Stock (2008), Accelerated decline in the Arctic sea ice cover, *Geophys. Res. Lett*., 35, L01703, doi:10.1029/2007GL031972.

Cunningham, S., T. Kanzow, D. Rayner, M. Baringer, W. Johns, J. Marotzke, H. Longworth, E. Grant, J.-M. Hirschi, L. Beal, C. Meinen and H. Bryden. Temporal Variability of the Atlantic MeridionalOverturning Circulation at 26.5_N. (2005), *Science*, 317(5840), 935–938.

Cudlip, W., D. R. Mantripp, C. L. Wrench, H. D. Griffiths, D. V. Sheehan, M. Lester, R. P. Leigh, and T. R. Robinson (1994), Corrections for altimeter low-level processing at the Earth Observation Data Centre, Int. J. Remote Sens., 15, 889 – 914.

Curry, R. and C. Mauritzen (2005), Dilution of the Northern North Atlantic Ocean in Recent Decades, *Science*, *308*, 1772-1774.

Curry, R.,Dickson R., Yashayaev I., (2003) A change in the fresh water balance of the Atlantic over the past four decades. *Nature*, 426 (6968), 826-829.

De Steur, L., Hansen, E., Gerdes, R., Karcher, M., Fahrbach, E. and co-authors, (2009) Freshwater fluxes in the East Greenland Current: a decade of observations. *Geophys. Res. Lett.* **36**, L23611, doi:10.1029/2009GL041278.

Dee D.P et al., (2011), The ERA-Interim reanalysis: configuration and performance of the data assimilation system. *Quarteley Journal of the Royal Meterological Society*, 137, pp. 553-597.

Deser, C.,Walsh, J.E., Timlin, M.S., 2000. Arctic sea ice variability in the context of recent atmospheric circulation trends. *J. Climate*. 13, 617–633.

Dickson, R., J. Meincke, S.-A. Malmberg, and A.J. Lee (1988), The "Great Salinity Anomaly" in the Northern North Atlantic 1968-1982, *Progress in Oceanography*, *20*, 103-151.

Dickson, R. R., and J. Brown (1994). The production of North Atlantic Deep Water: sources, rates, and pathways, *J. Geophys. Res*., 99, 12,319–12,341.

Dickson, R., J. Lazier, J. Meincke, P. Rhines, and J. Swift,(1996) Long-term coordinated changes in the convective activity of the North Atlantic, *Progress in Oceanography*, *38*, 241-295.

REFERENCES

Dickson, R.R., T.J. Osborne, J.W. Hurrell, J. Meincke, J. Blindheim, B. Adlandsvik, T. Vinje, G. Alekseev, and W. Maslowski, (2000) The Arctic Ocean Response to the North Atlantic Oscillation, *Journal of Climate*, *13* (15), 2671-2696.

Dickson, B., I. Yashayaev, J. Meincke, B. Turrell, S. Dye, and J. Holfort, Rapid freshening of the deep North Atlantic Ocean over the past four decades (2002), *Nature*, *416*, 832 - 837.

Doornbos E., Scharoo R. (2004) Improved ERS and Envisat Precise Orbit Determination. Proc. Of the 2004 Envisat and ERS Symposium, Salzburg, Austra.

Drinkwater, M. R. (1991), Ku band airborne radar altimeter observations of marginal sea ice during the 1984 Marginal Ice Zone Experiment, *J. Geophys. Res*., 96, 4555–4572.

Emery, W., and R. Thomson (2001), *Data Analysis Methods in Physical Oceanography,*2nd ed., 638 pp., Elsevier Sci., New York.

Fahrbach, E., J. Meincke, S. Østerhus, G. Rohardt, U. Schauer, V. Tverberg, and J. Verduin, (2001), Direct measurements of heat and mass transports through Fram Strait, *Polar Research*, *20* (2), 217-224.

Fang, Z., and J. M. Wallace,(1994) Arctic sea-ice variability on a time-scale of weeks and its relation to atmospheric forcing. *J. Climate,* **7,** 1897–1914.

Faugere Y, Dorandeu J, Picot N. and Femenias P., (2006) Envisat Ocean altimetry performance assessment: Continuity and improvement of the ERS series. *Sensors*, vol. 6, pp. 100-130.

Foldvik, A., K. Aagaard, and T. Torresen, (1988) On the velocity field of the East Greenland Current. *Deep-Sea Research*, **35**, 1335-1354.

Fu L. and Cazenave A. (2001) *Satellite altimetry and Earth Sciences*. San Diego. Academic Press.

Fu, L.-L., E. Christensen, M. Lefebvre, and Y. Menard, (1994) "TOPEX/POSEIDON mission overview", *J. Geophys. Res*.

Furevik T. (2000). On anomalous sea surface temperatures in the Nordic Seas. J. Climate, 13(5), 1044--1053.

Furevik, T. and J.E.Ø. Nilsen (2005). Large-Scale Atmospheric Circulation Variability and its Impacts on the Nordic Seas Ocean Climate – a Review, in Drange et al. (eds.), *The Nordic Seas: An Integrated Perspective*, *Geophysical Monograph Series* 158, AGU

Furevik, T., Nilsen, J.E.O., (2007) Large-scale atmospheric circulation variability and itsimpacts on the Nordic seas ocean climate — a review. In: Drange, H., Dokken, T., Furevik, T., Gerdes, R., Berger,W. (Eds.), *The Nordic Seas, An Integrated Perspective*. AGU Geophys. Monogr., vol. 158, pp. 105–136.

Furevik T., Richter, K. and K. A. Orvik (2009), Effect of wintertime low-pressure systems on the Atlantic inflow to the Nordic seas, *J. Geophys. Res*., 114, C09006.

Gascard, J.-C., C. Kergomard, P.-F. Jeannin, and M. Fily (1988), Diagnostic Study of the Fram Strait Marginal Ice Zone During Summer From 1983 and 1984 Marginal Ice Zone Experiment Lagrangian Observations, *J. Geophys. Res.*, 93(C4), 3613–3641.

Gascard, J.C., A.J. Watson, M.-J. Messias, K.A. Olsson, T. Johannessen, and K. Simonsen, (2002) Long-lived vortices as a mode of deep ventilation in the Greenland Sea, *Nature*, *416*, 525 - 527.

Giles, K. A., S. Laxon, and A. L. Ridout (2008), Circumpolar thinning of Arctic sea ice following the 2007 record ice extent minimum, *Geophys.Res. Lett.*, 35, L22502.

Gill A.E. and Niiler P.P., (1973), The theory of the seasonal variability in the ocean. *Deep Sea Research*, Vol. 20, pp. 141-177.

Gill, A., *Atmosphere-Ocean Dynamics*, Academic Press, London, 1982.

Gjevik B. and Straumer T. (1989) `Model simulation of the M2 and the K1 tide in the Nordic Seas and the Arctic ocean. *Tellus,* 41A, 73--96.

Griffies, S.M., and K. Bryan (1997), Predictability of North Atlantic Multidecadal Climate Variability, *Science*, *275*, 181-184.

Grist J.P., Josey S.A. Sinha B. (2007), Impact on the ocean of extreme Greenland Sea heat loss in the HadCM3 coupled ocean-atmosphere model. *Journal of Geophysical Research*, 112, doi:10.1029/2006JC003629.

Grist, J. P., Josey, S. A., Marsh, R., Good, S., Coward, A. C., de- Cuevas, B. A., Alderson, S. G., New, A. L., and Madec, G (2010), The Roles of Surface Heat Flux and Ocean Heat Transport During Four Decades of Atlantic Ocean Temperature Variability, Ocean Dynam., 61.

Guinehut S., Le Traon P.Y, Larnicol G. (2006), What can we learn from Global Altimetry/Hydrography comparisons? *Geophysical Research Letters*, vol. 33, L10604, doi:10.1029/2005GL025551

Hansen, B., and S. Østerhus, (2000) North Atlantic - Nordic Seas exchanges, *Progress in Oceanography*, *45*, 109 - 208.

Hansen, B., S. Østerhus, H. Hatun, R. Kristiansen, and K.M.H. Larsen,(2003) The Iceland-Faroe inflow of Atlantic water to the Nordic Seas, in *ICES Annual Science Conference*, Tallinn, Estonia..

Hatun H., Sando A.B., Drange H., Hansen B., Valdimarsson H. (2005) Influence of the Atlantic Subpolar Gyre on the Thermohaline Circulation. *Science*, vol 309, 1841-1844.

REFERENCES

Helland-Hansen, B., and F. Nansen, (1909) The Norwegian Sea, its physical oceanography. Based on the Norwegian researches 1900-1904., pp. 390, Mallingske, Christiania.

Hilmer, M., Jung, T., (2000) Evidence for a recent change in the link between the North Atlantic Oscillation and Arctic sea ice export. *Geophys. Res. Lett*. 27, 989–992.

Holliday, N.P., Hughes, S.L., Bacon, S., Beszczynska-Möller, A., Hansen, B., Lavin, A., Loeng, H., Mork, K.A., Østerhus, S., Sherwin, T. and Walczowski, W. (2008) Reversal of the 1960s to 1990s freshening trend in the northeast North Atlantic and Nordic Seas. *Geophysical Research Letters*, 35, L03614.

Hopkins, T.S., (1991) "The Gin Sea: review of physical oceanography and literature from 1972." *Earth Science Reviews* , 30, 175-318.

Hotelling, H., (1936) Relations between two sets of variates; *Biometrika*, 28, 321-377.

Houghton JT, Y Ding, DJ Griggs, M Noguer, PJ van~der Linden, X Dai, K Maskell, and CA Johnson, editors (2001). *Climate Change 2001: The Scientific Basis. Contribution of Working Group I to the Third Assessment Report of the Intergovernmental Panel on Climate Change*. Cambridge University Press. 801 pp.

Hughes C.W. and de Cuevas B.A, (2001), Why Western Boundary Currents in Realistic Oceans are Inviscid: A Link between Form Stress and Bottom Pressure Torques. *Journal of Physical Oceanography*, vol. 31,pp. 2871- 2885.

Hurrell J.W. and H. van Loon, (1997), Decadal variations in climate associated with the North Atlantic oscillation. *Climatic Change,* 36**,** 301–326.

Hurrell, J.W., Kushnir, Y., Visbeck, M., Ottersen, G., 2003. An overview of the North Atlantic Oscillation. In: Hurrell, J.W., Kushnir, Y., Ottersen, G., Visbeck, M. (Eds.), The North Atlantic Oscillation, Climatic Significance and Environmental Impact. *AGU Geophysical Monograph*, vol. 134, pp. 1–35.

Hurrell, J.,(1995) Decadal Trends in the North Atlantic Oscillation Regional Temperatures and Precipitation, *Science*, *269*, 676-679.

Ingvaldsen R, H Loeng, G Ottersen and B Ådlandsvik (2003). Climate variability in the Barents Sea during the 20th century with a focus on the 1990s. ICES Marine Science Symposia, 219, 160-168.

Ingvaldsen R, L Asplin and H Loeng (2004). The seasonal cycle in the Atlantic transport to the Barents Sea during the years 1997-2001. Cont. Shelf Res., 24 (2004), 1015-1032.

Isachsen P.E., LaCasce J.H., Mauritzen C., (2003) Wind-Driven Variability of the Large-Scale Recirculating Flow in the Nordic Seas and Arctic Ocean. *Journal of Physical Oceanography*, 33, pp. 2534-2550.

JAHNKE-BORNEMANN, A. and BRÜMMER, B. (2009), The Iceland–Lofotes pressure difference: different states of the North Atlantic low-pressure zone. Tellus A, 61: 466–475.

Jakobsen, P.K., M.H. Nielsen, D. Quadfasel, and T. Schmith, (2003) Variability of the surface circulation of the Nordic Seas during the 1990s, *ICES Marine Science Symposia*, *219*, 367-370.

Jakobsen, P.K., M.H. Ribergaard, D. Quadfasel, T. Schmith, and C.W. Hughes, (2003) Near-surface circulation in the northern North Atlantic as inferred from Lagrangian drifters: Variability from the mesoscale to interannual, *Journal of Geophysical Research*, *108* (C8), 3251.

Jacobson M. Z. (2009), Review of solutions to global warming, air pollution, and energy security,Energy Environ. Sci., 2, 148–173,.

Janssen, Peter A. E. M., Saleh Abdalla, Hans Hersbach, Jean-Raymond Bidlot, (2007) Error Estimation of Buoy, Satellite, and Model Wave Height Data. *J. Atmos. Oceanic Technol.*, 24, 1665–1677.

Jeansson E., Jutterström S., Rudels B., Anderson L.G, Olsson K.A, Jones E.P , Smethie W. M., Swift J.H, (2008) "Sources to the East Greenland Current and its contribution to the Denmark Strait Overflow" ,*Progress in Oceanography,* 78, 12-28.

Johannessen, O. M., J. A. Johannessen, J. Morison, B. A. Farrelly, and E. A. S. Svendsen, (1983) Oceanographic conditions in the marginal ice zone north of Svalbard in early fall 1979 with an emphasis on mesoscale processes, *J. Geophys. Res*., 88, 2755-2769,

Johannessen J.A., Johanessen O.M., Svendsen E., Shuchman R., Manley T, Campell W.J., Johsberger E.G., Sandyen S., Gascard J.C., Olaussen T., Davidson K., Van Leer J. (1987), Mesoscale Eddies in the Fram Strait Marginal Ice Zone during the 1983 and 1984 Marginal Ice Zone Experiments. *Journal of Geophysical Research*, vol. 92, pp. 6754-6772.

Johannessen, J.A., Svendsen, E., Sandven, S., Johannessen, O.M., and Lygre, K., (1989). 3-Dimensional structure of mesoscale eddies in the Norwegian Coastal Current. *Journal of Physical Oceanography*, 19, 3-19.

Johannessen, O.M., L. Bengtsson, M.W. Miles, S.I. Kuzmina, V.A. Semenov, G.V. Alekseev, A.P. Nagurnyi, V.F. Zakharov, L. Bobylev, L.H. Pettersson, K. Hasselmann, and H.P. Cattle, (2004) Arctic Climate Change - observed and modeled temperature and sea ice variability, *Tellus*, *56A*, 328-341.

Jones, P.D., Jónsson, T. and Wheeler, D., (1997) Extension to the North Atlantic Oscillation using early instrumental pressure observations from Gibraltar and South-West Iceland. *Int. J. Climatol.* **17**, 1433-1450.

Jones, E; Anderson, L; Jutterstrom, S; Swift, J (2008). Sources and distribution of fresh water in the East Greenland Current. *Progress in Oceanography* ,78: 37.

REFERENCES

Josey, S.A. (2003) Changes in the heat and freshwater forcing of the eastern Mediterranean and their influence on deep water formation. *Journal of Geophysical Research*, 108, (C7), 3237-[23pp].

Karstensen, J., Schlosser, P., Wallace, D., Bullister, J. and Blindheim, J. (2005). Water mass transformation in the Greenland Sea during the 1990s. *J. Geophys. Res.* 110, C07022.

Kay, J. E., T. L'Ecuyer, A. Gettelman, G. Stephens, and C. O'Dell (2008), Contribution of cloud and radiation anomalies to the 2007 Arctic sea ice extent minimum, *Geophys. Res. Lett*., 35, L08503, doi:10.1029/2008GL033451.

Killworth P.D., D. B. Chelton, and R. A. de Szoeke, (1997) The speed of observed and theoretical long extratropical planetary waves. *J.Phys. Oceanogr.,* **27,** 1946–1966.

Knudsen, M. (1899), Hydrography, in *The Danish Ingolf Expedition 1 (2)*, pp. 23-161, Bianco Luno, Copenhagen.

Kohl A. (2007), Generation and Stability of a Quasi-Permanent Vortex in the Lofoten Basin. *Journal of Physical Oceanography*, vol 37, pp. 2637-2651.

Koszalka I., LaCasce J.H, Andersson M., Orvik K.A., Mauritzen C. (2011), *Deep Sea Research I*, 58, 468-485.

Kuragano T. and Kamachi M. (2000) Global statistical space-time scales of oceanic variability estimated from the TOPEX/POSEIDON altimeter data. *Journal of Geophysical Research,* vol. 105, 955-974.

Kutzbach, J.E., (1970) Large-scale features of monthly mean Northern Hemisphere anomaly maps of sea-level pressure. *Mon. Weather Rev*. 98, 708–716.

Kwok, R. (2007), Near zero replenishment of the Arctic multiyear sea ice cover at the end of 2005 summer, *Geophys. Res. Lett.*, 34, L05501.

Kwok, R. (2008), Summer sea ice motion from the 18 GHz channel of AMSR-E and the exchange of sea ice between the Pacific and Atlantic sectors, *Geophys. Res. Lett*., 35, L03504.

Kwok, R., and D. A. Rothrock, (1999), Variability of Fram Strait ice flux and the North Atlantic oscillation. *J. Geophys. Res. Oceans,***104,** 5177–5189.

Lapeyre G. (2009) "What vertical mode does the altimeter reflect? On the decomposition in baroclinic modes and on a surface-trapped mode". *Journal of Physical Oceanography*.

Latarius K. and Quadfasel D., (2010) Seasonal to inter-annual variability of temperature and salinity in the Greenland Sea Gyre: heat and freshwater budgets. *Tellus*, 62A, 497-515.

REFERENCES

Laxon, S. (1994), Sea ice altimeter processing scheme at the EODC, *Int. J. Remote Sens.,* **15**, 915–924.

Legutke, S. (1991), A numerical investigation of the circulation in the Greenland and Norwegian Seas. *J. Phys. Oceanogr*., 21*,* 118–148.

Lettmann K. and Olbers D. (2005) Investigation of ACC transport and variability through the Drake Passage using the simple ocean model BARBI. CLIVAR Exchanges. vol 10, 30-32.

Linz, P., and R. L. C. Wang, (2003) , Exploring Numerical Methods: An Introduction to Scientific Computing Using MATLAB. *Jones and Bartlett*

Madec, G., Delecluse, P., Imbard, M., Lévy, C., (1999). OPA 8.1 Ocean General Circulation Model reference manual. Notes du Pôle de modélisation, Institut Pierre-Simon Laplace (IPSL), France, X, 91 pp

Marsh, R., Desbruyères, D., Bamber, J.L., de Cuevas, B.A., Coward, A.C. and Aksenov, Y. (2010) Short-term impacts of enhanced Greenland freshwater fluxes in an eddy-permitting ocean model. Ocean Science, 6, (3), 749-760.

Marshall, J. F., and F. Schott, (1999) Open-ocean convection: Observations, theory, and models, *Rev. Geophys*., 37, 1 – 64.

Martin, T. and P. Wadhams, (1999) Sea-ice flux in the East Greenland Current. *Deep-Sea Research* Part II, **46**, 1063-1082.

Martin M. L., Valero F., Morata A., Luna, M.Y.,A. Pascual A. and Santos-Munoz D. (2010) Springtime coupled modes of regional wind in the Iberian Penisula and large scale variability patterns. *International Journal of Climatology,* 31,pp. 880–895.

Martin S. (2002) *An Introduction to Ocean Remote Sensing*, , pp. 454. Cambridge, UK: Cambridge University Press.

Mauritzen, C. (1996), Production of dense overflow waters feeding the North Atlantic across the Greenland-Scotland Ridge. Part I: Evidence for a revised circulation scheme., *Deep Sea Research*, *43* (6), 769-806.

Mauritzen, C. (1996), Production of dense overflow waters feeding the North Atlantic across the Greenland-Scotland Ridge. Part 2: An inverse model., *Deep Sea Research*, *43* (6), 807-835.

*MDT*_CNES-CLS09 was produced by *CLS* Space Oceanography Division and distributed by *Aviso*, with support from *Cnes* (http://www.aviso.oceanobs.com/)

Morison J. (1991), Variations in the West Spitsbergen Current Estimated From Bottom Pressure Measurements. *Journal of Geophysical Research*, vol. 96, no. C10, pp.18.381-18.395.

REFERENCES

Mork K.A., Skagseth O. (2005), Annual Sea Surface Height Variability in the Nordic Seas*,The Nordic Seas: An Integrated Perspective*, AGU, pp. 51-64.

Muench, R.D., M.G. Mc Phee, C.A. Paulson, and J.H. Morrison, (1992) Winter oceanographic conditions in the Fram Strait Yermak Plateau region. *Journal of Geophysical Research*, **97**, 3469-3483.

Newman, M. and P. D. Sardeshmukh, (1995), A Caveat Concerning Singular Value Decomposition. *J. Climate*, 8, 352-360.

North, G.R., Bell, T.L., Cahalan, R.F., Moeng, F.J., (1982) Sampling errors in the estimation of empirical orthogonal functions. *Mon. Weather Rev*. 110, 699–706.

Nøst, O.A., and P.E. Isachsen (2003), The large-scale time-mean ocean circulation in the Nordic Seas and the Arctic Ocean estimated from simplified dynamics., *Journal of Marine Research*, *61*, 175-210.

Ogi M, Rigor I. G., Mc Phee M.G, Wallace J.M. (2008) Summer retreat of the Arctic sea ice: Role of summer winds. *Geophysical Research Letters*, vol. 35, L24701

Lettemann K. and Olbers D. (2005) "Investigation of ACC transport and variability through Drake Passage using the simple ocean model BARBI." *CLIVAR Exchanges*, **10**,pp. 30-32

Orvik, K.A., and P. Niiler (2002), Major pathways of Atlantic water in the northern North Atlantic and Nordic Seas toward Arctic, *Journal of Geophysical Research Letters*, *29* (19), 1-4.

Orvik, K. and Skagseth,Ø. (2003). The impact of the wind stress curl in theNorth Atlantic on the Atlantic inflow to the Norwegian Sea toward the Arctic. *Geophys. Res. Lett.* **30**, 1884.

Orvik, K.A., O. Skagseth, and M. Mork (2001), Atlantic inflow to the Nordic Seas: current structure and volume fluxes from moored current meters, VM-ADCP and SeaSoar CTD observations, 1995 - 1999, *Deep Sea Research I*, *48*, 937 -957.

Overland J.E, Preisendorfer R. (1982), A significance test for principal components applied to a cyclone climatology. *Mon. Weather Rev*., 110, 1-4.

Overland, J., J. Turner, J. Francis, N. Gillett, G. Marshall, and M. Tjernstrom, (2008), The Arctic and Antarctic: Two faces of climate change. *EOS, 89* (19), 177–178.

Overland, J. and M. Wang, (2010), Large-scale atmospheric circulation changes are associated with the recent loss of Arctic sea ice. *Tellus A*, 62 (1), 1–9.

Padman, L., and S. Erofeeva (2004), A barotropic inverse tidal model for the Arctic Ocean, *Geophys. Res. Lett.*, 31, L02303.

Peacock N.R., Laxon S.W. (2004) Sea Surface Determination in the Arctic Ocean from ERS Altimetry. *J. Geophys. Res*. vol **109**, C07001.

Polyakov, I. V., Alexeev, V. A., Ashik, I. M., Bacon, S., Beszczynska-Möller, A., Carmack, E. C., Dmitrenko, I. A., Fortier, L., Gascard, J. -C., Hansen, E., Hölemann, J., Ivanov, V. V., Kikuchi, T., Kirillov, S., Lenn, Y. -D., McLaughlin, F. A., Piechura, J., Repina, I., Timokhov, L. A., Walczowski, W. (2011) NOWCAST: fate of early-2000s Arctic warm water pulse. BULLETIN OF THE METEOROLOGICAL SOCIETY.

Pond, S., and G.L. Pickard, (1983) *Introductory Dynamical Oceanography*, Butterworth-Heinemann, Oxford.

Ponte, R.M., D.A. Salstein and R.D. Rosen, (1991) Sea level response to pressure forcing in a barotropic numerical model. *J. Phys. Oceanog*., 21, 1043-1057.

Ponte R.M. (2006) Low Frequency Sea Level Variability and the Inverted Barometer Effect. Journal of Atmospheric and Oceanic Technology, 23, 619-629.

Poulain, P. M., A. Warn-Varnas, and P. P. Niiler, (1996) Near-surface circulation of the Nordic Seas as measured by Lagrangian drifters. *J. Geophys. Res*., 101 (C8), 18 237–18 258.

Proshutinsky, A.Y., and M.A. Johnson, (1997) Two circulation regimes of the wind-driven Arctic Ocean, *Journal of Geophysical Research*, *102* (C6), 12493-12514.

Rahmstorf, S., and A. Ganopolski, (1999) Long-term global warming scenarios computed with an efficient coupled climate model. *Climatic Change,* 43**,** 353–367.

Randall, D.A., R.A. Wood, S. Bony, R. Colman, T. Fichefet, J. Fyfe, V. Kattsov, A. Pitman, J. Shukla, J. Srinivasan, R.J. Stouffer, A. Sumi and K.E. Taylor, (2007), Cilmate Models and Their Evaluation. In: Climate Change (2007) The Physical Science Basis. Contribution of Working Group I to the Fourth Assessment Report of the Intergovernmental Panel on Climate Change [Solomon, S., D. Qin, M. Manning, Z. Chen, M. Marquis, K.B. Averyt, M.Tignor and H.L. Miller (eds.)]. Cambridge University Press, Cambridge, United Kingdom and New York, NY, USA.

Rossby, T., Ozhigin, V., Ivshin, V., Bacon, S., (2009). An isopycnal view of the Nordic Seas hydrography with focus on properties of the Lofoten Basin. Deep-Sea Res. I 56 (11), 1955–1971.

Rudels, B. (1995), The thermohaline circulation of the Arctic Ocean and the Greenland Sea, *Phil. Trans. R. Soc. London A*, *352*, 287-299, 1995.

Rudels B., Jones E.P., Anderson L.G., Kattner G. (1994), On the intermediate depth waters of the Arctic Ocean In: Muench R., Johannessen O.M. *The role of the Polar Oceans in shaping the global climate*. American Geophysical Union, New York, pp 33-46.

Rudels, B., E. Fahrbach, J. Meincke, G. Budeus, and P. Eriksson, (2002) The East Greenland Current and its contribution to the Denmark Strait overflow, *ICES Journal of Marine Science*, *59*, 1133-1154.

Rudels B., Bjork G.,Nilsson J., Winsor P., Lake I., Nohr C. (2005) The interaction between waters from the arctic Ocean and the Nordic Seas north of Fram Strait and

along the East Greenland current: results from the Arctic Ocean-02 Oden expedition. *Journal of Marine systems*, 55,1-30.

Saenko, O.A., A. Schmittner and A.J. Weaver (2002), On the role of wind-driven sea ice motion on ocean ventilation, *J. Phys. Oceanogr.* 32 3376-3395.

Scharroo, R., and P. Visser (1998), Precise orbit determination and gravity field improvement for the ERS satellites, J. Geophys. Res., 103, 8113–8127.

Scharoo R (2002) A Decade of ERS Satellite Orbits and Altimetry. PhD thesis. Delf University Press.

Schauer U., Fahrbach E., Osterhus S., Rohardt G. (2004) Arctic warming through the Fram Strait: Oceanic heat transport from 3 years of measurements., *Journal of Geophysical Research*, 109, C06026.

Schlichtholz P, (2007) Density-dependent variations of the along-isobath flow in the East Greenland Current from the Fram Strait to the Denmark Strait, *J. Geophys. Res.* 112, p. C12022.

Schlichtholz, P., and M.-N. Houssais, (1999) An inverse modeling study in Fram Strait. Part II: water mass distribution and transports, *Deep Sea Research II*, *46*, 1137-1168.

Schlichtholz, P. and M.N. Houssais, (1999) An investigation of the dynamics of the East Greenland Current in Fram Strait based on a simple analytical model. *Journal of Physical Oceanography*, 29, 2240-2265.

Schlichtholz, P. (2005), Climatological baroclinic forcing of the barotropic flow in the East Greenland Current in Fram Strait, J. Geophys. Res., 110, C08013.

Schmith, T., and C. Hansen (2003), Fram Strait ice export during the Nineteenth and twentieth centuries reconstructed from a multiyear sea ice index from southwestern Greenland, *J. Clim*., 16, 2782 – 2791.

Schmittner, A., M. Latif and B. Schneider, (2005) Model projections of the North Atlantic thermohaline circulation for the 21st century assessed by observations. Geophysical Research Letters, 32, L23710.

Sciermammano F. (1979) A suggestion for the presentation of correlations and their significance levels. *Journal of Physical Oceanography*, 9, 1273-1276.

Seager, R., D. Battisti, J. Yin, N. Gordon, N. Naik, A. Clement and M. Cane. (2002) Is the Gulf Stream responsible for Europe's mild winters? Quarterly Journal of the Royal Meteorological Society, 128, 2563–2586.

Serreze M.C., Carse, R. G. Barry, and J. C. Rogers, (1997) Icelandic low activity: Climatological features, linkages with the NAO, and relationships with recent changes in the Northern Hemisphere circulation. *J. Climate,* 10**,** 453–464.

Serreze, M.C., J.E. Walsh, F.S. Chaplin, T. Osterkamp, M. Dyurgerov, V. Romanovsky, W.C. Oechel, J. Morison, T. Zhang, and R.G. Barry (2000), Observational evidence of recent changes in the northern high-latitude environment., *Climatic Change*, *46*, 159-207.

Simmonds, I. and K. Keay (2009), Extraordinary September Arctic sea ice reductions and their relationships with storm behavior over 1979-2008. *Geophysical Research Letters*, 36, L19 715,

Simmons A.J., Uppala S., Dee D., Kobayashi S. (2007). ERA–Interim: New ECMWF reanalysis products from 1989 onwards. Newsletter 110. ECMWF: Reading, UK.

Simonsen, K., and P.M. Haugan, (1996) Heat budgets of the Arctic Mediterranean and sea surface heat flux parameterizations for the Nordic Seas, *Journal of Geophysical Research*, *101* (C3), 6553-6576.

Skagseth, Ø., and K. A. Orvik (2002), Identifying fluctuations in the Norwegian Atlantic Slope Current by means of empirical orthogonal functions, *Cont. Shelf Res*., 22, 547– 563.

Skagseth Ø, KA Orvik, and T Furevik (2004). Coherent variability of the Norwegian Atlantic slope current determined by using TOPEX/ERS altimeter data, *Geophys. Res. Lett.*, 31, L14304.

Smith, W.H.F. and Sandwell, D.T., (1997). Global sea floor topography from satellite altimetry and ship depth soundings. *Science* 277, pp. 1956–1962

Smith, K. S. and G. K. Vallis, (2001), The scales and equilibration of midocean eddies: Freely evolving flow. *J. Phys. Oceanogr.,* 31, 554—571.

Solomon, S., D. Qin, M. Manning, Z. Chen, M. Marquis, K.B. Averyt, M. Tignor and H.L. Miller (2007). Contribution of Working Group I to the Fourth Assessment Report of the Intergovernmental Panel on Climate Change, *Cambridge University Press*, Cambridge United Kingdom and New York, NY, USA.

Spielhagen R.F., Werner K., Sørensen S.A., Zamelczyk K., Kandiano E., Budeus G.,Husum K., Marchitto T.M., Hald M. (2011) Enhanced Modern Heat Transfer to the Arctic by Warm Atlantic Water. *Science* ,vol. 331 no. 6016 pp. 450-453.

Strass, V., E. Fahrbach, U. Schauer, and L. Sellmann, Formation of Denmark Strait Overflow Water by Mixing in the East Greenland Current (1993), *Journal of Geophysical Research*, *98* (C4), 6907-6919.

Sverdrup, H.U., M.S. Johnson, and R.H. Flemming (1942) *The Oceans.*, 1087 pp., Prentice-Hall, New York.

Thompson, D. W., and J. M. Wallace, (1998) The Arctic Oscillation signature in the wintertime geopotential height and temperature fields. *Geophys. Res. Lett*., 25, 1297–1300.

REFERENCES

Thompson, D., and J. Wallace, (1998), The Arctic Oscillation signature in the wintertime geopotential height and temperature fields, *Geophysical Research Letters*, *25* (9), 1297-1300.

Thomson D.W.J, Wallace J.M., Hegerl G. C., (2000) Annular modes in the extratropical circulation. Part II: Trends. *J. Climate,* in press.

Thompson, A.F., (2008). The atmospheric ocean: eddies and jets in the Antarctic Circumpolar Current. *Philosophical Transactions of the Royal Society A*, 366, 4529-4541.

Thompson, A.F., P.H. Haynes, C. Wilson & K.J. Richards, (2010). Rapid Southern Ocean front transitions in an eddy-resolving ocean GCM. *Geophysical Research Letters*, 37, L2360237.

Tomczak, M., and J. S. Godfrey (2003), Regional Oceanography: An Introduction, 2nd ed., 390 pp., Daya, New Delhi.

Trenberth, Kevin E., Julie M. Caron, (2001) Estimates of Meridional Atmosphere and Ocean Heat Transports. *J. Climate*, 14, 3433–3443.

Trenberth KE, Fasullo JT, Kiehl J. (2009). Earth's global energy budget. *Bull. Amer. Meteorol. Soc.* 90, 311–324.

Venegas S.A., Mysak L.A., Straub D.N. (1996) Evidence for interannual and interdecadal climate variability in the South Atlantic. *Geophysical Research Letters*, 23: 2673-2676.

Vinje, T., N. Nordlund, and A. Kvambekk, (1998) Monitoring ice thickness in Fram Strait, *Journal of Geophysical Research*, *103*(C5), 10437-10449.

Vinogradov S.V, Ponte R.M., Heimbach P.,Wunsch C., (2008) "The mean seasonal cycle in sea level estimated from a data-constrained general circulation model" *Journal of Geophysical Research*, **113**, C03032.

Voet G., Quadfasel D., Mork K.A., Soiland H., (2010) The mid-depth circulation of the Nordic Seas derived from profiling float observations. Tellus A, Volume 62, Issue 4, pp. 516-529.

Von Storch, H., and F.W. Zwiers, (1999) *Statistical Analysis in Climate Research*. Cambridge University Press, 484 pp.

Wahr J. M. (1985), Deformation induced by polar motion, *J. Geophys. Res*., 90(B11), pp. 9363 – 9368.

Wallace J.M, Smith C., Bretherton C.S. (1992) Singular value decomposition of wintertime sea surface temperature and 500-mb height anomalies. *Journal of Climate*, 5, 561-576.

REFERENCES

Wang M. and Overland J.E. A sea ice free summer Arctic within 30 years? Geophysical Research Letters, vol. 36, L07502.

Welch P.D. (1967) The Use of Fast Fourier Transform for the Estimation of Power Spectra: A Method Based on Time Averaging Over Short, Modified Periodograms", *IEEE Transactions on Audio Electroacoustics*, vol. AU-15, pp. 70–73.

Widell, K., S. Østerhus, and T. Gammelsrød (2003), Sea ice velocity in the Fram Strait monitored by moored instruments, *Geophys. Res. Lett.*, 30(19),

Woodgate, R.A., E. Fahrbach, and G. Rohardt (1999) Structure and transports of the East Greenland Current at 75N from moored current meters, *Journal of Geophysical Research*, *104* (C8), 18059-18072.

Wunsch C, Stammer D. (1997). Atmospheric loading and the "inverted barometer" effect. *Rev. Geophys.* **35**, 79–107.

Wunsch, C., and Stammer, D. (1998). "Satellite altimetry, the marine geoid, and the oceanic general circulation." *Annu. Rev. Earth Planet. Sci*., **26**, 219-253

Wunsch, C. (1967), The long-period tides, *Rev. Geophys*., 5(4), 447–475.

Wunsch, C., and B. Grant (1982), Towards the general circulation of the North Atlantic Ocean., *Progress in Oceanography*, *11*, 1-59,.

Wunsch, C. (1994), Dynamically consistent hydrography and absolute velocity in the eastern North Atlantic Ocean, J. Geophys. Res., **99**, 14,071-14,090.

Young, W. R., (1981) The vertical structure of the wind-driven circulation. *Woods Hole Oceanographic Institution Tech. Rep.* 81–89, 215 pp.

Yu, L., Weller, R. A. and Sun, B. (2004) Mean and variability of the WHOI daily latent and sensible heat fluxes at in situ flux measurement sites in the Atlantic Ocean. *J. Clim.* **17**, 2096–2118.

Zhang, X., and J. E. Walsh (2006), Towards a seasonally ice-covered Arctic Ocean: Scenarios from the IPCC AR4 simulations, J. Clim, 19, 1730 – 1747.

Zhang, X., Sorteberg, A., Zhang, J., Gerdes, R. and Comiso, J. (2008) Recent radical shifts of atmospheric circulations and rapid changes in Arctic climate system. *Geophys. Res. Lett.* **35**, L22701.

Zhang X., R. Lindsay, M. Steele, and A. Schweiger, (2008) What drove the dramatic retreat of Arctic sea ice during summer 2007? *Geophys. Res. Lett.,* **35,** L11505.

APPENDIX

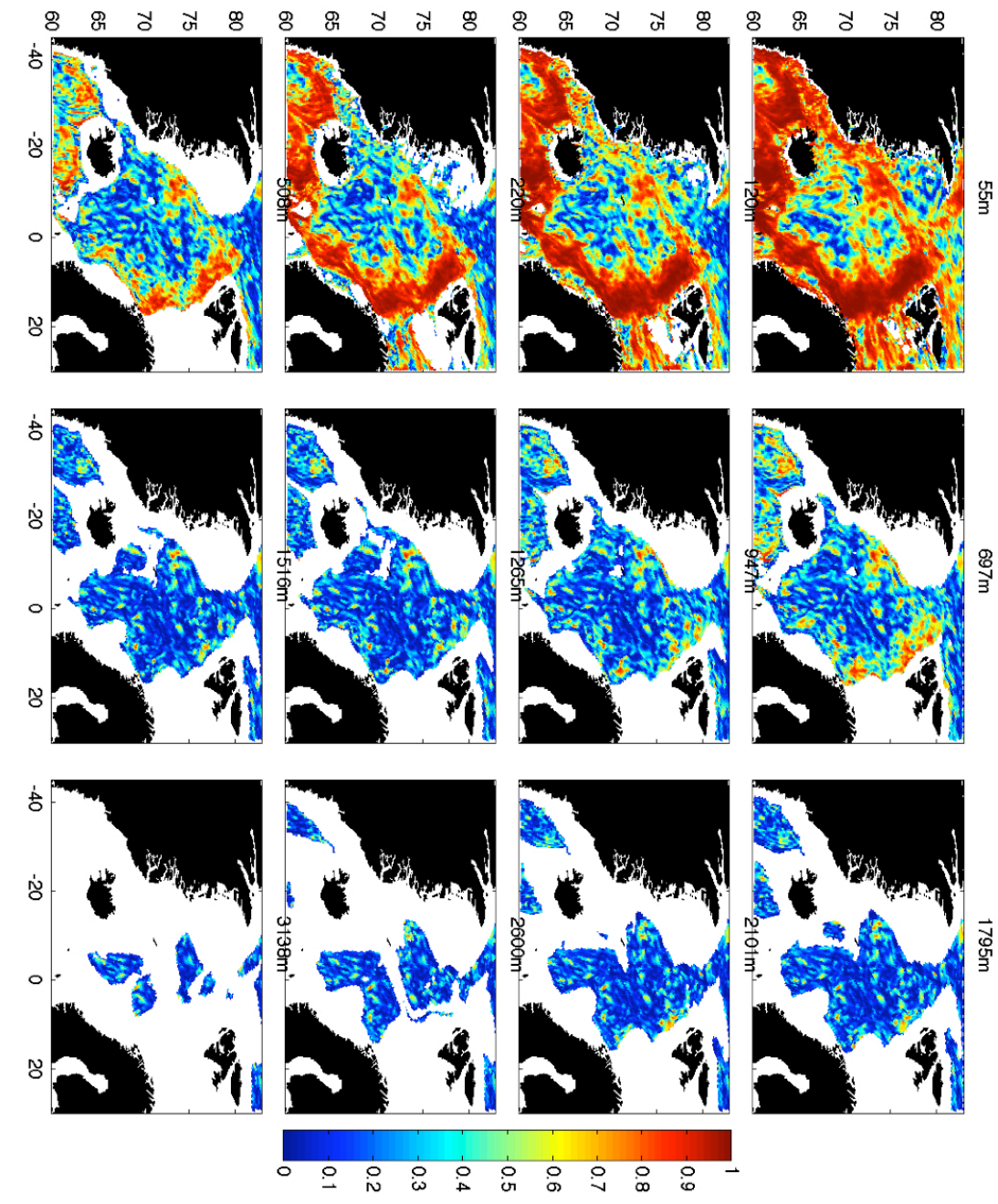

Squared coherence for the surface velocity and velocity at other depths for the whole Nordic Seas at the period of 3.6 months.

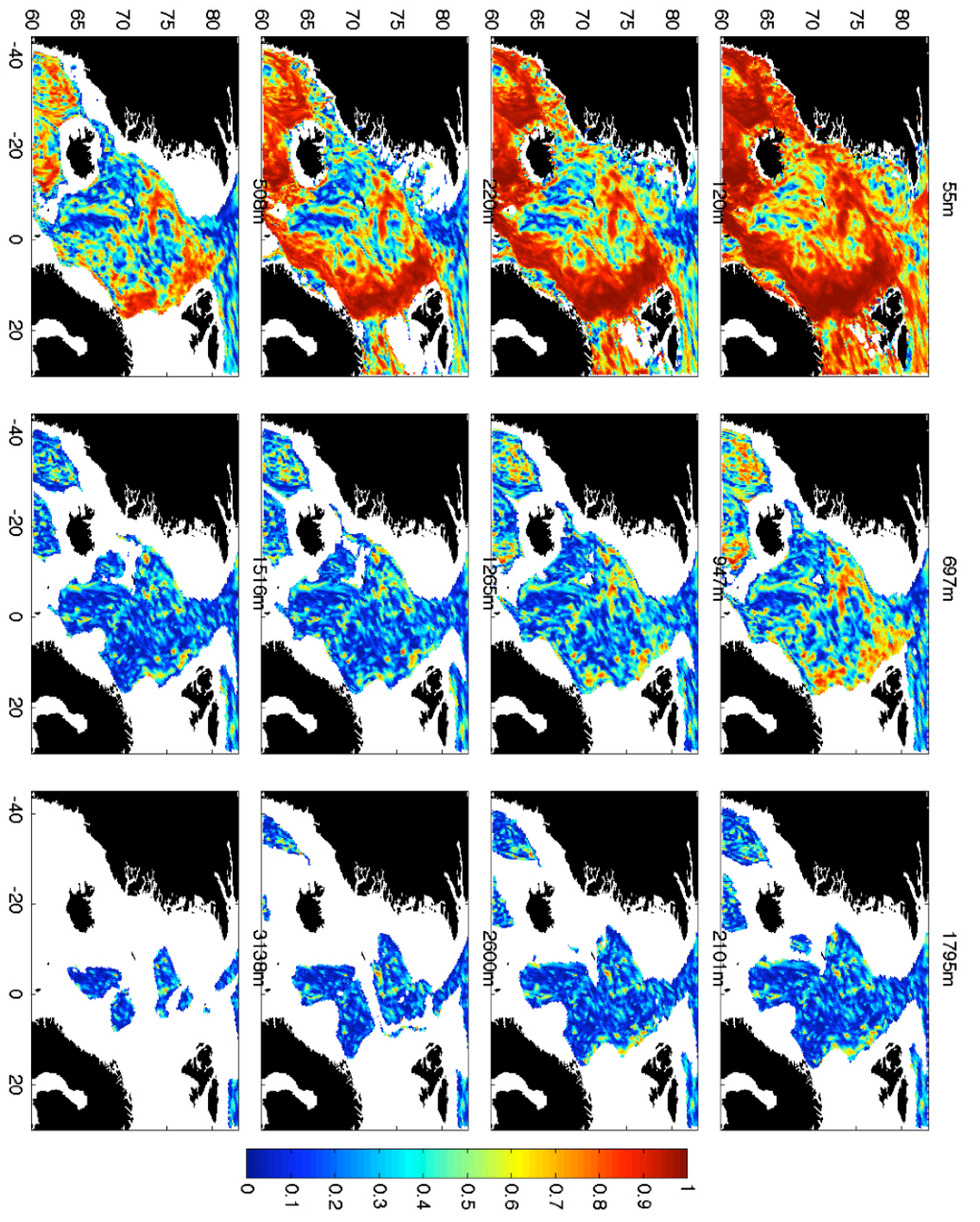

Squared coherence for the surface velocity and velocity at other depths for the whole Nordic Seas at the period of 5 months.

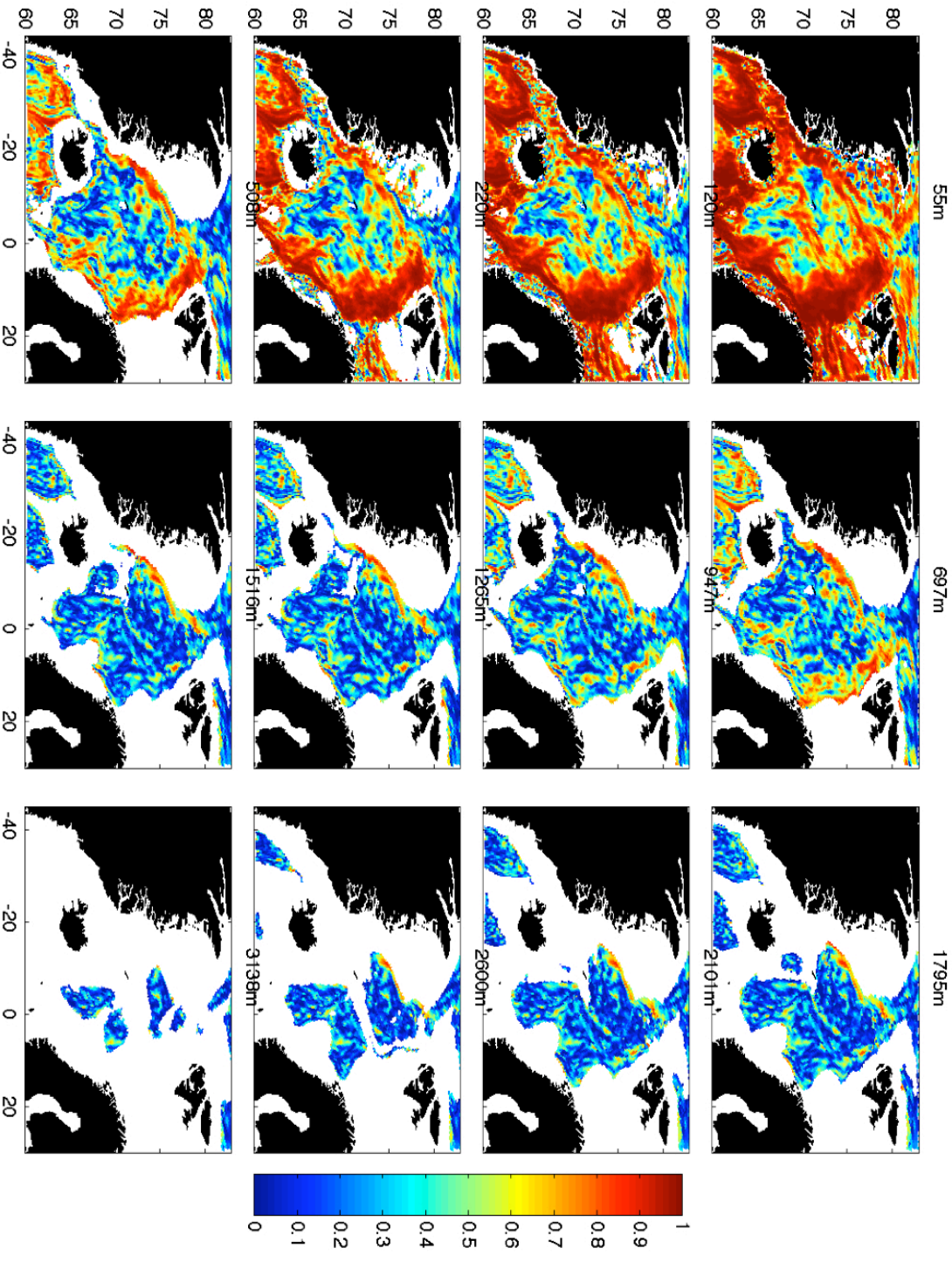

.Squared coherence for the surface velocity and velocity at other depths for the whole Nordic Seas at the period of 6 months.

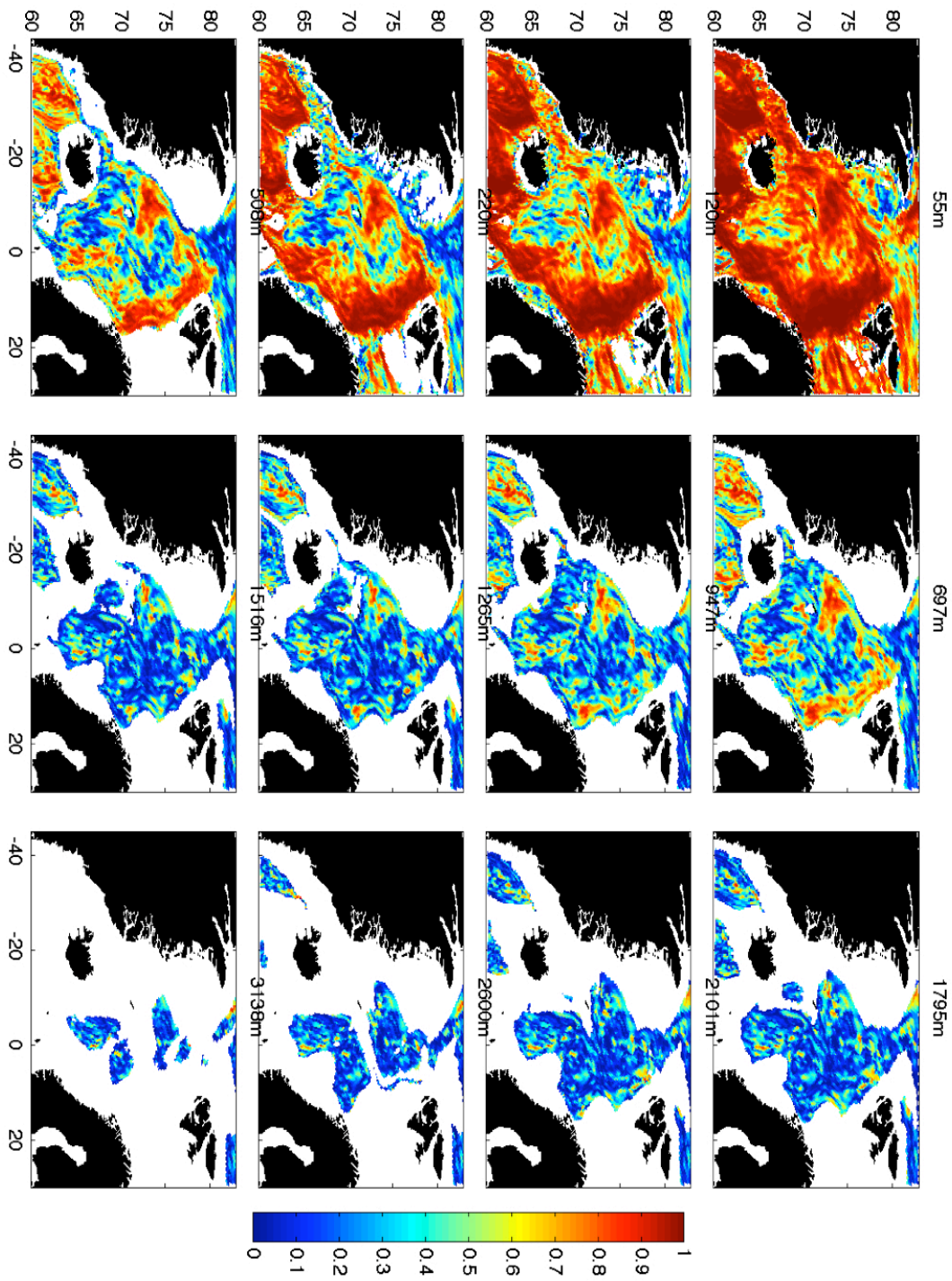

Squared coherence for the surface velocity and velocity at other depths for the whole Nordic Seas at the annual period of 9 months.

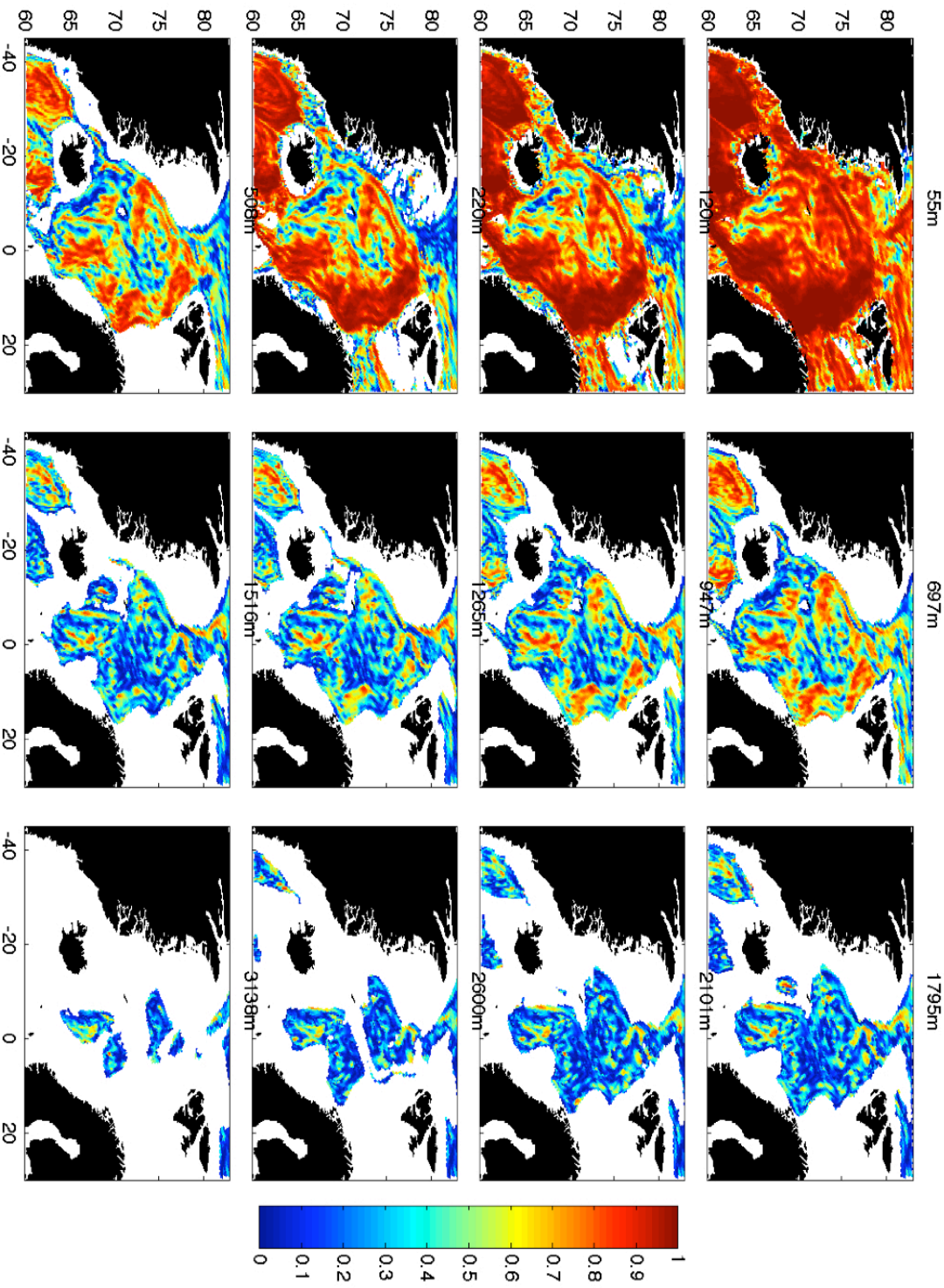

Squared coherence for the surface velocity and velocity at other depths for the whole Nordic Seas at the annual period of 1.8 years.

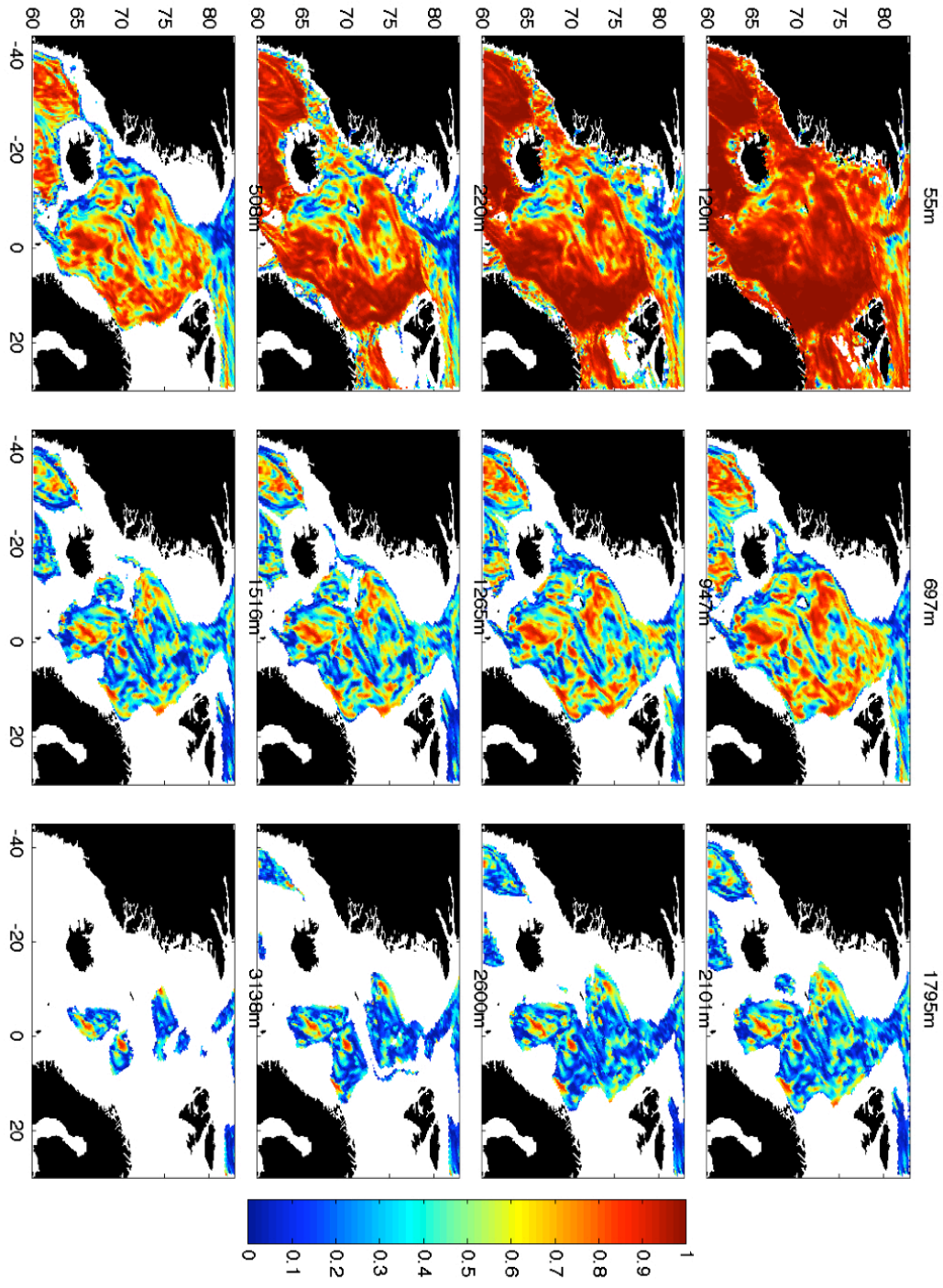

Squared coherence for the surface velocity and velocity at other depths for the whole Nordic Seas at the annual period of 3.5 years.

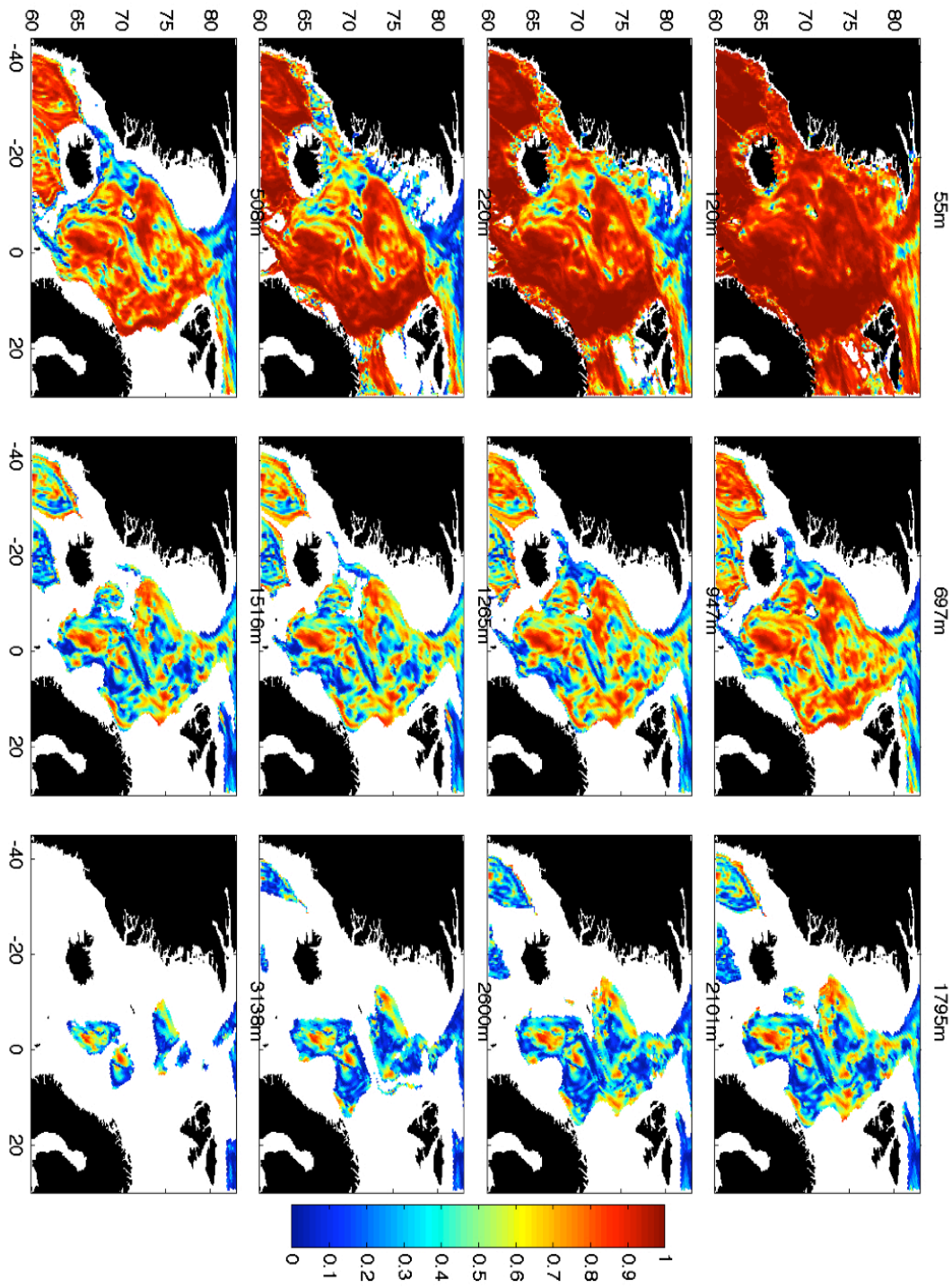

Squared coherence for the surface velocity and velocity at other depths for the whole Nordic Seas at the annual period of 5.3 years.